

Vascular and valvular tissue engineering: Treating and modeling vasculopathies and valvulopathies

Edited by

Laura Iop, Adrian Chester and Anthal Smits

Published in

Frontiers in Cardiovascular Medicine



FRONTIERS EBOOK COPYRIGHT STATEMENT

The copyright in the text of individual articles in this ebook is the property of their respective authors or their respective institutions or funders. The copyright in graphics and images within each article may be subject to copyright of other parties. In both cases this is subject to a license granted to Frontiers.

The compilation of articles constituting this ebook is the property of Frontiers.

Each article within this ebook, and the ebook itself, are published under the most recent version of the Creative Commons CC-BY licence. The version current at the date of publication of this ebook is CC-BY 4.0. If the CC-BY licence is updated, the licence granted by Frontiers is automatically updated to the new version.

When exercising any right under the CC-BY licence, Frontiers must be attributed as the original publisher of the article or ebook, as applicable.

Authors have the responsibility of ensuring that any graphics or other materials which are the property of others may be included in the CC-BY licence, but this should be checked before relying on the CC-BY licence to reproduce those materials. Any copyright notices relating to those materials must be complied with.

Copyright and source acknowledgement notices may not be removed and must be displayed in any copy, derivative work or partial copy which includes the elements in question.

All copyright, and all rights therein, are protected by national and international copyright laws. The above represents a summary only. For further information please read Frontiers' Conditions for Website Use and Copyright Statement, and the applicable CC-BY licence.

ISSN 1664-8714
ISBN 978-2-83250-822-0
DOI 10.3389/978-2-83250-822-0

About Frontiers

Frontiers is more than just an open access publisher of scholarly articles: it is a pioneering approach to the world of academia, radically improving the way scholarly research is managed. The grand vision of Frontiers is a world where all people have an equal opportunity to seek, share and generate knowledge. Frontiers provides immediate and permanent online open access to all its publications, but this alone is not enough to realize our grand goals.

Frontiers journal series

The Frontiers journal series is a multi-tier and interdisciplinary set of open-access, online journals, promising a paradigm shift from the current review, selection and dissemination processes in academic publishing. All Frontiers journals are driven by researchers for researchers; therefore, they constitute a service to the scholarly community. At the same time, the *Frontiers journal series* operates on a revolutionary invention, the tiered publishing system, initially addressing specific communities of scholars, and gradually climbing up to broader public understanding, thus serving the interests of the lay society, too.

Dedication to quality

Each Frontiers article is a landmark of the highest quality, thanks to genuinely collaborative interactions between authors and review editors, who include some of the world's best academicians. Research must be certified by peers before entering a stream of knowledge that may eventually reach the public - and shape society; therefore, Frontiers only applies the most rigorous and unbiased reviews. Frontiers revolutionizes research publishing by freely delivering the most outstanding research, evaluated with no bias from both the academic and social point of view. By applying the most advanced information technologies, Frontiers is catapulting scholarly publishing into a new generation.

What are Frontiers Research Topics?

Frontiers Research Topics are very popular trademarks of the *Frontiers journals series*: they are collections of at least ten articles, all centered on a particular subject. With their unique mix of varied contributions from Original Research to Review Articles, Frontiers Research Topics unify the most influential researchers, the latest key findings and historical advances in a hot research area.

Find out more on how to host your own Frontiers Research Topic or contribute to one as an author by contacting the Frontiers editorial office: frontiersin.org/about/contact

Vascular and valvular tissue engineering: Treating and modeling vasculopathies and valvulopathies

Topic editors

Laura Iop — University of Padua, Italy

Adrian Chester — The Magdi Yacoub Institute, United Kingdom

Anthal Smits — Eindhoven University of Technology, Netherlands

Citation

Iop, L., Chester, A., Smits, A., eds. (2022). *Vascular and valvular tissue engineering: Treating and modeling vasculopathies and valvulopathies*. Lausanne: Frontiers Media SA. doi: 10.3389/978-2-83250-822-0

Table of contents

- 05 **Editorial: Vascular and valvular tissue engineering: Treating and modeling vasculopathies and valvulopathies**
Anthal I. P. M. Smits, Laura Iop and Adrian H. Chester
- 08 **Sevelamer Attenuates Bioprosthetic Heart Valve Calcification**
Zhen Meng, Zhe Li, Erli Zhang, Li Zhang, Qingrong Liu and Yongjian Wu
- 19 **Biocompatibility and Application of Carbon Fibers in Heart Valve Tissue Engineering**
Yuan-Tsan Tseng, Nabil F. Grace, Heba Aguib, Padmini Sarathchandra, Ann McCormack, Ahmed Ebeid, Nairouz Shehata, Mohamed Nagy, Hussam El-Nashar, Magdi H. Yacoub, Adrian Chester and Najma Latif
- 31 **Recent Progress in *in vitro* Models for Atherosclerosis Studies**
Jun Chen, Xixi Zhang, Reid Millican, Tyler Lynd, Manas Gangasani, Shubh Malhotra, Jennifer Sherwood, Patrick Taejoon Hwang, Younghye Cho, Brigitta C. Brott, Gangjian Qin, Hanjoong Jo, Young-sup Yoon and Ho-Wook Jun
- 54 **Development of the Human Arterial Valves: Understanding Bicuspid Aortic Valve**
Deborah J. Henderson, Lorraine Eley, Jasmin E. Turner and Bill Chaudhry
- 65 **Understanding Pulmonary Autograft Remodeling After the Ross Procedure: Stick to the Facts**
Lucas Van Hoof, Peter Verbrugghe, Elizabeth A. V. Jones, Jay D. Humphrey, Stefan Janssens, Nele Famaey and Filip Rega
- 85 **A Biohybrid Material With Extracellular Matrix Core and Polymeric Coating as a Cell Honing Cardiovascular Tissue Substitute**
Jahnavi Mudigonda, Dongyang Xu, Alan Amedi, Brooks A. Lane, Daniella Corporan, Vivian Wang and Muralidhar Padala
- 100 **Engineering Efforts to Refine Compatibility and Duration of Aortic Valve Replacements: An Overview of Previous Expectations and New Promises**
Stefano Rizzi, Sara Ragazzini and Maurizio Pesce
- 110 **Marker-Independent Monitoring of *in vitro* and *in vivo* Degradation of Supramolecular Polymers Applied in Cardiovascular *in situ* Tissue Engineering**
Julia Marzi, Emma C. Munnig Schmidt, Eva M. Brauchle, Tamar B. Wissing, Hannah Bauer, Aurelie Serrero, Serge H. M. Söntjens, Anton W. Bosman, Martijn A. J. Cox, Anthal I. P. M. Smits and Katja Schenke-Layland
- 124 **Stem Cell Based Approaches to Modulate the Matrix Milieu in Vascular Disorders**
Sajeesh S, Shataakshi Dahal, Suraj Bastola, Simran Dayal, Jimmy Yau and Anand Ramamurthi

- 144 **3D Printed Bioreactor Enabling the Pulsatile Culture of Native and Angioplastied Large Arteries**
Rolando S. Matos, Davide Maselli, John H. McVey, Christian Heiss and Paola Campagnolo
- 161 **Serial assessment of early antibody binding to decellularized valved allografts**
Firdavs Oripov, Robert Ramm, Christine Falk, Tobias Goecke, Johannes Ebken, Ramadan Jashari, Dietmar Böthig, Alexander Horke, Murat Avsar, Dmitry Bobylev, Axel Haverich, Andres Hilfiker and Samir Sarikouch
- 172 **Macrophage-extracellular matrix interactions: Perspectives for tissue engineered heart valve remodeling**
Nikolaos Poulis, Marcy Martin, Simon P. Hoerstrup, Maximilian Y. Emmert and Emanuela S. Fioretti



OPEN ACCESS

EDITED AND REVIEWED BY

Elena Aikawa,
Brigham and Women's Hospital,
United States

*CORRESPONDENCE

Anthal I. P. M. Smits
a.i.p.m.smits@tue.nl
Laura Iop
laura.iop@unipd.it

SPECIALTY SECTION

This article was submitted to
Heart Valve Disease,
a section of the journal
Frontiers in Cardiovascular Medicine

RECEIVED 07 November 2022

ACCEPTED 18 November 2022

PUBLISHED 30 November 2022

CITATION

Smits AIPM, Iop L and Chester AH
(2022) Editorial: Vascular and valvular
tissue engineering: Treating and
modeling vasculopathies and
valvulopathies.
Front. Cardiovasc. Med. 9:1092102.
doi: 10.3389/fcvm.2022.1092102

COPYRIGHT

© 2022 Smits, Iop and Chester. This is
an open-access article distributed
under the terms of the [Creative
Commons Attribution License \(CC BY\)](#).
The use, distribution or reproduction
in other forums is permitted, provided
the original author(s) and the copyright
owner(s) are credited and that the
original publication in this journal is
cited, in accordance with accepted
academic practice. No use, distribution
or reproduction is permitted which
does not comply with these terms.

Editorial: Vascular and valvular tissue engineering: Treating and modeling vasculopathies and valvulopathies

Anthal I. P. M. Smits^{1,2*}, Laura Iop^{3*} and Adrian H. Chester^{4,5}

¹Department of Biomedical Engineering, Eindhoven University of Technology, Eindhoven, Netherlands, ²Institute for Complex Molecular Systems (ICMS), Eindhoven University of Technology, Eindhoven, Netherlands, ³Department of Cardiac, Thoracic, Vascular Sciences and Public Health, Padua Medical School, University of Padua, Padua, Italy, ⁴Heart Science Centre, Magdi Yacoub Institute, Harefield, United Kingdom, ⁵Imperial College London, National Heart and Lung Institute, London, United Kingdom

KEYWORDS

tissue engineering and regenerative medicine, cardiovascular development, cardiovascular disease, biomaterials, heart valve replacement, biocompatibility, bioprosthetic heart valve, *in vitro* disease model

Editorial on the Research Topic

Vascular and valvular tissue engineering: Treating and modeling vasculopathies and valvulopathies

Considerable progress has been made in recent years with the development of tissue-engineered heart valves and blood vessels. As these laboratory-based projects make translational steps toward the clinic, a new set of hurdles need to be negotiated. The articles in this Research Topic address some of the most imminent question regarding cardiovascular tissue engineering: what inspiration can we draw from native valvular and vascular development? How is the integration and remodeling of a tissue-engineered graft influenced by immunological or hemodynamic conditions? Can we use tissue engineering methodologies to engineer *in vitro* and *ex vivo* disease models to systematically unravel pathophysiological processes and the result of interventions?

Learning from and modeling biology

The main benefit of tissue-engineered substitutes is their intrinsic potential to grow and remodel in response to changing environmental conditions, analog to the native tissue that is being replaced. In-depth knowledge on the development and pathophysiological remodeling of native cardiovascular tissues is therefore indispensable. Starting from embryonic development, [Henderson et al.](#) provide an in-depth description on the state-of-the-art of (patho-)physiological development of the human arterial valves (i.e. semilunar; aortic and pulmonary valves). Importantly, they highlight that, while most of our knowledge regarding valve development is directly extrapolated from animal models, it is essential to also study these processes directly

in humans; a challenge which is hampered by scarcity of donor material (Henderson et al.). When looking at postnatal valve remodeling, a quintessential characteristic is the capacity of the valves to remodel in response to changes in the hemodynamic loads. Van Hoof et al. review experimental and clinical data regarding pulmonary homograft remodeling after the Ross procedure, representing an extremely interesting study case, as it provides for a situation where a mature pulmonary valve is exposed to an extreme change in hemodynamic loads, being transplanted from the low pressure to the high pressure circulation.

Both these reviews highlight that there are still important knowledge gaps in our understanding of cardiovascular development and remodeling. Bioengineering and tissue engineering methodologies enable the development of *ex vivo* and *in vitro* tissue models to study cardiovascular remodeling and interventions in a mechanistic, well-controlled and potentially high-throughput manner, complementary to *in vivo* studies. In this context, Matos et al. describe the development of an *ex vivo* blood vessel culture setup in which vascular pathologies can be induced in a well-controlled biomimicking hydrodynamic environment. Chen et al. provide an overview of the literature with respect to bottom-up engineered *in vitro* models of atherosclerosis.

Translatable tissue engineering methods: Natural matrix-based valve replacements

Despite considerable technical progress in cardiovascular tissue engineering, the translational challenges that have hampered clinical use of tissue-engineered cardiovascular substitutes so far, have become increasingly evident. Rizzi et al. provide an opinionated review on the various methodologies for heart valve tissue engineering, specifically focusing on broad translational potential. They advocate for the potential of *in situ* tissue engineering approaches, given their inherent reduced costs and logistical complexity when compared to *in vitro* cultured methods, and particularly, the use of natural scaffolds (e.g., decellularized allografts/xenografts) as the most native-like constructs available to date (Rizzi et al.).

One of the most important considerations for the use of decellularized valvular grafts is to minimize or harness the immunological response to the allogeneic or xenogeneic tissue, to prevent acute immunological rejection and adverse tissue remodeling (e.g. calcification, accelerated matrix degradation). Meng et al. describe the use of Sevelamer and an alternative cross-linking method to reduce the risk of calcification of bioprosthetic valves based on cross-linked bovine pericardium. Nevertheless, cross-linking inherently limits cellular ingrowth and functional matrix remodeling, and thereby abolishes the regenerative potential of bioprosthetic matrices. This

has cued the development of matrix decellularization as an alternative treatment to create non-immunological matrices whilst maintaining regenerative potential. Oripov et al. report on a clinical study in which early binding of antibodies to decellularized allografts was longitudinally quantified in 20 patients with repaired congenital heart disease (median age 18 years). Their main finding is that there was increased antibody binding in some patients who received a decellularized aortic allograft, who subsequently developed valve degeneration within 28 days post-operatively (Oripov et al.). In addition, they observed interesting potential influences of patient age, sex, and patient-donor sex mismatch on antibody binding risk, although larger patient cohorts would be needed to draw robust conclusions on this (Oripov et al.).

As an alternative approach to using decellularized native tissues as source for bioprostheses, the use of decellularized *de novo in vitro* engineered tissues is being pursued to create natural-based cardiovascular replacements without the need for donor tissue. Poulis et al. provide an interesting perspective on the role of macrophages in the process of tissue remodeling and their reciprocal interactions with the extracellular matrix. This is building on the notion that, instead of avoiding the inflammatory response to the implanted graft, its potential can be harnessed to trigger and coordinate functional tissue regeneration. The importance of the extracellular matrix is further emphasized in the review by Sajeesh et al., who elaborate on the use of stem cell-secreted extracellular vesicles as a source of immunomodulatory and pro-regenerative factors to enhance functional matrix regeneration.

Translatable tissue engineering methods: Using resorbable synthetic polymers for *in situ* tissue engineering

One of the downsides of natural-based cardiovascular grafts is the limited control over the structural and mechanical properties. Therefore, the use of resorbable synthetic polymers for regenerative cardiovascular grafts is being investigated, which offer relatively easy processing and a great level of control to engineer the ideal substitute. However, synthetic biomaterials lack the intrinsic bioactivity that is associated with the natural extracellular matrix. In an effort to combine the best of both worlds, Mudigonda et al. describe the development of a biohybrid scaffold material, consisting of decellularized pericardium coated with electrospun polycaprolactone-chitosan nanofibers to enhance mechanical strength and to improve cell homing.

One of the most critical challenges when using resorbable synthetic grafts for *in situ* tissue engineering is the balancing of resorption of the synthetic graft material with the formation of

new tissue *in situ*, and to sustain function while the polymer is replaced by new tissue. Addressing this challenge, Tseng et al. report on the proof-of-concept for incorporation of carbon fibers into polycaprolactone heart valve scaffolds with the aim to sustain valve functionality while the polymeric mesh is replaced by new tissue. The balance between scaffold resorption and tissue formation is also addressed by Marzi et al., who report on the use of Raman microspectroscopy to characterize the extent and type of resorption of *in situ* tissue-engineered carotid artery grafts based on electrospun supramolecular elastomers implanted up to 12 months in sheep. Interestingly, they showed feasibility of measuring both the local scaffold degradation stage and the collagen maturation stage in the same location by obtaining the local molecular fingerprint using Raman microspectroscopy, thereby uniquely enabling the detailed and marker-free assessment of the local tissue-scaffold balance (Marzi et al.).

Taken together, the articles in this Research Collection address some of the most imminent current challenges pertaining to cardiovascular tissue engineering. Common denominators are the importance of cell-matrix interactions, inspired by the dynamism of native cardiovascular tissues, as well as immunological processes and the tailoring of biomaterials to modulate those. What is also apparent from this collection is that the scientific questions addressed within the tissue engineering field are increasingly converging with clinical and translational needs, rather than to be driven by

technology push. These trends will accelerate translation of tissue engineering technologies and derivatives from bench to bed.

Author contributions

AS prepared the initial draft. LI and AC reviewed and edited the manuscript. All authors contributed to the article and approved the submitted version.

Conflict of interest

The authors declare that the research was conducted in the absence of any commercial or financial relationships that could be construed as a potential conflict of interest.

Publisher's note

All claims expressed in this article are solely those of the authors and do not necessarily represent those of their affiliated organizations, or those of the publisher, the editors and the reviewers. Any product that may be evaluated in this article, or claim that may be made by its manufacturer, is not guaranteed or endorsed by the publisher.



Sevelamer Attenuates Bioprosthetic Heart Valve Calcification

Zhen Meng¹, Zhe Li^{1*}, Erli Zhang¹, Li Zhang², Qingrong Liu¹ and Yongjian Wu¹

¹ State Key Laboratory of Cardiovascular Disease, Fuwai Hospital, National Center for Cardiovascular Diseases, Chinese Academy of Medical Sciences and Peking Union Medical College, Beijing, China, ² Analytical Instrumentation Center, College of Chemistry and Molecular Engineering, Peking University, Beijing, China

OPEN ACCESS

Edited by:

Laura Iop,
University of Padua, Italy

Reviewed by:

Yingfei Xue,
Columbia University, United States
Yunbing Wang,
Sichuan University, China

*Correspondence:

Zhe Li
ada521521@126.com

Specialty section:

This article was submitted to
Heart Valve Disease,
a section of the journal
Frontiers in Cardiovascular Medicine

Received: 12 July 2021

Accepted: 30 August 2021

Published: 29 September 2021

Citation:

Meng Z, Li Z, Zhang E, Zhang L, Liu Q
and Wu Y (2021) Sevelamer
Attenuates Bioprosthetic Heart Valve
Calcification.
Front. Cardiovasc. Med. 8:740038.
doi: 10.3389/fcvm.2021.740038

Objective: Sevelamer hydrochloride is a phosphate binder used to treat hyperphosphatemia in chronic kidney disease (CKD) patients that can reduce valvular and vascular calcification. The aim of this study was to examine the effects of sevelamer treatment on calcification in bioprosthetic heart valves (BHVs).

Methods: Wistar rats were randomly divided into three groups according to sevelamer intake and implantation (sham–sham operation; implant–implantation and normal diet, implant+S implantation, and sevelamer diet). Two kinds of BHVs—bovine pericardium treated with glutaraldehyde (GLUT) or non-GLUT techniques—were implanted in rat dorsal subcutis at 4 weeks. After implantation, sevelamer was administered to the implant+S group. The animals were executed at days 0 (immediately after implantation), 7, 14, 28, and 56. Calcium levels were determined by atomic absorption spectroscopy and von Kossa staining. Serum biochemistry analysis, Western blotting, real-time quantitative polymerase chain reaction, alkaline phosphatase activity measurement, histopathologic analysis, immunohistochemistry, and enzyme-linked immunosorbent assay were conducted to identify the anti-calcification mechanism of sevelamer.

Results: Non-GLUT crosslinking attenuates BHV calcification. Serum phosphate and calcium remained unreactive to sevelamer after a 14-day treatment. However, the mean calcium level in the implant+S group was significantly decreased after 56 days. In addition, the PTH level, inflammatory cell infiltration, system and local inflammation, and expression of Bmp2, Runx2, Alp, IL-1 β , IL-6, and TNF- α were significantly reduced in the implant+S group.

Conclusion: Sevelamer treatment significantly attenuated the calcification of BHVs and had anti-inflammation effects that were independent from serum calcium and phosphate regulation. Thus, sevelamer treatment might be helpful to improve the longevity of BHVs.

Keywords: valvular heart disease, bioprosthetic heart valve, structural valve degeneration, sevelamer, anti-calcification

INTRODUCTION

Valvular heart disease (VHD) is a common disease accounting for substantial morbidity and mortality in developed countries. According to a study in 2006, the prevalence of VHD is 2.5% in the US population (1). So far, no drug treatment can improve the long-term outcome of VHD compared with its natural history, and valve replacement surgery is the first-line therapy for the patients (2). Approximately 2,80,000 valvular substitutes are now implanted worldwide each year, with a predicted increment to 8,50,000 per year by 2050 (3). Currently available prosthetic valves can be divided into mechanical heart valves (MHVs) and bioprosthetic heart valves (BHVs). Each of the valves has inherent limitations. MHVs are durable yet highly thrombogenic, which requires lifelong anticoagulation therapy. BHVs do not require anticoagulant therapy but their durability is limited due to the inevitable structural valve degeneration (SVD) (2).

SVD, including calcification, leaflet fibrosis, tear, or flail leading to degeneration and/or hemodynamic dysfunction, is an intrinsic permanent change of BHVs. The rate of SVD is 10–30% at year 10 and 20–50% at year 15. Approximately 74% of valve failure requiring reoperation arises from SVD (4). As of today, there is no Food and Drug Administration-approved therapy to control SVD. SVD is believed to depend on the mechanical properties of the valve and the immunologic and calcification process (3). The general mechanisms of the native valve and BHV calcification seem to be related. Calcium and phosphate in the blood can form crystal cores in BHVs, which play important roles in BHV calcification (5). These findings indicated that attenuating the calcification might prolong the durability of BHVs (3).

Sevelamer hydrochloride (Renagel), a crosslinked poly(allylamine hydrochloride), hereafter referred to as sevelamer, is a non-absorbed calcium-free and aluminum-free phosphate binder used for the treatment of hyperphosphatemia in end-stage renal disease (ESRD) patients. A previous study has shown that sevelamer can reduce the calcification of vasculature and naïve aortic valves in chronic kidney disease (CKD) animal models and patients (6, 7). In addition, observational studies reported that a 0.1 mmol/L increase in serum phosphate was associated with a 50% increase in the risk of naïve aortic valve calcification (8). Based on these findings, we hypothesized that sevelamer could attenuate BHV calcification by decreasing serum phosphate levels in patients with normal renal function. In this study, we used a subdermal implantation model of normal rats to evaluate the effects of sevelamer therapy on post-implantation tissue changes in commercially available BHVs.

Abbreviations: VHD, valvular heart disease; MHV, mechanical heart valve; BHV, bioprosthetic heart valve; SVD, structural valve degeneration; CKD, chronic kidney disease; ESRD, end-stage renal disease; BP, bovine pericardium; GLUT, glutaraldehyde; ALP, alkaline phosphatase; RUNX2, RUNX family transcription factor 2; BMP2, bone morphogenetic protein 2; IL-1 β , interleukin 1 beta; IL-6, interleukin 6; TNF- α , tumor necrosis factor-alpha; PTH, parathyroid hormone; GAPDH, glyceraldehyde-3-phosphate dehydrogenase; LDL-C, low-density lipoprotein cholesterol.

MATERIALS AND METHODS

Materials

Commercial sevelamer hydrochloride (Renagel), a crosslinked poly(allylamine hydrochloride), was purchased from Sanofi. In addition, two kinds of commercial BHVs were kindly provided by the Peijia Medical Limited laboratory. Briefly, bovine pericardium (BP) sheets were treated with two different chemical treatment techniques as previously described (9): (a) BP sheets treated by glutaraldehyde (GLUT), and (b) BP sheets treated by an alternative, irreversible carbodiimide-based crosslinking chemistry (non-GLUT) (9). The rat diet was provided by Beijing HFK bioscience CO., LTD. containing 18% protein, 4% fat, 1.0–1.8% calcium, and 0.6–1.2% phosphorus. Sevelamer was administered together with the diet as a 3% w/w mix with animal chow as previously described (10).

Experimental Design

This animal study was performed according to the guidelines for animal care and approved by the Animal Care and Utilization Committee, Experimental Animal Center, Fuwai Hospital, National Center for Cardiovascular Diseases, China. Ninety healthy specific-pathogen-free (SPF) 4-week-old male Wistar rats weighing 50 ± 2.51 g purchased from Beijing Vital River Laboratory Animal Technology Corporation were used in the present study. The rats were housed in a specific-pathogen-free animal facility at 25°C with a 12-h light/dark cycle. The rats had free access to chow diets and water. These rats were randomly assigned to three groups with 30 animals in each: sham group (standard diet), implant group (standard diet), and implant+S group (standard diet with 3% w/w sevelamer). One GLUT cusp and one non-GLUT BHV cusp were surgically implanted in the dorsal subcutis of rats of implant group and implant+S group. In each group, five to six rats were euthanized by tribromoethanol, and samples were harvested at the designated time points (days 0, 7, 14, 28, and 56).

Animal Operation

Four-week-old rats were euthanized by tribromoethanol (Sigma-Aldrich). One dorsal midline surgical incision was made, and two subdermal pockets were created on either side of the sagittal plane. For each rat of implant and implant+S groups, one GLUT and one non-GLUT BHV cusps (1×1 cm) were implanted and positioned to lie as flat as possible in each of the pockets. One sample was placed per pocket. The incision was closed with a surgical suture. For rats from the sham group, surgery was performed without implanting cusps. After surgery, 20,000 IU benzylpenicillin sodium was injected intramuscularly for injection prophylaxis for 3 days. After the designated period, the rats were euthanized by tribromoethanol. The whole blood was collected *via* post-cava. After clotting at room temperature, serum samples were obtained by centrifugation at 4,000 rpm for 30 min at 4°C and stored at -80°C until further analysis. The heart with the aortic root, kidneys, and thoracic aorta was harvested and fixed in 10% neutralized buffered formalin (Leagene Biotech, Beijing, China) for histological analysis. The BHV cusps and surrounding capsules were removed from

the subdermal sites. The middle section was fixed in 10% neutralized buffered formalin for histological analysis. The remaining sections were placed immediately in liquid nitrogen and stored at -80°C as soon as possible for molecular analysis and quantitative calcium determination.

Serum Biochemistry

Serum phosphate, calcium, alkaline phosphatase (ALP), and creatinine were measured by the Center of Laboratory Medicine, Fuwai Hospital. Briefly, phosphate was determined with a phosphate test kit (molybdate method) (Biosino, Beijing, China). Calcium was determined with a calcium test kit (o-Cresolphthalein complexone, OCPC method; Biosino, Beijing, China). Phosphate and calcium were measured using an AU 5800 automatic analyzer (Beckman Coulter, USA). ALP was determined with the ALP kit (NPP substrate-AMP buffer method; Biosino, Beijing, China). Creatine was determined with creatinine kit (Jaffé method; Biosino, Beijing, China). ALP and creatinine were measured using a Hitachi LABOSPECT 008AS automatic analyzer (Hitachi, Tokyo, Japan).

Enzyme-Linked Immunosorbent Assay (ELISA)

Serum parathyroid hormone (PTH) interleukin- 1β (IL- 1β), interleukin-6 (IL-6), and tumor necrosis factor- α (TNF- α) were detected by ELISA (R&D Systems, MN, USA for IL- 1β , IL-6, TNF- α ; Meimian, Wuhan, China for PTH), according to the manufacturer's instructions. Dilutions and determination of standards were performed according to the manufacturer's instructions. The amounts of inflammatory markers in each serum sample were determined by matching the optical density in solution at 450 nm with a standard curve.

Quantitative Calcium Determination

Quantitative calcium determination was performed by the Analytical Instrumentation Center, Peking University. Briefly, one section of each cusp (without surrounding connective tissue) was weighed and acid hydrolyzed in 6N Ultrex II HCl, dried under nitrogen gas, and resuspended in 6N Ultrex II HCl. Samples were centrifuged to remove the remaining particles and diluted in nano-filtered water. Calcium was analyzed using a prodigy 7 inductively coupled plasma-atomic emission (ICP-AES) spectrometer (Leeman, USA). Standards of calcium ions were prepared by diluting the commercial -1000 ppm ICP standards. The calibration was linear, with a maximum error of 5%. The solutions were diluted to appropriate concentration using 1% HNO_3 (w/w). The intensity was obtained using a 10-s exposure, and the result was an average of three reads. Dilution ratios were used to calculate the calcium content of the sample, and values were normalized to dry sample weight.

Histopathologic Analysis

Histopathologic analysis was performed by the Pathology Department of Fuwai Hospital. Rat heart, kidney, aorta, and BHV cusps fixed in 10% neutralized buffered formalin were embedded in paraffin. Sections of $5\text{-}\mu\text{m}$ thickness were stained with hematoxylin and eosin (Leagene Tech, Beijing, China).

Histopathologic evaluation was performed by two experienced pathologists. The evaluation criteria are described in the **Supplementary Material**.

Immunohistochemistry (IHC)

For IHC, endogenous peroxidase activity of paraffin-embedded sections was blocked with 0.3% hydrogen peroxide in methanol. Sections, each separated by $3\text{--}5\text{ }\mu\text{m}$, were washed with PBS and incubated with rabbit anti-CD68 monoclonal antibody (Abcam, 1:500) to stain macrophages and rabbit anti-CD11b monoclonal antibody (Abcam, 1:500) to stain neutrophils at 4°C overnight. Specimens were then treated with a peroxidase conjugated goat anti-mouse secondary antibody (ZSGB Biotech, CA) and diaminobenzene substrate (ZSGB Biotech). Images were taken using a Leica DM 6000B microscope (Leica, Germany). The semi-quantitative analysis was performed by ImageJ analysis software.

Von Kossa Staining

Paraffined sections were washed with distilled water and incubated with 5% aqueous AgNO_3 (Abcam) under ultraviolet light for 45 min, then treated with 2.5% sodium thiosulfate (Abcam) for 2 min, and finally incubated with 0.1% nuclear fast red (Abcam) for 1 min. Images were taken using a panoramic SCAN image system (3DHISTECH). The semi-quantitative analysis was performed by ImageJ analysis software.

Real-Time Quantitative Polymerase Chain Reaction (RT-qPCR)

Total RNAs were isolated from BHV cusps with surrounding capsules using a RNeasy mini kit (Qiagen) following the manufacturer's instructions. Reverse transcription (RT) was performed using PrimeScriptTM RT Master Mix (Takara, CA, USA). qPCR was performed with SYBRTM Green Master Mix (Applied Biosystems) and run on 7500 or QuantStudio 3/5 Real-Time PCR systems (Applied Biosystems). Rat Gapdh was used as internal control unless specified otherwise. RT-qPCR assay primers used in this study are listed in **Table 1**.

Western Blot

The proteins of BHV cusps and the surrounding capsules were extracted with RIPA Lysis Buffer (Beyotime). The proteins were boiled with SDS-PAGE sample loading buffer for 5 min. The samples were then loaded onto a NuPAGE Bis-Tris gel (Thermo) followed by electrophoresis and transferred onto PVDF membranes. Membranes were blocked with TBST containing 5% milk powder, incubated with rabbit anti-RUNX2, BMP2, and GAPDH (Abcam) antibodies overnight at 4°C . The membranes were then washed and incubated with HRP-labeled goat anti-rabbit secondary antibodies (Beyotime Biotech). Detection was done using SuperSignal West Femto Maximum Sensitivity Substrate (Thermo Fisher Scientific). The images were acquired using the FluorChem M system (ProteinSimple). Quantification analyses were performed using ImageJ analysis software.

ALP Activity Measurement

The proteins of BHV cusps and the surrounding capsule were extracted with RIPA Lysis Buffer (Beyotime). The ALP activity was measured with Alkaline Phosphatase Assay Kit (Beyotime) following the manufacturer's instructions. Briefly, certain dilutions of samples were incubated with para-nitrophenyl phosphate to produce p-nitrophenol in diethanolamine (DEA, pH 9.8) buffer. The amount of ALP activity in each serum sample was determined by matching the optical density in the solution at 405 nm with a standard curve. A series dilution of p-nitrophenol (10 mM) were used to create a standard curve.

Statistics

Continuous data were expressed as mean \pm standard deviation (SD) and compared using Student's *t*-test (when two groups were compared) or one-way analysis of variance with Dunnett's or Tukey's multiple comparisons tests (when more than two groups were compared). Normal data distribution was checked using the Shapiro–Wilk test. Finally, categorical data were expressed as sample numbers and compared with Kruskal–Wallis one-way analysis of variance. A *p*-value < 0.05 for the two-sided test was considered statistically significant. All analyses were performed with IBM SPSS statistics 25 and GraphPad Prism 8.0.

TABLE 1 | qPCR primers used in this study.

| Gene | Forward | Reverse |
|---------------|---------------------------|----------------------------|
| BMP2 | TCTGGAAGCTGTGGGATAGA | GAGGAGCCTGTGGAGAAATAC |
| RUNX2 | GACTGTGGTTACCGTCATGGC | ACTTGGTTTTTCATAACAGCGGA |
| IL-1 β | ATGGCAACTGTCCCTGAACCTCACT | CAGGACAGGTATAGATTCAACCCCTT |
| TNF- α | GCAGATGGGCTGTACCTTATC | GAAATGGCAAATCGGCTGAC |
| IL-6 | GTTGCCTTCTTGGGACTG | ACTGGTCTGTTGTGGGTG |
| GAPDH | GGAGTCTACTGGCGTCTTCAC | ATGAGCCCTTCCACGATGC |

Runx2, RUNX family transcription factor2; *Bmp2*, bone morphogenetic protein 2; *IL-1 β* , interleukin 1 beta; *IL-6*, interleukin 6; *TNF- α* , tumor necrosis factor-alpha; *Gapdh*, glyceraldehyde-3-phosphate dehydrogenase.

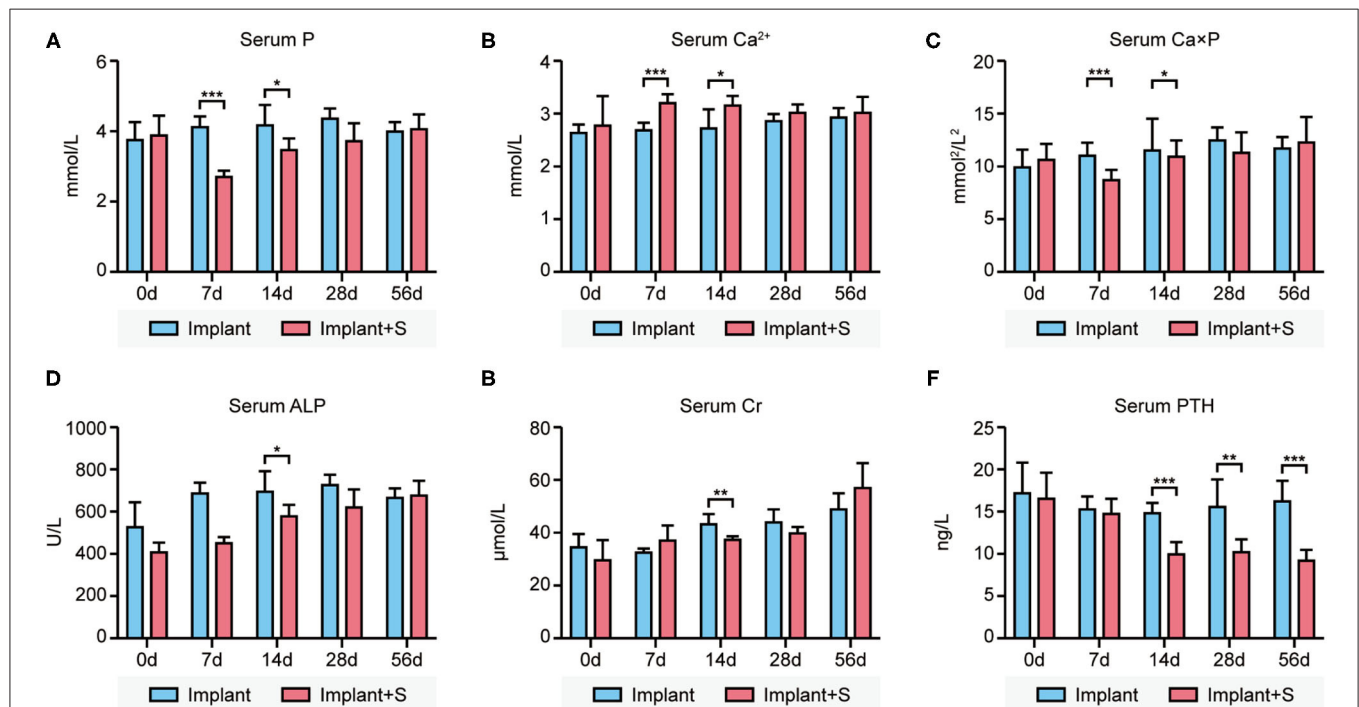


FIGURE 1 | Difference of serum biochemistry parameters between the implant and implant+S groups at days 0, 7, 14, 28, and 56 after implantation. **(A)** Compared to implant and implant+S group concerning serum phosphate levels, serum phosphate level decreased transiently in implant+S groups in 7–14 days. **(B)** Comparison between the implant and implant+S group concerning serum calcium levels. Serum calcium level increases transiently in the implant+S group in 7–14 days. **(C)** Comparison between the implant and implant+S group concerning serum calcium-phosphate product; serum calcium-phosphate product level decreased transiently in the implant+S group at 7 days. **(D)** Comparison between the implant and implant+S group concerning serum ALP. **(E)** Comparison between the implant and implant+S group concerning serum creatine. **(F)** Comparison between the implant and implant+S group concerning serum PTH level; serum PTH was decreased continuously in the implant+S group after 14 days. *N* = 4–6, data are mean \pm SD, **p* < 0.05, ***p* < 0.01, ****p* < 0.001.

RESULTS

Effect of Sevelamer on Serum Biochemistry and Body Weight

No difference was observed between the three groups in food intake and body weight (data not shown). No abnormality was observed in the heart, kidneys, and thoracic aorta of rats treated with sevelamer. No difference was observed between sham and implant groups in the concentrations of serum phosphate, calcium, calcium-phosphate product ($\text{Ca} \times \text{P}$), ALP, PTH, and creatine, except for a transient increment of ALP at day 7 because of stress response to the implantation (Supplementary Figure 1).

Serum phosphate was significantly lower in the implant+S group than in the implant group at days 7 and 14. In contrast, serum calcium was significantly higher in the implant+S group than the implant group at days 7 and 14. $\text{Ca} \times \text{P}$ was decreased in the implant+S group at 7 days. At day 14, serum ALP and creatine was slightly lower in the implant+S group than in the implant group. All differences mentioned above disappeared after 28 days (Figures 1A–E). However, serum PTH decreased

continuously in the implant+S group than in the implant group after 14 days (Figure 1F).

Effect of Sevelamer on Calcium Levels in the Implants

The calcium level was quantified by ICP-AES. The calcium level of GLUT BHVs was significantly higher than that of non-GLUT BHVs in the implant group after 56 days (GLUT vs. non-GLUT calcium: 47.44 ± 25.49 vs. 19.89 ± 7.95 $\mu\text{g}/\text{mg}$), suggesting that non-GLUT linking BHV implantation resulted in fewer valvular calcification. Accordingly, we evaluated the effect of sevelamer in rats implanted with GLUT and non-GLUT linking BHVs. Furthermore, BHVs of the implant group had a higher calcium level than that of the implant+S group (Figures 2A,B). The implant+S group showed significantly lower levels of *de novo* BHV calcification at all measured time points from 7 to 56 days. Heavy calcification on BHVs in the implant group was verified by von Kossa staining 56 days after implantation (Figure 2C). von Kossa staining of BHVs in the implant+S group showed less calcification after implantation (Figure 2C). These results were confirmed using a quantitative analysis (Figure 2D).

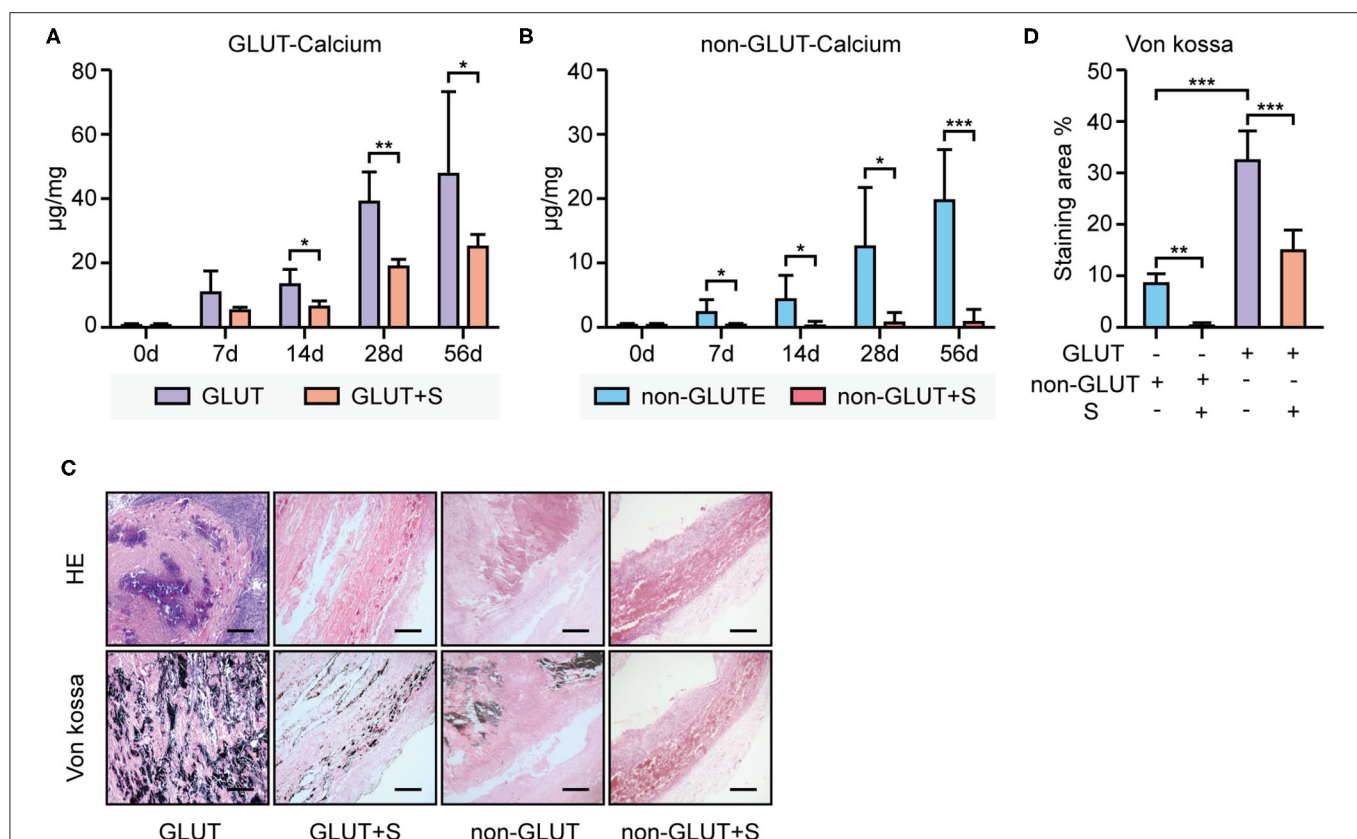


FIGURE 2 | Calcium deposition analysis of BHVs between the implant and implant+S group. **(A)** Calcium levels of GLUT BHVs between the implant and implant+S group, at days 0, 7, 14, 28, and 56 after implantation. **(B)** Calcium level of non-GLUT BHVs between the implant and implant+S groups at days 0, 7, 14, 28, and 56 after implantation. **(C)** Representative images and quantification of von Kossa staining and hematoxylin–eosin (HE) staining of BHVs in implant and implant+S groups 56 days after implantation; scale bars represent 400 μm . **(D)** Quantification of von Kossa staining of BHVs in implant and implant+S groups 56 days after implantation. GLUT represents GLUT BHVs in the implant group, GLUT+S represents GLUT BHVs in the implant+S group, non-GLUT represents non-GLUT BHVs in the implant group, and non-GLUT+S represents non-GLUT BHVs in the implant+S group. $N = 4-6$, data are mean \pm SD, $*p < 0.05$, $**p < 0.01$, $***p < 0.001$.

Effect of Sevelamer on the Expression of Osteoblast Markers in the Implants

RT-qPCR revealed that Runx2 and Bmp2 mRNA expression were higher in BHVs of the implant group than the implant+S group on the 56th day after implantation (Figures 3A,B, 4A,B). Western blot confirmed these changes in protein level (Figures 3D–F, 4D–F). In addition, the ALP activity measure showed that BHVs of the implant group have a higher ALP activity than those of the implant+S group (Figures 3C, 4C) on the 56th day after implantation.

Effect of Sevelamer on the Local and Systemic Inflammatory

RT-qPCR showed that BHVs of the implant group have higher levels of the inflammatory marker, including IL-1 β , IL-6, and TNF- α , than those of the implant+S group on the 56th day after implantation (Figures 3G–I, 4G–I). After 56 days of implantation, IL-1 β , IL-6, and TNF- α in serum were significantly increased in the implant group than the sham group (Figures 5A–C). However, sevelamer significantly suppressed the increments of IL-1 β , IL-6, and TNF- α in serum (Figures 5A–C). Pathological analysis and immunohistochemistry showed that BHVs of the implant group have higher levels in degeneration, granulation tissue invasion, neutrophils, and macrophages than that of the implant+S group at day 56 after implantation (Table 2; Figures 2C, 5D–H).

DISCUSSION

Studies have reported that sevelamer can lower serum phosphate concentration and thus attenuate the progression of cardiovascular calcification in both CKD animal models and real-world patients (11, 12). The present study demonstrated that 3% w/w sevelamer supplementation in chow diet was sufficient to reduce bioprosthesis calcification in subdermal BHV implantation rat models. However, sevelamer did not significantly affect the levels of serum phosphate, calcium, calcium-phosphate products, serum ALP activity, and creatinine in rats implanted with non-GLUT linking BHVs at day 56 of treatment, but caused transient fluctuations of these parameters between days 7 and 14. Our further research confirmed that this anti-calcification function may resort to decreasing PTH levels, attenuating local and system inflammatory and downregulating factors in the calcification signaling pathway, including BMP2, RUNX2, and ALP.

As sevelamer is not absorbed from the gut, it cannot induce hypophosphatemia and direct effects on the vascular system. Our study showed that sevelamer does not affect body weight and food intake, corroborating previous studies (13). Bone parameters were not measured in this study, but according to the literature, sevelamer cannot reduce bone density (5, 14). Since sevelamer cannot be absorbed in the gut and cannot induce hypophosphatemia and hypocalcemia, we can conclude that sevelamer is a safe treatment to attenuate BHV calcification.

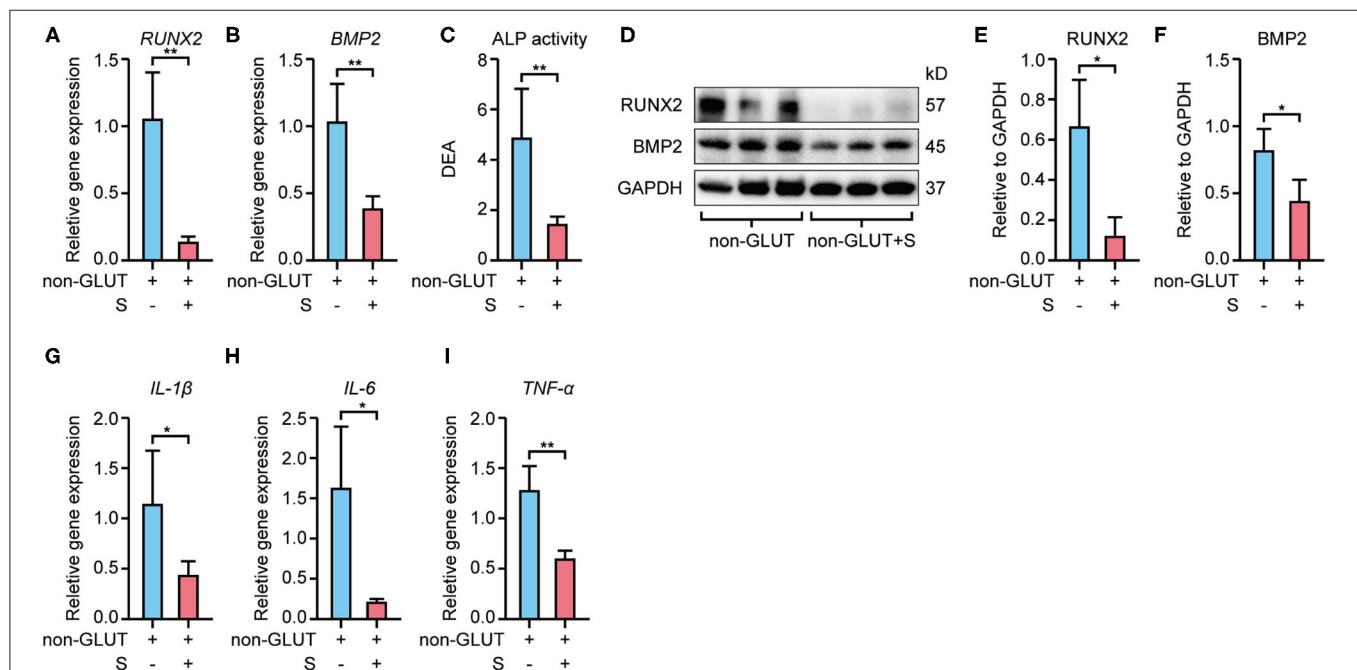


FIGURE 3 | Expression of osteoblast and inflammatory markers of non-GLUT BHVs in implant and implant+S groups 56 days after implantation. (A,B) Sevelamer reduces Runx2 and Bmp2 mRNA levels. (C) Sevelamer reduces ALP activity. (D–F) Protein expression of RUNX2 and BMP2 quantification analysis (E,F) and representative blotting (D). (G–I) mRNA expression of IL-1 β (G), IL-6 (H), and TNF- α (I) decreased in the implant+S group. $N = 3$ for Western blot, $N = 4$ for RT-qPCR, $N = 5$ for ALP activity. non-GLUT represents non-GLUT BHVs in the implant group, and non-GLUT+S represents non-GLUT BHVs in the implant+S group. Data are mean \pm SD, * $p < 0.05$, ** $p < 0.01$.

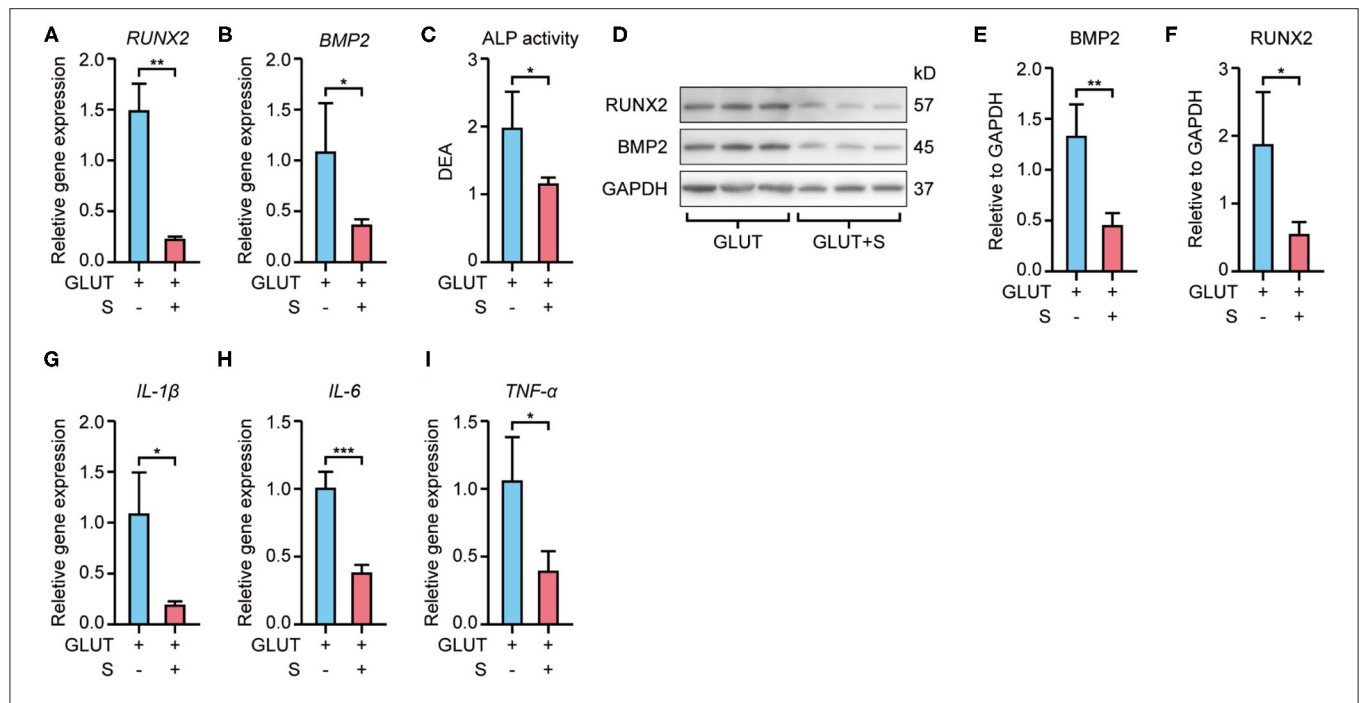


FIGURE 4 | Expression of osteoblast and inflammatory markers of GLUT BHVs in implant and implant+S groups 56 days after implantation. **(A,B)** Sevelamer reduces Runx2 and Bmp2 mRNA levels. **(C)** Sevelamer reduces ALP activity. **(D-F)** Protein expression of RUNX2 and BMP2 quantification analysis **(E,F)** and representative blotting **(D)**. **(G-I)** mRNA expression of IL-1β **(G)**, IL-6 **(H)**, and TNF-α **(I)** decreased in the implant+S group. $N = 3$ for Western blot, $N = 4$ for RT-qPCR and ALP activity. GLUT represents GLUT BHVs in the implant group, and GLUT+S represents GLUT BHVs in the implant+S group. Data are mean \pm SD, * $p < 0.05$, ** $p < 0.01$, *** $p < 0.001$.

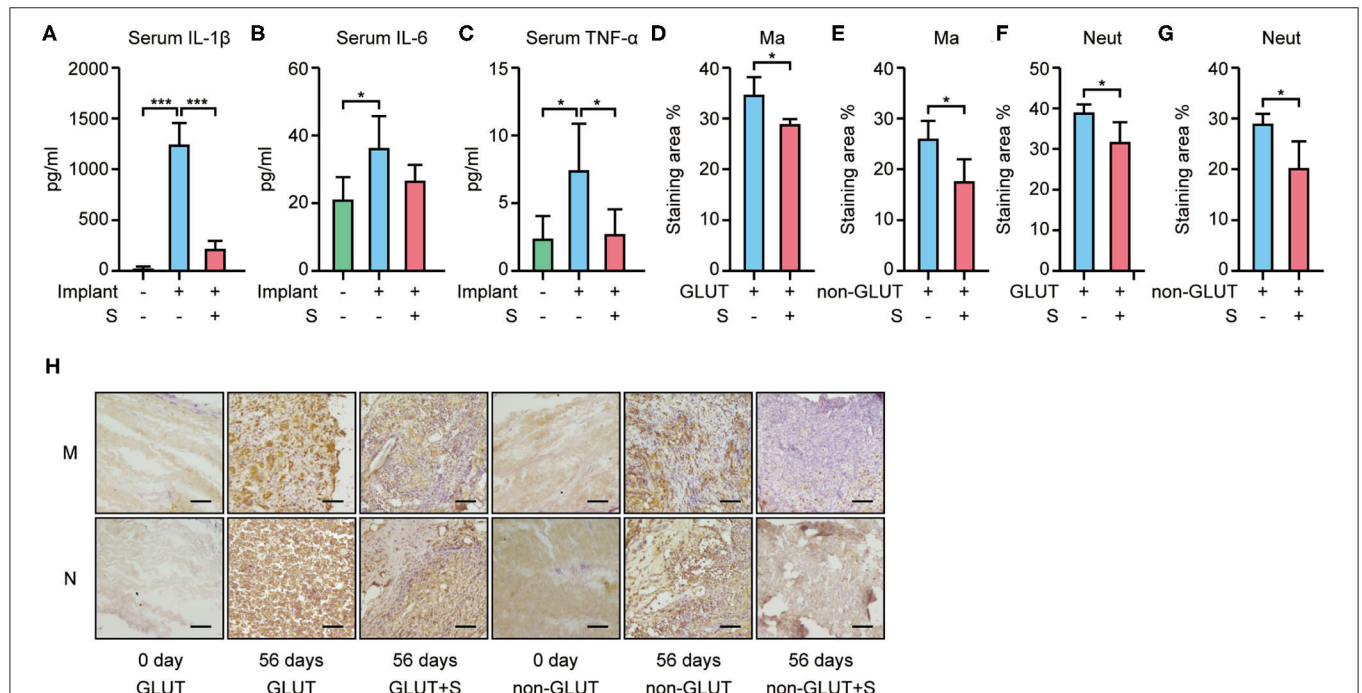


FIGURE 5 | Inflammatory markers in serum and macrophage/neutrophil infiltration in BHVs in implant and implant+S groups 56 days after implantation. **(A-C)** Serum level of IL-1β **(A)**, IL-6 **(B)**, and TNF-α **(C)** increased in the implant group and attenuated by sevelamer. **(D-H)** Macrophage and neutrophil infiltration in BHVs and attenuated by sevelamer, and representative images **(H)** and quantification analysis of IHC staining; scale bars represent 100 μ m **(D-G)**. GLUT represents GLUT BHVs in the implant group, GLUT+S represents GLUT BHVs in the implant+S group, non-GLUT represents non-GLUT BHVs in the implant group, and non-GLUT+S represents non-GLUT BHVs in the implant+S group. M/Ma represents macrophage, and N/Neut represents neutrophil. $N = 4$, data are mean \pm SD, * $p < 0.05$, *** $p < 0.001$.

TABLE 2 | Histopathologic analysis of non-GLUT BHVs in implant and implant+S groups after 56 days of implantation.

| | Class | Implant+S | Implant | p-value |
|----------------------------|-------|-----------|---------|---------|
| Number | | 5 | 5 | |
| Degeneration | - | 5 | 0 | 0.003 |
| | I | 0 | 0 | |
| | II | 0 | 0 | |
| | III | 0 | 0 | |
| | IV | 0 | 5 | |
| Necrosis | - | 4 | 0 | 0.063 |
| | I | 0 | 0 | |
| | II | 0 | 1 | |
| | III | 0 | 2 | |
| | IV | 1 | 2 | |
| Calcification | - | 3 | 0 | 0.163 |
| | I | 1 | 2 | |
| | II | 0 | 1 | |
| | III | 0 | 2 | |
| | IV | 1 | 0 | |
| GranulationTissue invasion | - | 0 | 4 | 0.011 |
| | I | 2 | 1 | |
| | II | 3 | 0 | |
| | III | 0 | 0 | |
| | IV | 0 | 0 | |
| Neutrophil | - | 4 | 0 | 0.007 |
| | I | 1 | 0 | |
| | II | 0 | 2 | |
| | III | 0 | 1 | |
| | IV | 0 | 2 | |
| Macrophage | - | 2 | 0 | 0.033 |
| | I | 3 | 2 | |
| | II | 0 | 1 | |
| | III | 0 | 2 | |
| | IV | 0 | 0 | |

Approximately 20% of cardiac surgery is used to treat VHD, and about half of the valve replacements use BHVs (15). BHVs are recommended strongly especially in patients with high bleeding risk and young women contemplating pregnancy (2). Up to now, three basic types of BHVs exist: xenografts, homografts, and autografts. Xenografts account for most of BHVs since biomaterials of animal origin are widely available. Most commercially available BHVs are fabricated out of porcine aortic valve leaflets or BP sheets crosslinked with glutaraldehyde (GLUT). GLUT crosslinking can make BHVs resistant against enzymatic degradation and reduce tissue antigenicity. However, GLUT-crosslinked BHVs experience failure due to calcification or degeneration within 10–20 years and seem to fail faster in younger patients (15). BHV calcification shares some general mechanisms with native aortic valve calcification involving passive and active mechanisms. The passive mechanism prosthesis-related dystrophic calcification is due to precipitation of calcium phosphate on cell debris and

fibrous. The active mechanism means valvular infiltration of cell or cell elements (calcium-binding proteins, macrophage, T lymphocyte, and matrix metalloproteinase). Several studies have suggested an association between inflammation, reactive oxygen species, thrombogenicity, coagulation, and calcification. Mechanical stress and cyclic loading are more likely to cause BHV calcification than native valves because, structurally, BHVs are different from native valves. The immune response to xenograft antigens such as galactose- α -1,3-galactose (α -Gal) and N-glycolylneuraminic acid (NeuGc), which are not expressed in humans, contributes to BHV calcification. Clinical studies also documented the relationship between BHV calcification and impaired lipid metabolism (3, 5).

GLUT crosslinking does not stabilize components such as elastin and glycosaminoglycans (GAGs) of extracellular matrix (ECM), making BHVs rigid and more prone to mechanical calcification degeneration than normal valves. Calcification has been shown to originate at devitalized cells and damaged ECM components (4). We test a new generation of non-GLUT BHVs provided by Peijia Medical Ltd. These BHVs use an alternative, irreversible carbodiimide-based crosslinking chemistry to stabilize more of the ECM component such as elastin and GAGs and produce stronger and more compliant BHVs (9). In our study, non-GLUT BHVs are less prone to calcification than traditional GLUT BHVs in subdermal implantation animal models, demonstrating that non-GLUT BHVs may be more durable heart valve implants in future.

A previous study has reported that 1% w/w sevelamer did not show any effect on serum phosphate in normal rat and normal rats treated with 3% w/w sevelamer showed a significant decrease in serum phosphate in 2–8 days (11). Since many studies chose 3% w/w sevelamer to treat rats (6, 11, 13), we decided to follow these studies. However, dosages of sevelamer should be screened in further studies to find an optimal dosage. Several studies showed that sevelamer has no effect on serum phosphate and calcium level of normal rat models after weeks of treatments (6, 13). A clinical study also failed to detect a significant decrease in serum phosphate level in patients with aortic stenosis using sevelamer for 6 weeks (8). These studies are consistent with our finding that sevelamer can only cause a transient decrease of serum phosphate levels in normal rats. Serum phosphate decreased transiently after sevelamer treatment in 7–14 days. Meanwhile, serum calcium increased to maintain the calcium-phosphate product. However, these changes disappear after 14 days. A clinical study showed that phosphate excretion from urine reduced during sevelamer treatment periods in the non-CKD population (8). We speculated that serum calcium and phosphate returning to the normal level could be attributed to renal and endocrine regulation. Our study found that PTH levels in the implant+S group consistently decreased after 14 days. Calcium and phosphate in the blood can support the growth of calcium phosphates on cell debris and fibrous components of BHVs, although serum calcium and phosphate are unchanged during most periods of sevelamer treatment. Sevelamer's influence on phosphate metabolism may affect the passive mineralization of BHVs, which needs further studies.

A relationship between inflammation and calcification has been demonstrated in many studies (3, 5). Macrophage is the most found immune cell in BHVs, whereas T lymphocytes and B lymphocytes, neutrophils, and eosinophils are less frequent. The macrophage can produce matrix metalloproteinases (MMPs), reactive oxygen species, multiple cytokines, and chemokines to promote calcification. Besides local inflammation, system inflammation also plays an important role in BHV calcification. C/T genotype of the rs 2229238 polymorphism within the IL6R gene has been proved to be associated with an increased risk of severe BHV calcification, as the genotype was significantly associated with a higher IL-6 level (16). Previous studies have shown that sevelamer can decrease serum levels of C-reactive proteins in CKD patients (17, 18). Sevelamer-treated uremic rats have less interstitial fibrosis and inflammation (13). Our study found that sevelamer can reduce macrophage and neutrophil infiltration in BHVs and inflammatory cytokine levels, including IL-1 β , IL-6, and TNF- α . Serum IL-1 β in both BHVs and serum suggested that sevelamer can attenuate local and system inflammation. The anti-inflammation effect may explain the reason for the anti-calcification effect of sevelamer. In addition, a marked reduction of calcium deposition and lower expressions of osteoblast markers such as BMP2, RUNX2, and ALP in mRNA and protein levels were found in the sevelamer-treated group.

The relationship between BHV calcification and impaired lipid metabolism has also been documented. A clinical study showed that increasing serum cholesterol levels are associated with increased BHV calcification. The odds ratio for valve explanation was 3.9-fold higher in patients with serum cholesterol levels higher than 200 mg/dl (19). Animal studies showed that statin significantly attenuated calcification of bovine pericardial valves in a subcutaneous rat model (20). However, no clinical data supported the anti-calcification effects of statin in BHVs. Dysfunctional BHVs display a considerable lipid deposition and foam cells. Oxidized LDL (low-density lipoprotein) can be produced by reactive oxygen species released by infiltrating neutrophils and macrophages (3). Studies have confirmed that sevelamer can reduce total and low-density lipoprotein cholesterol (LDL-C) levels. Wilkes et al. reported a 35.9% decrease in serum LDL-C in hemodialysis patients treated with sevelamer (21). Sevelamer can also attenuate oxidative stress (22). However, our subdermal implantation model used a widely used rat without a gene modification strain, with a normal diet. Thus, it is a limited model to study the effect of sevelamer on BHV calcification resorting of regulation lipid metabolism. Sevelamer also has pleiotropic effects such as decreasing the phosphaturic hormone fibroblast growth 23 (FGF23), which is secreted by osteocytes and osteoblasts in response to oral phosphate loading and is associated with the development of endothelial dysfunction and cardiac hypertrophy in CKD (23) and regulation of the expression of cell cycle proteins (6), among other effects. More studies are required to explore the mechanism of the anti-calcification effect of sevelamer in BHVs.

Several techniques are being developed to avoid BHV calcifications (5, 15, 24), including a new crosslinking method to stabilize more ECM components, a decellularization

technique to eliminate cellular debris, proper heart valve tissue sources from gene knockout animals with no immunological antigens, such as α -Gal and NeuGc, and new implantation techniques. However, considering that millions of BHVs have already been implanted, a therapy for BHV calcification prevention is required. Currently, there is no FDA-approved treatment to manage BHV calcification. Apart from a statin, anticoagulant therapy, immunosuppressive therapy, and MMP inhibitors under exploration to prevent BHV calcification (3), our study provided a new choice to prevent BHV calcification. However, more studies are needed to prove the effect.

LIMITATION AND CONCLUSION

This study has several limitations. First, we used a subcutaneous animal model that is different from the blood circulation model. However, this is the traditional first step when developing tissue-engineered heart valves in the rat, which is an animal model that is considerably easier and less expensive than the larger animal models. Second, we only used two types of BHVs and one dosage of sevelamer. More commercial BHVs and dosages of sevelamer need to be tested in the future. Third, sevelamer has many effects besides the anti-inflammatory action. More studies are needed to identify these effects on the prevention of BHV calcification. Finally, the relationship between the animal model and clinical outcomes has not been established. More clinical studies, including randomized controlled trials, are needed to prove the clinical value of sevelamer in the prevention of BHV calcification.

In conclusion, sevelamer treatment significantly attenuated the calcification of BHVs in a subcutaneous rat model and had anti-inflammation effects, which are independent from serum calcium and phosphate regulation. Thus, our results suggest that sevelamer treatment might be helpful for the prevention of BHV calcification.

DATA AVAILABILITY STATEMENT

The original contributions presented in the study are included in the article/**Supplementary Material**, further inquiries can be directed to the corresponding author.

ETHICS STATEMENT

The animal study was reviewed and approved by the animal care and utilization committee, experimental animal center, Fuwai hospital National Center for Cardiovascular Diseases, China.

AUTHOR CONTRIBUTIONS

ZL and EZ contributed to the design and manuscript preparation of this study. ZM and QL contributed to the animal experiment, molecular study, and data collection. LZ contributed to the ICP-AES experiment. YW is an expert in valvular heart

disease field who gave knowledge support to the study. All authors contributed to the article and approved the submitted version.

FUNDING

This work was supported by grants from the National Natural Science Foundation of China (NSFC) (81700405) and China Scholarship Committee (CSC) award 201406210335 to EZ, from NSFC (91339103) to YW, Capital health development scientific research program (W01-ZD-02_W_2019) to YW, and from Special Research Fund for Central Universities, Peking Union Medical College (3332018052) to ZL.

REFERENCES

1. Nkomo VT, Gardin JM, Skelton TN, Gottdiener JS, Scott CG, Enriquez-Sarano M. Burden of valvular heart diseases: a population-based study. *Lancet*. (2006) 9540:1005–11. doi: 10.1016/S0140-6736(06)69208-8
2. Otto CM, Nishimura RA, Bonow RO, Carabello BA, Erwin JP 3rd, Gentile F, et al. 2020 ACC/AHA Guideline for the management of patients with valvular heart disease: a report of the American college of cardiology/American heart association joint committee on clinical practice guidelines. *Circulation*. (2020) 143:e72–227. doi: 10.1161/CIR.0000000000000923
3. Kostyunin AE, Yuzhalin AE, Rezvova MA, Ovcharenko EA, Glushkova TV, Kutikhin AG. Degeneration of bioprosthetic heart valves: update 2020. *J Am Heart Assoc*. (2020) 9:e018506. doi: 10.1161/JAHA.120.018506
4. Capodanno D, Petronio AS, Prendergast B, Eltchaninoff H, Vahanian A, Modine T, et al. Standardized definitions of structural deterioration and valve failure in assessing long-term durability of transcatheter and surgical aortic bioprosthetic valves: a consensus statement from the European Association of Percutaneous Cardiovascular Interventions (EAPCI) endorsed by the European Society of Cardiology (ESC) and the European Association for Cardio-Thoracic Surgery (EACTS). *Eur Heart J*. (2017) 45:3382–90. doi: 10.1093/eurheartj/ehx303
5. Badria AF, Koutsoukos PG, Mavrilas D. Decellularized tissue-engineered heart valves calcification: what do animal and clinical studies tell us? *J Mater Sci Mater Med*. (2020) 12:132. doi: 10.1007/s10856-020-06462-x
6. Maizel J, Six I, Dupont S, Secq E, Dehedin B, Barreto FC, et al. Effects of sevelamer treatment on cardiovascular abnormalities in mice with chronic renal failure. *Kidney Int*. (2013) 3:491–500. doi: 10.1038/ki.2013.110
7. Block GA, Spiegel DM, Ehrlich J, Mehta R, Lindbergh J, Dreisbach A, et al. Effects of sevelamer and calcium on coronary artery calcification in patients new to hemodialysis. *Kidney Int*. (2005) 68:1815–24. doi: 10.1111/j.1523-1755.2005.00600.x
8. Wald DS, Chambers J, Bestwick J. P., and Wald N. J. (2019). Randomized crossover trial of phosphate-binding medication on serum phosphate levels in patients with aortic stenosis. *Clin. Ther*. 10, 2066–2072.e2. doi: 10.1016/j.clinthera.2019.08.004
9. Tam H, Zhang W, Infante D, Parchment N, Sacks M, Vyavahare N. Fixation of bovine pericardium-based tissue biomaterial with irreversible chemistry improves biochemical and biomechanical properties. *J Cardiovasc Transl Res*. (2017) 2:194–205. doi: 10.1007/s12265-017-9733-5

ACKNOWLEDGMENTS

We thank Yuyan Xiong, Wence Shi, and Ruijie Tang from State Key Laboratory of Cardiovascular Disease, Fuwai Hospital and Fei Zhao from Blood Disease Hospital, Chinese Academy of Medical Science, for their assistance with the animal operation.

SUPPLEMENTARY MATERIAL

The Supplementary Material for this article can be found online at: <https://www.frontiersin.org/articles/10.3389/fcvm.2021.740038/full#supplementary-material>

10. Cozzolino M, Dusso AS, Liapis H, Finch J, Lu Y, Burke SK, et al. The effects of sevelamer hydrochloride and calcium carbonate on kidney calcification in uremic rats. *J Am Soc Nephrol*. (2002) 9:2299–308. doi: 10.1097/01.ASN.0000025782.24383.0D
11. Nagano N, Miyata S, Obana S, Eto N, Fukushima N, Burke SK, et al. Renal mineral handling in normal rats treated with sevelamer hydrochloride (Renagel), a noncalcemic phosphate binder. *Nephron*. (2001) 3:321–8. doi: 10.1159/000046093
12. Chertow GM, Burke SK, Raggi P. Sevelamer attenuates the progression of coronary and aortic calcification in hemodialysis patients. *Kidney Int*. (2002) 1:245–52. doi: 10.1046/j.1523-1755.2002.00434.x
13. Finch JL, Lee DH, Liapis H, Ritter C, Zhang S, Suarez E, et al. Phosphate restriction significantly reduces mortality in uremic rats with established vascular calcification. *Kidney Int*. (2013) 6:1145–53. doi: 10.1038/ki.2013.213
14. Mathew S, Lund RJ, Strebeck F, Tustison KS, Geurs T, Hruska KA. Reversal of the adynamic bone disorder and decreased vascular calcification in chronic kidney disease by sevelamer carbonate therapy. *J Am Soc Nephrol*. (2007) 1:122–30. doi: 10.1681/ASN.2006050490
15. Manji RA, Ekser B, Menkis AH, Cooper DK. Bioprosthetic heart valves of the future. *Xenotransplantation*. (2014) 1:1–10. doi: 10.1111/xen.12080
16. Ponasenko AV, Khutornaya MV, Kutikhin AG, Rutkovskaya NV, Tsepokina AV, Kondyukova NV, et al. A Genomics-based model for prediction of severe bioprosthetic mitral valve calcification. *Int J Mol Sci*. (2016) 17:1385. doi: 10.3390/ijms17091385
17. Nikolov IG, Joki N, Maizel J, Lacour B, Drüeke TB, Massy ZA. Pleiotropic effects of the non-calcium phosphate binder sevelamer. *Kidney Int Suppl*. (2006) 105:S16–23. doi: 10.1038/sj.ki.5001994
18. Goldberg DI, Dillon MA, Slatopolsky EA, Garrett B, Gray JR, Marbury T, et al. Effect of RenaGel, a non-absorbed, calcium- and aluminium-free phosphate binder, on serum phosphorus, calcium, and intact parathyroid hormone in end-stage renal disease patients. *Nephrol Dial Transplant*. (1998) 9:2303–10. doi: 10.1093/ndt/13.9.2303
19. Farivar RS, Cohn LH. Hypercholesterolemia is a risk factor for bioprosthetic valve calcification and explantation. *J Thorac Cardiovasc Surg*. (2003) 4:969–75. doi: 10.1016/S0022-5223(03)00708-6
20. Lee S, Kim DH, Youn YN, Joo HC, Yoo KJ, Lee SH. Rosuvastatin attenuates bioprosthetic heart valve calcification. *J Thorac Cardiovasc Surg*. (2019) 3, 731–41.e1. doi: 10.1016/j.jtcvs.2018.12.042
21. Wilkes BM, Reiner D, Kern M, Burke S. Simultaneous lowering of serum phosphate and LDL-cholesterol by sevelamer hydrochloride (RenaGel) in dialysis patients. *Clin Nephrol*. (1998) 6:381–6.
22. Phan O, Ivanovski O, Nguyen-Khoa T, Mothu N, Angulo J, Westenfeld R, et al. Sevelamer prevents uremia-enhanced atherosclerosis progression in apolipoprotein E-deficient mice. *Circulation*. (2005) 18:2875–82. doi: 10.1161/CIRCULATIONAHA105.541854

23. Koiwa F, Kazama JJ, Tokumoto A, Onoda N, Kato H, Okada T, et al. Sevelamer hydrochloride and calcium bicarbonate reduce serum fibroblast growth factor 23 levels in dialysis patients. *Ther Apher Dial.* (2005) 4:336–9. doi: 10.1111/j.1744-9987.2005.00293.x
24. Bonetti A, Marchini M, Ortolani F. Ectopic mineralization in heart valves: new insights from *in vivo* and *in vitro* procalcific models and promising perspectives on noncalcifiable bioengineered valves. *J Thorac Dis.* (2019) 5:2126–43. doi: 10.21037/jtd.2019.04.78

Conflict of Interest: The authors declare that the research was conducted in the absence of any commercial or financial relationships that could be construed as a potential conflict of interest.

Publisher's Note: All claims expressed in this article are solely those of the authors and do not necessarily represent those of their affiliated organizations, or those of the publisher, the editors and the reviewers. Any product that may be evaluated in this article, or claim that may be made by its manufacturer, is not guaranteed or endorsed by the publisher.

Copyright © 2021 Meng, Li, Zhang, Zhang, Liu and Wu. This is an open-access article distributed under the terms of the Creative Commons Attribution License (CC BY). The use, distribution or reproduction in other forums is permitted, provided the original author(s) and the copyright owner(s) are credited and that the original publication in this journal is cited, in accordance with accepted academic practice. No use, distribution or reproduction is permitted which does not comply with these terms.



Biocompatibility and Application of Carbon Fibers in Heart Valve Tissue Engineering

Yuan-Tsan Tseng^{1,2}, Nabil F. Grace³, Heba Aguib^{1,2,4}, Padmini Sarathchandra², Ann McCormack¹, Ahmed Ebeid⁴, Nairouz Shehata⁴, Mohamed Nagy⁴, Hussam El-Nashar⁴, Magdi H. Yacoub^{1,2,4}, Adrian Chester^{1,2} and Najma Latif^{1,2*}

¹ Heart Science Centre, Magdi Yacoub Institute, Harefield, United Kingdom, ² Imperial College London, National Heart and Lung Institute, London, United Kingdom, ³ Centre for Innovative Materials Research, Lawrence Technological University, Southfield, MI, United States, ⁴ Biomedical Engineering and Innovation Laboratory, Aswan Heart Centre, Aswan, Egypt

OPEN ACCESS

Edited by:

Philippe Sucosky,
Kennesaw State University,
United States

Reviewed by:

Craig Simmons,
University of Toronto, Canada
Peter Zilla,
University of Cape Town, South Africa

*Correspondence:

Najma Latif
n.latif@imperial.ac.uk

Specialty section:

This article was submitted to
Heart Valve Disease,
a section of the journal
Frontiers in Cardiovascular Medicine

Received: 12 October 2021

Accepted: 29 November 2021

Published: 24 December 2021

Citation:

Tseng Y-T, Grace NF, Aguib H, Sarathchandra P, McCormack A, Ebeid A, Shehata N, Nagy M, El-Nashar H, Yacoub MH, Chester A and Latif N (2021) Biocompatibility and Application of Carbon Fibers in Heart Valve Tissue Engineering. *Front. Cardiovasc. Med.* 8:793898. doi: 10.3389/fcvm.2021.793898

The success of tissue-engineered heart valves rely on a balance between polymer degradation, appropriate cell repopulation, and extracellular matrix (ECM) deposition, in order for the valves to continue their vital function. However, the process of remodeling is highly dynamic and species dependent. The carbon fibers have been well used in the construction industry for their high tensile strength and flexibility and, therefore, might be relevant to support tissue-engineered hearts valve during this transition in the mechanically demanding environment of the circulation. The aim of this study was to assess the suitability of the carbon fibers to be incorporated into tissue-engineered heart valves, with respect to optimizing their cellular interaction and mechanical flexibility during valve opening and closure. The morphology and surface oxidation of the carbon fibers were characterized by scanning electron microscopy (SEM). Their ability to interact with human adipose-derived stem cells (hADSCs) was assessed with respect to cell attachment and phenotypic changes. hADSCs attached and maintained their expression of stem cell markers with negligible differentiation to other lineages. Incorporation of the carbon fibers into a stand-alone tissue-engineered aortic root, comprised of jet-sprayed polycaprolactone aligned carbon fibers, had no negative effects on the opening and closure characteristics of the valve when simulated in a pulsatile bioreactor. In conclusion, the carbon fibers were found to be conducive to hADSC attachment and maintaining their phenotype. The carbon fibers were sufficiently flexible for full motion of valvular opening and closure. This study provides a proof-of-concept for the incorporation of the carbon fibers into tissue-engineered heart valves to continue their vital function during scaffold degradation.

Keywords: carbon fibers, biocompatibility, heart valve, tissue engineering, biomaterials, composite, adipose-derived stem cells

INTRODUCTION

Tissue-engineered heart valves offer the potential to overcome the limitations of current prosthetics. The success of tissue-engineered heart valves rely upon several factors: first, the scaffold material being strong and flexible enough to withstand the hemodynamic cycle of loading and unloading at a frequency corresponding to a range of heart rates during rest and exercise. Second, the construct needs to be receptive to the population by cells either seeded during *in vitro*

production of the valve or following implantation. Last, the scaffold should be biodegradable to allow the replacement of the own extracellular matrix (ECM) of the hosts. However, the process is highly dynamic and species dependent (1). Rapid cellular ingrowth and ECM deposition are often observed in animal models, but these observations typically fail to be observed in humans (1–4). Therefore, the potential risk for scaffold degradation and fatigue to occur prior to sufficient laying down of functional ECM leads to structural failure of the constructs.

Textile support as part of heart valve leaflets has been proposed previously by our group and others (5–9). However, most of the literature has been focused on reinforcement of the leaflet with mono- or multifilament yarns, which will still suffer from creep, fatigue, and unpredictable degradation over time. To ensure the stability of the construct during the remodeling process, we have assessed the suitability of incorporating carbon fibers into tissue-engineered heart valves to reinforce the biodegradable scaffold. The carbon fiber is a thin fiber between 5 and 20 μm in diameter composed of mostly carbon atoms. It has been used in the repair of damaged tendons and ligaments to provide additional support and strength during surgical repair and regeneration (10–12). More recently, the carbon fibers have been used to provide additional strength in scaffold materials used for bone, cartilage, and trachea tissue-engineered constructs (13–17). The low density and high strength properties of the carbon fibers, which are also flexible and have complete elastic recovery after unloading, give them excellent fatigue resistance (18). This profile of mechanical properties makes them good candidates for inclusion in scaffolds for heart valve tissue engineering.

The carbon fibers are usually combined with other polymers to reinforce the strength to weight ratio of the composite. This often required surface enhancement on the chemically inert carbon fiber surface that improves its chemical bonding and adhesion between the carbon fibers and matrix. Plasma oxidization is a simple and residue-free surface activation technique for the carbon fibers; thus, the focus of this *in-vitro* study was to investigate the biocompatibility of the carbon fibers in their pristine and plasma oxidized forms with human adipose-derived stem cells (hADSCs) to determine how binding of cells to the carbon fibers can be maximized. We have assessed the flexibility of the carbon fibers with respect to the motion of tissue-engineered valve cusps in a pulse duplicator. We envisage these findings that will provide a rationale for further studies into the use of carbon fibers as a part of composite scaffold to provide strength and durability of the engineered tissue.

MATERIALS AND METHODS

Carbon Fibers

The carbon fibers used in this study were produced by the treatment of a polyacrylonitrile (PAN) precursor, with pyrolysis, surface treatment, and sizing processes (Toray Carbon Fibers Europe, Paris, and France). The size and shape of the carbon fibers were analyzed with a scanning electron microscope (SEM) to assess the uniformity of size and shape. For experiments with cells, the carbon fibers were sterilized by incubating in 70%

ethanol for 1 h followed by washing in sterile phosphate-buffered saline (PBS) three times prior to cell seeding.

Plasma Oxidation

The carbon fibers were mounted on a 24-well CellCrown™ 24 (Scaffdex Oy, Finland) and treated with plasma oxidation at 0.16 mbar oxygen (Diener Electronic, Germany). The carbon fibers were exposed to 30 W for 10, 20, and 30 min, which were compared to 30 min of 90 W. All the following analysis and cell seeding were performed within 24 h of plasma oxidization treatment.

Cell Culture

The hADSCs were purchased from Lonza (PT-5006; Lonza, Switzerland) and cultured in a culture medium comprising adipose-derived stem cell basal medium, 10% fetal calf serum (FCS), 1% L-glutamine, and 0.1% gentamicin–amphotericin B (ADSC Growth Medium BulletKit™, PT-4505; Lonza, Switzerland). The cells were fed every 3 days and subcultured at 90% confluency.

Cell Seeding

The hADSCs (3×10^5 cells) were simultaneously cultured on the pristine and plasma oxidized (30 W) carbon fibers (fixed on CellCrown™ 24) for 3 weeks under rotatory seeding at 10 rpm with a rotator (Bibby Scientific, UK) as described previously (19). In addition, the hADSCs (5,000 cells) were seeded on coverslips and cultured for 3 weeks as a control. At the end of this period, the coverslips and the carbon fibers were washed twice in PBS and fixed in 4% paraformaldehyde for 10 min. The fixative solution was removed with three rinses of PBS. The carbon fibers were removed from the CellCrown™ 24. Cells on coverslips and the carbon fibers were permeabilized with Triton X-100 (0.5% v/v in PBS) for 3 min and washed two times in PBS-Tween (PBS-T) (0.1% v/v). Cells were blocked using 3% (w/v) bovine serum albumin (BSA) and incubated with primary antibodies [α -smooth muscle actin (α -SMA) (Dako, US), vimentin (Dako, US), calponin (Dako, US), SM22 (Abcam, US), vinculin (Sigma-Aldrich, US), Ectodysplasin A (EDA)-fibronectin (Dinova, Germany), alkaline phosphatase (Sigma-Aldrich, US), CD44 (BD Pharmingen™, US), osteocalcin (Abcam, US), CD105 (Abcam, US), CD90 (Dinova, Germany), CD31 (Dako, US), SRY-Box transcription factor 9 (Sox9) (R&D Systems, US), and peroxisome proliferator-activated receptor gamma (PPAR γ) (Abcam, US)] in BSA 1.5% w/v for 1 h. After thorough washing in PBS-T, the cells were incubated with secondary antibodies for 1 h, washed 3 times during 5 min in PBS-T, and incubated 10 min with 4,6-diamidino-2-phenylindole (DAPI) (Sigma-Aldrich, US). Cells were washed again twice in PBS-T and mounted on glass slides in the PermaFluor Aqueous Mounting Fluid (Beckman Coulter, Fullerton, California, USA). Observations were performed with an inverted confocal microscope (Zeiss, LSM 510 Meta Inverted).

Scanning Electron Microscopy

The hADSCs grown on coverslips and the carbon fibers were fixed in 2.5% glutaraldehyde in 0.1 M sodium cacodylate buffer for at least 2 h followed by two buffer washes. Specimens were

then postfixing with 1% osmium tetroxide in 0.1 M sodium cacodylate buffer for 1 h. After two buffer washes, specimens were dehydrated through ascending series of ethanol starting from 25 to 100%. Then, the specimens were chemically dried using hexamethylenedizilazine (HMDS), mounted on SEM stubs, and coated with gold/palladium. Images of the carbon fibers with and without cells were taken on JEOL JSM-6010LA analytical scanning microscope. hADSCs on coverslips and the carbon fibers were added to aluminum sample holders with carbon tape, air dried overnight, and coated with gold/palladium. An energy dispersive X-ray analyzer energy dispersive spectroscopy (EDS) (JEOL JED-2300 X-ray Microanalysis System) was used to investigate the surface structure of the carbon fibers.

Proliferation Assay

After 3 weeks of cell seeding with the carbon fibers, proliferation assays were carried out with the CellTiter 96[®] Aqueous Non-radioactive Cell Proliferation Assay Kit (Promega G-5421, US) by adding 20 μ l of (3-(4,5-dimethylthiazol-2-yl)-5-(3-carboxymethoxyphenyl)-2-(4-sulfophenyl)-2H-tetrazolium) (MTS)/phenazine methosulfate (PMS) solution with 100 μ l of dulbecco's modified eagle medium (DMEM) on cells. Plates were incubated for 1 h at 37°C, 5% carbon dioxide (CO₂), and the absorbance was read at 490 nm.

Mechanical Testing

Samples of the carbon fibers between 3 and 5 mm in length [measured using a caliper (Mitutoyo, Japan)] and cross-sectional area measured by SEM (JEOL JSM-6010LA) were subjected to uniaxial tensile testing (TA Electroforce TestBench, Minnesota, USA) at a speed of 0.1 mm/s. For each condition, 4 repeated samples, cut longitudinally, were measured. The resulting stress strain curve was fitted with six-order polynomial trend line. The gradient of elastic modulus was taken from the steepest curve.

Analysis of Cusp Movement/Hinge Mechanism

It is well known that the carbon fibers suffer from brittle snap when bend in 90° angles against the direction of the carbon fibers; therefore, motion analysis of a human heart valve was conducted. The Aswan Heart Science Center Ethics Committee approval and informed consent were obtained to use the CT images from a normal adult individual (female, aged 54 years). The hinge range of movement of the aortic valve was measured using CT images (Siemens Somatom definition flash dual source multislice CT machine with retrospective ECG gating, slice thickness 0.6 mm, pitch 0.18, and gantry rotation time 0.28 s). Three-dimensional (3D) segmentation was used to reconstruct cusp and sinus shape (Mimics Innovation Suite 21 research edition, Materialize NV, Leuven, Belgium). The segmented model was rotated to visualize the leaflet and sinus side perpendicular to the leaflet and sinus plane (side view).

Three nadir points of the three sinuses were determined and a plane representing the annular plane was created (Figure 5C). A cross-section through the middle of the cusp as a vertical plan (perpendicular to the annular plane) was marked to each sinus and the movement of the cusp and sinus wall to this vertical plan

was tracked at five points of the cardiac cycle (0, 10, 20, 30, and 40%) covering the complete systolic phase.

To identify the movement of the hinge, the angles and radii of each cusp and sinus were measured. The radii (R) of the best fit circles are recorded and curvature is calculated by the relation $k = 1/R$. A plane (Pp) perpendicular to the annular plane (Pa) through each of the nadirs was created to measure the angle of the tangent of each cusp at the nadirs to Pp and, thus, track its movement.

Bioreactor Testing

To demonstrate their utility and functionality in a tissue-engineered valve construct, the carbon fibers were sutured using a standard needle into the hinge region of the jet-sprayed nanofibrous polycaprolactone (PCL) scaffold (20). The carbon fibers were not incorporated into the jet-spraying process because they are not compatible with the spinning process. In addition, carbon fibers are only required at regions of high stress to alleviating the stress on the nanofiber scaffold. The nanofibrous scaffolds were first constructed into a 3D functional valve root using a preparatory process (patent pending) followed by suturing the carbon fibers along the hinge to the belly region and halfway up toward the coapting edge in a defined spatial manner (5 equally spaced markers were used as a guide in the center of this region). Each strand consists of 50 individual carbon fibers. The carbon fibers were tethered on the outside edge of the commissure and a running stitch was stitched following the marked parallel lines (Figure 6). We sutured the carbon fibers in the radial direction to demonstrate the worst-case scenario in the carbon fiber movement in the radial direction. Valve roots with and without the embedded carbon fibers were subjected to a hydrodynamic pulmonary profile as set in ISO 5840 (20 mm Hg mean pressure, 70 bpm, 5 L/min cardiac output, and 35% systolic duration) using the Aptus[®] Bioreactors (Aptus Bioreactors, USA). High speed camera (500 frames per second) (Sony, Japan) was used to capture the opening and closure of the valve over cardiac cycles. The relative geometric orifice area was calculated using in-house matrix laboratory (MATLAB) code based on the percentage of the observed opened area over the maximum observable viewing area.

Statistical Analysis

Data were tested for normality using the Kolmogorov–Smirnov test and the Shapiro–Wilk test. A two-tailed *t*-test was used to test the means between the different groups using the GraphPad Prism software, US. $p < 0.05$ was considered as statistically significant.

RESULTS

Scanning Electron Microscopy Demonstrates the Carbon Fibers of Uniform Diameter and Structure

The topology of the carbon fibers showed a uniform, smooth, and solid structure. It consisted of numerous individual carbon fibers (Figure 1A) with a uniform diameter of 7 μ m. The carbon fibers had no visible defects such as cracks, pits, or splits, and no

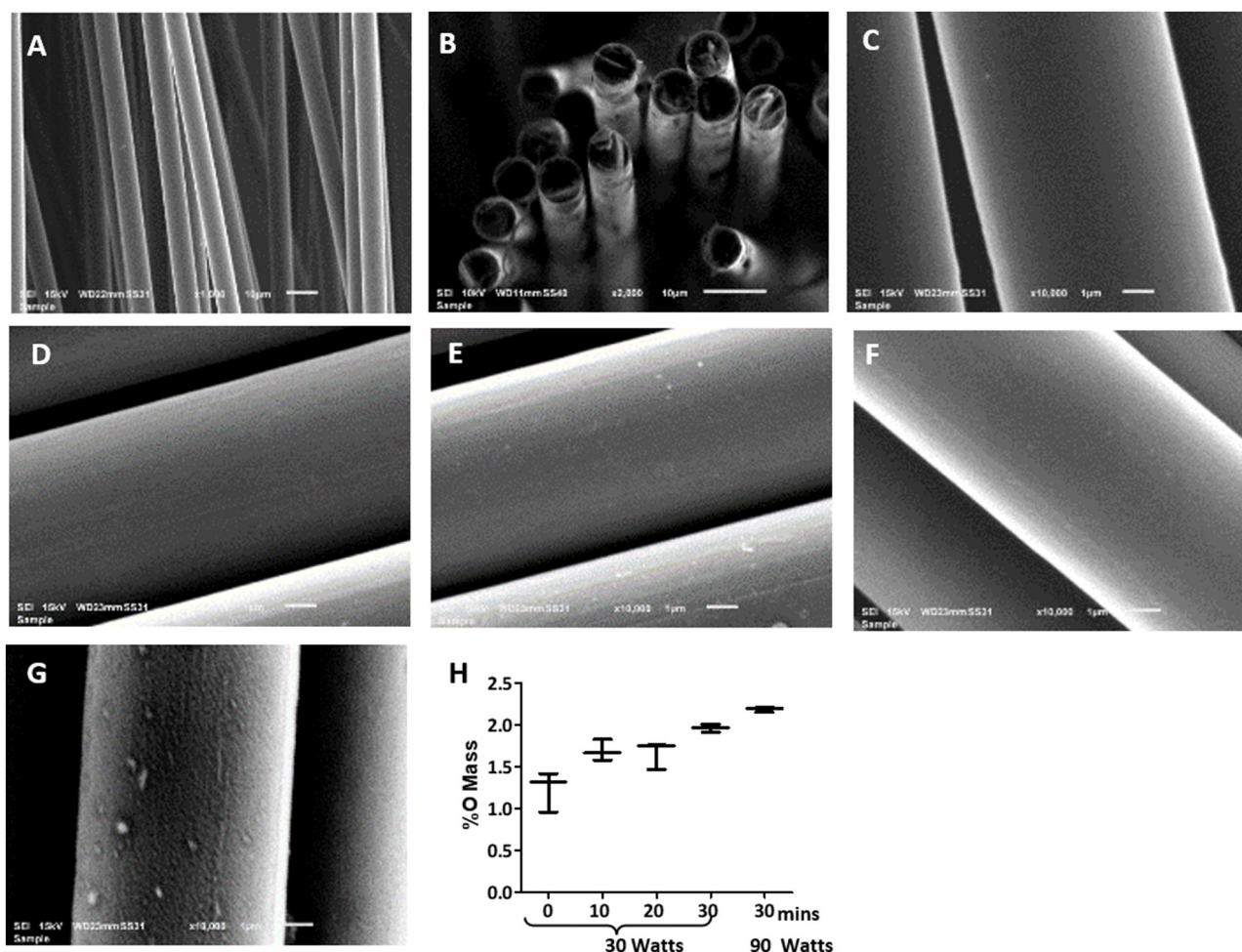


FIGURE 1 | Scanning electron microscopy (SEM) images of uniform diameter and smooth surface of the carbon fibers. Images of the pristine carbon fibers as shown in (A) 1,000X, (B) 2,000X, and (C) 10,000X magnification show the pristine carbon fibers. Images of the carbon fibers with various oxygen plasma treatment, where (D) 10 min plasma oxidation at 30 W; (E) 20 min plasma oxidation at 30 W; (F) 30 min plasma oxidation at 30 W; (G) 30 min plasma oxidation at 90 W. Surface remains smooth up to 30 min of the oxygen plasma treatment at 30 W, but significant itching was observed with 90 W treatment. (H) shows the EDS analysis of the carbon fibers surface with the increase in oxygen content with increasing the time of plasma oxidation and the wattage.

pores (Figure 1C). The cross-section of the carbon fibers showed a solid structure with no internal pores, although some staggering was observed due to uneven cutting and fracturing (Figure 1B).

Plasma Oxidation Disrupts the Smooth Surface of the Carbon Fibers

Plasma oxidation modified the carbon fibers with an oxide surface layer. The EDS showed oxygen mass increased from 1.4 to 2% with increased treatment time from untreated to 30 min at 30 W (Figure 1H). This treatment maintained the smooth surface of the carbon fibers without any signs of damage (Figures 1C–F). However, an enhanced wattage to 90 W showed the surface becoming rough with random indentations (Figure 1G) and a marginal enhancement of oxide formation to 2.1%. Therefore, it is concluded that 30 min of 30 W plasma oxidation could be administered without any damage to the

surface of the fibers. This level of plasma oxidation was used in subsequent cellular experiments with carbon fibers.

Morphology of the hADSCs on Coverslips and the Carbon Fibers

The hADSCs were able to attach and spread on the carbon fibers in an aligned and elongated manner, along the length of both the pristine and plasma oxidized carbon fibers (Figures 2A–D). In addition, the hADSCs were able to wrap around a single carbon fiber as well as form a sheet of the hADSCs across the multiple fibers. Morphology of the hADSCs on the single carbon fibers was dissimilar to the hADSCs cultured on coverslips in such that they were elongated and spindly. The hADSCs grown on coverslips showed the typical flattened, spread out morphology with numerous filopodia extending from the cell surface. On reaching confluency, the hADSCs made good contact between adjacent cells with some overlapping of cells (Figure 2F).

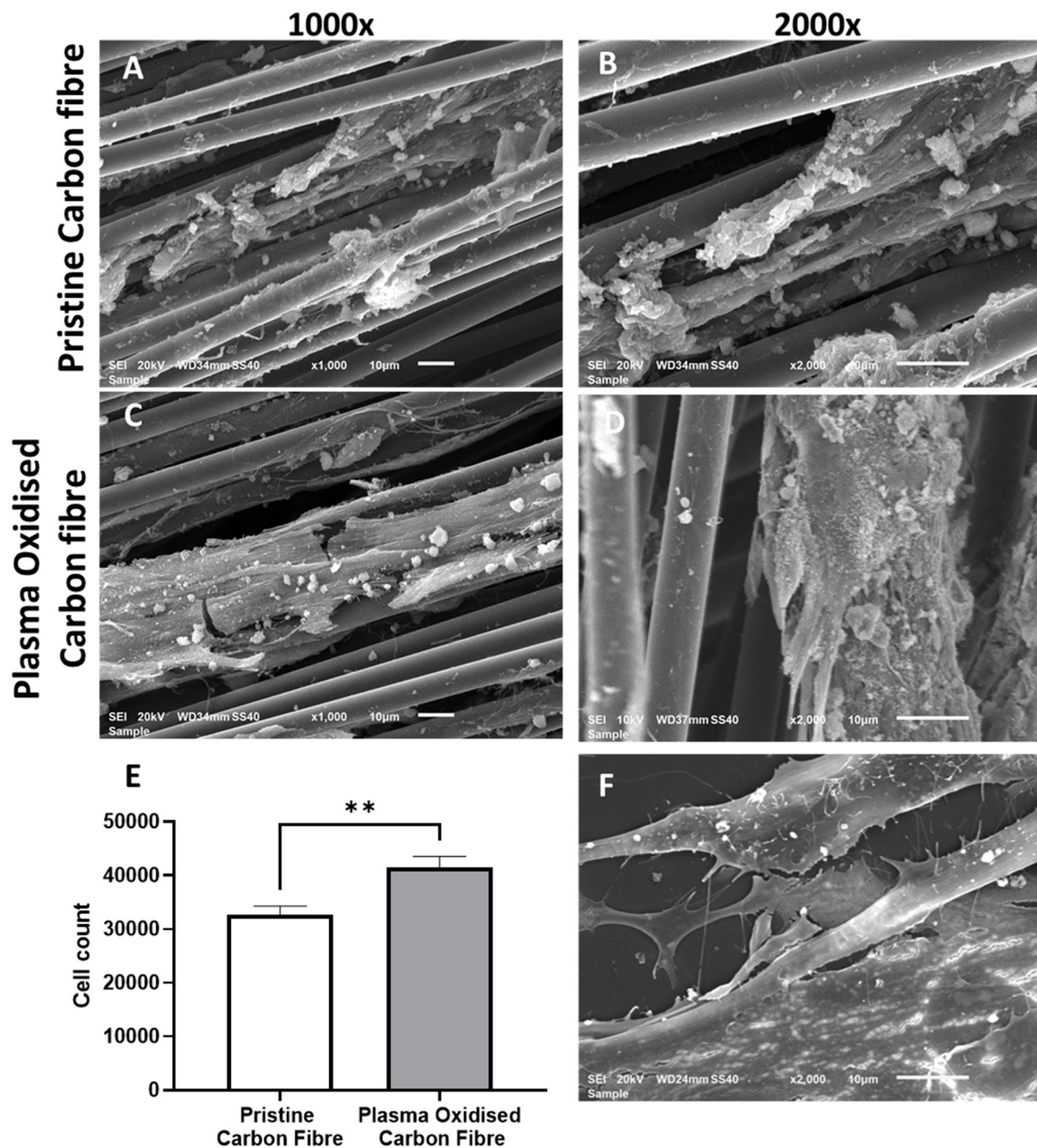
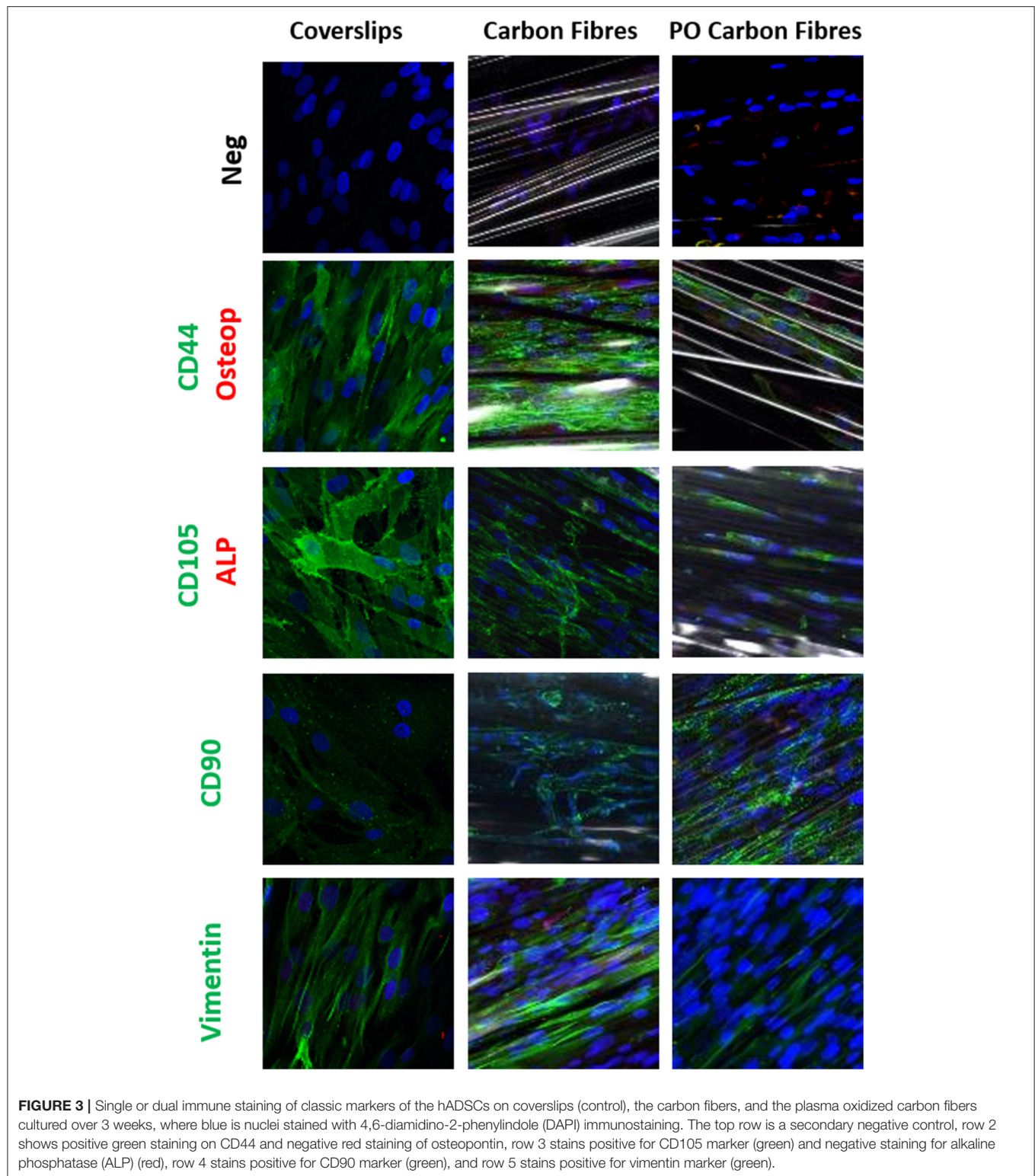


FIGURE 2 | The SEM images of the cultured human adipose-derived stem cells (hADSCs) on the pristine carbon fiber at a magnification of 1,000X (A) and 2,000X (B). (C,D) Show the cultured hADSCs on the plasma oxidized carbon fiber at a magnification of X1,000 and X2,000, respectively. (E) shows the proliferation (MTS) assay of the hADSCs on the pristine and plasma oxidized carbon fibers (* significant different with $p < 0.05$ base on the two-tailed t -test). (F) shows the SEM image of the control hADSCs on the coverslip at a magnification of X2,000.

Cell Colonization to the Carbon Fibers

Cell colonization of the hADSCs on the pristine and plasma oxidized carbon fibers was performed with and without dynamic seeding. Static seeding of 3×10^5 hADSCs to the carbon fibers resulted in poor adhesion, which was not quantifiable (not shown). This is most likely due to the settling of the hADSCs on the bottom of the well with little contact time to the carbon fibers. The dynamic seeding improved the contact time of cells

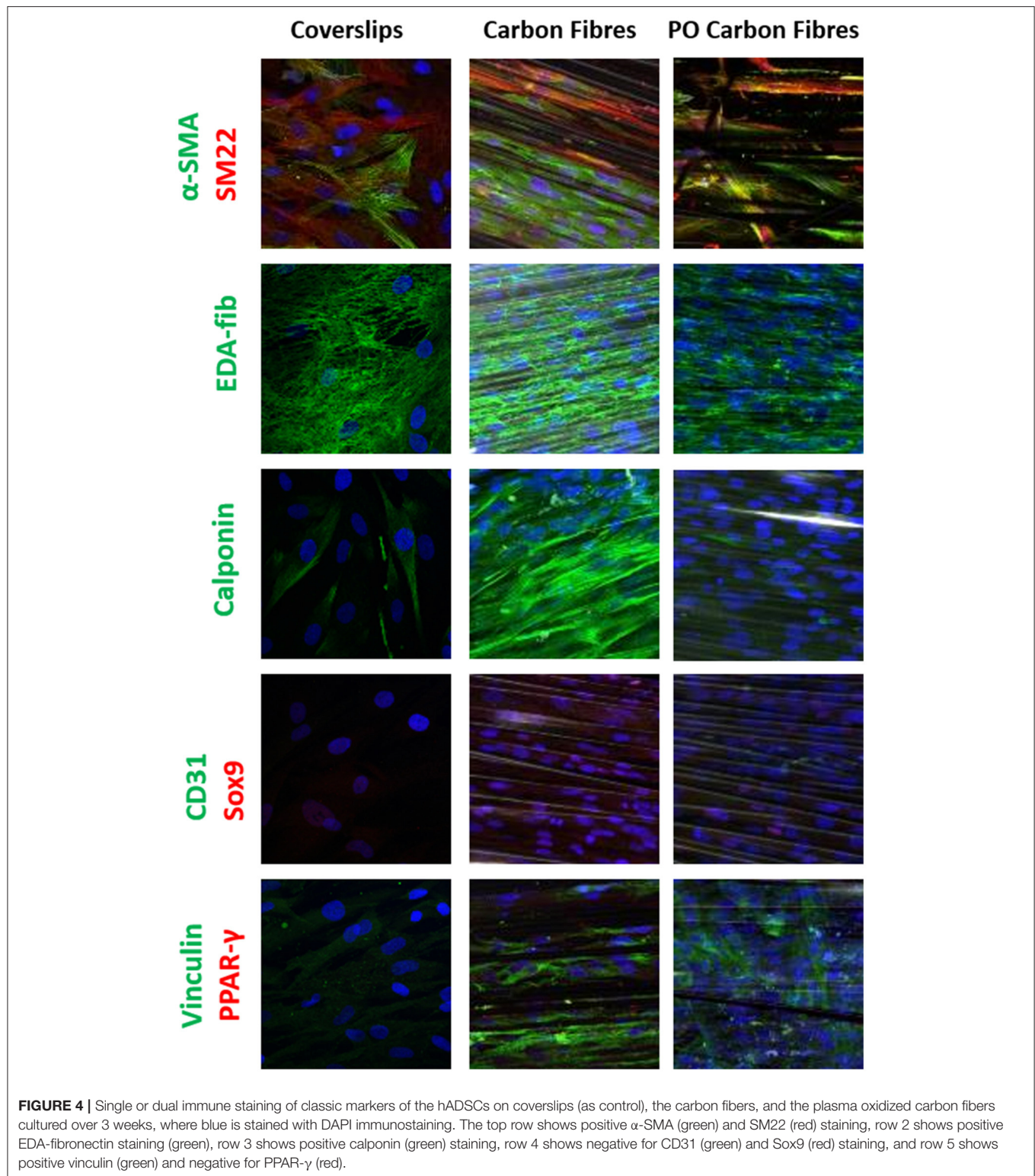
to the carbon fibers resulting in quantifiable colonization. The MTS assay showed the cell colonization on the pristine carbon fibers (mean cell number 32,662, SD 1,609), which was further significantly improved by plasma oxidation (mean cell number 41,558, SD 1,982), $p \leq 0.05$ (Figure 2E). The detected cell numbers in the non-plasma- and plasma-treated carbon fibers are 30 and 40 K, respectively. Therefore, the attachment efficiency is < 10%, as there would be some proliferation.



The Phenotype of the hADSCs on the Carbon Fibers

Immunostaining was used to compare the phenotype of the hADSCs grown on coverslips, the pristine carbon fibers, and the

plasma oxidized carbon fibers (Figures 3, 4). CD44 and CD105 were highly expressed on the hADSCs in all the 3 formats. CD90, another marker of mesenchymal stem cells, showed strong expression on both forms of the carbon fibers. The intermediate



filament protein vimentin showed consistent staining of the hADSCs on all the formats.

Differentiation of the hADSCs was assessed by using markers for myofibroblastic, adipogenic, chondrogenic, and

osteogenic differentiation. The hADSCs on coverslips showed weak homogeneous expression of SM22 (<20%) and a very low incidence of α -SMA (<10%) -positive hADSCs showed stress fiber staining. This expression was slightly higher

between coverslips and the carbon fibers (**Figure 4**), indicating a low level of myofibroblastic activation. EDA-fibronectin, an early marker of myofibroblastic differentiation, showed enhanced expression on the untreated carbon fibers, but a similar low expression on the oxidized carbon fibers. Calponin showed a marked increase in expression on the untreated carbon fibers. There was no expression of CD31 on the hADSCs in any format; however, Sox9 showed weak expression in the hADSCs on the carbon fibers. There was no expression of PPAR γ , osteopontin, or alkaline phosphatase. The expression of vinculin was enhanced on the carbon fibers (**Figure 4**).

Mechanical Properties of the Carbon Fibers

The mechanical testing of the carbon fibers was performed with multifiber strands to mimic the application scenario. Stress/strain curves were generated (**Supplementary Figure 2**) using the carbon fibers in the longitudinal direction with the mechanical properties shown in **Table 1**. The stress-strain curve showed an initial toe region, which might

TABLE 1 | Mechanical properties of the carbon fibers measured and human heart valve from literature.

| Mechanical parameter | Carbon fiber | Heart valve (21) |
|-------------------------|-------------------------|--|
| Modulus of elasticity | 140 GPa (± 4.14) | 0.015 GPa (circumferential) and 0.002 GPa (radial) |
| Failure strain | 0.039 (± 0.0036) | 0.22 (circumferential) and 0.3 (radial) |
| Ultimate tensile stress | 3.52 GPa (± 0.11) | 0.0026 GPa (circumferential) and 0.0004 GPa (radial) |

have resulted due to the initial straightening of the multiple carbon fibers strands. The modulus of elasticity, ultimate tensile stress, and failure strain of the carbon fibers were 140 (± 4.14), 3.52 (± 0.11), and 0.039 GPa (± 0.0036), respectively.

Analysis of the Range of Movement of Cusps and Sinuses

An example of a normal human valvular root stained with Alcian blue is shown in **Figure 5A**. The cusp of the valve is hinged onto the sinus wall as part of its structural support. Changes in the angles of each cusp and sinus over the cardiac cycle were measured in the region as shown in **Figures 5B, 6C**. It showed that the cusps—non-coronary cusp (NCC), right coronary cusp (RCC), and left coronary cusp (LCC) had a greater range of motion of 9–70° compared to a limited range of motion, 30–48°, for the coronary sinuses (**Table 2**).

Measurements of the radii of the sinuses and cusps during valve opening and closure, and, consequently, of the curvature, showed a maximum range of 0.09–0.50 for the LCC and 0.08–0.15 for the corresponding sinus, left coronary sinus (LCS) (**Table 3**). Curvature was similarly greater for the NCC and RCC compared to their corresponding sinuses.

Carbon Fiber Reinforced Cusp and Geometric Orifice Area of the Valve

To demonstrate the proof-of-principle that the carbon fibers can be embedded into PCL-sprayed nanofibers and maintained normal valvular cusp function, functional PCL nanofibrous heart valve roots with and without the carbon fibers (**Figure 6A**) were subjected to hydrodynamic testing in a pulse duplicator. The geometric orifice area at the end of the systolic phase in the model

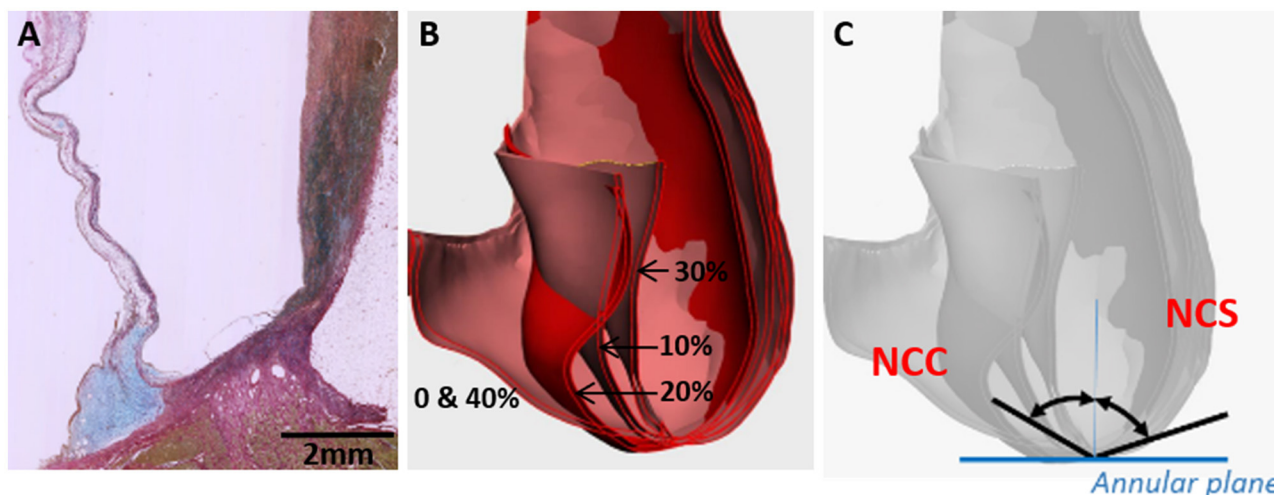


FIGURE 5 | Cross-section through a normal human valvular root stained with Alcian blue (blue) and Sirius red (pink) showing the expression of glycosaminoglycans (blue) and collagens (pink), respectively (**A**). The cusp is on the left and the sinus is on the right side. Overlaid CT images through a cross-section of a normal human valve at different phases of the systolic cycle (between 0 and 40% of the cardiac cycle is shown) (**B**) and angles, which were measured for all the 3 cusps and sinuses [non-coronary cusp shown in (**C**)].

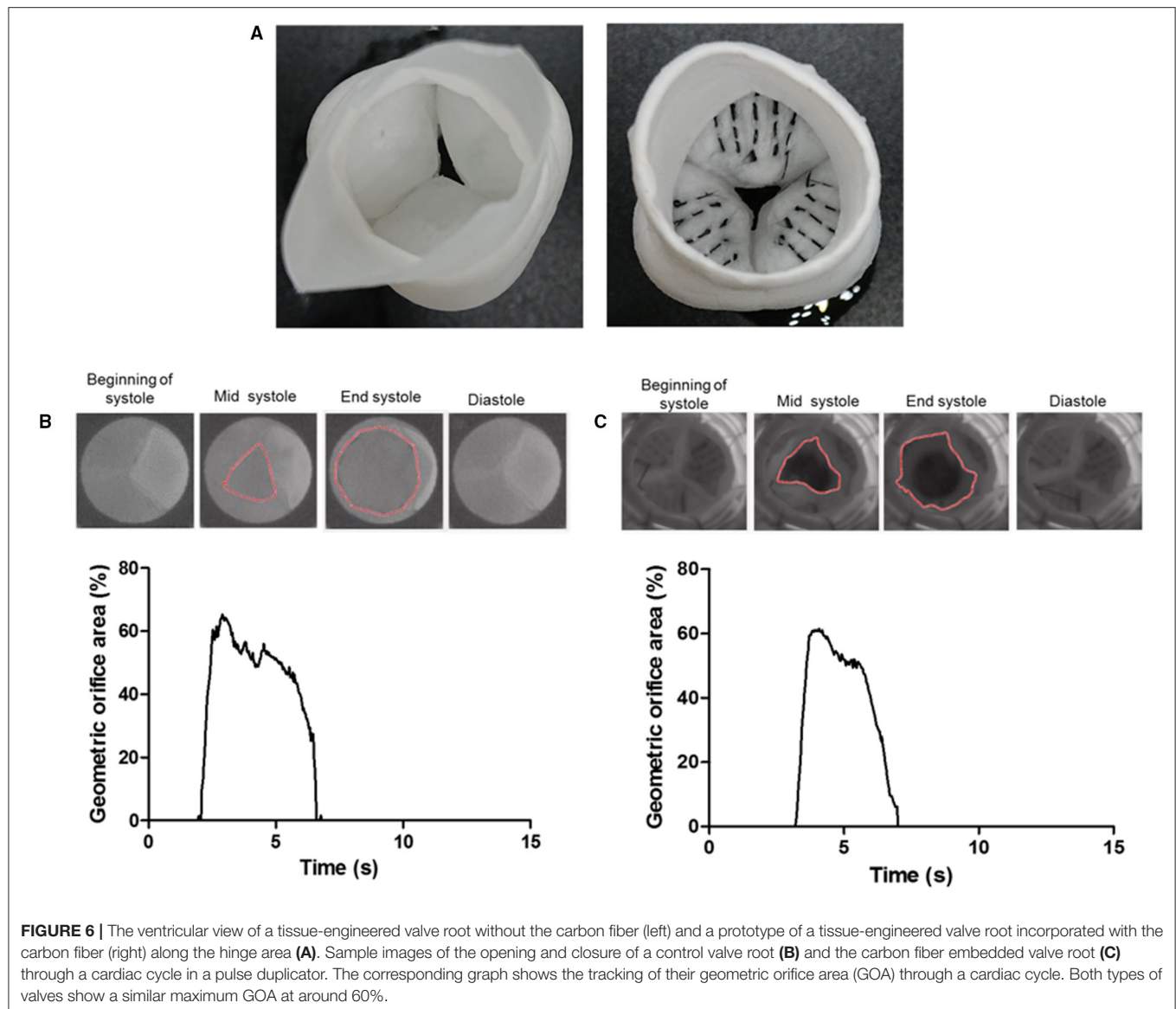


TABLE 2 | The angle of the cusps and sinuses formed to the perpendicular line going through the nadir of the annulus at different phases of the cardiac cycles.

| Phase | NCC | NCS | RCC | RCS | LCC | LCS |
|-------|--------|--------|-------|--------|--------|--------|
| 0% | 70° | 33° | 62° | 41° | 68° | 36° |
| 10% | 37° | 38° | 14° | 30° | 29° | 34° |
| 20% | 44° | 42° | 9° | 32° | 20° | 42° |
| 30% | 27° | 48° | 11° | 41° | 23° | 44° |
| 40% | 70° | 33° | 62° | 41° | 68° | 36° |
| Range | 27–70° | 33–48° | 9–62° | 30–41° | 20–68° | 34–44° |

NCC, non-coronary cusp; NCS, non-coronary sinus; RCC, right coronary cusp; RCS, right coronary sinus; LCC, left coronary cusp; LCS, left coronary sinus.

without the carbon fibers was 65% and this was very similar to the model with the carbon fibers at 62%. Both the models closed fully in the diastolic phase (**Figures 6B,C**).

DISCUSSION

In a load-bearing application such as the heart valve, biodegradable materials present a significant challenge in balancing the rate of polymer degradation vs. the continued mechanical function of the construct (2). Therefore, a strategy that incorporates the carbon fibers into the tissue-engineered constructs to ensure the continued function is proposed in this study.

Carbon fiber is a well-established material that is currently used in the construction industry such as suspension bridges for its superior strength, fatigue resistance, durability, flexibility, and elastic recovery. Thus, strategic incorporation of the carbon fibers into a biodegradable scaffold can ensure the continued load-bearing function of the targeted tissue. In addition, previous *in-vitro* and *in-vivo* studies on the other carbon fibers have yielded controversial results showing that the carbon fibers induced

TABLE 3 | Radius (mm) of the first third of cusp mid-curve and sinus mid-curve.

| Phase | NCC | NCS | RCC | RCS | LCC | LCS |
|-------|------|-----|--------|------|------|--------|
| 0% | 12 | 5 | 11 | 12 | 11 | 6.5 |
| 10% | 3 | 6 | 3 | 9 | 2 | 12 |
| 20% | 4.5 | 5.5 | 4 | 10 | 5 | 8 |
| 30% | 3 | 7 | 2.5 | 11 | 2 | 11 |
| 40% | 12 | 5 | 11 | 12 | 11 | 6.5 |
| Range | 3–12 | 5–7 | 2.5–11 | 9–12 | 2–11 | 6.5–12 |

NCC, non-coronary cusp; NCS, non-coronary sinus; RCC, right coronary cusp; RCS, right coronary sinus; LCC, left coronary cusp; LCS, left coronary sinus.

the growth of new tissue (11, 22) and other studies yielded opposite results (23, 24). Bone, ligaments, and tendon application have been previously the main focus of biocompatibility studies for carbon fibers. With the increased interest in regenerative medicine and tissue engineering, the interaction of the carbon fibers with stem cells is now relevant but has not been tested. In this study, we demonstrate that the carbon fibers are compatible with the hADSCs, support ECM deposition as evidenced by the expression of EDA-fibronectin, have superior strength, and are flexible enough to allow the free movement of the valve cusps when stitched into a tissue-engineered valve construct from the sinus wall, across the hinge region and into the belly of the cusp. This study has shown the potential use of these carbon fibers in heart valve tissue engineering.

We chose to examine the biocompatibility of the carbon fibers with the hADSCs since these cells are good candidates in seeding scaffolds for *in-vitro* tissue engineering strategies (25). In addition, the differentiation capacity of the hADSCs permits these cells to serve as an indicator for conditions that may favor the expression of adipogenic, chondrogenic, and osteogenic cell phenotypes (26). The hADSCs were able to adhere to the smooth surface of the pristine carbon fibers as shown with the SEM images and the MTS assay (**Figure 2**). Furthermore, the number of cells adhering could be significantly enhanced by prior activation of the surface by plasma oxidation, a process that leads to the production of acid oxides on the surface of the carbon fibers that enhances surface hydrophilicity, thereby enhancing surface activation energy suitable for matrix bonding (27).

The hADSCs that were cultured onto the carbon fibers retained their stem cell phenotype with no evidence of differentiation into adipogenic, chondrogenic, osteogenic, or endothelial cell phenotypes. However, there was some myofibroblastic differentiation with upregulation of α -SMA, calponin, and EDA-fibronectin. The plasma oxidized carbon fiber reduced this level of activation. The lack of differentiation to other phenotypes indicates that the cells are essentially inert to the carbon fibers as previously reported (28). With respect to *in vitro* heart valve tissue engineering, the use of hADSCs and the carbon fibers may prove useful especially, as the hADSCs were shown to retain their phenotype and specific differentiation can be induced and guided by the application of growth factors, peptides, and compounds. We have previously shown that using an active lysine-threonine-threonine-lysine-serine (KTTKS) peptide motif enhanced the secretion of

ECM components (29) and using specific motifs can drive the expression of tissue-specific ECM proteins. Combining surface activation with plasma oxidation, the carbon fibers can be easily linked to specific bioactive peptides or biomolecules through carbodiimide chemistry.

The native heart valves have mechanical stiffness in the range of 1 to 2 MPa in the radial and 10 to 20 MPa in the circumferential directions, with ultimate tensile stress (UTS) of 0.4 MPa in the radial and 2.6 MPa in the circumferential directions (21, 30, 31) as shown in **Table 1** and a typical polymeric porous scaffold used in heart valve tissue engineering has significantly lower mechanical stiffness in the range of 3 to 6 MPa and UTS in the range of 0.4 to 0.7 MPa (31) due to its porous nature to allow for cell colonization. Furthermore, tissue-engineered scaffolds suffer from further deterioration during long implantation periods due to biodegradation and repetitive stress. The engineering application of carbon fibers has been used extensively as a reinforcement component in composite materials due to their ultra-high strength. Therefore, the carbon fiber could be used to form part of a composite scaffold to reinforce it. Mechanical testing of the carbon fibers showed them to have an extremely high modulus of 140 GP (± 4.14) and ultimate tensile strength at 3.52 Gpa (± 0.11) in the direction of the carbon fibers. These fall in the range of the other carbon fibers produced from PAN and mesophase pitch (MPP) (32).

Despite the high modulus of the carbon fibers, one important design constraint with the carbon fibers was that they became brittle and snapped if they were forced to bend at a sharp 90° angle. This has been reported previously when used in reconstruction for chronic anterior cruciate ligaments, where they found that the carbon fibers broke under twisting or angular forces (33). The brittleness of the carbon fibers at a sharp 90° angle could be a design constraint for heart valve tissue engineering. As a first step, we calculated the angle between the sinus wall and the valve cusp varied during the opening and closing phases of the valve. CT-based analysis of the movement of the aortic cusps in relation to each corresponding sinus showed a great range of movement of the cusps and a maintained curvature at the hinge area, despite the significant changes in angles in the hinge area. These calculations showed that the angle between the sinus wall and each of the three valve cusps did not exceed a 90° angle. Furthermore, as a proof-of-principle, the embedding of carbon fibers across the radial direction of the tissue-engineered heart valve showed that the geometric orifice area and leaflet motion of a tissue-engineered valve in a bioreactor were unaffected by the incorporation of the carbon fibers. In this configuration, the carbon fibers utilized the sinus wall as a pillar in a suspension bridge to transfer the load on the valvular cusp during the diastolic phase, while allowing the heart valve to open without significant obstruction.

This study establishes the potential utility of the carbon fibers in tissue-engineered heart valves. There remain several additional studies that are required to assess if the carbon fibers will provide any benefit to the durability and function of tissue-engineered heart valves. The carbon fibers used in this study were sewn into the cusps in a radially orientated line across the width of the cusp; these carbon fibers may not necessarily be the optimal width

apart or in the best orientation. Further studies are required to establish the potential long-term benefits of the reinforcement of scaffold material on the durability and functions of tissue-engineered heart valves both *in vitro* and *in vivo* studies. This study has used one cell type to assess the biocompatibility of the carbon fibers. Previous studies have also shown the carbon fibers to be compatible with cells, but this may be dependent upon the types of carbon fiber used (34–36). Assessment of the cellularization of scaffold materials containing the carbon fibers *in vivo* will be the ultimate test of biocompatibility.

CONCLUSION AND FUTURE STUDY

In this study, we demonstrated that the carbon fibers can be populated by the hADSCs without stimulating their differentiation. The carbon fibers were sufficiently flexible to be incorporated into an *in vitro* functioning tissue-engineered heart valve without restricting the motion of the cusps. Further study is required to optimize the carbon fiber distribution/pattern and embedding method in order to optimize their potential to enhance the durability and hemodynamic performance of tissue-engineered heart valves.

DATA AVAILABILITY STATEMENT

The original contributions presented in the study are included in the article/**Supplementary Material**, further inquiries can be directed to the corresponding author/s.

REFERENCES

- Zilla P, Bezuidenhout D, Human P. Prosthetic vascular grafts: wrong models, wrong questions and no healing. *Biomaterials*. (2007) 28:5009–27. doi: 10.1016/j.biomaterials.2007.07.017
- Zilla P, Deutsch M, Bezuidenhout D, Davies NH, Pennel T. Progressive reinvention or destination lost? half a century of cardiovascular tissue engineering. *Front Cardiovasc Med*. (2020) 7:159. doi: 10.3389/fcvm.2020.00159
- Berger K, Sauvage LR, Rao AM, Wood SJ. Healing of arterial prostheses in man: its incompleteness. *Ann Surg*. (1972) 175:118–27. doi: 10.1097/0000658-197201000-00018
- Pennel T, Zilla P, Bezuidenhout D. Differentiating transmural from transanastomotic prosthetic graft endothelialization through an isolation loop-graft model. *J Vasc Surg*. (2013) 58:1053–61. doi: 10.1016/j.jvs.2012.11.093
- Liberski A, Ayad N, Wojciechowska D, Zielińska D, Struszczyk MH, Latif N, et al. Knitting for heart valve tissue engineering. *Glob Cardiol Sci Pract*. (2016) 2016:e201631. doi: 10.21542/gcsp.2016.31
- Lieshout MV, Peters G, Rutten M, Baaijens F. A knitted, fibrin-covered polycaprolactone scaffold for tissue engineering of the aortic valve. *Tissue Eng*. (2006) 12:481–7. doi: 10.1089/ten.2006.12.481
- Albanna MZ, Bou-Akl TH, Walters HL, Matthew HWT. Improving the mechanical properties of chitosan-based heart valve scaffolds using chitosan fibers. *J Mech Behav Biomed Mater*. (2012) 5:171–80. doi: 10.1016/j.jmbbm.2011.08.021
- Vaessen A, Pidancier C, Chakfe N, Heim F. Hybrid textile heart valve prosthesis: preliminary in vitro evaluation. *Biomed Tech*. (2018) 63:333–9. doi: 10.1515/bmt-2016-0083
- Heim F, Gupta BS. Textile heart valve prosthesis: the effect of fabric construction parameters on long-term durability. *Tex Res J*. (2009) 79:1001–13. doi: 10.1177/0040517507101457
- Strover AE, Firer P. The use of carbon fiber implants in anterior cruciate ligament surgery. *Clin Orthop Relat Res*. (1985) 88–98. doi: 10.1097/00003086-198506000-00014
- Jenkins DH, Forster IW, McKibbin B, Ralis ZA. Induction of tendon and ligament formation by carbon implants. *J Bone Joint Surg Br*. (1977) 59:53–7. doi: 10.1302/0301-620X.59B1.845228
- Alexander H, Weiss AB, Parsons JR. Ligament and tendon repair with an absorbable polymer-coated carbon fiber stent. *Bull Hosp Jt Dis Orthop Inst*. (1986) 46:155–73.
- Lewandowska-Szumieł M, Komender J, Chłopek J. Interaction between carbon composites and bone after intrabone implantation. *J Biomed Mater Res*. (1999) 48:289–296.
- Brantigan JW, Steffee AD. Carbon fiber implant to aid interbody lumbar fusion: 1-year clinical results in the first 26 patients. In: Yonenobu K, Ono K, Takemitsu Y, editors. *Lumbar Fusion and Stabilization*. Tokyo: Springer Japan. p. 379–95. doi: 10.1007/978-4-431-68234-9_41
- Baba K, Mikhailov A, Sankai Y. Long-term safety of the carbon fiber as an implant scaffold material. In: *2019 41st Annual International Conference of the IEEE Engineering in Medicine and Biology Society (embc)*. New York, NY: IEEE. p. 1105–10. doi: 10.1109/EMBC.2019.8856629
- Ortega Z, Alemán ME, Donate R. Nanofibers and microfibers for osteochondral tissue engineering. *Adv Exp Med Biol*. (2018) 1058:97–123. doi: 10.1007/978-3-319-76711-6_5
- Vearick SB, Demétrio KB, Xavier RG, Moreschi AH, Muller AF, Dos Santos LAL, et al. Fiber-reinforced silicone for tracheobronchial stents: an experimental study. *J Mech Behav Biomed Mater*. (2018) 77:494–500. doi: 10.1016/j.jmbbm.2017.10.013

ETHICS STATEMENT

The studies involving human participants were reviewed and approved by Aswan Heart Science Centre Ethics Committee. The patients/participants provided their written informed consent to participate in this study.

AUTHOR CONTRIBUTIONS

YT-T and NL contributed to the experimental plan, concept, data collection, analysis, and writing of the manuscript. NG and HA contributed to the concept. PS, AM, AE, NS, MN, and H-EN contributed to the data collection and analysis. MY and AC involved in the concept and editing and reviewing of the manuscript. All authors contributed to the article and approved the submitted version.

FUNDING

We would like to thank the Magdi Yacoub Institute for funding this study.

SUPPLEMENTARY MATERIAL

The Supplementary Material for this article can be found online at: <https://www.frontiersin.org/articles/10.3389/fcvm.2021.793898/full#supplementary-material>

18. Balasubramanian M. *Composite Materials And Processing*. Amsterdam: Elsevier (2017).
19. Colazzo F, Sarathchandra P, Smolenski RT, Chester AH, Tseng Y-T, Czernuszka JT, et al. Extracellular matrix production by adipose-derived stem cells: implications for heart valve tissue engineering. *Biomaterials*. (2011) 32:119–27. doi: 10.1016/j.biomaterials.2010.09.003
20. Sohler J, Carubelli I, Sarathchandra P, Latif N, Chester AH, Yacoub MH. The potential of anisotropic matrices as substrate for heart valve engineering. *Biomaterials*. (2014) 35:1833–44. doi: 10.1016/j.biomaterials.2013.10.061
21. Balgud A, Rubbens MP, Mol A, Bank RA, Bogers AJJC, van Kats JP, et al. The role of collagen cross-links in biomechanical behavior of human aortic heart valve leaflets—relevance for tissue engineering. *Tissue Eng*. (2007) 13:1501–11. doi: 10.1089/ten.2006.0279
22. Jenkins DH. The repair of cruciate ligaments with flexible carbon fibre. a longer term study of the induction of new ligaments and of the fate of the implanted carbon. *J Bone Joint Surg Br*. (1978) 60:520–522. doi: 10.1302/0301-620X.60B4.711800
23. Pesakova V, Klezl Z, Balik K, Adam M. Biomechanical and biological properties of the implant material carbon-carbon composite covered with pyrolytic carbon. *J Mater Sci Mater Med*. (2000) 11:793–8.
24. Rohe K, Braun A, Cotta H. Carbon band implants in animal experiments. light and transmission electron microscopy studies of biocompatibility. *Z Orthop Ihre*. (1986) 124:569–77. doi: 10.1055/s-2008-1045002
25. Hassan M, Latif N, Yacoub M. Adipose tissue: friend or foe? *Nat Rev Cardiol*. (2012) 9:689–702. doi: 10.1038/nrcardio.2012.148
26. Gir P, Oni G, Brown SA, Mojallal A, Rohrich RJ. Human adipose stem cells: current clinical applications. *Plast Reconstr Surg*. (2012) 129:1277–90. doi: 10.1097/PRS.0b013e31824ecae6
27. Boroj MB, Shoushtari AM, Sabet EN, Haji A. Influence of oxygen plasma treatment parameters on the properties of carbon fiber. *J Adhes Sci Technol*. (2016) 30:2372–82. doi: 10.1080/01694243.2016.1182833
28. Rajzer I, Menaszek E, Bacakova L, Rom M, Blazewicz M. In vitro and in vivo studies on biocompatibility of carbon fibres. *J Mater Sci Mater Med*. (2010) 21:2611–22. doi: 10.1007/s10856-010-4108-3
29. Krishnamoorthy N, Tseng Y, Gajendrarao P, Sarathchandra P, McCormack A, Carubelli I, et al. Strategy to enhance secretion of extracellular matrix components by stem cells: relevance to tissue engineering. *Tissue Eng Part A*. (2018) 24:145–56. doi: 10.1089/ten.tea.2017.0060
30. Pham T, Sulejmani F, Shin E, Wang D, Sun W. Quantification and comparison of the mechanical properties of four human cardiac valves. *Acta Biomater*. (2017) 54:345–55. doi: 10.1016/j.actbio.2017.03.026
31. Hasan A, Ragaert K, Swieszkowski W, Selimović Š, Paul A, Camci-Unal G, et al. Biomechanical properties of native and tissue engineered heart valve constructs. *J Biomech*. (2014) 47:1949–63. doi: 10.1016/j.jbiomech.2013.09.023
32. Loidl D, Peterlik H, Paris O, Muller M, Burghammer M, Riekel C. Structure and mechanical properties of carbon fibres: a review of recent microbeam diffraction studies with synchrotron radiation. *J Synchrotron Radiat*. (2005) 12:758–64. doi: 10.1107/S0909049505013440
33. Bray RC, Flanagan JP, Dandy DJ. Reconstruction for chronic anterior cruciate instability. a comparison of two methods after six years. *J Bone Joint Surg Br*. (1988) 70:100–5. doi: 10.1302/0301-620X.70B1.3339039
34. Blazewicz M. Carbon materials in the treatment of soft and hard tissue injuries. *Eur Cell Mater*. (2001) 2:21–9. doi: 10.22203/eCM.v002a03
35. Grabinski C, Hussain S, Lafdi K, Braydich-Stolle L, Schlager J. Effect of particle dimension on biocompatibility of carbon nanomaterials. *Carbon N Y*. (2007) 45:2828–35. doi: 10.1016/j.carbon.2007.08.039
36. Elias KL, Price RL, Webster TJ. Enhanced functions of osteoblasts on nanometer diameter carbon fibers. *Biomaterials*. (2002) 23:3279–87. doi: 10.1016/S0142-9612(02)00087-X

Conflict of Interest: The authors declare that the research was conducted in the absence of any commercial or financial relationships that could be construed as a potential conflict of interest.

Publisher's Note: All claims expressed in this article are solely those of the authors and do not necessarily represent those of their affiliated organizations, or those of the publisher, the editors and the reviewers. Any product that may be evaluated in this article, or claim that may be made by its manufacturer, is not guaranteed or endorsed by the publisher.

Copyright © 2021 Tseng, Grace, Aguib, Sarathchandra, McCormack, Ebeid, Shehata, Nagy, El-Nashar, Yacoub, Chester and Latif. This is an open-access article distributed under the terms of the Creative Commons Attribution License (CC BY). The use, distribution or reproduction in other forums is permitted, provided the original author(s) and the copyright owner(s) are credited and that the original publication in this journal is cited, in accordance with accepted academic practice. No use, distribution or reproduction is permitted which does not comply with these terms.



Recent Progress in *in vitro* Models for Atherosclerosis Studies

Jun Chen^{1†}, Xixi Zhang^{1†}, Reid Millican², Tyler Lynd¹, Manas Gangasani¹, Shubh Malhotra¹, Jennifer Sherwood², Patrick Taejoon Hwang², Younghye Cho^{1,3}, Brigitta C. Brott^{1,2,4}, Gangjian Qin¹, Hanjoong Jo⁵, Young-sup Yoon^{6,7} and Ho-Wook Jun^{1,2*}

¹ Department of Biomedical Engineering, The University of Alabama at Birmingham, Birmingham, AL, United States,

² Endomimetics, LLC., Birmingham, AL, United States, ³ Family Medicine Clinic, Obesity, Metabolism, and Nutrition Center and Research Institute of Convergence of Biomedical Science and Technology, Pusan National University Yangsan Hospital, Yangsan, South Korea, ⁴ Division of Cardiovascular Disease, School of Medicine, The University of Alabama at Birmingham, Birmingham, AL, United States, ⁵ Wallace H. Coulter Department of Biomedical Engineering, Georgia Institute of Technology and Emory University, Atlanta, GA, United States, ⁶ Division of Cardiology, Department of Medicine, Emory University, Atlanta, GA, United States, ⁷ Severance Biomedical Science Institute, Yonsei University College of Medicine, Seoul, South Korea

OPEN ACCESS

Edited by:

Anthal Smits,
Eindhoven University of
Technology, Netherlands

Reviewed by:

Ayman Al Haj Zen,
Hamad Bin Khalifa University, Qatar
Claudia Goettsch,
RWTH Aachen University, Germany

*Correspondence:

Ho-Wook Jun
hwjun@uab.edu

[†]These authors have contributed
equally to this work and share first
authorship

Specialty section:

This article was submitted to
Heart Valve Disease,
a section of the journal
Frontiers in Cardiovascular Medicine

Received: 06 October 2021

Accepted: 21 December 2021

Published: 27 January 2022

Citation:

Chen J, Zhang X, Millican R, Lynd T, Gangasani M, Malhotra S, Sherwood J, Hwang PT, Cho Y, Brott BC, Qin G, Jo H, Yoon Y-s and Jun H-W (2022) Recent Progress in *in vitro* Models for Atherosclerosis Studies. *Front. Cardiovasc. Med.* 8:790529. doi: 10.3389/fcvm.2021.790529

Atherosclerosis is the primary cause of hardening and narrowing arteries, leading to cardiovascular disease accounting for the high mortality in the United States. For developing effective treatments for atherosclerosis, considerable efforts have been devoted to developing *in vitro* models. Compared to animal models, *in vitro* models can provide great opportunities to obtain data more efficiently, economically. Therefore, this review discusses the recent progress in *in vitro* models for atherosclerosis studies, including traditional two-dimensional (2D) systems cultured on the tissue culture plate, 2D cell sheets, and recently emerged microfluidic chip models with 2D culture. In addition, advanced *in vitro* three-dimensional models such as spheroids, cell-laden hydrogel constructs, tissue-engineered blood vessels, and vessel-on-a-chip will also be covered. Moreover, the functions of these models are also summarized along with model discussion. Lastly, the future perspectives of this field are discussed.

Keywords: atherosclerosis, disease models, tissue-engineered blood vessels, microfluidic chips, *in vitro* models and methods

INTRODUCTION

Cardiovascular disease (CVD) is the severest global health concern and the primary leading cause of mortality in the United States, resulting primarily from atherosclerosis (1, 2). *In vivo* models, ranging from rats to pigs to non-human primates, have been employed as the gold standard to explore valuable insights into atherosclerosis and predict novel drug safety and efficacy for atherosclerosis treatment (3, 4). However, current *in vivo* atherosclerosis models suffer issues, such as inevitable interspecies differences in the genome, biological varieties, limited genetic variability, and low throughput. In particular, large-sized *in vivo* atherosclerosis model development requires a costly high-fat diet, genetic manipulation, and extensively long induction time, leading to a prolonged life cycle of pharmaceutical research with increased expense (3). In addition, these issues in large animal models also have hindered the widespread use of these systems in research. In contrast, the induction of atherosclerosis models in small animals, such as mice and rabbits, is cheaper and less time consuming; however, these models commonly develop atherosclerotic lesions in carotid arteries and aortic arches, different from the patients who often develop atherosclerosis

in their coronary arteries (3, 4). Given these unsolved issues, there is a high chance that the newly discovered lead compounds showing therapeutic efficacy in the animal models would fail to demonstrate comparable efficacy in patients. In comparison to *in vivo* models, *in vitro* models provide great opportunities to assess drug efficiency and toxicity as well as explore biological mechanisms in a reproducible, economical, high throughput, and controllable manner (5, 6). Those advantages render them valuable platforms for atherosclerosis-associated mechanistic investigations and new therapy development.

In vitro models are usually classified into 2D and 3D models. The traditional *in vitro* 2D models generally refer to the monolayer of cells created by seeding cells on the tissue culture plates (TCP) followed by cell culture in a static condition. In this system, the cells usually adhere and spread on the flat surface. Due to their high availability and low cost, such systems are the most widely used to evaluate drug efficacy and toxicity and study biological processes. In addition to the traditional 2D systems, cell sheet tissue engineering and microfluidic technology have brought about tissue-engineered 2D cell sheets and microfluidic chips with 2D culture to improve the recapitulation of the human physiological and pathological environment (7–9). However, despite being more advanced than traditional 2D systems, both models still cannot faithfully replicate the human pathophysiology, thereby encouraging more advanced *in vitro* models. An ideal *in vitro* system should emulate the 3D human tissue architecture with proper cellular components and disease features. Therefore, a considerable effort has been made to develop *in vitro* 3D models with structures that mimic human 3D tissues for modeling pathological processes for elucidating disease development and new drug evaluation, ranging from cancer (10), the blood-brain barrier (11, 12), neurodegenerative diseases (13), cardiac fibrosis (14), to atherosclerosis (15).

In this review, we summarize the recent progress in *in vitro* models for atherosclerosis studies, including 2D *in vitro* models, such as traditional 2D cultures on TCP, 2D tissue-engineered cell sheets, and newly emerging microfluidic chip models with 2D culture. Moreover, we discuss the state-of-the-art *in vitro* three-dimensional (3D) models in the context of spheroids, cell-laden hydrogel constructs, tissue-engineered blood vessels (TEBVs), and vessel-on-a-chips (**Figure 1**). Pathology of atherosclerosis is also included to facilitate understanding of these models and their applications for mechanistic studies. Lastly, we also highlight the future perspectives of this field.

PATHOLOGY OF ATHEROSCLEROSIS

Atherosclerosis, a chronic inflammatory disease, results in plaque formation within the intimal layer of arteries (22). Several risk factors can increase the likelihood of atherosclerosis development. The most well-known is low-density lipoprotein cholesterol (LDL-C). Typically, atherosclerosis is initiated by the passage of LDL-C through arterial endothelium and accumulates within the intima, which induces endothelial dysfunction with adhesion molecule expression, an essentially biological process for atherosclerosis initiation (**Figure 2A**) (23). Similar to LDL-C,

an abnormal and turbulent flow within the arterial lumen also elevates the risk of atherosclerosis by inducing adhesive molecule expression (24). High-density lipoprotein cholesterol (HDL-C) is inversely related to the risk of developing atherosclerosis; however, evidence suggests no protective role for HDL-C against atherosclerosis (25). The seemingly futile behavior could be due to compositional and functional modifications of HDL-C by inflammatory mediators (26). Other risk factors may include hypertension, chronic kidney disease, aging, and hyperglycemia (27).

Although there is controversy, the most prevalent theory describes the progression of atherosclerosis strongly depending on the activation of the inflammatory response; thus, circulating monocytes, critical players within innate immunity playing a crucial role in inflammation activation. Specifically, those monocytes are responsible for infiltrating the lesion site, differentiating into macrophages, and internalizing oxidized LDL (Ox-LDL) that gives rise to foam cells, the primary cellular components found in the plaque, thereby triggering an inflammatory reaction (**Figure 2B**) (23, 28). Additionally, some evidence suggests that macrophages may locally proliferate to accelerate foam cell genesis (29). As the disease progresses, a fatty streak composed of aggregated foam cells forms in the lesion and further aggravates the inflammation. As the disease advances by increased inflammation, an atheroma may grow in the lesion and becomes increasingly fibrous. With the inflammation continuously becoming severe, local cells undergo apoptosis. The intense inflammatory response in the plaque may be mitigated if efferocytosis occurs, whereby macrophages clear apoptotic cells; however, in most cases, as the atherosclerotic plaque advances, macrophages experience cellular reprogramming that restrains their efferocytotic capacity. As more and more apoptotic cells fail to be removed, a necrotic core forms within the lesion (**Figure 2C**) (23, 30).

In addition to monocytes and macrophages, smooth muscle cells (SMCs) play a vital but paradoxical role in atherosclerosis by either advancing or protecting disease progression. Since SMCs are not terminally differentiated, they undergo phenotype transition in an atherosclerotic environment. The phenotype variations of SMCs may implicate a loss of contractility, reduced SMC contractile markers, increased proliferation and migration of SMCs (31), and upregulated production of proteoglycans. It is worth noting that SMCs can express macrophage and endothelial cell markers instigating ambiguity among the atherosclerotic players. Additionally, recent studies showed that SMCs could transform into macrophage-like cells, internalize Ox-LDL, and become foam cells (31, 32), thus contributing to the generation of the necrotic core and promoting atherosclerosis progression. Despite that, SMC phenotypes can also produce a fibrous cap that stabilizes the plaque, reduces the risk of rupture, and prevents thrombus formation. Without such stabilization, the plaque may rupture, leading to thrombosis that often occurs in advanced stages of atherosclerosis (**Figure 2D**) (23). In addition, SMCs present within the atheromatous plaque may form a mineralized matrix resulting in calcium deposits. Early microcalcifications have been shown to destabilize the plaque, while more extensive

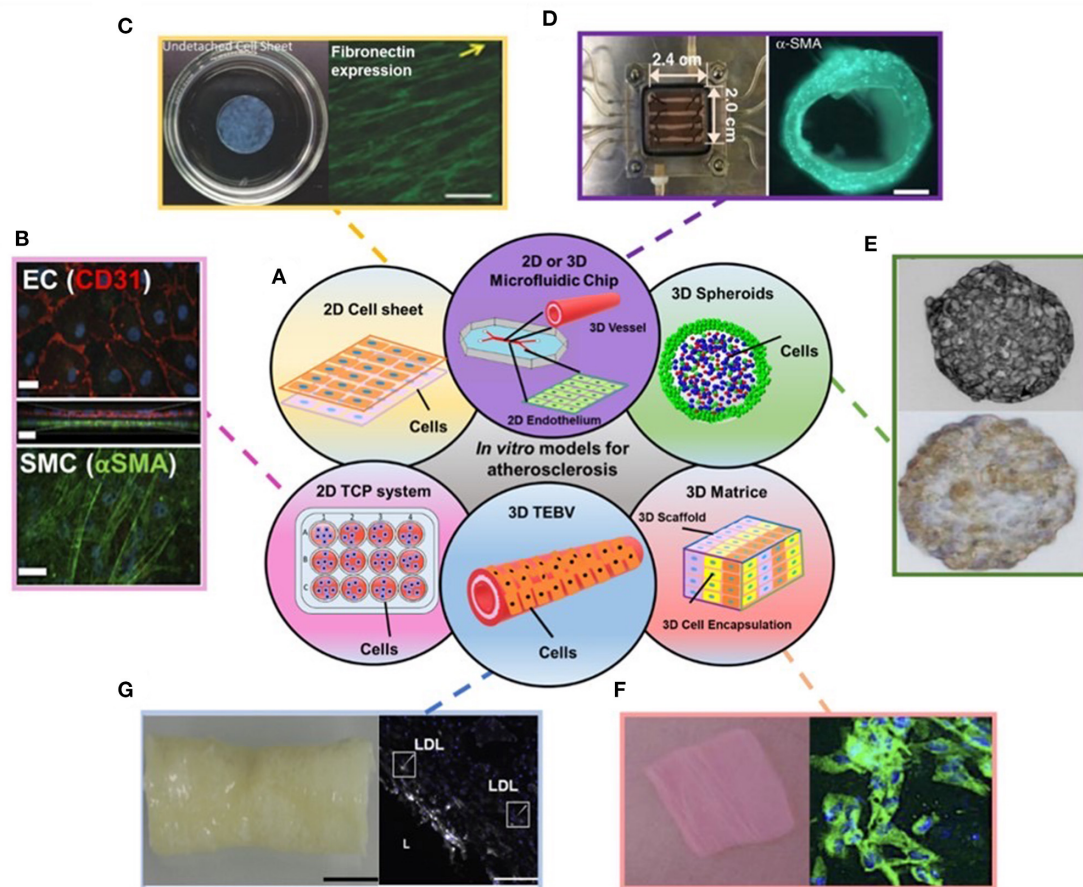


FIGURE 1 | (A) Schematic showing the disused *in vitro* models for atherosclerosis studies in the review. (B–G) Examples of data regarding different *in vitro* models covered in the review: (B) Endothelial cells (ECs) (top) and Smooth muscle cells (SMCs) (bottom) stained with EC and SMC phenotype markers in 2D transwell model. (C) 2D cell sheet (left) that expresses fibronectin (right). (D) 3D microfluidic vessel on a chip (left) made of green fluorescence protein-expressing human umbilical vein endothelial cells (right). (E) SMC spheroid (top) and EC/SMC spheroid (bottom). (F) 3D SMC laden hydrogel constructs (left) and stained with SMA- α (right, green). (G) 3D tissue-engineered blood vessels (left) and stained with monocytes and LDL (right). Adapted, with permission from (16) (B), (17) (C), (18) (D), (19) (E), (20) (F), and (21) (G).

calcifications serve as a stabilizing component to the atheroma (33, 34).

IN VITRO 2D MODELS FOR ATHEROSCLEROSIS STUDIES

2D *in vitro* models are essential for studying the pathology of various diseases and drug evaluation, which have been extensively used for decades. The most common 2D *in vitro* models are single-cell culture systems, which contain only one type of cell component observed in the atherosclerotic plaque, such as ECs, SMCs, macrophages, and foam cells. Single-cell cultures have been used to assess new types of therapeutics, such as microRNA (35, 36) and exosomes (37, 38), and investigate mechanistic studies associated with atherosclerosis. However, recently they have been widely applied for evaluating the efficacy of drug-loaded delivery systems for treating atherosclerosis due

to the issues observed in free drug administration (Table 1). Despite the wide use of single-cell models, single-cell models may not be sufficient to obtain a reliable prediction for therapeutic efficacy in patients due to their inability to mimic the native structure of vessels and features of human plaques. Thus, to gain significant insights into therapeutic efficacy and atherosclerosis pathogenesis, single-cell models are commonly used along with *in vivo* models.

In addition to the single-cell culture systems, research has been focused on developing co-culture models for atherosclerosis-associated studies. The co-culture systems include direct cell-to-cell and indirect transwell co-cultures. It was reported that, as far back as 1986, various cell types involved in atherosclerosis pathology—including ECs, SMCs, and macrophages—were used in various direct and indirect co-culture studies to create blood vessels for examining inflammation and its role in atherosclerosis (59–63). Furthermore, with the advancement of the engineering approach,

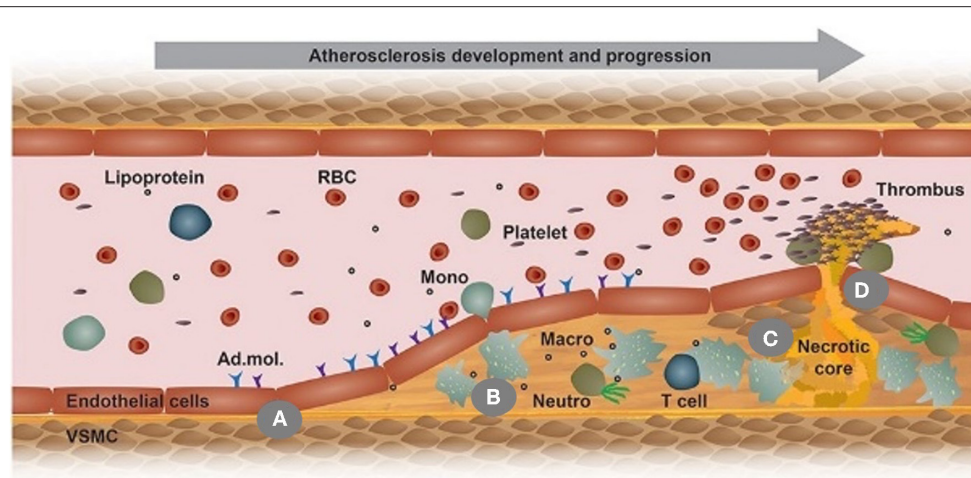


FIGURE 2 | This scheme illustrates the development of an atherosclerotic plaque from left to right in a longitudinal section of an arterial vessel: **(A)** Upon activation by metabolic or inflammatory triggers, endothelial cells express adhesion molecules (Ad. mol.) that promote the recruitment of monocytes (Mono); **(B)** Monocyte differentiate into macrophages (Macro) and uptake Ox-LDL, leading to foam cell formation; **(C)** Macrophage (Macro) and foam cells eventually die and fall apart, thereby forming a necrotic core; **(D)** Advanced, vulnerable plaques can rupture and thereby form an arterial thrombus. Adapted, with permission, from (23) **(A–D)**.

TABLE 1 | Summary of *in vitro* 2D single-cell culture model and its specific function for evaluating drug delivery system for atherosclerosis.

| Model | Model function (biological process studied) | References |
|------------|--|--------------------------|
| Macrophage | To evaluate drug delivery system targeting ability to plaque | (39) |
| | To evaluate drug delivery system effects on macrophage polarization | (40) |
| | To evaluate drug delivery system effects on cholesterol removal (efflux) | (41–43) |
| | To evaluate drug delivery system effects on inflammation resolution | (44–50) |
| | To evaluate drug delivery system effects on Reactive oxygen species generation | (41, 47, 49, 51–54) |
| | To evaluate drug delivery system effects on nitric oxide production | (52) |
| | To evaluate drug delivery system effects on efferocytosis and phagocytosis | (55, 56) |
| | To evaluate cellular uptake of drug delivery system | (41, 43, 44, 49, 55, 56) |
| | To evaluate drug delivery system effects on cellular apoptosis | (49, 57) |
| | To evaluate drug delivery system effects on foam cell formation | (41, 42, 46, 49, 57) |
| SMC | To evaluate drug delivery system effects on the cellular proliferation | (44) |
| | To evaluate drug delivery system effects on foam cell formation | (49, 58) |
| EC | To evaluate the cellular uptake of drug delivery systems | (49) |
| | To evaluate the cellular uptake of drug delivery systems | (44) |
| Foam cell | To evaluate cellular binding of drug delivery systems | (51) |
| | To evaluate drug delivery system effects on cholesterol removal (efflux) | (54) |
| | To evaluate drug delivery system effects on inflammation resolution | (54) |

considerable efforts have been made to develop advanced *in vitro* 2D systems, where cells are seeded in 2D scaffolds or microfluidic chips for better mimicry of the physiology and pathology of atherosclerosis environment. In this section, we summarize these systems.

SINGLE-CELL MODEL

Single-cell models have been widely used for assessing drug delivery systems due to their high availability and ease of fabrication. These single systems include only macrophages, SMCs, ECs, or foam cells (Table 1). One of the applications

of these single-cell systems in the drug delivery field is to evaluate the cellular uptake of those systems. In one study, Schwendeman et al. developed a single-cell model composed of THP-1 monocytes differentiated macrophages to evaluate the cellular uptake of these DiD dye-labeled synthetic high-density lipoproteins (DiD-sHDL) (41). It was shown that 99% of macrophages showed DiD positive after 2 h incubation with the particles. In addition to macrophages, other cell types, such as TNF- α treated HUVECs and mouse vascular smooth muscle cells (VSMCs), have also been employed to demonstrate the efficient cellular uptake of DiD labeled macrophage membrane functionalized biomimetic nanoparticles

and Cy5 labeled β -cyclodextrin nanoparticles, respectively (44). Besides, the Liu group reported the development of single-cell systems composed of either HUVECs, RAW cells, or foam cells to investigate the cellular binding of platelet mimicking nanoparticles to these cells. Using these single-cell systems, they found those platelet mimicking nanoparticles showed strong binding to foam cells in contrast to no binding to other types of cells (51).

The anti-atherosclerotic function of a therapeutic loaded drug delivery system is dependent on the effects of these drug delivery systems on several critical biological processes strongly associated with macrophages or macrophage-derived foam cells, such as ROS generation, foam cell formation, and cholesterol efflux, and inflammation resolution (**Table 1**). Thus, macrophages have been widely used to evaluate the drug delivery system's effect on these processes. One typical example is using the macrophages to evaluate the regulation of the cholesterol efflux and influx resulting from drug delivery systems by Ghosh et al. They showed that the simultaneous delivery of siRNA and LXR ligand *via* mannose-functionalized dendrimeric nanoparticles (mDNPs) could significantly decrease cholesterol content in the macrophages (42). In addition, macrophages in the plaque have been demonstrated to express Ca^{2+} /calmodulin-dependent solid protein kinase (CaMKII γ) and suppress the efferocytosis receptor, thereby leading to plaque necrosis and efferocytosis suppression. Macrophage systems have been used to investigate the drug delivery system's effect on efferocytosis and plaque stability. For checking the effect of siRNA nanoparticles on efferocytosis, bone marrow-derived macrophages were incubated with siRNA-loaded nanoparticles by the Shi group. It was shown that the CaMKII γ expression was significantly decreased by the siRNA-loaded nanoparticles, thus increasing macrophage efferocytosis and plaque stability (55). Besides enhancing efferocytosis, the induction of inflammation resolution by therapeutic-loaded drug delivery systems is also investigated for treating atherosclerosis. One typical example demonstrated by the Scott group, where the macrophages were treated with the anti-inflammatory nanocarriers, celastrol-loaded nanocarriers, showed significantly less production of TNF- α than those untreated ones (45).

In addition to evaluating therapeutic loaded drug delivery systems, single-cell models have been applied to explore the mechanism associated with atherosclerosis pathogenesis. For instance, ECs have been used to evaluate various pathophysiological stimuli, such as pro-inflammatory cytokines, hemodynamic forces, hypercholesterolemia, and hypertension, on endothelial dysfunction, inflammation, and cellular senescence in atherogenesis (24, 64–70). In addition, Single-cell systems composed of SMCs or monocytes have been used to assess these stimuli's effects on SMC phenotype change, monocyte differentiation, and foam cell formation, which may be a critical process in developing atherosclerosis (71–80). **Table 2** summarizes some recent typical single-cell model examples of atherosclerosis mechanism exploration.

CO-CULTURE SYSTEMS

Direct Cell-to-Cell Interaction

Direct cell-to-cell interaction involves the culture and seeding of different cell types either on top of one another or next to each other with direct contact on TCP. This type of co-culture system has been used to study cell interaction and adhesion influenced by specific factors involved in the pathogenesis of atherosclerosis. For example, Goldschmidt-Clermont et al. developed a co-culture system consisting of vascular smooth muscle cells (VSMCs), monocytes, and macrophage colony-stimulating factor (M-CSF), to investigate macrophage activation and adhesion to VSMCs. Their results showed significant adhesion and clustering of M-CSF activated macrophages on the VSMCs and a VSMC apoptosis rate up to 60% (96). Later, Natarajan et al. expanded upon using diabetic VSMCs and the monocyte system to study diabetic condition impact on monocyte adhesion and atherosclerosis development. Through such a co-culture model, they found that monocyte binding on VSMCs was significantly higher in the presence of glucose in a dose-dependent manner, indicating diabetes may promote atherogenesis (97). Changes in VSMC phenotype due to vascular injury play a critical role in developing atherosclerotic lesions. Thus, in another study, Panitch et al. developed a hyperplastic cell co-culture model to the close mimicry of vascular injury and studied vascular injury's effect on SMC phenotype changes. For creating the injury model, a low density of ECs was seeded onto aortic smooth muscle cells (ASMCs). Utilizing this model, they showed that incomplete endothelialization resulted in switching the phenotype of ASMCs from healthy and contractile to an uncontrolled proliferative state, which plays an essential role in promoting atherosclerotic lesion development (98).

Besides that, using 2D co-culture systems, many studies have examined the correlation between chronic multi-bacterial infections, such as periodontal bacteria, and their impact on atherosclerosis development (99–102). Specifically, Yamamoto et al. created a co-culture of monocytes and human umbilical vein endothelial cells (HUVECs). They demonstrated that introducing *Porphyromonas gingivalis* (*P. gingivalis*), a common bacterium in periodontal infections, to a co-culture led to a significant increase in monocyte attachment to HUVECs and inflammation (103). To further study this risk factor, Huck et al. examined *P. gingivalis* and its modulatory effects on EC apoptosis using a co-culture system composed of *P. gingivalis* and activated ECs. It was found that EC metabolic activity and cell viability significantly decreased when ECs were co-cultured with *P. gingivalis* (104). Also, establishing a co-culture system composed of *A. Actinomycetemcomitans* and EC, Lafaurie et al. showed the human coronary ECs incubated with *A. actinomycetemcomitans* generated a severer pro-inflammatory environment compared to the controls (105). These studies discussed here demonstrated that the co-culture models are crucial tools for analyzing chronic multi-bacterial infections and studying their effects on the risk factors for atherosclerosis, including inflammation, EC apoptosis, and monocyte adhesion.

TABLE 2 | Some examples in recent studies using a single-cell model for atherosclerosis mechanism exploration.

| Model | Biological process | Model function | References |
|------------|--|---|------------|
| Macrophage | Efferocytosis or/and phagocytosis, or pyroptosis | To study the effect of allele G of rs9349379, an intron of PHACTR1 gene, on impairing the efferocytosis in human atherosclerotic lesional macrophages | (81) |
| | | To explore whether GATA2 overexpression can impair macrophage phagocytosis and efferocytosis | (82) |
| | | To study the mitochondrial outer membrane protein effect on inhibiting macrophage pyroptosis resulting from Ox-LDL | (83) |
| | Cellular senescence | To explore the mechanism of formation of senescent macrophages during atherosclerosis and whether LPS can induce macrophage senescence | (84) |
| | Lipid uptake or/and foam cell formation | To investigate the direct role of IgE on macrophage-sterol-responsive-network gene expression and foam cell formation | (85) |
| | | To study the relationship between the phenotype-specific difference of macrophages and their ability of LDL uptake, cellular cholesterol levels, and cholesterol efflux. | (86) |
| | | To explore whether the inhibition of bromodomain-containing protein 4 could prevent lipid accumulation in senescent macrophages | (84) |
| | | To study the function of the RAC1 gene on regulating inflammatory cytokine secretion and lipid uptake of macrophages | (87) |
| | | To explore the underlying mechanism of vascular inflammation effect on the foam cell formation derived from macrophages, mainly focusing on the role of NOS1 in macrophage lipid uptake | (88) |
| | | To investigate whether the role of TREML4 in human macrophages and the pathogenesis of atherosclerosis | (89) |
| EC | Inflammation | To investigate whether NOS1 could enhance the pro-inflammatory cytokine secretion by macrophages | (88) |
| | | To explore the molecular mechanism of FGF21 function against atherosclerosis and the effect of FGF21 on suppressing proteins associated with pyroptosis in HUVECs | (90) |
| | Pyroptosis | To explore whether NLRP3 activation in ECs can promote atherosclerosis development associated with diabetes | (91) |
| | | To study how disturbed flow regulating enzymes as well as their roles in the apoptosis and inflammation | (92) |
| | | To explore how exosome lncRNA GAS5 regulates apoptosis of HUVECs in atherosclerosis | (93) |
| | Cell senescence | To study whether the disturbed flow can induce HUVEC senescence and associated pathway | (94) |
| SMC | Phenotypic modulation | To study the oxidized lipid effect and SMC phenotype changes | (72) |
| | | To study whether there are differences between Ox-LDL-loaded SMCs <i>in vitro</i> and <i>in vivo</i> at a genetic level. | (95) |

LPS, Lipopolysaccharide; PHACTR1, Phosphatase and Actin Regulator 1; IgE, Immunoglobulin E; NOS1, Nitric oxide synthase; lncRNA, Long non-coding RNAs; FGF21, Fibroblast growth factor 21; HUVECs, Human umbilical vein endothelial cells; GAS5, Growth Arrest Specific 5; ECs, endothelial cells; Ox-LDL, Oxidized lipoprotein.

Apart from mechanistic studies, 2D co-culture models have also been employed to evaluate potential treatments for atherosclerosis; nevertheless, they are not as popular as single-cell culture. One recent associated study was shown by Porrini et al., where the authors investigated the effects of polyphenols on atherosclerosis initiation using a co-culture inflammatory model composed of HUVECs, THP-1 cells, and TNF- α (106). Moreover, the Wong group reported a similar study, where the authors developed a human microvascular endothelial cell (HMVEC) and THP-1 cell co-culture system to demonstrate the remarkable efficacy of miR-146a-loaded microparticles on EC inflammation and monocyte adhesion on HMVECs (107). In another study, Li et al. also created EC and THP-1 co-culture systems to show that the newly developed peptide-based high-density lipoprotein

(pHDL) could inhibit THP-1 cell adhesion and achieve a similar inhibition effect human HDL (108). Thus, these studies demonstrated an *in vitro* EC/monocyte platform for testing potential treatments for suppressing atherosclerosis initiation.

In-direct Transwell Co-culture

Unlike direct co-culture, the indirect co-culture model utilizes transwells, providing a platform to investigate cellular responses by secretory pathways and cytokine production. The model utilizes a well plate with transwell inserts, where at least one cell type is grown on the transwell membrane filter insert or the bottom of the well of the plates.

Studies utilizing the transwell indirect co-culture model aim to explore the non-contact interactions between ECs,

monocytes, and SMCs, thereby gaining a deeper understanding of atherogenesis. For instance, Natarajan et al. examined direct and indirect interactions of THP-1 cells with VSMCs using a transwell model. In this study, THP-1 cells were cultured with HVSMCs at the bottom of the well plate or in the transwell insert alone. The binding of VSMCs to THP-1 cells in the well plate led to increased Akt phosphorylation and THP-1 proliferation. In contrast, the THP-1 cells alone in the transwell insert did not show increased proliferation. This finding demonstrated that physical contact of monocytes and VSMCs might represent a critical mechanism accounting for abnormal accumulation of monocytes in the plaque, a crucial step leading to the development of atherosclerosis (109). A similar study performed by Maffia et al. demonstrated a new 2D co-culture transwell model to investigate the interaction among three key cell players in atherosclerosis development without any direct cell-cell contact. The model consisted of THP-1 in the well as well as SMCs and ECs on the underside and upper surface of the transwell insert, respectively. Findings showed that soluble factors released from ECs/THP-1 along with SMCs promoted CDH5 expression, indicating that the co-culture systems could improve the EC junction integrity (16). Similarly, Lee et al. used a transwell model to examine how the glycolaldehyde-induced advanced glycation end products (glycol-AGEs) would affect the proliferation and inflammation of SMCs. The transwell system was created by seeding SMCs in the well plate and then co-culturing HUVECs and THP-1 cells in the transwell insert. Interestingly, using this system, it was found that SMC proliferation and inflammatory cytokine production were increased upon adding glycol-AGEs in the co-culture system, while no differences were observed in the SMC-only group. Thus, this study suggested that a transwell co-culture system was of great importance for evaluating the effects of a specific compound on cell proliferation and inflammation for atherosclerosis research (110).

Various research groups have reported using transwell models to study the effects of interactions between ECs and monocytes on trans-endothelial migration, promoting atherosclerosis development. For instance, Hajishengallis et al. incorporated a transwell co-culture model to investigate monocyte adhesion and migration under chemoattractant-induced inflammatory conditions induced by *P. gingivalis* (111). For making this model, a confluent monolayer of HUVECs was first seeded in the transwell insert and cultured with THP-1 cells transfected with human CD14 and *P. gingivalis*. By utilizing such a system, substantial evidence showed that the activation of the CD11b/CD18 receptors by *P. gingivalis* increased THP-1 cell adhesion to the HUVECs and improved the THP-1 migration rate and amount through the confluent HUVEC layer to the well plate (111). In addition, to study the development of foam cells from peripheral blood mononuclear cells (PBMCs) in an atherogenesis environment, Muller et al. created a unique transwell model with HUVECs, TNF- α , and LDL in a transwell insert and PBMCs in the well plate. Through this specifically designed system, the authors found that TNF- α activated HUVEC led to a modification of LDL into Ox-LDL and resulted in the formation of foam cells derived from PBMCs

(112). The study demonstrated the significance of using the transwell system to understand foam cell formation's mechanism in an early stage of atherosclerosis.

2D Cell Sheets

As discussed in the previous sections, many co-culture methods have been established for studies of cell-cell interactions; however, culture plate surfaces do not adequately mimic extracellular matrix (ECM) conditions, therefore impacting the cell behaviors (113). In contrast, native scaffolds with a unique avenue to overcome these limitations have been used in developing tissue-engineered 2D cell sheets (114). Taking decellularized ECM scaffolds as examples, they can provide a biocompatible and physiological mimicking environment necessary for cell adhesion, migration, proliferation, tissue morphogenesis, differentiation, and eventual homeostasis (17, 115, 116). In addition to decellularized ECM, scaffolds made by collagen and fibrin, the predominant structural proteins within the ECM, also allow cell adhesion and growth, cell-matrix interaction, and tissue function regulation, which have also been employed for cell sheet fabrication. One interesting study was conducted by the Kim group, where the authors generated cell sheets by decellularizing carotid arteries first, then using the obtained ECM from the arteries for bone-marrow cells (BMCs) seeding and differentiating the BMCs into EC and SMCs (117). In addition to carotid arteries, Choi et al. created decellularized ECM from human adipose tissue and utilized it to fabricate cell sheets with fibroblasts, SMCs, chondrocytes, and ECs (118–120). Those sheets mimic the cell components of an artery, which may serve as great tools for exploring atherosclerosis development mechanisms. Although decellularized ECM was shown to generate cell sheets in these studies, 2D models using decellularized ECM for atherosclerosis models are limited by mechanical stability, batch-to-batch variability, and ECM content qualification (121).

In addition to decellularized ECM, other scaffolds have also been used to develop cell sheets that can partially mimic artery structure. For instance, Wong et al. seeded VSMCs on degradable, tyramine-conjugated carboxymethyl cellulose and alginate hydrogel scaffold to create patterned VSMC cell sheets that could be stacked in alternating angles to mimic the native arterial medial layer (122). Kim et al. also made SMC cell sheets by seeding SMCs on dishes coated with a thermo-responsive polymer film composed of polyurethane acrylate, glycidyl methacrylate, polyethylene terephthalate with amine-terminated poly (N-isopropyl acrylamide) (PIPAAm) (123). Because of the temperature-responsive property of PIPAAm, the cell sheets could be detached by reducing the culture temperature (123). PIPAAm based approach has been widely used for cell sheet fabrication, which was discussed in the previous review (124). Nevertheless, because of the long detachment process and high cost of PIPAAm coated dishes, polystyrene has been investigated as a cost-effective alternative to fabricating the pre-vascularized SMC sheets (125). Although cell sheets have not been employed as *in vitro* models for atherosclerosis-related application, they hold great potentials for atherosclerosis research

due to their layered structures with cellular components similar to the tunica intima and media of the human artery.

2D Microfluidic Chips

Recently, advanced *in vitro* systems, microfluidic chips, which combine micro-analysis and dynamic culture, have emerged as innovative platforms for various applications, ranging from life sciences research to drug screening and analysis (7, 8). Compared to conventional 2D systems on TCP, microfluidic chips have distinct advantages, such as enhanced sensitivity, continuous monitoring and feedback, the inclusion of flow, and continuous medium supply, making them promise candidates for conducting research associated with atherosclerosis. Generally, microfluidic devices can be classified into 2D or 3D models, dependent on the culture methods. However, in this section, we only summarize the 2D microfluidic chips (126). The 3D microfluidic chips will be discussed in the later 3D model section.

Endothelium plays an essential role in maintaining vessel functions, vascular integrity, and homeostasis. Dysfunctional endothelium with high permeability is regarded as one of the hallmarks of atherosclerosis initiation (127). Modeling functional endothelium *in vitro* is particularly important to improve our knowledge of atherogenesis at the molecular level. Thus, tremendous efforts have been devoted to the rational design of endothelium-on-a-chip to understand the effects of various factors on EC function. For instance, Jiang et al. developed an endothelium-on-a-chip to investigate the effects of shear stress, glucose, LDL on reactive oxidative species (ROS) production and EC function in the early atherosclerosis stage. To generate a model to closely mimic the hyperglycemia or hyperlipidemia environment in the atherosclerosis prone area, ECs were seeded in the chip to form an endothelium-like monolayer, followed by treating the EC layer with glucose or LDL under low fluid shear stress and cyclic stretch, respectively. Using this model, the authors found that the ECs seeded on the hyperlipidemia chip model showed a sharper decrease of VE-cadherin level than the ECs exposed to the same condition but cultured on the peri dish (128). This observation indicated a more pronounced cellular response from the chip model than the peri dish model, demonstrating the advantages of using chip models for atherosclerosis studies. Also, to investigate the effects of two ECM proteins, fibronectin and collagen, on endothelial inflammation, Gweon et al. created a microfluidic EC chip model by incorporating fibronectin or collagen-coated polyacrylamide hydrogel onto a chip followed by EC seeding (129). An interesting result was obtained by using this model—the ECs on fibronectin hydrogel showed a more disrupted barrier, higher permeability, and less prominent cellular elongation and orientation than the ECs on collagen-coated hydrogel upon shear stress (129). In addition, in a recent study, an endothelium-on-a-chip with specially designed ridged-shaped patterns was developed by Baratchi et al. to explore how disturbed flow affected the EC orientation, size, and nuclear shape using an endothelium-on-a-chip with specially designed ridged-shaped patterns (Figure 3A) (130). This unique design allowed the system to generate disturbed flow with low shear stress between the ridges on the chip. With the application of such system, it was revealed that,

under the disturbed flow generated by the chip, EC stress fiber orientation was perpendicular to the flow, in great contrast to the ECs exposed to laminar flow or static condition, of which the fibers showed alignment along with the flow or no specific pattern, respectively (Figure 3B). Additionally, the disturbed flow was found to increase the nucleus circularity index of the cells but decrease the nucleus area compared to the laminar or static flow (130). This study demonstrated the great value of endothelium-on-a-chip for studying the hemodynamic force effect on ECs. In another study, Liu et al. endeavored to use an endothelium-on-a-chip model, and ICAM-1 modified nanoparticles for real-time evaluation of TNF- α triggered endothelium activation. This chip system included two channels separated by a semi-permeable membrane for seeding cells and activating endothelium, allowing the real-time monitoring of ICAM-1 expression on the activated endothelium by analyzing the amount of ICAM-1 antibody-modified NPs binding to the endothelium-on-a-chip. The study showed the great potential of using endothelium-on-a-chip for real-time atherosclerosis mechanism study (132).

Monocyte recruitment by dysfunctional endothelium promotes atherosclerosis progression. The design of endothelium-on-a-chip to elucidate the mechanism of monocyte-endothelium interaction has attracted increasing research interest. An example was demonstrated by Hou et al., who developed a constriction controllable endothelium-on-a-chip to investigate the monocyte attachment to the ECs stimulated by 50 or 80% constriction conditions (132). Remarkably, the authors demonstrated that the THP-1 cell attachment to the ECs was strongly dependent on constriction (132). In another study, Jeon et al. designed an endothelium-on-a-chip model to explore the interaction between THP-1 cells and ECs upon lipopolysaccharide (LPS) stimulation. Utilizing such a chip, the authors found that LPS could induce a longer migration distance of THP-1 through endothelium (133).

Along with elucidating the crucial factors regulating EC function and interaction between ECs and monocytes, the endothelium-on-a-chip has also been employed to evaluate nanoparticle behaviors in an atherosclerosis environment. For example, in one study, an endothelium-on-a-chip system was developed to evaluate the translocation of lipid-hybrid nanoparticles over dysfunctional endothelium (134). Dysfunctional endothelium was induced by treating the endothelium-on-a-chip with TNF- α and controllable shear stress. Notably, using this chip system, the authors found that the nanoparticles could translocate through the dysfunctional endothelium but were excluded by the healthy endothelium. Notably, the *in vitro* data obtained from the chip system was well-correlated with the result observed *in vivo*, indicating that the *in vitro* chip model can predict nanoparticle behavior *in vivo* (134). Likely, Jiang et al. demonstrated the combined use of endothelium-on-a-chip models and animal models to evaluate the potential of using platinum-NPs to treat atherosclerosis. The *in vitro* chip model results showed great consistency with the *in vivo* model's data, which demonstrated that the antioxidant property of platinum-NPs that scavenged hyperlipidemia induced ROS in ECs *in vitro* and decreased the expression

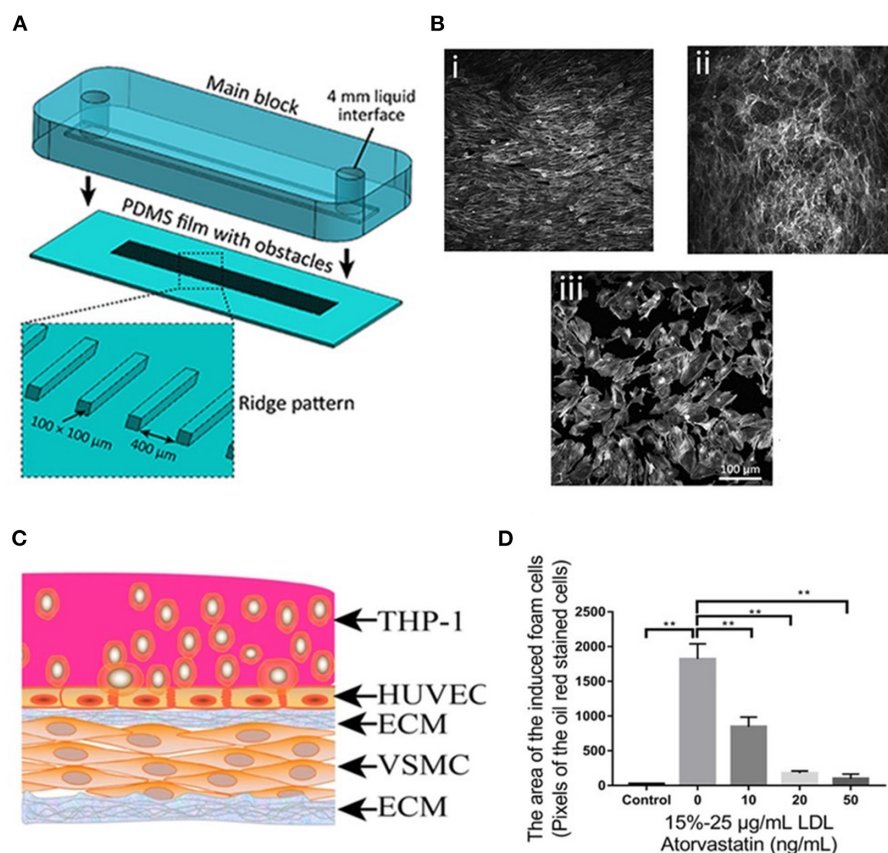


FIGURE 3 | (A) The process of assembling the main block and the PDMS substrate with ridge obstacles, with the inset showing the zoomed-in PDMS substrate. **(B)** A confluent layer of HAECs cultured under (i) laminar flow, (ii) disturbed flow, and (iii) static condition, following which the actin cytoskeleton was labeled with Atto 565-phalloidin. **(C)** Diagram of the co-culture model. **(D)** Foam cell formation after being treated with atorvastatin and LDL at different concentrations. Adapted, with permission from (130) **(A,B)** and (131) **(C,D)**. ** $P < 0.01$.

of vascular cell adhesion protein 1 (VCAM-1) *in vivo* (128). These studies discussed here showed a good promise of the endothelium-on-a-chip system to study the nanomedicine effect on dysfunctional endothelium.

Apart from the simple chip systems only including ECs, Ding et al. established a stretchable microfluidic chip model composed of VSMC layer, HUVEC layer, foam cells, LDL, and a non-uniform stretched chip film to investigate the efficacy of atorvastatin and associated underlining molecular mechanism (Figure 3C). The stretching was induced by the manual deformation of the chip film where the cells were cultured, thus, generating an atheroprone-like microenvironment with disturbed shear stress. Using this model, the authors found that atorvastatin (50 ng/mL) significantly inhibited foam cell formation (Figure 3D), reduced ROS, and led to an up-regulation or down-regulation of crucial genes associated with atherosclerosis. More importantly, based on these data generated by utilizing the model, the authors proposed an appealing working mechanism of atorvastatin in atherosclerosis (131). This study demonstrated that endothelium-on-a-chip could not only be applied for drug evaluation but also a mechanistic investigation related to atherosclerosis development.

IN VITRO 3D MODELS FOR ATHEROSCLEROSIS STUDIES

Traditional *in vitro* 2D platforms for atherosclerosis studies are limited to 2D, lacking physiological 3D structure observed in *in vivo* and failing to provide proper pathological compositions of human atherosclerotic plaque. In addition, 2D culture also has issues with substrate topography and stiffness (135). Therefore, the data obtained from the 2D culture system may provide misleading information regarding the safety and efficacy of the lead compound. In contrast, 3D culture, which has emerged as a helpful approach, can generate cell constructs that recapitulate the 3D structure of the organ with more naturally grown ECM, thus providing better EMC-cell and cell-cell interaction and allowing appropriate cell behaviors observed in *in vivo* (126, 136). Moreover, the 3D models can improve the predictability of therapeutic toxicity and sensitivity. It has been reported that the drug response of the 3D model is different from that of the 2D model; significantly higher drug resistance has been observed in the 3D model compared to 2D models (10). Given their unique advantages, developing *in vitro* 3D models has been of growing interest for atherosclerosis modeling and drug testing. Generally,

in vitro 3D models can be developed by bio-fabrication, an approach that generates organized structures with biological function using living cells, cell aggregates, biomaterials, and bioactive molecules *via* bio-assembly or bio-printing followed by tissue maturation (137).

IN VITRO 3D SPHEROIDS

3D spheroid is three-dimensional cellular aggregates that approximately resemble a sphere, increasingly being utilized to evaluate therapeutics because of its better similarity to natural tissue than 2D culture systems. The formation of spheroid cultures involves extracellular matrix fibers with a ligand motif, such as tripeptide Arg-Gly-Asp, and their binding with integrin membrane proteins on the cell surface (138). This binding is essential as it allows the numerous cells to aggregate and facilitates the binding of homophilic cadherins between cells, resulting in solid adhesion and compaction of the cell mass, leading to a spheroid formation (138). Several fabrication methods have been used to develop spheroid culture over the past several decades. One of the earliest methods used is the hanging drop method (139), in which cells aggregate form when inverting a plate with a suspension of cells. A centrifuge (140) or a spinner flask has been applied to force cells to assemble into cell aggregates to form spheroids (19, 141). Spheroids have also been produced by culturing a suspension of cells on a non-adherent substrate, forcing the cells to form spheroids (142). It should be noted that, as a result of spheroid formation, the gene expression (143, 144), metabolism (145), and cellular motility differentiation (146–148), and polarity of cells (149) within the spheroid culture were found different from that of monolayer cultures in 2D. With more accurate mimicry of structures of native tissue than traditional 2D monolayer cultures, spheroid models have been increasingly utilized for studying and modeling atherosclerosis.

As stated earlier, foam cells are differentiated macrophages that uptake lipids, the main cellular component in atherosclerotic plaque. In recent years, scientific efforts have focused on the generation of foam cell spheroid model to investigate the effects of specific compounds on foam cell formation and associated inflammation. For example, using a 3D spheroid model of foam cells, Nguyen et al. demonstrated that foam cell formation could be significantly decreased by dexamethasone (Dex) and fluocinolone acetonide (FA), but FA was more effective than Dex (150). Hydroxyl beta-cyclodextrin (HBCD) is a polysaccharide that increases cholesterol efflux and solubility. In another study, Kwan et al. used the foam cell spheroid model to evaluate the efficacy of co-delivery of HBCD and sirolimus loaded poly-co-lactic-co-glycolic acid microparticles (mc-PLGA-MPs) on foam cell formation under ultrasound stimulation (151). These studies shed light on the utility of the foam cell spherical model for atherosclerosis studies.

VSMC is another significant factor that affects arterial wall thickening, promotes atherosclerotic plaque formation, and regulates atherosclerotic plaque stability. Therefore, a study reported by Chun et al. demonstrated the effects of membrane-type 1 matrix metalloproteinase (MT1-MMP) on mouse VSMC

proliferation using 3D spheroid models composed of mouse VSMCs with silenced MT1-MMP gene (152). Their results demonstrated that MT1-MMP gene, when silenced, remarkably increased the proliferation of mouse VSMCs in this 3D model; while using a 2D model, minimal effects of such gene on VSMC proliferation was observed. This study potentiated the importance of using 3D spheroid models to investigate biological processes associated with atherosclerosis other than 2D models. Furthermore, the focal adhesion kinase (FAK) has been reported to control the proliferation of VSMCs through N-Cadherin and is significant to cell adhesion. Then, Vaidyanathan et al. created a spheroid VSMC model to study the focal adhesion FAK gene and the regulation of its downstream genes, such as Rac, Rho, and Cdc42, aiming to identify potential pathways to treat neointima formation (153). By quantifying the expression of Rac and Rho in the VSMC spheroids, the authors found that FAK-Rac-N-cadherin or FAK-Rho-N-cadherin are necessary for VSMC spheroid formation, which might be considered a future target for treating atherosclerosis-related neointima formation (153).

The models demonstrated above have focused on developing an early atherosclerosis model with one type of cell component; however, it is worth noting that atherosclerosis is a chronic inflammatory disease encompassing various stages. When it comes to an advanced atherosclerosis model, Weber et al. pioneered an *in vitro* spheroid pseudo-atherosclerotic plaque composed of a spheroid core and a layer of myofibroblasts surrounding the core to emulate the late-stage atherosclerotic lesion, human fibroatheroma (15). Specifically, two types of pseudo-atherosclerotic plaque, b- and t-plaques, were developed using blood-derived myeloid cells and THP-1 cells for core fabrication. In addition to monocytes, their spheroid cores were also filled with collagen, lipid matrix with macrophages, and dendritic cells. It was found that the cell population distribution between the t-plaques and b-plaques was similar, including main components such as monocytes, macrophages, activated dendritic cells, plasmacytoid dendritic cells. Nevertheless, their components differed from human carotid plaques, primarily composed of activated dendritic cells and plasmacytoid dendritic cells (15). Moreover, native carotid plaques showed significant down-regulation of pro-inflammatory and remodeling genes than pseudo-plaques (15). Although this may be the most cohesive *in vitro* spheroid atherosclerosis model, age, sex, or genetic predisposition has not been taken into account.

IN VITRO 3D CELL-LADEN HYDROGEL CONSTRUCTS

Cell-laden hydrogel constructs are composed of growth factors, hydrogels, and cells, providing a 3D *in vitro* environment beneficial for studying atherosclerosis. In contrast to the 2D cell sheet fabricated by seeding cells on a 2D scaffold, the cell-laden hydrogel system is usually fabricated by embedding cells into 3D hydrogel matrices with growth factors followed by static or dynamic culture (154). Notably, cell-laden hydrogel construct can be developed with desirable geometries, sizes, and compositions, thus providing an environment allowing cells to

behave similarly to *in vivo* (154). With respect to atherosclerosis applications, cell-laden hydrogel constructs implement a 3D *in vivo* mimicking model to observe cellular interactions and pathophysiology and permit lower cost, improved controllability, and higher throughput compared to animal models.

An ideal hydrogel for fabricating a cell-laden hydrogel system should be biodegradable and biocompatible with good porosity and high-water content. It also should enable cell growth, proliferation, and migration by allowing the diffusion of nutrients throughout the scaffold (155). As previously mentioned, collagen is the predominant structural protein within the ECM (20, 156). Thus, to date, the cell-laden collagen hydrogel construct has been the most widely used for elucidating the effect of a particular factor on monocyte attachment. For example, Chiu et al. created a model composed of a collagen gel, ECs, and SMCs to study the influence of SMCs on inflammation and monocyte adhesion for atherosclerosis development (157). The SMC-laden collagen hydrogel was fabricated by embedding SMCs within the collagen hydrogel and seeding an EC monolayer over the SMC-laden hydrogel. Additionally, in another study, the SMC-laden collagen hydrogel was utilized to elucidate the roles of SMCs and flow in leukocyte adhesion and transmigration (157). In addition, due to the ability to mimic vessel intima-media structure mimicking, EC-seeded SMC-laden collagen-based hydrogel construct was used to model early atherosclerosis by the Hou group in a recent study. The authors induced EC dysfunction and SMC migration by treating the cell-hydrogel construct with IL-1 β , TNF α and Ox-LDL. Notably, the SMC migration into the EC layer could be easily quantified using such a system, which cannot be achieved through a traditional transwell assay. Moreover, the potential of this system as a drug screening tool was demonstrated by the atheroprotective effect of vitamin D, and metformin was observed when tested using this model (158). However, the main limitation of this study is that the EC layer is not monolayer and is as thick as the SMC layer, and lacks tunica adventitia. In another case, the Teo group manipulated the monocyte-laden collagen hydrogel construct with low or high densities to resemble the early or late-stage atheroma atherosclerotic tissues to study the ECM (collagen) effects on macrophage behaviors in these two environments. To generate the construct, THP-1 cells were first embedded within the collagen hydrogel with Ox-LDL, then differentiated into macrophages and activated into pro- (M1) and anti-inflammatory (M2) phenotypes. By detecting the inflammatory cytokines produced by the model, the authors found that M1 macrophages, M2 macrophages, and THP-1 monocytes showed different responses in high and low tissue density hydrogel construct (159).

Besides collagen hydrogels, a fibrin gel-based model was used to model early atherosclerosis by the Vahl group. Briefly, SMCs were encapsulated into the fibrin gel first, and ECs were seeded onto the SMC-laden fibrin gel to form an EC seeded SMC-laden fibrin construct; then, lipoproteins and monocytes were added to the culture to induce atherogenesis and foam cell formation. Additionally, this model was used to study atherosclerosis development for up to 6 weeks, indicating its long-term stability. This study demonstrated an autologous *in vitro* vascular model for studying the development of early atherosclerotic lesions

(160). Similarly, by using 3D engineered SMC-fibrin construct of a specific geometry, Vogel et al. discovered that the balance between metalloproteinase (MMP) and their inhibitors are flow-dependent—high shear stress could protect the *de novo* ECM, whereas low shear stress would cause SMC proteolytic activity leading to more collagen, less elastin, and shifted SMC phenotype (161). This study demonstrated the potential of using cell hydrogel construct for evaluating hemodynamic force effect on cells associated with atherosclerosis development.

IN VITRO 3D VESSEL BASED SYSTEMS

Tissue-Engineered Blood Vessels (TEBVs)

Over the past decade, significant advancements in tissue engineering, regenerative medicine, biomaterials, and cell biology enabled the fabrication of tissue-engineered blood vessels (TEBVs) as vascular grafts for treating atherosclerosis. Until recently, TEBVs have emerged as valuable models for studying atherogenesis or developed into *in vitro* atherosclerosis platforms that replicate the key features of atherosclerosis, offering an alternative to 2D and animal models for atherosclerosis and associated therapy studies.

In the case of TEBV fabrication, TEBVs have been developed by seeding vascular cells in biodegradable polymeric scaffolds. For instance, Arai et al. developed single-layered TEBV by seeding fibronectin and gelatin-coated mouse smooth muscle cells on poly-(L-lactide-co- ϵ -caprolactone) (PLCL) scaffold followed by maturing tissue in a perfusion system. The resultant TEBVs achieved similar mechanical properties to that of native arteries. Similarly, Lissy et al. created 2-layered TEBVs by seeding ECs and SMCs on PCL conduit with controllable wall thickness and shear stress (162). In addition to the seeding strategy, cell sheet technology has also been used as an alternative approach. For instance, single-layered TEBVs were created by the Germain group by rolling the fibroblast cell sheets into a vessel-like structure. Then, the cell sheets were fabricated by culturing fibroblasts on TCP for 1 month. With the results from single-layered TEBV, the same group also developed a multi-layered TEBV using decellularizing a single-layered TEBV followed by seeding SMCs and ECs in the decellularized TEBV and maturing the TEBV in a bioreactor (163). Besides this, an innovative strategy was unveiled by Rolle et al. recently, where the authors developed spatially controlled TEBV by fusing SMC ring units into a vessel structure with heterogeneous compositions similar to those observed in intimal hyperplasia or atherosclerosis. In particular, the human aortic SMCs (hAoSMC) ring units were self-assembled structures by culturing hAoSMCs in agarose molds. Then, the TEBV was created by threading the hAoSMC ring units on a mandrel and then culturing the mandrel with ring units in a static condition, followed by a dynamic environment using a bioreactor (164). Although some TEBVs have been generated by seeding cells on 2D scaffolds followed by rolling and maturing of the vessel structure, we still discuss them in the 3D section as those TEBVs provide a 3D vessel shape.

For atherosclerosis-associated applications, 2-layered TEBVs were developed by the Truskey group to demonstrate that PCSK9 might affect atherogenesis, independent of LDL. Apart from

PCSK9, the same group also explored the effect of oxidative stress on inflammation and senescence on vascular cells using a 2-layered TEBV composed of endothelium and fibroblast layers. The data generated from the model suggested that oxidative stress promoted atherosclerosis by increasing vascular cell inflammation (165–167). Likely, Chen et al. developed a 2-layered EC-SMC TEBV. Using an imaging chamber, the authors observed the real-time dynamic process of leukocyte recruitment and penetration through the endothelium into the intima using the developed TEBV. This study was the first demonstration of the real-time monitor for *in vitro* pathogenesis, which enable a more thorough investigation of drug effects on cellular behavior in a micro-physiological system for understanding atherosclerosis pathogenesis (168).

Although significant early attempts were made with the design of TEBVs without curvature, recently, the interest in developing branched TEBVs for disease studying has been grown, attributed to the fact that different vascular geometries leading to varied flow patterns may significantly affect atherogenesis. One typical example was demonstrated by the Leong group, where the authors constructed a branched TEBV to study the flow pattern effect on atherogenesis. They found that the athero-prone region (branched side outlets) demonstrated more monocyte adhesion than other areas (169). In another study, Cardinal et al. developed an angulated TEBV that mimics the bent human vessel to study the stent effects on atherogenesis in athero-prone regions (170). The TEBV was developed by seeding HUVECs on the expanded polytetrafluoroethylene tubular scaffold with bent geometry. The authors found a significantly reduced endothelialization on the stented TEBV compared with the un-stented control (170). These studies demonstrated that an *in vitro* TEBV platform with controllable geometry could mimic the athero-prone condition of the artery, which is well-suited for future intravascular device evaluation.

Compared to TEBV, TEBVs with atherosclerotic features, later referring as diseased TEBVs, have brought more enthusiasm to the field. However, due to the complexity of atherosclerotic plaque, only a few studies have developed diseased TEBVs with some key features of atherosclerosis. One representative example was demonstrated by Hoerstrup et al., who fabricated a 2-layered diseased TEBV by seeding vascular cells on a biodegradable tubular scaffold and adding LDL and inflammatory cells under high/low shear stress. The diseased TEBV platform demonstrated early atherosclerosis features such as monocyte attachment and LDL (21). Besides 2-layered diseased TEBV, Truskey et al. endeavored to fabricate a 3-layered TEBV (ECs, SMCs, and dermal fibroblast, from inside to outside) and induced early atherosclerosis using LDL with/without TNF- α (18). Their method maintained the vascular cell phenotype and early atherosclerosis symptoms in the TEBV, including endothelial activation, vasoactivity, monocyte accumulation, foam cell formation, and macrophage polarization. Moreover, they used this model to test the effects of LDL, lovastatin, and P2Y₁₁ inhibitor (NF157) on disease progression and found that lovastatin can block the altered vasoactivity and NO production induced by eLDL and TNF- α (18). Therefore, this diseased TEBV could be used to study specific vascular functions that might be

challenging to evaluate *in vivo*. Similarly, in another study, Cho et al. fabricated atherosclerotic three-layered vascular construct conduits with tunable geometry (stenosis and tortuous structure), a monolayer of the confluent endothelium, and condensed SMC layers using cell printing technology (Figures 4A–C). Significantly, the turbulent flow in the TEBVs with stenosis and tortuous structure and co-culture of SMCs and ECs led to higher endothelial dysfunction LDL accumulation (Figure 4D), foam cell formation (Figure 4E), and THP-1 cell recruitment (Figure 4F), hallmarks of early atherosclerosis compared to other conditions. These results indicated the importance of athero-prone vascular structure and the co-existence of vascular cell types to generate atherogenesis in the model. Remarkably, the authors showed the significant role of TEBV in atherosclerosis drug testing by demonstrating that atorvastatin efficacy for atherosclerosis was observed in the TEBV, including endothelial dysfunction, monocyte recruitment, LDL oxidation, and uptake, and improvement of free cholesterol efflux. Hence, this study substantiated the TEBV as a promising tool for biomedical applications, including pathological study and novel drug identification and evaluation (171).

Vessel-on-a-Chip

Vessel-on-a-chip is one type of organ-on-a-chip (OOC) system, which has aroused significant interest in researchers working in the field of atherosclerosis studies. Notably, an OOC system is a biomimetic *in vitro* microfluidic platform developed by combining cell biology, microfluidic technology, biomaterial science, and tissue engineering. Typically, an OOC system possesses an engineered architecture built in a chamber of a micron-sized electron fluidic chip, recapitulating the micro-physiological environment and architectures of functional human organs (172, 173). The chamber can be connected to a pump with a controlled flow rate and shear stress (174). In other cases, critical features of certain human diseases in a specific tissue can be induced in the OOC for modeling disease (175). Compared to traditional 2D static cultures, OOC systems provide a dynamic environment with more accurate vascular physiology, morphology, and response. Furthermore, high throughput capacity is a compelling feature of OOC systems in comparison to animal models, which is important for reducing the R&D cost (176). Therefore, OOC systems, particularly vessel-on-a-chip, have emerged as cost-effective platforms to fundamentally study biochemical and metabolic processes, investigate cellular responses during atherogenesis, and evaluate the therapeutic efficacy and safety for atherosclerosis (177). Hence, in the following section, we overview the recent progress in this field.

Vessel-on-a-chip comprises a vessel-like structure on a chip with or without disease features. Vessel-on-a-chip systems have been fabricated by seeding cells on a fiber scaffold. For instance, to tackle the issues commonly observed in vessels developed in static conditions, such as endothelium shedding and irregular orientation, the Li group fabricated a chip by seeding ECs on a highly oriented electrospun poly(ϵ -caprolactone fibers) scaffold. The ECs grown on the chip showed improved endothelialization under perfusion and achieved alignment under a flow similar

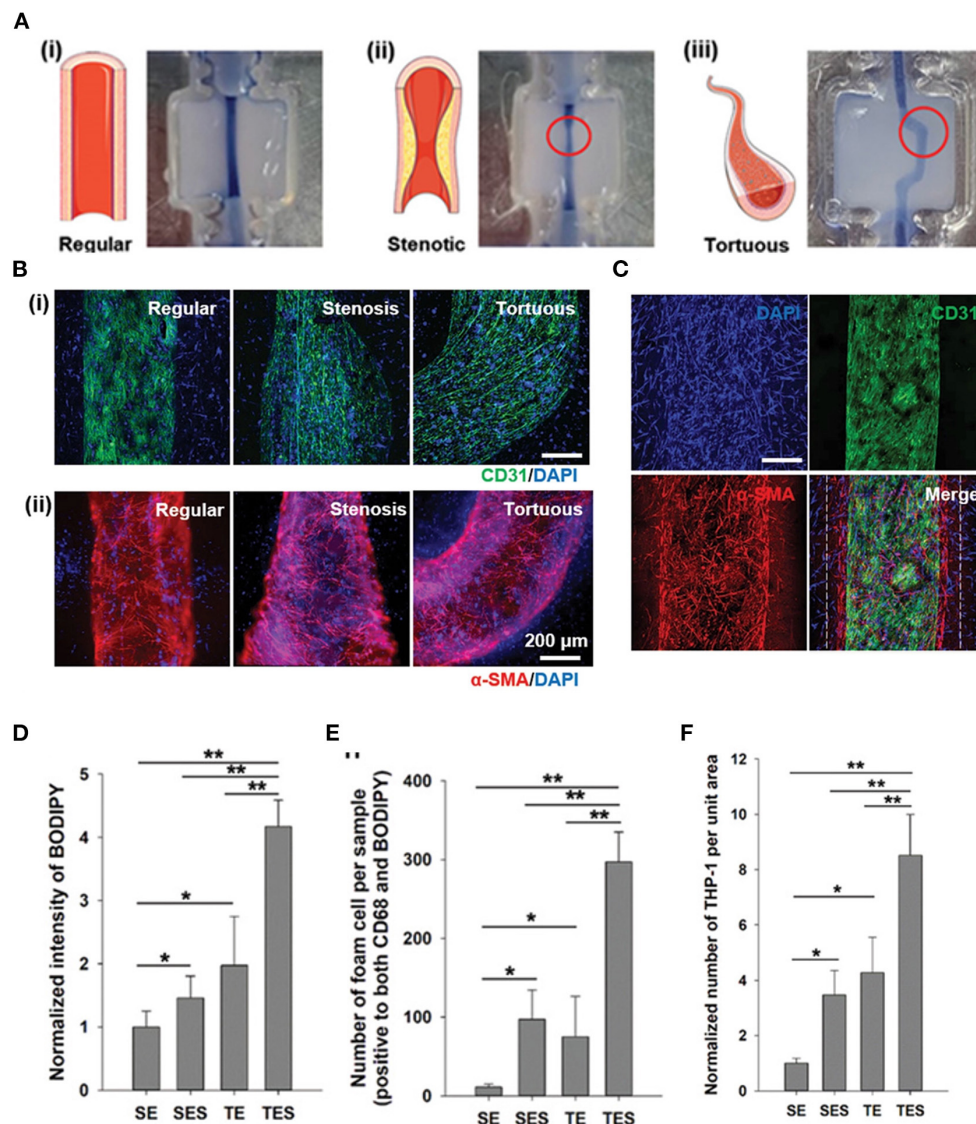


FIGURE 4 | Construction of a novel *in vitro* atherosclerotic model from geometry-tunable artery equivalents engineered via in-bath coaxial cell printing. **(A)** By programming the printing path and moving speed, triple-layer arterial constructs with controlled geometries were achieved, including (i) regular straight, (ii) stenotic, and (iii) tortuous models. **(B)** (i) Confluent endothelium and (ii) dense smooth muscle tissues were generated in the constructed artery equivalents on day 7, regardless of the designed geometries (Scale: 200 μ m). **(C)** The distributions of a monolayer endothelium surrounded by compartmentalized smooth muscle cells and fibroblasts (white dashes) are distinguishable **(D)** Quantification of LDL accumulation, **(E)** foam cells, and **(F)** adhered THP-1 cells. SE: steady-flow model containing only ECs; SES: steady-flow model containing ECs and SMCs/fibroblasts; TE: turbulent-flow model containing only ECs; TES: turbulent-flow model containing EC and SMS/fibroblasts. Adapted, with permission from (171). * $P < 0.05$; ** $P < 0.005$.

to natural vessel endothelium (178). Besides direct seeding cells on a scaffold, vessel-on-a-chip has also been made by fabricating cell-laden constructs and seeding cells on the hybrid constructs. For example, Khademhosseini et al. fabricated by constructing fibroblast and SMC laden-gelatin methacryloyl gel, followed by seeding ECs on the SMC-laden construct through perfusion (179). After 3 days of perfusion, the vessel showed a confluent endothelium layer, with significantly better barrier function than the vessel without an EC layer (179). This vessel-on-a-chip system is highly applicable for drug safety screening

because of its three-layered structure and perfusion system. In another study, Li et al. reported their blood-vessel-on-chip with controllable vessel structures (straight, wavy, or helical) to mimic various blood vessel physiological environments. First, the authors fabricated hollow microfiber with a straight, wavy, or helical structure by controlling the flow rate, injection device radius, and fluid composition of each channel. Then, a fully covered endothelium layer was achieved by seeding HUVECs in the inner surface of collagen and alginate-coated hollow microfibers. Additionally, a proof-of-concept test was conducted

to show that this cell-laden microfiber could be fabricated into a vessel-on-a-chip (180).

Although the progress of significance toward the development of vessel-on-a-chip systems has been made, most studies have focused on the generation of non-diseased vessel-on-a-chip with limited applications, with only one study demonstrating the development of atherosclerotic vessel-on-a-chip. In this study, Hoerstrup et al. induced atherosclerosis on a chip with tissue-engineered arteries (hiTEV) made from cells derived from human-induced pluripotent stem cells (hiPSCs) (181). To generate the hiTEV, the authors firstly induced SMC, EC, and macrophage-derived from hiPSCs and showed that the hiPSCs-derived SMCs and ECs could express SMC contractile phenotype markers and endothelial phenotype markers. Then, the authors fabricated two-layered hiTEV by seeding hiPSC-derived SMCs in the biodegradable tubular-shaped conduits carrying fibrin scaffold and cultured, followed by seeding the hiPSC-derived ECs in the inner lumen of the conduits on a microfluidic chip. It was found that the matured hiTEV was composed of endothelium and SMC layer with good expressions of EC and SMC phenotype markers, respectively. Furthermore, plaque-like structures were induced in the hiTEV after the vessel was treated with hiPSC derived macrophages and LDL. The authors also found that populations of dendritic cells for conducting antigen-presenting, ECs, and macrophages from the tissue-engineered plaque showed resemblance to those found in native plaque. Notably, the transcription expression of ECM assembly and remodeling of tissue-engineered plaques also displayed similarity to native plaques (181). Although this model emulated the native plaque closely, some limitations and drawbacks existed. For instance, hiPSC derived cells did not possess aged but fetal-like cell phenotype, while atherosclerosis occurred in young and older adults. Secondly, T and B cells play essential roles in atherosclerosis development; however, T and B cells were not included in the developed model. In addition, the applications of such a system were not demonstrated in the study.

Vessel-on-a-chip systems have been applied to investigate the biological process associated with atherosclerosis and evaluate the safety of specific compounds. For example, Joore et al. designed tubular vessels-on-a-chip to study monocyte adhesion to endothelium. The tubular vessels were fabricated by seeding human coronary artery ECs into collagen gel and culturing the cell-gel complex using perfused flow. The authors showed that after being treated with TNF- α , the vessels expressed significant ICAM-1 proteins and recruited significant monocytes. Moreover, using this model, the authors found that aerosol extract was far less toxic than cigarettes exact to the endothelium by showing that aerosol extract induced significantly lower expression of ICAM-1 and monocyte adhesion (182). In another study, Li et al. reported the generation of an endothelial carotid artery model using EC and gelatin (183). More importantly, this study demonstrated the first tuning fork-shaped artery (Figure 5A), which was composed of four parts able to mimic the common carotid artery (CCA), internal carotid artery (ICA), external carotid artery (ECA), and carotid sinus (CS), respectively (Figure 5A). In addition, a perfusion loop consisted of a medium, and a pump was used to generate a flow for this

model (Figure 5B). Interestingly, when the flow was applied, the laminar flow in the CCA region changed into a disturbed flow with lower WSS in CS regions because of its curvature structure. However, when the flow reached the ICA and ECA regions, it transformed into laminar flow with higher WSS. Due to the chip's unique design leading to various flow conditions in different chip areas, the authors were able to study the hemodynamics effect, such as wall shear stress (WSS), on ECs. Remarkably, they found that the ECs in the chip showed different responses to the flow changes. In the ECA region, the EC becomes elongated and aligned following the flow direction, whereas, in the region of CS, the ECs demonstrated a round shape and are more disorganized (Figure 5C). In addition, an endothelialized monolayer was found to form in the region of ECA (Figures 5D,E). Moreover, the expression of ICAM-1 and VCAM-1 in the CS region was more significant than that in the ECA region (Figures 5F,G). In addition, the WSS was found to increase the nitric oxide production in the system with time (Figure 5H). Also, a decreased expression of ZO-1, the primary EC tight junction marker, was observed in CS regions compared to the ECA region (Figure 5I) (183). This study demonstrated an example of creating and using a vessel-on-a-chip of unique characteristics to investigate the hemodynamic force effect on crucial cellular components associated with atherogenesis, which is not feasible in most other *in vitro* systems that depend on static culture.

CONCLUSION AND FUTURE PERSPECTIVES

A considerable number of *in vitro* models have been developed as potential platforms for studying atherosclerosis mechanisms and exploring new treatment, ranging from a traditional 2D single-cell culture system on TCP (Tables 1, 2) to advanced 3D TEBVs and vessel-on-a-chip models (Table 3). The advantage of using *in vitro* systems for drug evaluation is that the disease indicators, risk levels, and the determination of efficacy and toxicity of specific drug treatment can be studied with reduced cost, time, and resources before advancing to complicated *in vivo* models or clinical studies. This review discusses each system and associated studies in detail and summarizes the advantages, limitations, and future perspectives of each *in vitro* system (Table 4). Although, by far, the established *in vitro* models are not yet capable of fully modeling human atherosclerosis, these models, particularly the 3D models, show excellent potential for improving atherosclerosis research and revolutionizing the drug development process.

Due to the ease of creation, traditional *in vitro* 2D models, including single-cell culture and direct or indirect co-culture models on TCP, have been widely used to evaluate drug delivery systems and conduct a mechanistic investigation for atherosclerosis. Still, these models have some limitations in the aspects related to closely resembling physiological structures *in vivo* and promoting adequate development of ECM interactions, thus leading to improper regulation of cell signaling and behaviors and making it challenging to translate

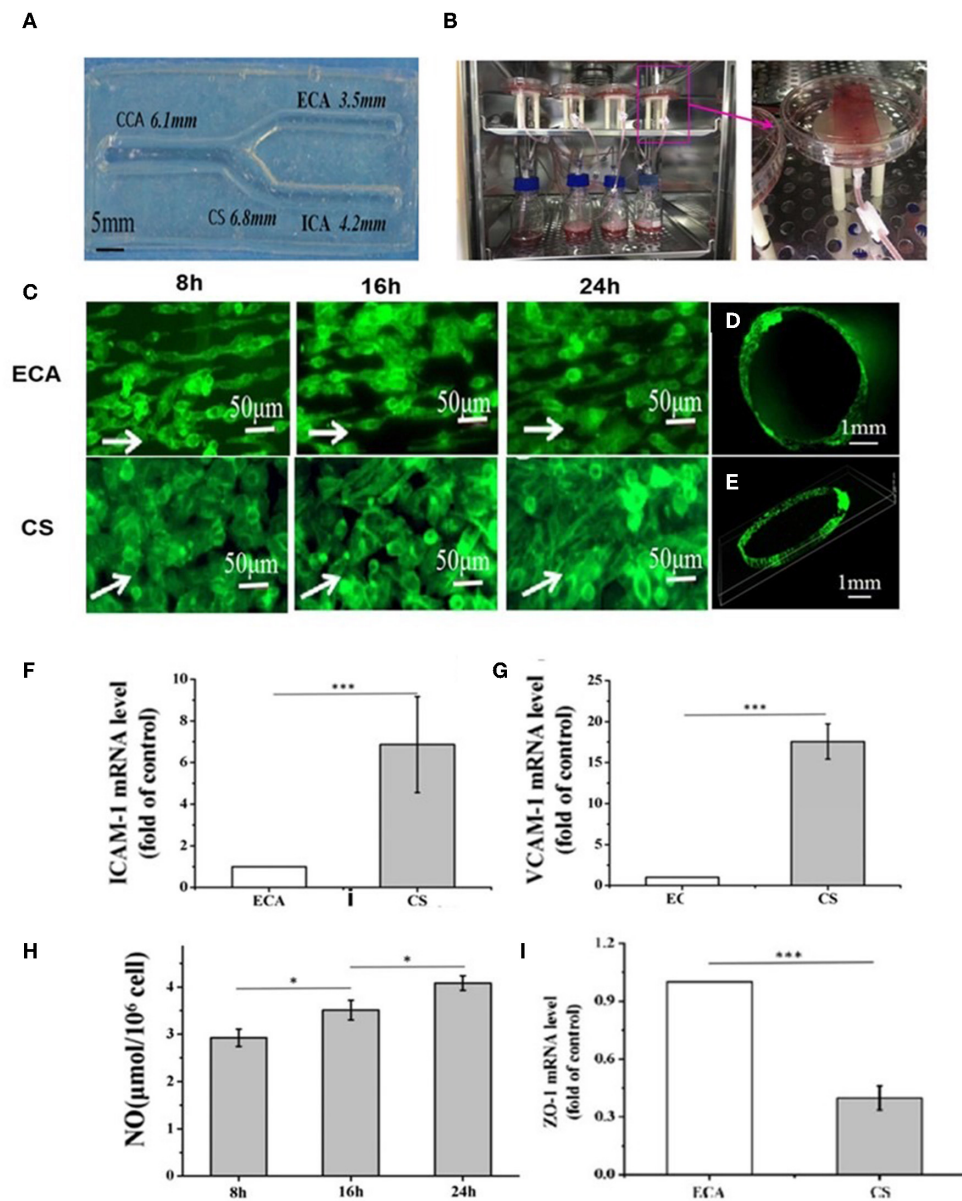


FIGURE 5 | (A) Gelatin-based carotid artery model. **(B)** Actual assembled carotid artery system. **(C)** ECs morphology in Region ECA after dynamic experiment 8, 16, and 24 h or ECs in Region ECA. ECs morphology in Region CS after dynamic experiment 8, 16, and 24 h. **(D,E)** Distribution of ECs in cross-section of Region ECA (The white arrows point in the direction of flow). **(F–I)** The expression of ICAM-1 **(F)** and VCAM-1 **(G)** was studied in the Regions ECA and CS after 24-h perfusion experiment; **(H)** The vasoactive substances NO; **(I)** Expression of ZO-1 was studied in the Regions ECA and CS after 24 h perfusion. Adapted, with permission from (183). * $P < 0.05$; *** $P < 0.001$.

data to animal and human studies. In addition to these problems, indirect culture systems also suffer a notable drawback of insufficient cell attachment to the surface of trans wells.

Taking advantage of cell sheet engineering, a more advanced *in vitro* 2D cell sheet model has been developed to mimic the layered structure of the artery wall. The 2D cell sheets include EC, SMC single layer, or EC-SMC bilayer sheets, showing great potential for evaluating drug toxicity and developing new atherosclerosis models. However, 2D cell sheets, mainly

made from a scaffold-free approach, suffer drawbacks of low mechanical property and spontaneous contraction and shrinkage. In addition to cell sheet models, with the recent advancement of microfluidic technology, endothelium-on-a-chip has been created to provide an improved *in vitro* environment to study the mechanism associated with endothelial dysfunction and monocyte attachment. Even though substantial evidence has shown that endothelium-on-a-chip systems had brought new insights into atherogenesis, such a system by far can

TABLE 3 | Summarization of the models, cell types, and biological processes studied using *in vitro* 2D culture systems and *in vitro* 3D systems covered in the current review.

| Model | Cell types | Model function (biological process) | References |
|--------------------------------------|--|--|---------------------|
| Direct cell-to-cell Interaction (2D) | VSMCs, monocytes, ECs | To study the effect of diseased conditions (M-CSF, diabetic, or vascular injury) on atherosclerotic development, including macrophage activation/adhesion to VSMC, or SMC phenotype switch | (96–98) |
| | Monocytes, HUVECs, bacterium | To study the impact of bacterial infection on atherosclerosis development (inflammation and EC apoptosis) | (99–105) |
| | ECs, THP-1s | To evaluate potential atherosclerosis treatment | (106–108) |
| In-direct Transwell Co-culture (2D) | SMCs, THP-1s | To study the significance of physical contact between SMC and monocyte for atherosclerosis development | (109) |
| | SMCs, ECs, THP-1s | To study the interactions between different cell types and their effects on atherogenesis. | (16, 110–112) |
| Cell Sheet (2D) (Decellularized ECM) | ECs and SMCs differentiated from BMCs; fibroblast, SMCs, ECs, chondrocytes | To mimic the native ECM component to improve vascular cell spreading and proliferation. | (117–121) |
| Cell Sheet (Polymer Scaffold) | SMCs | To partially mimic arterial structure | (122–124) |
| Microfluidic Chip (2D) | ECs (endothelium-on-a-chip), THP-1s | To observe endothelial response, inflammation, and interaction with monocytes during atherosclerosis. | (127–130, 132, 133) |
| | | To evaluate the effect of nanomedicine on dysfunctional endothelium | (128, 134) |
| | Multi-layer including SMCs, ECs, and foam cells | To study the mechanism of atorvastatin under the atherosclerotic condition | (131) |
| Spheroid (3D) | Foam cells | To evaluate therapeutic effects on atherosclerosis | (150, 151) |
| | SMCs | To study SMC remodeling during atherosclerosis | (152, 153) |
| | Myeloid cells, THP-1s, macrophage, dendritic, myofibroblasts | To emulate late-stage fibroatheroma | (15) |
| Cell-laden Hydrogel Construct (3D) | ECs, SMCs, monocytes neutrophil in collagen gel | To mimic early atherosclerosis and study the effect of SMC on monocyte adhesion | (157, 158) |
| | THP-1s in collagen gel | To study ECM effect on macrophage behavior under early and late atherosclerosis | (159) |
| Tissue-engineered Blood Vessel (3D) | ECs, SMCs, monocytes | To study early atherosclerosis development | (160, 161) |
| | ECs, fibroblasts, or SMCs (2-layered vessels) | To study the mechanism of atherogenesis or drug screening | (165–167) |
| | ECs, monocytes (branched geometry) | To study the endothelial behavior in the athero-prone region | (169, 170) |
| Vessel-on-a-chip (3D) | ECs, SMCs, monocytes, fibroblasts | To mimic key early atherosclerotic plaque features for mechanism study or drug screening | (18, 21, 171) |
| | ECs, SMCs | To mimic the natural vascular features on a chip with controlled geometry | (178–180) |
| | ECs, SMCs, and macrophages | To emulate atherosclerotic plaque on a chip | (181–183) |

only be applied to study biological processes in the early atherosclerosis stage. However, atherosclerosis is a complicated process, sequentially transiting from early to the advanced stage as inflammation increases, and only advanced atherosclerosis may drive severe cardiovascular disease. Thus, it is imperative to develop advanced-stage atherosclerosis models to facilitate the development of therapeutic options with improved efficacy for treating late-stage atherosclerosis.

Thanks to the advancement in tissue engineering and microfluidic technologies and the innovation of biomaterials, the fabrication of 3D *in vitro* models that recapitulate the physiological architecture and provide a pathological environment better than 2D models has become a reality. 3D

in vitro models discussed in the review include spheroid, cell-laden hydrogel constructs, TEBV, and vessel-on-a-chip. Although the spheroid system has become a new breakout for cancer drug screening, to date, the development of the spheroid model for atherosclerosis is still in its infancy, and its application is limited. This is possibly due to its limited capability to faithfully mimic the layered structures of an atherosclerotic vessel. The most impressive spheroid system developed so far can only replicate the features of atherosclerotic plaque, not the vessel wall structure. In addition to the spheroid models, cell-laden hydrogel models have also been created for atherosclerosis studies. In contrast to the spheroid model, the distinctive advantage of the cell-laden hydrogel system is its ability to recapitulate layered

TABLE 4 | Summarize the features, advantages, application, challenges, and future directions of models discussed in the review.

| Model | Features | Advantages | Applications | Challenges | Directions |
|-------------------------------------|--|---|---|---|--|
| Single-cell Systems (2D) | Seeding only one cell type in a tissue culture plate (TCP) | <ul style="list-style-type: none"> - High availability - Easy to make - Cost-effective - High reproducibility - High throughput | <ul style="list-style-type: none"> - Evaluation of drug and drug delivery system - Mechanistic studies | <ul style="list-style-type: none"> - Fail to mimic the native plaque composition and vascular structure | <ul style="list-style-type: none"> - Creating a co-culture system |
| Direct Co-culture (2D) | Direct cell-to-cell seeding of multicell types in a TCP | | <ul style="list-style-type: none"> - Study of cell-cell interaction and adhesion | <ul style="list-style-type: none"> - Difficulty mimicking native physiological structures and proper development of cellular interactions with ECM | <ul style="list-style-type: none"> - Using ECM-mimicking scaffold |
| In-direct Transwell Co-culture (2D) | Cells seeded in a TCP and trans-well inserts | | <ul style="list-style-type: none"> - Study of cellular responses <i>via</i> secretory pathways and cytokine production | | <ul style="list-style-type: none"> - Improving cell attachment - Using ECM mimicking scaffold |
| Cell Sheet (2D) | Layered structure seeded on the 2D scaffolds or no scaffolds | <ul style="list-style-type: none"> - Better mimicking the vascular wall structure than other 2D systems - Relatively easy to fabricate | <ul style="list-style-type: none"> - Potential for therapeutic evaluation - Potential for studying cell-cell interaction | <ul style="list-style-type: none"> - Prone to spontaneous shrinkage or contraction - Lacking adequate mechanical properties - More expensive than TCP based systems | <ul style="list-style-type: none"> - Increasing mechanical property through other types of scaffolds - Exploration of applications of such systems |
| Microfluidic Chip (2D) | Endothelium seeded on a chip with a flow | <ul style="list-style-type: none"> - Micro-analysis - Providing continuous monitoring and medium supply - Enhanced sensitivity - Dynamic culture - Relatively easy to make | <ul style="list-style-type: none"> - Mechanistic studies - Nanomedicine evaluation - Allowing real-time imaging | <ul style="list-style-type: none"> - Require additional types of equipment, such as pumps, tubing, and connectors - Not adequately model 3D native environments - Costly | <ul style="list-style-type: none"> - Using ECM mimicking scaffold - Using multiple vascular cells observed in the plaque |
| Spheroid (3D) | Cellular aggregates to provide 3D structures | <ul style="list-style-type: none"> - Providing spherical structures - Advanced plaque | <ul style="list-style-type: none"> - Mechanistic studies | <ul style="list-style-type: none"> - Limited capability or function in comparison to native tissue - Failing to provide the layered vascular structure - Low quantity of spheroids | <ul style="list-style-type: none"> - Large production of this model |
| Cell-laden Hydrogel Construct (3D) | Cells embedded within hydrogel scaffolds | <ul style="list-style-type: none"> - Ability to provide an ECM mimicking environment provided by the scaffold - relatively easy to make | <ul style="list-style-type: none"> - Mechanistic studies | <ul style="list-style-type: none"> - Difficult to reproduce - Poor mechanical properties | <ul style="list-style-type: none"> - Increase mechanical properties and reproducibility - Controlling the properties of hydrogels - Using these systems for various applications |
| Tissue-engineered Blood Vessel (3D) | Models reproducing native vessel structure and size with or without disease features | <ul style="list-style-type: none"> - Allowing controlled stimuli - Providing partially vessel-like structure - Dynamic culture - Providing similar size to that of native vessels | <ul style="list-style-type: none"> - Drug evaluation - Mechanistic studies - Potential for medical device evaluation - Allowing real-time imaging | <ul style="list-style-type: none"> - Majority are not developed using arterial cells - Lacking the fibroblast layer - Challenging to have a monolayer of endothelium - Failing to induce advanced atherosclerotic plaques - Expensive and difficult to reproduce - Time-consuming | <ul style="list-style-type: none"> - Producing three-layered vessel - Using arterial cells or stem cells - Incorporating T and B cells in the system - Large scale production for pharmaceutical use - Improving reproducibility - Providing advanced plaque |
| Vessel-on-a-chip (3D) | Models reproducing vessel structures with or without disease feature on a micro-sized chip | <ul style="list-style-type: none"> - Allowing controlled stimuli and real-time imaging - Providing partially vessel-like structure - Dynamic culture | <ul style="list-style-type: none"> - Applicable for drug screening - Mechanistic studies - Allowing real-time imaging | <ul style="list-style-type: none"> - Expensive and difficult to reproduce - Additional equipment to create a dynamic microenvironment - Lacking three-layered structures - Time-consuming - Inability to provide actual size vessel for medical device evaluation - Limited to drug screening | |

structures similar to the human vessel wall. In comparison to the 2D cell sheets, the cells embedded in the layered cell-laden hydrogel behave more closely to those observed *in vivo*. Among the cell-laden hydrogel systems, collagen and fibrin-based cell-laden hydrogels are the most widely used models due to their ECM mimicking property. Although significant progress in developing cell-laden collagen and fibrin hydrogel models is highly encouraging, these systems still have drawbacks of poor reproducibility issues, lack of homogeneity, and insufficient mechanical properties. It is, therefore, worth exploring a new method to improve the reproducibility and homogeneity of cell-laden hydrogel constructs in the future. In addition, the incorporation of cell-laden collagen into microfluidic devices to generate more advanced atherosclerosis models can also be an exciting future direction. Besides, future focus can move toward the development of a cell-laden hydrogel model with improved disease features using hydrogel scaffolds made from other biomaterials, such as alginate, chitosan, hyaluronic acid, gelatin, or poly(ethylene glycol), to overcome current limitations.

With respect to *in vitro* 3D models, TEBVs and vessel-on-a-chip systems are the most prominent systems with the greatest complexities and physiological relevance, which can reproduce vessel structures and provide a disease-like spatial environment with controlled mechanical stimuli. In addition, both systems empower potent tools allowing for real-time imaging and investigating multifaceted biological processes and mechanisms contributing to atherosclerosis. However, different from vessel-on-a-chip, which is limited to drug screening, TEBVs can be fabricated to possess the actual vessel size, thereby offering an opportunity to evaluate medical devices. Although the recent achievement in TEBV and vessel-on-a-chip systems is highly encouraging and has significantly contributed to atherosclerosis studies, some limitations remain. For instance, (1) vessels in some studies were made with the mouse, dermal, or venous cells instead of human inflammatory and arterial cells; (2) most of the vessels developed were single or double-layered vessels, lacking the fibroblast layer; (3) it is still challenging to create vessel structure composed of a complete monolayer of the endothelium in vessels; (4) no studies have explored an approach for the induction of advanced atherosclerotic plaques. Therefore, future studies may focus on several vital perspectives, such as how to (1) fabricate a 3-layered vessel wall using human artery cells and (2) how to create advanced atherosclerotic features including calcification necrotic core and thrombosis in the vessels. Such advanced systems will significantly impact the development of new therapeutics for treating late atherosclerosis. In addition, with the substantial improvement in stem cell technology, future research can also explore whether the incorporation of hiPSC isolated from the patient will create a system faithfully

mimicking atherosclerosis for personalized precision medicine. It is also important to address whether including immune cells (T and B cells) would generate an improved disease system. Besides that, it is imperative to explore how to produce TEBV and vessel-on-a-chip models on a large scale with excellent reproducibility. In addition, how to achieve commercialization and translation of these systems for medical end-users remain to be achieved. Moreover, the standardization of the manufacturing process of those models still needs to be performed in the near future. Lastly, in addition to the use of drugs as a therapeutic approach for atherosclerosis, medical devices such as drug-eluting stents (DESs) and drug-coated balloons (DCBs) have also been developed to treat in-stent restenosis associated with atherosclerosis. However, current commercially available DES and DCBs are found to have their issues; thus, a new coating design for improving the performance of these medical devices is needed. As aforementioned, most *in vitro* models have been developed for drug screening, with no study reporting *in vitro* systems suitable for assessing new coating designs for medical devices. Hence, developing powerful *in vitro* models for the effective evaluation of medical devices with a novel coating material is vital and should be regarded as a future research focus.

AUTHOR CONTRIBUTIONS

JC and XZ designed and outlined the article and primarily revised the draft. TL and YC drafted as well as JC edited the pathology of atherosclerosis section. RM, SM, and JS drafted as well as JC and PH edited the *in vitro* 2D model section. JC, XZ, TL, and MG drafted as well as JC and XZ edited the *in vitro* 3D model section. JC drafted the introduction and conclusion section. BB, GQ, Y-sY, and HJ provided suggestions for article writing and figure selection. SM, MG, and JC formatted references. H-WJ conceived, supervised, and reviewed outline and article writing. All the authors have reviewed and approved the manuscript for submission.

FUNDING

The authors gratefully acknowledge the financial support from the National Institutes of Health (1R01HL125391 to H-WJ), Alabama Research and Development Enhancement Fund (1ARDEF22 09 to H-WJ), American Heart Association (18POST34080260 to JC and 20PRE35210599 to XZ), National Institutes of Health (1R01HL150887 to Y-sY), and National Research Foundation of Korea (NRF) funded by the Korea government (MSIT) (Nos. 2020R1A2C3003784 and 2020M3A9I4038454 to Y-sY).

REFERENCES

- Herrington W, Lacey B, Sherliker P, Armitage J, Lewington S. Epidemiology of atherosclerosis and the potential to reduce the global burden of atherothrombotic disease. *Circ Res.* (2016) 118:535–46. doi: 10.1161/CIRCRESAHA.115.307611
- Libby P, Bornfeldt KE, Tall AR. Atherosclerosis: successes, surprises, and future challenges. *Am Heart Assoc.* (2016) 118:531–4. doi: 10.1161/CIRCRESAHA.116.308334
- Veseli BE, Perrotta P, De Meyer GR, Roth L, Van der Donckt C, Martinet W, et al. Animal models of atherosclerosis. *Eur Pharmacol J.* (2017) 816:3–13. doi: 10.1016/j.ejphar.2017.05.010

4. Getz GS, Reardon CA. Animal models of atherosclerosis. *Arter Thromb Vasc Biol.* (2012) 32:1104–15. doi: 10.1161/ATVBAHA.111.237693
5. Geraili A, Jafari P, Hassani MS, Araghi BH, Mohammadi MH, Ghafari AM, et al. Controlling differentiation of stem cells for developing personalized organ-on-chip platforms. *Adv Healthc Mater.* (2018) 7:1700426. doi: 10.1002/adhm.201700426
6. Ma C, Peng Y, Li H, Chen W. Organ-on-a-chip: a new paradigm for drug development. *Trends Pharmacol Sci.* (2021) 42:119–33. doi: 10.1016/j.tips.2020.11.009
7. Liao Z, Wang J, Zhang P, Zhang Y, Miao Y, Gao S, et al. Recent advances in microfluidic chip integrated electronic biosensors for multiplexed detection. *Biosens Bioelectron.* (2018) 121:272–80. doi: 10.1016/j.bios.2018.08.061
8. Cui P, Wang S. Application of microfluidic chip technology in pharmaceutical analysis: a review. *Pharm J Anal.* (2019) 9:238–47. doi: 10.1016/j.jpba.2018.12.001
9. Zurina IM, Presniakova VS, Butnaru DV, Svistunov AA, Timashev PS, Rochev YA. Tissue engineering using a combined cell sheet technology and scaffolding approach. *Acta Biomater.* (2020) 113:63–83. doi: 10.1016/j.actbio.2020.06.016
10. Carvalho MR, Lima D, Reis RL, Oliveira JM, Correlo VM. Anti-Cancer drug validation: the contribution of tissue-engineered models. *Stem Cell Rev.* (2017) 13:347–63. doi: 10.1007/s12015-017-9720-x
11. Grifno GN, Farrell AM, Linville RM, Arevalo D, Kim JH, Gu L, et al. Tissue-engineered blood-brain barrier models via directed differentiation of human-induced pluripotent stem cells. *Sci Rep.* (2019) 9:13957. doi: 10.1038/s41598-019-50193-1
12. Campisi M, Shin Y, Osaki T, Hajal C, Chiono V, Kamm RD. 3D self-organized microvascular model of the human blood-brain barrier with endothelial cells, pericytes and astrocytes. *Biomaterials.* (2018) 180:117–29. doi: 10.1016/j.biomaterials.2018.07.014
13. Lin YT, Seo J, Gao F, Feldman HM, Wen HL, Penney J, et al. APOE4 causes widespread molecular and cellular alterations associated with alzheimer's disease phenotypes in human iPSC-derived brain cell types. *Neuron.* (2018) 98:1141–54. doi: 10.1016/j.neuron.2018.05.008
14. Deddens JC, Sadeghi AH, Hjortnaes J, van Laake LW, Buijsrogge M, Doevendans PA, et al. Modeling the human scarred heart *in vitro*: toward new tissue engineered models. *Adv Healthc Mater.* (2017) 6:1600571. doi: 10.1002/adhm.201600571
15. Mallone A, Stenger C, Von Eckardstein A, Hoerstrup SP, Weber B. Biofabricating atherosclerotic plaques: *in vitro* engineering of a three-dimensional human fibroatheroma model. *Biomaterials.* (2018) 150:49–59. doi: 10.1016/j.biomaterials.2017.09.034
16. Noonan J, Grassia G, Mac Ritchie N, Garside P, Guzik TJ, Bradshaw AC, et al. A novel triple-cell two-dimensional model to study immune-vascular interplay in atherosclerosis. *Front Immunol.* (2019). 10:849. doi: 10.3389/fimmu.2019.00849
17. Xing Q, Vogt C, Leong KW, Zhao F. Highly aligned nanofibrous scaffold derived from decellularized human fibroblasts. *Adv Funct Mater.* (2014) 24:3027–35. doi: 10.1002/adfm.201303460
18. Zhang X, Bishawi M, Zhang G, Prasad V, Salmon E, Breithaupt JJ, et al. Modeling early stage atherosclerosis in a primary human vascular microphysiological system. *Nat Commun.* (2020) 11:1–17. doi: 10.1038/s41467-020-19197-8
19. Korff T, Kimmina S, Martiny-Baron G, Augustin HG. Blood vessel maturation in a 3-dimensional spheroidal coculture model: direct contact with smooth muscle cells regulates endothelial cell quiescence and abrogates VEGF responsiveness. *FASEB J.* (2001) 15:447–57. doi: 10.1096/fj.00-0139com
20. Dash BC, Setia O, Gorecka J, Peyvandi H, Duan K, Lopes L, et al. A dense fibrillar collagen scaffold differentially modulates secretory function of iPSC-derived vascular smooth muscle cells to promote wound healing. *Cells.* (2020) 9:40966. doi: 10.3390/cells9040966
21. Robert J WB, Frese L, Emmert MY, Schmidt D, von Eckardstein A, et al. A three-dimensional engineered artery model for *in vitro* atherosclerosis research. *PLoS ONE.* (2013) 8:e79821. doi: 10.1371/journal.pone.0079821
22. Pahwa R, Jialal I. *Atherosclerosis*. Treasure Island, FL: StatPearls. (2021).
23. Oppi S, Luscher TF, Stein S. Mouse models for atherosclerosis research-which is my line? *Front Cardiovasc Med.* (2019) 6:46. doi: 10.3389/fcvm.2019.00046
24. Gimbrone MA, Garcia-Cardena G. Endothelial cell dysfunction and the pathobiology of atherosclerosis. *Circ Res.* (2016) 118:620–36. doi: 10.1161/CIRCRESAHA.115.306301
25. Musunuru K, Kathiresan S. Surprises from genetic analyses of lipid risk factors for atherosclerosis. *Circ Res.* (2016) 118:579–85. doi: 10.1161/CIRCRESAHA.115.306398
26. Chiesa ST, Charakida M. High-density lipoprotein function and dysfunction in health and disease. *Cardiovasc Drugs Ther.* (2019) 33:207–19. doi: 10.1007/s10557-018-06846-w
27. Glasser SP, Selwyn AP, Ganz P. Atherosclerosis: risk factors and the vascular endothelium. *Am Heart J.* (1996) 131:379–84. doi: 10.1016/S0002-8703(96)90370-1
28. Goldstein JL, Brown MS. A century of cholesterol and coronaries: from plaques to genes to statins. *Cell.* (2015) 161:161–72. doi: 10.1016/j.cell.2015.01.036
29. Robbins CS, Hilgendorf I, Weber GF, Theurl I, Iwamoto Y, Figueiredo JL, et al. Local proliferation dominates lesional macrophage accumulation in atherosclerosis. *Nat Med.* (2013) 19:1166–72. doi: 10.1038/nm.3258
30. Yurdagül A, Doran AC, Cai B, Fredman G, Tabas IA. Mechanisms and consequences of defective efferocytosis in atherosclerosis. *Front Cardiovasc Med.* (2017) 4:86. doi: 10.3389/fcvm.2017.00086
31. Bennett MR, Sinha S, Owens GK. Vascular smooth muscle cells in atherosclerosis. *Circ Res.* (2016) 118:692–702. doi: 10.1161/CIRCRESAHA.115.306361
32. Allahverdian S, Chaabane C, Boukais K, Francis GA, Bochaton-Piallat ML. Smooth muscle cell fate and plasticity in atherosclerosis. *Cardiovasc Res.* (2018) 114:540–50. doi: 10.1093/cvr/cvy022
33. Ruiz JL, Weinbaum S, Aikawa E, Hutcheson JD. Zooming in on the genesis of atherosclerotic plaque microcalcifications. *J Physiol.* (2016) 594:2915–27. doi: 10.1113/JP271339
34. Shi X, Gao J, Lv Q, Cai H, Wang F, Ye R, Liu X. Calcification in atherosclerotic plaque vulnerability: friend or foe? *Front Physiol.* (2020) 11:56. doi: 10.3389/fphys.2020.00056
35. Su G, Sun G, Liu H, Shu L, Liang Z. Downregulation of miR-34a promotes endothelial cell growth and suppresses apoptosis in atherosclerosis by regulating Bcl-2. *Heart Vessels.* (2018) 33:1185–94. doi: 10.1007/s00380-018-1169-6
36. Tang F, Yang TL. MicroRNA-126 alleviates endothelial cells injury in atherosclerosis by restoring autophagic flux via inhibiting of PI3K/Akt/mTOR pathway. *Biochem Biophys Res Commun.* (2018) 495:1482–9. doi: 10.1016/j.bbrc.2017.12.001
37. Xu L, Geng T, Zang G, Bo L, Liang Y, Zhou H, et al. Exosome derived from CD137-modified endothelial cells regulates the Th17 responses in atherosclerosis. *Cell J. Mol Med.* (2020) 24:4659–67. doi: 10.1111/jcmm.15130
38. Ma J, Chen L, Zhu X, Li Q, Hu L, Li H. Mesenchymal stem cell-derived exosomal miR-21a-5p promotes M2 macrophage polarization and reduces macrophage infiltration to attenuate atherosclerosis. *Acta Biochim. Biophys.* (2021) 53:1227–36. doi: 10.1093/abbs/gmab102
39. Lee GY, Kim JH, Choi KY, Yoon HY, Kim K, Kwon IC, et al. Hyaluronic acid nanoparticles for active targeting atherosclerosis. *Biomaterials.* (2015) 53:341–8. doi: 10.1016/j.biomaterials.2015.02.089
40. Beldman TJ, Senders ML, Alaarg A, Pérez-Medina C, Tang J, Zhao Y, et al. Hyaluronan nanoparticles selectively target plaque-associated macrophages and improve plaque stability in atherosclerosis. *ACS Nano.* (2017) 11:5785–99. doi: 10.1021/acsnano.7b01385
41. Yuan W, Yu B, Yu M, Kuai R, Morin EE, Wang H, et al. Synthetic high-density lipoproteins delivering liver X receptor agonist prevent atherogenesis by enhancing reverse cholesterol transport. *J Control Release.* (2021) 329:361–71. doi: 10.1016/j.jconrel.2020.11.016
42. He H, Wang J, Yannie PJ, Korzun WJ, Yang H, Ghosh S. Nanoparticle-based “two-pronged” approach to regress atherosclerosis by simultaneous modulation of cholesterol influx and efflux. *Biomaterials.* (2020) 260:120333. doi: 10.1016/j.biomaterials.2020.120333

43. Kim H, Kumar S, Kang DW, Jo H, Park JH. Affinity-driven design of cargo-switching nanoparticles to leverage a cholesterol-rich microenvironment for atherosclerosis therapy. *ACS Nano*. (2020) 14:6519–31. doi: 10.1021/acsnano.9b08216
44. Wang Y, Zhang K, Li T, Maruf A, Qin X, Luo L, et al. Macrophage membrane functionalized biomimetic nanoparticles for targeted anti-atherosclerosis applications. *Theranostics*. (2021) 11:164. doi: 10.7150/thno.47841
45. Allen SD, Liu YG, Kim T, Bobbala S, Yi S, Zhang X, et al. Celastrol-loaded PEG-b-PPS nanocarriers as an anti-inflammatory treatment for atherosclerosis. *Biomater Sci*. (2019) 7:657–68. doi: 10.1039/C8BM01224E
46. Gao C, Huang Q, Liu C, Kwong CH, Yue L, Wan JB, et al. Treatment of atherosclerosis by macrophage-biomimetic nanoparticles via targeted pharmacotherapy and sequestration of proinflammatory cytokines. *Nat Commun*. (2020) 11:1–14. doi: 10.1038/s41467-020-16439-7
47. Pham LM, Kim EC, Ou W, Phung CD, Nguyen TT, Pham TT, et al. Targeting and clearance of senescent foamy macrophages and senescent endothelial cells by antibody-functionalized mesoporous silica nanoparticles for alleviating aorta atherosclerosis. *Biomaterials*. (2021) 269:120677. doi: 10.1016/j.biomaterials.2021.120677
48. Hossaini Nasr S, Rashidjahanabad Z, Ramadan S, Kauffman N, Parameswaran N, Zinn KR, et al. Effective atherosclerotic plaque inflammation inhibition with targeted drug delivery by hyaluronan conjugated atorvastatin nanoparticles. *Nanoscale*. (2020) 12:9541–56. doi: 10.1039/D0NR00308E
49. Wang Y, Li L, Zhao W, Dou Y, An H, Tao H, et al. Targeted therapy of atherosclerosis by a broad-spectrum reactive oxygen species scavenging nanoparticle with intrinsic anti-inflammatory activity. *ACS Nano*. (2018) 12:8943–60. doi: 10.1021/acsnano.8b02037
50. Chen F, Chen J, Han C, Yang Z, Deng T, Zhao Y, et al. Theranostics of atherosclerosis by the indole molecule-templated self-assembly of probucol nanoparticles. *Mater J Chem B*. (2021) 9:4134–42. doi: 10.1039/D1TB00432H
51. Ma Y, Ma Y, Gao M, Han Z, Jiang W, Gu Y, et al. Platelet-mimicking therapeutic system for noninvasive mitigation of the progression of atherosclerotic plaques. *Adv Sci*. (2021) 8:2004128. doi: 10.1002/adv.202004128
52. Kim M, Sahu A, Hwang Y, Kim GB, Nam GH, Kim IS, et al. Targeted delivery of anti-inflammatory cytokine by nanocarrier reduces atherosclerosis in Apo E^{-/-} mice. *Biomaterials*. (2020) 226:119550. doi: 10.1016/j.biomaterials.2019.119550
53. Ma B, Xu H, Zhuang W, Wang Y, Li G, Wang Y, et al. responsive nanoplatform with two-photon AIE imaging for atherosclerosis diagnosis and “two-pronged” therapy. *Small*. (2020) 16:2003253. doi: 10.1002/sml.202003253
54. Wu G, Zhang J, Zhao Q, Zhuang W, Ding J, Zhang C, et al. Molecularly engineered macrophage-derived exosomes with inflammation tropism and intrinsic heme biosynthesis for atherosclerosis treatment. *Angew Chem Int*. (2020) 59:4068–74. doi: 10.1002/anie.201913700
55. Tao W, Yurdagul A, Kong N, Li W, Wang X, Doran AC, et al. siRNA nanoparticles targeting CaMKII γ in lesional macrophages improve atherosclerotic plaque stability in mice. *Sci Transl Med*. (2020) 12:aay1063. doi: 10.1126/scitranslmed.aay1063
56. Flores AM, Hosseini-Nassab N, Jarr KU, Ye J, Zhu X, Wirka R, et al. Pro-efferocytic nanoparticles are specifically taken up by lesional macrophages and prevent atherosclerosis. *Nat Nanotechnol*. (2020) 15:154–61. doi: 10.1038/s41565-019-0619-3
57. Guo C, Ma R, Liu X, Chen T, Li Y, Yu Y, et al. Silica nanoparticles promote oxLDL-induced macrophage lipid accumulation and apoptosis via endoplasmic reticulum stress signaling. *Sci Tot Environ*. (2018) 631–2:570–9. doi: 10.1016/j.scitotenv.2018.02.312
58. Gao W, Sun Y, Cai M, Zhao Y, Cao W, Liu Z, et al. Copper sulfide nanoparticles as a photothermal switch for TRPV1 signaling to attenuate atherosclerosis. *Nat Commun*. (2018) 9:231. doi: 10.1038/s41467-017-02657-z
59. Islam K, Timraz S, Nasser R, Gater D, Pearson Y, Christoforou N. Co-culture methods used to model atherosclerosis in vitro using endothelial, smooth muscle, and monocyte cells. *SM J Biomed Eng*. (2016) 2:1008.
60. Armentano RL, Levenson J, Barra JG, Fischer GJ, Breitbart GJ, Pichel RH, et al. Assessment of elastin and collagen contribution to aortic elasticity in conscious dogs. *Am J Physiol heart C*. (1991) 260:H1870–7. doi: 10.1152/ajpheart.1991.260.6.H1870
61. Hennig B, Chow CK. Lipid peroxidation and endothelial cell injury: implications in atherosclerosis. *Free Radio Biol Med*. (1988) 4:99–106. doi: 10.1016/0891-5849(88)90070-6
62. van Buul-Wortelboer MF, Brinkman HJ, Dingemans KP, de Groot PG, van Aken WG, van Mourik JA. Reconstitution of the vascular wall *in vitro*. A novel model to study interactions between endothelial and smooth muscle cells. *Exp Cell Res*. (1986) 162:151–8. doi: 10.1016/0014-4827(86)90433-7
63. Davies PF, Truskey GA, Warren HB, O'Connor SE, Eisenhaure BH. Metabolic cooperation between vascular endothelial cells and smooth muscle cells in co-culture: changes in low density lipoprotein metabolism. *J Cell Biol*. (1985) 101:871–9. doi: 10.1083/jcb.101.3.871
64. Zeuke S, Ulmer AJ, Kusumoto S, Katus HA, Heine H. TLR4-mediated inflammatory activation of human coronary artery endothelial cells by LPS. *Cardiovasc Res*. (2002) 56:126–34. doi: 10.1016/S0008-6363(02)00512-6
65. Takahara N, Kashiwagi A, Maegawa H, Shigeta Y. Lysophosphatidylcholine stimulates the expression and production of MCP-1 by human vascular endothelial cells. *Metabolism*. (1996) 45:559–64. doi: 10.1016/S0026-0495(96)90024-4
66. Andueza A, Kumar S, Kim J, Kang DW, Mumme HL, Perez JI, et al. Endothelial reprogramming by disturbed flow revealed by single-cell RNA and chromatin accessibility study. *Cell Rep*. (2020) 33:108491. doi: 10.1016/j.celrep.2020.108491
67. Blackman BR, Garcia-Cardena G, Gimbrone MA. A new *in vitro* model to evaluate differential responses of endothelial cells to simulated arterial shear stress waveforms. *J Biomech Eng*. (2002) 124:397–407. doi: 10.1115/1.1486468
68. Cominacini L, Rigoni A, Pasini AF, Garbin U, Davoli A, Campagnola M, et al. The binding of oxidized low-density lipoprotein (ox-LDL) to ox-LDL receptor-1 reduces the intracellular concentration of nitric oxide in endothelial cells through an increased production of superoxide. *J Biol Chem*. (2001) 276:13750–5. doi: 10.1074/jbc.M01061200
69. Yu Y, Fukuda N, Yao EH, Matsumoto T, Kobayashi N, Suzuki R, et al. Effects of an ARB on endothelial progenitor cell function and cardiovascular oxidation in hypertension. *Am J Hypertens*. (2008) 21:72–7. doi: 10.1038/ajh.2007.5
70. Krishnaswamy G, Smith JK, Mukkamala R, Hall K, Joyner W, Yerra L, et al. Multifunctional cytokine expression by human coronary endothelium and regulation by monokines and glucocorticoids. *Microvasc Res*. (1998) 55:189–200. doi: 10.1006/mvre.1998.2079
71. Hayashi K, Takahashi M, Nishida W, Yoshida K, Ohkawa Y, Kitabatake A, et al. Phenotypic modulation of vascular smooth muscle cells induced by unsaturated lysophosphatidic acids. *Circ Res*. (2001) 89:251–8. doi: 10.1161/hh1501.094265
72. Pidkova NA, Cherepanova OA, Yoshida T, Alexander MR, Deaton RA, Thomas JA, et al. Oxidized phospholipids induce phenotypic switching of vascular smooth muscle cells *in vivo* and *in vitro*. *Circ Res*. (2007) 101:792–801. doi: 10.1161/CIRCRESAHA.107.152736
73. Clement N, Gueguen M, Glorian M, Blaise R, Andreani M, Brou C, et al. Notch3 and IL-1 β exert opposing effects on a vascular smooth muscle cell inflammatory pathway in which NF- κ B drives crosstalk. *J Cell Sci*. (2007) 120:3352–61. doi: 10.1242/jcs.007872
74. Chen CN, Li YS, Yeh YT, Lee PL, Usami S, Chien S, et al. Synergistic roles of platelet-derived growth factor-BB and interleukin-1 β in phenotypic modulation of human aortic smooth muscle cells. *Proc Natl Acad Sci USA*. (2006) 103:2665–70. doi: 10.1073/pnas.0510973103
75. Yoshida T, Gan Q, Owens GK. Kruppel-like factor 4, Elk-1, and histone deacetylases cooperatively suppress smooth muscle cell differentiation markers in response to oxidized phospholipids. *Am J Physiol Cell Physiol*. (2008) 295:C1175–1182. doi: 10.1152/ajpcell.00288.2008
76. Holycross BJ, Blank RS, Thompson MM, Peach MJ, Owens GK. Platelet-derived growth factor-BB-induced suppression of smooth muscle cell differentiation. *Circ Res*. (1992) 71:1525–32. doi: 10.1161/01.RES.71.6.1525
77. Wang Z, Wang DZ, Hockemeyer D, McAnally J, Nordheim A, Olson EN. Myocardin and ternary complex factors compete for SRF to control smooth muscle gene expression. *Nature*. (2004) 428:185–9. doi: 10.1038/nature02382

78. Oh J, Riek AE, Weng S, Petty M, Kim D, Colonna M, et al. Endoplasmic reticulum stress controls M2 macrophage differentiation and foam cell formation. *J Biol Chem.* (2012) 287:11629–41. doi: 10.1074/jbc.M111.338673
79. Finn AV, Nakano M, Polavarapu R, Karmali V, Saeed O, Zhao X, et al. Hemoglobin directs macrophage differentiation and prevents foam cell formation in human atherosclerotic plaques. *J Am Coll Cardiol.* (2012) 59:166–77. doi: 10.1016/j.jacc.2011.10.852
80. McLaren JE, Michael DR, Salter RC, Ashlin TG, Calder CJ, Miller AM, et al. IL-33 reduces macrophage foam cell formation. *J Immunol.* (2010) 185:1222–9. doi: 10.4049/jimmunol.1000520
81. Kasikara C, Schilperoort M, Gerlach B, Xue C, Wang X, Zheng Z, et al. Deficiency of macrophage PHACTR1 impairs efferocytosis and promotes atherosclerotic plaque necrosis. *J Clin Invest.* (2021) 131:e145275. doi: 10.1172/JCI145275
82. Yin C, Vrieze AM, Rosoga M, Akingbasote J, Pawlak EN, Jacob RA, et al. Efferocytic defects in early atherosclerosis are driven by GATA2 overexpression in macrophages. *Front Immunol.* (2020) 11:594136. doi: 10.3389/fimmu.2020.594136
83. Peng X, Chen H, Li Y, Huang D, Huang B, Sun D. Effects of NIX-mediated mitophagy on ox-LDL-induced macrophage pyroptosis in atherosclerosis. *Cell Biol Int.* (2020) 44:1481–90. doi: 10.1002/cbin.11343
84. Wang H, Fu H, Zhu R, Wu X, Ji X, Li X, et al. BRD4 contributes to LPS-induced macrophage senescence and promotes progression of atherosclerosis-associated lipid uptake. *Aging.* (2020) 12:9240–59. doi: 10.18632/aging.103200
85. Zhang X, Li J, Luo S, Wang M, Huang Q, Deng Z, et al. IgE contributes to atherosclerosis and obesity by affecting macrophage polarization, macrophage protein network, and foam cell formation. *Arterioscler Thromb Vasc Biol.* (2020) 40:597–610. doi: 10.1161/ATVBAHA.119.313744
86. BaidZajevs K, Hadadi É, Lee B, Lum J, Shihui F, Sudbery I, et al. Macrophage polarisation associated with atherosclerosis differentially affects their capacity to handle lipids. *Atherosclerosis.* (2020) 305:10–8. doi: 10.1016/j.atherosclerosis.2020.05.003
87. Bandaru S, Ala C, Ekstrand M, Akula MK, Pedrelli M, Liu X, et al. Lack of RAC1 in macrophages protects against atherosclerosis. *PLoS ONE.* (2020) 15:e0239284. doi: 10.1371/journal.pone.0239284
88. Roy A, Saqib U, Wary K, Baig MS. Macrophage neuronal nitric oxide synthase (NOS1) controls the inflammatory response and foam cell formation in atherosclerosis. *Int Immunopharmacol.* (2020) 83:106382. doi: 10.1016/j.intimp.2020.106382
89. Gonzalez-Cotto M, Guo L, Karwan M, Sen SK, Barb J, Collado CJ, et al. TREM14 promotes inflammatory programs in human and murine macrophages and alters atherosclerosis lesion composition in the apolipoprotein E deficient mouse. *Front Immunol.* (2020) 11:397. doi: 10.3389/fimmu.2020.00397
90. Zeng Z, Zheng Q, Chen J, Tan X, Li Q, Ding L, et al. FGF21 mitigates atherosclerosis via inhibition of NLRP3 inflammasome-mediated vascular endothelial cells pyroptosis. *Exp Cell Res.* (2020) 393:112108. doi: 10.1016/j.yexcr.2020.112108
91. Huang D, Gao W, Zhong X, Ge J. NLRP3 activation in endothelia promotes development of diabetes-associated atherosclerosis. *Aging.* (2020) 12:18181–91. doi: 10.18632/aging.103666
92. Heo KS, Le NT, Cushman HJ, Giancursio CJ, Chang E, Woo CH, et al. Disturbed flow-activated p90RSK kinase accelerates atherosclerosis by inhibiting SENP2 function. *J Clin Invest.* (2015) 125:1299–310. doi: 10.1172/JCI76453
93. Chen L, Yang W, Guo Y, Chen W, Zheng P, Zeng J, et al. Exosomal lncRNA GAS5 regulates the apoptosis of macrophages and vascular endothelial cells in atherosclerosis. *PLoS ONE.* (2017) 12:e0185406. doi: 10.1371/journal.pone.0185406
94. Warboys CM, de Luca A, Amini N, Luong L, Duckles H, Hsiao S, et al. Disturbed flow promotes endothelial senescence via a p53-dependent pathway. *Arterioscler Thromb Vasc Biol.* (2014) 34:985–95. doi: 10.1161/ATVBAHA.114.303415
95. Conklin AC, Nishi H, Schlamp F, Örd T, Öunap L, Kaikkonen MU, et al. Meta-analysis of smooth muscle lineage transcriptomes in atherosclerosis and their relationships to *in vitro* models. *Immunometabolism.* (2021) 3:e210022. doi: 10.20900/immunometab20210022
96. Vasudevan SS, Lopes NH, Seshiah PN, Wang T, Marsh CB, Kereiakes DJ, et al. Mac-1 and Fas activities are concurrently required for execution of smooth muscle cell death by M-CSF-stimulated macrophages. *Cardiovasc Res.* (2003) 59:723–33. doi: 10.1016/S0008-6363(03)00514-5
97. Meng L, Park J, Cai Q, Lanting L, Reddy MA, Natarajan R. Diabetic conditions promote binding of monocytes to vascular smooth muscle cells and their subsequent differentiation. *Am J Physiol Heart Circ Physiol.* (2010) 298:H736–45. doi: 10.1152/ajpheart.00935.2009
98. Chaterji S, Park K, Panitch A. Scaffold-free *in vitro* arterial mimetics: the importance of smooth muscle-endothelium contact. *Tissue Eng A.* (2010) 16:1901–12. doi: 10.1089/ten.tea.2009.0271
99. Beck JD, Elter JR, Heiss G, Couper D, Mauriello SM, Offenbacher S. Relationship of periodontal disease to carotid artery intima-media wall thickness. *Arterioscler Thromb Vasc Biol.* (2001) 21:1816–22. doi: 10.1161/hq1101.097803
100. Gibson FC, Yumoto H, Takahashi Y, Chou HH, Genco CA. Innate immune signaling and porphyromonas gingivalis-accelerated atherosclerosis. *Dent J Res.* (2006) 85:106–21. doi: 10.1177/154405910608500202
101. Tous M, Ribas V, Escolà-Gil JC, Blanco-Vaca F, Calpe-Berdiel L, Coll B, et al. Manipulation of inflammation modulates hyperlipidemia in apolipoprotein E-deficient mice: a possible role for interleukin-6. *Cytokine.* (2006) 34:224–32. doi: 10.1016/j.cyto.2006.05.007
102. Herzberg MC, Meyer MW. Dental plaque, platelets, and cardiovascular diseases. *Ann Periodontol.* (1998) 3:151–60. doi: 10.1902/annals.1998.3.1.151
103. Hashizume T, Kurita-Ochiai T, Yamamoto M. Porphyromonas gingivalis stimulates monocyte adhesion to human umbilical vein endothelial cells. *FEMS Microbiol Immunol.* (2011) 62:57–65. doi: 10.1111/j.1574-695X.2011.00786.x
104. Bugueno IM, Khelif Y, Seelam N, Morand DN, Tenenbaum H, Davideau JL, et al. Porphyromonas gingivalis differentially modulates cell death profile in Ox-LDL and TNF- α pre-treated endothelial cells. *PLoS ONE.* (2016) 11:e0154590–e0154590. doi: 10.1371/journal.pone.0154590
105. Gualtero DF, Viafara-Garcia SM, Morantes SJ, Buitrago DM, Gonzalez OA, Lafaurie GI. Rosuvastatin inhibits interleukin (IL)-8 and IL-6 production in human coronary artery endothelial cells stimulated with aggregatibacter actinomycetemcomitans serotype b. *Periodontol J.* (2017) 88:225–35. doi: 10.1902/jop.2016.160288
106. Marino M, Bo' CD, Tucci M, Klimis-Zacas D, Riso P, Porrini M. Modulation of adhesion process, E-Selectin and VEGF production by anthocyanins and their metabolites in an *in vitro* model of atherosclerosis. *Nutrients.* (2020) 12:655. doi: 10.3390/nu12030655
107. Ma S, Tian XY, Zhang Y, Mu C, Shen H, Bismuth J, et al. E-selectin-targeting delivery of microRNAs by microparticles ameliorates endothelial inflammation and atherosclerosis. *Sci Rep.* (2016) 6:22910. doi: 10.1038/srep22910
108. Xu R, Li S, Shi M, Li Z, Wang Y, Li J, et al. Peptide-based high-density lipoprotein promotes adipose tissue browning and restrains development of atherosclerosis and type 2 diabetes. *Nano Today.* (2021) 36:101054. doi: 10.1016/j.nantod.2020.101054
109. Cai Q, Lanting L, Natarajan R. Interaction of monocytes with vascular smooth muscle cells regulates monocyte survival and differentiation through distinct pathways. *Arterioscler Thromb Vasc Biol.* (2004) 24:2263–70. doi: 10.1161/01.ATV.0000146552.16943.5e
110. Nam MH, Lee HS, Seomun Y, Lee Y, Lee KW. Monocyte-endothelium-smooth muscle cell interaction in co-culture: proliferation and cytokine productions in response to advanced glycation end products. *Biochim Biophys Acta.* (2011) 1810:907–12. doi: 10.1016/j.bbagen.2011.06.005
111. Harokopakis E, Albrez MH, Martin MH, Hajishengallis G. TLR2 transmodulates monocyte adhesion and transmigration via Rac1- and PI3K-mediated inside-out signaling in response to *Porphyromonas gingivalis* fimbriae. *J Immunol.* (2006) 176:7645–56. doi: 10.4049/jimmunol.176.12.7645
112. Westhorpe CL, Dufour EM, Maisa A, Jaworowski A, Crowe SM, Muller WA. Endothelial cell activation promotes foam cell formation by monocytes

- following transendothelial migration in an *in vitro* model. *Exp Mol Pathol.* (2012) 93:220–6. doi: 10.1016/j.yexmp.2012.03.014
113. Zuniga MC, White SL, Zhou W. Design and utilization of macrophage and vascular smooth muscle cell co-culture systems in atherosclerotic cardiovascular disease investigation. *Vasc Med.* (2014) 19:394–406. doi: 10.1177/1358863X14550542
 114. Zhou J, Fritze O, Schleicher M, Wendel HP, Schenke-Layland K, Harasztsi C, et al. Impact of heart valve decellularization on 3-D ultrastructure, immunogenicity and thrombogenicity. *Biomaterials.* (2010) 31:2549–54. doi: 10.1016/j.biomaterials.2009.11.088
 115. Frantz C, Stewart KM, Weaver VM. The extracellular matrix at a glance. *J Cell Sci.* (2010) 123:4195–200. doi: 10.1242/jcs.023820
 116. Crapo PM, Gilbert TW, Badylak SF. An overview of tissue and whole organ decellularization processes. *Biomaterials.* (2011) 32:3233–43. doi: 10.1016/j.biomaterials.2011.01.057
 117. Cho SW, Lim SH, Kim IK, Hong YS, Kim SS, Yoo KJ, et al. Small-diameter blood vessels engineered with bone marrow-derived cells. *Ann Surg.* (2005) 241:506–15. doi: 10.1097/01.sla.0000154268.12239.ed
 118. Choi JS, Yang HJ, Kim BS, Kim JD, Kim JY, Yoo B, et al. Human extracellular matrix (ECM) powders for injectable cell delivery and adipose tissue engineering. *J Control Release.* (2009) 139:2–7. doi: 10.1016/j.jconrel.2009.05.034
 119. Choi JS, Kim BS, Kim JY, Kim JD, Choi YC, et al. Decellularized extracellular matrix derived from human adipose tissue as a potential scaffold for allograft tissue engineering. *J Biomed Mater Res A.* (2011) 97:292–9. doi: 10.1002/jbm.a.33056
 120. Kim BS, Choi JS, Kim JD, Choi YC, Cho YW. Recellularization of decellularized human adipose-tissue-derived extracellular matrix sheets with other human cell types. *Cell Tissue Res.* (2012) 348:559–67. doi: 10.1007/s00441-012-1391-y
 121. McCrary MW, Bousalis D, Mobini S, Song YH, Schmidt CE. Decellularized tissues as platforms for *in vitro* modeling of healthy and diseased tissues. *Acta Biomater.* (2020) 111:1–19. doi: 10.1016/j.actbio.2020.05.031
 122. Rim NG, Yih A, Hsi P, Wang Y, Zhang Y, Wong JY. Micropatterned cell sheets as structural building blocks for biomimetic vascular patches. *Biomaterials.* (2018) 181:126–39. doi: 10.1016/j.biomaterials.2018.07.047
 123. Williams NP, Rhodehamel M, Yan C, Smith AST, Jiao A, Murry CE, et al. Engineering anisotropic 3D tubular tissues with flexible thermoresponsive nanofabricated substrates. *Biomaterials.* (2020) 240:119856. doi: 10.1016/j.biomaterials.2020.119856
 124. Owaki T, Shimizu T, Yamato M, Okano T. Cell sheet engineering for regenerative medicine: current challenges and strategies. *Biotechnol J.* (2014) 9:904–14. doi: 10.1002/biot.201300432
 125. Jia Z, Guo H, Xie H, Bao X, Huang Y, Yang G, et al. Harvesting prevascularized smooth muscle cell sheets from common polystyrene culture dishes. *PLoS ONE.* (2018) 13:e0204677. doi: 10.1371/journal.pone.0204677
 126. Coluccio ML, Perozziello G, Malara N, Parrotta E, Zhang P, Gentile F, et al. Microfluidic platforms for cell cultures and investigations. *Microelectron Eng.* (2019) 208:14–28. doi: 10.1016/j.mee.2019.01.004
 127. Davignon J, Ganz P. Role of endothelial dysfunction in atherosclerosis. *Circulation.* (2004) 109:27–32. doi: 10.1161/01.CIR.0000131515.03336.f8
 128. Zheng W, Huang R, Jiang B, Zhao Y, Zhang W, Jiang X. An early-stage atherosclerosis research model based on microfluidics. *Small.* (2016) 12:2022–34. doi: 10.1002/smll.201503241
 129. Shin Y, Lim S, Kim J, Jeon JS, Yoo H, Gweon B. Emulating endothelial dysfunction by implementing an early atherosclerotic microenvironment within a microfluidic chip. *Lab Chip.* (2019) 19:3664–77. doi: 10.1039/C9LC00352E
 130. Tovar-Lopez F, Thurgood P, Gilliam C, Nguyen N, Pirogova E, Khoshmanesh K, et al. A microfluidic system for studying the effects of disturbed flow on endothelial cells. *Front Bioeng Biotechnol.* (2019) 7:81. doi: 10.3389/fbioe.2019.00081
 131. Gu X, Xie S, Hong D, Ding Y. An *in vitro* model of foam cell formation induced by a stretchable microfluidic device. *Sci Rep.* (2019) 9:1–11. doi: 10.1038/s41598-019-43902-3
 132. Venugopal Menon N, Tay HM, Pang KT, Dalan R, Wong SC, et al. A tunable microfluidic 3D stenosis model to study leukocyte-endothelial interactions in atherosclerosis. *APL Bioeng.* (2018) 2:016103. doi: 10.1063/1.4993762
 133. Nam U, Kim S, Park J, Jeon JS. Lipopolysaccharide-induced vascular inflammation model on microfluidic chip. *Micromachines.* (2020) 11:747. doi: 10.3390/mi11080747
 134. Kim Y, Lobatto ME, Kawahara T, Chung BL, Mieszawska AJ, Sanchez-Gaytan BL, et al. Probing nanoparticle translocation across the permeable endothelium in experimental atherosclerosis. *Proc Natl Acad Sci USA.* (2014) 111:1078–83. doi: 10.1073/pnas.1322725111
 135. Skardal A, Murphy SV, Devarasetty M, Mead I, Kang HW, Seol YJ, et al. Multi-tissue interactions in an integrated three-tissue organ-on-a-chip platform. *Sci Rep.* (2017) 7:1–16. doi: 10.1038/s41598-017-08879-x
 136. Cukierman E, Pankov R, Stevens DR, Yamada KM. Taking cell-matrix adhesions to the third dimension. *Science.* (2001) 294:1708–12. doi: 10.1126/science.1064829
 137. Moroni L, Burdick JA, Highley C, Lee SJ, Morimoto Y, Takeuchi S, et al. Biofabrication strategies for 3D *in vitro* models and regenerative medicine. *Nat Rev Mater.* (2018) 3:21–37. doi: 10.1038/s41578-018-0006-y
 138. Lin RZ, Chang HY. Recent advances in three-dimensional multicellular spheroid culture for biomedical research. *Biotechnol J.* (2008) 3:1172–84. doi: 10.1002/biot.200700228
 139. Fennema E, Rivron N, Rouwkema J, van Blitterswijk C, de Boer J. Spheroid culture as a tool for creating 3D complex tissues. *Trends Biotechnol.* (2013) 31:108–15. doi: 10.1016/j.tibtech.2012.12.003
 140. Handschel JG, Depprich RA, Kübler NR, Wiesmann HP, Ommerborn M, Meyer U. Prospects of micromass culture technology in tissue engineering. *Head Face Med.* (2007) 3:4. doi: 10.1186/1746-160X-3-4
 141. Sutherland RM, McCredie JA, Inch WR. Growth of multicell spheroids in tissue culture as a model of nodular carcinomas. *Natl Cancer Inst J.* (1971) 46:113–20.
 142. Yuhas JM, Li AP, Martinez AO, Ladman AJ. A simplified method for production and growth of multicellular tumor spheroid. *Cancer Res.* (1977) 37:3639–43.
 143. Narayanan RA, Rink A, Beattie CW, Hu WS. Differential gene expression analysis during porcine hepatocyte spheroid formation. *Mammalian Genome.* (2002) 13:515–23. doi: 10.1007/s00335-002-2179-2
 144. Timmins NE, Maguire TL, Grimmond SM, Nielsen LK. Identification of three gene candidates for multicellular resistance in colon carcinoma. *Cytotechnology.* (2004) 46:9–18. doi: 10.1007/s10616-005-1476-5
 145. Lagies S, Schlimpert M, Neumann S, Wäldin A, Kammerer B, Börner C, et al. Cells grown in three-dimensional spheroids mirror *in vivo* metabolic response of epithelial cells. *Commun Biol.* (2020) 3:246. doi: 10.1038/s42003-020-0973-6
 146. Mahmud G, Campbell CJ, Bishop KJM, Komarova YA, Chaga O, Soh S, et al. Directing cell motions on micropatterned ratchets. *Nat Phys.* (2009) 5:606–12. doi: 10.1038/nphys1306
 147. Kilian KA, Bugarija B, Lahn BT, Mrksich M. Geometric cues for directing the differentiation of mesenchymal stem cells. *Proc Natl Acad Sci USA.* (2010) 107:4872–7. doi: 10.1073/pnas.0903269107
 148. Shih YR, Tseng KF, Lai HY, Lin CH, Lee OK. Matrix stiffness regulation of integrin-mediated mechanotransduction during osteogenic differentiation of human mesenchymal stem cells. *J Bone Miner Res.* (2011) 26:730–8. doi: 10.1002/jbmr.278
 149. Liu H, Radisky DC, Wang F, Bissell MJ. Polarity and proliferation are controlled by distinct signaling pathways downstream of PI3-kinase in breast epithelial tumor cells. *Cell Biol J.* (2004) 164:603–12. doi: 10.1083/jcb.200306090
 150. L.Nguyen TH, Muktabar A, Tang J, Wong YS, Thaxton CS, Venkatraman SS, et al. The potential of fluocinolone acetonide to mitigate inflammation and lipid accumulation in 2D and 3D foam cell cultures. *Biomed Res Int.* (2018) 2018:3739251. doi: 10.1155/2018/3739251
 151. Thomas RG, Su X, Vizetto-Duarte C, Muktabar A, Ng KW, Kwan JJ. Targeted ultrasound enhanced drug delivery to foam cell spheroids. *Acoust J Soc Am.* (2019) 146:2751–2751. doi: 10.1121/1.5136524
 152. Barnes RH, Akama T, Öhman MK, Woo MS, Bahr J, Weiss SJ, et al. Membrane-tethered metalloproteinase expressed by vascular smooth muscle cells limits the progression of proliferative atherosclerotic lesions. *Am Heart Assoc J.* (2017) 6:3693. doi: 10.1161/JAHA.116.03693

153. Vaidyanathan K, Wang C, Krajnik A, Yu Y, Choi M, Lin B, et al. Machine learning reveals heterogeneous responses to FAK, Rac, Rho, and Cdc42 inhibition on vascular smooth muscle cell spheroid formation and morphology. *bioRxiv*. (2020). doi: 10.1101/2020.01.30.927616
154. Yang J, Zhang YS, Yue K, Khademhosseini A. Cell-laden hydrogels for osteochondral and cartilage tissue engineering. *Acta Biomater*. (2017) 57:1–25. doi: 10.1016/j.actbio.2017.01.036
155. Peppas NA, Hilt JZ, Khademhosseini A, Langer R. Hydrogels in biology and medicine: from molecular principles to bionanotechnology. *Adv Mater*. (2006) 18:1345–60. doi: 10.1002/adma.200501612
156. Lin K, Zhang D, Macedo MH, Cui W, Sarmiento B, Shen G. Advanced collagen-based biomaterials for regenerative biomedicine. *Adv Funct Mater*. (2019) 29:1804943. doi: 10.1002/adfm.201804943
157. Chen CN, Chang SF, Lee PL, Chang K, Chen LJ, Usami S, et al. Neutrophils, lymphocytes, and monocytes exhibit diverse behaviors in transendothelial and subendothelial migrations under coculture with smooth muscle cells in disturbed flow. *Blood*. (2006) 107:1933–42. doi: 10.1182/blood-2005-08-3137
158. Su C, Menon NV, Xu X, Teo YR, Cao H, Dalan R, et al. A novel human arterial wall-on-a-chip to study endothelial inflammation and vascular smooth muscle cell migration in early atherosclerosis. *Lab Chip*. (2021) 21:2359–71. doi: 10.1039/d1lc00131k
159. Garcia-Sabaté W, Mohamed KE, Sapudom J, Alatoon A, Al Safadi L, Teo J. Biomimetic 3D models for investigating the role of monocytes and macrophages in atherosclerosis. *Bioengineering*. (2020) 7:113. doi: 10.3390/bioengineering7030113
160. Dorweiler B, Torzewski M, Dahm M, Ochsenhirt V, Lehr HA, Lackner KJ, et al. Novel *in vitro* model for the study of plaque development in atherosclerosis. *Thromb Haemost*. (2006) 95:182–9. doi: 10.1160/TH05-05-0357
161. Hosseini V, Mallone A, Mirkhani N, Noir J, Salek M, Pasqualini FS, et al. A pulsatile flow system to engineer aneurysm and atherosclerosis mimetic extracellular matrix. *Adv Sci*. (2020) 7:2000173. doi: 10.1002/advs.202000173
162. Ragaseema V, Columbus S, Ramesh R, Krishnan KL. Potential of tissue engineered blood vessel as model to study effect of flow and wall thickness on cellular communication. *Curr Tissue Eng*. (2014) 3:39–46. doi: 10.2174/2211542002666131209233849
163. Laterreur V, Ruel J, Auger FA, Vallières K, Tremblay C, Lacroix D, et al. Comparison of the direct burst pressure and the ring tensile test methods for mechanical characterization of tissue-engineered vascular substitutes. *J Mech Behav Biomed Mater*. (2014) 34:253–63. doi: 10.1016/j.jmbbm.2014.02.017
164. Strobel HA, Hookway TA, Piola M, Fiore GB, Soncini M, Alsberg E, et al. Assembly of tissue-engineered blood vessels with spatially controlled heterogeneities. *Tissue Eng A*. (2018) 24:1492–503. doi: 10.1089/ten.tea.2017.0492
165. Fernandez CE, Yen RW, Perez SM, Bedell HW, Povsic TJ, Reichert WM, et al. Human vascular microphysiological system for *in vitro* drug screening. *Sci Rep*. (2016) 6:21579. doi: 10.1038/srep21579
166. Breithaupt JJ, Kwon J, Etttyreddy A, Zhang X, Gersbach C, Truskey GA. PCSK9 knockdown decreases inflammatory markers and U937 monocyte accumulation in a tissue-engineered blood vessel model. *Circulation*. (2019) 140:A13133–A13133.
167. Salmon EE, Breithaupt JJ, Truskey GA. Application of oxidative stress to a tissue-engineered vascular aging model induces endothelial cell senescence and activation. *Cells*. (2020) 9:1292. doi: 10.3390/cells9051292
168. Chen Z, Tang M, Huang D, Jiang W, Li M, Ji H, et al. Real-time observation of leukocyte–endothelium interactions in tissue-engineered blood vessel. *Lab Chip*. (2018) 18:2047–54. doi: 10.1039/C8LC00202A
169. Lee JH, Chen Z, He S, Zhou JK, Tsai A, Truskey GA, et al. Emulating early atherosclerosis in a vascular microphysiological system using branched tissue-engineered blood vessels. *Adv Biology*. (2021) 5:2000428. doi: 10.1002/adbi.202000428
170. Chavez RD, Walls SL, Cardinal KOH. Tissue-engineered blood vessel mimics in complex geometries for intravascular device testing. *PLoS ONE*. (2019) 14:e0217709. doi: 10.1371/journal.pone.0217709
171. Gao G, Park W, Kim BS, Ahn M, Chae S, Cho WW, et al. Construction of a novel *in vitro* atherosclerotic model from geometry-tunable artery equivalents engineered via in-bath coaxial cell printing. *Adv Funct Mater*. (2021) 31:2008878. doi: 10.1002/adfm.202008878
172. Zheng F, Fu F, Cheng Y, Wang C, Zhao Y, Gu Z. Organ-on-a-chip systems: microengineering to biomimic living systems. *Small*. (2016) 12:2253–82. doi: 10.1002/smll.201503208
173. Rogal J, Zbinden A, Schenke-Layland K, Loskill P. Stem-cell based organ-on-a-chip models for diabetes research. *Adv Drug Deliv Rev*. (2019) 140:101–28. doi: 10.1016/j.addr.2018.10.010
174. Cochran A, Albers HJ, Passier R, Mummery CL, van den Berg A, Orlova VV, et al. Advanced *in vitro* models of vascular biology: human induced pluripotent stem cells and organ-on-chip technology. *Adv Drug Deliv Rev*. (2019) 140:68–77. doi: 10.1016/j.addr.2018.06.007
175. Tian C, Tu Q, Liu W, Wang J. Recent advances in microfluidic technologies for organ-on-a-chip. *Trends Analyt Chem*. (2019) 117:146–56. doi: 10.1016/j.trac.2019.06.005
176. Franzen N, van Harten WH, Retèl VP, Loskill P, van den Eijnden J, Jzerman JM. Impact of organ-on-a-chip technology on pharmaceutical R&D costs. *Drug Discov Today*. (2019) 24:1720–4. doi: 10.1016/j.drudis.2019.06.003
177. Yesil-Celiktas O, Hassan S, Miri AK, Maharjan S, Al-kharboosh R, Quiñones-Hinojosa A, et al. Mimicking human pathophysiology in organ-on-chip devices. *Adv Biosyst*. (2018) 2:1800109. doi: 10.1002/adbi.201800109
178. Zhang X, Wang Z, Zhang YS, Yan S, Hou C, Gong Y, et al. Studying endothelial cell shedding and orientation using adaptive perfusion-culture in a microfluidic vascular chip. *Biotechnol Bioeng*. (2021) 118:963–78. doi: 10.1002/bit.27626
179. Hasan A, Paul A, Memic A, Khademhosseini A. A multilayered microfluidic blood vessel-like structure. *Biomed Microdevices*. (2015) 17:1–13. doi: 10.1007/s10544-015-9993-2
180. Jia L, Han F, Yang H, Turnbull G, Wang J, Clarke J, et al. Microfluidic fabrication of biomimetic helical hydrogel microfibers for blood-vessel-on-a-chip applications. *Adv Healthc Mater*. (2019) 8:1900435. doi: 10.1002/adhm.201900435
181. Mallone A, Gericke C, Hosseini V, Chahbi K, Haenseler W, Emmert MY, et al. Human induced pluripotent stem cell-derived vessels as dynamic atherosclerosis model on a chip. *bioRxiv*. (2021). doi: 10.1101/2020.11.27.401034
182. Poussin C, Kramer B, Lanz HL, Van den Heuvel A, Laurent A, Olivier T, et al. 3D human microvessel-on-a-chip model for studying monocyte-to-endothelium adhesion under flow-application in systems toxicology. *Altex*. (2020) 37:47–63. doi: 10.14573/altex.1811301
183. Chen R, Wang B, Liu Y, He J, Lin R, Li D. Gelatin-based perfusable, endothelial carotid artery model for the study of atherosclerosis. *Biomed Eng*. (2019) 18:1–13. doi: 10.1186/s12938-019-0706-6

Conflict of Interest: RM, JS, PH, BB, and H-WJ were employed by the company Endomimetics, LLC.

The remaining authors declare that the research was conducted in the absence of any commercial or financial relationships that could be construed as a potential conflict of interest.

Publisher's Note: All claims expressed in this article are solely those of the authors and do not necessarily represent those of their affiliated organizations, or those of the publisher, the editors and the reviewers. Any product that may be evaluated in this article, or claim that may be made by its manufacturer, is not guaranteed or endorsed by the publisher.

Copyright © 2022 Chen, Zhang, Millican, Lynd, Gangasani, Malhotra, Sherwood, Hwang, Cho, Brott, Qin, Jo, Yoon and Jun. This is an open-access article distributed under the terms of the Creative Commons Attribution License (CC BY). The use, distribution or reproduction in other forums is permitted, provided the original author(s) and the copyright owner(s) are credited and that the original publication in this journal is cited, in accordance with accepted academic practice. No use, distribution or reproduction is permitted which does not comply with these terms.



Development of the Human Arterial Valves: Understanding Bicuspid Aortic Valve

Deborah J. Henderson*, Lorraine Eley, Jasmin E. Turner and Bill Chaudhry

Biosciences Institute, Newcastle University, Newcastle upon Tyne, United Kingdom

Abnormalities in the arterial valves are some of the commonest congenital malformations, with bicuspid aortic valve (BAV) occurring in as many as 2% of the population. Despite this, most of what we understand about the development of the arterial (semilunar; aortic and pulmonary) valves is extrapolated from investigations of the atrioventricular valves in animal models, with surprisingly little specifically known about how the arterial valves develop in mouse, and even less in human. In this review, we summarise what is known about the development of the human arterial valve leaflets, comparing this to the mouse where appropriate.

Keywords: arterial valve, semilunar valve, outflow tract cushions, human, development, remodelling, sculpting, bicuspid aortic valve

OPEN ACCESS

Edited by:

Michel Puceat,
Institut National de la Santé et de la
Recherche Médicale
(INSERM), France

Reviewed by:

José Luis De La Pompa,
Spanish National Centre for
Cardiovascular Research, Spain
Choon Hwai Yap,
Imperial College London,
United Kingdom

*Correspondence:

Deborah J. Henderson
deborah.henderson@ncl.ac.uk

Specialty section:

This article was submitted to
Heart Valve Disease,
a section of the journal
Frontiers in Cardiovascular Medicine

Received: 27 October 2021

Accepted: 16 December 2021

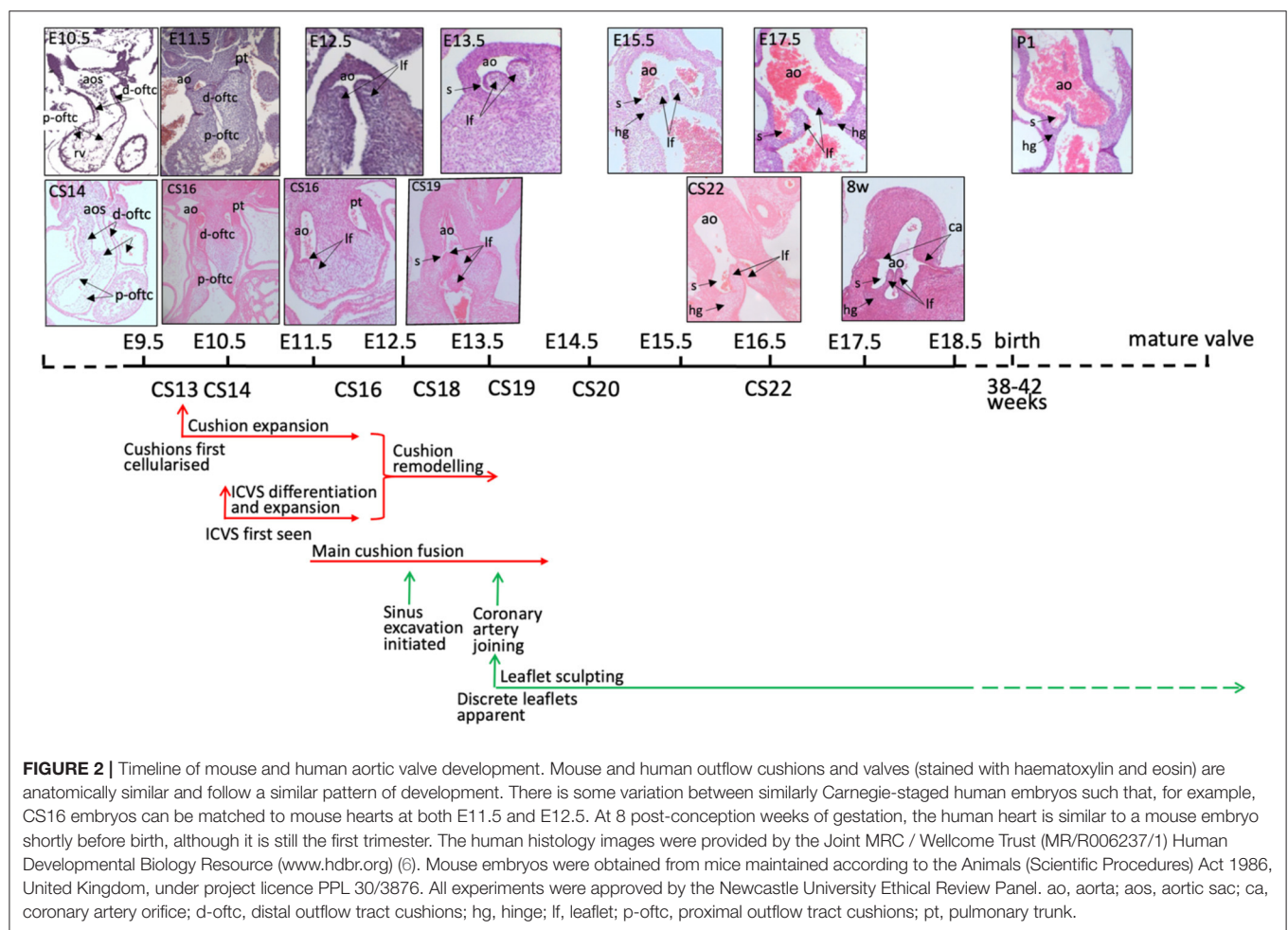
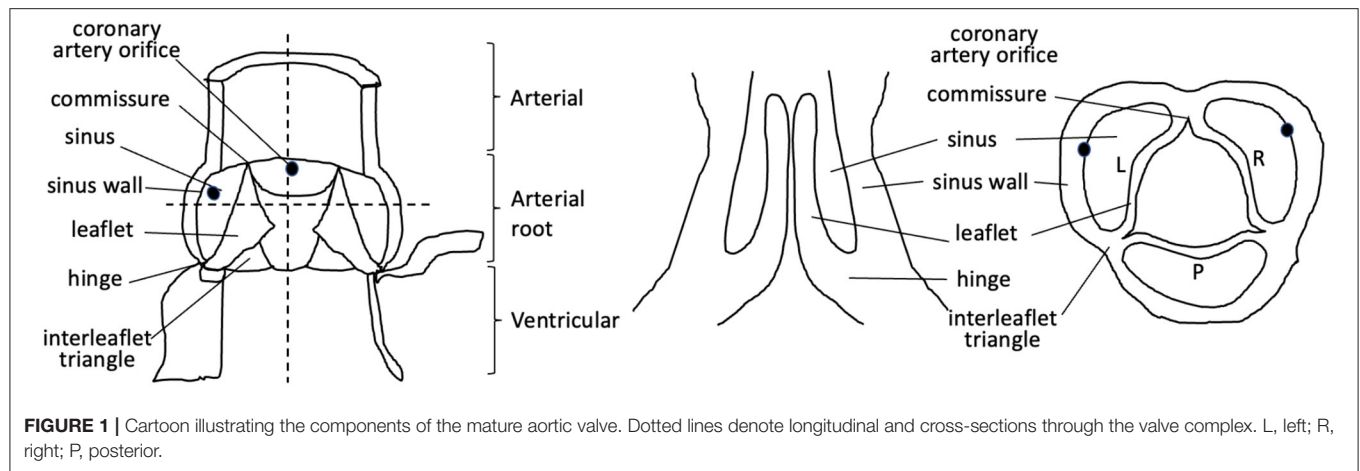
Published: 27 January 2022

Citation:

Henderson DJ, Eley L, Turner JE and
Chaudhry B (2022) Development of
the Human Arterial Valves:
Understanding Bicuspid Aortic Valve.
Front. Cardiovasc. Med. 8:802930.
doi: 10.3389/fcvm.2021.802930

ANATOMY AND NOMENCLATURE OF THE MATURE ARTERIAL (SEMILUNAR) VALVES

Abnormalities of the arterial valves (sometimes known as the semilunar valves), including bicuspid aortic valve and leaflet dysplasia, are amongst the commonest congenital anomalies (1, 2). Although they may be asymptomatic at birth and thus missed during neonatal health checks, they do predispose to severe cardiovascular disease, including valve stenosis, regurgitation, calcification, and thoracic aortic aneurysm in later life (2). Thus, understanding their aetiology is of great interest. The arterial valves sit between the aorta and pulmonary trunk and their respective left and right ventricular outflow tracts in both human and mouse hearts, and are structurally very similar (3–5) (**Figures 1, 2**). These valves are complex structures that are composed of more than just the three moving leaflets. They also include the hinges that attach the leaflets to the wall, the commissures that are the points of apposition of the leaflets close to the wall, and the sinuses, which are the pockets that form between the leaflets and the wall. The regions of the wall that lie immediately upstream of the hinges (on the ventricular side) are called the interleaflet triangles (**Figure 1**). For the purposes of this review, we will refer to the coronary leaflets of the aortic valve (and their homologues in the pulmonary valve) as the right and left leaflet, and the non-coronary leaflet of the aortic valve as the posterior leaflet (its homologue in the pulmonary valve is the anterior leaflet). There have been several excellent reviews over recent years that have described in detail how the arterial valves develop based on studies in animal models (7–12). It is not our intention to extensively re-review the mouse, chicken, or zebrafish literature, but to instead focus on what is known directly from studies carried out with human material, relating this to key studies in animal models for perspective. The aim is to highlight some of the seminal work that has been done in the past, suggest what still needs to be done, and speculate on how this helps or hinders our understanding of one of the main congenital abnormalities of the arterial valves, bicuspid aortic valve (BAV).



ENDOCARDIAL TO MESENCHYME TRANSITION AND CUSHION FORMATION

The first and probably best understood process required for the development of the cardiac valves is the process of endocardial

to mesenchyme transition (EndMT). This process, which has mostly been studied in mouse and chicken, has been reviewed extensively (7–12). In its primitive state, the heart tube consists of an outer layer of the myocardium, with an inner lining of the endocardium. Between these two cell layers is a layer of

extracellular matrix (ECM), often known as cardiac jelly. This ECM is an essential component of the forming and mature valve leaflets, with the knockout of ECM components found in the early cushions, such as Hyaluronan and Versican, resulting in acellular cushions in mouse embryos [e.g. (13, 14)]. During the process of EndMT, endocardial cells change their epithelial-like phenotype into a mesenchymal one and migrate into the cardiac jelly to form primitive endocardial cushions (sometimes referred to as ridges). Whilst the regulation of the localisation and mechanisms of this complex process are beyond the scope of this review, some key points are relevant here. Cushions are first seen in the developing mouse outflow tract at about embryonic day (E)10, approximately 12 hours after they are seen in the atrioventricular canal. The cushions are cellularised between E10 and E11.5 by EndMT in the proximal region, which is regulated by Bone Morphogenetic Protein (BMP), Transforming Growth Factor beta (TGF β), and Notch signalling [reviewed in (7–12)], and neural crest cells (NCCs) migrating into the distal cushions (described in more detail below). By E12.5, valve mesenchymal cells derived from both populations are found throughout the length of the cushions, thus contributing distally to the valve leaflets and proximally to the cushions that will give rise to the outlet septum (7–12).

Much less is specifically known about the early stages of cushion formation in the human heart. The outflow cushions are first apparent at the end of the 4th week of human gestation (CS10–13; 5–6mm crown-rump length; CRL. See **Table 1** legend for explanation of staging used throughout this manuscript). Maron and Hutchins (1974) (16) saw cushions at approximately 33 days post conception (dpc; CS15) with Hutchins et al. (17) reporting the presence of outflow cushions in more than half of 32 dpc (CS14) hearts and all 33 dpc (CS15) hearts; these were recognised as taking on a spiralling configuration from their first appearance (18). There do not appear to be any studies directly investigating EndMT using cushion explant culture in human embryos. However, it was shown (19) that Nuclear Factor Of Activated T Cells 1 (NFATC1), which appears to repress EndMT in mice (20–22), was absent from nuclei of valve endocardial cells (VECs) of embryos at 4 weeks of gestation, but then appeared in the nuclei of these cells of embryos at 4–6 weeks (CS13–17) of gestation (19). This suggests that the absence of NFATC1 may allow VECs to undergo EndMT prior to 4 weeks of gestation. This correlates with when the outflow cushions first become apparent but, as in mice, may be important for repressing EndMT during the next phase when the cushions expand and septation occurs. Interestingly, the repressive effects of Vascular Endothelial Growth Factor A (VEGFA) on EndMT (23) also appear to be conserved (19).

NCC, OUTFLOW TRACT SEPTATION, AND VALVE DEVELOPMENT

Outflow tract septation is intimately involved in arterial valve formation through shared progenitor cell lineages, cushions, and timing of events. These progenitor lineages include EndMT-derived cells (which in the outflow tract originate in the second

heart field; SHF) and NCCs. The NCCs are a progenitor population that play a crucial role in the process of outflow tract septation; in their absence, septation does not occur [reviewed in (24–26)]. Whilst NCCs form smooth muscle cells in the developing walls of the great arteries and are important in cardiac innervation, it may be that their role in outflow septation is mainly as a ‘filler,’ acting to bulk out the outflow cushions to bring them into contact and thus allow fusion; the majority of NCCs in the proximal part of the cushions die by apoptosis shortly after septation occurs (12, 27). It has been recognised that outflow tract septation cannot be initiated before the formation of the 6th pharyngeal arch arteries (28), which does not occur until approximately 32 dpc [CS14 or 6–8 mm; (29)]. The aorta and pulmonary blood flows are separated by around the end of the 5th week of gestation (CS15–16; 9 mm CRL) (16), with the initiation of outflow septation apparent in most 37 dpc embryos (CS16; 11–14 mm CRL) (17). Kramer (15) showed that this septation produces the precursors of the right and left leaflets of the forming arterial valves, with the parietal main outflow cushion contributing to the left leaflets of the aortic and pulmonary valve and the septal cushion contributing to the right leaflets. Notably, at least in the mouse, both EndMT-derived cells and NCCs are abundant in the left and right leaflets of the aortic and pulmonary valves at comparable and later stages of development (30, 31). Fusion of the main cushions separates the channels of the aorta and pulmonary trunk and subsequent separation of the aorta from the pulmonary trunk in a plane perpendicular to the line of cushion fusion results in the formation of two, free-standing arterial trunks with their distinct valves. The aortic and pulmonary valves are approximately lateral to one another at 37 dpc (CS16), with the pulmonary valve only slightly more cranial. This is much exaggerated by 48 dpc (CS19) with, similarly to mouse, the pulmonary valve positioned more superior and anterior (16) (anterior and ventral in the mouse).

Although it is accepted that NCCs are crucial for human outflow tract development as they are in birds and mice [reviewed in (24, 25)], there is limited information available, at least in part because of the difficulty in labelling this progenitor cell population in the human heart. It has been shown, using AP2 α as a marker, that NCCs are found within the distal outflow cushions at 33 dpc [CS15; (32)]. This expression was downregulated by 37 dpc (CS16) of development and thus could not be used to track them within the developing arterial valves. However, the characteristic condensed mesenchyme within the outflow cushions, which is shown to be made up of NCCs in the mouse, is apparent in the human outflow cushions from approximately 32 dpc (CS14) (33).

FORMATION OF INTERCALATED LEAFLET VALVE SWELLINGS

The intercalated leaflet valve swellings (ICVSs; sometimes referred to as intercalated valve cushions) that are the precursors of the anterior and posterior leaflets of the arterial valves were first noted in human embryos (15) and are seen clearly

TABLE 1 | Staging criteria for human embryos.

| CS | Somite stage | Days post ovulation | Crown rump length (mm) | Morphological landmarks |
|----|--------------|---------------------|------------------------|---|
| 9 | 1–3 | 19–21 | 1.5–3.0 | Head fold present |
| 10 | 4–12 | 22 | 2.0–3.5 | Neural tube closing. First and second branchial arches visible |
| 11 | 13–21 | 24 | 2.5–4.5 | Rostral neuropore closing. Otic placodes present. Optic vesicles formed. |
| 12 | 21–29 | 26 | 3–5 | Upper limb buds appear. Rostral neuropore closed. Caudal neuropore closing. Otic pits present. Three pairs of branchial arches visible. |
| 13 | 30+ | 28 | 4–6 | Embryo has C-shaped curve. Caudal neuropore closed. Upper limb buds flipper like. Four pairs of branchial arches visible. Lower limb buds appear. Otic vesicles present. Lens placodes distinct. Attenuated tail present. |
| 14 | | 32 | 5–7 | Upper limbs paddle-shaped. Lens pits and nasal pits visible. Optic cups present. |
| 15 | | 33 | 7–9 | Hand plates formed. Lens vesicles present. Nasal pits prominent. Lower limbs paddle-shaped. Cervical sinuses visible. |
| 16 | | 37 | 11–14 | Foot plates formed. Pigment visible in retina. Auricular hillocks developing. |
| 17 | | 41 | 11–14 | Digital rays clearly visible in hand plates. Auricle hillocks outline future auricle of external ear. Trunk beginning to straighten. Cerebral vesicles prominent. |
| 18 | | 44 | 13–17 | Digital rays clearly visible in foot plates. Elbow region visible. Eyelids forming. Notches between the digital rays in the hand. |
| 19 | | 47.5 | 17–20 | Limbs extend ventrally. Trunk elongating and straightening. Midgut herniation prominent. Prominent toe rays. |
| 20 | | 50.5 | 21–23 | Upper limbs longer and bent at elbows. Fingers distinct but webbed. Notches between the digital rays in the feet. Scalp vascular plexus appears. |
| 21 | | 52 | 22–24 | Hands and feet approach each other. Fingers free and longer. Toes distinct but webbed. Stubby tail present. |
| 22 | | 54 | 25–27 | Toes free and longer. Eyelids and auricles or external ears more developed |
| 23 | | 56.5 | 28–30 | Head more rounded and shows human characteristics. External genitalia still have sexless appearance. Distinct bulge still present in umbilical cord caused by herniation of intestines. |

(See <http://hdbatlas.org/staging-criteria/carnegie-staging.html>). Note on staging: The papers we have referenced use a range of staging methods, including Carnegie Stages (CS), days/weeks post conception (dpc/pcw), and crown-rump length (CRL). For comparative purposes and to aid understanding for the non-embryologist, these have been converted into days/weeks post conception. Where relevant, the original staging method follows in *italics*.

in cross sections through the outflow tract at 33 dpc (CS15; 9 mm CRL) as lateral bulges within the outflow wall; they have since been described in the mouse at comparable stages of development (E10.5–E12.5). Kramer (15) recognised during his original observations that the ICVSs contribute solely to the valve leaflets and do not play roles in outflow tract septation. Moreover, he recognised that they are distinct from the main outflow cushions; this has since been confirmed by studies in mouse (31). The ICVSs of human embryos were also discussed by Thompson et al. (34) who described them as midline cellular condensations close to the myocardial rim, although he did not recognise their role in valve formation. He noted, however, that the ‘condensations’ were less distinct in other species, including the rat and chicken (34). Of note, care should be taken when using the word ‘condensations’ with respect to the ICVSs, as this could lead to confusion with the more frequently referred to condensations of NCCs that occur in the main outflow cushions (see above). More recently, and after a gap of more than 20 years, several authors have recognised the ICVSs in mouse and human embryos and have begun their molecular characterisation (31, 32, 35, 36). This has shown that they lie at the boundary between the SHF-derived myocardium (proximally) and SHF-derived smooth muscle cells (distally) within the walls of the outflow vessels

at E10.5–E12.5 (human 28–33 dpc; CS13–15) (31, 35). In terms of their cellular origin, it has been shown that whilst there are small numbers of EndMT-derived and NCC-derived cells within the ICVSs, the majority of cells at these early stages express Isl1, a marker of undifferentiated SHF-derived cells, suggesting that they have a different origin (directly differentiating from SHF progenitors) to the majority of cells in the main outflow cushions that are formed by EndMT and the immigration of NCCs (31, 32).

CUSHION EXPANSION TO FORM ARTERIAL VALVE PRIMORDIA

Once the relevant progenitor lineages have contributed cells to the mesenchyme in the mouse heart, they undergo a period of proliferation that results in rapid cushion growth (as shown in **Figures 2, 3**), with too much [e.g. (37, 38)] or too little [e.g. (39, 40)] cell division associated with defects in the leaflets as development proceeds. More than 60% of outflow cushion mesenchymal cells express proliferation markers during the 4th week of human development, with the levels falling gradually to <20% after the 10th week of gestation (19). RNASeq analysis suggested that this might be regulated by MYC proto-oncogene

(MYC), a known regulator of cell cycle progression. Thus, as in the mouse, there is rapid proliferation leading up to the period when cushions remodel into valve leaflets (see below) (19).

As well as its early roles in supporting EndMT, ECM also appears to be important for remodelling of the cushion/valve mesenchyme. Knockout of the ECM component Perlecan in mice results in excessive numbers of cells within the outflow cushions, resulting in cushion hyperplasia and dysplastic arterial valve leaflets (41). Similarly, Versican, which is essential for early cushion formation, also plays an essential role during later remodelling stages of cushion to valve morphogenesis. If Versican cleavage is impaired by knockout of the matrix metalloprotease ADAMTS5, then the arterial valve leaflets become dysplastic, with abnormal deposition of other matrix components including Collagen and Elastin (42). In the human heart, CD44 (Hyaluronan receptor) has been found in cushion mesenchyme cells at 4 weeks of gestation (approximately CS13) and slightly later in valve endocardium (19). Elastin staining using specific antibodies was seen from 7 weeks of gestation (CS19–20) in the developing arterial valve leaflets (although at lower levels than in the arterial wall) and already showed evidence of stratification, being more abundant on the ventricular side of the forming leaflets (43). Elastin expression declined with gestational age. RNASeq showed enrichment for a number of other microfibril-associated proteins, including Fibronectin, Fibrillin 2 and 3, Fibulin 2, 4 and 5, LOX, and Emilin, in first trimester valve tissue, with Fibronectin and Fibrillin 1–3 found by immunohistochemistry from 4 weeks (43).

Recently, there has been much interest in the potential role of cilia in the development and maintenance of valve leaflets, largely because of the association between mutations in cilia-associated genes and human valve defects [e.g. (44)]. Primary cilia are small projections of the membrane with a microtubule core, which are implicated in cell signalling and mechano-sensing (45). Currently, there do not appear to be any published studies characterising cilia in human embryonic or foetal arterial valve leaflets; this is an area that would benefit from further work.

VALVE SCULPTING

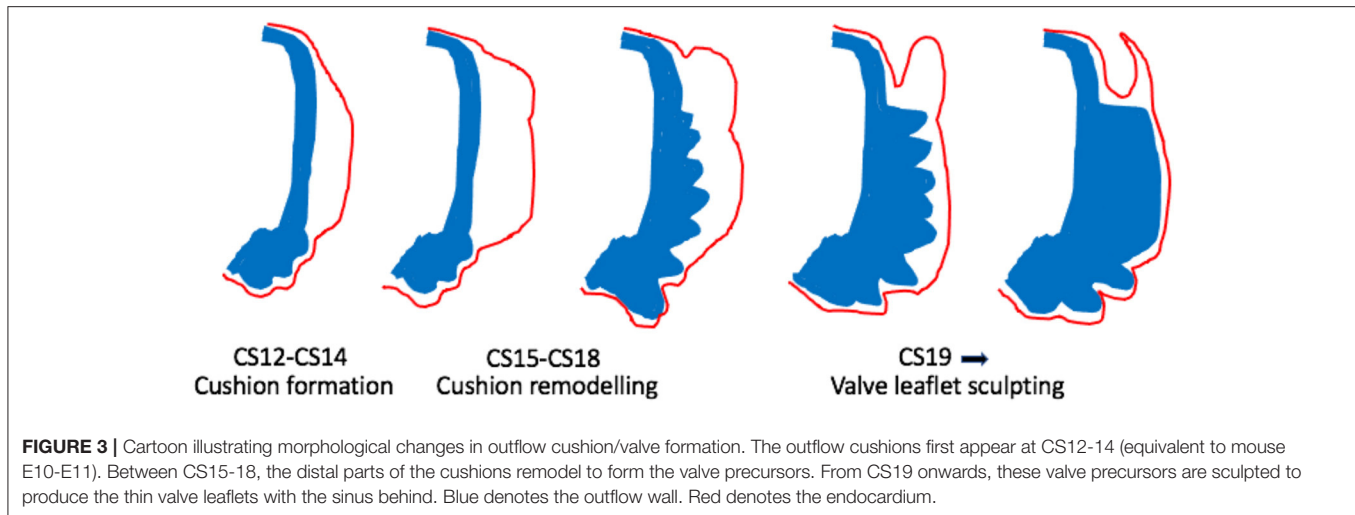
Once the cushions have formed and outflow tract septation is underway (from approximately E12.5 in mouse; CS16 in human), the distal parts of the main cushions remodel to form the arterial valve leaflets and are distinct from the proximal cushions that will remodel to form the outlet septum of the ventricular outflow tracts (Figures 2, 3). During this process of leaflet remodelling, the details of which remain unclear, the bulky, primitive valve precursors (cushions and ICVSs) are sculpted into thin fibrous leaflets, connected to the vessel wall by hinges that delineate the sinuses (Figure 3). A number of mouse mutants have been described as having thickened, abnormally shaped (dysplastic) leaflets [for example (41, 42, 46–49)]. The leaflets in these mutants are characterised by having

excessive cell numbers and/or abnormalities in the ECM; if this leads to the cushions being pushed against one another, it can result in BAV (42, 49). However, in most cases, the pathomechanisms leading to valve dysplasia are unclear. Thus, these sculpting stages of arterial valve development remain the least well-understood but may be the most relevant to human disease.

Since the arterial valve leaflets form from the distal ends of the outflow cushions (15, 50), it may be possible to determine where they will form from as early as 33 dpc (CS15) as the lumen narrows and the overlying endocardium takes on a distinct cobble-stone appearance. However, at 37 dpc (CS16), the mesenchyme of the distal cushions, where the leaflets will form, swells relative to the more proximal regions of the cushions (33). The first appearance of valve structures from the cushions is at approximately 41 dpc (CS17), with the sinuses first apparent as shallow depressions between the arterial wall and the developing valve (16) (Figures 2, 3). At this stage, it was also observed that the VECs on the arterial side of the leaflet are cuboidal whereas those on the ventricular side are flattened (16), suggesting responses to differential blood flow patterns. This was later confirmed using molecular markers [CD31; (19)]. At this stage, the forming valves have a considerable length within the middle part of the septating outflow tract, coinciding with the boundary between the arterial and ventricular components (33). By around the 50th day of gestation (CS20), the sinus walls are becoming apparent but are still surrounded by a cuff of the myocardium, whilst by 52 dpc (CS21; 23mm CRL), the leaflets are short and thick with only a slit-like sinus. At the same time, the cellular density of the leaflets is increasing. By the end of the 8th week of gestation (CS23), the leaflets appear longer and are more delicate (16) (see Figures 2, 3). The leaflets continue to become more refined as development proceeds.

MATURATION OF THE ARTERIAL VALVE LEAFLETS

At the same time as the leaflets are sculpting, they are also maturing in respect to their cellular and extracellular components. Mature valve leaflets contain valvular interstitial cells (VICs) that are derivatives of the cushion mesenchyme. These VICs reside within three layers, characterised by distinct ECM profiles: the fibrosa (on the arterial side of the leaflet), composed mostly of Collagens; the spongiosa, made up mostly of Proteoglycans; and the ventricularis, which contains Elastin fibres. The leaflets are also covered by a specialised endocardial layer (VECs) (51). Animal studies have shown that abnormalities in, for example, matrix remodelling enzymes can disrupt the stratification of the valve leaflets during development (42, 51), whereas in other models [e.g. (51, 52)], the leaflets are initially stratified, but become disorganised and myxomatous as the animals age. The timing of leaflet stratification in human embryos is rather unclear as in the limited studies that have been carried out, there are large gaps between stages. One study suggested that the arterial valve leaflets lose their homogeneous character in the 60 mm CRL foetus (approximately 12 pcw),



with Collagen fibrils apparent in the proximal parts of the leaflets and in the subendocardial region of their ventricular side (16). Analyses of more mature valves were carried out in this study (16), however, CRL was used to determine the maturity of the samples, which is not generally considered to be reliable after 80 mm due to a high degree of variation between fetuses. Thus, the precise staging of larger fetuses from this study has to be interpreted with caution. Collagen fibres increased in the leaflets of the 90 mm foetus (approximately 14 pcw) and by 100 mm (approximately 14.5 pcw), a distinct subendocardium, with elastic fibres in the ventricular side, was observed. Collagen continued to increase in the 100 mm and 125 mm foetus (approximately 16 pcw). The valve leaflets began to take on a mature structure in the 150 mm foetus with a dense collagenous middle layer and looser connective tissue on the ventricular side of the leaflets (16). Analysis of human hearts from 14 gestational weeks (using Movat's pentachrome staining) indicated that, at this earliest stage, the valves were homogeneous with no clear layers apparent. At these stages, the valves were mainly composed of Proteoglycans, with limited Collagen and Elastin (52). By 20 weeks, a bilaminar structure was observable, but the mature trilaminar structure was not apparent until 36 weeks of gestation. It was also noted that VIC density decreased in the 2nd and 3rd trimesters, and this was matched by a decrease in proliferation from approximately 26% in the second trimester, to only 6% in the third trimester; by this stage, most of the proliferation was close to the arterial side of the leaflets. The second trimester foetal valve leaflets had a myofibroblast-like appearance and expressed high levels of proteolytic enzymes such as Matrix metalloproteases (MMPs); these decreased with advancing gestational age (53).

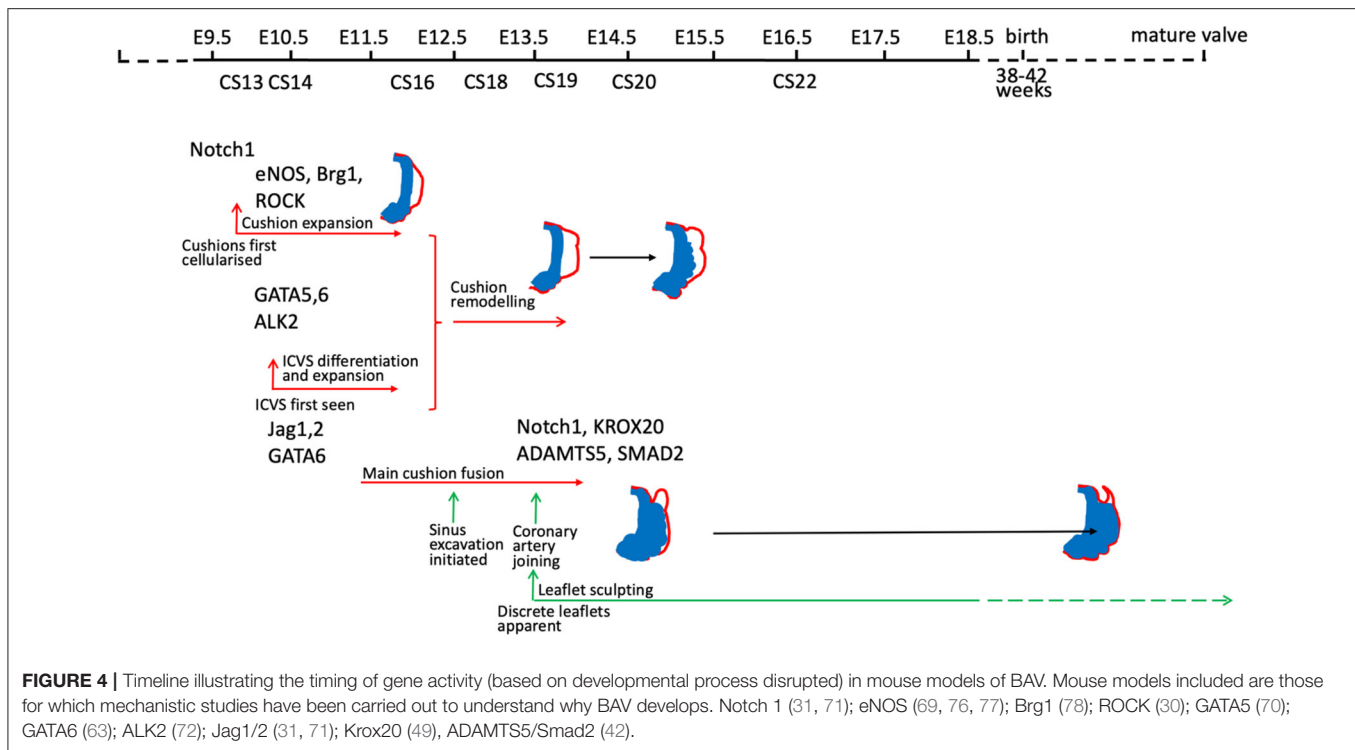
THE APPEARANCE OF THE CORONARY ARTERIES

Coronary arteries were seen in the left and right sinuses of the aortic valve during the 6th week of human development (CS18)

(17). This was confirmed recently (33) with data showing that the left coronary artery is first seen at CS18, whereas the right coronary artery was only seen a few days later at CS19. Notably, it has been suggested that apart from the association of the coronary arteries with the right and left leaflets of the aortic valve only, the aortic and pulmonary valves appear morphologically similar until birth (16).

ARTERIAL VALVE MALFORMATIONS – GENETIC CAUSES?

Congenital malformations of the arterial valves are very common and include valves with abnormal numbers of leaflets, including unicuspid, bicuspid, and quadricuspid variants, and valve leaflet dysplasia, in which the leaflets are typically thickened and/or shortened (1, 2). In the case of BAV, which is by far the most common abnormality, a similar range of leaflet patterns has been observed in human and mouse, including apparent fusions between the left and right and right and posterior (non-coronary) leaflets; fusions between the left and posterior leaflets are rare in humans (1, 2). Moreover, it has been suggested that BAV can also result from the absence of a leaflet, presumably the posterior leaflet derived from the ICVS, as an absence of one of the main outflow cushions would prevent outflow tract septation (12, 31, 54). A well-recognised feature of bicuspid valves is the presence or absence of a raphe, presumed to represent a fusion seam, which in some cases is associated with a notch or an asymmetry suggesting a third leaflet formed during development, but fused with one of the others. Studies in animal models have suggested that leaflet fusion occurs because the cushions or leaflets are pushed against one another resulting in their fusion, either because they are hyperplastic or misplaced, with the raphe being what remains of the endocardium at the fusion seam e.g. (49, 54). Although it is commonly stated that 85–90% of human BAVs have a raphe (1, 2), recent studies suggest that as many as 25% may have no raphe (55). This implies that in these cases, either the fusion seam is completely remodelled and cannot be seen,



or the leaflet primordium may have been missing throughout development. All of these abnormalities predispose the valves to stenosis and/or regurgitation, and to degeneration in later life. Interestingly, there appear to be differences in the patterns of abnormalities seen in populations from different ethnic groups. For example, studies from Europe and the United States have suggested that approximately 85% of non-syndromic patients with BAV present with a common left-right leaflet (1, 2). In contrast, studies from Japan and South Korea suggest that the left-right pattern may be found in <60% of East Asian patients with BAV, with a common right-posterior leaflet increasing in prevalence in this population (56, 57). Common left-posterior leaflets are rare in any population. Although this requires further investigation, this suggests that there may be a genetically inherited predisposition to particular types of malformation. Recent studies have also suggested that genetic syndromes can be associated with different patterns of leaflet fusion. For example, whilst Turner and DiGeorge syndromes most commonly present with a common left-right leaflet, Down syndrome is associated with a common right-posterior leaflet (58). Together, these data suggest that there is likely to be a genetic element to leaflet patterning.

There have been several large (and small) studies that have sought to establish the genetic causes of BAV and aortic stenosis in the human population [for example (59–67)]. Despite some success [most notably in the case of ROBO4; (68)], many of these studies have taken a targeted-sequencing approach based on data from studies of animal models and/or filtered the large numbers of gene variants obtained from exome sequencing based on whether the gene is known to play a role in heart/valve

development. Thus, these studies are heavily reliant on the quality of the data from previous genomic studies and from cardiovascular developmental biology using animal models.

There are many good examples of mouse gene knockouts that result in valve dysplasia and/or BAV [for example (30, 31, 42, 49, 63, 68–73)] and also in other species such as the Syrian hamster (54, 74, 75). These animal models have given essential insights into how disruption of different developmental mechanisms, genes, and signalling pathways can lead to different types of BAV and valve dysplasia (Figure 4). For a comprehensive overview of this topic, we recommend several excellent reviews where these have been summarised (12, 54, 79, 80). It should be noted that only rarely (68) has the mouse been used to model human BAV gene variants, confirming their pathogenicity, and thus it remains unclear in the majority of cases whether the gene variants observed are directly and specifically causative for BAV.

Although each of the different patterns of BAV has been reported in mouse models, there appears to be an under-representation of the left-right fusion pattern relative to the human population, and an over-representation of the cases where there appears to be an absence of the posterior leaflet, with no visible raphe in the remaining leaflets. Some of these differences may be explained by a lack of detailed description of the tiny mouse leaflets, where a raphe may be difficult to see. It could also be that the nature of most mouse models, where genes are ‘knocked out’ and are therefore non-functional may lead to different effects on cell behaviour. Point mutations may alter the function of the associated genes in more subtle ways, perhaps altering interactions with binding partners leading to gain of function rather than loss of function phenotypes. Alternatively,

most human BAV series involve adult patients and it may be that this is not fully representative of the full spectrum of anomalies. For example, a study of babies under 3 months of age with critical aortic stenosis revealed different leaflet and commissure patterns to those of older children (81). Whether this is a maturity issue or reflects a failure of survival of babies with the severest phenotypes is not clear, but it does suggest that an analysis of only adults may miss some phenotypic variations. It is also possible that there are biological differences between mouse and human arterial valve development and anatomy. Some minor differences are apparent (**Figure 2**), but whether these are enough to explain the reported differences in aortic valve phenotypes between mouse and human remains unclear.

There is a great interest in the idea of using zebrafish to model human BAV gene variants, despite the zebrafish aortic valve naturally having only two leaflets; there is no pulmonary valve in fish as there are no lungs. There would be enormous advantages of using the zebrafish to model BAV variants, as it develops externally, is easy to manipulate physically and genetically, and lack of dependence on a functional cardiovascular system for the first 5 days of its development, coupled with its transparency as a larva, makes it ideal for live imaging of the developing heart and for investigating the more genetically intractable effects of, for example, blood flow on valve development (82). However, this major anatomical difference between fish and mammals means that it is not easy to directly correlate abnormal phenotypes in the zebrafish valve with the human phenotype. Despite this, aortic stenosis and/or regurgitation across the aortic valve has been used as supportive evidence for gene variant significance (68, 83, 84). The use of zebrafish to model BAV is also currently hampered by a lack of clarity about whether the zebrafish arterial valve develops in the same way as the mammalian valve. For example, do the same progenitor lineages contribute to the aortic valve in mammals and fish, and does EndMT play a crucial role in zebrafish as it does on mouse? Elucidation of these issues will improve our understanding of the key features of valve development and will help to establish whether zebrafish can be a useful model for understanding how gene variants in human patients can lead to the well-recognised pathology.

Much is known about arterial valve development from animal models, although there are still some areas, particularly relating to the sculpting of the leaflets and the maturation of their supporting structures, that remain to be clarified. In terms of understanding the extent to which knowledge from animal studies can be applied to human arterial valve development, we still do not have a detailed timeline of how the arterial valves develop in the human embryo/foetus, particularly in the period from 8 to 40 weeks of gestation. Although the samples are limited, it will be important to establish when the key events

take place and to establish the maturity of the human foetal and neonatal arterial valves relative to what we see in rodents. In terms of morphogenetic mechanisms, remarkably little is known specifically about these processes in human embryos. Although direct extrapolation from mouse to human is routine, we still do not know if cardiac progenitor populations make the same contributions in mouse and human. This is hampered by the difficulties in carrying out lineage tracing experiments in human embryos, although this could be overcome by the development of specific markers for differentiated NCCs and EndMT-derived cells. Alternatively, tracking somatic mutations as a form of lineage tracing is becoming a reality and may solve the issue (85). Extending from this, we do not know whether the same mechanisms that seem to underpin the patho-development of BAV in mice, for example, hypercellularity of the cushions/leaflets or absence of the ICVS, are similarly of relevance in humans. Thus, whilst it is likely that the basic mechanisms are similar, there may be crucial differences that limit the usefulness of animal models for studying both normal and abnormal valve development and disease. Whilst the possibility of offering genetic counselling for isolated BAV may seem some way off, and anyway may not be considered appropriate for a malformation that is frequently asymptomatic for much of life, it would be useful to understand the link between BAV and adult cardiovascular disease. This might allow us to stratify patients with BAV into groups who would be likely to go on to develop calcified leaflets or thoracic aortic aneurysms, perhaps based on the leaflet pattern or the nature of the progenitor lineage that was disrupted, and those in which this is unlikely. This would allow targeted drug interventions and perhaps influence surgical decisions about whether to replace the aortic valve with the patient's own pulmonary valve (as in the Ross procedure), rather than a porcine, synthetic, or metallic valve. It is only with further analysis of scarce human embryos that we will properly be able to address these important issues.

AUTHOR CONTRIBUTIONS

DH and BC wrote, reviewed, and revised the manuscript. LE and JT produced the histological sections and reviewed the document. All authors contributed to the article and approved the submitted version.

FUNDING

This work was supported by the British Heart Foundation Programme Grant RG/19/2/34256 and MRC/Wellcome Trust (MR/R006237/1).

REFERENCES

1. Sievers HH, Schmidtke C. A classification system for the bicuspid aortic valve from 304 surgical specimens. *J Thorac Cardiovasc Surg.* (2007) 133:1226–33. doi: 10.1016/j.jtcvs.2007.01.039
2. Siu SC, Silversides CK. Bicuspid aortic valve disease. *J Am Coll Cardiol.* (2010) 55:2789–800. doi: 10.1016/j.jacc.2009.12.068
3. Webb S, Qayyum SR, Anderson RH, Lamers WH, Richardson MK. Septation and separation within the outflow tract of the developing heart. *J Anat.* (2003) 202:327–42. doi: 10.1046/j.1469-7580.2003.00168.x
4. Anderson RH, Mori S, Spicer DE, Brown NA, Mohun TJ. Development and morphology of the ventricular outflow tracts. *World J Pediatr Congenit Heart Surg.* (2016) 7:561–77. doi: 10.1177/2150135116651114

5. Richardson R, Eley L, Donald-Wilson C, Davis J, Curley N, Alqahtani A, et al. Development and maturation of the fibrous components of the arterial roots in the mouse heart. *J Anat.* (2018) 232:554–67. doi: 10.1111/joa.12713
6. Gerrelli D, Liso S, Copp AJ, Lindsay S. Enabling research with human embryonic and fetal tissue resources. *Development.* (2015) 142:3073–6. doi: 10.1242/dev.122820
7. Combs MD, Yutzy KE. Heart valve development: regulatory networks in development and disease. *Circ Res.* (2009) 105:408–21. doi: 10.1161/CIRCRESAHA.109.201566
8. de Vlaming A, Sauls K, Hajdu Z, Visconti RP, Mehesz AN, Levine RA, et al. Atrioventricular valve development: new perspectives on an old theme. *Differentiation.* (2012) 84:103–16. doi: 10.1016/j.diff.2012.04.001
9. Pucéat M. Embryological origin of the endocardium and derived valve progenitor cells: from developmental biology to stem cell-based valve repair. *Biochim Biophys Acta.* (2013) 1833:917–22. doi: 10.1016/j.bbamcr.2012.09.013
10. MacGrogan D, Luxán G, Driessen-Mol A, Bouten C, Baaijens F, de la Pompa JL. How to make a heart valve: from embryonic development to bioengineering of living valve substitutes. *Cold Spring Harb Perspect Med.* (2014) 4:a013912. doi: 10.1101/cshperspect.a013912
11. O'Donnell A, Yutzy KE. Mechanisms of heart valve development and disease. *Development.* (2020) 147:dev183020. doi: 10.1242/dev.183020
12. Henderson DJ, Eley L, Chaudhry B. New concepts in the development and malformation of the arterial valves. *J Cardiovasc Dev Dis.* (2020) 7:38. doi: 10.3390/jcdd7040038
13. Mjaatvedt CH, Yamamura H, Capehart AA, Turner D, Markwald RR. The Cspg2 gene, disrupted in the hdf mutant, is required for right cardiac chamber and endocardial cushion formation. *Dev Biol.* (1998) 202:56–66. doi: 10.1006/dbio.1998.9001
14. Camenisch TD, Spicer AP, Brehm-Gibson T, Biesterfeldt J, Augustine ML, Calabro A Jr, et al. Disruption of hyaluronan synthase-2 abrogates normal cardiac morphogenesis and hyaluronan-mediated transformation of epithelium to mesenchyme. *J Clin Invest.* (2000) 106:349–60. doi: 10.1172/JCI10272
15. Kramer TC. The partitioning of the truncus and conus and the formation of the membranous portion of the interventricular septum in the human heart. *Am J Anat.* (1942) 71:343–70. doi: 10.1002/aja.1000710303
16. Maron BJ, Hutchins GM. The development of the semilunar valves in the human heart. *Am J Pathol.* (1974) 74:331–44.
17. Hutchins GM, Kessler-Hanna A, Moore GW. Development of the coronary arteries in the embryonic human heart. *Circulation.* (1988) 77:1250–7. doi: 10.1161/01.CIR.77.6.1250
18. Goor DA, Dische R, Lillehei CW. The conotruncus. I Its normal inversion and conus absorption. *Circulation.* (1972) 46:375–84. doi: 10.1161/01.CIR.46.2.375
19. Monaghan MG, Linneweh M, Liebscher S, Van Handel B, Layland SL, Schenke-Layland K. Endocardial-to-mesenchymal transformation and mesenchymal cell colonization at the onset of human cardiac valve development. *Development.* (2016) 143:473–82. doi: 10.1242/dev.133843
20. de la Pompa JL, Timmerman LA, Takimoto H, Yoshida H, Elia AJ, Samper E, et al. Role of the NF-ATc transcription factor in morphogenesis of cardiac valves and septum. *Nature.* (1998) 392:182–6. doi: 10.1038/32419
21. Ranger AM, Grusby MJ, Hodge MR, Gravalles EM, de la Brousse FC, Hoey T, et al. The transcription factor NF-ATc is essential for cardiac valve formation. *Nature.* (1998) 392:186–90. doi: 10.1038/32426
22. Chang CP, Neilson JR, Bayle JH, Gestwicki JE, Kuo A, Stankunas K, et al. A field of myocardial-endocardial NFAT signaling underlies heart valve morphogenesis. *Cell.* (2004) 118:649–63. doi: 10.1016/j.cell.2004.08.010
23. Dor Y, Camenisch TD, Itin A, Fishman GI, McDonald JA, Carmeliet P, et al. novel role for VEGF in endocardial cushion formation and its potential contribution to congenital heart defects. *Development.* (2001) 128:1531–8. doi: 10.1242/dev.128.9.1531
24. Hutson MR, Kirby ML. Model systems for the study of heart development and disease. Cardiac neural crest and conotruncal malformations. *Semin Cell Dev Biol.* (2007) 18:101–10. doi: 10.1016/j.semcdb.2006.12.004
25. Keyte AL, Alonzo-Johnsen M, Hutson MR. Evolutionary and developmental origins of the cardiac neural crest: building a divided outflow tract. *Birth Defects Res C Embryo Today.* (2014) 102:309–23. doi: 10.1002/bdrc.21076
26. George RM, Maldonado-Velez G, Firulli AB. The heart of the neural crest: cardiac neural crest cells in development and regeneration. *Development.* (2020) 147:dev188706. doi: 10.1242/dev.188706
27. Poelmann RE, Mikawa T, Gittenberger-de Groot AC. Neural crest cells in outflow tract septation of the embryonic chicken heart: differentiation and apoptosis. *Dev Dyn.* (1998) 212:373–84. doi: 10.1002/(SICI)1097-0177(199807)212:3<373::AID-AJA5>3.0.CO;2-E
28. Orts-Llorca F, Puerta Fonolla J, Sobrado J. The formation, septation and fate of the truncus arteriosus in man. *J Anat.* (1982) 134(Pt 1):41–56.
29. Congdon ED. Transformation of the aortic arch system during the development of the human embryo. *Contrib Embryol.* (1922) 14:47–110.
30. Phillips HM, Mahendran P, Singh E, Anderson RH, Chaudhry B, Henderson DJ. Neural crest cells are required for correct positioning of the developing outflow cushions and pattern the arterial valve leaflets. *Cardiovasc Res.* (2013) 99:452–60. doi: 10.1093/cvr/cvt132
31. Eley L, Alqahtani AM, MacGrogan D, Richardson RV, Murphy L, Salguero-Jimenez A, et al. A novel source of arterial valve cells linked to bicuspid aortic valve without raphe in mice. *Elife.* (2018) 7:e34110. doi: 10.7554/eLife.34110
32. Sizarov A, Lamers WH, Mohun TJ, Brown NA, Anderson RH, Moorman AF. Three-dimensional and molecular analysis of the arterial pole of the developing human heart. *J Anat.* (2012) 220:336–49. doi: 10.1111/j.1469-7580.2012.01474.x
33. Hikspoors J, Kruepunga N, Mommen, G, Koehler E, Anderson R, Lamers. Spatial and temporal aspects of the human embryonic heart between 3.5 and 8 weeks of development. Preprint (In review). Available online at: <https://www.researchsquare.com/article/rs-129074/v1> (accessed December 28, 2020).
34. Thompson RP, Sumida H, Abercrombie V, Satow Y, Fitzharris TP, Okamoto N. Morphogenesis of human cardiac outflow. *Anat Rec.* (1985) 213:578–86, 538–9. doi: 10.1002/ar.1092130414
35. Anderson RH, Chaudhry B, Mohun TJ, Bamforth SD, Hoyland D, Phillips HM, et al. Normal and abnormal development of the intrapericardial arterial trunks in humans and mice. *Cardiovasc Res.* (2012) 95:108–15. doi: 10.1093/cvr/cvs147
36. Milos NC, Nordstrom DB, Ongaro I, Chow AK. Variations in structure of the outflow tract of the human embryonic heart: a new hypothesis for generating bicuspid aortic semilunar valves. *Ann Anat.* (2017) 211:88–103. doi: 10.1016/j.aanat.2016.12.004
37. Lakkis MM, Epstein JA. Neurofibromin modulation of ras activity is required for normal endocardial-mesenchymal transformation in the developing heart. *Development.* (1998) 125:4359–67. doi: 10.1242/dev.125.22.4359
38. Chen YH, Ishii M, Sun J, Sucov HM, Maxson RE Jr. Msx1 and Msx2 regulate survival of secondary heart field precursors and post-migratory proliferation of cardiac neural crest in the outflow tract. *Dev Biol.* (2007) 308:421–37. doi: 10.1016/j.ydbio.2007.05.037
39. Combs MD, Yutzy KE. VEGF and RANKL regulation of NFATc1 in heart valve development. *Circ Res.* (2009) 105:565–74. doi: 10.1161/CIRCRESAHA.109.196469
40. Zhang H, von Gise A, Liu Q, Hu T, Tian X, He L, et al. Yap1 is required for endothelial to mesenchymal transition of the atrioventricular cushion. *J Biol Chem.* (2014) 289:18681–92. doi: 10.1074/jbc.M114.554584
41. Costell M, Carmona R, Gustafsson E, González-Iriarte M, Fässler R, Muñoz-Chápuli R. Hyperplastic conotruncal endocardial cushions and transposition of great arteries in perlecan-null mice. *Circ Res.* (2002) 91:158–64. doi: 10.1161/01.RES.0000026056.81424.DA
42. Dupuis LE, Osinska H, Weinstein MB, Hinton RB, Kern CB. Insufficient versican cleavage and Smad2 phosphorylation results in bicuspid aortic and pulmonary valves. *J Mol Cell Cardiol.* (2013) 60:50–9. doi: 10.1016/j.yjmcc.2013.03.010
43. Votteler M, Berrio DA, Horke A, Sabatier L, Reinhardt DP, Nsair A, et al. Elastogenesis at the onset of human cardiac valve development. *Development.* (2013) 140:2345–53. doi: 10.1242/dev.093500
44. Durst R, Sauls K, Peal DS, deVlaming A, Toomer K, Leyne M, et al. Mutations in DCHS1 cause mitral valve prolapse. *Nature.* (2015) 525:109–13. doi: 10.1038/nature14670

45. Anvarian Z, Mykytyn K, Mukhopadhyay S, Pedersen LB, Christensen ST. Cellular signalling by primary cilia in development, organ function and disease. *Nat Rev Nephrol.* (2019) 15:199–219. doi: 10.1038/s41581-019-0116-9
46. Koenig SN, Bosse KM, Nadorlik HA, Lilly B, Garg V. Evidence of aortopathy in mice with haploinsufficiency of *Notch1* in *Nos3*-null background. *J Cardiovasc Dev Dis.* (2015) 2:17–30. doi: 10.3390/jcdd2010017
47. Wang Y, Wu B, Farrar E, Lui W, Lu P, Zhang D, et al. Notch-Tnf signalling is required for development and homeostasis of arterial valves. *Eur Heart J.* (2017) 38:675–86. doi: 10.1093/eurheartj/ehv520
48. Ridge LA, Kewbank D, Schütz D, Stumm R, Scambler PJ, Ivins S. Dual role for CXCL12 signaling in semilunar valve development. *Cell Rep.* (2021) 36:109610. doi: 10.1016/j.celrep.2021.109610
49. Odelin G, Faure E, Couplier F, Di Bonito M, Bajolle F, Studer M, et al. Krox20 defines a subpopulation of cardiac neural crest cells contributing to arterial valves and bicuspid aortic valve. *Development.* (2018) 145:dev151944. doi: 10.1242/dev.151944
50. Shaner RF. Abnormal pulmonary and aortic semilunar valves in embryos. *Anat Rec.* (1963) 147:5–13. doi: 10.1002/ar.1091470103
51. Hinton RB Jr, Lincoln J, Deutsch GH, Osinska H, Manning PB, Benson DW, et al. Extracellular matrix remodeling and organization in developing and diseased aortic valves. *Circ Res.* (2006) 98:1431–8. doi: 10.1161/01.RES.0000224114.65109.4e
52. Hulin A, Moore V, James JM, Yutzey KE. Loss of *Axin2* results in impaired heart valve maturation and subsequent myxomatous valve disease. *Cardiovasc Res.* (2017) 113:40–51. doi: 10.1093/cvr/cvw229
53. Aikawa E, Whittaker P, Farber M, Mendelson K, Padera RF, Aikawa M, et al. Human semilunar cardiac valve remodeling by activated cells from fetus to adult: implications for postnatal adaptation, pathology, and tissue engineering. *Circulation.* (2006) 113:1344–52. doi: 10.1161/CIRCULATIONAHA.105.591768
54. Sans-Coma V, Fernández B, Durán AC, Thiene G, Arqué JM, Muñoz-Chápuli R, et al. Fusion of valve cushions as a key factor in the formation of congenital bicuspid aortic valves in Syrian hamsters. *Anat Rec.* (1996) 244:490–8. doi: 10.1002/(SICI)1097-0185(199604)244:4<490::AID-AR7>3.0.CO;2-Z
55. Koenraadt WM, Grewal N, Gaidoukevitch OY, DeRuiter MC, Gittenberger-de Groot AC, Bartelings MM, et al. The extent of the raphe in bicuspid aortic valves is associated with aortic regurgitation and aortic root dilatation. *Neth Heart J.* (2016) 24:127–33. doi: 10.1007/s12471-015-0784-4
56. Kinoshita T, Naito S, Suzuki T, Asai T. Valve phenotype and risk factors of aortic dilatation after aortic valve replacement in Japanese patients with bicuspid aortic valve. *Circ J.* (2016) 80:1356–61. doi: 10.1253/circj.CJ-15-1378
57. Sun BJ, Jin X, Song JK, Lee S, Lee JH, Park JB, et al. Clinical characteristics of Korean patients with bicuspid aortic valve who underwent aortic valve surgery. *Korean Circ J.* 2018 48:48–58. doi: 10.4070/kcj.2017.0124
58. Niaz T, Poterucha JT, Olson TM, Johnson JN, Craviari C, Nienaber T, et al. Characteristic morphologies of the bicuspid aortic valve in patients with genetic syndromes. *J Am Soc Echocardiogr.* (2018) 31:194–200. doi: 10.1016/j.echo.2017.10.008
59. Wooten EC, Iyer LK, Montefusco MC, Hedgepeth AK, Payne DD, Kapur NK, et al. Application of gene network analysis techniques identifies *AXIN1/PDIA2* and endoglin haplotypes associated with bicuspid aortic valve. *PLoS ONE.* (2010) 5:e8830. doi: 10.1371/journal.pone.0008830
60. Martin LJ, Pilipenko V, Kaufman KM, Cripe L, Kottyan LC, Keddache M, et al. Whole exome sequencing for familial bicuspid aortic valve identifies putative variants. *Circ Cardiovasc Genet.* (2014) 7:677–83. doi: 10.1161/CIRCGENETICS.114.000526
61. Bonachea EM, Zender G, White P, Corsmeier D, Newsom D, Fitzgerald-Butt S, et al. Use of a targeted, combinatorial next-generation sequencing approach for the study of bicuspid aortic valve. *BMC Med Genomics.* (2014) 7:56. doi: 10.1186/1755-8794-7-56
62. Dargis N, Lamontagne M, Gaudreault N, Sbarra L, Henry C, Pibarot P, et al. Identification of gender-specific genetic variants in patients with bicuspid aortic valve. *Am J Cardiol.* (2016) 117:420–6. doi: 10.1016/j.amjcard.2015.10.058
63. Gharibeh L, Komati H, Bossé Y, Boodhwani M, Heydarpour M, Fortier M, et al. Bicuspid Aortic Valve Consortium. *GATA6* regulates aortic valve remodeling, and its haploinsufficiency leads to right-left type bicuspid aortic valve. *Circulation.* (2018) 138:1025–38. doi: 10.1161/CIRCULATIONAHA.117.029506
64. Giusti B, Sticchi E, De Caro R, Magi A, Nistri S, Pepe G. Genetic bases of bicuspid aortic valve: the contribution of traditional and high-throughput sequencing approaches on research and diagnosis. *Front Physiol.* (2017) 8:612. doi: 10.3389/fphys.2017.00612
65. Yang B, Zhou W, Jiao J, Nielsen JB, Mathis MR, Heydarpour M, et al. Protein-altering and regulatory genetic variants near *GATA4* implicated in bicuspid aortic valve. *Nat Commun.* (2017) 8:15481. doi: 10.1038/ncomms15481
66. McKellar SH, Tester DJ, Yagubyan M, Majumdar R, Ackerman MJ, Sundt TM 3rd. Novel NOTCH1 mutations in patients with bicuspid aortic valve disease and thoracic aortic aneurysms. *J Thorac Cardiovasc Surg.* (2007) 134:290–6. doi: 10.1016/j.jtcvs.2007.02.041
67. Mohamed SA, Aherrahrou Z, Liptau H, Erasmi AW, Hagemann C, Wrobel S, et al. Novel missense mutations (p.T596M and p.P1797H) in NOTCH1 in patients with bicuspid aortic valve. *Biochem Biophys Res Commun.* (2006) 345:1460–5. doi: 10.1016/j.bbrc.2006.05.046
68. Gould RA, Aziz H, Woods CE, Seman-Senderos MA, Sparks E, Preuss C, et al. ROBO4 variants predispose individuals to bicuspid aortic valve and thoracic aortic aneurysm. *Nat Genet.* (2019) 51:42–50. doi: 10.1038/s41588-018-0265-y
69. Lee TC, Zhao YD, Courtman DW, Stewart DJ. Abnormal aortic valve development in mice lacking endothelial nitric oxide synthase. *Circulation.* (2000) 101:2345–8. doi: 10.1161/01.CIR.101.20.2345
70. Laforest B, Andelfinger G, Nemer M. Loss of *Gata5* in mice leads to bicuspid aortic valve. *J Clin Invest.* (2011) 121:2876–87. doi: 10.1172/JCI44555
71. MacGrogan D, D'Amato G, Travasano S, Martinez-Poveda B, Luxán G, Del Monte-Nieto G, et al. Sequential ligand-dependent notch signaling activation regulates valve primordium formation and morphogenesis. *Circ Res.* (2016) 118:1480–97. doi: 10.1161/CIRCRESAHA.115.308077
72. Thomas PS, Sridurongrit S, Ruiz-Lozano P, Kaartinen V. Deficient signaling via *Alk2* (*Acvr1*) leads to bicuspid aortic valve development. *PLoS ONE.* (2012) 7:e35539. doi: 10.1371/journal.pone.0035539
73. Mommersteeg MT, Yeh ML, Parnavelas JG, Andrews WD. Disrupted Slit-Robo signalling results in membranous ventricular septum defects and bicuspid aortic valves. *Cardiovasc Res.* (2015) 106:55–66. doi: 10.1093/cvr/cvv040
74. Sans-Coma V, Cardo M, Thiene G, Fernández B, Arqué JM, Durán AC. Bicuspid aortic and pulmonary valves in the Syrian hamster. *Int J Cardiol.* (1992) 34:249–54. doi: 10.1016/0167-5273(92)90021-T
75. Fernández B, Fernández MC, Durán AC, López D, Martire A, Sans-Coma V. Anatomy and formation of congenital bicuspid and quadricuspid pulmonary valves in Syrian hamsters. *Anat Rec.* (1998) 250:70–9. doi: 10.1002/(SICI)1097-0185(199801)250:1<70::AID-AR7>3.0.CO;2-I
76. Fernández B, Durán AC, Fernández-Gallego T, Fernández MC, Such M, Arqué JM, Sans-Coma V. Bicuspid aortic valves with different spatial orientations of the leaflets are distinct etiological entities. *J Am Coll Cardiol.* (2009) 54:2312–8. doi: 10.1016/j.jacc.2009.07.044
77. Peterson JC, Chughtai M, Wisse LJ, Gittenberger-de Groot AC, Feng Q, Goumans MTH, et al. Bicuspid aortic valve formation: *Nos3* mutation leads to abnormal lineage patterning of neural crest cells and the second heart field. *Dis Model Mech.* (2018) 11:dmm034637. doi: 10.1242/dmm.034637
78. Akerberg BN, Sarangam ML, Stankunas K. Endocardial *Brg1* disruption illustrates the developmental origins of semilunar valve disease. *Dev Biol.* (2015) 407:158–72. doi: 10.1016/j.ydbio.2015.06.015
79. Soto-Navarrete MT, López-Unzu MÁ, Durán AC, Fernández B. Embryonic development of bicuspid aortic valves. *Prog Cardiovasc Dis.* (2020) 63:407–418. doi: 10.1016/j.pcad.2020.06.008
80. Fernández B, Soto-Navarrete MT, López-García A, López-Unzu MÁ, Durán AC, Fernández MC. Bicuspid aortic valve in 2 model species and review of the literature. *Vet Pathol.* (2020) 57:321–31. doi: 10.1177/0300985819900018
81. McKay R, Smith A, Leung MP, Arnold R, Anderson RH. Morphology of the ventriculoaortic junction in critical aortic stenosis. Implications for hemodynamic function and clinical management. *J Thorac Cardiovasc Surg.* (1992) 104:434–42. doi: 10.1016/S0022-5223(19)34800-7
82. Liu J, Stainier DY. Zebrafish in the study of early cardiac development. *Circ Res.* (2012) 110:870–4. doi: 10.1161/CIRCRESAHA.111.246504
83. Rambeau P, Faure E, Thérion A, Avierinos JF, Jopling C, Zaffran S, et al. Reduced aggrecan expression affects cardiac outflow tract development

- in zebrafish and is associated with bicuspid aortic valve disease in humans. *Int J Cardiol.* (2017) 249:340–43. doi: 10.1016/j.ijcard.2017.09.174
84. Fulmer D, Toomer K, Guo L, Moore K, Glover J, Moore R, et al. Defects in the exocyst-cilia machinery cause bicuspid aortic valve disease and aortic stenosis. *Circulation.* (2019) 140:1331–41. doi: 10.1161/CIRCULATIONAHA.119.038376
 85. Spencer Chapman M, Ranzoni AM, Myers B, Williams N, Coorens THH, Mitchell E, et al. Lineage tracing of human development through somatic mutations. *Nature.* (2021) 595:85–90. doi: 10.1038/s41586-021-03548-6

Conflict of Interest: The authors declare that the research was conducted in the absence of any commercial or financial relationships that could be construed as a potential conflict of interest.

Publisher's Note: All claims expressed in this article are solely those of the authors and do not necessarily represent those of their affiliated organizations, or those of the publisher, the editors and the reviewers. Any product that may be evaluated in this article, or claim that may be made by its manufacturer, is not guaranteed or endorsed by the publisher.

Copyright © 2022 Henderson, Eley, Turner and Chaudhry. This is an open-access article distributed under the terms of the Creative Commons Attribution License (CC BY). The use, distribution or reproduction in other forums is permitted, provided the original author(s) and the copyright owner(s) are credited and that the original publication in this journal is cited, in accordance with accepted academic practice. No use, distribution or reproduction is permitted which does not comply with these terms.



Understanding Pulmonary Autograft Remodeling After the Ross Procedure: Stick to the Facts

Lucas Van Hoof^{1*}, Peter Verbrugghe¹, Elizabeth A. V. Jones², Jay D. Humphrey³, Stefan Janssens⁴, Nele Famaey⁵ and Filip Rega¹

¹ Department of Cardiac Surgery, University Hospitals Leuven, Leuven, Belgium, ² Center for Molecular and Vascular Biology, KU Leuven, Leuven, Belgium, ³ Department of Biomedical Engineering, Yale University, New Haven, CT, United States, ⁴ Department of Cardiology, University Hospitals Leuven, Leuven, Belgium, ⁵ Biomechanics Section, KU Leuven, Leuven, Belgium

OPEN ACCESS

Edited by:

Anthal Smits,
Eindhoven University of
Technology, Netherlands

Reviewed by:

Paul Human,
University of Cape Town, South Africa
Najma Latif,
The Magdi Yacoub Institute,
United Kingdom

*Correspondence:

Lucas Van Hoof
lucas.vanhoof@kuleuven.be;
lucasvanhoof1@gmail.com

Specialty section:

This article was submitted to
Heart Valve Disease,
a section of the journal
Frontiers in Cardiovascular Medicine

Received: 04 December 2021

Accepted: 17 January 2022

Published: 09 February 2022

Citation:

Van Hoof L, Verbrugghe P, Jones EAV, Humphrey JD, Janssens S, Famaey N and Rega F (2022) Understanding Pulmonary Autograft Remodeling After the Ross Procedure: Stick to the Facts. *Front. Cardiovasc. Med.* 9:829120. doi: 10.3389/fcvm.2022.829120

The Ross, or pulmonary autograft, procedure presents a fascinating mechanobiological scenario. Due to the common embryological origin of the aortic and pulmonary root, the conotruncus, several authors have hypothesized that a pulmonary autograft has the innate potential to remodel into an aortic phenotype once exposed to systemic conditions. Most of our understanding of pulmonary autograft mechanobiology stems from the remodeling observed in the arterial wall, rather than the valve, simply because there have been many opportunities to study the walls of dilated autografts explanted at reoperation. While previous histological studies provided important clues on autograft adaptation, a comprehensive understanding of its determinants and underlying mechanisms is needed so that the Ross procedure can become a widely accepted aortic valve substitute in select patients. It is clear that protecting the autograft during the early adaptation phase is crucial to avoid initiating a sequence of pathological remodeling. External support in the freestanding Ross procedure should aim to prevent dilatation while simultaneously promoting remodeling, rather than preventing dilatation at the cost of vascular atrophy. To define the optimal mechanical properties and geometry for external support, the ideal conditions for autograft remodeling and the timeline of mechanical adaptation must be determined. We aimed to rigorously review pulmonary autograft remodeling after the Ross procedure. Starting from the developmental, microstructural and biomechanical differences between the pulmonary artery and aorta, we review autograft mechanobiology in relation to distinct clinical failure mechanisms while aiming to identify unmet clinical needs, gaps in current knowledge and areas for further research. By correlating clinical and experimental observations of autograft remodeling with established principles in cardiovascular mechanobiology, we aim to present an up-to-date overview of all factors involved in extracellular matrix remodeling, their interactions and potential underlying molecular mechanisms.

Keywords: Ross procedure, pulmonary autograft, mechanobiology, remodeling, extracellular matrix, external support

INTRODUCTION

The aortic valve opens and closes continuously, upwards of 100,000 times per day. Smooth functioning of the valve throughout a lifetime is enabled by its innate remodeling ability (1). Yet, the valve may need to be replaced in cases of unrepairable aortic valve disease, as, for example, in the setting of a bicuspid aortic valve. Especially in young adults with a long life expectancy, an aortic valve substitute should optimally restore aortic root biomechanics and hemodynamic function.

Disappointing outcomes of the first prosthetic valves led to the search for biological alternatives and in 1962, Donald N. Ross commenced implanting aortic valve homografts in patients (2). The lack of availability of homografts in all sizes, the lack of growth potential in children, and their limited durability prompted the quest for a living valve alternative (3). In the Ross procedure, first performed in a patient in 1967, the diseased aortic valve is replaced by the patient's own pulmonary valve and a pulmonary homograft is implanted in the pulmonary position (**Figure 1**) (5). As the so-called pulmonary autograft is a native tissue substitute, it offers an excellent hemodynamic profile and resistance to endocarditis without the need for anticoagulant therapy (6, 7). This translates into superior exercise capacity and freedom from valve-related complications when compared to mechanical or bioprosthetic valve replacement (8–10). Therefore, the Ross procedure is the only aortic valve replacement that can restore long-term survival and quality-of-life to that of the age-matched population (11–13). Yet, due to a perceived risk of increased operative mortality and the fear of complex reoperations on two valves, there remains skepticism toward the procedure (14, 15).

The Ross procedure presents a fascinating mechanobiological scenario. After devascularizing the autograft, it is placed in the systemic circulation and suddenly exposed to a five- to eight-fold greater blood pressure. In the freestanding root technique (**Figure 1.1**), the pulmonary autograft often dilates immediately (16). Nevertheless, many patients have a well-functioning neo-aortic valve multiple decades post-operatively, indicating a living, remodeling valve (17, 18). As the aorta and pulmonary root share a common embryological origin, the conotruncus, several authors have hypothesized that the pulmonary autograft has the innate ability to remodel into an aortic phenotype (19–22). Unfortunately, there are few data on successfully remodeled tissue. Rather, most *ex vivo* studies on human autografts evaluated tissue acquired at reoperation and even detailed histological reports of well-functioning autografts are scarce. Therefore, the adaptive mechanisms of the pulmonary autograft are poorly understood. It appears, however, that stress-shielding the pulmonary autograft using meticulous surgical technique, blood pressure control, or external support may further promote adaptation to the systemic circulation (19, 23).

Previous clinical studies and animal models have shown an increase in collagen in both autograft walls and leaflets (24–26). Remodeling of collagen, a key mechanism in cardiovascular biology that can increase tensile stiffness and strength, is also seen in pulmonary hypertension, systemic hypertension and aortic aneurysms (27–29). Therefore, it is likely an essential component

of successful remodeling after the Ross procedure. Additional mechanisms such as an increase in cell-extracellular matrix (ECM) connections or collagen cross-linking may contribute to autograft remodeling, but have not yet been identified for the Ross procedure. Proteomic characterization of dilated autografts suggests a unique (mal)adaptive process that differs from that of ascending aortic aneurysms (30). Because all mechanisms aiming to restore tissue stress levels have the greatest chance of succeeding before overt dilatation, the early remodeling phase appears crucial. Furthermore, it is uncertain whether the pulmonary valve has a greater inherent remodeling ability than the wall, or if the wall is just more likely to suffer maladaptation in the freestanding Ross procedure because it sits unrestrained.

Prior reviews on the Ross procedure have focused mainly on patient selection and surgical technique yet speculate about autograft remodeling (19, 23). Nevertheless, long-term success of the Ross procedures relies in the first place on a living, remodeling autograft. Therefore, a comprehensive understanding of autograft adaptation and its determinants is needed so that we can identify patient-specific strategies to promote remodeling and make the pulmonary autograft a permanent aortic valve substitute. Starting with a comparison between the pulmonary artery and aorta, we review autograft mechanobiology in relation to the distinct clinical failure mechanisms. Furthermore, we evaluate the evidence regarding strategies to promote pulmonary autograft adaptation. By correlating clinical and experimental observations of autograft remodeling with established principles in cardiovascular mechanobiology, we aim to present an overview of factors involved in ECM remodeling and their interactions. Simultaneously, we aim to indicate unmet clinical needs, gaps in current knowledge, and areas for further research.

SURGICAL TECHNIQUES OF THE ROSS PROCEDURE

The Ross procedure was first performed with the scalloped pulmonary autograft implanted in subcoronary position, avoiding the need for coronary reimplantation (**Figure 1.2**) (31). The freestanding root replacement technique was introduced in 1974, once reimplantation of the coronary arteries became technically feasible (3). As this iteration is more reproducible and applicable over a wide range of anatomies, it is the most commonly used today (32). Furthermore, this technique enables neo-aortic root expansion during somatic growth in children.

Upon realizing the risk of dilatation with the root technique, the autologous inclusion technique was introduced whereby the autograft is included within the native aortic wall (**Figure 1.3**). Although this technique reliably prevents dilatation, it is not applicable in cases of severe size mismatch (16, 18, 33). Prosthetic external support also has the potential to prevent neo-aortic dilatation and is nowadays most commonly performed by placing the autograft within a cylinder of Dacron vascular graft (**Figure 2B**) (34–36). The long-term effect on reoperation rate and mechanobiological adaptation have yet to be determined (13). The use of external subvalvular annuloplasty

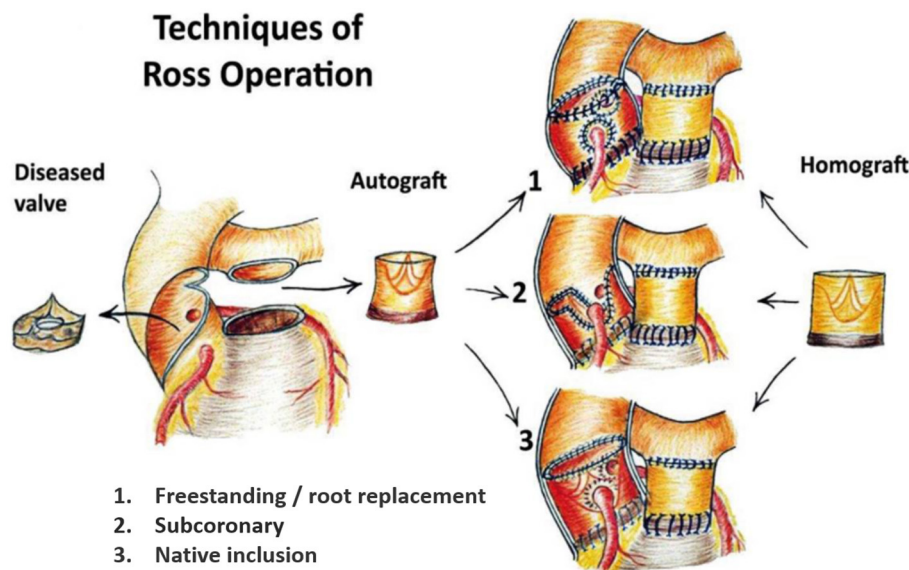


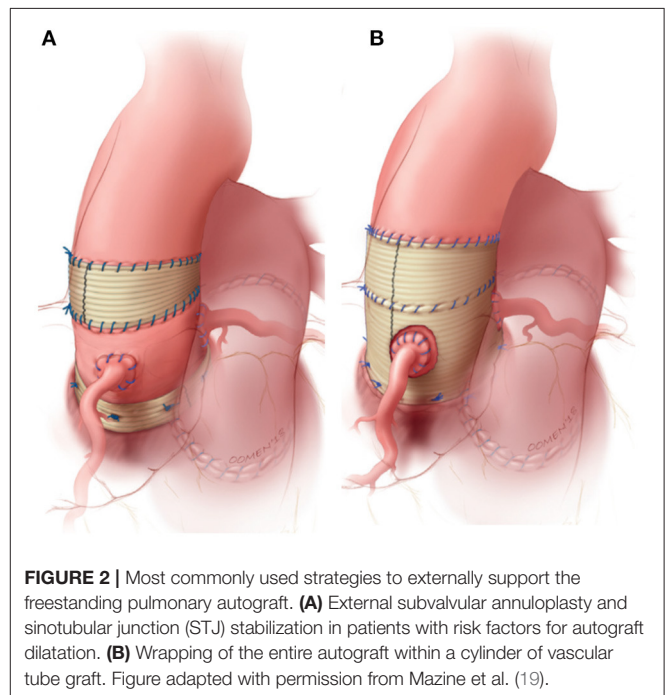
FIGURE 1 | The 3 main techniques of the Ross procedure. 1. Freestanding root replacement technique with implantation of the entire pulmonary root into the left ventricular outflow tract. 2. Subcoronary technique: implantation of the pulmonary valve only within the native aortic annulus. 3. Autologous/native inclusion technique with implantation of the pulmonary autograft within the native aortic wall to prevent dilatation. Figure reproduced from Sievers (4), journal ceased publication no permission could be requested.

and sinotubular junction (STJ) stabilization in patients with an enlarged annulus or STJ was introduced in a systematic fashion by Ismail El-Hamamsy (**Figure 2A**) (19). Using this “tailored approach” combined with strict blood pressure control, it appears possible to mitigate dilatation while avoiding the potentially deleterious hemodynamic and histological effects of total external support (37).

CLINICAL FAILURE MECHANISMS

Clinical autograft failure, and subsequent reoperation, can be related to wall dilatation, leaflet degeneration, or both. Occurring exclusively after the root replacement technique, non-structural valve degeneration is defined as greater than moderate aortic regurgitation ($AR \geq 3/4$) caused by dilatation or autograft wall dilatation beyond 50 mm, with or without associated AR (38). Structural valve degeneration, defined as greater than moderate AR caused by leaflet degeneration or prolapse, is the most common mode of failure for the subcoronary technique, yet it can occur in all variations of the Ross procedure (38). An overview of possible failure patterns, based on anatomical site and underlying mechanism, and correlation with the functional classification of AR as proposed by the group of El Khoury is shown in **Figure 3** (39). As the wall and leaflets can degenerate concomitantly, combinations of the described mechanisms are possible, depending on the specific failure phenotype.

In expert hands, durability of the subcoronary technique may exceed that of the root replacement technique, without the risk of dilatation. As a leader in his field, Dr. Hans-Hinrich Sievers reports excellent freedom from reoperation of



89.8% at 20 years post-operatively (17). On the other hand, by maximally respecting leaflet anatomy and relations, the root replacement technique has early superiority over the subcoronary and inclusion techniques (18). For any technique, imperfect surgical implantation may result in early AR, progressive in



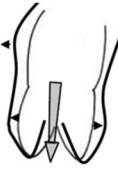
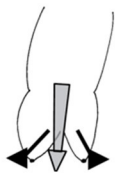



| | NSVD | | | | SVD | | |
|-------------------|--|---|---|---|--|---|---|
| Site of failure | Wall | | | | Leaflet | | |
| Mechanism | Surgical technique, technical failure Repetitive overdistension and maladaptation Clinical risk factors for dilatation | | | | Surgical technique, technical failure Repetitive trauma and maladaptation Endocarditis | | |
| Manifestation | Sinus ≥ 50 mm | STJ dilatation | Sinus dilatation | Annulus dilatation | Perforation | Prolapse | Restriction |
| Clinical failure | Dissection risk? | AR $\geq 3/4$ | | | AR $\geq 3/4$ | | |
| Illustration |  |  |  |  |  |  |  |
| AR classification | NA | Type Ia | Type Ib | Type Ic | Type Id | Type II | Type III |

FIGURE 3 | Classification of the failure mechanisms of the Ross procedure and correlation with El Khoury's functional classification of aortic regurgitation. AR, aortic regurgitation; SVD, structural valvular degeneration; NSVD, non-structural valvular degeneration. Illustrations adapted with permission from Boodhwani et al. (39).

nature due to increased leaflet stress, and potentially lead to early technical failure.

For the root replacement technique, initial elastic dilatation occurs immediately upon release of the aortic cross-clamp due to the pulmonary artery's compliance (**Figure 5**) (40, 41). Furthermore, up to 60% of the dilatation that is present at 1 year manifested prior to hospital discharge (42). An intuitive hypothesis dictates that in patients with pronounced early dilatation, in itself leading to thinning of the wall, a cycle of pathological remodeling is initiated as the autograft is not permitted to adapt; dilatation begets dilatation (37). Progressive annular or STJ dilatation is known to cause leaflet malcoaptation with a central regurgitant jet (**Figure 3**) (39, 43, 44). Isolated autograft sinus dilatation on the other hand, is less likely to lead to AR (45).

Although chronic dilatation, related to tissue remodeling, appears to be a slow process in most patients, autograft diameter will exceed 40 mm in up to 50% of patients at 12 years post-operatively (33, 46). At 15 years, up to 24% of patients will require a reoperation for non-structural valve degeneration (13, 32, 38, 47). For the root replacement technique, risk factors for dilatation and subsequent reoperation are pre-operative isolated AR, a large aortic annulus, size mismatch between aortic and pulmonary annulus, pre-existing aortic dilatation, younger age, male sex and post-operative hypertension (13, 32, 38, 47, 48). These variables should be kept in mind when selecting candidates for the Ross procedure (19).

While less straightforward than for genetically determined aortic aneurysms, there appears to be an association between autograft diameter and dissection. Pulmonary autograft dissection has been described in at least 9 cases, occurring between 5 and 18 years after index surgery at an autograft

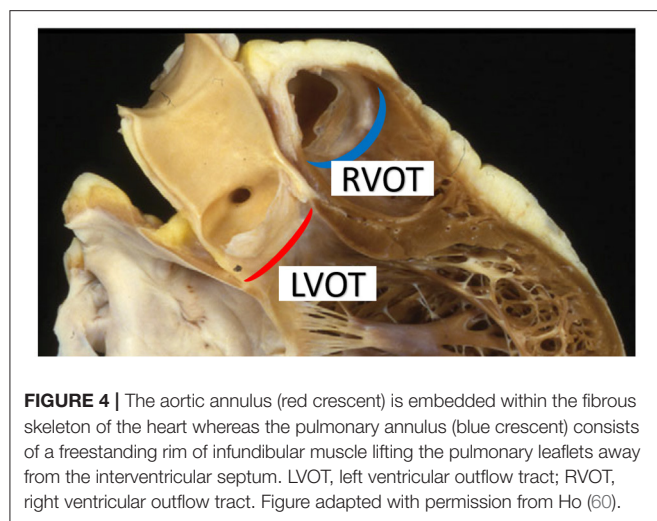
diameter of 54–64 mm (49–57). All patients presented with aortic insufficiency related to a bicuspid aortic valve (BAV) at initial operation. Furthermore, a common feature was pronounced early or sudden dilatation, for example during pregnancy, indicating compromised mechanical homeostasis. In 6 out of 9 cases, the dissection originated in the non-coronary cusp, possibly related to elevated local wall stress. As all dissections were localized without crossing suture-lines, most were incidental findings on imaging, and histopathological assessment confirmed the subacute-to-chronic nature of these dissections (51, 53, 54). In one case, the non-coronary sinus ruptured (56). The critical size threshold for reoperation, when the risk of dissection exceeds the risk of reoperation, is still uncertain. It seems that the risk of autograft dissection or rupture is very low for a diameter below 50 mm, indicating that the decision to reoperate for dilatation should be tailored individually.

AUTOGRAFT CHARACTERISTICS

A thorough understanding of pulmonary autograft mechanobiology begins with studying the differences between the pulmonary and aortic root. As both vessels have the same embryological origin, the conotruncus, their basic histological composition and anatomy are initially similar (58). Due to diverging hemodynamic conditions post-natally, after the ductus arteriosus closes, the aorta and pulmonary artery and their respective valves develop distinct microstructural and mechanical properties (59).

Surgical Anatomy

Both arteries are said to arise from an “annulus,” but the shape of the ventriculo-aortic junction does not constitute a true circle.



The aortic root has a crown like band of fibrous tissue at its base with the ventriculo-aortic junction embedded centrally in the heart and inserted on both the atrioventricular valves and the thick left ventricular myocardium (**Figure 4**). The pulmonary root on the other hand, has no fibrous annulus and originates from the right ventricular infundibulum, a freestanding rim of muscle seated on the right ventricle and septum (61). Both valves consist of three semilunar leaflets, inserted on the annulus in a crown like fashion and meeting at the level of the STJ, forming the commissures (60, 61).

In healthy individuals, the aortic STJ diameter is 10–15% smaller than the annulus diameter and $\pm 25\%$ smaller than the maximal sinus diameter (62, 63). Furthermore, the pulmonary valve diameter is about 2 mm greater than that of the aortic valve and both are closely related in height (64). However, in patients undergoing the Ross operation, the relation between pulmonary artery and aorta may be distorted.

Microstructure of the Wall and Valve

Both arteries possess a tunica media rich with elastin, endowing the wall with resilience and elastic recoil, and a tunica adventitia consisting primarily of thick collagen fibers, providing strength (58). Compared to the pulmonary artery, the aorta has a thicker wall with a greater content of structural proteins. Furthermore, its tunica media has a greater number of elastic laminae which are more organized with a denser weave (61, 65–67). As most functional elastic fibers are assembled before adulthood, they are susceptible to mechanical fatigue and proteolytic degradation. Collagen fibers, on the other hand, have a short half-life and are subject to constant turn-over in response to changes in wall stress (27). Therefore, *via* the action of mainly fibroblasts, the adventitia plays a crucial role in maintaining mechanical homeostasis. The tunica media consists of concentric elastic laminae interspaced with reticular collagen and smooth muscle cells (SMCs), the latter making up $\sim 35\%$ of the wall by dry weight. Finally, a modest amount of glycosaminoglycans contributes to compressive stiffness and likely mechanosensing.

Because the contractile filaments of the SMCs are connected to elastic fibers by focal adhesions, forming so-called elastin-contractile units, the SMCs are the main mechanosensing cells of the tunica media (68). While SMCs are typically considered to have either a contractile or synthetic phenotype, with the latter representing a matrix-remodeling function, it seems that these are two ends of a spectrum (69, 70). Furthermore, the SMC population in the aortic and pulmonary media is inhomogenous with cells from various lineages possessing different matrix-producing abilities in response to changes in wall stress or hypoxia (71).

The aortic and pulmonary leaflets, or cusps, are richly innervated and capable of actively responding to changes in mechanical load (19, 72, 73). The cusps are delineated by endothelium on both the arterial and ventricular side. Their core consists of three layers: the collagen-rich fibrosa on the arterial side, the central spongiosa consisting mainly of glycosaminoglycans, and the ventricularis on the ventricular side, rich in elastin sheets (60). Valvular endothelial cells play an important role in the valve's response to changes in flow-induced shear stress by modulating inflammation, calcification, and ECM remodeling (72, 74). They are different from vascular endothelial cells due to their high proliferation rate, unique gene expression profile and orientation perpendicular to blood flow (72). Valve interstitial cells (VICs), present in all three layers of the leaflet, are the primary matrix remodeling cells that maintain structure and function. The mechanical environment of the VICs is sensed by, amongst others, mechanosensitive ion channels (21). When compared to pulmonary VICs, aortic VICs are stiffer and display a greater ability to contract the ECM (75). Additional functional differences include the greater potential for a pro-inflammatory and pro-osteogenic response in aortic VICs, indicating why valve calcification is common in the aortic valve yet rare in the pulmonary position (76).

Aortic and Pulmonary Root Biomechanics

The pulmonary autograft undergoes a radical change in environment after the Ross procedure due to differences in hemodynamic conditions. The blood pressure in the aorta is around 120/80 mmHg at rest whereas that in the pulmonary artery is around 25/10 mmHg (77). In the healthy pulmonary and aortic root, blood flow is laminar with sinus vortices behind the leaflets, acting as low-pressure zones to facilitate smooth opening and closing (78, 79). The blood flow acceleration and peak velocity in the aorta are approximately double that of the pulmonary root (80). Furthermore, powerful left ventricular contractions subject the aortic root to cyclic elongation and torsional deformation (81). Sufficient aortic distensibility is required to reduce cardiac workload and provide diastolic coronary flow (82). Cyclic expansion of aortic root volume is nearly twice that of the pulmonary root (37.7 vs. 20.9 %), with the greatest distension occurring at the STJ and commissures (82).

Both arterial walls display non-linear mechanical behavior and are most compliant in their physiological pressure ranges because their ECM components are deposited and interlinked at vessel-specific levels of transmural pressure and stretch. At physiological

arterial pulsatility, the mechanical load is carried mainly by elastic fibers. With increasing distension, collagen fibers are recruited and the artery stiffens (66, 70). As the pulmonary sinuses are most compliant within the physiological transmural pressure range of 0–30 mmHg, the greatest diameter changes are seen in this range (Figure 5). Beyond 30 mmHg, proportionally less distension is seen with increasing pressures as the wall stiffens (40, 83). Therefore, once exposed to systemic pressures after the Ross procedure, and before any remodeling takes place, the autograft wall will behave significantly stiffer than the aorta, evident by a steeper incline of the pressure-diameter curve (Figure 5) (40, 66, 84, 85).

The leaflets of the semilunar valves are exposed to flexural and shear stress in systole and tensile and compressive stress in diastole (1). To accommodate this complex cyclical loading, the leaflets are highly anisotropic: they are stiffer in the circumferential than axial direction, related to the circumferential orientation of collagen fibers as opposed to axially oriented elastin bundles (1, 86). Due to the trans-aortic pressure drop of 60–100 mmHg, the autograft leaflets will suddenly experience a far greater tensile and compressive stress on their arterial surface post-operatively. While the microstructure of pulmonary and aortic leaflets is similar, the latter are typically 50–60% thicker and contain more collagen (87, 88). The mechanical properties of both valves also seem to be similar, yet discrepancies in testing protocols between different studies make it challenging to draw definitive conclusions (86, 87, 89, 90). It seems nonetheless that the pulmonary valve is mechanically sound as an aortic valve substitute, given it is implanted symmetrically with perfect coaptation.

Implications for Surgical Technique

The relation between annular and STJ dimensions determine leaflet coaptation (39, 43, 44). A dilated aortic annulus (≥ 27 mm) may indicate an underlying connective tissue

problem. Furthermore, in cases of size mismatch, implantation of the autograft within a larger aortic annulus may impart additional pre-stretch. To ensure that the leaflets remain constrained within the aortic annulus, the autograft should be implanted deep within the annulus so that it can benefit from support of the fibrous skeleton of heart. In patients with a large annulus, an external annuloplasty using a band of prosthetic material may be indicated to further stabilize the annulus (19).

There are regional biomechanical differences within both arterial walls: the ascending aorta and main pulmonary artery are more compliant than their respective sinuses due to a greater elastin content (61, 66). Furthermore, because aortic expansion during the cardiac cycle is most pronounced at the level of the commissures, the STJ is at risk for dilatation after the freestanding root Ross (82). The autograft must be trimmed distally, leaving at most 2 mm of pulmonary wall above the commissures. In patients with pre-operative aortic dilatation, the STJ can be stabilized using a prosthetic interposition graft (91). Externally supporting the STJ with a resorbable band of polydioxanone (PDS) has shown to reduce the incidence of neo-aortic regurgitation in children, further confirming the importance of the STJ.

There appear to be no histological or biomechanical differences between the 3 pulmonary sinuses (66). However, during autograft harvesting, the left-facing, septal autograft sinus is stripped of most of its adventitial tissue where it is adherent to the aorta. In the freestanding Ross, this sinus is therefore usually placed in the left coronary sinus so that it benefits from support of the surrounding heart structures (91).

CONDITIONS AFFECTING AUTOGRAFT PROPERTIES

The underlying pathology forming the clinical indication for the Ross procedure may affect the pulmonary autograft characteristics. In the general population, degenerative aortic valve stenosis in the elderly is the primary indication for valve replacement (92). BAV disease, characterized by abnormal fusion of the aortic leaflets so that only 2 functional leaflets exist, is of special interest to the Ross procedure. While BAV occurs in 0.5–1.2% of the population, it is present in up to 74% of patients undergoing the Ross procedure as it typically manifests at a younger age than degenerative aortic stenosis (32, 38, 93).

Histological features in the aortic wall of BAV include SMC apoptosis and degeneration of ECM (94). While there is evidence for a genetic basis, increased leaflet stress and abnormal flow patterns influence both the development of BAV and its clinical manifestation (95). For the aorta and pulmonary root, both the leaflets and the cells populating the sinus walls are derived from neural crest and second heart field lineages (96). This provides a developmental link between pathologies affecting the leaflets and sinus walls like the aortic dilatation in up to 50% of patients with BAV disease (97). Neural crest cells, implicated in BAV and congenital aortic stenosis, are less commonly seen in the pulmonary than in the aortic root in murine embryological studies (96). This may explain why anatomic pulmonary valve anomalies, precluding use as an autograft, are rare (incidence

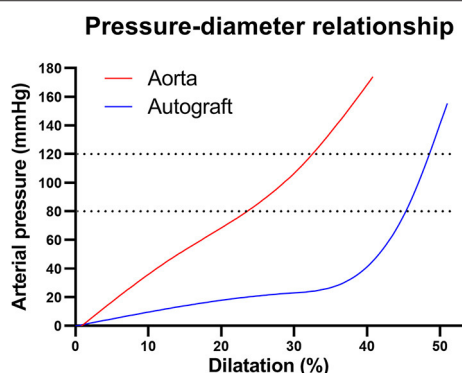


FIGURE 5 | Pressure-diameter behaviors for the healthy aortic and pulmonary root illustrating non-linear mechanical behavior. In the aortic pressure range of 80–120 mmHg (dotted lines), the pulmonary artery behaves very stiff, evident by the steep incline. Figure recreated using data available in the article by Nagy et al. (40).

of 0.1%) and usually associated with other congenital heart defects (98–100).

While de Sa et al. observed degenerative histological features in the main pulmonary artery of BAV patients (101), the association between aortic and pulmonary degenerative features was not confirmed by other groups (94, 102). Furthermore, when assessed by planar biaxial mechanical testing, there is no difference in mechanical properties of the pulmonary artery according to aortic valve phenotype (67). On the other hand, when assessed *in vivo* by echocardiography, elastic properties of the pulmonary artery are impaired with a correlation between aortic and pulmonary stiffness and diameter in BAV patients (103, 104).

Importantly, the presence of BAV in itself is not a risk factor for autograft failure or dilatation after the freestanding Ross. There are, however, risk factors for dilatation that are associated with BAV and may indicate an underlying connective tissue anomaly, such as aortic insufficiency, a large aortic annulus, or pre-operative aortic dilatation (13, 47, 48). This is in keeping with the observation that the aortic and main pulmonary artery walls of patients with predominantly AR are more compliant than those of patients with predominantly aortic stenosis or mixed stenosis/regurgitation (67). Furthermore, all described cases of autograft dissection occurred in patients with BAV disease. These data highlight the importance of understanding autograft mechanobiology to guide patient selection and predict the risk of dilatation.

Marfan syndrome (MFS) is the most common genetic form of thoracic aortic aneurysm disease, caused by pathogenic variants of the microfibrillar protein fibrillin-1, an ECM component acting as scaffold for elastin, as well as contributing to TGF- β signaling (105). The aorta of patients with MFS is susceptible to dissection or rupture because of its increased stiffness and impaired remodeling ability. MFS and other genetically driven aortopathies are a contra-indication for the Ross procedure because the underlying histologic anomalies, medial degeneration with elastic fiber fragmentation and loss of SMCs may also affect the pulmonary wall (106). Indeed, arterial elastic properties are impaired in MFS, and patients have a larger pulmonary artery diameter with an aneurysm in up to 15.3% (107). If the pulmonary artery of these patients potentially cannot withstand pulmonary pressures, it does not appear fit for use as an aortic autograft.

CLINICAL EVIDENCE FOR AUTOGRAFT REMODELING

In 2006, Sir Magdi Yacoub wrote: “An evolutionary point in the Ross operation is the inherent capacity of the autograft to adapt to the new environment by altering its structure and physical properties” (108). The potential longevity of the pulmonary autograft, several decades in many patients, strongly supports this notion (17, 18). If the autograft leaflets would not remodel and function simply as passive structures, it is highly unlikely that they would be able to withstand the systemic circulation for several decades.

For the freestanding Ross, it seems that repetitive supraphysiological distension of the pulmonary autograft may lead to progressive wall damage, while also eliciting a mechanobiological response. Clinical explants of autograft walls acquired within the first 3 months after the Ross procedure show SMC loss and fragmented elastic fibers yet also an increase in myofibroblasts (24). Late explants acquired at reoperation for dilatation show fragmentation of elastic fibers and deposition of mucoid material as well as hyperplastic intimal remodeling, marked adventitial fibrosis and an increase in synthetic SMCs and myofibroblasts (24, 25, 109–112). Yacoub et al. investigated dilated autograft wall samples with a mean implantation period of 14.1 ± 4.1 years and contrary to previous studies, they observed a seemingly well-remodeled and revascularized arterial wall with preserved architecture and a mixture of increased organization of elastic lamellae and degenerative features (20). **Table 1** provides an overview of the main histological reports evaluating autograft samples acquired from patients and their key findings.

Based on *in vivo* imaging at 1–5 years post-operatively in adults and children who underwent the Ross procedure as a root technique, the pulmonary autograft sinuses appeared significantly stiffer than the native aorta of healthy controls (85, 114, 115). Stiffening of the pulmonary autograft wall upon dilatation is easily explained by the non-linear mechanical behavior of the intramural constituents, and is likely an inevitable early consequence of the Ross procedure. On the other hand, mechanical testing of dilated, “failed” autograft walls shows that they are not only less stiff than healthy aorta, they are also less stiff than normal pulmonary root at aortic and pulmonary pressure ranges, respectively (116, 117). An artery’s mechanical behavior *in vivo* is determined by its inherent material stiffness but also by its structural stiffness, related to its anatomical configuration and pre-stretch. As it is uncertain if the described mechanical tests of each unique arterial sample were performed at representative levels of *in vivo* pre-stretch, it is challenging to correlate the mechanical data of these studies with expected *in vivo* behavior. It is unknown if long-term ECM remodeling can restore autograft stiffness to normal values in well-functioning autografts. Furthermore, the long-term implications of wall stiffness on valve and ventricular function remain uncertain.

Several investigators had the opportunity to investigate autograft leaflets explanted at reoperation, transplantation or at autopsy. While leaflets usually retained their typical trilayered architecture, increased leaflet thickness mainly due to the apposition of an extra layer of tissue/pannus on the ventricular side was consistently observed in multiple reports of both failed and well-functioning valves (20, 24, 25, 109, 113). This layer was characterized by intimal hyperplasia, dense collagen and the presence of myofibroblasts and matrix-remodeling enzymes. Even in “failed” autografts, overall leaflet architecture and microstructure were rather well-preserved while the autograft walls exhibited pronounced degeneration. The excellent freedom from reoperation for the subcoronary and inclusion techniques, with some patients surviving 44 years after surgery, support the notion that the pulmonary leaflets may adapt better than the wall (17, 18, 20).

TABLE 1 | Overview of the main histological reports evaluating autograft samples acquired from patients and their key findings (20, 24, 25, 109–111, 113).

| References | Sample origin | Timing | Wall | Valve |
|---------------------------|--|--|--|---|
| Goffin et al. (113) | Autopsy after death from ventricular arrhythmia ($n = 1$). | 1.5 years | Normal elastin and SMC architecture. Disappearance of dendritic cells. | Thickening of ventricular aspect of leaflets with large numbers of fibroblasts. Disappearance of dendritic cells. |
| Takkenberg et al. (111) | Reintervention (aortic homograft) for dilatation with AR ($n = 1$). | 7 years. | Focal interruption of elastin fibers, intimal hyperplasia, fibrosis. | - |
| Ishizaka et al. (110) | Reintervention for dilatation with AR ($n = 4$). | 1, 3, 4, and 8 years. | Elastin fragmentation, mucopolysaccharide deposition. | - |
| Rabkin-Aikawa et al. (24) | Reintervention for dilatation with AR ($n = 4$), transplantation ($n = 3$), autopsy ($n = 2$). | 3 early (2–10 weeks) and 6 late (2.5–6 years). | Early: elastin fragmentation, granulation tissue. Late: fibrosis, loss of normal SMCs, elastin and collagen without inflammation or calcification. | Trilayered architecture preserved yet leaflets thicker due to pannus with intimal hyperplasia and myofibroblasts on ventricular side of cusp. Reduction of myofibroblast and MMP-13 counts in early vs. late explants. |
| Schoof et al. (25) | Reintervention for dilatation with AR ($n = 26$), reintervention for AR after subcoronary Ross ($n = 2$), autopsy after freestanding Ross ($n = 2$). | Mean 6.1 ± 3.1 years, range 0.1–11.7 years. | Elastin fragmentation, mucopolysaccharide deposition, adventitial fibrosis, myofibroblast presence and SMC hypertrophy, intimal hyperplasia. | Trilayered architecture preserved yet leaflets thicker due to apposition of extra tissue layer on ventricular side of cusp with intimal hyperplasia, myofibroblasts, collagen and elastin. Similar features in non-failed explant acquired at autopsy. Failed subcoronary implants: grossly disturbed architecture. |
| Mookhoek et al. (109) | Reintervention for dilatation with AR ($n = 10$), for isolated dilatation ($n = 1$). | Median 11, range 7.3–15.4 years. | - | Trilayered architecture preserved yet leaflets thicker due to apposition of fibrous tissue on ventricular side. Ventricularis contains myofibroblasts and cells positive for MMP1, IL-6 and TGF- β . Increase in collagen fiber density. Evidence of ongoing remodeling at 10 years. |
| Yacoub et al. (20) | Reintervention for dilatation with AR ($n = 7$), for AR after subcoronary Ross ($n = 1$), autopsy after subcoronary Ross ($n = 1$), autopsy after freestanding Ross ($n = 1$). | Freestanding: mean 14 ± 4 years. Subcoronary: 42 and 44 years. | Mixture of adaptation (increased number of continuous elastic fibers), and disarray (elastin fragmentation and scarce collagen in between). Notable presence of vasa vasorum in outer tunica media and adventitia. | Trilayered architecture preserved yet leaflets thicker due to apposition of tissue on ventricular side, containing elastin, collagen, glycosaminoglycans Thickness of fibrosa layer increased to that of aortic valve. Subcoronary: architecture distorted, calcifications. |

AR, aortic regurgitation; SMC, smooth muscle cell.

EXPERIMENTAL EVIDENCE FOR AUTOGRAFT REMODELING

One might argue that animal models are not clinically relevant as they often use young, healthy animals and short implantation times compared to the development of clinically relevant autograft dilatation. Nevertheless, they provide the opportunity to study the early adaptation mechanisms in seemingly well remodeled autografts. **Table 2** shows an overview of all animal models relevant to the Ross procedure and their main findings. In an ovine model of a main pulmonary artery interposition graft in the descending aorta, pulmonary architecture was well-preserved in some areas while vascular atrophy was observed in others. A proportion of explanted tissue samples exhibited aorta-like mechanical behavior during biaxial tensile testing, indicating the pulmonary artery's ability to remodel (84, 118, 119). In a similar animal model using resorbable external support, Nappi et al. suggest that a “neovessel” developed with an increase in

elastic wall components (120). This finding is in stark contrast to findings by Schoof et al., who noted preservation of the typical pulmonary arterial microstructure in pigs (26). While new elastin can be produced during adulthood, it is uncertain to what extent these new fibers can contribute to mechanical adaptation, and to what extent the data by Nappi et al. can be extrapolated to humans (27).

In a porcine model of the freestanding Ross procedure, Schoof et al. reported a revascularized wall lacking degenerative features after 10 months. Furthermore, enlarged and rearranged SMCs were seen alongside adventitial fibrosis (26, 121). In the longest experimental evaluation to date, Tudorache et al. observed preservation of typical tri-layered leaflet histology with normal cellular distribution at 22 ± 2.7 months in lambs after the freestanding Ross procedure. Unfortunately, they did not investigate the dilated autograft wall or ECM remodeling of the valve (122). Our group recently developed an ovine model of the Ross procedure performed as a freestanding root replacement

TABLE 2 | Overview of animal models relevant to the Ross procedure with main findings (22, 26, 84, 118–124).

| Model | References | Animal | Objective | Follow-up | Main findings |
|---|-------------------------------|--------|---|-----------------|---|
| Pulmonary (valve) interposition graft in the descending aorta | Lower et al. (124) | Dog | Feasibility study. | Up to 12 months | The pulmonary valve and artery can withstand the systemic circulation. |
| | Nappi et al. (22, 120) | Sheep | Dilatation, remodeling, resorbable and composite external support. | 6 months | Resorbable support prevents excessive dilatation, enables diameter increase in proportion to somatic growth. Wall erosion underneath stiff materials. |
| | Vanderveken et al. (118, 119) | Sheep | Dilatation, remodeling, mechanical properties, porous mesh support. | 6 months | Remodeling in line with earlier studies. Support halts dilatation yet with risk of vascular atrophy. Mechanical adaptation in some samples. |
| Ross procedure | Pillsbury et al. (125) | Dog | Feasibility study. | 12–14 months | The subcoronary Ross procedure is technically feasible. |
| | Schoof et al. (26, 121) | Pig | Dilatation in growing animals, tissue remodeling. | 10 months | Increase in size along with somatic growth. Wall: revascularized, typical architecture preserved, SMC's enlarged, collagen increase. Valve: enlarges more than can be explained by merely somatic growth. |
| | Tudorache et al. (122) | Sheep | Dilatation, valve function, cellular characterization. | 20 months | Valve: native cell distribution, neovascularization in leaflet base, trilayered architecture preserved. |

SMC, smooth muscle cell. Adapted with permission from Van Hoof et al. (123).

(123). Preliminary histological evaluation is consistent with previous clinical and experimental explant studies (**Figure 6**). Future work will include a comprehensive evaluation of autograft mechanobiology with analysis of hemodynamic parameters, imaging, histology, gene expression response and mechanical testing of explanted tissues.

DISCUSSION

Understanding Pulmonary Autograft Adaptation

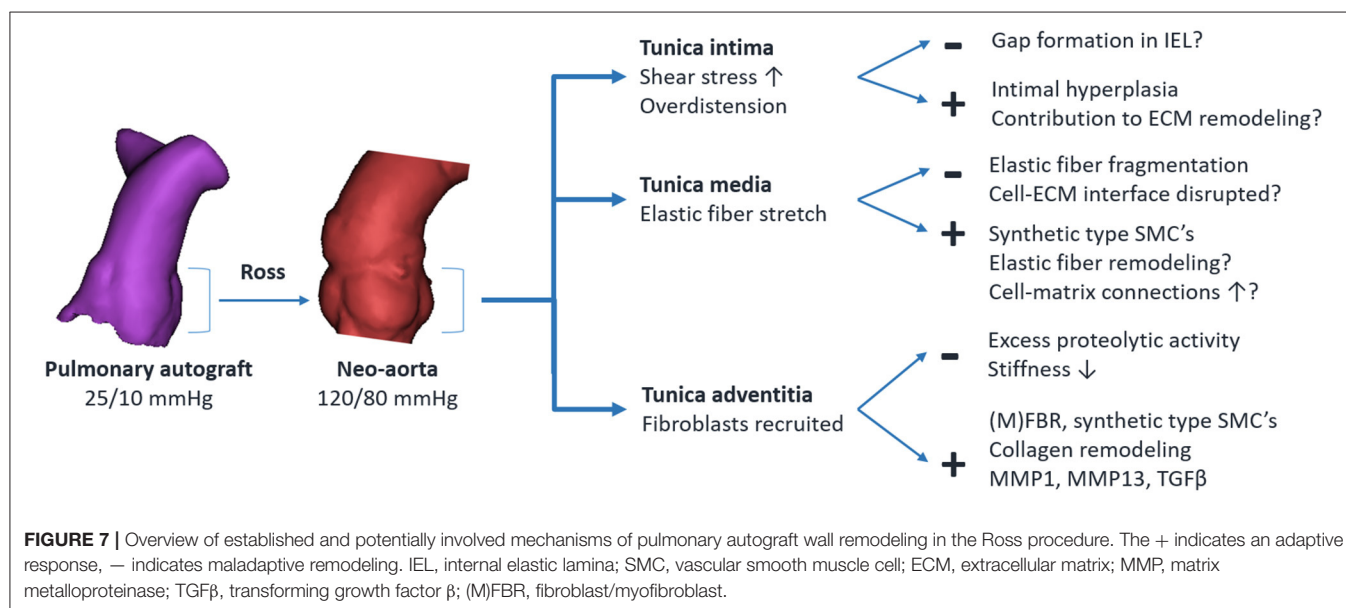
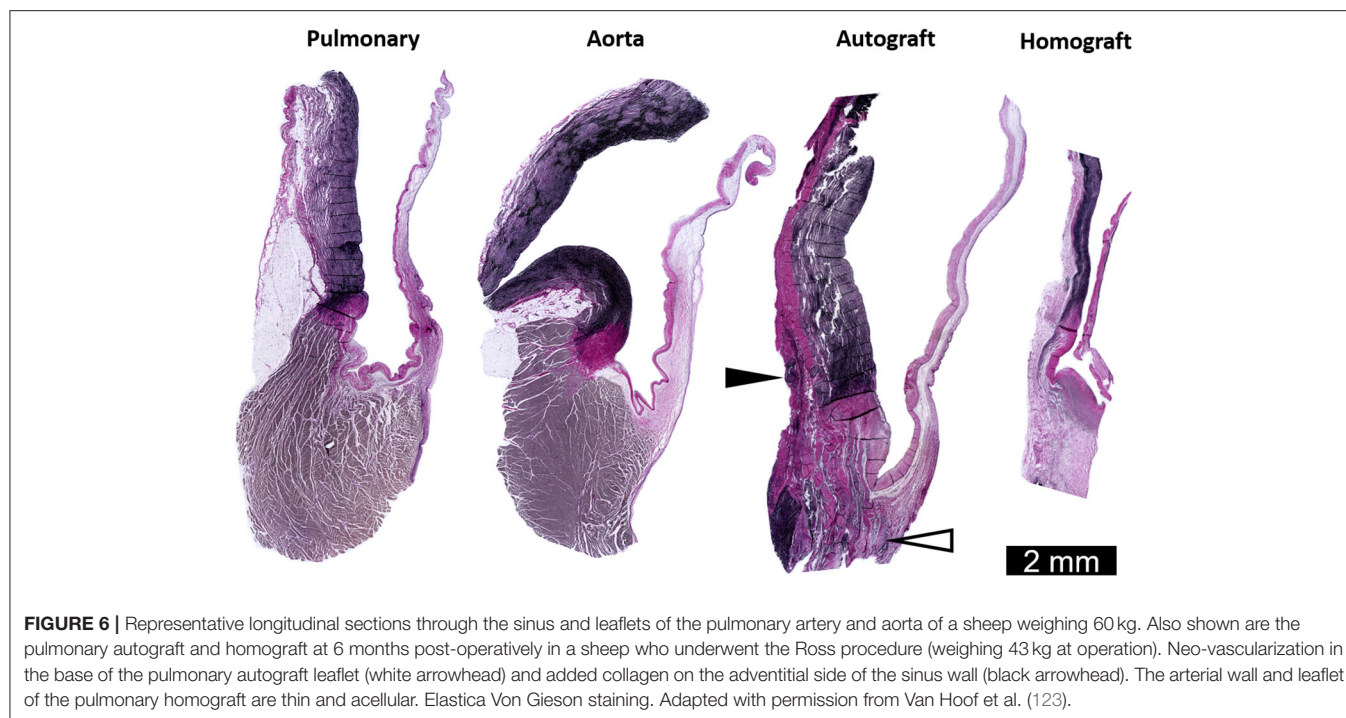
ECM Damage and Remodeling

Insight into the underlying mechanisms can be gained by correlating established principles of arterial mechanobiology with changes observed in the pulmonary autograft. In physiological conditions, SMCs and adventitial fibroblasts are stress-shielded mainly by elastic fibers. Upon completion of the freestanding Ross procedure, the autograft wall dilates, resulting in a 5- to 10-fold greater circumferential wall stress (126). As the elastic fibers become stretched and the mechanical load is transmitted to previously underrecruited collagen fibers, the artery behaves stiffer (28). This disruption of baseline stress values prompts a response to restore mechanical homeostasis. *Via* cell-ECM and cell-cell connections, cells sense the stress acting on the ECM. Changes in the mechanical environment are translated into intracellular signals *via* specific mechanotransduction pathways, inducing the production of ECM proteins, adhesion molecules and matrix metalloproteinases (MMPs) (70). **Figure 7** provides an overview of known and potentially involved mechanisms of ECM remodeling.

Fibroblasts located mainly in the adventitia are among the first to be activated by overdistension (127). These fibroblasts proliferate, and *via* the release of growth factors, induce the

differentiation of SMCs from the contractile to the synthetic phenotype. Fibroblasts differentiate into myofibroblasts by the influence of transforming growth factor β (TGF- β) and mechanical stresses (69, 128). Collagen is deposited at the newly imposed mechanical load while existing fibers are removed by MMPs or modulated, for example by changing collagen cross-linking patterns (27). Increased adventitial collagen is observed in all autograft samples acquired at reoperation and in all animal studies, suggesting a common mode of remodeling in both failed and well-adapted autografts. This form of ECM remodeling is a crucial part of arterial homeostasis in arterial aging, pulmonary arterial hypertension and aneurysm development (27, 129, 130). Elevated myofibroblast, MMP1, MMP13 and TGF- β levels are seen in clinical autograft explants at over 10 years post-operatively (24, 25, 30, 109). This persistent ECM remodeling likely indicates the inability to restore the homeostatic state.

As regeneration of elastic fibers is limited, certainly in comparison with collagen, they are susceptible to mechanical fatigue by repetitive overdistension. Currently, the threshold pressure or diameter which causes acute elastic damage is unknown. In an *ex vivo* inflation set-up, the main pulmonary artery became susceptible to damage upon acute exposure to a transmural pressure beyond 60 mmHg, with pressures above 100 mmHg likely to induce collagen damage as well (131). Because this study by Wang et al. employed previously frozen porcine pulmonary arteries, it is uncertain if these data can be extrapolated to the Ross procedure in humans. Previous studies of dilated, explanted pulmonary autografts show fragmented elastin fibers and an increase in synthetic-type smooth muscle cells. As the stress in SMCs is typically concentrated at focal adhesions, connecting the cytoskeleton to surrounding elastic fibers, it seems likely that damage to the elastic-contractile units occurs (68). Besides representing a change in mechanical properties, elastic fiber fragments have a signaling function



by inducing SMC proliferation and a phenotype switch, and will undergo proteolytic degradation by MMPs and cathepsins (28, 132).

Immediately after the Ross procedure, autograft leaflets are exposed to elevated shear, compressive and tensile stresses. Furthermore, aortic root dilatation may contribute to cusp stretching. It is likely that collagen production plays an important role in valve remodeling in response to increased stress, as it does in the wall, with an important role for VICs in the cusps (133). Previous histological studies suggest successful

leaflet adaptation to the systemic circulation, with increased cusp mass mainly due to the apposition of an extra layer of fibrous tissue on the ventricular cusp side (20, 24, 25, 109). While this suggests improved mechanical properties, there are no data to support this. The absence of the degenerative features which are seen in dilated autograft walls could indicate a greater ability of the leaflet to adapt to the systemic circulation. By preventing excessive deformation and providing reciprocal support, good leaflet coaptation in the early phase after the Ross procedure likely protects the cusps from acute ECM damage,

thereby permitting adaptation. Endothelial to mesenchymal transition may also play a role in maintaining leaflet integrity (1).

Blood Flow, Shear Stress, and the Endothelium

Endothelial hyperplasia is consistently observed in wall samples explanted late after the Ross procedure (20, 25). This feature, commonly seen in aortic aneurysms, suggests remodeling in response to elevated shear or intramural stress (134). Furthermore, endothelial cells of explanted autograft valves express Ephrin B2. While this may indicate a stable systemic VEC phenotype, it cannot be excluded that these cells migrated from the native aorta or endocardium (24).

Among all aortic valve substitutes, blood flow patterns are closest to normal after the Ross operation (7, 41). In BAV disease, abnormal flow patterns with elevated wall shear stress associate with aneurysm progression and focal elastin degeneration (135). The changes in flow and shear stress that occur in the pulmonary autograft, upon transposition from pulmonary to aortic position, have not been quantified. Therefore, the role of abnormal flow patterns, pre-existent or related to neo-aortic regurgitation which develops later, on autograft remodeling remains unknown.

Ischemia and Inflammation

As their wall is thicker than 0.5 mm, the external layers of the pulmonary sinuses are supplied by vasa vasorum (136). Disruption thereof during autograft harvesting may lead to damage or impair remodeling. Both in a porcine model of the Ross procedure and in clinical explant studies, a well-revascularized arterial wall with normal to slightly increased presence of vasa vasorum in the tunica media and adventitia was seen (20, 25, 26). The magnitude of this contribution and the role of neovascularization in mechanobiological adaptation after the Ross procedure are unknown. The autograft leaflets are likely less affected by ischemia as they are supplied by diffusion from both the aortic and ventricular side.

Goffin et al. observed a disappearance of dendritic cells in an explanted autograft of a 14-year old patient who died of unrelated causes (113). While these accessory immune cells play a role in regulating early ECM remodeling, the significance of this finding is uncertain (127). *In vitro*, repetitive overstretching of valvular endothelial cells leads to an upregulation of inflammatory pathways (74). However, there is no evidence for relevant inflammatory activity or calcification in samples explanted several years after the Ross procedure.

Molecular Mechanisms Warranting Further Research

A recent study by Chiarini et al. suggests a unique maladaptive process in the autograft which differs from that of aortic aneurysms (30). They compared the proteomic signature of the tunica media of dilated autografts, acquired 8–16 years post-operatively, against that for normal PA, aorta and aortic aneurysm samples. An upregulation of paxillin, a key component of focal adhesions, was observed. As the integrin-containing focal adhesions mechanically link the ECM and actin cytoskeleton, their finding may represent abnormal cytoskeleton remodeling and impaired mechanotransduction (70). Vimentin,

a component of the SMC cytoskeleton, was also upregulated, confirming the activation of pathways involving synthetic SMCs. A downregulation of MAGP1 was seen, suggesting impaired elastic fiber buildup. They also found evidence of a disturbed JAG1-Notch1 signaling, potentially impeding tissue remodeling by limiting cell-cell interactions. Unfortunately, it is unknown if the observed proteomic changes represent a cause or consequence of maladaptation and repetitive overdilation.

In the general population, pulmonary artery aneurysm is a rare entity, reported only 8 times in 109,571 autopsies and mainly associated with pulmonary arterial hypertension in the setting of congenital heart disease (130, 137). There are yet several molecular pathways implied in thoracic aortic aneurysms which are also involved in the development of pulmonary arterial hypertension and pulmonary artery aneurysm. Analogous with BAV disease, a combination of hemodynamics and underlying molecular pathways likely impair mechanoregulation in both the aorta and pulmonary artery (130). With regards to collagen integrity, deficiencies in the following proteins are relevant: biglycan (an ECM component regulating collagen formation) and collagen 3 α 1 chain (implied in Ehlers-Danlos Syndrome type IV). For elastic fibers: fibrillin-1 (elastic fiber core glycoprotein with signaling function, implicated in MFS) and fibulin 4 (regulation of elastic fiber assembly). Reduced expression of lysyl oxidase, a collagen and elastin cross-linking enzyme, also leads to mural degeneration. For the actin cytoskeleton, proteins like smooth muscle α -actin and filamin A are relevant. With regards to mechanoregulation, TGF- β receptors (implicated in Loeys-Dietz syndrome) and Notch1 (impaired signaling seen in dilated autografts) are implicated (130). These interesting associations provide insight into possible underlying mechanisms of pulmonary autograft maladaptation. Finally, the role of mechanosensitive ion channels should be explored (21).

Strategies to Prevent Pulmonary Autograft Dilatation

Antihypertensive Treatment

Undoubtedly, blood pressure is one of the main determinants of remodeling. As early remodeling is crucial to avoid initiating a vicious cycle of pathological remodeling, strict blood pressure control (systolic pressure <110 mmHg) is advocated by many experts starting immediately post-operatively and continued for 6–12 months (19). While there is currently no direct evidence for an effect on dilatation, reoperation rate or histological outcome, aggressive blood pressure control appears justified as there are many indirect arguments that antihypertensive medication can improve autograft remodeling. In ascending aortic aneurysms, hypertension is associated with aneurysm growth rate as well as dissection (138). While the decrease in wall stress is non-linearly related to blood pressure lowering, antihypertensive treatment can achieve a marked reduction in wall stress, even in patients with mildly elevated blood pressure. Therefore, even in patients with normal or slightly elevated blood pressure, antihypertensive treatment can achieve a marked reduction in wall stress. In the Ross procedure, this could make the difference needed to allow autograft adaptation.

The underlying idea is to gradually expose the autograft to aortic pressures. There is anecdotal evidence that preoperative pulmonary arterial hypertension pre-conditions the autograft by promoting ECM organization (65). In animal models of pulmonary hypertension, thickness of the tunica media is increased (29). This concept is further supported by numerical simulations of saphenous vein remodeling when used as arterial bypass graft, whereby gradual loading improves remodeling (139).

In both MFS and after the Ross procedure, a repetitive cycle of overdistension occurs in an arterial wall at risk for pathological remodeling (140). Aortic stiffness is inherently increased in MFS. Similarly, the pulmonary autograft wall behaves stiffer than the aorta at systemic pressures, at least before remodeling (84). By lowering blood pressure and the force and velocity of ventricular contraction, beta-blockers reduce aortic wall stress, thereby lowering the risk of aortic dissection in patients with MFS and potentially enabling the wall to heal. Angiotensin-converting enzyme inhibitors and angiotensin II receptor blockers reduce blood pressure and aortic stiffness (105). In murine models of MFS, prenatal initiation of angiotensin II receptor blockers has the potential to prevent pathological remodeling and aortic dilatation. As this effect is related to hemodynamic and vasomotor changes as well as the interference with TGF- β signaling, it may be of interest to the Ross procedure (141).

Mechanobiology of External Autograft Support

The technical considerations of currently used strategies to prevent autograft dilatation were recently reviewed by Chauvette et al. (23). While it is uncertain at this point what the best strategy is, external support should be biocompatible in terms of geometry, compliance and tissue reaction. The primary goal of external support is to stabilize root dimensions; this will inevitably reduce distensibility, and therefore circumferential wall stress and strain. Repetitive strain is crucial to arterial homeostasis, just as mechanical loading is essential for the maintenance of bone density and skeletal muscle mass (142). In a landmark study, Courtman et al. banded the infrarenal abdominal aorta in rabbits, thereby reducing local strain. At 6 weeks, they observed apoptotic loss of 30% of SMCs and a 45% reduction of medial area. No endothelial cell loss was seen, nor was neo-intimalization impaired in animals undergoing banding and endothelial balloon denudation (143). In an experiment involving iliac artery wrapping in baboons, a tighter wrap induced more ECM loss and SMC atrophy (144). These banding studies indicate that excessive stress-shielding, so that cells experience low tensile stress, is undesirable. This is analogous to applying a tight cast to a fractured leg without allowing movement of the limb, resulting in muscle and bone atrophy (142). Furthermore, damage induced by compression between the wrap and pulsatile blood flow cannot be excluded. Numerical simulations of prosthetic external support of the descending aorta indicate the potential of external support to ameliorate the arterial homeostatic response to elevated pressure, and also point to stiffness of the support material as a crucial determinant of remodeling (145). It seems that the autograft needs to feel just the right amount of stress in order

to heal after being devascularized during the operation, and subsequently remodel.

Any type of prosthetic external support induces a tissue reaction, influenced by the material, presence of a coating and porosity. Early cellular inflammation soon shifts to a foreign body giant cell reaction, characterized by macrophages and giant cells attempting to encapsulate the implanted material (146). For external support, porosity is one of the most important parameters. A porous material will permit the ingrowth of a fibrotic neo-adventitia and blood vessels, thereby enabling the transport of oxygen and nutrients through the material (147, 148). Furthermore, the graft will become anchored to the arterial wall, forming a composite. A non-biodegradable low-porosity material, on the other hand, will prevent tissue ingrowth and elicit the formation of a thick sheath of fibrosis, potentially further increasing arterial stiffness (148, 149). As the inflammatory reaction induced by the graft is situated in the peri-adventitia, its contribution to vascular remodeling is unknown.

Autologous Inclusion Technique

In the autologous inclusion technique (**Figure 1.3**), the autograft is sutured into the aortic annulus and then included within the native aortic wall, which is reduced or enlarged to achieve the desired dimension (18). From an anatomical and biomechanical point of view, this technique optimally preserves functional aortic root integrity and compliance. The native aorta naturally augments the autograft's structural properties to withstand systemic pressures, though without a detailed analysis of changes in wall stress from homeostatic values. While this technique is technically challenging, an exceptionally low incidence of significant root dilatation and reoperation can be achieved (18). To our knowledge, there are no histological reports of autografts explanted after the inclusion technique.

Dacron Vascular Prosthesis

The autograft can be included within a segment of Dacron vascular tube or Valsalva graft before implantation into the aortic annulus (**Figure 8A**), stabilizing neo-aortic dimensions up to 5 years post-operatively (34–36). While this may seem a straightforward and reproducible technique, it risks distorting the autograft and preventing it from settling into its natural post-operative shape. As a microporous and sealed graft allows limited tissue ingrowth, seroma formation, erosion and graft migration have been a great concern for conventional aortic wrapping of aneurysms using the same material (151, 152). Because the rigid, woven material impairs pulsatility, there are also concerns about elevated leaflet stress and abnormal flow patterns, as evidenced by 4D MRI studies after valve-sparing root replacement (79). Finally, vascular atrophy seems inevitable with this stiff material due to excessive stress-shielding (148). To date, these complications have not been reported for the supported Ross procedure.

Personalized External Aortic Root Support

In Personalized External Aortic Root Support (PEARS), a soft, custom-made mesh is used to stabilize a moderately dilated aortic

root with at most mild AR, primarily in patients with MFS (153). The porous support (**Figure 8B**) becomes well-incorporated into a neo-adventitia and stabilizes root dimensions (148, 150, 154–156). Subsequently, the risk of dissection is mitigated by avoiding repetitive overdilation. Pepper et al. had the opportunity to histologically examine the aorta of a patient with MFS who underwent PEARS and later died of unrelated causes. The supported region of his aorta showed a normal tunica media whereas the unsupported aortic arch showed features of Marfan syndrome, suggesting that the external support allowed the aorta to heal (156).

This flexible, porous material that conforms to aortic anatomy holds great promise for the Ross procedure and has currently been applied in nearly 50 patients (157). In conventional aortic PEARS, the support is modeled using the patient's pre-operative aortic CT scan. The challenge in the Ross procedure has been to predict external support morphology based on pre-operative imaging, as the pulmonary autograft changes shape and dilates immediately upon exposure to aortic pressures. In an ovine model of a pulmonary artery interposition graft in the descending aorta, the mesh material used in PEARS successfully stabilized dimensions at 2 months after allowing some initial dilatation. All supported samples showed thinning of the media with SMC atrophy (119). While this atrophy may be an inevitable consequence of stress-shielding, it indicates that improvements to the material's mechanical properties are possible. Furthermore, a major difference with conventional aortic PEARS is that the pulmonary autograft is devascularized during the operation, and external support may influence healing and the development of vasa vasorum.

Resorbable Materials

If protection during the early phase, when the risk of dilatation is greatest, will promote appropriate pulmonary autograft remodeling, external support might not be required permanently.

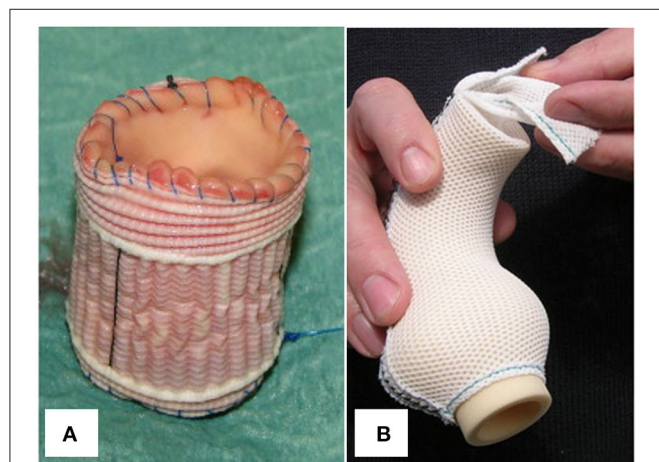


FIGURE 8 | (A) Pulmonary autograft wrapped with a cylinder of microporous Dacron graft. **(B)** Personalized external aortic root support implant fashioned from porous, soft mesh. Figure adapted with permission from Carrel et al. (34) and Treasure et al. (150).

One could envision a composite external support, partially consisting of resorbable material, gradually resorbing and allowing some initial dilatation while the degree of support decreases. A similar strategy is used to promote *in vivo* neovessel development using biodegradable tissue engineering scaffolds (158).

The clinical use of resorbable support was already described in 1993 by Moritz et al., who used a VICRYL® mesh composed of polyglactin 910. Unfortunately, data on the effect on dilatation is not available (159). Nappi et al. designed a composite support consisting of a resorbable polydioxanone mesh interwoven with fibers of expanded polytetrafluoroethylene, the latter allowing gradual expansion but serving as permanent support. They used this material as support for a pulmonary artery interposition graft in the descending aorta of 10 growing sheep. At 6 months, dilatation was effectively prevented and the material was well-incorporated without marked inflammatory changes (22). Unfortunately, their report lacks reliable measurements of wall thickness, protein fractions, elastin integrity and mechanical testing to confirm remodeling. While composite resorbable support holds great promise to prevent neo-aortic root dilatation, like in the Ross procedure, its clinical implementation is currently not justified.

Remaining Questions and Future Perspectives

Understanding and Promoting Pulmonary Autograft Remodeling

The available evidence indicates that the pulmonary autograft can become a permanent solution for a wide range of patients. Several fundamental questions remain to be answered before this can become reality (**Table 3**). Besides the universally observed collagen remodeling by myofibroblasts and synthetic type SMCs, it is unknown which mechanoregulation pathways enable some autografts to withstand systemic conditions for several decades. Candidate mechanisms include changes in collagen cross-linking or an increase in cell-ECM connections.

A greater understanding of the relation between patient characteristics and autograft remodeling may identify biomarkers or cardiac imaging features related to autograft maladaptation. This will enable us to define in which patients the autograft's innate remodeling ability will likely suffice to withstand systemic conditions, and in whom additional measures are needed to guarantee adaptation. A pre-operative *in vivo* assessment of the pulmonary autograft using dynamic imaging studies may indicate whether a patient is a good candidate for the Ross procedure. Serial post-operative imaging studies evaluating changes in stiffness may identify patients at risk for excessive dilatation or reoperation (85, 114, 115). As in aortic aneurysms, localized changes in shear stress may signal underlying elastin degradation (135). In patients with congestive heart failure, excessive myocardial collagen cross-linking indicates undue cardiac stiffness and associates with adverse clinical outcome. This collagen cross-linking can be quantified non-invasively on blood samples or based on the urinary proteome (160). Furthermore, diastolic left ventricular function can be predicted

TABLE 3 | Remaining fundamental questions and unmet clinical needs regarding pulmonary autograft remodeling after the Ross procedure.**Understanding pulmonary autograft remodeling****Mechanotransduction and -regulation mechanisms in wall and valve**

Established mechanism: collagen deposition

Additional mechanisms which determine (mal)adaptation?

Cell-cell or cell-ECM adhesions

Collagen cross-linking

Role of endothelial cells, shear stress and blood flow?

Timeline of adaptation? Is it ever complete?**What defines (mal)adaptation?**

Aorta and PA have common embryological origin → Can the autograft truly develop aorta-like microstructure and mechanical properties?

Have they diverged too far apart? Is any observed remodeling merely a coping mechanism, leading to a new equilibrium at best?

Risk of dissection in dilated autograft—criteria for reintervention?

Are pulmonary leaflets better suited than wall to withstand systemic conditions?

Different innate remodeling ability? Related to distinct mechanical loading?

Strategies to improve autograft longevity and adaptation**Ideal conditions for autograft?**

Geometry: sinus/cusp orientation, proportions annulus-sinus-STJ, ...

How much stress is ideal/acceptable for wall and leaflet?

Blood pressure target?

How much autograft wall dilatation is desirable or can be tolerated?

Threshold for damage—start of pathological cycle of remodeling?

Optimizing patient selection

Can we go beyond anatomical and demographic variables?

In vivo quantification of arterial properties and autograft (mal)adaptation

Mechanical properties: stiffness, elasticity > Imaging

Biological processes: collagen cross-linking, ... > Biomarkers

> Pre-operative: predict dilatation, guide patient selection

> Post-operative: identify maladaptation, risk of reoperation/dissection

External support

Can we reduce the reintervention rate without collateral damage?

Risk of erosion, seroma formation, graft migration?

Effect on LV and leaflet stress?

Ideal material properties? Role for resorbable materials?

Outcome of PEARS for the Ross operation?

Antihypertensive treatment

Effect on reintervention rate?

Hemodynamic effect vs. direct influence on remodeling pathways?

Other strategies to pharmacologically influence remodeling?

based on the urinary proteome in individuals without heart failure (161). Similarly, serial biochemical studies in patients before and after the Ross procedure might identify biomarkers to guide patient selection or confirm the presence of maladaptation in the post-operative setting.

In vitro culture of a pulmonary artery in a bioreactor may provide valuable insights into the timeline of early remodeling and the role of shear stress, pre-stretch at implantation and acute hypertension. Large animal models also hold great promise to evaluate whether current strategies to prevent dilatation—external support and antihypertensive treatment—promote

remodeling, either by modifying the mechanical environment or by interfering with molecular pathways (123). To assess whether the autograft remains viable—capable of healing and regulating its mechanical properties—active mechanical testing of freshly explanted leaflets and wall would be required (162). A rat model with heterotopic implantation of the pulmonary root of a syngeneic donor animal into the abdominal aorta would allow a serial evaluation of adaptation in the first post-operative months at a lower cost.

By providing data on microstructure, mechanical properties, geometry, hemodynamics and the underlying pathways, experimental models can enable numerical simulation of autograft remodeling (163, 164). Subsequently, the ideal conditions for remodeling, or conversely, the risk of dissection, could be identified in so-called *in silico* trials (165). Until now, available computational studies have mainly confirmed important *in vivo* observations, such as the importance of STJ dimensions on wall and leaflet stress (126, 163, 166, 167). It has proven very challenging to mathematically simulate the complex torsional deformation of the aortic root which results in spiraling blood flow and flow vortices behind leaflets (41).

Preventing Autograft Dilatation in the Freestanding Ross Procedure

Notwithstanding its clinical use since 2004, several questions about prosthetic external support of the autograft sinuses should be resolved (36). First, concerns about the deleterious hemodynamic effects on the left ventricle and autograft leaflets should be addressed by echocardiographic and 4D flow MRI studies. Second, once placed in the aortic position, optimal autograft geometry must be clearly defined. Quantitative comparison of pre-operative and post-operative imaging in patients undergoing the Ross procedure might yield a predictive algorithm for ideal autograft geometry and subsequent external support configuration.

The mechanical properties of external support should be determined by how much stress-shielding is needed in each phase of remodeling. To this end, the timeline of changes in mechanical properties should be evaluated in clinical imaging studies and in an animal model. Finally, polymer materials are required which truly augment the autograft. Even the best currently used polymer materials, including resorbable ones, are relatively stiff and inelastic (119). Therefore, the mechanical behavior will be dominated by the external support, potentially leading to excessive stress-shielding and deleterious hemodynamic effects. Polyglycerol sebacate (PGS) is a promising new resorbable elastomer which has been used as tissue-engineered vascular grafts to serve as scaffold for cellularization (168). More futuristic options include a bioengineered matrix of collagen and elastin, containing growth factors, or even seeded with stem cells, immediately optimizing mechanical properties while promoting autograft incorporation into the aortic root (169).

CONCLUSIONS

Long-term clinical success of the Ross procedure relies on a well-functioning, living valve integrated into an aortic root having a normal hemodynamic profile. From this point of view,

the subcoronary and autologous inclusion technique may be superior to the freestanding root technique, yet the latter is applicable over a wider spectrum of cardiac anatomy and is more surgically reproducible. All evidence indicates that the autograft valve is suited to withstand the systemic circulation and remodel, given that it is implanted symmetrically with stable annular and STJ dimensions over time. Therefore, one of the key surgical principles of the Ross procedure is to ensure that the proximal autograft is constrained within the native aortic annulus. The autograft sinuses, on the other hand, sit unrestrained after a freestanding Ross procedure and are at risk of dilating and subsequently causing the valve to fail. The currently available evidence indicates that the pulmonary autograft wall is not capable of truly achieving mechanical homeostasis and remodeling into an aortic phenotype. Perhaps the aortic and pulmonary root have diverged too far apart after arising from a common embryological origin.

Protecting the autograft during the early adaptation phase is crucial to avoid initiating a sequence of pathological remodeling. Therefore, strict blood pressure control during the first 6–12 post-operative months is justified to reduce wall and leaflet stress. Adequate patient selection is critical and the surgical technique should be tailored individually, aiming to minimize the amount of wall tissue exposed to aortic pressures. While external autograft support may stabilize root dimensions, its efficacy should be measured by a reduction in reinterventions, without negatively affecting valve or left ventricular function.

Remodeling of the ECM with mainly the production of additional collagen is a common feature in both autograft walls and leaflets. A distinct feature of autograft leaflets is the apposition of an extra layer of tissue on the ventricular side, resulting in increased leaflet thickness. Future studies should pinpoint the remodeling processes in well-remodeled and externally supported autografts. Several molecular pathways are proposed. To this end, animal models or bioreactor studies should include a comprehensive mechanobiological assessment at different time-points consisting of microstructural evaluation,

transcriptional and proteomic characterization, mechanical testing of tissue samples and dynamic imaging studies with complete hemodynamic profile.

Numerical simulations of tissue growth and remodeling may aid in distilling the ideal conditions for autograft adaptation. Subsequently, a patient-specific strategy for autograft protection and external support could be determined, and the indications for the Ross procedure might be expanded. Widespread clinical implementation of the PEARS concept for the Ross procedure is greatly anticipated because of the many advantages over microporous vascular grafts. Future innovations to external support may include the use of resorbable materials or bio-engineered scaffolds to augment the autograft's mechanical properties and guide remodeling.

AUTHOR CONTRIBUTIONS

This manuscript is the result of 3 years of research into the mechanobiology of the Ross procedure in the context of the PhD program of LV, performed under supervision of FR, PV, NF, and EJ. LV wrote the first draft and edited the figures and tables. Subsequent revisions were written based on multidisciplinary discussions involving LV, PV, EJ, JH, SJ, NF, and FR, including written feedback. All authors approved the final version.

FUNDING

KU Leuven Research Project (C2 Project: C24/16/026 24ZKD1128-00-W01) + LV is the holder of a predoctoral grant Strategic basic research (SB 1S70220N) from the Research Foundation Flanders (FWO).

ACKNOWLEDGMENTS

The authors would like to thank Piet Claus for the knowledge he shared on cardiovascular imaging and dynamics which contributed to the realization of this manuscript.

REFERENCES

- Chester AH, El-Hamamsy I, Butcher JT, Latif N, Bertazzo S, Yacoub MH. The living aortic valve: From molecules to function. *Glob Cardiol Sci Pract.* (2014) 2014:11. doi: 10.5339/gcsp.2014.11
- Somerville J. The origins of the Ross operation. *Images Paediatr Cardiol.* (2012) 14:3–5.
- Spray TL. Technique of pulmonary autograft aortic valve replacement in children (the Ross procedure). *Semin Thorac Cardiovasc Surg Pediatr Card Surg Annu.* (1998) 1:165–78. doi: 10.1016/S1092-9126(98)70022-5
- Sievers HH. Ross procedure H.H. *HSR Proc Intensive Care Cardiovasc Anesth.* (2012) 4:119–23. Available online at: <https://citeseerx.ist.psu.edu/viewdoc/download?doi=10.1.1.680.9781&rep=rep1&type=pdf>
- Ross DN. Replacement of aortic and mitral valves with a pulmonary autograft. *Lancet.* (1967) 290:956–8. doi: 10.1016/S0140-6736(67)90794-5
- Torii R, El-Hamamsy I, Donya M, Babu-Narayan SV, Ibrahim M, Kilner PJ, et al. Integrated morphologic and functional assessment of the aortic root after different tissue valve root replacement procedures. *J Thorac Cardiovasc Surg.* (2012) 143:1422–8.e2. doi: 10.1016/j.jtcvs.2011.12.034
- Bissell MM, Loudon M, Hess AT, Stoll V, Orchard E, Neubauer S, et al. Differential flow improvements after valve replacements in bicuspid aortic valve disease: A cardiovascular magnetic resonance assessment. *J Cardiovasc Magn Reson.* (2018) 20:1–10. doi: 10.1186/s12968-018-0431-5
- Nötzold A, Hüppe M, Schmidtke C, Blömer P, Uhlig T, Sievers HH. Quality of life in aortic valve replacement: pulmonary autografts versus mechanical prostheses. *J Am Coll Cardiol.* (2001) 37:1963–6. doi: 10.1016/S0735-1097(01)01267-0
- Buratto E, Shi WY, Wynne R, Poh CL, Larobina M, Keefe MO, et al. Improved survival after the Ross procedure compared with mechanical aortic valve replacement. *J Am Coll Cardiol.* (2018) 71:1337–44. doi: 10.1016/j.jacc.2018.01.048
- Sharabiani MTA, Dorobantu DM, Mahani AS, Turner M, Peter Tometzki AJ, Angelini GD, et al. Aortic valve replacement and the Ross operation in children and young adults. *J Am Coll Cardiol.* (2016) 67:2858–70. doi: 10.1016/j.jacc.2016.04.021
- McClure GR, Belley-Cote EP, Um K, Gupta S, Bouhout I, Lortie H, et al. The Ross procedure versus other aortic valve replacement: a systematic review and meta-analysis. *Eur J Cardio-thoracic Surg.* (2018) 59:462–70. doi: 10.1093/ejcts/ezy247

12. Etnel JRG, Grashuis P, Huygens SA, Pekbay B, Papageorgiou G, Helbing WA, et al. The ross procedure: a systematic review, meta-analysis, and microsimulation. *Circ Cardiovasc Qual Outcomes*. (2018) 11:e004748. doi: 10.1161/CIRCOUTCOMES.118.004748
13. Sievers HH, Stierle U, Charitos EI, Takkenberg JJM, Hörer J, Lange R, et al. A multicentre evaluation of the autograft procedure for young patients undergoing aortic valve replacement: update on the German Ross Registry. *Eur J Cardio-thoracic Surg*. (2016) 49:212–8. doi: 10.1093/ejcts/ezv001
14. Reece TB, Welke KF, O'Brien S, Grau-Sepulveda MV, Grover FL, Gammie JS. Rethinking the ross procedure in adults. *Ann Thorac Surg*. (2014) 97:175–81. doi: 10.1016/j.athoracsur.2013.07.036
15. Stulak JM, Burkhart HM, Sundt TM, Connolly HM, Suri RM, Schaff H V, et al. Spectrum and outcome of reoperations after the ross procedure. *Circulation*. (2010) 122:1153–8. doi: 10.1161/CIRCULATIONAHA.109.897538
16. Takkenberg JJM, van Herwerden LA, Galema TW, Bekkers JA, Kleyburg-Linkers VA, Eijkemans MJ, et al. Serial echocardiographic assessment of neo-aortic regurgitation and root dimensions after the modified Ross procedure. *J Hear Valve Dis*. (2006) 15:100–6.
17. Sievers HH, Stierle U, Petersen M, Klotz S, Richardt D, Diwoky M, et al. Valve performance classification in 630 subcoronary Ross patients over 22 years. *J Thorac Cardiovasc Surg*. (2018) 156:79–86. doi: 10.1016/j.jtcvs.2018.03.015
18. Skillington PD, Mokhles MM, Takkenberg JJM, Larobina M, O'Keefe M, Wynne R, et al. The Ross procedure using autologous support of the pulmonary autograft: Techniques and late results. *J Thorac Cardiovasc Surg*. (2015) 149:S46–52. doi: 10.1016/j.jtcvs.2014.08.068
19. Mazine A, El-Hamamsy I, Verma S, Peterson MD, Bonow RO, Yacoub MH, et al. Ross procedure in adults for cardiologists and cardiac surgeons. *J Am Coll Cardiol*. (2018) 72:2761–77. doi: 10.1016/j.jacc.2018.08.2200
20. Yacoub MH, Tsang V, Sarathchandra P, Jensen H, Hughes S, Latif N. Long-term adaptive versus maladaptive remodelling of the pulmonary autograft after the Ross operation. *Eur J Cardiothorac Surg*. (2020) 57:977–85. doi: 10.1093/ejcts/ezaa019
21. Al-Shammari H, Latif N, Sarathchandra P, McCormack A, Rog-Zielinska EA, Raja S, et al. Expression and function of mechanosensitive ion channels in human valve interstitial cells. *PLoS ONE*. (2020) 15:e0240532. doi: 10.1371/journal.pone.0240532
22. Nappi F, Spadaccio C, Fraldi M, Montagnani S, Fouret P, Chachques JC, et al. A composite semiresorbable armoured scaffold stabilizes pulmonary autograft after the Ross operation: Mr Ross's dream fulfilled. *J Thorac Cardiovasc Surg*. (2016) 151:155–64. doi: 10.1016/j.jtcvs.2015.09.084
23. Chauvette V, Chamberland MÈ, El-Hamamsy I. A review of pulmonary autograft external support in the Ross procedure. *Expert Rev Med Devices*. (2019) 16:981–8. doi: 10.1080/17434440.2019.1685380
24. Rabkin-Aikawa E, Aikawa M, Farber M, Kratz JR, Garcia-Cardena G, Kouchoukos NT, et al. Clinical pulmonary autograft valves: Pathologic evidence of adaptive remodeling in the aortic site. *J Thorac Cardiovasc Surg*. (2004) 128:552–61. doi: 10.1016/j.jtcvs.2004.04.016
25. Schoof PH, Takkenberg JJM, van Suylen RJ, Zondervan PE, Hazekamp MG, Dion RAE, et al. Degeneration of the pulmonary autograft: An explant study. *J Thorac Cardiovasc Surg*. (2006) 132:1426–32. doi: 10.1016/j.jtcvs.2006.07.035
26. Schoof PH, Gittenberger-de Groot AC, De Heer E, Bruijn JA, Hazekamp MG, Huysmans HA. Remodeling of the porcine pulmonary autograft wall in the aortic position. *J Thorac Cardiovasc Surg*. (2000) 120:55–65. doi: 10.1067/mtc.2000.106970
27. Humphrey JD, Dufresne ER, Schwartz MA. Mechanotransduction and extracellular matrix homeostasis. *Nat Rev Mol Cell Biol*. (2014) 15:802–12. doi: 10.1038/nrm3896
28. Thompson RW, Geraghty PJ, Lee JK. Abdominal aortic aneurysms: Basic mechanisms and clinical implications. *Curr Probl Surg*. (2002) 39:110–230. doi: 10.1067/msg.2002.121421
29. Zuckerman BD, Orton EC, Stenmark KR, Trapp JA, Murphy JR, Coffeen PR, et al. Alteration of the pulsatile load in the high-altitude calf model of pulmonary hypertension. *J Appl Physiol*. (1991) 70:859–68. doi: 10.1152/jappl.1991.70.2.859
30. Chiarini A, Dal Prà I, Faggian G, Armato U, Luciani GB. Maladaptive remodeling of pulmonary artery root autografts after Ross procedure: a proteomic study. *J Thorac Cardiovasc Surg*. (2020) 159:621–32.e3. doi: 10.1016/j.jtcvs.2019.07.083
31. Somerville J. The origins of the Ross operation. *Images Paediatr Cardiol*. (2012) 14:3–5.
32. David TE, David C, Woo A, Manlhiot C. The Ross procedure: outcomes at 20 years. *J Thorac Cardiovasc Surg*. (2014) 147:85–94. doi: 10.1016/j.jtcvs.2013.08.007
33. de Kerchove L, Rubay J, Pasquet A, Poncelet A, Ovaert C, Pirotte M, et al. Ross operation in the adult: long-term outcomes after root replacement and inclusion techniques. *Ann Thorac Surg*. (2009) 87:95–102. doi: 10.1016/j.athoracsur.2008.09.031
34. Carrel T, Schwerzmann M, Eckstein F, Aymard T, Kadner A. Preliminary results following reinforcement of the pulmonary autograft to prevent dilatation after the Ross procedure. *J Thorac Cardiovasc Surg*. (2008) 136:472–5. doi: 10.1016/j.jtcvs.2008.02.004
35. Juthier F, Banfi C, Vincentelli A, Ennezat PV, Le Tourneau T, Pinçon C, et al. Modified Ross operation with reinforcement of the pulmonary autograft: Six-year results. *J Thorac Cardiovasc Surg*. (2010) 139:1420–3. doi: 10.1016/j.jtcvs.2010.01.032
36. Slater M, Shen I, Welke K, Komanapalli C, Ungerleider R. Modification to the Ross procedure to prevent autograft dilatation. *Pediatr Card Surg Annu*. (2005) 8:181–4. doi: 10.1053/j.pcsu.2005.01.022
37. Bouhout I, Ghoneim A, Tusch M, Stevens LM, Semplonius T, Tarabzoni M, et al. Impact of a tailored surgical approach on autograft root dimensions in patients undergoing the Ross procedure for aortic regurgitation. *Eur J Cardio-thoracic Surg*. (2019) 56:959–67. doi: 10.1093/ejcts/ezz105
38. Martin E, Mohammadi S, Jacques F, Kalavrouziotis D, Voisine P, Doyle D, et al. Clinical outcomes following the Ross procedure in adults: A 25-year longitudinal study. *J Am Coll Cardiol*. (2017) 70:1890–9. doi: 10.1016/j.jacc.2017.08.030
39. Boodhwani M, de Kerchove L, Glineur D, Poncelet A, Rubay J, Astarci P, et al. Repair-oriented classification of aortic insufficiency: Impact on surgical techniques and clinical outcomes. *J Thorac Cardiovasc Surg*. (2009) 137:286–94. doi: 10.1016/j.jtcvs.2008.08.054
40. Nagy ZL, Fisher J, Walker PG, Watterson KG. The *in vitro* hydrodynamic characteristics of the porcine pulmonary valve and root with regard to the Ross procedure. *J Thorac Cardiovasc Surg*. (2000) 120:284–9. doi: 10.1067/mtc.2000.107473
41. Torii R, Xu XY, El-Hamamsy I, Mohiaddin R, Yacoub MH. Computational biomechanics of the aortic root. *Aswan Hear Cent Sci Pract Ser*. (2011) 2011:16. doi: 10.5339/ahcsp.2011.16
42. Hokken RB, Bogers AJJC, Taams MA, Schiks-Berghout MB, Van Herwerden LA, Roelandt JRTC, et al. Does the pulmonary autograft in the aortic position in adults increase in diameter? An echocardiographic study. *J Thorac Cardiovasc Surg*. (1997) 113:667–74. doi: 10.1016/S0022-5223(97)70223-X
43. Bellhouse BJ, Bellhouse F, Abbott JA, Talbot L. Mechanism of valvular incompetence in aortic sinus dilatation. *Cardiovasc Res*. (1973) 7:490–4. doi: 10.1093/cvr/7.4.490
44. Kim DH, Handschumacher MD, Levine RA, Joo Sun B, Jang JY, Yang DH, et al. Aortic valve adaptation to aortic root dilatation insights into the mechanism of functional aortic regurgitation from 3-dimensional cardiac computed tomography. *Circ Cardiovasc Imaging*. (2014) 7:828–35. doi: 10.1161/CIRCIMAGING.113.001976
45. Matalanis G, Perera NK. Aortic valve sparing root surgery for Marfan syndrome. *Ann Cardiothorac Surg*. (2017) 6:682–91. doi: 10.21037/acs.2017.11.05
46. Frigiola A, Ranucci M, Carlucci C, Giamberti A, Abella R, Donato M Di, et al. The Ross procedure in adults: long-term follow-up and echocardiographic changes leading to pulmonary autograft reoperation. *Ann Thorac Surg*. (2008) 86:482–90. doi: 10.1016/j.athoracsur.2008.04.001
47. Charitos EI, Takkenberg JJM, Hanke T, Gorski A, Botha C, Franke U, et al. Reoperations on the pulmonary autograft and pulmonary homograft after the Ross procedure: an update on the German Dutch Ross Registry. *J Thorac Cardiovasc Surg*. (2012) 144:813–23. doi: 10.1016/j.jtcvs.2012.07.005

48. David TE, Ouzounian M, David CM, Lafreniere-Roula M, Manlhiot C. Late results of the Ross procedure. *J Thorac Cardiovasc Surg.* (2019) 157:201–8. doi: 10.1016/j.jtcvs.2018.06.037
49. Kincaid EH, Maloney JD, Lavender SW, Kon ND. Dissection in a pulmonary autograft. *Ann Thorac Surg.* (2004) 77:707–8. doi: 10.1016/S0003-4975(03)01402-4
50. Luciani GB, Favaro A, Viscardi F, Bertolini P, Mazzucco A. Valve-sparing root replacement for pulmonary autograft dissection late after the Ross operation. *J Thorac Cardiovasc Surg.* (2004) 128:753–6. doi: 10.1016/j.jtcvs.2004.03.031
51. Klieverik LMA, Takkenberg JJM, Elbers BCJ, Oei FBS, van Herwerden LA, Bogers AJJC. Dissection of a dilated autograft root. *J Thorac Cardiovasc Surg.* (2007) 133:817–8. doi: 10.1016/j.jtcvs.2006.11.006
52. Venkataraman R, Vaidyanathan KR, Sankar MN, Cherian KM. Late dissection of pulmonary autograft treated by valve-sparing aortic root replacement. *J Card Surg.* (2009) 24:443–5. doi: 10.1111/j.1540-8191.2008.00764.x
53. Rabkin DG, Reid BB, Doty JR. Acute on chronic pulmonary autograft dissection. *Interact Cardiovasc Thorac Surg.* (2015) 20:563–4. doi: 10.1093/icvts/ivu427
54. Myers MR, Magruder JT, Crawford TC, Grimm JC, Halushka MK, Baumgartner WA, et al. Surgical repair of aortic dissection 16 years post-Ross procedure. *J Surg Case Reports.* (2016) 4:1–3. doi: 10.1093/jscr/rjw059
55. Richey S, Fiore AC, Huddleston CB. Type A aortic dissection after the ross procedure. *Ann Thorac Surg.* (2018) 106:e105–6. doi: 10.1016/j.athoracsur.2018.02.042
56. Peeters G, Arrigoni SC, Schoof P, Accord RE, Mariani MA. Acute type A dissection 18 years after a Ross operation: the old prejudice. *Ann Thorac Surg.* (2019) 107:e255–7. doi: 10.1016/j.athoracsur.2018.08.075
57. Siudalska H, Kuśmierczyk M, Rózański J, Petryka-Mazurkiewicz J, Kumor M, Michałowska AM, et al. Aortic dissection after the Ross procedure. *Kardiologia Pol.* (2021) 79:702–3. doi: 10.33963/KP.15957
58. Goor DA, Dische R, Lillehei CW. The conotruncus. I Its normal inversion and conus absorption. *Circulation.* (1972) 46:634–6. doi: 10.1161/01.CIR.46.3.635
59. Leung DYM, Glagov S, Mathews MB. Elastin and collagen accumulation in rabbit ascending aorta and pulmonary trunk during postnatal growth. Correlation of cellular synthetic response with medial tension. *Circ Res.* (1977) 41:316–23. doi: 10.1161/01.RES.41.3.316
60. Ho SY. Structure and anatomy of the aortic root. *Eur J Echocardiogr.* (2009) 10:3–10. doi: 10.1093/ejehoccard/jen243
61. Hokken RB, Bartelings MM, Bogers AJJC, Gittonberger-De Groot AC. Morphology of the pulmonary and aortic roots with regard to the pulmonary autograft procedure. *J Thorac Cardiovasc Surg.* (1997) 113:453–61. doi: 10.1016/S0022-5223(97)70357-X
62. Tamás E, Nylander E. Echocardiographic description of the anatomic relations within the normal aortic root. *J Heart Valve Dis.* (2007) 16:240–6.
63. Kunzelman KS, Grande KJ, David TE, Cochran RP, Verrier ED. Aortic root and valve relationships: impact on surgical repair. *J Thorac Cardiovasc Surg.* (1994) 107:162–70. doi: 10.1016/S0022-5223(94)70465-1
64. Capps SB, Elkins RC, Fronk DM. Body surface area as a predictor of aortic and pulmonary valve diameter. *J Thorac Cardiovasc Surg.* (2000) 119:975–82. doi: 10.1016/S0022-5223(00)70092-4
65. Carr-White GS, Afoke A, Birks EJ, Hughes S, O'Halloran A, Glennen S, et al. Aortic root characteristics of human pulmonary autografts. *Circulation.* (2000) 102:III15–I21. doi: 10.1161/01.CIR.102.suppl_3.III-15
66. Azadani AN, Chitsaz S, Matthews PB, Jaussaud N, Leung J, Wisneski A, et al. Biomechanical comparison of human pulmonary and aortic roots. *Eur J Cardio-thoracic Surg.* (2012) 41:1111–6. doi: 10.1093/ejcts/ezr163
67. Dionne PO, Wener E, Emmott A, Cartier R, Mongrain R, Leask R, et al. The Ross procedure: biomechanical properties of the pulmonary artery according to aortic valve phenotype. *Interact Cardiovasc Thorac Surg.* (2016) 23:371–6. doi: 10.1093/icvts/ivw148
68. Karimi A, Milewicz DM. Structure of the elastin-contractile units in the thoracic aorta and how genes that cause thoracic aortic aneurysms and dissections disrupt this structure. *Can J Cardiol.* (2016) 32:26–34. doi: 10.1016/j.cjca.2015.11.004
69. Tomasek JJ, Gabbiani G, Hinz B, Chaponnier C, Brown RA. Myofibroblasts and mechano: regulation of connective tissue remodelling. *Nat Rev Mol Cell Biol.* (2002) 3:349–63. doi: 10.1038/nrm809
70. Humphrey JD, Schwartz MA, Tellides G, Milewicz DM. Role of mechanotransduction in vascular biology. *Circ Res.* (2015) 116:1448–61. doi: 10.1161/CIRCRESAHA.114.304936
71. Frid MG, Dempsey EC, Durmowicz AG, Stenmark KR. Smooth muscle cell heterogeneity in pulmonary and systemic vessels: importance in vascular disease. *Arterioscler Thromb Vasc Biol.* (1997) 17:1203–9. doi: 10.1161/01.ATV.17.7.1203
72. El-Hamamsy I, Chester AH, Yacoub MH. Cellular regulation of the structure and function of aortic valves. *J Adv Res.* (2010) 1:5–12. doi: 10.1016/j.jare.2010.02.007
73. Marron K, Yacoub MH, Polak JM, Sheppard MN, Fagan D, Whitehead BF, et al. Innervation of human atrioventricular and arterial valves. *Circulation.* (1996) 94:368–75. doi: 10.1161/01.CIR.94.3.368
74. Metzler SA, Pregonero CA, Butcher JT, Burgess SC, Warnock JN. Cyclic strain regulates pro-inflammatory protein expression in porcine aortic valve endothelial cells. *J Heart Valve Dis.* (2008) 17:571–8. doi: 10.1161/JAHA.117.006339
75. Rutkovskiy A, Malashicheva A, Sullivan G, Bogdanova M, Kostareva A, Stenslökken KO, et al. Valve interstitial cells: the key to understanding the pathophysiology of heart valve calcification. *J Am Heart Assoc.* (2017) 6:1–23. doi: 10.1161/JAHA.117.006339
76. Yang X, Fullerton DA, Su X, Ao L, Cleveland JC, Meng X. Pro-osteogenic phenotype of human aortic valve interstitial cells is associated with higher levels of toll-like receptors 2 and 4 and enhanced expression of bone morphogenetic protein 2. *J Am Coll Cardiol.* (2009) 53:491–500. doi: 10.1016/j.jacc.2008.09.052
77. Boron WF, Boulpaep EL. *Medical Physiology: A Cellular and Molecular Approach.* Philadelphia, PA: Saunders/Elsevier (2009).
78. Barker AJ, Roldán-Alzate A, Entezari P, Shah SJ, Chesler NC, Wieben O, et al. Four-dimensional flow assessment of pulmonary artery flow and wall shear stress in adult pulmonary arterial hypertension: results from two institutions. *Magn Reson Med.* (2015) 73:1904–13. doi: 10.1002/mrm.25326
79. Oechtering TH, Frydrychowicz A, Sievers HH. Malrotated sinus vortices in straight graft valve-sparing aortic root treatment: a matter of concern? *J Thorac Cardiovasc Surg.* (2017) 154:794–7. doi: 10.1016/j.jtcvs.2017.02.024
80. Gardin JM, Burn CS, Childs WJ, Henry WL. Evaluation of blood flow velocity in the ascending aorta and main pulmonary artery of normal subjects by Doppler echocardiography. *Am Heart J.* (1984) 107:310–9. doi: 10.1016/0002-8703(84)90380-6
81. Beller CJ, Labrosse MR, Thubrikar MJ, Robicsek F. Role of aortic root motion in the pathogenesis of aortic dissection. *Circulation.* (2004) 109:763–9. doi: 10.1161/01.CIR.0000112569.27151.F7
82. Lansac E, Lim HS, Shomura Y, Lim KH, Goetz W, Rice NT, et al. Aortic and pulmonary root: are their dynamics similar? *Eur J Cardio-thoracic Surg.* (2002) 21:268–75. doi: 10.1016/S1010-7940(01)01132-0
83. Bia D, Armentano RL, Grignola JC, Craiem D, Zócalo YA, Ginés FF, et al. The vascular smooth muscle of great arteries: local control site of arterial buffering function? *Rev Esp Cardiol.* (2003) 56:1202–9. doi: 10.1016/S0300-8932(03)77039-0
84. Vastmans J, Fehervary H, Verbrughe P, Verbelen T, Vanderveken E, Vander Sloten J, et al. Biomechanical evaluation of a personalized external aortic root support applied in the Ross procedure. *J Mech Behav Biomed Mater.* (2018) 78:164–74. doi: 10.1016/j.jmbbm.2017.11.018
85. Lenoir M, Emmott A, Bouhout I, Poirier N, Tusch M, El-Hamamsy I, et al. Autograft remodeling after the Ross procedure by cardiovascular magnetic resonance imaging: aortic stenosis versus insufficiency. *J Thorac Cardiovasc Surg.* (2022) 163:578–87.e1. doi: 10.1016/j.jtcvs.2020.03.185
86. Hasan A, Ragaert K, Swieszkowski W, Selimović Š, Paul A, Camci-Unal G, et al. Biomechanical properties of native and tissue engineered heart valve constructs. *J Biomech.* (2014) 47:1949–63. doi: 10.1016/j.jbiomech.2013.09.023
87. Stradins P, Lacis R, Ozolanta I, Purina B, Ose V, Feldmane L, et al. Comparison of biomechanical and structural properties between human aortic and pulmonary valve. *Eur J Cardio-thoracic Surg.* (2004) 26:634–9. doi: 10.1016/j.ejcts.2004.05.043

88. Leeson-Dietrich J, Boughner D, Vesely I. Porcine pulmonary and aortic valves: a comparison of their tensile viscoelastic properties at physiological strain rates. *J Heart Valve Dis.* (1995) 4:88–94.
89. Soares ALF, van Geemen D, van den Bogaardt AJ, Oomens CWJ, Bouten CVC, Baaijens FPT. Mechanics of the pulmonary valve in the aortic position. *J Mech Behav Biomed Mater.* (2014) 29:557–67. doi: 10.1016/j.jmbbm.2013.07.009
90. Christie GW, Barratt-Boyes BG. Mechanical properties of porcine pulmonary valve leaflets: how do they differ from aortic leaflets? *Ann Thorac Surg.* (1995) 60(Suppl. 2):S195–9. doi: 10.1016/S0003-4975(95)00279-T
91. Mazine A, Ghoneim A, El-Hamamsy I. The Ross procedure: how I teach it. *Ann Thorac Surg.* (2018) 105:1294–8. doi: 10.1016/j.athoracsur.2018.01.048
92. Iung B, Baron G, Butchart EG, Delahaye F, Gohlke-Bärwolf C, Levang OW, et al. A prospective survey of patients with valvular heart disease in Europe: The Euro Heart Survey on valvular heart disease. *Eur Heart J.* (2003) 24:1231–43. doi: 10.1016/S0195-668X(03)00201-X
93. Robicsek F, Thubrikar MJ, Cook JW, Fowler B. The congenitally bicuspid aortic valve: How does it function? Why does it fail? *Ann Thorac Surg.* (2004) 77:177–85. doi: 10.1016/S0003-4975(03)01249-9
94. Schmid FX, Bielenberg K, Holmer S, Lehle K, Djavidani B, Prasser C, et al. Structural and biomolecular changes in aorta and pulmonary trunk of patients with aortic aneurysm and valve disease: Implications for the Ross procedure. *Eur J Cardio-thoracic Surg.* (2004) 25:748–53. doi: 10.1016/j.ejcts.2004.02.028
95. Michelena HI, Prakash SK, Della CA, Bissell MM, Anavekar N, Mathieu P, et al. Bicuspid aortic valve identifying knowledge gaps and rising to the challenge from the international bicuspid aortic valve consortium (BAVCON). *Circulation.* (2014) 129:2691–704. doi: 10.1161/CIRCULATIONAHA.113.007851
96. Richardson R, Eley L, Donald-Wilson C, Davis J, Curley N, Alqahtani A, et al. Development and maturation of the fibrous components of the arterial roots in the mouse heart. *J Anat.* (2018) 232:554–67. doi: 10.1111/joa.12713
97. Verma S, Siu SC. Aortic dilatation in patients with bicuspid aortic valve. *N Engl J Med.* (2014) 370:1920–9. doi: 10.1056/NEJMra1207059
98. Vistarini N, Gebhard C, Desjardins G, El-Hamamsy I. Successful repair of a bicuspid pulmonary autograft valve causing early insufficiency after a Ross procedure. *Ann Thorac Surg.* (2016) 101:e99–101. doi: 10.1016/j.athoracsur.2015.06.119
99. Kajingu Enciso S, Elens M, Rubay J. Congenital bicuspid pulmonary valve. An uncommon impede for Ross procedure. *Acta Chir Belg.* (2017) 117:115–7. doi: 10.1080/00015458.2016.1220121
100. Jashari R, Van Hoeck B, Goffin Y, Vanderkelen A. The incidence of congenital bicuspid or bileaflet and quadracuspid or quadrileaflet arterial valves in 3,861 donor hearts in the European Homograft Bank. *J Heart Valve Dis.* (2009) 18:337–44.
101. De Sa M, Moshkovitz Y, Butany J, David TE, Robicsek F, Gardner TJ, et al. Histologic abnormalities of the ascending aorta and pulmonary trunk in patients with bicuspid aortic valve disease: clinical relevance to the Ross procedure. *J Thorac Cardiovasc Surg.* (1999) 118:588–96. doi: 10.1016/S0022-5223(99)70002-4
102. Luciani GB, Barozzi L, Tomezzoli A, Casali G, Mazzucco A. Bicuspid aortic valve disease and pulmonary autograft root dilatation after the Ross procedure: a clinicopathologic study. *J Thorac Cardiovasc Surg.* (2001) 122:74–9. doi: 10.1067/mtc.2001.114638
103. Celik M, Yuksel UC, Yalcinkaya E, Gokoglan Y, Yildirim E, Bugan B, et al. Elasticity properties of pulmonary artery in patients with bicuspid aortic valve. *Echocardiography.* (2014) 31:759–64. doi: 10.1111/echo.12455
104. Kutty S, Kaul S, Danford CJ, Danford DA. Main pulmonary artery dilation in association with congenital bicuspid aortic valve in the absence of pulmonary valve abnormality. *Heart.* (2010) 96:1756–61. doi: 10.1136/hrt.2010.199109
105. Cañadas V, Vilacosta I, Bruna I, Fuster V. Marfan syndrome. Part 1: pathophysiology and diagnosis. *Nat Rev Cardiol.* (2010) 7:256–65. doi: 10.1038/nrcardio.2010.30
106. Chiu P, Irons M, van de Rijn M, Liang DH, Miller DC. Giant pulmonary artery aneurysm in a patient with Marfan syndrome and pulmonary hypertension. *Circulation.* (2016) 133:1218–21. doi: 10.1161/CIRCULATIONAHA.115.020537
107. Sheikhzadeh S, De Backer J, Gorgan NR, Rybczynski M, Hillebrand M, Schüler H, et al. The main pulmonary artery in adults: a controlled multicenter study with assessment of echocardiographic reference values, and the frequency of dilatation and aneurysm in Marfan syndrome Orphanet. *J Rare Dis.* (2014) 9:203. doi: 10.1186/s13023-014-0203-8
108. Yacoub MH. The Ross operation - an evolutionary tale. *Asian Cardiovasc Thorac Ann.* (2006) 14:1–2. doi: 10.1177/021849230601400101
109. Mookhoek A, de Heer E, Bogers AJJC, Takkenberg JJM, Schoof PH. Pulmonary autograft valve explants show typical degeneration. *J Thorac Cardiovasc Surg.* (2010) 139:1416–9. doi: 10.1016/j.jtcvs.2010.01.020
110. Ishizaka T, Devaney EJ, Ramsburgh SR, Suzuki T, Ohye RG, Bove EL. Valve sparing aortic root replacement for dilatation of the pulmonary autograft and aortic regurgitation after the Ross procedure. *Ann Thorac Surg.* (2003) 75:1518–22. doi: 10.1016/S0003-4975(02)04904-4
111. Takkenberg JJM, Zondervan PE, Van Herwerden LA. Progressive pulmonary autograft root dilatation and failure after ross procedure. *Ann Thorac Surg.* (1999) 67:551–4. doi: 10.1016/S0003-4975(98)01274-0
112. Sundt TM, Moon MR, Xu H, Stelzer P. Reoperation for dilatation of the pulmonary autograft after the ross procedure. *J Thorac Cardiovasc Surg.* (2002) 122:1249–52. doi: 10.1067/mtc.2001.116320
113. Goffin YA, Narine KR, Alexander JP, Van Goethem J, Daenen WJ. Histopathologic comparison of a pulmonary autograft and pulmonary homograft in a patient 17 months after a Ross procedure: an autopsy study. *J Heart Valve Dis.* (1998) 7:327–30.
114. Ando Y, Ochiai Y, Tokunaga S, Hisahara M, Baba H, Miyagi C, et al. Size and stiffness of the pulmonary autograft after the Ross procedure in children. *Pediatr Cardiol.* (2019) 40:776–83. doi: 10.1007/s00246-019-02064-9
115. Xuan Y, Alonso E, Emmott A, Wang Z, Kumar S, Mongeon F-P, et al. Wall stresses of early remodeled pulmonary autografts. *J Thorac Cardiovasc Surg.* (2021). doi: 10.1016/j.jtcvs.2021.08.058. [Epub ahead of print].
116. Mookhoek A, Krishnan K, Chitsaz S, Kuang H, Ge L, Schoof PH, et al. Biomechanics of failed pulmonary autografts compared with normal pulmonary roots. *Ann Thorac Surg.* (2016) 102:1996–2002. doi: 10.1016/j.athoracsur.2016.05.010
117. Mookhoek A, Krishnan K, Chitsaz S, Kuang H, Ge L, Schoof PH, et al. Biomechanics of failed pulmonary autografts compared to native aortic roots. *Ann Thorac Surg.* (2017) 103:1482–8. doi: 10.1016/j.athoracsur.2016.08.061
118. Vanderveken E, Vastmans J, Verbelen T, Verbrugghe P, Famaey N, Verbeken E, et al. Reinforcing the pulmonary artery autograft in the aortic position with a textile mesh: a histological evaluation. *Interact Cardiovasc Thorac Surg.* (2018) 27:566–73. doi: 10.1093/icvts/ivy134
119. Vanderveken E, Vastmans J, Claus P, Verbeken E, Fehervary H, Van Hoof L, et al. Mechano-biological adaptation of the pulmonary artery exposed to systemic conditions. *Sci Rep.* (2020) 10:1–12. doi: 10.1038/s41598-020-59554-7
120. Nappi P, Spadaccio C, Fouret P, Hammoudi N, Chachques JC, Chello M, et al. An experimental model of the Ross operation: development of resorbable reinforcements for pulmonary autografts. *J Thorac Cardiovasc Surg.* (2015) 149:1134–42. doi: 10.1016/j.jtcvs.2014.12.056
121. Schoof PH, Hazekamp MG, Van Wermeskerken GK, De Heer E, Bruijn JA, Gittenberger-De Groot AC, et al. Disproportionate enlargement of the pulmonary autograft in the aortic position in the growing pig. *J Thorac Cardiovasc Surg.* (1998) 115:1264–72. doi: 10.1016/S0022-5223(98)70208-9
122. Tudorache I, Theodoridis K, Baraki H, Sarikouch S, Bara C, Meyer T, et al. Decellularized aortic allografts versus pulmonary autografts for aortic valve replacement in the growing sheep model: haemodynamic and morphological results at 20 months after implantation. *Eur J Cardio-thoracic Surg.* (2016) 49:1228–38. doi: 10.1093/ejcts/ezv362
123. Van Hoof L, Claus P, Jones EAV, Meuris B, Famaey N, Verbrugghe P, et al. Back to the root: a large animal model of the Ross procedure. *Ann Cardiothorac Surg.* (2021) 10:444–53. doi: 10.21037/acs-2020-rp-21
124. Lower RR, Stoffer RC, Shumway NE. Autotransplantation of the pulmonic valve into the aorta. *J Thorac Cardiovasc Surg.* (1960) 39:680–7. doi: 10.1016/S0022-5223(20)31814-6
125. Pillsbury RC, Shumway NE. Replacement of the aortic valve with the autologous pulmonic valve. *Surg Forum.* (1966) 17:176–7.

126. Wisneski AD, Matthews PB, Azadani AN, Chitsaz S, Lui N, Takabe K, et al. Finite element modeling of the human pulmonary autograft: a quantitative analysis of wall stress after the Ross procedure. *J Am Coll Surg.* (2012) 215:S46. doi: 10.1016/j.jamcollsurg.2012.06.137
127. Stenmark KR, Nozik-Grayck E, Gerasimovskaya E, Anwar A, Li M, Riddle S, et al. The adventitia: Essential role in pulmonary vascular remodeling. *Compr Physiol.* (2011) 1:141–61. doi: 10.1002/cphy.c090017
128. Rensen SSM, Doeveendans PAFM, Van Eys GJJM. Regulation and characteristics of vascular smooth muscle cell phenotypic diversity. *Netherlands Hear J.* (2007) 15:100–8. doi: 10.1007/BF03085963
129. Van Varik BJ, Rennenberg RJMW, Chris P, Kroon AA, De Leeuw PW, Schurgers LJ. Mechanisms of arterial remodeling: lessons from genetic diseases. *Front Genet.* (2012) 3:1–10. doi: 10.3389/fgene.2012.00290
130. Nuche J, Palomino-Doza J, Ynsaurriaga FA, Delgado JF, Ibáñez B, Oliver E, et al. Potential molecular pathways related to pulmonary artery aneurysm development: Lessons to learn from the aorta. *Int J Mol Sci.* (2020) 21:509. doi: 10.3390/ijms21072509
131. Wang Y, Gharahi H, Grobbl MR, Rao A, Roccabianca S, Baek S. Potential damage in pulmonary arterial hypertension: an experimental study of pressure-induced damage of pulmonary artery. *J Biomed Mater Res.* (2021) 109:579–89. doi: 10.1002/jbm.a.37042
132. Patel A, Fine B, Sandig M, Mequanint K. Elastin biosynthesis: The missing link in tissue-engineered blood vessels. *Cardiovasc Res.* (2006) 71:40–9. doi: 10.1016/j.cardiores.2006.02.021
133. Ku CH, Johnson PH, Batten P, Sarathchandra P, Chambers RC, Taylor PM, et al. Collagen synthesis by mesenchymal stem cells and aortic valve interstitial cells in response to mechanical stretch. *Cardiovasc Res.* (2006) 71:548–56. doi: 10.1016/j.cardiores.2006.03.022
134. Tang PCY, Coady MA, Lovoulos C, Dardik A, Aslan M, Elefteriades JA, et al. Hyperplastic cellular remodeling of the media in ascending thoracic aortic aneurysms. *Circulation.* (2005) 112:1098–105. doi: 10.1161/CIRCULATIONAHA.104.511717
135. Guzzardi DG, Barker AJ, Van Ooij P, Malaisrie SC, Puthumana JJ, Belke DD, et al. Valve-related hemodynamics mediate human bicuspid aortopathy: insights from wall shear stress mapping. *J Am Coll Cardiol.* (2015) 66:892–900. doi: 10.1016/j.jacc.2015.06.1310
136. Wolinsky H, Glagov S. Nature of species differences in the medial distribution of aortic vasa vasorum in mammals. *Circ Res.* (1967) 20:409–21. doi: 10.1161/01.RES.20.4.409
137. Bartter T, Irwin RS, Nash G. Aneurysms of the pulmonary arteries. *Chest.* (1988) 94:1065–75. doi: 10.1378/chest.94.5.1065
138. Tong J, Rabkin S. The relationship between hypertension and thoracic aortic aneurysm of degenerative or atherosclerotic origin: a systematic review. *Austin Hypertens.* (2016) 1:1004.
139. Ramachandra AB, Humphrey JD, Marsden AL. Gradual loading ameliorates maladaptation in computational simulations of vein graft growth and remodelling. *J R Soc Interface.* (2017) 14:e0995. doi: 10.1098/rsif.2016.0995
140. Pyeritz RE. The Marfan syndrome. *Annu Rev Med.* (2000) 51:481–510. doi: 10.1146/annurev.med.51.1.481
141. Habashi JP, Judge DP, Holm TM, Cohn RD, Loeys BL, Cooper TK, et al. Losartan, an AT1 antagonist, prevents aortic aneurysm in a mouse model of Marfan syndrome. *Science.* (2006) 312:117–21. doi: 10.1126/science.1124287
142. Ceroni D, Martin X, Delhumeau C, Rizzoli R, Kaelin A, Farpour-Lambert N. Effects of cast-mediated immobilization on bone mineral mass at various sites in adolescents with lower-extremity fracture. *J Bone Jt Surg A.* (2012) 94:208–16. doi: 10.2106/JBJS.K.00420
143. Courtman DW, Cho A, Langille L, Wilson GJ. Eliminating arterial pulsatile strain by external banding induces medial but not neointimal atrophy and apoptosis in the rabbit. *Am J Pathol.* (1998) 153:1723–9. doi: 10.1016/S0002-9440(10)65687-8
144. Min SK, Kenagy RD, Jeanette JP, Clowes AW. Effects of external wrapping and increased blood flow on atrophy of the baboon iliac artery. *J Vasc Surg.* (2008) 47:1039–47. doi: 10.1016/j.jvs.2007.12.043
145. Ramachandra AB, Latorre M, Szafron JM, Marsden AL, Humphrey JD. Vascular adaptation in the presence of external support - a modeling study. *J Mech Behav Biomed Mater.* (2020) 110:103943. doi: 10.1016/j.jmbbm.2020.103943
146. Schürmann K, Vorwerk D, Bückner A, Neuerburg J, Klosterhalfen B, Müller G, et al. Perigraft inflammation due to Dacron-covered stent-grafts in sheep iliac arteries: correlation of MR imaging and histopathologic findings. *Cardiovasc Radiol.* (1997) 204:757–63. doi: 10.1148/radiology.204.3.9280255
147. Orenstein SB, Saberski ER, Kreutzer DL, Novitsky YW. Comparative analysis of histopathologic effects of synthetic meshes based on material, weight, and pore size in mice. *J Surg Res.* (2012) 176:423–9. doi: 10.1016/j.jss.2011.09.031
148. Van Hoof L, Verbrugghe P, Verbeken E, Treasure T, Famaey N, Meuris B, et al. Support of the aortic wall: a histological study in sheep comparing a macroporous mesh with low-porosity vascular graft of the same polyethylene terephthalate material. *Interact Cardiovasc Thorac Surg.* (2017) 25:89–95. doi: 10.1093/icvts/ivx009
149. White RA. The effect of porosity and biomaterial on the healing and long-term mechanical properties of vascular prostheses. *Trans Am Soc Artif Intern Organs.* (1988) 34:95–100. doi: 10.1097/00002480-198804000-00004
150. Treasure T, Petrou M, Rosendahl U, Austin C, Rega F, Pirk J, et al. Personalized external aortic root support: a review of the current status. *Eur J Cardio-Thorac Surg.* (2016) 50:400–4. doi: 10.1093/ejcts/ezw078
151. Treasure T. A “compare and contrast” exercise: wrapping versus personalised external aortic root support (PEARS). *J Cardiothorac Surg.* (2016) 11:10–1. doi: 10.1186/s13019-016-0499-7
152. Plonek T, Dumanski A, Nowicki R, Kustrzycki W. Computed tomography angiography of aorta subjected to external wrapping. *J Cardiothorac Surg.* (2016) 11:1–5. doi: 10.1186/s13019-016-0487-y
153. Van Hoof L, Rega F, Golesworthy T, Verbrugghe P, Austin C, Takkenberg JJM, et al. Personalised external aortic root support for elective treatment of aortic root dilation in 200 patients. *Heart.* (2021) 107:1790–5. doi: 10.1136/heartjnl-2021-319300
154. Verbrugghe P, Verbeken E, Pepper J, Treasure T, Meyns B, Meuris B, et al. External aortic root support: a histological and mechanical study in sheep. *Interact Cardiovasc Thorac Surg.* (2013) 17:334–9. doi: 10.1093/icvts/ivt165
155. Izgi C, Newsome S, Alpendurada F, Nyktari E, Boutsikou M, Pepper J, et al. External aortic root support to prevent aortic dilatation in patients with Marfan syndrome. *J Am Coll Cardiol.* (2018) 72:1095–105. doi: 10.1016/j.jacc.2018.06.053
156. Pepper J, Goddard M, Mohiaddin R, Treasure T. Histology of a Marfan aorta 45 years after personalized external aortic root support. *Eur J Cardio-Thorac Surg.* (2015) 48:502–5. doi: 10.1093/ejcts/ezu415
157. Golesworthy T. *ExoVasc® Personalised External Aortic Root Support Project Status – 6 August 2021.* (2021).
158. Drews JD, Pepper VK, Best CA, Szafron JM, Cheatham JP, Yates AR, et al. Spontaneous reversal of stenosis in tissue-engineered vascular grafts. *Sci Transl Med.* (2020) 12:1–14. doi: 10.1126/scitranslmed.aax6919
159. Mortiz A, Domanig E, Marx M, Moidl R, Simon P, Laufer G, et al. Pulmonary autograft valve replacement in the dilated and asymmetric aortic root. *Eur J Cardio-Thorac Surg.* (1993) 7:405–8. doi: 10.1016/1010-7940(93)90003-T
160. López B, Ravassa S, González A, Zubillaga E, Bonavita C, Bergés M, et al. Myocardial collagen cross-linking is associated with heart failure hospitalization in patients with hypertensive heart failure. *J Am Coll Cardiol.* (2016) 67:251–60. doi: 10.1016/j.jacc.2015.10.063
161. Zhang ZY, Ravassa S, Yang WY, Petit T, Pejchinovski M, Zürbig P, et al. Diastolic left ventricular function in relation to urinary and serum collagen biomarkers in a general population. *PLoS ONE.* (2016) 11:1–17. doi: 10.1371/journal.pone.0167582
162. El-Hamamsy I, Balachandran K, Yacoub MH, Stevens LM, Sarathchandra P, Taylor PM, et al. Endothelium-dependent regulation of the mechanical properties of aortic valve cusps. *J Am Coll Cardiol.* (2009) 53:1448–55. doi: 10.1016/j.jacc.2008.11.056
163. Famaey N, Vastmans J, Fehervary H, Maes L, Vanderveken E, Rega F, et al. Numerical simulation of arterial remodeling in pulmonary autografts. *Z Angew Math Mech.* (2018) 98:2239–57. doi: 10.1002/zamm.201700351
164. Vastmans J, Maes L, Peirlinck M, Vanderveken E, Rega F, Kuhl E, et al. Growth and remodeling in the pulmonary autograft: computational evaluation using kinematic growth models and constrained mixture theory. *Int J Numer Method Biomed Eng.* (2021) e3545:1–24. doi: 10.1002/cnm.3545

165. Morrison TM, Pathmanathan P, Adwan M, Margerrison E. Advancing regulatory science with computational modeling for medical devices at the FDA's office of science and engineering laboratories. *Front Med.* (2018) 5:1–11. doi: 10.3389/fmed.2018.00241
166. Qiao A, Pan Y, Dong N. Modeling study of aortic root for ross procedure: a structural finite element analysis. *J Heart Valve Dis.* (2014) 23:683–7.
167. Alonso E, Xuan Y, Emmott A, Wang Z, Kumar S, Mongeon F-P, et al. Alonso 2020 wall stress after Ross operation. *Circulation.* (2020) 142:A16230. doi: 10.1161/circ.142.suppl_3.16230
168. Wu W, Allen RA, Wang Y. Fast-degrading elastomer enables rapid remodeling of a cell-free synthetic graft into a neoartery. *Nat Med.* (2012) 18:1148–53. doi: 10.1038/nm.2821
169. Breuer CK, Brennan MP, Dardik A, Hibino N, Roh JD, Nelson GN, et al. Tissue-engineered vascular grafts demonstrate evidence of growth and development when implanted in a juvenile animal model. *Ann Surg.* (2008) 248:370–6. doi: 10.1097/SLA.0b013e318184dcbd

Conflict of Interest: The authors declare that the research was conducted in the absence of any commercial or financial relationships that could be construed as a potential conflict of interest.

Publisher's Note: All claims expressed in this article are solely those of the authors and do not necessarily represent those of their affiliated organizations, or those of the publisher, the editors and the reviewers. Any product that may be evaluated in this article, or claim that may be made by its manufacturer, is not guaranteed or endorsed by the publisher.

Copyright © 2022 Van Hoof, Verbrugghe, Jones, Humphrey, Janssens, Famaey and Rega. This is an open-access article distributed under the terms of the Creative Commons Attribution License (CC BY). The use, distribution or reproduction in other forums is permitted, provided the original author(s) and the copyright owner(s) are credited and that the original publication in this journal is cited, in accordance with accepted academic practice. No use, distribution or reproduction is permitted which does not comply with these terms.



A Biohybrid Material With Extracellular Matrix Core and Polymeric Coating as a Cell Honing Cardiovascular Tissue Substitute

Jahnvi Mudigonda^{1,2}, Dongyang Xu^{1,2}, Alan Amedi^{1,2}, Brooks A. Lane^{1,2}, Daniella Corporan^{1,2}, Vivian Wang¹ and Muralidhar Padala^{1,2*}

¹ Structural Heart Research & Innovation Laboratory, Carlyle Fraser Heart Center, Emory University Hospital Midtown, Atlanta, GA, United States, ² Division of Cardiothoracic Surgery, Emory University School of Medicine, Atlanta, GA, United States

OPEN ACCESS

Edited by:

Laura Iop,
University of Padua, Italy

Reviewed by:

Andrea Bagno,
University of Padua, Italy
Archana Bhaw-Luximon,
University of Mauritius, Mauritius
Xiaojun Yu,
Stevens Institute of Technology,
United States

*Correspondence:

Muralidhar Padala
spadala@emory.edu

Specialty section:

This article was submitted to
Heart Valve Disease,
a section of the journal
Frontiers in Cardiovascular Medicine

Received: 01 November 2021

Accepted: 20 January 2022

Published: 24 March 2022

Citation:

Mudigonda J, Xu D, Amedi A, Lane BA, Corporan D, Wang V and Padala M (2022) A Biohybrid Material With Extracellular Matrix Core and Polymeric Coating as a Cell Honing Cardiovascular Tissue Substitute. *Front. Cardiovasc. Med.* 9:807255. doi: 10.3389/fcvm.2022.807255

Objective: To investigate the feasibility of a hybrid material in which decellularized pericardial extracellular matrix is functionalized with polymeric nanofibers, for use as a cardiovascular tissue substitute.

Background: A cardiovascular tissue substitute, which is gradually resorbed and is replaced by host's native tissue, has several advantages. Especially in children and young adults, a resorbable material can be useful in accommodating growth, but also enable rapid endothelialization that is necessary to avoid thrombotic complications. In this study, we report a hybrid material, wherein decellularized pericardial matrix is functionalized with a layer of polymeric nanofibers, to achieve the mechanical strength for implantation in the cardiovascular system, but also have enhanced cell honing capacity.

Methods: Pericardial sacs were decellularized with sodium deoxycholate, and polycaprolactone-chitosan fibers were electrospun onto the matrix. Tissue-polymer interaction was evaluated using spectroscopic methods, and the mechanical properties of the individual components and the hybrid material were quantified. *In-vitro* blood flow loop studies were conducted to assess hemocompatibility and cell culture methods were used to assess biocompatibility.

Results: Encapsulation of the decellularized matrix with 70 μ m thick matrix of polycaprolactone-chitosan nanofibers, was feasible and reproducible. Spectroscopy of the cross-section depicted new amide bond formation and C–O–C stretch at the interface. An average peel strength of 56.13 ± 11.87 mN/mm² was measured, that is sufficient to withstand a high shear of 15 dynes/cm² without delamination. Mechanical strength and extensibility ratio of the decellularized matrix alone were $18,000 \pm 4,200$ KPa and $0.18 \pm 0.03\%$ whereas that of the hybrid was higher at $20,000 \pm 6,600$ KPa and $0.35 \pm 0.20\%$. Anisotropy index and stiffness of the biohybrid were increased as well. Neither thrombus formation, nor platelet adhesion or hemolysis was measured in the *in-vitro* blood flow loop studies. Cellular adhesion and survival were adequate in the material.

Conclusion: Encapsulating a decellularized matrix with a polymeric nanofiber coating, has favorable attributes for use as a cardiovascular tissue substitute.

Keywords: biomaterial, tissue engineering, xenogeneic, cardiovascular, extracellular matrix

INTRODUCTION

Cardiovascular surgical procedures often require tissue reconstruction, and appropriate materials for this purpose are lacking. Autologous tissue from the patient would be the most ideal, but such materials are scarcely available and are variable in quality. Thus, non-autologous or fully synthetic materials are needed to fulfill this gap, with the most ideal material being one that gradually resorbs and integrates into the host's body (1). This is especially desirable in children undergoing cardiac surgery where long-term durability, hemocompatibility, and implant remodeling are essential to withstand pulsatile hemodynamics and somatic growth.

There is currently a dearth of such materials and this gap is acknowledged by the scientific community (2–5). Currently, glutaraldehyde-fixed bovine pericardium (Glut BP), that was introduced in the 1970s is utilized for its hemocompatibility and mechanical strength. This material is used widely, both as surgical patches and as leaflets in prosthetic heart valves (6). Glutaraldehyde, a common fixative, makes the BP inert to bioactivity and hydrophobic and increases its mechanical strength by crosslinking collagen fibers in the BP, making it suitable for use in the cardiovascular system. However, it also can promote tissue calcification and lead to structural deterioration of the material over time (7, 8). Glycation and albumin infiltration into these materials has also been shown to occur, leading to non-calcific tissue deterioration as well (9). These shortcomings make it less than ideal for long-term efficacy and host integration (1, 4, 6, 10, 11).

To overcome these challenges, glutaraldehyde-free, detergent-based decellularized pericardia have been introduced. Though of superior immunogenicity, these tissues lack adequate mechanical strength for use in the cardiovascular system (12). Cell seeding and *in-vitro* mechanical preconditioning were tried, but such attempts have also not yielded tangible outcomes that could improve their clinical translation (13, 14). The failure mechanisms are often attributed to weak mechanical properties, residual detergents, and remnant cellular materials that cause structural degeneration and calcification and prevents active remodeling (15–17). Synthetic grafts made from polymers, such as Gore-Tex and Dacron, have gained significant use in the past few decades due to excellent mechanical properties, and some success in achieving hemocompatibility (2, 3, 18). However, the immune response elicited by these grafts creates fibrosis and calcification, reproducing the challenges observed with currently used materials (19).

Recently, a distinct *in-situ* tissue engineering approach has gained traction, in which synthetic materials that are inert at the time of implantation, but remodel and are resorbed *in situ* are being used. These are made from biodegradable supramolecular polymers, which elicit a host immune response, but gradually

breakdown and are replaced by the own tissue of the host (12, 20, 21). Successful remodeling of these materials is dependent on the chemical nature of the material, its porosity and surface profile that enables cellular attachment, degradation profile in relation to the host tissue formation, and hemocompatibility. Tissue engineered materials so far have been very promising in animal models with short and intermediate follow-ups (22–25) and some of these materials are being tested preclinically with some success (24, 26). Though the preclinical results are promising, the long-term immune response and mechanistic studies that elucidate long-term fibrotic phenotypes are unknown (1). One of the main challenges for designing a desired acellular biomaterial is to achieve a balance between scaffold degradation and neotissue formation without eliciting unfavorable chronic immune and fibrotic response (15, 22, 27, 28).

Hybrid tissue engineering is a more recent approach, in which instead of using a fully synthetic degradable scaffold, a combination of two materials is used. Often, one of the materials is a synthetic polymer that baits cells from the host, in a programmed manner and the second material is another natural polymer or a native decellularized matrix that provides a 3-dimensional scaffold for the cells to hone into and thrive (29–35). Combining synthetic and natural polymers allows programmed mechanical properties, but is susceptible to enzymatic degradation over time (6, 30). On the contrary, combining synthetic polymers with natural decellularized tissues, provides adequate and tunable mechanical strength and also a native tissue architecture that is highly conducive for cellular honing and proliferation (29, 31, 33–40). Porcine heart valve tissue constructs that were modified with biopolymers improved their *in-vivo* mechanical stability, antithrombogenicity, remodeling, and prevented calcification (31, 40, 41). We previously adapted the hybrid tissue engineering approach to fabricate a planar hybrid biomaterial with multiple applications for cardiovascular reconstruction. We modified BP, which is widely used as a cardiovascular replacement (42, 43) with a biodegradable [polycaprolactone (PCL):chitosan (Ch)] polymer blend to construct a biohybrid material (44). The concept was deduced to a prototype by using non-degradable decellularized BP, with a detergent mixture that removed all the cells, but preserved the extracellular matrix (ECM) architecture. This native ECM core was then overlaid with a matrix of PCL:Ch using an electrospinning technique to deposit nanofibers onto the matrix core in a directionally aligned manner. The hypothesis is that the polymeric mesh restores mechanical function of the pericardia lost due to the decellularization process, and thus is more suitable to evolving cardiovascular mechanical environments. The polymeric mesh will also hypothetically act as a non-thrombogenic, bioactive layer that enables cellular adhesion that precedes cellular infiltration and ultimately, gradual polymer degradation as seen in another scaffold using the same synthetic polymer blend (25). In this study, we report extensive *in-vitro* characterization of this biohybrid material, its mechanical strength using a variety of testing methods, hemocompatibility in blood flow loops with high and low shear stresses and flow disturbances, biocompatibility, and feasibility

Abbreviations: SEM, scanning electron microscopy; FT-IR, Fourier-transform infrared spectroscopy; XPS, X-ray photon spectroscopy; GAG, glycosaminoglycans; DAPI, 4,6-diamidino-2-phenylindole; PCL, polycaprolactone; Ch, chitosan; H&E, hematoxylin and eosin; Glut, glutaraldehyde; BP, bovine pericardium; ECM, extracellular matrix; Glut-BP, glut fixed untreated BP.

of this hybrid composite material as a potential cardiovascular replacement material.

MATERIALS AND METHODS

Matrix-Polymer Composite Material (Biohybrid)

Bovine pericardium was sourced from a commercial vendor (Collagen Solutions, Eden Prairie, Minnesota, USA) and the biohybrid material was prepared. The pericardium was decellularized with 2% sodium deoxycholate [D6750; Sigma-Aldrich, St. Louis, Mosby, USA; average molecular weight (MW) 1,200–5,000] for 48 h, followed by 1% sodium deoxycholate for 24 h, and treatment with DNase (D4527; Sigma-Aldrich, St. Louis, Mosby, USA) and RNase (R6513; Sigma-Aldrich, St. Louis, Mosby, USA) for 2 h at 37°C, in a shaker incubator (Model 420; Orbital shaker, Forma Scientific, USA). Acellularity was confirmed by DNA estimation, histology [H&E and 4,6-diamidino-2-phenylindole (DAPI) staining], and scanning electron microscopy (SEM). Twelve percent PCL (Catalog # 440744, Sigma-Aldrich, St. Louis, Mosby, USA, molecular weight 70,000–90,000) and 1% Ch (Catalog # 417963, Sigma-Aldrich, St. Louis, Mosby, USA, molecular weight >1,00,000) blend was prepared in a mixture of 80:20 trifluoroacetic acid (TFA) (L06374, Alfa Aesar, USA) and dichloromethane (DCM) (39116, Alfa Aesar, USA). The polymer solution was then electrospun onto a 10 cm × 12 cm decellularized pericardial core mounted on a rotating mandrel. Polymer fibers (134.68 ± 49.4 nm) were deposited in the circumferential direction on the fibrosa side of the decellularized pericardium, 3 h upto at room temperature, until a thickness of about 70 μ m was achieved. The sample was then neutralized in 0.5 M NaOH for 10 min for the free amine of Ch to interact with the decellularized tissue. The sample was then washed in distilled water and preserved in 70% ethanol. Detailed protocols for each method are described in **Supplementary Section 1.0**.

Mechanical Integrity of the Decellularized Core and Core-Polymer Interaction

Efficacy of decellularization and its structural integrity were assessed by staining with Masson's trichrome, Verhoeff's Van Gieson, and alcian blue stains. Quantitative estimation of DNA, collagen, elastin, and glycosaminoglycans (GAGs) was performed with DNA Estimation Kit (PureGenome™ Tissue DNA Extraction Kit, Millipore Sigma, USA), Hydroxyproline Assay (MAK008, Sigma-Aldrich, St. Louis, Mosby, USA), Fastin™ Elastin Assay (F2000, Biocolor, UK), and Dimethylmethylene Blue (DMMB) Assay, respectively, using techniques reported earlier (44). Detailed protocols for each step are described in the **Supplementary Section 1.1**. Polymer-core interface was examined with SEM and molecular interactions were quantified with Fourier transform infrared spectroscopy (FT-IR) and X-ray photoelectron spectroscopy (XPS). FTIR spectra were recorded for PCL, Ch, PCL-Ch blend, decellularized BP, and the biohybrid samples to identify the differences in their functional groups. XPS was used to determine the

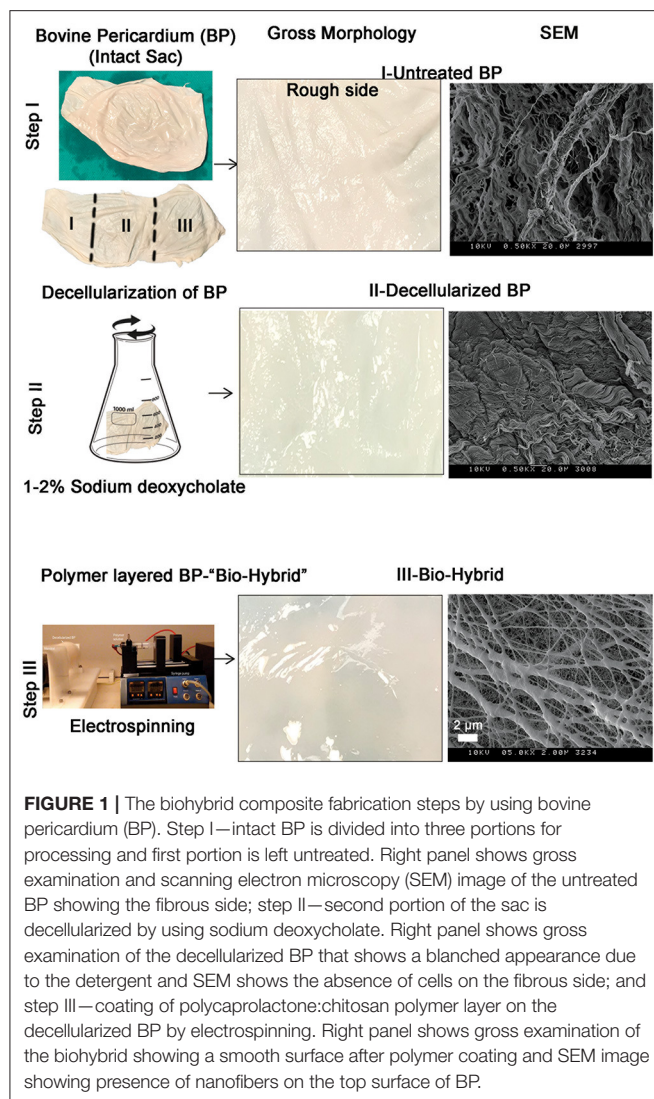
elemental and chemical composition of each material. Sample preparation techniques and details of each method are provided in **Supplementary Section 1.2**.

Core-Polymer Peel and Shear Strength

Strength of the polymer-core interaction was quantified by using two methods—a custom setup to measure the tangential peel force required to delaminate the polymer off the decellularized core and a second experiment in which tubes of the material were prepared and mounted into a flow loop to induce shear stress on the polymer. Details of both the setups are provided in **Supplementary Section 1.3**. The peel force was plotted against time and the instance of peeling was defined as a point when a sharp change in the force-displacement curve was observed. Peel strength was then calculated as the load imposed tangentially at the time of peel, to the longitudinal cross-sectional area of the material (width × length). In the flow experiments, a shear stress of 15 dynes/sq cm was imposed on the inner walls of the tube made from this material, with a glycerin-water mixture with viscosity equivalent to that of blood. The conduits were exposed to flow for 24 h, after which they were removed and examined with SEM. In another experiment, the conduit was constricted to form a 50% stenosis, to create high velocity flow through the channel and downstream recirculating zones and the experiment was repeated.

Mechanical Testing

Unconstrained uniaxial testing was performed on untreated BP ($n = 7$), decellularized BP ($n = 7$), and the biohybrid material ($n = 7$). A dog-boned shape die (W: 5 mm × L: 30 mm) was used to cut uniform samples, oriented so the polymer fibers were aligned with the loading direction. Thickness of the samples were measured at multiple regions with a digital caliper and averaged to get an estimated sample thickness. Prior to testing, graphite markers were placed on the sample for optical strain measurements. The sample was mounted in a universal testing machine (Test Resources 100Q, Shakopee, Minnesota, USA) and preconditioned for 10 cycles, with 50% of maximum strain in the elastic region for 10 cycles. The samples were then loaded to failure at a strain rate of 10 mm/min. From the resultant stress-strain data, the uniaxial ultimate tensile strength (UTS), ultimate tensile extensibility (UTE), and the tangential moduli at the upper and lower response regions were calculated and compared between the groups. Constrained uniaxial testing was also performed on a biaxial mechanical testing system (CellScale Biomaterials Testing, Waterloo, Ontario, Canada) with 6 mm × 6 mm samples mounted by using rakes. Sample thicknesses were measured as described above. Four graphite optical markers were placed on the surface of the sample for optical strain measurements, and the samples were immersed in phosphate-buffered saline (PBS) maintained at 37°C throughout testing. All the tissue samples underwent 7 cycles of preconditioning, until hysteresis was absent. The samples were then constrained (fixed) in one direction (axial/circumferential) and then loaded to 10 and 20% strain in the orthogonal direction while recording force and marker positions. The green strains were measured, and the 2nd Piola-Kirchoff stress was calculated. Lastly, samples were loaded



equibiaxially by stretching the samples to 10% strain in both the directions uniformly while recording force and optical marker locations to measure green strain and calculate 2nd Piola-Kirchoff stress. Data were fit to a Fung's exponential strain energy function through minimization of an objective function to estimate best fit model parameters. The relationship between the axial and circumferential directions was assessed by using Fung's model coefficients to calculate an anisotropy index (*AI*), where a value of 1 would indicate the tissue was isotropic and values closer to 0 would suggest increasing material anisotropy. Further details can be found in **Supplementary Section 1.4**.

Cell Adhesion Study

Porcine mitral valve interstitial cells were isolated and seeded onto the material to assess their attachment to the surface. Though human valve cells would be ideal, we did not have access to these materials. Porcine mitral valves were used to isolate cells to in view of future animal testing of the biohybrid and due to

complexity to procure normal human valves. Techniques used to isolate the cells are described in **Supplementary Section 1.5**. Forty-eight hours after seeding the cells onto the material, the materials were fixed and stained with rhodamine phalloidin and DAPI. Retainment and viability of cells were observed under a microscope (Axioscope A1, Carl Zeiss Microscopy, LLC, USA).

Hemocompatibility

Hemocompatibility of the bio-hybrid and decellularized BP was assessed by percentage hemolysis assessment assay, clot formation assay, and platelet adhesion assays. Fresh porcine whole blood was collected with ethylenediaminetetraacetic acid (EDTA) (1.6 g/l) and maintained under constant agitation. Porcine blood was used as human blood to the desired volumes was not available. For hemolysis studies, sterile samples were incubated with 5 ml whole blood for 30 min at 37°C. One cc of blood was sampled at baseline and at the end of the experiment and percentage hemolysis was calculated as (free Hb/total Hb) × 100. To assess clot formation, the decellularized BP and the biohybrid samples were incubated in constantly agitated whole blood at 37°C for 30 min. Clot formation was assessed visually. For platelet adhesion assay, platelets were isolated from 30 ml whole blood by centrifugation at 2,000 rpm for 12 min and the supernatant was centrifuged at 5,000 rpm for 15 min. The platelet pellet was resuspended in 2 ml of platelet-poor plasma and 500 µl of platelet suspension was added to the samples. Samples were kept in shaker incubator for 30 min at 37°C at 100 rpm, fixed in formalin for 30 min, and stored in 70% ethanol. SEM was used to image adhered platelets on the surface of these materials.

Statistical Analysis

Statistical analysis was performed in GraphPad Prism software version 7 (GraphPad Software Incorporation, San Diego, California, USA). All the data were tested for normality by using the Shapiro-Wilk normality test. The untreated BP, decellularized BP, and the biohybrid groups were compared by using the Wilcoxon matched-pairs signed rank test for collagen, GAG, and elastin estimation. For DNA estimation data, a paired *t*-test was used for comparison between the untreated and decellularized groups. For the uniaxial and biaxial mechanical testing, one-way ANOVA was used to test the differences between the three groups tested. All the *p* < 0.05 were considered as statistically significant.

RESULTS

The bio-hybrid scaffold was fabricated by electrospinning PCL-Ch nanofibers onto the rough side of decellularized BP. The three groups of materials used for *in-vitro* experiments (untreated BP, decellularized BP, and the biohybrid) were characterized by gross morphology and surface characteristics, as shown in **Figure 1**. The untreated BP had a fibrous appearance both in the gross observation and electron microscopy, which also showed the presence of cells (**Figure 1—Step I**). The decellularized BP had fibrous structure on electron microscopy and in gross morphology and appeared blanched due to the treatment with detergent. Gross observation of the biohybrid showed a smooth glistening surface and the presence of polymer nanofibers in SEM

(Figure 1—Step III). The detailed characterization of the polymer nanofibers has been reported previously (44).

Decellularization of BP and ECM Characterization

Decellularization was a prerequisite for the fabrication of the bio-hybrid scaffold and decellularized BP was analyzed for acellularity and ECM integrity as shown in schematic Figure 2A. H&E and DAPI staining showed the absence of nuclei in the decellularized BP compared to the untreated BP (Figures 2A–F). DNA content significantly decreased after decellularization from 158.6 ± 115.1 to 49.06 ± 41.1 ng/mg ($p < 0.05$) in the untreated BP and decellularized BP, respectively (Figure 2D). Major ECM components were preserved after decellularization and after biohybrid fabrication as shown by histology and ECM assays (Figures 2G–K). Collagen did not significantly decrease after decellularization and the hybrid tissue fabrication (Figure 2G). Collagen was quantified at 5.6 ± 0.58 , 5.0 ± 0.64 , and 5.5 ± 0.44 $\mu\text{g}/\text{mg}$ in the untreated BP, decellularized BP, and the bio-hybrid, respectively. Collagen retention was also seen in trichrome staining indicated by blue fibrils, as shown in Figures 2G–I. Similarly, elastin and GAG did not significantly decrease (Figures 2J–O) after fabrication of the bio-hybrid. GAG and elastin concentration were 58.9 ± 43.31 , 74.29 ± 58.79 , and 59.14 ± 63.39 $\mu\text{g}/\text{mg}$ and quantified as 8.73 ± 2.48 , 8.84 ± 3.83 , and 5.43 ± 1.7 $\mu\text{g}/\text{mg}$ in the untreated BP, decellularized BP, and the bio-hybrid, respectively. Figures 2B–F show the reduction of nuclei in the decellularized BP in comparison to the untreated BP, both quantitatively and qualitatively. Large variability was observed in the ECM protein components due to the heterogeneity in the pericardia between animals, and the relatively smaller sample size. Such heterogeneity was reported by other studies as well (43, 45).

Polymer-Tissue Interface Characterization

Scanning electron microscopy images of the untreated BP, decellularized BP, and the biohybrid are shown in Figures 3A–C. Bovine pericardial surface depicts cells integrated with the fibers (Figure 3A), whereas decellularization removed the cells while preserving the matrix architecture (Figure 3B). The biohybrid surface depicts nanofibers overlaid on the core and covering it (Figure 3C). The individual polymer blend nanofibers electrospun on aluminum foil are approximately 134.68 ± 49.4 nm (data not shown here) that fuse during the hybrid tissue preparation to form thicker fibers. Figures 3D–F depict the interface between the polymer and the matrix core and a SEM image of the cross-section depicting adherence of the polymer to the underlying matrix core. XPS results of each of the materials are shown in Figure 3G, which provide elemental analysis in a quantitative manner. In the bio-hybrid material, new peaks corresponding to C=O, C-O, and C-N were observed, which were not seen in the decellularized BP alone or the polymer blend alone. FTIR data in Figure 3H depict the spectra of the newly formed chemical bonds between the polymer and the underlying ECM. Two new peaks at 1548.8 and 1638.2 cm^{-1} corresponding to the amide groups and two new peaks

at 877.1 and 1044.2 cm^{-1} corresponding to C–O–C stretch were measured.

Peel Strength of the Bio-Hybrid

Results of the peel strength and shear-induced delamination experiments are shown in Figure 4. The load required to peel the polymer from the surface of the matrix core is given in Figure 4A from the four distinct bio-hybrid samples ranging from 40 to 75 g, with an average force of 56.13 ± 11.87 mN/mm² g required to delaminate the polymer. The samples induced with two different shear stress conditions are shown in Figure 4B, depicting the cylindrical sample with and without a constriction. SEM images of the luminal surfaces of the decellularized BP and the biohybrid, with and without flow, are shown in Figure 4C and Supplementary Figure 1. At 15 and 30 dynes/cm² of shear stress, disarray of the decellularized fibers was observed, with higher damage associated with higher shear rates. In the bio-hybrid, the polymer nanofibers did not peel or disrupt, but formed a more uniform layer on the tissue, aligned along the flow direction. In either case, the polymer was not delaminated from the underlying pericardium.

Mechanical Testing of the Biohybrid Composite Material

Unconstrained uniaxial mechanical testing of the untreated BP, decellularized BP, and the bio-hybrid samples did not show any difference in the ultimate tensile strength (untreated BP: $18,000 \pm 4,200$ kPa, decellularized BP: $20,000 \pm 6,600$ kPa, and the bio-hybrid: $20,000 \pm 6,600$ kPa), as shown in Figure 5A. However, there was a significant increase in the tensile extensibility (Figure 5B) of the biohybrid compared to the untreated BP (untreated BP: $18 \pm 3.7\%$, decellularized BP: $23 \pm 9\%$, and the bio-hybrid: $35 \pm 2\%$). While constraining the samples by 10% in the axial direction and stretching in the circumferential direction to 10%, the bio-hybrid material had an increased upper and lower tangential moduli compared to BP and decellularized BP [bio-hybrid upper tangent modulus (UTM) and lower tangent modulus (LTM) = $3,071 \pm 693$ and $1,481 \pm 289$ KPa; decellularized BP UTM and LTM = 930 ± 370 and 467 ± 174 KPa; and untreated BP UTM and LTM = 435 ± 129 and 200 ± 42 KPa], but was not evident when constraining the sample by 20% or when constrained in the circumferential direction and loaded in the axial direction for either condition (Figure 6). Results from equibiaxial testing are shown in Figures 5C,D, which highlight the native intraspecimen variability in mechanical response of BP that leads to samples with large variations in mechanical properties, which limited statistical findings. Supplementary Figure 3 depicts the biaxial stress strain curves for all the samples tested. The Fung model was appropriately fitted to each individual data sets with an average root mean square error (RMSE) of 9.49 ± 2.53 kPa, 11.11 ± 9.97 kPa, and 13.74 ± 15.22 kPa for the untreated BP, decellularized BP, and the bio-hybrid materials, respectively. Decellularization of BP trended toward an increase in material anisotropy (AI: 0.32 ± 0.15) compared to untreated BP (AI: 0.55 ± 0.21), although not statistically significant. Deposition of

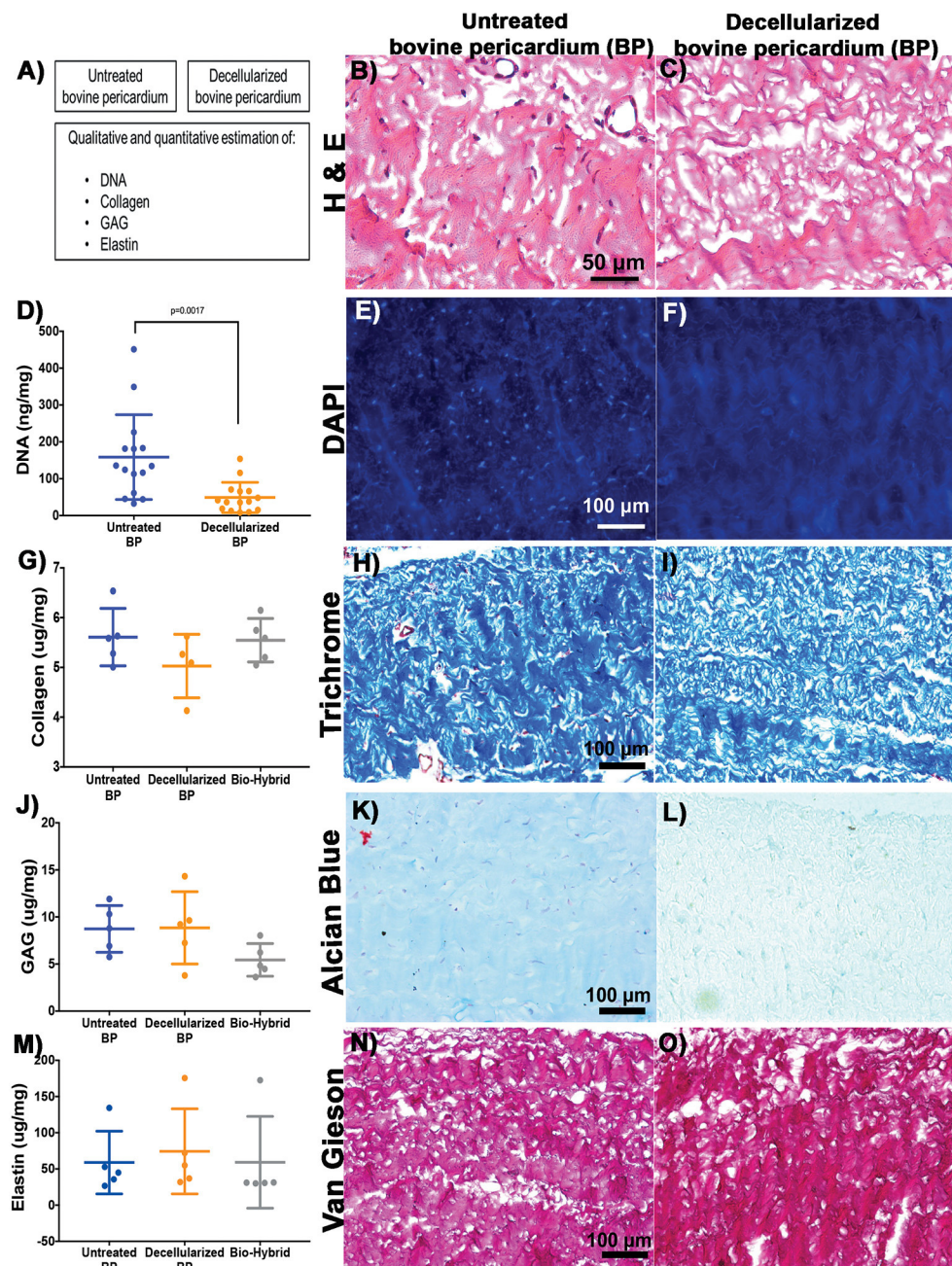


FIGURE 2 | Characterization of the untreated BP and decellularized BP by using histopathology and biological estimation of extracellular matrix proteins. **(A–C)** Schematic representation of the characterization and H&E staining showing absence of cells in the decellularized BP. **(D–F)** Quantification of total DNA showing significant reduction in the decellularized BP and 4,6-diamidino-2-phenylindole (DAPI) staining showing absence of DNA in the decellularized BP. **(G–I)** Quantification of collagen showing no reduction of collagen in the decellularized BP and the biohybrid and trichrome staining showing presence of collagen represented by blue color in the decellularized BP. **(J–L)** Quantification of glycosaminoglycans (GAGs) showing no significant reduction of GAGs in the decellularized BP and the biohybrid and Alcian blue staining showing presence of GAG represented by cyan color in the decellularized BP. **(M–O)** Quantification of elastin showing no significant reduction of GAGs in the decellularized BP and the biohybrid and Verhoeff's Van Gieson staining showing presence of elastin represented by black fibers in the decellularized BP.

the PCL/Ch nanofibers on the biohybrid appeared to partially restore the AI of the material ($AI: 0.45 \pm 0.25$) to that of BP prior to decellularization, although not statistically significant (Table 1).

Biocompatibility and Hemocompatibility of the Biohybrid

The *in-vitro* biocompatibility of the bio-hybrid composite is shown in Figures 7B,C where the bio-hybrid and decellularized

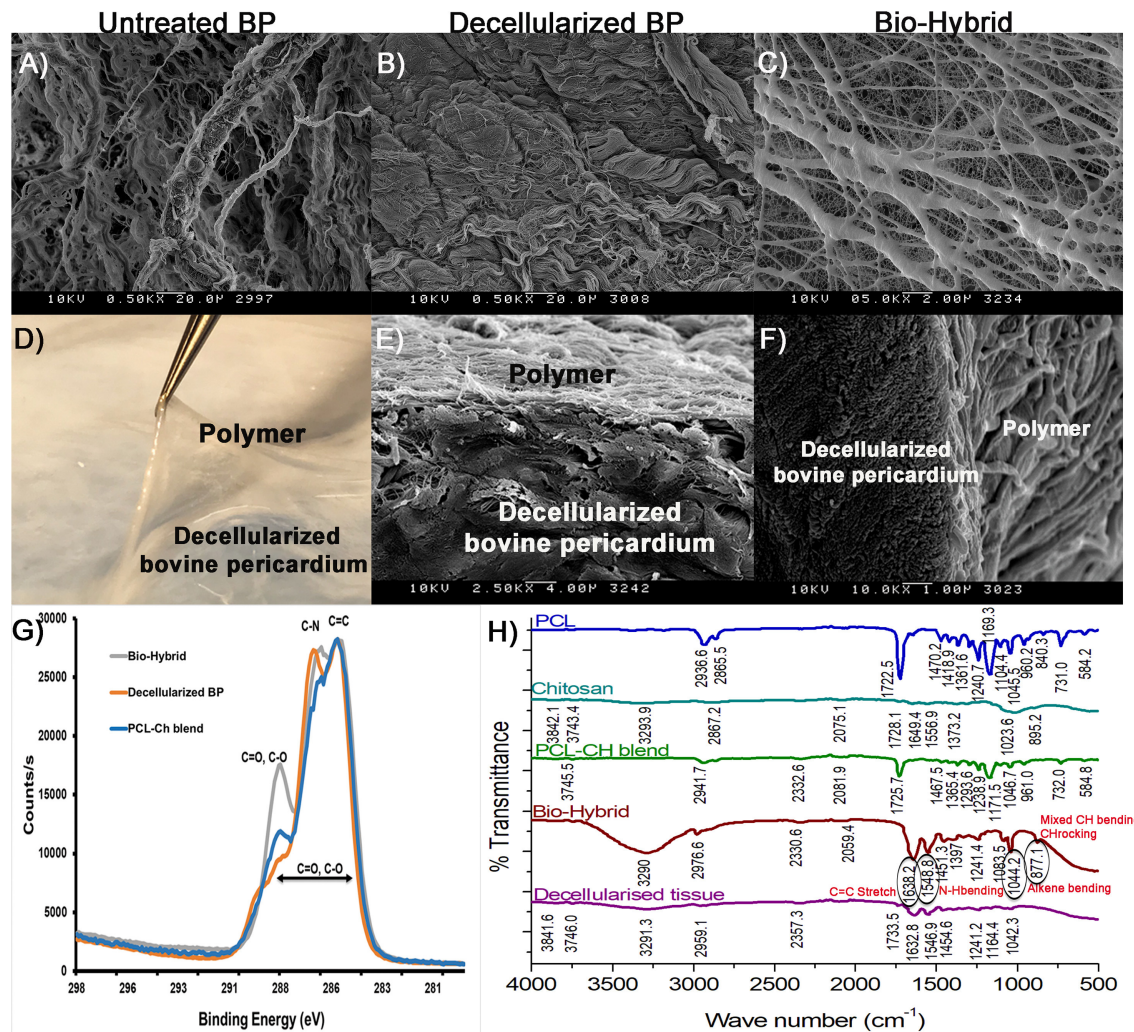


FIGURE 3 | Polymer-tissue interface characterization in the biohybrid composite. **(A–C)** SEM images of the untreated BP, decellularized BP, and the biohybrid showing the presence of cells in the untreated BP, absence of cells in decellularized BP, and coating of electrospun polymer nanofibers on the decellularized BP in the biohybrid composite, **(D–F)** photograph of the biohybrid composite showing lifting of polymer from the decellularized BP followed by SEM images of the cross-sectional views of the biohybrid showing presence of polymer fibers at the interface without separation at the interface, **(G)** carbon scanning of the biohybrid, decellularized BP, and polycaprolactone:chitosan blend by X-ray photoelectron spectroscopy showing difference in binding energy corresponding to peaks C=C, C=O, C-O, and C-N in the biohybrid, and **(H)** Fourier transform IR spectroscopy of polycaprolactone, chitosan, blend, the biohybrid, and decellularized BP showing unique peaks in the biohybrid corresponding to changes in the C=C, C=O, N-H, and C-H groups.

BP showed similar and better attachment of porcine valve interstitial cells whereas the untreated BP (**Figure 7A**) showed less attachment of cells seen visually on these samples. **Figures 7D–H** show *in-vitro* hemocompatibility of the biohybrid by using three different tests. The bio-hybrid and the decellularized BP samples did not show any hemolysis (0 g/dl) of cells upon agitating with fresh blood as shown in **Figure 7D**. Clots did not form on the decellularized BP and the bio-hybrid samples demonstrating unchanged hemocompatibility of the bio-hybrid with the addition of polymer to the decellularized core (**Figures 7E,F**). Additionally, there was minimal platelet adhesion on the bio-hybrid in comparison to the decellularized BP core as shown in the SEM images (**Figures 7G,H**).

DISCUSSION

Data from this study demonstrate the feasibility of the biohybrid composite for use as a cardiovascular tissue substitute. Combining a non-reactive, base material such as decellularized ECM with native three-dimensional structure, with a reactive and slowly biodegrading polymeric covering, it provides a new approach for potential *in-situ* cardiovascular tissue engineering. Though this study does not demonstrate *in-vivo* results in support of this claim, the *ex-vivo* measurements demonstrate good mechanical strength of the layered scaffold, biocompatibility that is evident from cellular adhesion and viability, and hemocompatibility from minimal platelet adhesion

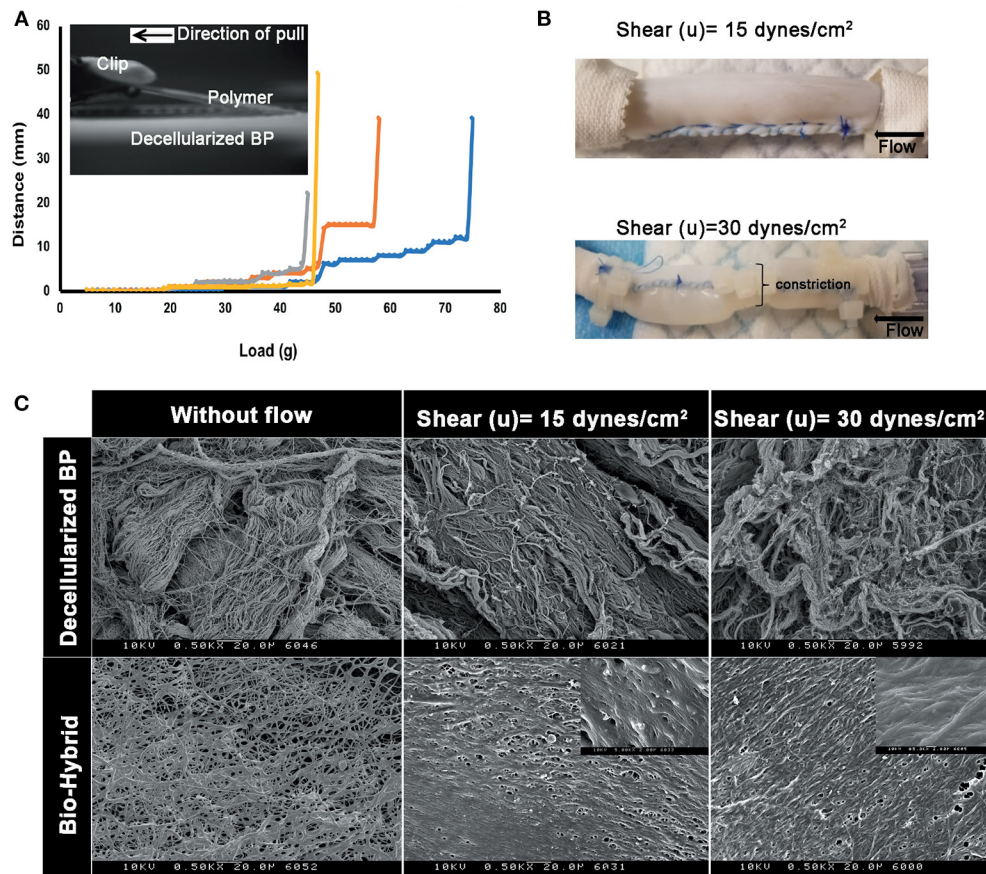


FIGURE 4 | Peel strength of the polymer in the biohybrid. **(A)** Peel profile of the biohybrid composite showing the load measured to peel the polymer in the biohybrid from the decellularized BP by using a customized setup where the polymer was peeled by using a clip attached to a weight hanger and a pulley, **(B)** image of the biohybrid composite conduit subjected to low shear and high shear (a portion of sample constricted to about 50% of original diameter) experienced by a normal artery (15 dynes/cm²) in a continuous flow loop, and **(C)** SEM images of the decellularized BP samples subjected without any shear (without flow), low (15 dynes/cm²) and high shears (30 dynes/cm²) showing extent of damage of the extracellular matrix fibers due to the shear. SEM images of the biohybrid samples subjected without any shear (without flow), low and high shears showing non-delamination and smoothening of the polymer surface when subjected to shear.

in blood flow loops. Altogether, this *ex-vivo* data demonstrate the potential feasibility of this new approach.

The choice of the two materials used in this study builds upon current clinical knowledge supporting the use of these materials independently in the cardiovascular system. Glutaraldehyde-treated BP is currently the gold standard in cardiac surgery, as it has good mechanical strength and stability, adequate shelf-life, and non-thrombogenicity (42, 46–48). Despite these favorable characteristics, structural deterioration and calcification are observed, primarily due to the host immune response to the glutaraldehyde fixative and the cells within the tissue (6, 48, 49). This issue was addressed previously, by decellularization of the BP, reducing the total DNA content, and maximizing the native ECM protein content such as collagen, elastin, and GAGs (50–52). Despite these measures, the mechanical strength upon decellularization is lessened, with uncontrolled material anisotropy from changes in the fiber architecture and alignment (53). Structural degradation of the decellularized material is a risk, decreasing its use in the cardiovascular system.

In the bio-hybrid material, under uniaxial loading, increased material extensibility along the fiber direction was observed, without significant bulk stiffening. When constrained in the axial direction with a 10% stretch and loading in the circumferential direction (fiber direction), the material appeared to stiffen. When the axial stretch was increased to 20%, this stiffening was not observed, suggesting that the polymer fibers were either reoriented to bear load or damaged at these loads. It is likely that reorientation had occurred at higher loads, as we did not observe any damage to the polymeric layer. The *in-vitro* scaffold stability and degradation of the decellularized BP and the bio-hybrid were previously studied by us and demonstrated that both the materials did not degrade significantly in stimulated physiological conditions (37°C, pH 7.0) for up to 30 days (44, 54). Also, the ultimate tensile strength of human cardiovascular tissue in uniaxial tension ranges from 1 to 3 MPa and the bio-hybrid scaffolds with the 70 μm thick polymer layer is significantly stronger as seen in **Figure 5** (55, 56). With a degradation of about 7% in 30 days [from our previous study (54)], we assume

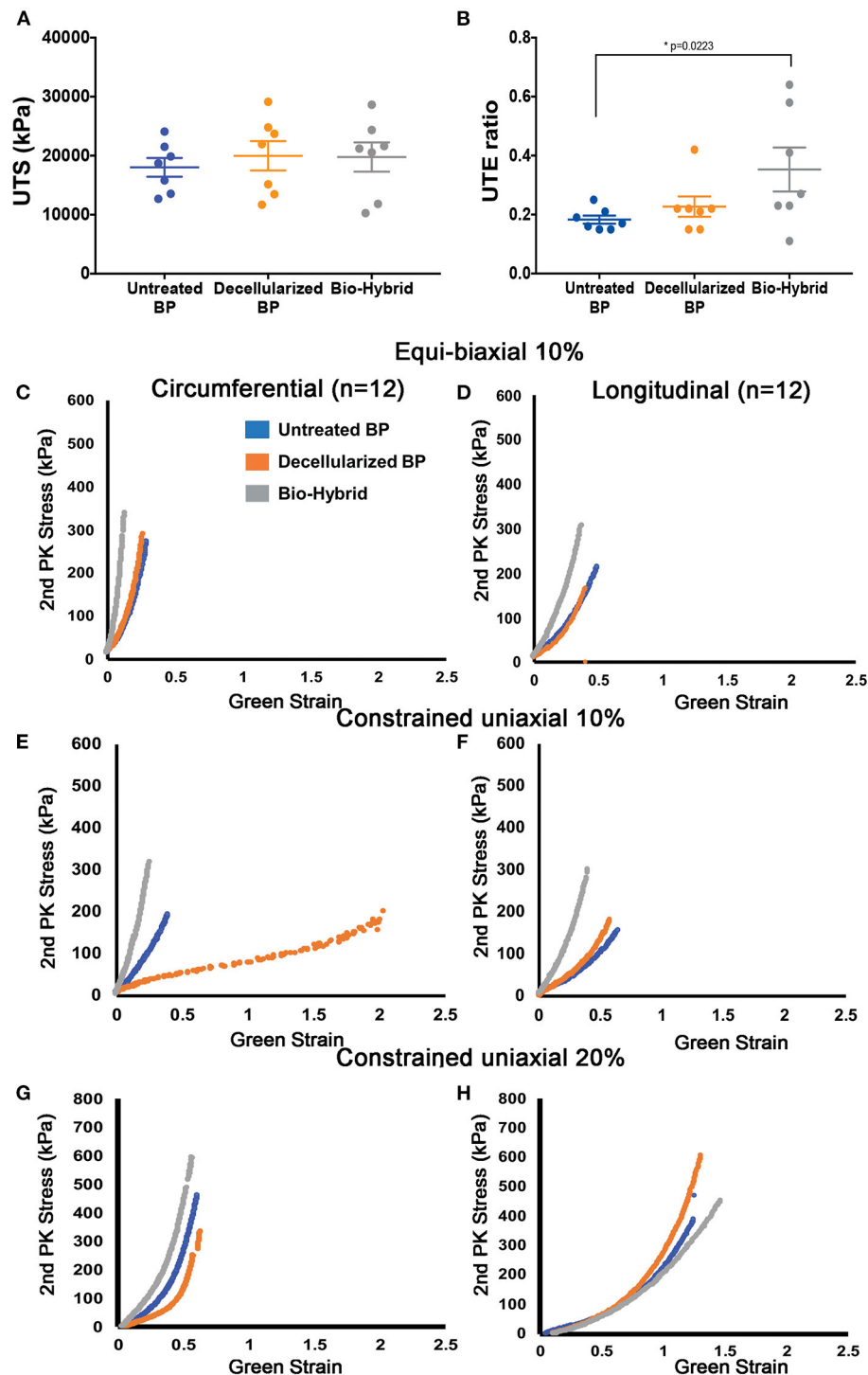
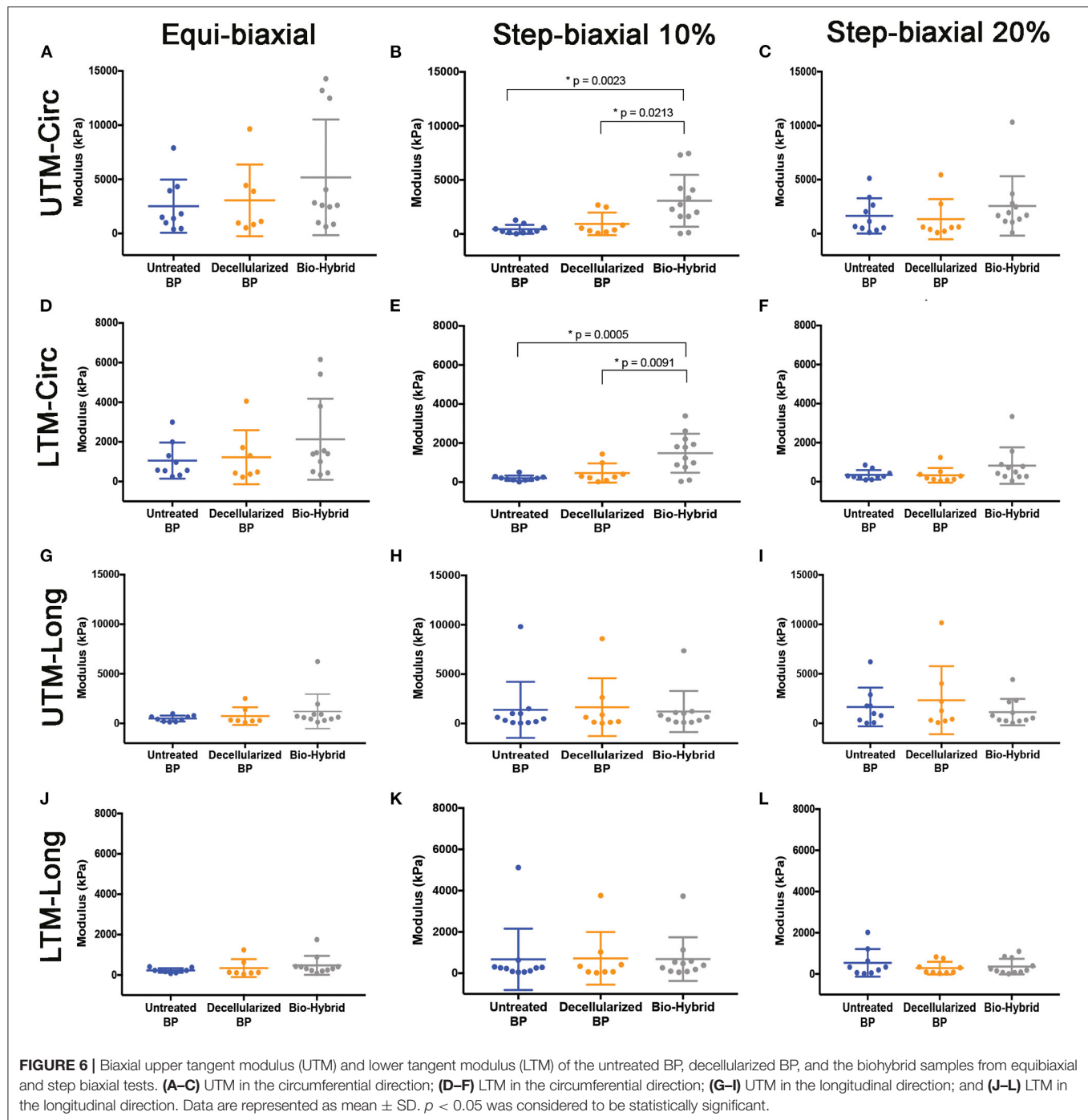


FIGURE 5 | *In-vitro* mechanical properties of the untreated BP, decellularized BP, and the biohybrid composite. **(A,B)** Uniaxial tensile strength (kPa) and uniaxial tensile extensibility ratio of the materials showing no difference in the tensile strength and a significant increase in the extensibility in the biohybrid, **(C,D)** equibiaxial (10%) testing of the three groups showing a stiffer response of the biohybrid in both the circumferential and longitudinal directions and similar response of the fresh BP and decellularized BP, **(E,F)** step biaxial testing with 10% strain in the direction of testing showing stiffer response of the biohybrid than the other two groups in both the directions whereas the decellularized BP is more compliant in the circumferential direction, and **(G,H)** step biaxial testing with 20% strain in the direction of testing showing stiffer response of the biohybrid in the circumferential direction followed by the untreated BP and decellularized BP and longitudinal direction shows stiffer response of the decellularized BP with absence of aligned polymer nanofibers in the biohybrid.



that the biohybrid will most likely remain stable and allow ECM remodeling when implanted *in vivo*, similar to other cardiovascular tissue replacement biomaterials (21, 57, 58). The *in-vivo* degradation is likely to differ from *in-vitro* conditions due to the complex interplay of immune response, expression of matrix degradation enzymes, and macrophage expression that is absent in *in-vitro* experiments (58). It is known that synthetic biomaterials are known to experience chronic inflammatory response and the decellularized tissues are less immunogenic,

but are weaker and more susceptible to structural degradation. Bio-hybrid scaffold material that has a non-degradable bovine pericardial core (degradation time about 10 years) with a biodegradable polymer coating (PCL degradation time is about 2 years) would possibly experience intermediary inflammatory response and provide enough duration for matrix remodeling as cardiovascular substitute material similar to the other hybrid scaffolds (23, 25, 58–61). Previous work has shown that PCL:Ch vascular grafts, by using similar concentrations of the polymers,

TABLE 1 | Fung model parameters and anisotropy metric.

| | c | a₁ | a₂ | a₃ | RMSE (kPa) | AI |
|-------------------|--------------------|----------------------|----------------------|----------------------|-------------------|-------------|
| Fresh BP | 528.9 ± 650.22 | 11.56 ± 24.19 | 7.06 ± 15.89 | 1.29 ± 2.95 | 9.49 ± 2.53 | 0.55 ± 0.21 |
| Decellularized BP | 19058.2 ± 46137.75 | 4.12 ± 4.15 | 1.17 ± 1.03 | 0.26 ± 0.22 | 11.11 ± 9.79 | 0.32 ± 0.15 |
| Biohybrid | 278.42 ± 302.94 | 25.33 ± 48.76 | 5.78 ± 7.83 | 1.92 ± 3.31 | 13.74 ± 15.22 | 0.45 ± 0.25 |

Fung exponential model parameters and anisotropy index (AI) for the each experimental group. RMSE is the root mean square error. Data are presented as mean ± SD.

showed good vascular remodeling (25); however, this has not been studied as a cardiovascular replacement tissue. FTIR and XPS data in this study demonstrate that the polymeric layer also formed bonds with the underlying collagen proteins in the decellularized matrix, which may promote anchoring of both the layers and reorientation under loading. Hydrogen bond formation between the hydroxyl group of Ch and the ester group of PCL were observed, which, in turn formed amide linkage between the PCL:Ch and decellularized core as shown in XPS and FTIR (Figure 3).

Polycaprolactone was chosen, as it is Food and Drug Administration (FDA)-approved synthetic polymer with tunable mechanical properties, hydrophobicity that inhibits platelet attachment and slow degradation making it suitable for use in the cardiovascular system. However, the inherent hydrophobicity does not enable cellular attachment and, thus, promote *in-situ* host tissue engineering of the scaffold (59). Ninety percent deacetylated Ch at a very low concentration (1%) was added to PCL, increasing its hydrophilicity to an extent that cellular infiltration and survival may be possible. Ch has a structure similar to native GAGs, which may provide the moieties required for cellular adhesion and further infiltration. Recently, PCL-Ch small-diameter vascular grafts, with high concentrations of Ch, were used successfully in sheep up to 6 months (25).

The polymer could be overlaid on the matrix in several ways, but electrospinning provided an approach that can create a 3-dimensional surface topography that would enable cellular attachment (44, 54). Electrospinning was preferred than commonly used dip coating for polymer-tissue combination due to the potential damage from organic solvents (41, 55). Additionally, the polymer deposition on the BP in this study in its native 3D form negates the risk of degeneration and calcification that has been otherwise seen previously in cryopreserved tissues (56, 62). The coating of a biocompatible polymer on decellularized tissue would act as an immune barrier to antigenic proteins present after decellularization that has shown to be beneficial to improve cellular adhesion and mechanotransduction that, in turn, improves *in-vivo* remodeling (31, 40, 41). Nanofiber-microdimension architecture has been shown by others to improve cellular adhesion with stronger attachment in comparison to the smoother biomaterial surfaces due to higher surface to volume ratio and similar 3D topography of natural tissues leading to enhanced deposition of ECM proteins (63, 64). We, thus, chose to electrospun PCL:Ch nanofibers (134.68 ± 49.4 nm) to mimic the surface similar to natural ECM fibers that fuse to form around

300 to 500 μm fibers during the bio-hybrid processing that allowed excellent cellular attachment and alignment on the bio-hybrid compared to the decellularized BP and untreated BP (Figure 7). While this investigation was limited to this specific polymeric blend, other polymers that are combined with small molecules can be used in the future for specific targeted outcomes.

With the specified modifications to the pericardial preparation, *in-vitro* biocompatibility studies showed better cellular attachment onto the bio-hybrid (Figure 7). The cellular attachment is likely from the hydrophilicity that the PCL:Ch blend imparts, which is not seen in the PCL-based biomaterials (59). The biohybrid material also exhibited adequate *in-vitro* hemocompatibility with no hemolysis or clot formation, and minimal platelet attachment when the material was agitated in blood (Figure 7). The hemocompatibility of the polymeric blend can be attributed to the hydrophobicity of the PCL and smooth surface of the polymer that does not allow the platelets to adhere. Such behavior was shown by others using this PCL:Ch combination for vascular tissue engineering (25, 65). In a dynamic *in-vitro* setup, the polymer layer did not delaminate when subjected to shear equivalent to that of a normal artery in a closed flow loop setup (Figure 4), suggesting its use as a cardiovascular replacement material. The lack of polymer delamination in the flow loop setup correlated with data from the peel strength experiments, which confirmed that adhered polymer layer in the bio-hybrid could withstand physiological flow (Figure 4). The biocompatible and hemocompatible bio-hybrid material with a time-bound degradable polymer layer (since PCL has a degradability of around 2 years *in vivo*) is hypothesized to provide a favorable interface to attract cells and at the same time provides matrix stability over the first few weeks to months after implantation that may redirect it toward remodeling and not fibrosis.

From a translational perspective, the proposed bio-hybrid composite material has several benefits, with a strong decellularized core that provides the mechanical strength for the tissues, while the degradable polymeric sacrificial layer that can enable anisotropy, acute and short chronic immune response until degradation, and cellular honing is achieved. This ensures that as the scaffold remodels, adequate mechanical strength to sustain the hemodynamic forces is available. Thus, the proposed material could be used in high pressure environments as well, such as for patching the carotid artery after endarterectomy, as arterial grafts in children, and potentially as valve leaflets as well. The clinical relevance of this material as

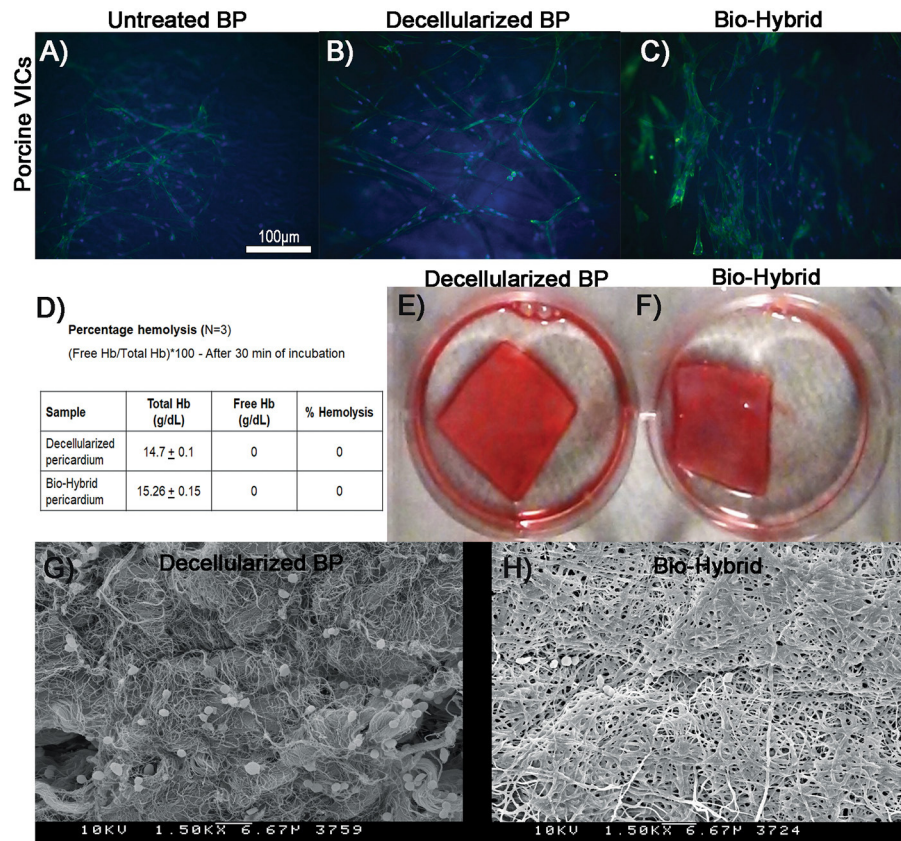


FIGURE 7 | *In-vitro* biocompatibility and hemocompatibility studies of the decellularized BP and the biohybrid composite. **(A–C)** *In-vitro* biocompatibility of the untreated glutaraldehyde-fixed BP, decellularized BP, and the biohybrid by cell adhesion assay. Cell adhesion of porcine valve interstitial cells showing good attachment on the decellularized BP and the biohybrid samples compared to untreated glutaraldehyde-fixed BP, **(D)** percentage hemolysis of cells on the decellularized BP and the biohybrid showing no hemolysis on both the samples when incubated with fresh porcine blood for 30 min, **(E,F)** clot formation assay showing no clots on both the decellularized BP and the biohybrid samples after 30 min of incubation with blood, and **(G,H)** SEM images of the decellularized BP and the biohybrid incubated with platelets showing very minimal platelet adhesion on the biohybrid compared to the decellularized BP.

a patch or shaped into different implants and their functional efficacy requires long-term studies in animals, which is our next step.

STUDY LIMITATIONS

As with any experimental study, some limitations should be considered. The materials and methods used in this study are off-the-shelf materials and custom build devices and, thus, are not built per good manufacturing practices (GMPs) standards. Thus, a higher degree of variability between samples is observed. Moreover, there is inter- and intraspecimen variability in native BP, which makes batch processing inconsistent and limits statistical findings of material responses. In future, the most homogenous region of BP will be considered for making the bio-hybrid. Secondly, the *in-vivo* large animal studies are needed to study the immune response along with long-term efficacy and remodeling. Lastly, the efficacy of the bio-hybrid can be better explained when compared to commercially available glutaraldehyde fixed and decellularized tissues that are used clinically.

CONCLUSION

The proposed bio-hybrid approach to combine a natural decellularized pericardium, with polymeric nanofibers, has adequate mechanical strength, biocompatibility and hemocompatibility, making it a potentially translatable cardiovascular tissue substitute.

DATA AVAILABILITY STATEMENT

The original contributions presented in the study are included in the article/**Supplementary Material**, further inquiries can be directed to the corresponding author.

AUTHOR CONTRIBUTIONS

JM worked on the idea generation, experimental design, execution of experiments, data analysis, and manuscript preparation. DX, VW, AA, BL, and DC contributed to the experimental work and data analysis of this study. MP

contributed to the experimental design, data validation, and editing of the manuscript. All authors edited and approved the final version of the manuscript.

FUNDING

This study was supported by grants from the American Heart Association (19POST34380522) and an infrastructure support

from the Carlyle Fraser Heart Center at Emory University Hospital Midtown.

SUPPLEMENTARY MATERIAL

The Supplementary Material for this article can be found online at: <https://www.frontiersin.org/articles/10.3389/fcvm.2022.807255/full#supplementary-material>

REFERENCES

- Siddiqui RE, Abraham JR, Butany J. Bioprosthetic heart valves: modes of failure. *Histopathology*. (2009) 55:135–44. doi: 10.1111/j.1365-2559.2008.03190.x
- Shoenfeld NA, Connolly R, Ramberg K, Valeri CR, Eldrup-Jorgensen J, Callow AD. The systemic activation of platelets by Dacron grafts. *Surg Gynecol Obstet*. (1988) 166:454–7.
- Ando M, Takahashi Y. Ten-year experience with handmade trileaflet polytetrafluoroethylene valved conduit used for pulmonary reconstruction. *J Thorac Cardiovasc Surg*. (2009) 137:124–31. doi: 10.1016/j.jtcvs.2008.08.060
- Cohn LH, Collins JJ, DiSesa VJ, Couper GS, Peigh PS, Kowalko W, et al. Fifteen-year experience with 1678 Hancock porcine bioprosthetic heart valve replacements. *Ann Surg*. (1989) 210:435–43.
- Iop L, Palmosi T, Dal Sasso E, Gerosa G. Bioengineered tissue solutions for repair, correction and reconstruction in cardiovascular surgery. *J Thorac Dis*. (2018) 10:S2390–411. doi: 10.21037/jtd.2018.04.27
- Ozaki S, Kawase I, Yamashita H, Uchida S, Nozawa Y, Takatoh M, et al. A total of 404 cases of aortic valve reconstruction with glutaraldehyde-treated autologous pericardium. *J Thorac Cardiovasc Surg*. (2014) 147:301–6. doi: 10.1016/j.jtcvs.2012.11.012
- Manji Rizwan A, Zhu Lin F, Nijjar Nimrit K, Rayner David C, Korbitt Greg S, Churchill Thomas A, et al. Glutaraldehyde-fixed bioprosthetic heart valve conduits calcify and fail from xenograft rejection. *Circulation*. (2006) 114:318–27. doi: 10.1161/CIRCULATIONAHA.105.549311
- Angell WW, Angell JD, Kosek JC. Twelve-year experience with glutaraldehyde-preserved porcine xenografts. *J Thorac Cardiovasc Surg*. (1982) 83:493–502. doi: 10.1016/S0022-5223(19)37236-8
- Frasca A, Xue Y, Kossar AP, Keeney S, Rock C, Zakharchenko A, et al. Glycation and serum albumin infiltration contribute to the structural degeneration of bioprosthetic heart valves. *JACC Basic Transl Sci*. (2020) 5:755–66. doi: 10.1101/2020.02.14.948075
- Vesely I. The evolution of bioprosthetic heart valve design and its impact on durability. *Cardiovasc Pathol*. (2003) 12:277–86. doi: 10.1016/S1054-8807(03)00075-9
- Butcher JT, Mahler GJ, Hockaday LA. Aortic valve disease and treatment: the need for naturally engineered solutions. *Adv Drug Deliv Rev*. (2011) 63:242–68. doi: 10.1016/j.addr.2011.01.008
- Helder MRK, Kouchoukos NT, Zehr K, Dearani JA, Maleszewski JJ, Leduc C, et al. Late durability of decellularized allografts for aortic valve replacement: a word of caution. *J Thorac Cardiovasc Surg*. (2016) 152:1197–9. doi: 10.1016/j.jtcvs.2016.03.050
- Lin C-H, Hsia K, Ma H, Lee H, Lu J-H. *In vivo* performance of decellularized vascular grafts: a review article. *Int J Mol Sci*. (2018) 19:2101. doi: 10.3390/ijms19072101
- Boyd R, Parisi F, Kalfa D. State of the art: tissue engineering in congenital heart surgery. *Semin Thorac Cardiovasc Surg*. (2019) 31:807–17. doi: 10.1053/j.semtcvs.2019.05.023
- Butcher JT. The root problem of heart valve engineering. *Sci Transl Med*. (2018) 10:eaa5850. doi: 10.1126/scitranslmed.aat5850
- Joudinaud TM, Baron F, Raffoul R, Pagis B, Vergnat M, Parisot C, et al. Redo aortic root surgery for failure of an aortic homograft is a major technical challenge. *Eur J Cardiothorac Surg*. (2008) 33:989–94. doi: 10.1016/j.ejcts.2008.01.054
- Khanna A, Zamani M, Huang NF. Extracellular matrix-based biomaterials for cardiovascular tissue engineering. *J Cardiovasc Dev Dis*. (2021) 8:137. doi: 10.3390/jcdd8110137
- Brown JW, Ruzmetov M, Vijay P, Rodefeld MD, Turrentine MW. Right ventricular outflow tract reconstruction with a polytetrafluoroethylene monocusp valve: a twelve-year experience. *J Thorac Cardiovasc Surg*. (2007) 133:1336–43. doi: 10.1016/j.jtcvs.2006.12.045
- Nappi F, Spadaccio C, Acar C, El-Hamamsy I. Lights and shadows on the Ross procedure: biological solutions for biological problems. *Semin Thorac Cardiovasc Surg*. (2020) 32:815–22. doi: 10.1053/j.semtcvs.2020.04.006
- Bell D, Prabhu S, Betts K, Justo R, Venugopal P, Karl TR, et al. Durability of tissue-engineered bovine pericardium (CardioCel®) for a minimum of 24 months when used for the repair of congenital heart defects. *Interact Cardiovasc Thorac Surg*. (2019) 28:284–90. doi: 10.1093/icvts/ivy246
- Kluin J, Talacua H, Smits AIPM, Emmert MY, Brugmans MCP, Fioretta ES, et al. *In situ* heart valve tissue engineering using a bioresorbable elastomeric implant - From material design to 12 months follow-up in sheep. *Biomaterials*. (2017) 125:101–17. doi: 10.1016/j.biomaterials.2017.02.007
- Shinoka T, Breuer C. Tissue-engineered blood vessels in pediatric cardiac surgery. *Yale J Biol Med*. (2008) 81:161–6.
- Sugiura T, Tara S, Nakayama H, Yi T, Lee Y-U, Shoji T, et al. Fast degrading bioresorbable arterial vascular graft with high cellular infiltration inhibits calcification of the graft. *J Vasc Surg*. (2017) 66:243–50. doi: 10.1016/j.jvs.2016.05.096
- Bockeria LA, Svanidze O, Kim A, Shatalov K, Makarenko V, Cox M, et al. Total cavopulmonary connection with a new bioabsorbable vascular graft: first clinical experience. *J Thorac Cardiovasc Surg*. (2017) 153:1542–50. doi: 10.1016/j.jtcvs.2016.11.071
- Fukunishi T, Best CA, Sugiura T, Shoji T, Yi T, Udelsman B, et al. Tissue-engineered small diameter arterial vascular grafts from cell-free nanofiber PCL/chitosan scaffolds in a sheep model. *PLoS ONE*. (2016) 11:e0158555. doi: 10.1371/journal.pone.0158555
- Zhang BL, Bianco RW, Schoen FJ. Preclinical assessment of cardiac valve substitutes: current status and considerations for engineered tissue heart valves. *Front Cardiovasc Med*. (2019) 6:72. doi: 10.3389/fcvm.2019.00072
- Schoen FJ, Levy RJ. Tissue heart valves: current challenges and future research perspectives. *J Biomed Mater Res*. (1999) 47:439–65. doi: 10.1002/(SICI)1097-4636(19991215)47:4<439::AID-JBM1>3.0.CO;2-O
- Kehl D, Weber B, Hoerstrup SP. Bioengineered living cardiac and venous valve replacements: current status and future prospects. *Cardiovasc Pathol*. (2016) 25:300–5. doi: 10.1016/j.carpath.2016.03.001
- Todesco M, Zardin C, Iop L, Palmosi T, Capaldo P, Romanato F, et al. Hybrid membranes for the production of blood contacting surfaces: physicochemical, structural and biomechanical characterization. *Biomater Res*. (2021) 25:26. doi: 10.1186/s40824-021-00227-5
- Heidenhain C, Weichert W, Schmidmaier G, Wildemann B, Hein M, Neuhaus P, et al. Polymer coating of porcine decellularized and cross-linked aortic grafts. *J Biomed Mater Res Part B Appl Biomater*. (2010) 94:256–3. doi: 10.1002/jbm.b.31650

31. Stamm C, Khosravi A, Grabow N, Schmohl K, Treckmann N, Drechsel A, et al. Biomatrix/polymer composite material for heart valve tissue engineering. *Ann Thorac Surg.* (2004) 78:2084–92; discussion: 2092–3. doi: 10.1016/j.athoracsur.2004.03.106
32. Sun X, Peng W, Yang Z, Ren M, Zhang S, Zhang W, et al. Heparin-chitosan-coated acellular bone matrix enhances perfusion of blood and vascularization in bone tissue engineering scaffolds. *Tissue Eng Part A.* (2011) 17:2369–78. doi: 10.1089/ten.tea.2011.0027
33. Jiang B, Akgun B, Lam RC, Ameer GA, Wertheim JA. A polymer–extracellular matrix composite with improved thromboresistance and recellularization properties. *Acta Biomater.* (2015) 18:50–8. doi: 10.1016/j.actbio.2015.02.015
34. Heydarkhan-Hagvall S, Schenke-Layland K, Dhanasopon AP, Rofail F, Smith H, Wu BM, et al. Three-dimensional electrospun ECM-based hybrid scaffolds for cardiovascular tissue engineering. *Biomaterials.* (2008) 29:2907–14. doi: 10.1016/j.biomaterials.2008.03.034
35. Reid JA, Callanan A. Hybrid cardiovascular sourced extracellular matrix scaffolds as possible platforms for vascular tissue engineering. *J Biomed Mater Res B Appl Biomater.* (2020) 108:910–24. doi: 10.1002/jbm.b.34444
36. Grabow N, Schmohl K, Khosravi A, Philipp M, Scharfschwerdt M, Graf B, et al. Mechanical and structural properties of a novel hybrid heart valve scaffold for tissue engineering. *Artif Organs.* (2004) 28:971–9. doi: 10.1111/j.1525-1594.2004.00007.x
37. Williams C, Budina E, Stoppel WL, Sullivan KE, Emani S, Emani SM, et al. Cardiac extracellular matrix–fibrin hybrid scaffolds with tunable properties for cardiovascular tissue engineering. *Acta Biomater.* (2015) 14:84–95. doi: 10.1016/j.actbio.2014.11.035
38. Fang Q, Gu T, Fan J, Zhang Y, Wang Y, Zhao Y, et al. Evaluation of a hybrid small caliber vascular graft in a rabbit model. *J Thorac Cardiovasc Surg.* (2020) 159:461–73. doi: 10.1016/j.jtcvs.2019.02.083
39. VeDepo MC, Detamore MS, Hopkins RA, Converse GL. Recellularization of decellularized heart valves: progress toward the tissue-engineered heart valve. *J Tissue Eng.* (2017) 8:2041731417726327. doi: 10.1177/2041731417726327
40. Wu S, Liu Y, Cui B, Tang Y, Wang Q, Qu X, et al. [Intravascular biocompatibility of decellularized xenogenic vascular scaffolds/PHBHHx hybrid material for cardiovascular tissue engineering]. *Sheng Wu Gong Cheng Xue Bao.* (2008) 24:610–6.
41. Wu S, Liu Y-L, Cui B, Qu X-H, Chen G-Q. Study on decellularized porcine aortic valve/poly (3-hydroxybutyrate-co-3-hydroxyhexanoate) hybrid heart valve in sheep model. *Artif Organs.* (2007) 31:689–97. doi: 10.1111/j.1525-1594.2007.00442.x
42. Li X, Guo Y, Ziegler K, Model L, Eghbalieh SDD, Brenes R, et al. Current usage and future directions for the bovine pericardial patch. *Ann Vasc Surg.* (2011) 25:561–8. doi: 10.1016/j.avsg.2010.11.007
43. Zouhair S, Dal Sasso E, Tuladhar SR, Fidalgo C, Vedovelli L, Filippi A, et al. A comprehensive comparison of bovine and porcine decellularized pericardia: new insights for surgical applications. *Biomolecules.* (2020) 10:371. doi: 10.3390/biom10030371
44. Jahnvi S, Kumary TV, Bhuvaneshwar GS, Natarajan TS, Verma RS. Engineering of a polymer layered bio-hybrid heart valve scaffold. *Mater Sci Eng C Mater Biol Appl.* (2015) 51:263–73. doi: 10.1016/j.msec.2015.03.009
45. Caballero A, Sulejmani F, Martin C, Pham T, Sun W. Evaluation of transcatheter heart valve biomaterials: biomechanical characterization of bovine and porcine pericardium. *J Mech Behav Biomed Mater.* (2017) 75:486–94. doi: 10.1016/j.jmbm.2017.08.013
46. Senthilnathan V, Treasure T, Grunkemeier G, Starr A. Heart valves: which is the best choice? *Cardiovasc Surg.* (1999) 7:393–7. doi: 10.1016/s0967-2109(99)00026-5
47. Oldenburg WA, Almercy T, Selim M, Farres H, Hakaim AG. Durability of carotid endarterectomy with bovine pericardial patch. *Ann Vasc Surg.* (2018) 50:218–24. doi: 10.1016/j.avsg.2017.11.062
48. Reul GJ, Cooley DA, Duncan JM, Frazier OH, Hallman GL, Livesay JJ, et al. Valve failure with the Ionescu-Shiley bovine pericardial bioprosthesis: analysis of 2680 patients. *J Vasc Surg.* (1985) 2:192–204. doi: 10.1016/0741-5214(85)90189-2
49. Liao J, Joyce EM, Sacks MS. Effects of decellularization on the mechanical and structural properties of the porcine aortic valve leaflet. *Biomaterials.* (2008) 29:1065–74. doi: 10.1016/j.biomaterials.2007.11.007
50. Nordmeyer S, Murin P, Schulz A, Danne F, Nordmeyer J, Kretzschmar J, et al. Results of aortic valve repair using decellularized bovine pericardium in congenital surgery. *Eur J Cardiothorac Surg.* (2018) 54:986–92. doi: 10.1093/ejcts/ezy181
51. Knight RL, Wilcox HE, Korossis SA, Fisher J, Ingham E. The use of acellular matrices for the tissue engineering of cardiac valves. *Proc Inst Mech Eng Part H J Eng Med.* (2008) 222:129–43. doi: 10.1243/09544119JE IM230
52. Choe JA, Jana S, Tefft BJ, Hennessy RS, Go J, Morse D, et al. Biomaterial characterization of off-the-shelf decellularized porcine pericardial tissue for use in prosthetic valvular applications. *J Tissue Eng Regen Med.* (2018) 12:1608–20. doi: 10.1002/term.2686
53. Hwang J, San BH, Turner NJ, White LJ, Faulk DM, Badylak SE, et al. Molecular assessment of collagen denaturation in decellularized tissues using a collagen hybridizing peptide. *Acta Biomater.* (2017) 53:268–78. doi: 10.1016/j.actbio.2017.01.079
54. Jahnvi S, Saravanan U, Arthi N, Bhuvaneshwar GS, Kumary TV, Rajan S, et al. Biological and mechanical evaluation of a bio-hybrid scaffold for autologous valve tissue engineering. *Mater Sci Eng C Mater Biol Appl.* (2017) 73:59–71. doi: 10.1016/j.msec.2016.11.116
55. Hong H, Dong N, Shi J, Chen S, Guo C, Hu P, et al. Fabrication of a novel hybrid heart valve leaflet for tissue engineering: an *in vitro* study. *Artif Organs.* (2009) 33:554–8. doi: 10.1111/j.1525-1594.2009.00742.x
56. Mitchell RN, Jonas RA, Schoen FJ. Pathology of explanted cryopreserved allograft heart valves: comparison with aortic valves from orthotopic heart transplants. *J Thorac Cardiovasc Surg.* (1998) 115:118–27. doi: 10.1016/S0022-5223(98)70450-7
57. de Valence S, Tille J-C, Mugnai D, Mrowczynski W, Gurny R, Möller M, et al. Long term performance of polycaprolactone vascular grafts in a rat abdominal aorta replacement model. *Biomaterials.* (2012) 33:38–47. doi: 10.1016/j.biomaterials.2011.09.024
58. Wissing TB, Bonito V, Bouten CVC, Smits AIPM. Biomaterial-driven *in situ* cardiovascular tissue engineering—a multi-disciplinary perspective. *NPJ Regen Med.* (2017) 2:18. doi: 10.1038/s41536-017-0023-2
59. Woodruff MA, Hutmacher DW. The return of a forgotten polymer—polycaprolactone in the 21st century. *Progr Polym Sci.* (2010) 35:1217–56. doi: 10.1016/j.progpolymsci.2010.04.002
60. Morell VO, Wearden PA. Experience with bovine pericardium for the reconstruction of the aortic arch in patients undergoing a Norwood procedure. *Ann Thorac Surg.* (2007) 84:1312–5. doi: 10.1016/j.athoracsur.2007.05.036
61. Pok S, Stupin IV, Tsao C, Pautler RG, Gao Y, Nieto RM, et al. Full-thickness heart repair with an engineered multilayered myocardial patch in rat model. *Adv Healthc Mater.* (2017) 6:1600549. doi: 10.1002/adhm.201600549
62. Lisy M, Kalender G, Schenke-Layland K, Brockbank KGM, Biermann A, Stock UA. Allograft heart valves: current aspects and future applications. *Biopreserv Biobank.* (2017) 15:148–57. doi: 10.1089/bio.2016.0070
63. Lee M, Wu BM, Dunn JCY. Effect of scaffold architecture and pore size on smooth muscle cell growth. *J Biomed Mater Res A.* (2008) 87:1010–6. doi: 10.1002/jbm.a.31816
64. Woo KM, Chen VJ, Ma PX. Nano-fibrous scaffolding architecture selectively enhances protein adsorption contributing to cell attachment. *J Biomed Mater Res A.* (2003) 67:531–7. doi: 10.1002/jbm.a.10098
65. Sarasam A, Madhally SV. Characterization of chitosan–polycaprolactone blends for tissue engineering applications. *Biomaterials.* (2005) 26:5500–8. doi: 10.1016/j.biomaterials.2005.01.071

Conflict of Interest: JM and MP are co-inventors of a patent application relevant to this technology, whose rights are assigned to Emory University. MP owns stock in Nyra Medical, and is an officer of this company. This entity did not have

any role in this study, nor did it sponsor or review it. MP has received personal consulting fees from Heart Repair Technologies, which again did not have any role in this work.

The remaining authors declare that the research was conducted in the absence of any commercial or financial relationships that could be construed as a potential conflict of interest.

Publisher's Note: All claims expressed in this article are solely those of the authors and do not necessarily represent those of their affiliated organizations, or those of the publisher, the editors and the reviewers.

Any product that may be evaluated in this article, or claim that may be made by its manufacturer, is not guaranteed or endorsed by the publisher.

Copyright © 2022 Mudigonda, Xu, Amedi, Lane, Corporan, Wang and Padala. This is an open-access article distributed under the terms of the Creative Commons Attribution License (CC BY). The use, distribution or reproduction in other forums is permitted, provided the original author(s) and the copyright owner(s) are credited and that the original publication in this journal is cited, in accordance with accepted academic practice. No use, distribution or reproduction is permitted which does not comply with these terms.



Engineering Efforts to Refine Compatibility and Duration of Aortic Valve Replacements: An Overview of Previous Expectations and New Promises

Stefano Rizzi^{1,2*}, Sara Ragazzini¹ and Maurizio Pesce^{1*}

¹ Tissue Engineering Unit, Centro Cardiologico Monzino, Istituto di ricovero e cura a carattere scientifico (IRCCS), Milan, Italy,

² Department of Chemistry, Materials and Chemical Engineering "Giulio Natta", Politecnico di Milano, Milan, Italy

OPEN ACCESS

Edited by:

Laura Iop,
University of Padua, Italy

Reviewed by:

Paul Human,
University of Cape Town, South Africa
Theodor Fischlein,
Nürnberg Hospital, Germany

*Correspondence:

Maurizio Pesce
maurizio.pesce@ccfm.it
Stefano Rizzi
stefano.rizzi@ccfm.it

Specialty section:

This article was submitted to
Heart Valve Disease,
a section of the journal
Frontiers in Cardiovascular Medicine

Received: 26 January 2022

Accepted: 28 March 2022

Published: 18 April 2022

Citation:

Rizzi S, Ragazzini S and Pesce M
(2022) Engineering Efforts to Refine
Compatibility and Duration of Aortic
Valve Replacements: An Overview of
Previous Expectations and New
Promises.

Front. Cardiovasc. Med. 9:863136.
doi: 10.3389/fcvm.2022.863136

The absence of pharmacological treatments to reduce or retard the progression of cardiac valve diseases makes replacement with artificial prostheses (mechanical or bio-prosthetic) essential. Given the increasing incidence of cardiac valve pathologies, there is always a more stringent need for valve replacements that offer enhanced performance and durability. Unfortunately, surgical valve replacement with mechanical or biological substitutes still leads to disadvantages over time. In fact, mechanical valves require a lifetime anticoagulation therapy that leads to a rise in thromboembolic complications, while biological valves are still manufactured with non-living tissue, consisting of aldehyde-treated xenograft material (e.g., bovine pericardium) whose integration into the host fails in the mid- to long-term due to unresolved issues regarding immune-compatibility. While various solutions to these shortcomings are currently under scrutiny, the possibility to implant fully biologically compatible valve replacements remains elusive, at least for large-scale deployment. In this regard, the failure in translation of most of the designed tissue engineered heart valves (TEHVs) to a viable clinical solution has played a major role. In this review, we present a comprehensive overview of the TEHVs developed until now, and critically analyze their strengths and limitations emerging from basic research and clinical trials. Starting from these aspects, we will also discuss strategies currently under investigation to produce valve replacements endowed with a true ability to self-repair, remodel and regenerate. We will discuss these new developments not only considering the scientific/technical framework inherent to the design of novel valve prostheses, but also economical and regulatory aspects, which may be crucial for the success of these novel designs.

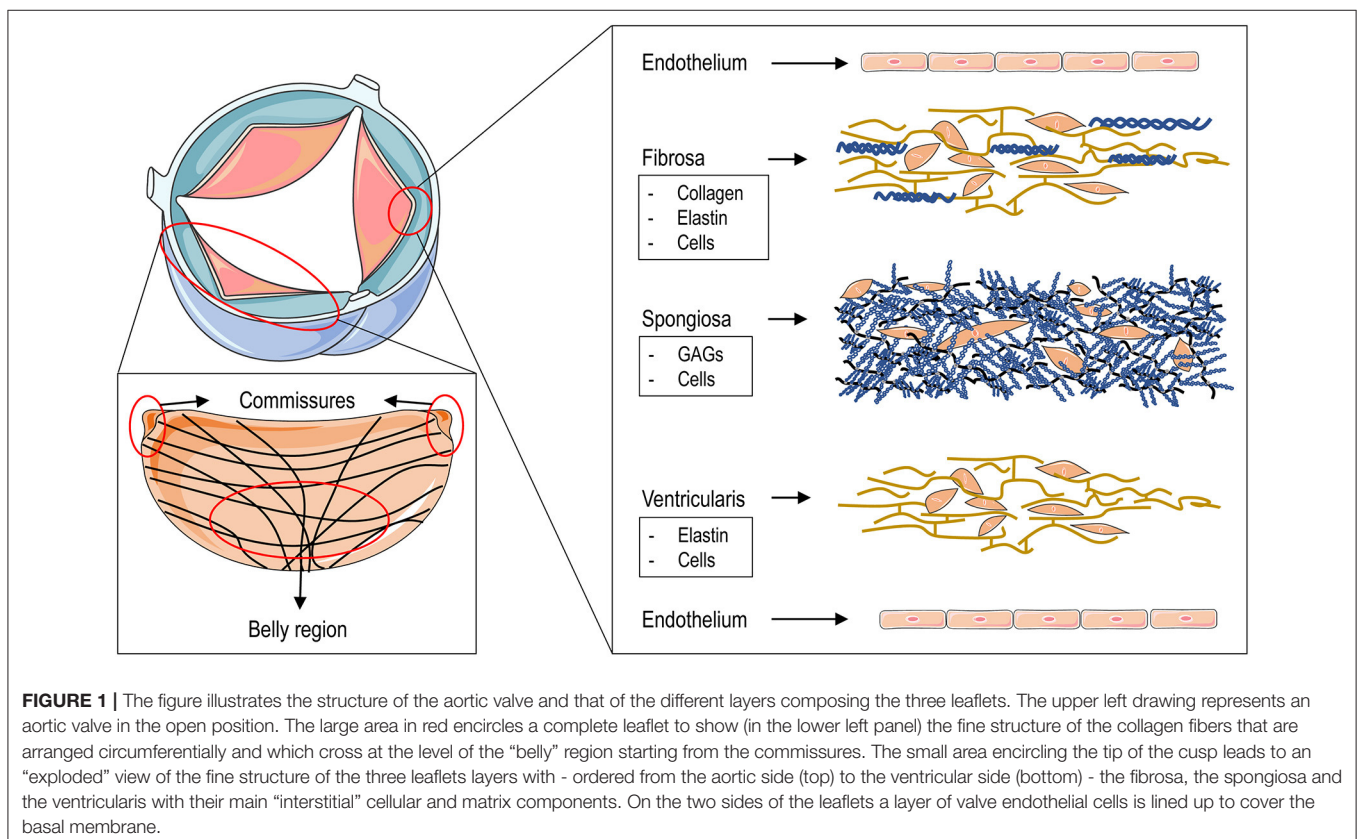
Keywords: calcific cardiac valve disease, valve substitution, tissue engineered heart valves, scaffold design, mechanical stress, TAVR, SAVR

HEART VALVE PATHOLOGY: BIOLOGICAL CAUSES AND CURRENT SOLUTIONS

Calcific Disease of the Aortic Valve

Heart valve pathologies have been described as a cause of disability and death since the seventeenth century. They still remain today a relevant contributor of loss of physical comfort and reduction of longevity and result in a considerable socio-economic burden (1, 2). Diseases of the cardiac valves can be divided into two main categories, namely congenital pathologies (e.g., the malformation of the aortic and pulmonary valves, the Ebstein's Anomaly, the Fallot tetralogy or the bicuspid aortic valve), with an impact especially during the neonatal period and infancy, and acquired pathologies which, depending on the etiology, can have an impact at all ages (i.e., the rheumatic or the infectious heart valve disease) or in the elderly (e.g., calcification of the mitral and aortic valves) (1, 3, 4). In this framework, a major contribution to the increase in the overall impact of cardiac valves pathologies worldwide is the rapid increase of conditions leading to the aortic valve (AoV) stenosis, specifically “calcific aortic valve disease” (CAVD)-a disease correlated primarily to aging (1, 3, 5, 6) with an important sex-related component (7). We will refer below to prostheses to treat CAVD, considering that those employed to treat other pathologies are very similar in design and performance.

The AoV is composed of three leaflets, each of which comprises three laminae: the *fibrosa*, the *spongiosa* and the *ventricularis*, each with different structural and mechanical characteristics. The *fibrosa*, the layer associated with the outflow, or aortic, side of the leaflet, is predominantly composed of collagen fibers arranged circumferentially in parallel bundles and crossing with a typical “X” geometry at the leaflet “belly” portion, surrounded by a matrix rich in elastin (8) (**Figure 1**). This is the layer that confers the maximal resistance of the leaflets to the compression forces acting on the aortic side, when the valve closes in diastole, and which can reach 80–120 mmHg (8). The *ventricularis*, the layer associated with the inflow side of the leaflet and facing the ventricular cavity, is a curvilinear structure mostly composed of elastin fibers oriented along the radial direction (**Figure 1**). The recoiling of these fibers supports the closure of the valve during the transition from systole (valve open) to diastole (valve closed) in the cardiac cycle (9). The *spongiosa*, finally, contains primarily glycosaminoglycans, a material with relatively low elastic modulus and an essential isotropic structure, which provide the deformability function of the valve leaflets and which serve to absorb the excessive mechanical forces (10). The three AoV layers are populated by specialized fibroblast-like cells, the so-called valve interstitial cells (VICs) (11). Although they are present in each of the valve layers, VICs are mostly abundant in the *spongiosa*, where they contribute



to repair the abundant extracellular matrix continuously exposed to mechanical workload. VICs have heterogeneous phenotypes depending on the developmental and pathologic status of the valve (12).

The evolution of aortic valve pathology begins with the occurrence of micro-ruptures of the endothelial layer covering the leaflets, especially on the outflow surface of the valve, due to perturbations of the shear forces. As with the initial events of atherosclerosis, these ruptures cause lipid infiltration and recruitment of inflammatory cells (13–15). This, in turn, determines a release of inflammatory cytokines and an oxidative stress burst that lead to pathological activation of the resident VICs whose functions are altered under these conditions. Specifically, these cells participate directly in the inflammatory process by responding *via* Toll-like receptors 2/4 to inflammatory signaling and, in turn, secreting an array of inflammatory cytokines (16). VICs also undergo a modification in their phenotype from one of matrix-repairing to one of matrix accumulating/remodeling with the potential to cause thickening of the leaflets—the so-called valve “sclerotic” phase—which is considered the first pathologic event in valve disease (13). The phase of AoV sclerosis persists in a clinically silent fashion until the beginning of the more rapid phase of valve calcification, characterized by transformation of VICs into calcific cells. These “osteoblastic” VICs have the ability to secrete initially small, but subsequently larger, calcific nodules that progressively deform the leaflet structure (17). This causes variations in the motion of the leaflets, incomplete valve closure at diastole and regurgitation with ensuing compromise of heart function. While inflammatory signaling is generally connected to the initial VICs matrix remodeling activity in the sclerotic phase, transformation from “activated” to osteoblastic “VICs” has been also linked to mechanical factors. In this respect, it has been hypothesized that the progressive hardening of the matrix surrounding VICs due to their remodeling activity prompts the activation of mechanosensitive-dependent pathways setting progression of the cells toward a calcific phenotype (18, 19).

Clinical Options for Valve Replacement

Until the beginning of the current century, surgical aortic valve replacement (SAVR) has been considered the elective option for surgical treatment of heart valve pathologies. Although highly effective, this is an invasive procedure requiring temporary cardiac arrest and extracorporeal circulation, which exposes patients to complications and side effects (20). For the majority of patients, the choice of the replacement device for SAVR is either a mechanical or a bioprosthetic valve. In a minority of patient's other options are adopted. These include the recuspidalization with autologous pericardium (the so-called Ozaki procedure) or transposition of the autologous pulmonary valve into the aortic position with replacement of the pulmonary valve with an aortic homograft—the Ross procedure adopted commonly for infants and children with congenital valve defects/stenosis and young adults (21–25).

A recent novel possibility to restore the functionality of a diseased aortic valve with reduced peri-procedural side effects involves trans-catheter aortic valve replacement (TAVR).

This technology, exploiting the pliability of pericardial tissue, allows deployment of a completely functional prosthesis using a minimally invasive procedure. These valves are currently approved for patients with severe, symptomatic aortic stenosis in all surgical risk categories given the favorable outcomes in the postoperative period (26, 27). Despite that TAVRs are based on a novel design and can be implanted with enormously lower risks, they still carry severe problems related to structural deterioration analogous to that of bioprosthetic grafts. For this reason, they are rarely implanted in patients younger than 60–65 years of age in accordance with the guidelines (28).

POLYMERIC VS. TISSUE-ENGINEERED VALVE REPLACEMENTS

Given the shortcomings of contemporary valve replacements, over the years, innovative designs have been sought using different approaches and manufacturing philosophies with the aim, in certain cases, to maximize the ease and minimize the cost of the approach (i.e., polymeric valves, PVs), and in other cases to ensure the maximal biocompatibility (tissue engineered heart valves, TEHV). We will discuss these two approaches separately, highlighting advantages and drawbacks.

Polymeric Valves

Polymeric valves are manufactured with elastomeric polymers by a simple fabrication procedure using molds. Typically, the process involves “injection molding” whereby synthetic (e.g., polyurethane or polystyrene) (29, 30) or natural polymers (e.g., fibrin) (31) are injected into tri-leaflet molds that give rise to complete sutureless valves, and can be readily mounted onto posts for implantation. This design provides advantages including easy scalability, low cost, natural hemodynamic performance and a relatively high long-term durability comparable to that of mechanical prostheses (32). On the other hand, when employed in animal valve replacement studies, polymeric valves, at least initially, did not lead to encouraging results due to calcification, thrombus and fibrous capsule formation, resulting in implant failure (33–35). Despite these shortcomings, in 2010, Quintessenza et al. (36) published a clinical study performed on 126 patients surgically treated with bicuspid pulmonary polytetrafluoroethylene (PTFE) valves. In particular, two types of valves with different thicknesses were used; the first was made with porous 0.6 mm PTFE while the second with non-porous 0.1 mm PTFE. Six patients treated with the porous PTFE valves needed reoperation due to leaflet calcification. In contrast, non-porous valves were less prone to stenosis as the lack of porosity prevented cellular in-growth and thickening (37). Moreover, 0.1 mm PTFE valves were characterized by higher leaflet mobility and lower transvalvular gradients (36). Stasiak et al. (29) recently introduced the so-called Poli-Valve (38)—a styrene triblock copolymer valve obtained by injection molding. This technique, besides being inexpensive and highly reproducible, appears to allow an optimal anisotropic distribution of forces on the leaflets and the polymeric fibers (39, 40) resulting in maximal mechanical durability due to

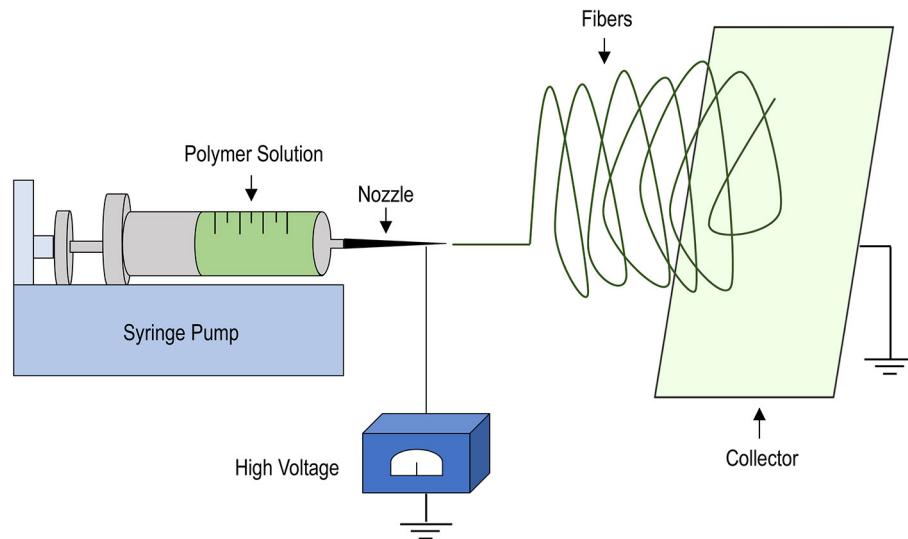


FIGURE 2 | Schematics of the electrospinning procedure. A liquid polymer solution is loaded into a syringe mounted into a syringe-pump and set to flow at defined rates through a nozzle of variable diameters (depending on the operational needs). The application of strong electric field allows the polymer to deposit onto a collector, consisting of a rotating mandrel or, as shown, a rotating plate onto which a non-woven scaffold can be manufactured due to solvent evaporation and solidification of the polymer fibers. Scaffold properties, such as porosity, fiber dimension and thickness can be easily adjusted by varying the dimension of the nozzle, the extrusion speed, the intensity of the electric field and the rotation speed of the collector.

a similar collagen fiber orientation to that of native heart valve tissue (39). The valve was bench-tested and validated according to ISO standards. Moreover, preliminary *ex vivo* and short-term *in vivo* feasibility tests were done, showing a good biocompatibility in the absence of mechanical failure and regurgitation. The lack of long-term tests *in vivo* still raises the question as to whether these valves offer an advantage over the most advanced mechanical replacements, in particular concerning the need for anti-coagulation therapies to prevent formation of thrombi on the surface of the leaflets.

First Generation TEHV: Advantages and Drawbacks

The general strategy to derive living replacements resembling native tissues was introduced in 1993 by Langer and Vacanti (41). These Authors, in their initial proposition of tissue engineering, defined three essential steps consisting of, (i) to seed autologous or allogenic-compatible cells inside scaffolds pre-fabricated with biocompatible/biodegradable materials, (ii) to enable tissue formation in bioreactors by exposing the tissue constructs to controlled mechanical loading and, (iii) to promote final tissue maturation, exploiting the ability of the pre-seeded cells to interact with circulating cells to complete the final evolution of the tissue constructs toward native leaflets (41). If induced to mature with appropriate instructing stimuli, the tissue constructs could therefore have regeneration and growing capacity. In the valve pathology scenario, this ability to grow would be especially indicated for use in pediatric patients, for whom the possible failure of the implants is compounded by the inability of the new valve to grow with the individual, making continuous surgical procedures necessary (42).

In vitro Strategy

During the years, several TEHVs manufactured with the classical tissue engineering approach [that we cite here as the “*in vitro strategy*” (32)] have been developed using various materials and manufacturing procedures. Particularly important in the scenario of this first type of valve replacement is the polymer deposition, or electrospinning technique (Figure 2). Electrospinning allows deposition of polymeric fibers by exploiting the ability of electric fields to direct these fibers onto rotating mandrels or planar/curvilinear surfaces (43). Given that the manufacturing process is performed by extruding liquid polymers through nozzles with different diameters, the dimension of the fibers, and the porosity of the scaffolds can be easily controlled. Moreover, by adjusting the rotation speed and/or the motion of the spotting surfaces, the orientation of the fiber deposition can be adjusted, thus allowing one to mimic, to a certain extent, the mechanical properties of the natural leaflets, thus allowing the scaffold to offer resistance to mechanical forces inherent to valve motion (44–46).

A first remarkable biodegradable polymeric material that was tested to produce electrospun meshes for assembly of valve scaffolds was polyglycolic acid (PGA). For example, in 1995, Shinoka et al. (47) manufactured a single leaflet valve constructed from non-woven PGA mesh sheets. The synthetic valve was seeded with ovine fibroblasts and endothelial cells, and then cultured up to 10 weeks. Initial *in vivo* tests performed on *in vitro* cell-seeded PGA scaffolds in lambs indicated absence of stenosis, especially when cells used to populate the scaffolds where autologous. In a more recent study, published in 2011, Schmidt et al. (48) tested a tri-leaflets synthetic pulmonary valve implanted in sheep using minimally-invasive surgery. The valve

was fabricated starting from nonwoven PGA meshes coated with poly-4-hydroxybutyrate (P4HB) using a heat-application welding technique. Scaffolds were then cultured *in vitro* with autologous myofibroblast and endothelial cells using dynamic bioreactors. *In vivo* tests confirmed adequate tissue formation and proper opening and closing of the valve.

In subsequent years, combinations of other polymers have been assessed to fabricate functional TEHV. One example is the valve developed by Gottlieb et al. composed by a mixture of PGA and poly-L-lactic acid (PLLA) fibers. The valve was assembled commencing with non-woven sheets containing PGA and PLLA fibers in a 1:1 ratio bonded by manual and machine needle punching. The scaffold was subsequently seeded with ovine bone marrow cells and cultured for 4 weeks prior to *in vivo* implantation (49). Valve insufficiency was, however, noted after 6 weeks. Moreover, although valve conduit diameter remained stable up to 20 weeks post-implantation, increasing valve regurgitation, corresponding to decreasing cusp length over time, was observed. The application of Hasan et al. (50) of a blend of polycaprolactone (PCL) and PLLA is of particular interest as it combined the high stiffness and the mechanical properties of PCL with the cell adhesive properties of PLLA, with cell-spreading and metabolic activity providing encouraging results.

The general and major shortcoming in the use of bioabsorbable materials such as PCL, PLLA or PGA is the failure to maintain a constant leaflet geometry and mechanical coherence, which results in retraction and thickening of the leaflets and valve insufficiency and regurgitation (49, 50). One of the most striking examples of this effect was described by Hoerstrup et al. (51) with respect to a valve composed by electrospun sheets of PGA coated with P4HB using a welding technique. Even if adapted for minimally invasive procedures, the scaffold design was insufficient to maintain a mechanical coherence over time after *in vivo* implantation, with general deterioration of the geometry and an overall thickening of the leaflets (48) which caused regurgitation and insufficiency (48).

The “retraction” and “compaction” effects of TEHV. s manufactured with biodegradable materials are mainly cell-mediated, and derive from the uncontrollable matrix degrading activity of the pre-seeded cells, or the cells recruited from the circulation (mainly monocytes/macrophages). While cell-mediated degradation can be reduced by optimizing the mechanical and surface characteristics of the polymers (e.g., stiffness, rigidity, wettability) and/or by performing functionalization of the electrospun fibers with natural or synthetic materials, an important factor is also the influence of mechanical load transmission from the scaffold to the cells. In fact, the unequal distribution of the strain forces on the curvilinear structure of the aortic valve leaflets, i.e., from the belly of the leaflet to the commissures (8), creates zones where the leaflet experiences maximal compression forces and other zones where forces are significant lower. Given the general mechano-sensitivity of adhering cells and, more in particular, that of the cells generally employed in valve tissue engineering (e.g., mesenchymal cells, valve cells, and fibroblasts) (19, 52) and the propensity of these cells toward a matrix remodeling and “pulling” phenotype when subjected to mechanical stress

(53, 54), an essential component in TEHV. s design is the possibility to achieve a mechanical adaptation of the cells to the microenvironment. According to findings by Cox et al. (55) this condition may be achieved, at least in part, by exposing TEHV. s constructs to controlled mechanical stimulation, which may promote maturation of the tissue with a native distribution of collagen fibers and a lower propensity to remodel over time after implantation. The combination of natural with synthetic polymers could, finally, prevent a precocious onset of the maladaptive cellular responses observed in TEHV. s manufactured with bio-absorbable non-woven materials, thus enabling the possibility to obtain structures with more stable and constant mechanical properties (56). However, the lack of long-term studies (49) and of an exhaustive knowledge of the cell-material interaction, nowadays excludes the transfer of these engineered valves to clinical practice.

***In-situ* Strategy**

The second approach for generating TEHV. s is the so-called “*in situ* strategy,” which exploits the ability of the human body to promote new tissue formation starting from an acellular implant due to the recruitment of circulating cells. In this setting, the postoperative adhesion of autologous cells to the scaffolds is a crucial event expected to provide a structure with performances as similar as possible to that of the native valves (57–59). An example of this approach is the electrospun valve fabricated by Kluin et al. (60) using a novel supramolecular elastomer; bis-urea-modified poly-carbonate (PC-BU). The function of the valve manufactured under these conditions was studied *in vitro*, while cellular recruitment and new tissue formation were evaluated during a long-term follow-up (12 months) in ovine model. Both phases of the study produced satisfactory results. In fact, the valves exhibited good functionality in terms of leaflets mobility, and did not show major signs of stenosis and thrombus and maintained a stable geometry and good cellular colonization *in vivo*.

Another example of an *in situ* TEHV is that recently developed by Cohan et al. (61). The scaffold was fabricated using a double component deposition (DCD) electrospinning strategy employing poly-(ester carbonate urethane)-urea (PCUU) as a material. With this procedure, the authors were able to obtain valves with a broad range of geometries suitable for stentless, stented and transcatheter applications (62). The valves were evaluated 24 h post implantation in a porcine model. Immediate postoperative analyses showed good valve kinematics and, at explant, no sign of stenosis, structural deterioration or thrombus was observed, even if the absence of a long-term study prevented full assessment of the effective regenerative potential of this PCUU valve.

An interesting *in vivo* study published by Emmert et al. (63) exploited a valve that combined both *in vitro* and *in situ* approaches. Briefly, a tri-leaflets heart valve was fabricated commencing with non-woven PGA sheets coated with P4HB as previously described (51). The scaffold was then seeded with ovine vascular derived cells and cultured in a dynamic bioreactor for 4 weeks. Before being implanted, the valve was decellularized

to obtain a structure suitable, as much as possible, for recolonization by autologous cells (64). At the end of the follow-up period (12 months), the valve exhibited good performance and tissue remodeling comparable to that of the native aortic valve.

Currently, concordance is lacking on the best approach to be followed given the pros and the cons of the two approaches. In fact, while the *in vitro* approach seems more appropriate to keep the phenotype of the cells under control until tissue maturation is complete, it requires complicate and time-consuming tissue engineering procedures which need to be performed in compliance with the rules for good manufacturing practice (GMP), and additionally necessitates huge monetary investments inappropriate for the increasing demand. In contrast, *in situ* TEHV, which lack a living component, could be produced with an off-the shelf strategy at enormously lower costs and could be easily implemented into the market. The shortcoming of this approach is that the efficiency of the *in situ* recellularization and tissue maturation is less controllable, given the anticipated patient-to-patient variability due to the effects of age, risk conditions and pathological settings, which could lead to a variable degree of inflammation and failure (65).

Second Generation of TEHVs: New Materials and Designs

In view of the growing awareness of the maladaptive interactions between cells and scaffolds used to produce TEHVs, more complex manufacturing concepts are now emerging based on more systematic views of the cells/scaffolds interactions (66) and the recognition of the role of the forces dominating cellular mechanosensitivity of the cells (20, 67). Central to this second-generation design is the change from scaffolds made of randomly interleaved fibers, to a design that is more compliant with the distribution of the strain and compression forces acting in the kinematics and mechanical loading of the natural valves. The idea underlying this new concept derives from the evidence that the natural ECM fibers in the valve are deposited from the very beginning of valve development mainly with anisotropic patterns instructed by mechanical forces, and that the cells residing within the anisotropically deposited fibers are adapted to maintain a quiescent phenotype (**Figure 1**) (68). In order to achieve this aim, one of the current trends is to manufacture scaffolds with oriented deposition of ECM components (e.g., collagen) by mechanically forcing cells to deposit fibers according to defined geometric patterns, and/or to employ polymers that can be deposited with anisotropic patterns in 3D. A further step in this biomimicry approach is the attempt to implement the natural tri-layered valve structure in scaffold design. An example of this new design has been provided by Masoumi et al. where a three-layer scaffold included an anisotropic fibrous layer deposited between two coatings of electrospun fibers. Cells were then seeded in an attempt to obtain a fully engineered heart valve with layers resembling the native structure of the aortic valve tissue (69). Despite the fact that the resulting valve differed from the native valve in its organization of the ECM (for example, that an anisotropic layer of PGS represented

the highly isotropic *spongiosa* layer), this type of scaffold gave good results when mechanical performance and maintenance of cellular viability was considered (70). Unfortunately, the lack of *in vivo* translation of this valve to date does not allow inferences on its behavior in a living organism. In a second example, Eslami et al. (71) employed a hydrogel made with a mixture of methacrylated hyaluronic acid and methacrylated gelatin, into which mitral valve interstitial cells were incorporated followed by its incorporation into a PGS-PCL electrospun scaffold. The author's speculated that this approach produces a more favorable environment for the remodeling of the ECM by the cells after *in vivo* implantation of the valve. Indeed, encasing cells into hydrogels before seeding a scaffold might mitigate the matrix digestion/remodeling activity of the cells and at the same time would favor the *de novo* deposition of matrix without affecting the mechanical function of the PGS-PCL layer. This may be particularly interesting considering that the behavior of the cells (and the resultant activation status) can be potentially modulated by mechanical tuning of the hydrogels characteristics, thereby crucially contributing to maintain them in a quiescent/self-renewing phenotype.

Numerous efforts toward the production of valve scaffolds with anisotropic mechanical characteristics have been made using novel fabrication techniques. For example, in a recent study by Wunner et al. (72) a polymeric scaffold with a highly controlled microarchitecture was manufactured using an "electrowriting" technique, which involves high voltage guided printing of a solvent-free, melted polymer onto a laterally sliding aluminum collector. Using this approach, the authors were able to orientate the polymeric fibers (made with medical grade PCL) to mimic that of the collagen and elastin fibers of the natural valve, resulting in a mechanical behavior comparable to that of native valve leaflet (73). Another method that has been exploited with the same aim has been developed by Moreira et al. (74) who introduced textile reinforcements into a scaffold containing a thin valve electrospun layer and fibrin cell-laden gel to confer anisotropic resistance against the forces acting in the valve motion cycle, which resembled the arrangement of collagen bundles of the native *fibrosa* layer. Preliminary bench testing of the resulting valve after 21 days dynamic conditioning, proved that mechanical stimulation enhanced matrix deposition (in particular collagen) by the cells, thus showing the versatility of a "mixed" fabrication approach to elaborate a design that more closely resembled the natural valve architecture. The utility of a tailored deposition of valve scaffolds fibers is, however, still under question, especially from the perspective of long-term scaffold remodeling after *in vivo* implantation. In fact, for example, Uiterwijk et al. (75) showed that the orientation of the collagen fibers in *in situ* TEHVs that were manufactured with isotropic or anisotropic fibers deposition and implanted for 1 year in sheep did not resemble the original arrangement of the fibers in the scaffold, but was instead dictated by the prevailing mechanical forces after implantation. While the authors concluded that the fiber's anisotropic deposition is insufficient to dictate the way the scaffold-populating cells mechanically adapt and deposit new matrix components, it has been discussed that other factors, such as the relatively rapid degradability of the scaffold

and inflammatory response, may contribute to override any instructive signals provided by the original geometry of the implant (76).

Finally, a promising technology that is still in its infancy but will undoubtedly provide a decisive future impact in cardiovascular medicine, is that of three-dimensional (3D) printing of valve scaffolds or direct bioprinting of valve leaflets using cell-laden polymers (77). The advantage of this manufacturing technology is that 3D printing/bioprinting allows deposition of matrix components with precise patterning and also exploits a layer-by-layer positioning of materials and cells with a high control of the output geometry (with μm accuracy). Potentially, given the possibility to translate the actual geometry of valves via imaging system data (i.e., CT-scan), this technique could be used for personalized manufacturing of valves tailored to the individual patient with maximal hemodynamic performance and adaptability (78). Despite these advantages, 3D printable materials or, in particular, bio-printable hydrogel/cellular mixtures still suffer from the lack of mechanical strength (79–81), especially with respect to the need to withstand an intense mechanical workload. In keeping with this conclusion, for example, the collagen Type I bioprinted valve described by Lee and co-authors (77) was efficiently cellularized with human endothelial cells, but its mechanical characteristics were insufficient to meet the standards required for mitral and aortic valves *in vivo*. While other valve-specific printable polymers are currently undergoing investigation, including methacrylated hydrogels, such as gelatin and hyaluronic acids (82), and PEG-DA hydrogels (83), further work is necessary to improve the mechanical characteristics of 3D/bioprinted valves to produce realistic alternatives.

RECELLULARIZATION OF DECELLULARIZED NATURAL TISSUES

Considering the above highlighted shortcomings of fully engineered TEHV's resulting from the combination of cells with artificial scaffolds, a further strategy that still has appealing features for engineering living valves, is to introduce human cells *de novo* into decellularized animal-derived materials, such as entire valves or pericardium. Prompted by remarkable examples such as the re-engineering of decellularized whole hearts (84), this strategy appears a realistic alternative, especially when considering the possibility to engineer tissues with full regeneration capacity and maximal biocompatibility for use in pediatric and young patients. The advantage of tissue decellularization includes the possibility of employing animal scaffolds already endowed with mechanical characteristic that closely resemble that of diseased tissues. For heart valve engineering, for example, porcine valves and porcine/bovine pericardium are elective materials either for the maximal mechanical compatibility (especially with respect to valves) and the easiness of valve manufacturability (especially for pericardium). Before being employed in a tissue engineered construct, the decellularized materials need to meet specific requirements to ensure maximum immunological compatibility

once implanted into the human body. In this respect, a principal element that needs to be addressed is the problem of xenoantigens, which is an overarching problem in the use of bioprosthetic valves as it is in vascularized solid organ xenotransplantation. Chemical cross-linking (using glutaraldehyde), which is normally performed to prepare bioprosthetic tissue for use in valve replacement procedures, fails to fully quench the immunogenicity thereof, including DNA and other cellular xenoantigens, such as Alpha-Gal (galactose- α -1,3-galactose) which, together with reactive aldehyde residues themselves, eventually lead to progressive deterioration of the valve (85, 86). In order to avoid the presence of xenoantigens, one possibility includes decellularization using ionic and/or non-ionic detergents (87, 88). Another possibility involves the use of “humanized” valve tissue through the generation of genetically engineered donor animals (89). Indeed, since the majority of human antibodies against the porcine material bind to the α Gal epitope (90), the use of pigs with a knockdown in the GGTA-1 locus (GTKO) would not give rise to xenograft rejections due to the α Gal epitope (91). Genetic ablation of other antigens, such as that encoding the SDa blood group or the N-glycolyl neuraminic acid offer potential advantages (91–94). The problem of residual immunogenicity of decellularized tissues is, however, not entirely resolved. In fact, there is a residual possibility of long-term rejection of decellularized tissues due to the persistence of residual contaminants deriving from the detergents employed, presence of ECM components that are not removed by the decellularization procedure and permanence of cellular debris not completely removed by post-decellularization washing procedures (95). This shortcoming might be overcome by elaborating a quality control system and toxicologic assessment of the decellularized material in view of clinical translation.

A second element to be considered in the employment of decellularized materials is the strategy to re-introduce the cells inside such scaffolds. In this respect, several unsuccessful attempts in the past have been performed based on culturing cells on the surface of the decellularized matrices (96, 97). The drawback of this approach is that decellularized matrices are mostly impervious to invasion by cells from the surface due to low porosity and permeability thereof. In this context our group developed a decellularization method for pericardium based on the employment of ionic and non-ionic detergents that both maintained the structural integrity and mechanical resistance of human (87) and porcine (98) pericardium and abolishes xenoantigens in the latter. Interestingly, when valve cells were statically cultured on the surface of the decellularized porcine pericardium, only minimal penetration was observed (98). In contrast, the increase in tissue permeability following decellularization rendered the tissue perfusable with an oscillating perfusion bioreactor (88), which led to a homogeneous distribution of the cells throughout the entire depth of the construct thereby effecting valve-like tissue maturation (99). Despite the lack, as yet, of confirmation of total biological compatibility of the recellularized tissue or the scalability of the method, the approach seems amenable to generate a fully engineered, personally tailored

(for example, using recipient mesenchymal cells), living valve for selected classes of patients (e.g., infants/children and young adults).

CONCLUSION

The present review describes past and present approaches in conceiving TEHV's and summarizes the current drawbacks that need to be overcome. While more historical design of TEHV's failed to consider the morphological design of matrices, which resulted in leaflets retraction/compaction and, thus, eventual failure, the overall trend emerging from more recent studies of new designs serves to elucidate the strict correlation between maintenance of proper cellular mechanosensitivity and the correct mechanical adaptation/maturation of the engineered tissues *in vivo*. This last consideration also underlines the urgent need of a more integrated work between engineers and biologists to come up with a systematic design of scaffolds and fine-tuning

of material characteristics to minimize the cell-mediated effects in scaffolds remodeling. In the context of modern valve tissue engineering, decellularized matrices still appear promising for TEHV's fabrication, despite the potentially high manufacturing costs which may limit their availability and use in well-suited recipient classes.

AUTHOR CONTRIBUTIONS

SRi and SRa drafted the manuscript and the figures. MP revised the work and elaborated the final version of the article. All authors contributed to the article and approved the submitted version.

FUNDING

MP is recipient of Institutional funding (Ricerca Corrente e Ricerca 5%), both from Ministero della Salute, Italy.

REFERENCES

- Coffey S, Roberts-Thomson R, Brown A, Carapetis J, Chen M, Enriquez-Sarano M, et al. Global epidemiology of valvular heart disease. *Nat Rev Cardiol.* (2021) 18:853–64. doi: 10.1038/s41569-021-00570-z
- Vaslef SN, Roberts WC. Early descriptions of aortic valve stenosis. *Am Heart J.* (1993) 125:1465–74. doi: 10.1016/0002-8703(93)91036-E
- Badiani S, Bhattacharyya S, Azimnia N, Treibel TA, Lloyd G. Moderate aortic stenosis: what is it and when should we intervene? *Interv Cardiol.* (2021) 16:e09. doi: 10.15420/icr.2021.04
- Mordi I, Tzemos N. Bicuspid aortic valve disease: a comprehensive review. *Cardiol Res Pract.* (2012) 2012:196037. doi: 10.1155/2012/196037
- Summerhill VI, Moschetta D, Orekhov AN, Poggio P, Myasoedova VA. Sex-specific features of calcific aortic valve disease. *Int J Mol Sci.* (2020) 21:5620. doi: 10.3390/ijms21165620
- Porras AM, McCoy CM, Masters KS. Calcific aortic valve disease: a battle of the sexes. *Circ Res.* (2017) 120:604–6. doi: 10.1161/CIRCRESAHA.117.310440
- Treibel TA, Kozor R, Fontana M, Torlasco C, Reant P, Badiani S, et al. Sex dimorphism in the myocardial response to aortic stenosis. *JACC Cardiovasc Imaging.* (2018) 11:962–73. doi: 10.1016/j.jcmg.2017.08.025
- Balguind A, Driessen NJ, Mol A, Schmitz JP, Verheyen F, Bouten CV, et al. Stress related collagen ultrastructure in human aortic valves—implications for tissue engineering. *J Biomech.* (2008) 41:2612–7. doi: 10.1016/j.jbiomech.2008.06.031
- Breuer CK, Mettler BA, Anthony T, Sales VL, Schoen FJ, Mayer JE. Application of tissue-engineering principles toward the development of a semilunar heart valve substitute. *Tissue Eng.* (2004) 10:1725–36. doi: 10.1089/ten.2004.10.1725
- Arjunon S, Rathan S, Jo H, Yoganathan AP. Aortic valve: mechanical environment and mechanobiology. *Ann Biomed Eng.* (2013) 41:1331–46. doi: 10.1007/s10439-013-0785-7
- Taylor PM, Batten P, Brand NJ, Thomas PS, Yacoub MH. The cardiac valve interstitial cell. *Int J Biochem Cell Biol.* (2003) 35:113–8. doi: 10.1016/S1357-2725(02)00100-0
- Liu AC, Joag VR, Gotlieb AI. The emerging role of valve interstitial cell phenotypes in regulating heart valve pathobiology. *Am J Pathol.* (2007) 171:1407–18. doi: 10.2353/ajpath.2007.070251
- Lerman DA, Prasad S, Alotti N. Calcific aortic valve disease: molecular mechanisms and therapeutic approaches. *Eur Cardiol.* (2015) 10:108–12. doi: 10.15420/ecr.2015.10.2.108
- Garoffolo G, Ferrari S, Rizzi S, Barbutto M, Bernava G, Pesce M. Harnessing Mechanosensation in Next Generation Cardiovascular Tissue Engineering. *Biomolecules.* (2020) 10:1419. doi: 10.3390/biom10101419
- Garoffolo G, Madonna R, de Caterina R, Pesce M. Cell based mechanosensing in vascular patho-biology: more than a simple go-with the flow. *Vascul Pharmacol.* (2018) 111:7–14. doi: 10.1016/j.vph.2018.06.013
- Yang X, Fullerton DA, Su X, Ao L, Cleveland JC, Meng X. Pro-osteogenic phenotype of human aortic valve interstitial cells is associated with higher levels of Toll-like receptors 2 and 4 and enhanced expression of bone morphogenetic protein 2. *J Am Coll Cardiol.* (2009) 53:491–500. doi: 10.1016/j.jacc.2008.09.052
- Bertazzo S, Gentleman E, Cloyd KL, Chester AH, Yacoub MH, Stevens MM. Nano-analytical electron microscopy reveals fundamental insights into human cardiovascular tissue calcification. *Nat Mater.* (2013) 12:576–83. doi: 10.1038/nmat3627
- Bouchareb R, Boulanger MC, Fournier D, Pibarot P, Messaddeq Y, Mathieu P. Mechanical strain induces the production of spheroid mineralized microparticles in the aortic valve through a RhoA/ROCK-dependent mechanism. *J Mol Cell Cardiol.* (2014) 67:49–59. doi: 10.1016/j.yjmcc.2013.12.009
- Santoro R, Scaini D, Severino LU, Amadeo F, Ferrari S, Bernava G, et al. Activation of human aortic valve interstitial cells by local stiffness involves YAP-dependent transcriptional signaling. *Biomaterials.* (2018) 181:268–79. doi: 10.1016/j.biomaterials.2018.07.033
- Fioretti ES, Motta SE, Lintas V, Loerakker S, Parker KK, Baaijens FPT, et al. Next-generation tissue-engineered heart valves with repair, remodelling and regeneration capacity. *Nat Rev Cardiol.* (2021) 18:92–116. doi: 10.1038/s41569-020-0422-8
- Ozaki S, Kawase I, Yamashita H, Uchida S, Takatoh M, Kiyohara N. Midterm outcomes after aortic valve neocuspidization with glutaraldehyde-treated autologous pericardium. *J Thorac Cardiovasc Surg.* (2018) 155:2379–87. doi: 10.1016/j.jtcvs.2018.01.087
- Kawase I, Ozaki S, Yamashita H, Uchida S, Nozawa Y, Matsuyama T, et al. Original aortic valve plasty with autologous pericardium for quadricuspid valve. *Ann Thorac Surg.* (2011) 91:1598–9. doi: 10.1016/j.athoracsurg.2010.10.068
- Ross DN. Homograft replacement of the aortic valve. *Lancet.* (1962) 2:487. doi: 10.1016/S0140-6736(62)90345-8
- Yacoub MH, Klieverik LM, Melina G, Edwards SE, Sarathchandra P, Bogers AJ, et al. An evaluation of the Ross operation in adults. *J Heart Valve Dis.* (2006) 15:531–9.
- Mazine A, El-Hamamsy I. Procedures and outcomes of surgical aortic valve replacement in adults. *Cardiol Clin.* (2020) 38:89–102. doi: 10.1016/j.ccl.2019.09.012
- Davidson LJ, Davidson CJ. Transcatheter treatment of valvular heart disease: a review. *JAMA.* (2021) 325:2480–94. doi: 10.1001/jama.2021.2133

27. Ak A, Porokhovnikov I, Kueth F, Schulze PC, Noutsias M, Schlattmann P. Transcatheter vs. surgical aortic valve replacement and medical treatment: Systematic review and meta-analysis of randomized and non-randomized trials. *Herz*. (2018) 43:325–37. doi: 10.1007/s00059-017-4562-5
28. Head SJ, Celik M, Kappetein AP. Mechanical versus bioprosthetic aortic valve replacement. *Eur Heart J*. (2017) 38:2183–91. doi: 10.1093/eurheartj/ehx141
29. Stasiak JR, Serrani M, Biral E, Taylor JV, Zaman AG, Jones S, et al. Design, development, testing at ISO standards and *in vivo* feasibility study of a novel polymeric heart valve prosthesis. *Biomater Sci*. (2020) 8:4467–80. doi: 10.1039/D0BM00412J
30. Bezuidenhout D, Williams DF, Zilla P. Polymeric heart valves for surgical implantation, catheter-based technologies and heart assist devices. *Biomaterials*. (2015) 36:6–25. doi: 10.1016/j.biomaterials.2014.09.013
31. Weber M, Gonzalez de Torre I, Moreira R, Frese J, Oedekoven C, Alonso M, et al. Multiple-step injection molding for fibrin-based tissue-engineered heart valves. *Tissue Eng Part C Method*. (2015) 21:832–40. doi: 10.1089/ten.tec.2014.0396
32. Fioretta ES, Dijkman PE, Emmert MY, Hoerstrup SP. The future of heart valve replacement: recent developments and translational challenges for heart valve tissue engineering. *J Tissue Eng Regen Med*. (2018) 12:e323–35. doi: 10.1002/term.2326
33. Hilbert SL, Ferrans VJ, Tomita Y, Eidbo EE, Jones M. Evaluation of explanted polyurethane trileaflet cardiac valve prostheses. *J Thorac Cardiovasc Surg*. (1987) 94:419–29. doi: 10.1016/S0022-5223(19)36257-9
34. Jansen J, Reul H. A synthetic three-leaflet valve. *J Med Eng Technol*. (1992) 16:27–33. doi: 10.3109/03091909209021954
35. Daebritz SH, Fausten B, Hermanns B, Schroeder J, Groetzner J, Autschbach R, et al. Introduction of a flexible polymeric heart valve prosthesis with special design for aortic position. *Eur J Cardiothorac Surg*. (2004) 25:946–52. doi: 10.1016/j.ejcts.2004.02.040
36. Quintessenza JA, Jacobs JP, Chai PJ, Morell VO, Lindberg H. Polytetrafluoroethylene bicuspid pulmonary valve implantation: experience with 126 patients. *World J Pediatr Congenit Heart Surg*. (2010) 1:20–7. doi: 10.1177/2150135110361509
37. Brown JW, Ruzmetov M, Vijay P, Rodefeld MD, Turrentine MW. Right ventricular outflow tract reconstruction with a polytetrafluoroethylene monocusp valve: a twelve-year experience. *J Thorac Cardiovasc Surg*. (2007) 133:1336–43. doi: 10.1016/j.jtcvs.2006.12.045
38. De Gaetano F, Serrani M, Bagnoli P, Brubert J, Stasiak J, Moggridge GD, et al. Fluid dynamic characterization of a polymeric heart valve prototype (Poli-Valve) tested under continuous and pulsatile flow conditions. *Int J Artif Organs*. (2015) 38:600–6. doi: 10.5301/ijao.5000452
39. Stasiak J, Brubert J, Serrani M, Nair S, de Gaetano F, Costantino ML, et al. A bio-inspired microstructure induced by slow injection moulding of cylindrical block copolymers. *Soft Matter*. (2014) 10:6077–86. doi: 10.1039/C4SM00884G
40. Stasiak J, Brubert J, Serrani M, Talhat A, De Gaetano F, Costantino ML, et al. Structural changes of block copolymers with bi-modal orientation under fast cyclical stretching as observed by synchrotron SAXS. *Soft Matter*. (2015) 11:3271–8. doi: 10.1039/C5SM00360A
41. Langer R, Vacanti JP. Tissue engineering. *Science*. (1993) 260:920–6. doi: 10.1126/science.8493529
42. Shinoka T, Miyachi H. Current status of tissue engineering heart valve. *World J Pediatr Congenit Heart Surg*. (2016) 7:677–84. doi: 10.1177/2150135116664873
43. Rutledge GC, Fridrikh SV. Formation of fibers by electrospinning. *Adv Drug Deliv Rev*. (2007) 59:1384–91. doi: 10.1016/j.addr.2007.04.020
44. Argento G, Simonet M, Oomens CW, Baaijens FP. Multi-scale mechanical characterization of scaffolds for heart valve tissue engineering. *J Biomech*. (2012) 45:2893–8. doi: 10.1016/j.jbiomech.2012.07.037
45. Oveissi F, Naficy S, Lee A, Winlaw DS, Dehghani F. Materials and manufacturing perspectives in engineering heart valves: a review. *Mater Today Bio*. (2020) 5:100038. doi: 10.1016/j.mtbio.2019.100038
46. Hasan A, Saliba J, Pezeshgi Modarres H, Bakhty A, Nasajpour A, Mofrad MRK, et al. Micro and nanotechnologies in heart valve tissue engineering. *Biomaterials*. (2016) 103:278–92. doi: 10.1016/j.biomaterials.2016.07.001
47. Shinoka T, Breuer CK, Tanel RE, Zund G, Miura T, Ma PX, et al. Tissue engineering heart valves: valve leaflet replacement study in a lamb model. *Ann Thorac Surg*. (1995) 60:S513–6. doi: 10.1016/S0003-4975(21)01185-1
48. Schmidt D, Dijkman PE, Driessen-Mol A, Stenger R, Mariani C, Puolakka A, et al. Minimally-invasive implantation of living tissue engineered heart valves: a comprehensive approach from autologous vascular cells to stem cells. *J Am Coll Cardiol*. (2010) 56:510–20. doi: 10.1016/j.jacc.2010.04.024
49. Gottlieb D, Kunal T, Emani S, Aikawa E, Brown DW, Powell AJ, et al. *In vivo* monitoring of function of autologous engineered pulmonary valve. *J Thorac Cardiovasc Surg*. (2010) 139:723–31. doi: 10.1016/j.jtcvs.2009.11.006
50. Flanagan TC, Sachweh JS, Frese J, Schnoring H, Gronloh N, Koch S, et al. *In vivo* remodeling and structural characterization of fibrin-based tissue-engineered heart valves in the adult sheep model. *Tissue Eng Part A*. (2009) 15:2965–76. doi: 10.1089/ten.tea.2009.0018
51. Hoerstrup SP, Kadner A, Melnitchouk S, Trojan A, Eid K, Tracy J, et al. Tissue engineering of functional trileaflet heart valves from human marrow stromal cells. *Circulation*. (2002) 106:143–50. doi: 10.1161/01.cir.0000032872.55215.05
52. Pesce M, Santoro R. Feeling the right force: How to contextualize the cell mechanical behavior in physiologic turnover and pathologic evolution of the cardiovascular system. *Pharmacol Ther*. (2017) 171:75–82. doi: 10.1016/j.pharmthera.2016.08.002
53. van Vlimmeren MA, Driessen-Mol A, Oomens CW, Baaijens FP. Passive and active contributions to generated force and retraction in heart valve tissue engineering. *Biomech Model Mechanobiol*. (2012) 11:1015–27. doi: 10.1007/s10237-011-0370-7
54. Balestrini JL, Billiar KL. Magnitude and duration of stretch modulate fibroblast remodeling. *J Biomech Eng*. (2009) 131:051005. doi: 10.1115/1.3049527
55. Cox MA, Kortsmat J, Driessen N, Bouten CV, Baaijens FP. Tissue-engineered heart valves develop native-like collagen fiber architecture. *Tissue Eng Part A*. (2010) 16:1527–37. doi: 10.1089/ten.tea.2009.0263
56. Neuenschwander S, Hoerstrup SP. Heart valve tissue engineering. *Transpl Immunol*. (2004) 12:359–65. doi: 10.1016/j.trim.2003.12.010
57. Erdbrugger W, Konertz W, Dohmen PM, Posner S, Ellerbrok H, Brodde OE, et al. Decellularized xenogenic heart valves reveal remodeling and growth potential *in vivo*. *Tissue Eng*. (2006) 12:2059–68. doi: 10.1089/ten.2006.12.2059
58. Jensen AB, Groff DE, McConahey PJ, Dixon FJ. Transmission of murine leukemia virus (Scripps) from parent to progeny mice as determined by p30 antigenemia. *Cancer Res*. (1976) 36:1228–32.
59. Konuma T, Devaney EJ, Bove EL, Gelehrter S, Hirsch JC, Tavakkol Z, et al. Performance of CryoValve SG decellularized pulmonary allografts compared with standard cryopreserved allografts. *Ann Thorac Surg*. (2009) 88:849–54. discussion 554–5. doi: 10.1016/j.athoracsur.2009.06.003
60. Kluijn J, Talacua H, Smits AI, Emmert MY, Brugmans MC, Fioretta ES, et al. *In situ* heart valve tissue engineering using a bioresorbable elastomeric implant - from material design to 12 months follow-up in sheep. *Biomaterials*. (2017) 125:101–17. doi: 10.1016/j.biomaterials.2017.02.007
61. Cohan GN, da Mota Silveira-Filho L, Matsumura Y, Luketich SK, Katz W, Badhwar V, et al. Acute *in vivo* functional assessment of a biodegradable stentless elastomeric tricuspid valve. *J Cardiovasc Transl Res*. (2020) 13:796–805. doi: 10.1007/s12265-020-09960-z
62. D'Amore A, Luketich SK, Raffa GM, Olia S, Menallo G, Mazzola A, et al. Heart valve scaffold fabrication: Bioinspired control of macro-scale morphology, mechanics and micro-structure. *Biomaterials*. (2018) 150:25–37. doi: 10.1016/j.biomaterials.2017.10.011
63. Emmert MY, Schmitt BA, Loerakker S, Sanders B, Spriestersbach H, Fioretta ES, et al. Computational modeling guides tissue-engineered heart valve design for long-term *in vivo* performance in a translational sheep model. *Sci Transl Med*. (2018) 10:eaa4587. doi: 10.1126/scitranslmed.aan4587
64. Dijkman PE, Driessen-Mol A, Frese L, Hoerstrup SP, Baaijens FP. Decellularized homologous tissue-engineered heart valves as off-the-shelf alternatives to xeno- and homografts. *Biomaterials*. (2012) 33:4545–54. doi: 10.1016/j.biomaterials.2012.03.015
65. Xue Y, Kossar AP, Abramov A, Frasca A, Sun M, Zyablitskaya M, et al. Age-related enhanced degeneration of bioprosthetic valves due to leaflet calcification, tissue crosslinking, and structural changes. *Cardiovasc Res*. (2022). doi: 10.1093/cvr/cvac002
66. Uspreck J, Chen WL, Simmons CA. Heart valve regeneration: the need for systems approaches. *Wiley Interdiscip*

- Rev Syst Biol Med.* (2016) 8:169–82. doi: 10.1002/wsbm.1329
67. Motta SE, Fioretta ES, Lintas V, Dijkman PE, Hilbe M, Frese L, et al. Geometry influences inflammatory host cell response and remodeling in tissue-engineered heart valves *in-vivo*. *Sci Rep.* (2020) 10:19882. doi: 10.1038/s41598-020-76322-9
 68. MacGrogan D, Luxan G, Driessen-Mol A, Bouten C, Baaijens F, de la Pompa JL. How to make a heart valve: from embryonic development to bioengineering of living valve substitutes. *Cold Spring Harb Perspect Med.* (2014) 4:a013912. doi: 10.1101/cshperspect.a013912
 69. Masoumi N, Annabi N, Assmann A, Larson BL, Hjortnaes J, Alemдар N, et al. Tri-layered elastomeric scaffolds for engineering heart valve leaflets. *Biomaterials.* (2014) 35:7774–85. doi: 10.1016/j.biomaterials.2014.04.039
 70. Masoumi N, Larson BL, Annabi N, Kharaziha M, Zamanian B, Shaperо KS, et al. Electrospun PGS:PCL microfibers align human valvular interstitial cells and provide tunable scaffold anisotropy. *Adv Healthc Mater.* (2014) 3:929–39. doi: 10.1002/adhm.201300505
 71. Eslami M, Vrana NE, Zorlutuna P, Sant S, Jung S, Masoumi N, et al. Fiber-reinforced hydrogel scaffolds for heart valve tissue engineering. *J Biomater Appl.* (2014) 29:399–410. doi: 10.1177/0885328214530589
 72. Wunner FM, Bas O, Saidy NT, Dalton PD, Pardo EMD, Huttmacher DW. Melt electrospinning writing of three-dimensional poly(epsilon-caprolactone) scaffolds with controllable morphologies for tissue engineering applications. *J Vis Exp.* (2017) 130:56289. doi: 10.3791/56289
 73. Saidy NT, Wolf F, Bas O, Keijden H, Huttmacher DW, Mela P, et al. Biologically inspired scaffolds for heart valve tissue engineering via melt electrowriting. *Small.* (2019) 15:e1900873. doi: 10.1002/smll.201900873
 74. Moreira R, Neusser C, Kruse M, Mulderrig S, Wolf F, Spillner J, et al. Tissue-engineered fibrin-based heart valve with bio-inspired textile reinforcement. *Adv Healthc Mater.* (2016) 5:2113–21. doi: 10.1002/adhm.201600300
 75. Uiterwijk M, Smits A, van Geemen D, van Klarenbosch B, Dekker S, Cramer MJ, et al. In situ remodeling overrules bioinspired scaffold architecture of supramolecular elastomeric tissue-engineered heart valves. *JACC Basic Transl Sci.* (2020) 5:1187–206. doi: 10.1016/j.jacbs.2020.09.011
 76. Mela P, D'Amore A. In situ heart valve tissue engineering: is scaffold structural biomimicry overrated? *JACC Basic Transl Sci.* (2020) 5:1207–9. doi: 10.1016/j.jacbs.2020.11.009
 77. Lee A, Hudson AR, Shiwarski DJ, Tashman JW, Hinton TJ, Yerneni S, et al. 3D bioprinting of collagen to rebuild components of the human heart. *Science.* (2019) 365:482–7. doi: 10.1126/science.aav9051
 78. Wang DD, Qian Z, Vukicevic M, Engelhardt S, Kheradvar A, Zhang C, et al. 3D printing, computational modeling, and artificial intelligence for structural heart disease. *JACC Cardiovasc Imaging.* (2021) 14:41–60. doi: 10.1016/j.jcmg.2019.12.022
 79. Budharaju H, Subramanian A, Sethuraman S. Recent advancements in cardiovascular bioprinting and bioprinted cardiac constructs. *Biomater Sci.* (2021) 9:1974–94. doi: 10.1039/D0BM01428A
 80. Sedlakova V, McTiernan C, Cortes D, Suuronen EJ, Alarcon EI. 3D bioprinted cardiac tissues and devices for tissue maturation. *Cells Tissues Organs.* (2021) 1–14. doi: 10.1159/000512792
 81. Vukicevic M, Mosadegh B, Min JK, Little SH. Cardiac 3D printing and its future directions. *JACC Cardiovasc Imaging.* (2017) 10:171–84. doi: 10.1016/j.jcmg.2016.12.001
 82. Duan B, Kapetanovic E, Hockaday LA, Butcher JT. Three-dimensional printed trileaflet valve conduits using biological hydrogels and human valve interstitial cells. *Acta Biomater.* (2014) 10:1836–46. doi: 10.1016/j.actbio.2013.12.005
 83. Hockaday LA, Kang KH, Colangelo NW, Cheung PY, Duan B, Malone E, et al. Rapid 3D printing of anatomically accurate and mechanically heterogeneous aortic valve hydrogel scaffolds. *Biofabrication.* (2012) 4:035005. doi: 10.1088/1758-5082/4/3/035005
 84. Ott HC, Matthiesen TS, Goh SK, Black LD, Kren SM, Netoff TI, et al. Perfusion-decellularized matrix: using nature's platform to engineer a bioartificial heart. *Nat Med.* (2008) 14:213–21. doi: 10.1038/nm1684
 85. Schoen FJ, Levy RJ. Calcification of tissue heart valve substitutes: progress toward understanding and prevention. *Ann Thorac Surg.* (2005) 79:1072–80. doi: 10.1016/j.athoracsur.2004.06.033
 86. Siddiqui RF, Abraham JR, Butany J. Bioprosthetic heart valves: modes of failure. *Histopathology.* (2009) 55:135–44. doi: 10.1111/j.1365-2559.2008.03190.x
 87. Vinci MC, Tessitore G, Castiglioni L, Prandi F, Soncini M, Santoro R, et al. Mechanical compliance and immunological compatibility of fixative-free decellularized/cryopreserved human pericardium. *PLoS ONE.* (2013) 8:e64769. doi: 10.1371/journal.pone.0064769
 88. Amadeo F, Boschetti F, Polvani G, Banfi C, Pesce M, Santoro R. Aortic valve cell seeding into decellularized animal pericardium by perfusion-assisted bioreactor. *J Tissue Eng Regen Med.* (2018) 12:1481–93. doi: 10.1002/term.2680
 89. Lila N, McGregor CG, Carpentier S, Rancic J, Byrne GW, Carpentier A. Gal knockout pig pericardium: new source of material for heart valve bioprostheses. *J Heart Lung Transplant.* (2010) 29:538–43. doi: 10.1016/j.healun.2009.10.007
 90. Galili U. Natural anti-carbohydrate antibodies contributing to evolutionary survival of primates in viral epidemics? *Glycobiology.* (2016) 26:1140–50. doi: 10.1093/glycob/cww088
 91. Byrne G, Ahmad-Villiers S, Du Z, McGregor C. B4GALNT2 and xenotransplantation: a newly appreciated xenogeneic antigen. *Xenotransplantation.* (2018) 25:e12394. doi: 10.1111/xen.12394
 92. Tector AJ, Mosser M, Tector M, Bach JM. The possible role of anti-Neu5Gc as an obstacle in xenotransplantation. *Front Immunol.* (2020) 11:622. doi: 10.3389/fimmu.2020.00622
 93. Chen G, Qian H, Starzl T, Sun H, Garcia B, Wang X, et al. Acute rejection is associated with antibodies to non-Gal antigens in baboons using Gal-knockout pig kidneys. *Nat Med.* (2005) 11:1295–8. doi: 10.1038/nm1330
 94. Byrne GW, Stalboerger PG, Davila E, Heppelmann CJ, Gazi MH, McGregor HC, et al. Proteomic identification of non-Gal antibody targets after pig-to-primate cardiac xenotransplantation. *Xenotransplantation.* (2008) 15:268–76. doi: 10.1111/j.1399-3089.2008.00480.x
 95. Naso F, Gandaglia A. Different approaches to heart valve decellularization: a comprehensive overview of the past 30 years. *Xenotransplantation.* (2018) 25:e12354. doi: 10.1111/xen.12354
 96. Vincentelli A, Wautot F, Juthier F, Fouquet O, Corseaux D, Marechaux S, et al. In vivo autologous recellularization of a tissue-engineered heart valve: are bone marrow mesenchymal stem cells the best candidates? *J Thorac Cardiovasc Surg.* (2007) 134:424–32. doi: 10.1016/j.jtcvs.2007.05.005
 97. Dainese L, Guarino A, Burba I, Esposito G, Pompilio G, Polvani G, et al. Heart valve engineering: decellularized aortic homograft seeded with human cardiac stromal cells. *J Heart Valve Dis.* (2012) 21:125–34.
 98. Santoro R, Consolo F, Spiccia M, Piola M, Kassem S, Prandi F, et al. Feasibility of pig and human-derived aortic valve interstitial cells seeding on fixative-free decellularized animal pericardium. *J Biomed Mater Res B Appl Biomater.* (2016) 104:345–56. doi: 10.1002/jbm.b.33404
 99. Amadeo F, Barbuto M, Bernava G, Savini N, Brioschi M, Rizzi S, et al. Culture into perfusion-assisted bioreactor promotes valve-like tissue maturation of recellularized pericardial membrane. *Front Cardiovasc Med.* (2020) 7:80. doi: 10.3389/fcvm.2020.00080

Conflict of Interest: The authors declare that the research was conducted in the absence of any commercial or financial relationships that could be construed as a potential conflict of interest.

Publisher's Note: All claims expressed in this article are solely those of the authors and do not necessarily represent those of their affiliated organizations, or those of the publisher, the editors and the reviewers. Any product that may be evaluated in this article, or claim that may be made by its manufacturer, is not guaranteed or endorsed by the publisher.

Copyright © 2022 Rizzi, Ragazzini and Pesce. This is an open-access article distributed under the terms of the Creative Commons Attribution License (CC BY). The use, distribution or reproduction in other forums is permitted, provided the original author(s) and the copyright owner(s) are credited and that the original publication in this journal is cited, in accordance with accepted academic practice. No use, distribution or reproduction is permitted which does not comply with these terms.



Marker-Independent Monitoring of *in vitro* and *in vivo* Degradation of Supramolecular Polymers Applied in Cardiovascular *in situ* Tissue Engineering

Julia Marzi^{1,2,3*}, Emma C. Munnig Schmidt⁴, Eva M. Brauchle^{1,2,3}, Tamar B. Wissing^{4,5}, Hannah Bauer⁶, Aurelie Serrero⁶, Serge H. M. Söntjens⁷, Anton W. Bosman⁸, Martijn A. J. Cox⁶, Anthal I. P. M. Smits^{4,5} and Katja Schenke-Layland^{1,2,3,9}

¹ Department for Medical Technologies and Regenerative Medicine, Institute of Biomedical Engineering, Eberhard Karls University Tübingen, Tübingen, Germany, ² NMI Natural and Medical Sciences Institute at the University of Tübingen, Reutlingen, Germany, ³ Cluster of Excellence iFIT (EXC 2180) "Image-Guided and Functionally Instructed Tumor Therapies," Eberhard Karls University Tübingen, Tübingen, Germany, ⁴ Department of Biomedical Engineering, Eindhoven University of Technology, Eindhoven, Netherlands, ⁵ Institute for Complex Molecular Systems (ICMS), Eindhoven University of Technology, Eindhoven, Netherlands, ⁶ Xeltis BV, Eindhoven, Netherlands, ⁷ SyMO-Chem BV, Eindhoven, Netherlands, ⁸ SupraPolix BV, Eindhoven, Netherlands, ⁹ Cardiovascular Research Laboratories, Department of Medicine, David Geffen School of Medicine at University of California, Los Angeles, Los Angeles, CA, United States

OPEN ACCESS

Edited by:

Najma Latif,
The Magdi Yacoub Institute,
United Kingdom

Reviewed by:

Yuan-Tsan Tseng,
Imperial College London,
United Kingdom
Toshiharu Shinoka,
Nationwide Children's Hospital,
United States

*Correspondence:

Julia Marzi
julia.marzi@uni-tuebingen.de

Specialty section:

This article was submitted to
Heart Valve Disease,
a section of the journal
Frontiers in Cardiovascular Medicine

Received: 28 February 2022

Accepted: 25 April 2022

Published: 17 May 2022

Citation:

Marzi J, Munnig Schmidt EC, Brauchle EM, Wissing TB, Bauer H, Serrero A, Söntjens SHM, Bosman AW, Cox MAJ, Smits AIPM and Schenke-Layland K (2022) Marker-Independent Monitoring of *in vitro* and *in vivo* Degradation of Supramolecular Polymers Applied in Cardiovascular *in situ* Tissue Engineering. *Front. Cardiovasc. Med.* 9:885873. doi: 10.3389/fcvm.2022.885873

The equilibrium between scaffold degradation and neotissue formation, is highly essential for *in situ* tissue engineering. Herein, biodegradable grafts function as temporal roadmap to guide regeneration. The ability to monitor and understand the dynamics of degradation and tissue deposition in *in situ* cardiovascular graft materials is therefore of great value to accelerate the implementation of safe and sustainable tissue-engineered vascular grafts (TEVGs) as a substitute for conventional prosthetic grafts. In this study, we investigated the potential of Raman microspectroscopy and Raman imaging to monitor degradation kinetics of supramolecular polymers, which are employed as degradable scaffolds in *in situ* tissue engineering. Raman imaging was applied on *in vitro* degraded polymers, investigating two different polymer materials, subjected to oxidative and enzymatically-induced degradation. Furthermore, the method was transferred to analyze *in vivo* degradation of tissue-engineered carotid grafts after 6 and 12 months in a sheep model. Multivariate data analysis allowed to trace degradation and to compare the data from *in vitro* and *in vivo* degradation, indicating similar molecular observations in spectral signatures between implants and oxidative *in vitro* degradation. *In vivo* degradation appeared to be dominated by oxidative pathways. Furthermore, information on collagen deposition and composition could simultaneously be obtained from the same image scans. Our results demonstrate the sensitivity of Raman microspectroscopy to determine degradation stages and the assigned molecular changes non-destructively, encouraging future exploration of this techniques for time-resolved quality assessment of *in situ* tissue engineering processes.

Keywords: Raman imaging, carotid implantation, tissue-engineered vascular grafts (TEVG), guided tissue engineering, resorption

INTRODUCTION

Current cardiovascular grafts are limited in their ability to replace native tissue. Hemodynamic changes require to adapt continuously, which is difficult to be artificially reproduced (1). As a result, complications often occur due to incompatibility between the native tissue and the grafted material (2). Tissue engineered grafts have been considered as promising cardiovascular replacements, but require time for cell harvesting, conditioning and production of rigid matrix, which is why these are not applicable for off-the-shelf usage (1). *In situ* tissue engineering or endogenous tissue restoration might be the solution, as in this method a degradable biomaterial is implanted in the patient to temporarily function as both, graft and scaffold for endogenous cells, directing regeneration directly at the intended site in the body (3). Biomaterials applied in *in situ* tissue engineering range from polymer scaffolds to *in vitro* generated matrices and decellularized xeno- or allografts (4–6). Over time the biomaterial will degrade, while matrix is produced by the cells that infiltrate and populate the scaffold. These two processes should happen at similar rates to preserve the integrity of the graft. Here, supramolecular materials enable the introduction of different molecular groups and so allow for tailoring of material characteristics, including degradation rates and mechanisms (7). Supramolecular materials can form stacks, as hydrogen bonds are formed between the supramolecular groups, which are non-covalent and therefore dynamic (7). This also enables integration of specific functional groups in a polymer. Under ideal conditions all biomaterial will degrade and a living tissue will remain with the ability to grow and adjust to its environment (8).

Implanted biomaterials degrade due to several processes, namely (1) enzymatic hydrolysis, also called enzymatic degradation when catalyzed by enzymes such as protease and esterase; (2) oxidation caused by reactive oxygen species (ROS) and (3) physical deterioration caused by water absorption (9). The immune system influences both enzymatic and oxidative degradation by way of macrophages and other activated immune cells, which secrete enzymes and ROS when in contact with the biomaterial scaffold (10). On a molecular level, hydrolytic degradation occurs when water molecules substitute ester bonds in a polymer (9). This causes breaking of the polymer chains and results in smaller polymer segments. In oxidative degradation, oxygen-comprising free radicals such as hydroxide or superoxide radicals react with the polymer (9). Especially, methylene protons next to functional groups in the polymer backbone are sensitive to hydrogen extraction, ultimately resulting in chain scission (or possibly cross-linking) of the degraded polymer. Typical molecules generated in oxidative degradation are water, carbon dioxide, and oligomeric chains with hydroxyl chain ends and/or carboxylic acid chain ends. Tissue engineered grafts will be constantly load-bearing during the transition from biomaterial to tissue. Accordingly, an appropriate degradation rate is of utmost importance for the success of the *in situ* procedure (9). Therefore, there is a need for tailoring the degradation kinetics of the used scaffold material. Furthermore, the biocompatibility and potential cytotoxicity of degradation products are an essential safety aspect of biodegradable polymers (11). Thus,

unraveling the mechanisms of polymer degradation and potential byproducts on a molecular level and correlating *in vitro* observations to *in vivo* processes is highly relevant for the design of successful implant materials providing long-term functionality as well as biocompatibility and immunocompatibility.

Methods to assess graft degradation *in vitro*, include scanning electron microscopy (SEM), gel permeation chromatography (GPC) or thermal and mechanical analyses to determine morphological changes and polymer integrity and have been thoroughly applied to study polymer degradation (10, 12, 13). These methods can similarly be applied for the analysis of *in vivo* degradation but require extensive sample processing or the removal of the implant material from the surrounding tissue and often do not allow to obtain spatially resolved information. Gaining spatial information on the local material degradation is highly important given that scaffold degradation is subject to strong spatiotemporal heterogeneities, due to differences in local microenvironment such as variations in cell influx or local hemodynamic loads (14, 15).

For more than two decades, material science employs Raman spectroscopy, but in the field of biological tissues this laser-based technique is relatively new (16, 17). Raman microspectroscopy is of great interest for both *in vitro* and *in vivo* applications due to its non-invasive nature and ease of sample preparation in comparison to more conventional methods, as it is label-free. Similar to infrared spectroscopy, which has been applied in a few studies to investigate *in vitro* as well as *in vivo* polymer degradation (18–20), Raman microspectroscopy allows for the non-destructive detection of molecular changes in both, synthetic as well as biological molecules, and in addition enables the simultaneous visualization of their spatial distribution in Raman imaging setups. In comparison to local polymer degradation, extracellular matrix formation and cellular infiltration in *in situ* tissue engineering can be studied at a spatial resolution by histological methods (21, 22), and were also in the focus in previous publications on *in situ* tissue-engineered heart valves and carotid implants, where Raman imaging was implemented as complementary method to routine histochemical and immunofluorescence staining (5, 15).

The aim of this study is to gain a better understanding of *in vivo* degradation pathways of supramolecular polymers which are promising candidates for *in situ* tissue engineering. Raman microspectroscopy and imaging were established in combination with multivariate analysis to assess degradation *in situ* and avoid further sample destruction by preprocessing steps. Molecular fingerprints of oxidative and enzymatic degradation were determined in fast and slow degrading polymer composites and transferred for the analysis of *in vivo* degradation in a carotid implant in a sheep model monitored over a period of 12 months.

MATERIALS AND METHODS

Polymer Scaffolds and Films

Polycaprolactone₂₀₀₀-Bisurea (PCL-BU) material (SyMO-Chem, Eindhoven, The Netherlands) and Poly(hexamethylene-) carbonate-Ureido-Pyrimidinone (PC-UPy) material (Xeltis, Eindhoven, The Netherlands) were prepared and electrospun

to form tubular scaffolds of 6–23 mm inner diameter. Scaffolds were fabricated in a climate-controlled electrospinning cabinet (IME Technologies, Geldrop, The Netherlands) according to the electrospinning method described previously by Pabittei et al. (23). Films were prepared by dissolving PC-UPy in HFIP, followed by casting the solution in a petri dish and dried at 37°C in a vacuum oven. Scaffolds and films were gamma sterilized.

In vitro Degradation

PCL-Bisurea Scaffolds

Samples for the *in vitro* study were degraded following methods previously described by Brugmans et al. (10). In brief, circles with a diameter of 8 mm were punched from the electrospun material ($n = 3$ per treatment). Prior to the degradation process, meshes were centrifuged at 4,500 rpm in purified water for 10 min to wetten the material and remove air bubbles. The material was enzymatically degraded by incubation at 37°C in 0.5 mL enzyme for either 12 or 36 h. The enzyme solution consisted of a 100x dilution of 10 U/mL cholesterol esterase from bovine pancreas (C-3766, Sigma-Aldrich, Saint Louis, US) in PBS. Cholesterol esterase is present in native serum, secreted by activated macrophages and known to be more dominant for the cleavage of urethane bonds than other secreted enzymes (24, 25). Oxidative degradation was done in a 2 mL oxidative degradation solution. The oxidative solution consisted of 20% hydrogen peroxide (#216763, Sigma-Aldrich) and 0.033 M cobalt(II) chloride (#232696, Sigma-Aldrich) in purified water. Hydrogen peroxide and cobalt(II) chloride undergo a Haber-Weiss reaction, creating reactive hydroxyl radicals, which react with the material (26). Incubation times of the scaffolds in oxidative solutions were 2.5 and 5 days. As control, samples were exposed to PBS for 12 and 36 h. The oxidative solutions were changed every 2.5 days to maintain a constant concentration of radicals.

PC-UPy Films and Scaffolds

Scaffolds were punched to 25 x 5 mm strips ($n = 4$ per timepoint). Films were cut to 1 x 1 cm samples ($n = 1$). Scaffolds were centrifuged at 4,500 rpm in purified water for 3 min. The scaffold and film were degraded using oxidative degradation with 50 wt% H₂O₂ (Honeywell) at 50°C for 2, 5 and 20 days. The oxidative solutions were changed every 3 days to maintain a constant concentration of radicals. The reaction was stopped by washing the samples with RO water and 1.3 M Na₂SO₃ solution.

Degradation Analysis

For routine degradation analysis, the mass averaged molecular weight (M_w) of three samples per condition were determined, by dissolving them in dimethylformamide (DMF) (Sigma-Aldrich) followed by gel permeabilization chromatography (GPC) analysis. This analysis was performed on a Varian/Polymer Laboratories PL-GPC 50, using DMF with 10 mmol/L lithium bromide as eluent and maintaining the temperature of the equipment at 50 °C. Furthermore, scaffold fiber morphology was visualized with scanning electron microscopy (SEM, Quanta 600F; Fei, Hillsboro, OR) to assess scaffold damage after *in vitro* degradation.

In vivo Degradation

Tissue sections of PC-UPy grafts were obtained from an *in vivo* study of a carotid implant in a sheep model (27). The animal study was conducted in compliance with ethical regulations and the Helsinki protocol. Furthermore, animal welfare was in compliance with the Directive 2010/63/ EU. PC-UPy scaffolds were implanted in 6 female Ile de France sheep (age 8–9 months, weight 45–90 kg at implantation) in the interposition of the carotid artery at IMMR (Paris, France). All animals received a 6–7 mm inner diameter, 3–5 cm long PC-UPy graft. The follow-up was 6 ($n = 3$) and 12 months ($n = 3$). All animals received Enoxaparin treatment (3000–4000IU SC/BID) until day 90 and Aspirin (125 mg IM/QD) until sacrifice. Patency was 100% at 6 months ($n = 3$) and 12 months ($n = 3$) follow-up with no indications of stenosis. After the endpoint of the study the explants were fixed in 4% neutral buffered formalin. The specimens were dehydrated, embedded in paraffin, and sectioned at 4 to 10 µm (performed by CVPPath Institute Inc., Gaithersburg, US). For orientation in the section and to define relevant regions for Raman imaging, overview staining *via* Movat Pentachrome were provided as well as von Kossa stains to detect calcifications (Supplementary Figure 1). Based on histochemical images, histo-scores were defined for semi-quantification of matrix degradation and collagen infiltration as previously described by Brugmans et al. (28). Histo-scores for polymer absorption, collagen infiltration and calcifications as well as the definition of score values are described in Supplementary Figure 2.

Raman Microspectroscopy

An inverse Raman microspectrometer (alpha 300R, WITec GmbH, Ulm, Germany), equipped with a 532 nm laser diode, was employed for all measurements with laser output power set to 50 mW for spectral acquisition (600 gr/mm, ±10 wavelengths).

Measurements of *in vitro* degraded scaffolds were performed using a 50x objective (LD EC Epiplan-Neofluor HD DIC 50x/0.55, Zeiss, Oberkochen, Germany). The integration time per spectrum was set to 0.2 s. For each sample, a minimum of three ROIs was chosen based on bright field images. Dimensions of the selected ROIs were 100 x 100 µm at a spatial resolution of 1 x 1 µm.

All measurements of *in vivo* degraded samples were performed with a 63x water-immersion objective (W Plan Apochromat 63x/1, Zeiss). Prior to Raman measurements, the tissue sections were deparaffinized and kept hydrated in PBS. Raman images were acquired from defined regions (500 x 500 µm, 2 x 2 µm/pixel, 0.05 s/pixel) within the implanted material and neointima, as well as the material-luminal tissue interface for the 12 months samples (Figure 1). ROIs were defined in histology overview images (Movat-Pentachrome stain performed by CVPPath Institute Inc., Gaithersburg, US) and transferred to unstained sections for Raman imaging. To avoid processing artifacts (e.g. by deparaffinization), *in vitro* degraded PC-UPy reference materials (see section *In vitro* Degradation) were additionally embedded, sectioned and deparaffinized before Raman imaging at the same conditions as the tissue sections to allow a direct comparison.

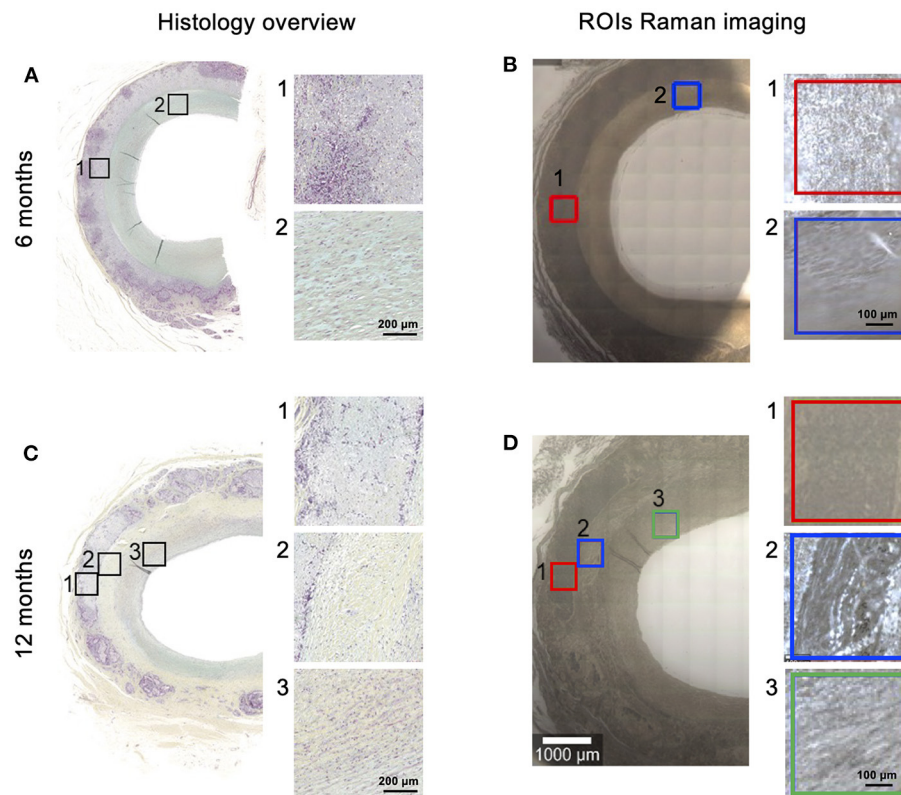


FIGURE 1 | Overview of analyzed scaffolds and regions of interest (ROIs). PC-UPy scaffolds were implanted in a sheep model. FFPE sections of 6-month (A,B) and 12-month (C,D) explants were analyzed. ROIs for Raman imaging (B,D) were defined in Movat-Pentachrome stained sections (A,C) (provided by CVPath). In 6-month samples scaffold material (1) and lumen (2) were distinguished, in 12-month samples scaffold material (1), material-tissue interface (2) and neointimal lumen (3) were defined as ROIs.

For spectral processing, *WITec Project FIVE* (5.3) software was used. Raman data was preprocessed by employing cosmic ray removal, cropping the spectra to the range between 300 and 3000 cm^{-1} , baseline-correction (shape algorithm) and normalization (Area under the curve = 1). Intensity distribution heatmaps at 1444 cm^{-1} were generated from non-normalized *in vitro* PC-UPy degradation data and compared by mean gray value analysis in *ImageJ* (Fiji).

Data Analysis

True Component Analysis

Processed images were analyzed using True Component Analysis (TCA), which aims to demix the different components in the measured spectra to find individual spectral components within the spectral dataset. Thus, it enables to generate false-color coded intensity distribution heatmaps based on different underlying spectral information in each pixel of the spectral maps. Spectra of non-degraded control material were used as reference.

Principal Component Analysis

Single spectra of the scaffold polymer component as well as the collagen component were exported using *Project FIVE* software by generating an image filter of the TCA heatmaps.

From each sample, a minimum of 100 spectra were randomly selected and exported to The Unscrambler X 10.3 (CAMO Software, Oslo, Norway). Principal component analysis (PCA) models were calculated for in-depth comparison of RM datasets of all conditions. PCA enables extraction of vector-dependent score values and loading spectra, which describe the spectral variances of a data set and depict the irregularities in a single Raman spectrum (29). PCA was performed employing the non-linear iterative partial least squares algorithm as described previously (30). All principal components (PCs) were screened for changes in Raman shifts found in the fingerprint regions of Raman spectra of the scaffold polymer or collagens. Outliers in PCA were determined using Hotelling T^2 test and excluded.

Statistical Analysis

Statistical analysis was performed in Graph Pad Prism 9. Data are presented as mean \pm standard deviation. Data were tested for Gaussian distribution (Shapiro-Wilk) and statistically compared using one-way ANOVA and Tukey test or Kruskal-Wallis and Dunn's test for multiple comparisons. P values < 0.05 were considered statistically significant.

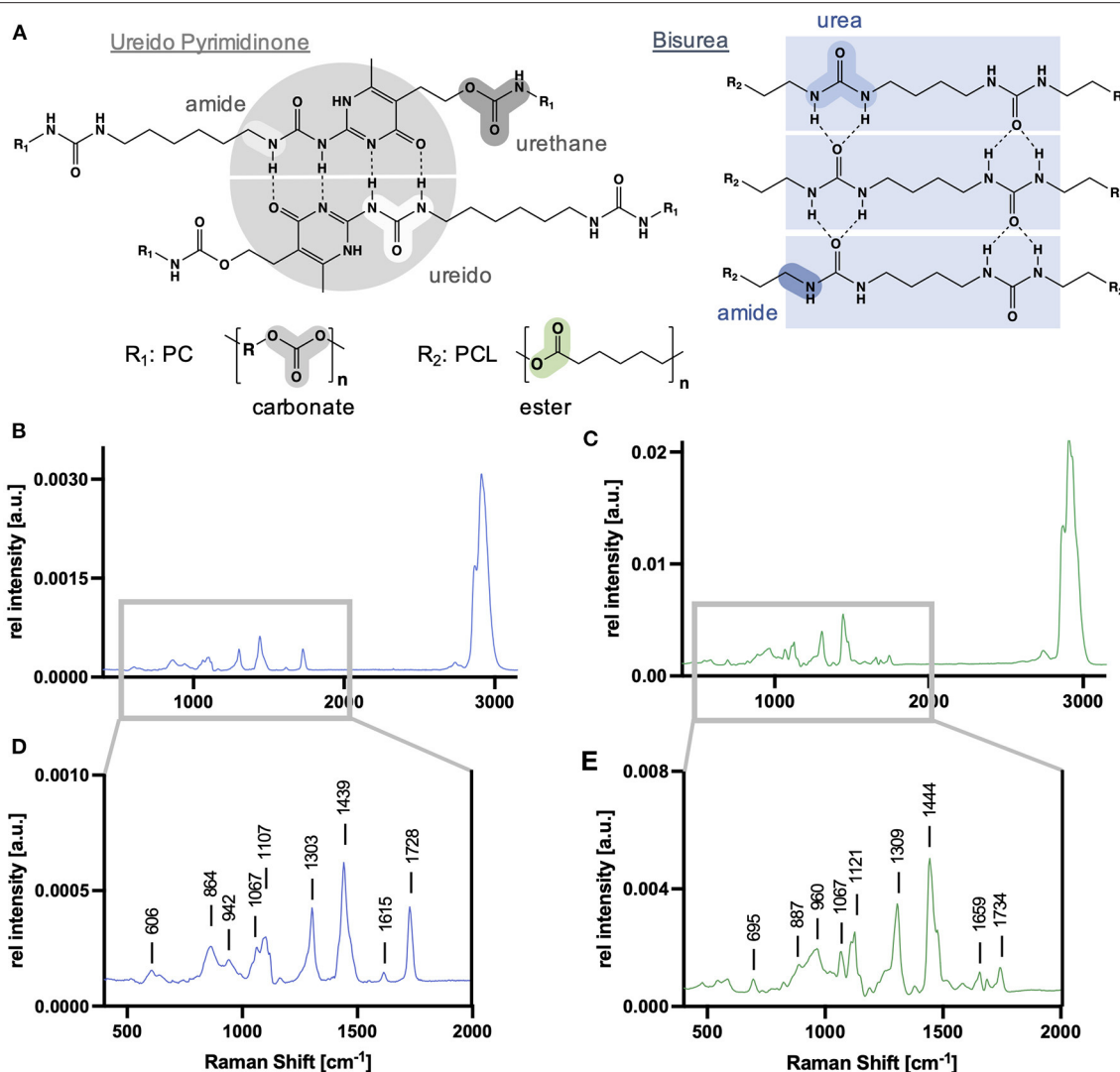


FIGURE 2 | Supramolecular building blocks and Raman spectra of scaffold polymer references. **(A)** Generic molecular structure of ureido pyrimidine polycarbonate (PC-UPy) and bisurea polycaprolactone (PCL-BU) including their molecular groups susceptible to degradation. PCL-BU **(B,D)** and PC-UPy **(C,E)** exhibit characteristic Raman signatures with bands assigned to their different building blocks.

RESULTS

Polymer Scaffolds Exhibit Characteristic Raman Signatures

Raman spectra of non-degraded electrospun PCL-BU and PC-UPy (**Figure 2**) were acquired and served as references to identify degradation-dependent spectral changes. Generic molecular structures for UPy and BU building blocks and relevant functional groups susceptible to degradation are described in **Figure 2A**. For PCL-BU (**Figures 2B,D**), a distinction could be made between the fingerprint regions resulting from the PCL chains and the urea blocks. When considering the PCL bands, peaks assigned to the C-C vibrations of the C-COO group (862 and 942 cm^{-1}), skeletal stretching (1,067 and 1,098 cm^{-1}), deformation vibrations of the CH_2 groups (1,303 and 1,442 cm^{-1}) and vibrations caused by C=O vibration (1,728 cm^{-1})

were identified (31). The fingerprint regions of the urea can be assigned to NCO and NCN vibrations (606 cm^{-1}) and N-H stretching at 1,615 cm^{-1} (32). The Raman spectrum of PC-UPy (**Figures 2C,E**) demonstrates assignments to the UPy blocks especially at 695 and 1,659 cm^{-1} . Spectral resonance typical for the PC chains is reflected by C-COO (960 cm^{-1}) and C=O groups (1,734 cm^{-1}), skeletal stretching (1,067 cm^{-1}) as well as CH_2 deformations (1,309 and 1,444 cm^{-1}). An overview of the most relevant bands and their molecular assignments is given in **Table 1**.

Comparison of Oxidative and Enzymatic *in vitro* Degradation in PCL-BU Scaffolds

First, the effect of different degradation mechanisms was investigated on PCL-BU material. PCL-BU was selected as it

was previously reported that this material is susceptible to both enzymatic and oxidative degradation (10). Electrospun PCL-BU scaffolds underwent oxidative degradation using $\text{H}_2\text{O}_2/\text{CoCl}_2$ or enzymatic degradation by cholesterol esterase. Raman images were acquired at three different timepoints for each of the degradation procedures and analyzed by True Component

Analysis (TCA) to generate intensity distribution heatmaps by fitting the non-degraded PCL-BU reference spectrum. In oxidative degradation, TCA of PCL-BU scaffolds allowed to visualize the fiber structures with no significant changes in fiber morphology over degradation time. However, for the 5 day degraded scaffolds, there was no good fit with the PCL-BU reference spectrum and an additional TCA component (light green) was identified (**Figure 3A**). TCA with the PCL-BU reference spectrum was also applied to generate Raman images of the enzymatically degraded scaffolds. Here, a clear change in fiber morphology to less and also thinner polymer fibers was observed (**Figure 3B**). Moreover, TCA identified a new spectral component (pink), starting to appear after 12 h of degradation at a spot wise localization. The two new spectral components were compared to the PCL-BU reference spectrum and showed changes in signal intensities in the Raman peaks at 606, 862, 1,107, 1,615 and 1,728 cm^{-1} (**Figure 3C**) but also in the overall spectral pattern, especially in the wavenumber range between 800 and 1,200 cm^{-1} (**Figure 3D**). New peaks which were either just present as spectral shoulder of another band or not expressed at all in the non-degraded PCL-BU spectrum were identified, i.e. at 910 and 1,039 cm^{-1} upon oxidative degradation and 992 and 1,121 cm^{-1} upon enzymatic degradation.

TABLE 1 | Relevant PCL-BU and PC-UPy peaks and their molecular assignments.

| Raman Shift [cm^{-1}] | | Molecular assignment |
|----------------------------------|--------|-----------------------------------|
| PCL-BU | PC-UPy | |
| 606 | | N-C-O and N-C-N vibrations (BU) |
| | 695 | Heterocycle ring vibrations (Upy) |
| 864 | 887 | C-O-C stretch |
| 942 | 960 | C=O |
| 1067 | 1067 | C-C bending (polymer backbone) |
| 1107 | | C-C stretch (PCL) |
| | 1121 | C-C stretch or C-OH/C-O-C |
| 1303 | 1309 | CH_2 twisting |
| 1439 | 1444 | CH_2/CH_3 bending |
| | 1520 | C=C |
| 1615 | | N-H |
| | 1659 | UPy |
| | 1685 | Amide (urethane) |
| 1728 | | C=O |
| | 1734 | C=O (PC) |

Monitoring of Oxidative *in vitro* Degradation in PC-UPy Scaffolds

Raman microspectroscopy was then performed on *in vitro* degraded PC-UPy polymer films and electrospun scaffolds

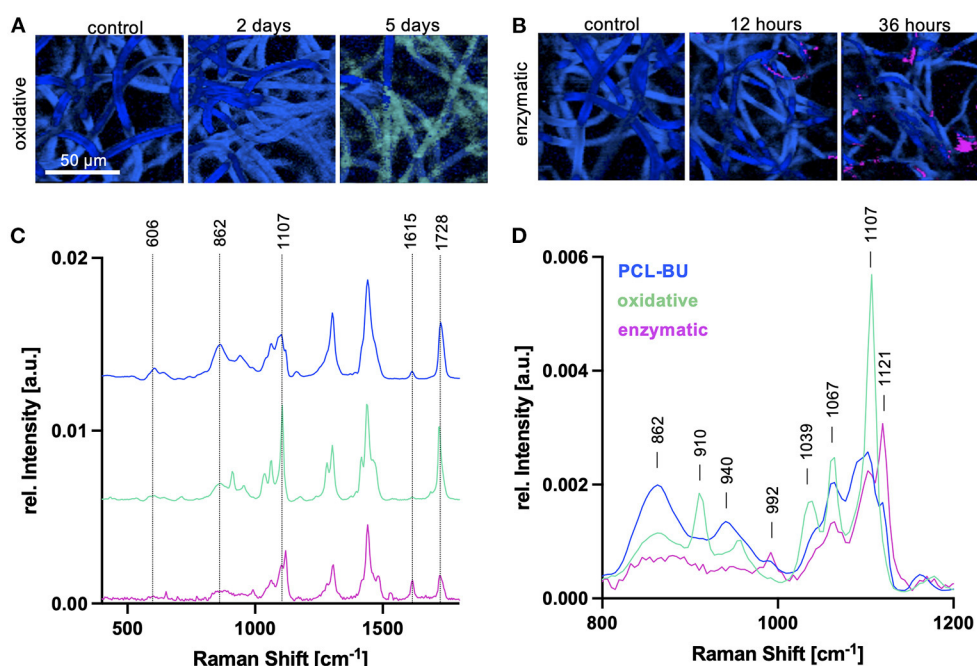


FIGURE 3 | Oxidative and enzymatic degradation in PCL-BU scaffolds. **(A)** TCA heatmaps of electrospun PCL-BU scaffolds at 0, 2 and 5 days of oxidative degradation. Scale bar equals 50 μm **(B)** TCA heatmaps of electrospun PCL-BU scaffolds at 0, 12 and 36 h of enzymatic degradation. **(C)** Average Raman spectra identified by TCA. blue—PCL-BU; light green—signature in 5d oxidatively degraded PCL-BU fibers; pink—signature appearing after 12 h of enzymatically degraded PCL-BU fibers. Labeled peaks correspond to bands with changes in peak intensity. **(D)** Zoom into the 800–1,200 cm^{-1} Raman shift range.

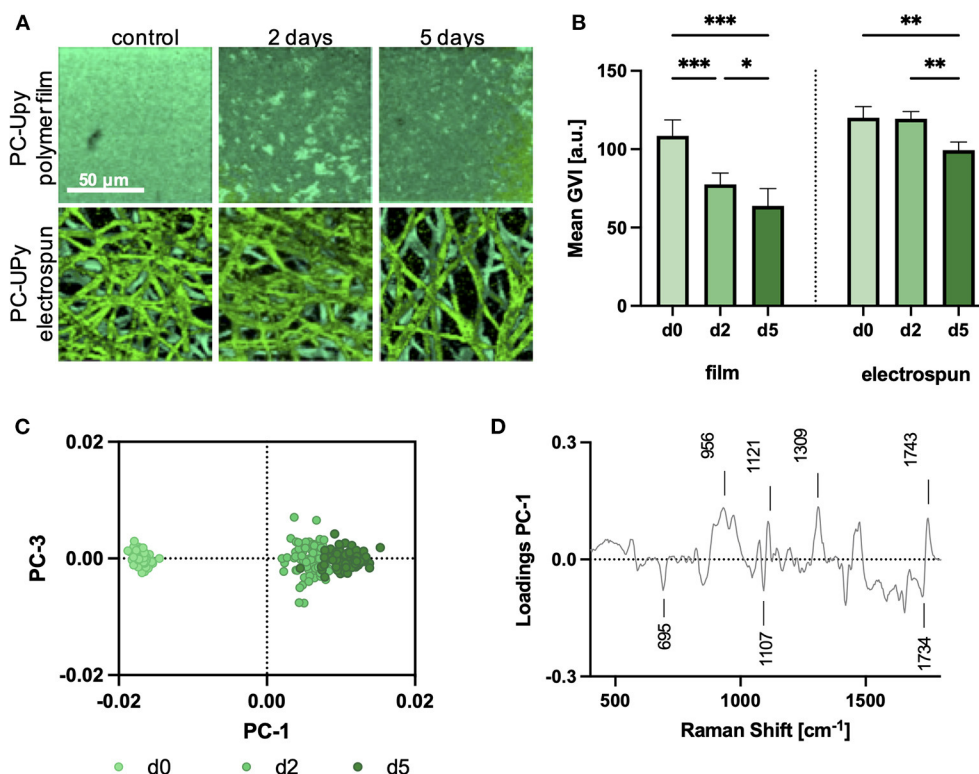


FIGURE 4 | Comparison of oxidative *in vitro* degradation of film and electrospun PC-UPy polymers. **(A)** TCA images of polymer films (upper row) and electrospun scaffolds (lower row) at 0 (d0), 2 (d2) and 5 (d5) days of oxidative *in vitro* degradation. Scale bar equals 50 μ m **(B)** Mean gray value intensities (GVI) of the PC-UPy polymer film and electrospun fiber intensity distribution heatmaps. Data are represented as mean \pm SD; $n = 3$, one-way ANOVA, * $p < 0.05$, ** $p < 0.01$, *** $p < 0.001$. **(C)** PC-1/PC-3 scores plot of a PCA performed on single extracted spectra from electrospun fibers **(A)** demonstrates a degradation time-dependent shift in the Raman signature. **(D)** The PC-1 loadings plot indicates relevant peaks for the spectral separation.

to determine the sensitivity of Raman microspectroscopy to investigate polymer degradation (Figure 4). Given that PC-UPy is barely susceptible to enzymatic degradation *in vitro* (33), the samples for this material were degraded by exposure to H₂O₂. TCA, with the non-degraded PC-UPy as reference spectrum, allowed for the mapping of the non-degraded material within the samples (Figure 4A). Control PC-UPy films showed a homogenous distribution of the Raman signal which decreased after 2 and 5 days within the degradation solution as quantified by the mean gray value intensity (GVI, Figure 4B). TCA images of electrospun control and degraded PC-UPy scaffolds expressed a good fit to the PC-UPy reference spectrum and showed tendencies toward a less dense fiber network after 5 days, as also reflected in the mean GVI (Figure 4B) but no further morphological differences. Therefore, a defined number of single spectra were randomly extracted from the TCA maps and analyzed by principal component analysis (PCA) to determine minor spectral changes and investigate the molecular composition of the degraded samples. The PC-1/PC-3 scores plot showed a clear separation of the spectral information derived from non-degraded, but also between day-2 and day-5 degraded polymer fibers. Control spectra clustered in the negative PC-1 scores range, whereas degraded samples clustered in the positive PC-1 range, with the strongest shift in day-5 scaffolds

(Figure 4C). The PC-1 loadings plot served to interpret the molecular changes that are assigned to the observed degradation time dependent separation (Figure 4D). The further a data point clusters at the positive PC scores range, the more pronounced are the bands which are described as positive peaks in the loadings. Data clustering in the negative scores range, exhibit stronger assignments to bands which are negative peaks in the corresponding loadings plot. Here, the bands at 695 (UPy) and 1,107 cm⁻¹ (C-C, skeletal stretch) decreased upon degradation, whereas an increase was observed for the bands at 956 (C=O), 1,121 (C-O-C, ether groups), 1,309 (CH₂ twisting) and 1,743 cm⁻¹ (C=O).

Molecular Characterization of *in vivo* Degradation of PC-UPy Scaffolds

Tissue sections of an *in vivo* study, where PC-UPy based electrospun scaffolds were implanted as carotid replacement in a sheep model, were investigated by Raman imaging. Spectral maps of the scaffold region (ROI1) of 6-month (Figure 5A) and 12-month explants (Figure 5B) were analyzed by TCA. In addition to a strong signal originating from the PC-UPy polymer, TCA allowed to localize and identify collagens, cells and fibrin depositions according to characteristic spectral signatures (Figure 5C). Whereas two of the 6-month explants showed

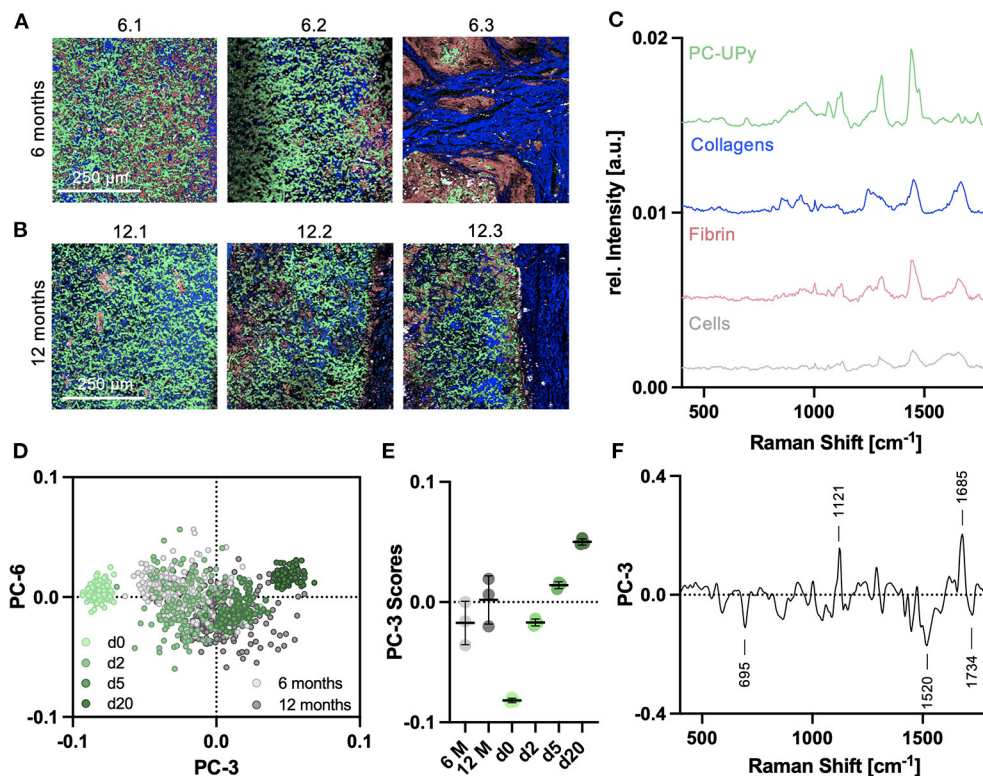


FIGURE 5 | Raman analysis of *in vivo* degradation of PC-UPy scaffolds. TCA Raman images of (A) 6-month and (B) 12-month explants; light green—PC-UPy, blue—collagens, light red—fibrin, white—cells, each image represents the explant from another animal, scale bar equals 250 μm (C) Identified TCA Raman spectra could be assigned to polymer and biological signatures. (D) Spectra extracted from *in vivo* degradation were compared to *in vitro* degradation by principal component analysis. (E) PC-3 scores indicated a degradation time dependent shift with 6 and 12-months *in vivo* samples clustering in the range between 2 and 5 day *in vitro* degraded samples, $n = 3$, mean score values \pm SD (F) Underlying spectral changes are explained by the PC-3 loadings plot.

a major contribution of the polymer fibers, in one explant (6.3) a strong collagen ingrowth was observed. Similarly, one of the 12-month implants (12.1) resulted in strong PC-UPy contributions compared to the other two 12-month explants, where the polymer assignments appeared less dense. Even though differences were visible between 6- and 12-month image distributions, 12-month explants still showed major assignments to polymer materials. Semi-quantitative analysis of polymer resorption was performed and defined in HistoScores, indicating a score of 25–50% matric absorption after 12 months (Supplementary Figure 2). In addition to morphological differences, spectra from the TCA images were extracted and analyzed by PCA to investigate molecular changes in PC-UPy polymer fibers upon *in vivo* degradation and to compare them to *in vitro* degradation. Therefore, a PCA including spectra from *in vitro* as well as *in vivo* degraded scaffolds was conducted. *In vitro* data were extended by an additional timepoint after 20 days of oxidative degradation. The PC scores plot demonstrated a degradation time dependent shift toward increasing PC-3 score values with progressing degradation time and showed a close overlay of *in vivo* and *in vitro* degraded samples (Figure 5D). Comparison of the PC score values (Figure 5E) demonstrated a clustering of the 6-month samples within the range of the 2-day *in vitro* degraded samples, whereas 12-month samples were

overlapping with the 5-day degraded samples. In accordance with the TCA images, the signatures of the 12.1. explant resembled rather the composition of the 6-month explants. An explant-wise comparison including an overview of the statistical testing is provided in Supplementary Figure 3. The PC-3 loadings plot (Figure 5F) allows to interpret the underlying molecular changes. Polymer fibers at later degradation stages, clustering at higher PC-3 ranges, were assigned to more pronounced bands at 1,121 (C-O) and 1,685 cm^{-1} (Amide, urethane), whereas signatures of non-degraded and early-stage degraded samples, clustering in the negative PC-3 range, had a higher contribution of the peaks at 695 and 1520 cm^{-1} (both UPy).

***In vivo* Tissue Remodeling Correlates to Polymer Degradation**

Raman histopathology enables the simultaneous detection and analysis of both, polymer and biological components, within the same tissue section and without the need for extensive sample processing or staining. In addition to polymer degradation at the implant material, the surrounding tissue was analyzed at three different regions—in between the scaffold fibers, at the polymer-tissue interface and in the neointima at the lumen (Figure 6A). The three-layer separation was only significantly expressed in the 12-month explants, whereas the 6-month explants were

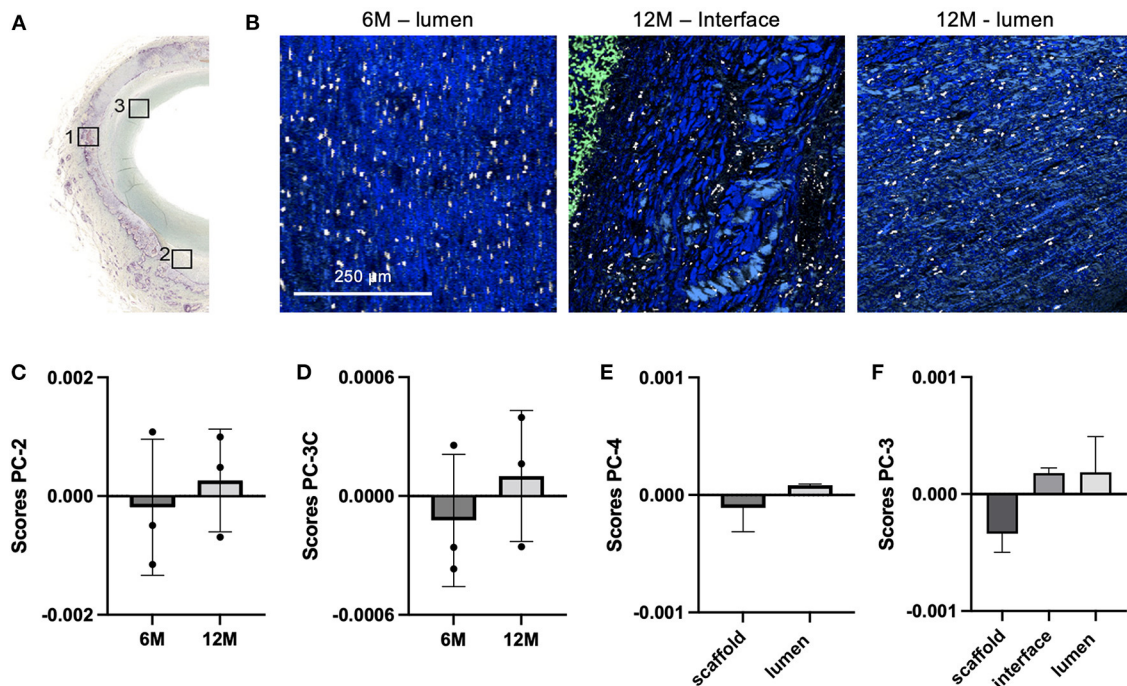


FIGURE 6 | Tissue maturation and collagen infiltration in carotid grafts. **(A)** Raman images were acquired from additional regions at the explant lumen (ROI3) and the interface (ROI2, only in 12-month samples), as defined in consecutive sections stained for Movat Pentachrome. **(B)** TCA intensity distribution heatmaps including collagen (blue), PC-UPy (light green) and cells (white) signatures; scale bar equals 250 μm . Extracted collagen spectra were compared by PCA for **(C)** 6 vs. 12-month scaffold region (ROI1), **(D)** 6 vs. 12-month luminal region (ROI3), **(E)** scaffold vs. luminal region in 6-month samples and **(F)** scaffold vs. interface vs. luminal region in 12-month samples; data are represented as mean score values \pm SD, $n = 3$.

separated to the scaffold site and the luminal tissue layer. In one of the 12-month samples (12.1) it was only possible to distinguish scaffold and lumen region (**Supplementary Figure 4**). The major extracellular matrix component identified in the adjacent tissue layers were collagen fibers as indicated in the TCA Raman images (**Figure 6B**). Single spectra were extracted from the TCA images for further in-depth analysis of collagen fiber maturity and integrity. PCAs were performed comparing collagen signatures of the same ROI at different timepoints and among different ROIs for the same timepoint. PCA of collagens infiltrating the scaffold region (**Figure 6C**) showed a shift from negative PC score values in 6-month spectra to positive PC score values in 12-month samples. However, both groups demonstrated data from one animal (6.3 and 12.1) clustering rather with the data from the other timepoint. A similar trend was shown for the collagens of the luminal tissue layer after 6 and 12 months of implantation (**Figure 6D**). The corresponding loadings plots (**Supplementary Figures 5A,B**) describe relevant peaks that explain the implantation time dependent changes in collagen fibers between 6 and 12 months. Both loadings indicate similar molecular changes in the scaffold and luminal region that are assigned to increased bands at 853, 935 (proline), 1,244 (amide III, β -sheet), 1,422 (CH_2 deformation) and 1,639 cm^{-1} (amide I) in 12-month explants and increased bands at 1,003 (phenylalanine), 1,310 (amide III, α -helix) and 1,690 cm^{-1} (amide I) for 6-month data. Separate PCAs were performed to compare collagens of the scaffold and luminal region at 6

months (**Figure 6E**) as well as collagens from scaffold, interface and luminal region at 12 months after implantation (**Figure 6F**). Six-month data clustered closely together with no significant difference between the regions for any of the calculated PCs, whereas 12-month data demonstrated a shift between collagen signatures from the implant region to collagen spectra derived from the interface and luminal region. However, also here no statistical significance was reached due to the heterogeneity among the animals. Peaks that contributed to the spectral differences were elaborated by the corresponding PC loadings plot (**Supplementary Figures 5C,D**) and could be assigned to differences in proline (853 cm^{-1}), amide III (1,240 cm^{-1}), the collagen backbone (960 and 1,440 cm^{-1}) and the amide I conformation (1,660 cm^{-1}).

DISCUSSION

Understanding the degradation of implants prospering from the recipient's endogenous regenerative capacity *via in situ* tissue engineering is of high relevance for the design and success of novel implant devices for cardiovascular replacements. In this study, Raman microspectroscopy was proposed as a complementary method to conventional analyses such as SEM or GPC analyses to study and evaluate local polymer degradation, as it allows to access information on the molecular composition and can be performed without extensive sample

processing, i.e. on tissue sections which are already prepared for histological analyses. Compared to destructive techniques such as chromatographic, mechanical or thermal analyses which have been reported for the investigation of *in vivo* polymer degradation (34, 35) and rather allow to assess the overall condition and characteristics of an implant material, Raman imaging obtains molecular-sensitive and spatially resolved information on the sample composition.

We have previously reported on the use of Raman microspectroscopy as a complementary method to evaluate the local balance between scaffold degradation and neotissue formation in *in situ* tissue-engineered heart valves (15) and arteries (5). In the current study, we specifically investigated whether the modus of degradation (i.e. enzymatic or oxidative) could be distilled from *in vivo* samples. To that end, Raman microspectroscopy was implemented to investigate different aspects of *in vitro* degradation such as the influence of the selected polymer, degradation over several timepoints as well as oxidative and enzymatically induced degradation. To further study the effect in native tissue, material degradation was monitored using Raman imaging on carotid explants of an *in vivo* sheep study.

Two different polymers were investigated for the *in vitro* study to assess the robustness of Raman spectroscopy to investigate degradation throughout different polymer materials. The two supramolecular polymer composites PC-UPy and PCL-BU were applied as model substances, as they are potential candidates for tissue engineering approaches (10, 36, 37) and provide different degradation kinetics. In general, PC-based polymers have been shown to degrade slower than PCL-based polymers (38). Despite similarities arising from similar molecular groups and assignments to skeletal vibrations of the polymer backbone, the Raman signatures of both polymers were significantly different, which in the future would also allow to discriminate oxidative processes in various other polymer materials applied in tissue engineering and simultaneously analyze implants composed of more than just one polymer.

Raman imaging of the degraded scaffolds allowed for the non-destructive visualization of the fiber morphology. Unlike SEM, which can only assess the fiber morphology, Raman spectroscopy allows for molecular imaging, investigating the molecular composition of the sample. Effects of oxidative degradation in PC-UPy polymers were less pronounced than in PCL-BU scaffolds but are in accordance with the slower degradation kinetics of PC-based polymers (38). Whereas changes in molecular composition upon PC-UPy degradation were only detectable *via* in-depth multivariate comparison by PCA, degradation in PCL-BU was already reflected in TCA images with a significantly different spectral signature of the polymer fibers after 5-day oxidative degradation. These data correlate with findings from an *in vivo* study of PCL-BU-based carotid implants in a rat model which showed highly accelerated degradation (39).

Degradation mechanisms for UPy and PCL based materials have been reported to be rather oxidative than hydrolytic (10, 33), therefore the *in vitro* degradation mainly focused on oxidative processes. However, an enzymatic degradation

step *via* cholesterol esterase was included for PCL-BU and compared to oxidative degradation. In addition to differences in fiber morphology, TCA images identified degradation-dependent spectral signatures which demonstrated different distribution patterns between oxidative and enzymatic degradation. The hypothesis here is that in enzymatic degradation entire molecules are cleaved, causing surface erosion which will decrease the fiber diameter and identify degradation-specific spectral changes at local spots. In contrast, the molecules in the oxidatively treated samples are believed to remain in place, while fiber length is reduced, which will not affect the fiber diameter but the overall molecular composition and spectral signature of the fibers. These conclusions are further supported by conventional degradation analyses by SEM and GPC (**Supplementary Figure 6**), where changes in fiber morphology are more pronounced in enzymatic degradation, but fiber density and composition, reflected by changes in the molecular weight, is rather observed in oxidative degradation. Furthermore, different molecular assignments of the TCA components appeared upon degradation. Compared to non-degraded PCL-BU, the spectrum in oxidatively degraded scaffolds showed a shift of the intensity ratios of the different building blocks. BU-related peaks ($606, 1,615\text{ cm}^{-1}$) decreased, whereas bands assigned to the skeletal vibrations and PCL ester groups ($1,067, 1,107, 1,728\text{ cm}^{-1}$) increased. This phenomenon can be assigned to relative changes in the polymer composition, as oxidative processes degrade the bisurea bonds first, resulting in higher contributions of the PCL-related bands to the overall polymer signature. Additional peaks occurring at 910 and $1,039\text{ cm}^{-1}$ could potentially be assigned to newly formed carboxyl groups derived from ester or urethane moieties and have been reported in correlation with a relative increase in crystallinity observed upon PCL degradation, which starts at the amorphous regions of the polymer (40). The degradation-specific spectrum in enzymatic degradation showed opposite spectral shifts. Here, a strong decrease of PCL-related bands, especially carbonyl ($1,728\text{ cm}^{-1}$) and ester (865 cm^{-1}) groups, was observed as well as a relative increase of the N-H band ($1,615\text{ cm}^{-1}$) and the shoulders at 992 and $1,121\text{ cm}^{-1}$. This signature is fully in line with ester hydrolysis taking place in the PCL-moieties of the fibers.

Following *in vitro* degradation, *in vivo* degradation of PC-UPy was assessed in 6 and 12-month carotid explants from a sheep model. Direct comparison to spectra from *in vitro* oxidative degradation supported the previous findings of Brugmans et al. (10) that oxidative mechanisms dominate in the degradation process for this material. Spectral signatures of 6-month *in vivo* data clustered closely with the 2-day *in vitro* degradation whereas 12-month spectra rather resembled the molecular composition of 5-day *in vitro* degraded samples. In addition to this overall trend, Raman spectroscopy also allowed to determine the individual degradational state for each explant. For each of the groups, an outlier explant was identified, rather clustering with the other explantation timepoint. Explant 6.3 showed an advanced degradation compared to the other 6-month samples, whereas spectra from explant 12.1 clustered closer to the 6-month or 2-day *in vitro* degraded samples. However, these observations are in line with the corresponding Raman and histology images, which show an advanced polymer degradation and collagen

infiltration for explant 6.3 as well as a dense polymer network and no separation into a material interface and luminal layer for explant 12.1., supporting the sensitivity of Raman spectroscopy to characterize a sample's molecular composition.

Degradation-dependent spectral changes as defined in the loadings plots, were similar between *in vitro* and *in vivo* analyses. Most robustly, degradation was assigned to a decrease in UPy related bands (695 , $1,520$ and $1,734\text{ cm}^{-1}$) and an increase in the $1,121\text{ cm}^{-1}$ peak. The assignment of the $1,121\text{ cm}^{-1}$ peak has not been fully defined yet, but had already been reported in a previous study on degradation of a pulmonary valve implants (15). Moreover, the *in vivo* degraded samples were assigned to a more pronounced $1,685\text{ cm}^{-1}$ band which corresponds to the amide in urethane groups, potentially indicating a UPy degradation product. Overall, these results suggest that *in vivo*, PC-UPy degradation is dominantly induced by oxidative pathways to which the UPy bonds are more susceptible than the PC chains.

This study demonstrates the potential of Raman microspectroscopy and imaging to further advance *in situ* tissue engineering. Supramolecular polymers can be synthesized to customize topography, durability, strength and degradability of a graft (38, 41). Further insights on molecular degradation mechanisms that can be modeled and characterized *in vitro*, have been shown to serve as reference measurements that can be transferred to define *in vivo* degradation pathways and could allow to tailor and design polymer materials that form implants with a better *in vivo* longevity. In addition, the identification of degradation-time dependent spectral changes can serve as an *in vivo* readout to monitor and spatially resolve polymer degradation *in situ*. First studies for *in vivo* Raman spectroscopy have been realized through endoscopic setups (42, 43), and could be transferred in the future to assess the performance and degradation of *in situ* tissue-engineered implants marker-independently and *in vivo*.

The *in vivo* follow-up in the presented study monitored PC-UPy polymers over a timeline of 12 months, but not over the complete degradation period. Whereas PCL-BU grafts demonstrated highly accelerated degradation *in vivo*, resulting in scaffold absorption after 60 days in an arterial graft (39), PC-UPy scaffolds even did not show complete absorption after 2 years as a pulmonary valve graft in a sheep model (15). However, over time, neotissue was formed and initial inflammation was reduced (15, 28, 44), demonstrating more advanced absorption and the absence of a chronic inflammatory response or severe calcifications. These promising results paved the way for the initiation of first clinical trials for PC-UPy based cardiovascular grafts (45).

One additional important feature of Raman imaging is that it enables to simultaneously assess collagen infiltration and polymer degradation within the same region of a sample. The balance between polymer degradation and tissue deposition and maturation is very important for the outcome of *in situ* tissue engineering; too slow degradation may lead to chronic inflammation and fibrotic encapsulation, while too rapid degradation (i.e. before sufficient neotissue has formed to take over the mechanical loads), will lead to structural failure (46). Scaffold degradation *in vivo* is an active cellular process driven by inflammatory cells such as macrophages and foreign

body giant cells, which also play a role in the coordination of tissue formation and maturation (47). This makes that scaffold degradation and tissue formation is dependent on the local influx and activation of cells and the local hemodynamic and biochemical environment, rather than a homogeneous time-dependent process. For example, Wissing et al. showed that macrophage-driven scaffold degradation is dependent on the scaffold microstructure (48) as well as hemodynamic loads (49). *In vivo*, Uiterwijk et al. observed a rapid unexpected accelerated remodeling of heart valve scaffolds with a bioinspired scaffold microstructure when implanted in sheep (50). Fukunishi et al. reported on species-dependent degradation rates of vascular grafts when implanted in rats or sheep (51). These reports emphasize the unpredictability of scaffold degradation and the tremendous value of accurately characterizing scaffold degradation and tissue formation simultaneously and *locally* in various regions of interest in a sample.

Therefore, in the present study, collagen spectra were extracted from the TCA images of the scaffold regions and compared to collagen signatures of newly formed tissue layers. Conventional methods to assess collagen deposition include histochemical or immunohistochemical staining (5) or can even be marker-independent when imaging collagen autofluorescence in SHG microscopy (4). In contrast to quantitative information, these methods are limited in their capability to address qualitative changes in structural composition of collagen fibers. Here, Raman spectroscopy has already been shown to be sensitive to changes in collagen fibers upon aging, tissue degradation or foreign body response (52–54) and was applied in this study to determine collagen maturation at different explantation timepoints and explant regions. Comparison between 6 and 12-month explants showed similar results in molecular changes for collagens between the polymer fibers and in the lumen. Upon implantation duration, collagen specific peaks assigned to proline, the collagen backbone and amides increased, whereas early-stage explants had a stronger phenylalanine peak assigned to proteins in general. Moreover, shifts in the amide I and amide III bands occurred which indicate different 2D and 3D structural orientation in α -helices and β -sheets, i.e. the prominent amide I shoulder at $1,690\text{ cm}^{-1}$ observed in 6-month samples can be linked to immature collagen crosslinks (55). Raman imaging of explant tissues served as a proof-of-principle experiment to study *in vivo* degradation, in combination with collagen maturation, and correlate it to observations of *in vitro* degradation. Sample heterogeneity was observed in this relatively small dataset in this study. Nevertheless, the ratios between polymer degradation and collagen infiltration and maturation were consistent throughout all samples, as the 6-month explant with faster polymer degradation kinetics simultaneously showed a more advanced collagen remodeling, same as for the slower degrading 12-month sample. These results encourage the further application and evaluation of PC-UPy scaffolds as carotid graft replacement.

CONCLUSION

In this study, we have demonstrated the suitability of Raman microspectroscopy to investigate morphological and molecular

changes during degradation of PCL- as well as PC-based supramolecular polymer composites. Raman imaging enables molecular sensitive *in situ* visualization of polymer degradation, overcoming the current limitations of conventional techniques. Characteristic peaks allowed to monitor degradation kinetics of different polymers and could distinguish oxidative and enzymatic degradation processes. Furthermore, partially degraded PC-UPy material could be identified and analyzed in *in vivo* degraded carotid implants, and was indicative of the predominant occurrence of oxidative degradation pathways. These findings underline the potential of Raman microspectroscopy and imaging to track the spatiotemporal progression of degradation and tissue maturation. The marker-independent accessibility of both, polymer and biological structures, open up a broad potential for *in situ* monitoring of tissue-engineered materials and will be further investigated in the future.

DATA AVAILABILITY STATEMENT

The raw data supporting the conclusions of this article will be made available by the authors, without undue reservation.

ETHICS STATEMENT

The animal study was reviewed and approved by Ethics Committee n°37, CNREEA, France.

AUTHOR CONTRIBUTIONS

EM and EB performed Raman measurements. TW performed PCL-BU *in vitro* degradation experiments. JM analyzed and

interpreted the data. HB, AS, AB, and SS validated the results. JM, HB, and AIS wrote the manuscript. KS-L, AS, AIS, and MC contributed to conceptualization, design and supervision of the study. All authors reviewed and edited the manuscript and approved the submitted version.

FUNDING

The collaboration between Eindhoven University of Technology and the University of Tübingen for Raman microspectroscopy of PCL-BU was facilitated by a traveling grant of the Dutch Heart Foundation to EM and a Short-Term Fellowship (8169) of the European Molecular Biology Organization (EMBO) to AIPMS. This study was financially supported by the Ministry of Science, Research and the Arts of Baden-Württemberg (33-729.55-3/214 and SI-BW 01222-91 to KS-L) and the Deutsche Forschungsgemeinschaft (INST 2388/64-1 GRK 2543/1 and under Germany's Excellence Strategy EXC 2180-390900677 to KS-L).

ACKNOWLEDGMENTS

The authors thank Bastiaan Ippel (TU Eindhoven) for support with GPC analyses and Daniel Carvajal Berrio (University of Tübingen) for technical assistance in Raman spectroscopy.

SUPPLEMENTARY MATERIAL

The Supplementary Material for this article can be found online at: <https://www.frontiersin.org/articles/10.3389/fcvm.2022.885873/full#supplementary-material>

REFERENCES

- Wissing TB, Bonito V, Bouten CV, Smits AI. Biomaterial-driven *in situ* cardiovascular tissue engineering—a multi-disciplinary perspective. *NPJ Regen Med.* (2017) 2:1–20. doi: 10.1038/s41536-017-0023-2
- Zilla P, Bezuidenhout D, Human P. Prosthetic vascular grafts: wrong models, wrong questions and no healing. *Biomaterials.* (2007) 28:5009–27. doi: 10.1016/j.biomaterials.2007.07.017
- Sengupta D, Waldman SD, Li S. From *in vitro* to *in situ* tissue engineering. *Ann Biomed Eng.* (2014) 42:1537–45. doi: 10.1007/s10439-014-1022-8
- Biermann AC, Marzi J, Brauchle E, Wichmann JL, Arendt CT, Puntmann V, et al. Improved long-term durability of allogeneic heart valves in the orthotopic sheep model. *Eur J Cardiothorac Surg.* (2019) 55:484–93. doi: 10.1093/ejcts/ezy292
- Bonito V, Koch SE, Krebber MM, Carvajal-Berrio DA, Marzi J, Duijvelshoff R, et al. Distinct effects of heparin and interleukin-4 functionalization on macrophage polarization and *in situ* arterial tissue regeneration using resorbable supramolecular vascular grafts in rats. *Adv Healthc Mater.* (2021) 10:2101103. doi: 10.1002/adhm.202101103
- Fang S, Ellman DG, Andersen DC. Tissue Engineering of small-diameter vascular grafts and their *in vivo* evaluation in large animals and humans. *Cells.* (2021) 10:713. doi: 10.3390/cells10030713
- Aida T, Meijer E, Stupp S. Functional supramolecular polymers. *Science.* (2012) 335:813–7. doi: 10.1126/science.1205962
- De Kort B, Koch S, Wissing T, Krebber M, Bouten C, Smits A. Immuno-regenerative biomaterials for *in situ* cardiovascular tissue engineering—do patient characteristics warrant precision engineering? *Adv Drug Deliv Rev.* (2021) 178:113960. doi: 10.1016/j.addr.2021.113960
- Lyu S, Untereker D. Degradability of polymers for implantable biomedical devices. *Int J Mol Sci.* (2009) 10:4033–65. doi: 10.3390/ijms10094033
- Brugmans M, Sijntens S, Cox M, Nandakumar A, Bosman A, Mes T, et al. Hydrolytic and oxidative degradation of electrospun supramolecular biomaterials: *in vitro* degradation pathways. *Acta Biomater.* (2015) 27:21–31. doi: 10.1016/j.actbio.2015.08.034
- Besseling PJ, Mes T, Bosman AW, Peeters JW, Janssen HM, Bakker MH, et al. The *in-vitro* biocompatibility of ureido-pyrimidinone compounds and polymer degradation products. *J Polym Sci.* (2021) 59:1267–77. doi: 10.1002/pol.20210072
- Wang Z, Wang Y, Ito Y, Zhang P, Chen X. A comparative study on the *in vivo* degradation of poly(L-lactide) based composite implants for bone fracture fixation. *Sci Rep.* (2016) 6:20770. doi: 10.1038/srep20770
- Nifant'ev I, Shlyakhtin A, Komarov P, Tavitkin A, Kananykhina E, Elchaninov A, et al. *In vitro* and *in vivo* studies of biodegradability and biocompatibility of poly(εCL)-b-Poly(EtOEP)-based films. *Polymers.* (2020) 12:3039. doi: 10.3390/polym12123039
- Kluin J, Talacua H, Smits AI, Emmert MY, Brugmans MC, Fioretta ES, et al. *In situ* heart valve tissue engineering using a bioresorbable elastomeric implant—from material design to 12 months follow-up in sheep. *Biomaterials.* (2017) 125:101–17. doi: 10.1016/j.biomaterials.2017.02.007
- De Kort BJ, Marzi J, Brauchle EM, Lichauco AM, Bauer HS, Serrero A, et al. Inflammatory and regenerative processes in bioresorbable synthetic pulmonary valves up to two years in sheep—spatiotemporal insights

- augmented by Raman microspectroscopy. *Acta Biomater.* (2021) 135:243–59. doi: 10.1016/j.actbio.2021.09.005
16. Jawhari T, Roid A, Casado J. Raman spectroscopic characterization of some commercially available carbon black materials. *Carbon N Y.* (1995) 33:1561–5. doi: 10.1016/0008-6223(95)00117-V
 17. Butler HJ, Ashton L, Bird B, Cinque G, Curtis K, Dorney J, et al. Using Raman spectroscopy to characterize biological materials. *Nat Protoc.* (2016) 11:664–87. doi: 10.1038/nprot.2016.036
 18. Ma Z, Wu Y, Wang J, Liu C. *In vitro* and *in vivo* degradation behavior of poly(trimethylene carbonate-co-d,l-lactic acid) copolymer. *Regen Biomater.* (2017) 4:207–13. doi: 10.1093/rb/rbx003
 19. Uhrich K, Ibim S, Larrier D, Langer R, Laurencin C. Chemical changes during *in vivo* degradation of poly (anhydride-imide) matrices. *Biomaterials.* (1998) 19:2045–50. doi: 10.1016/S0142-9612(98)00110-0
 20. Chlopek J, Morawska-Chochol A, Paluszkievicz C, Jaworska J, Kasperczyk J, Dobrzyński P, et al. and NMR study of poly (lactide-co-glycolide) and hydroxyapatite implant degradation under *in vivo* conditions. *Polym Degrad Stab.* (2009) 94:1479–85. doi: 10.1016/j.polymdegradstab.2009.05.010
 21. Zhu M, Wu Y, Li W, Dong X, Chang H, Wang K, et al. Biodegradable and elastomeric vascular grafts enable vascular remodeling. *Biomaterials.* (2018) 183:306–18. doi: 10.1016/j.biomaterials.2018.08.063
 22. Reinhardt JW, Rosado JdDR, Barker JC, Lee Y-U, Best CA, Yi T, et al. Early natural history of neotissue formation in tissue-engineered vascular grafts in a murine model. *Regen Med.* (2019) 14:389–408. doi: 10.2217/rme-2018-0133
 23. Pabitte DR, Heger M, Beek JF, van Tuijl S, Simonet M, van der Wal AC, et al. Optimization of suture-free laser-assisted vessel repair by solder-doped electrospun poly (ϵ -caprolactone) scaffold. *Ann Biomed Eng.* (2011) 39:223–34. doi: 10.1007/s10439-010-0157-5
 24. Wang G, Labow R, Santerre J. Biodegradation of a poly (ester) urea-urethane by cholesterol esterase: isolation and identification of principal biodegradation products. *J Biomed Mater Res.* (1997) 36:407–17. doi: 10.1002/(SICI)1097-4636(19970905)36:3<407::AID-JBM16>3.0.CO;2-A
 25. Tang Y, Labow R, Santerre J. Enzyme induced biodegradation of polycarbonate-polyurethanes: dose dependence effect of cholesterol esterase. *Biomaterials.* (2003) 24:2003–11. doi: 10.1016/S0142-9612(02)00563-X
 26. Schubert MA, Wiggins MJ, Anderson JM, Hiltner A. Role of oxygen in biodegradation of poly (etherurethane urea) elastomers. *J Biomed Mater Res.* (1997) 34:519–30. doi: 10.1002/(SICI)1097-4636(19970315)34:4<519::AID-JBM12>3.0.CO;2-7
 27. Cox MB, H; El-Kurdi, MS. Xeltis: towards grafts from supramolecular materials. In: Frédéric CNH, de Borst GJ, Hedin U, Meichelboeck W, editors. *12th European Symposium on Vascular Biomaterials*. Strasbourg: ESVB (2021). p. 348–58.
 28. Brugmans M, Serrero A, Cox M, Svanidze O, Schoen FJ. Morphology and mechanisms of a novel absorbable polymeric conduit in the pulmonary circulation of sheep. *Cardiovasc Pathol.* (2019) 38:31–8. doi: 10.1016/j.carpath.2018.10.008
 29. Spiers RM, Marzi J, Brauchle EM, Cross SE, Vaughan RH, Bateman PA, et al. Donor age significantly influences the Raman spectroscopic biomolecular fingerprint of human pancreatic extracellular matrix proteins following collagenase-based digestion. *Acta Biomater.* (2019) 99:269–83. doi: 10.1016/j.actbio.2019.09.013
 30. Wold S, Esbensen K, Geladi P. Principal component analysis. *Chemometr Intell Lab Syst.* (1987) 2:37–52. doi: 10.1016/0169-7439(87)80084-9
 31. Kotzianova A, Rebicek J, Mojzes P, Pokorný M, Palacký J, Hrbáč J, et al. Analysis of composite nanofibrous layers by confocal Raman microscopy. *Polymer.* (2014) 55:5036–42. doi: 10.1016/j.polymer.2014.08.032
 32. Frost RL, Kristof J, Rintoul L, Klopogge JT. Raman spectroscopy of urea and urea-intercalated kaolinites at 77 K. *Spectrochim Acta A Mol Biomol Spectrosc.* (2000) 56:1681–91. doi: 10.1016/S1386-1425(00)00223-7
 33. Dankers PYW, Zhang Z, Wisse E, Grijpma DW, Sijbesma RP, Feijen J, et al. Oligo(trimethylene carbonate)-based supramolecular biomaterials. *Macromolecules.* (2006) 39:8763–71. doi: 10.1021/ma061078o
 34. Lam CX, Hutmacher DW, Schantz JT, Woodruff MA, Teoh SH. Evaluation of polycaprolactone scaffold degradation for 6 months *in vitro* and *in vivo*. *J Biomed Mater Res A.* (2009) 90:906–19. doi: 10.1002/jbm.a.32052
 35. Hedberg EL, Kroese-Deutman HC, Shih CK, Crowther RS, Carney DH, Mikos AG, et al. *In vivo* degradation of porous poly (propylene fumarate)/poly (DL-lactic-co-glycolic acid) composite scaffolds. *Biomaterials.* (2005) 26:4616–23. doi: 10.1016/j.biomaterials.2004.11.039
 36. Morales DL, Herrington C, Bacha EA, Morell VO, Prodan Z, Mroczek T, et al. A novel restorative pulmonary valve conduit: early outcomes of two clinical trials. *Front Cardiovasc Med.* (2021) 7:583360. doi: 10.3389/fcvm.2020.583360
 37. Mollet BB, Bogaerts IL, van Almen GC, Dankers PY, A. bioartificial environment for kidney epithelial cells based on a supramolecular polymer basement membrane mimic and an organotypical culture system. *J Tissue Eng Regen Med.* (2017) 11:1820–34. doi: 10.1002/term.2080
 38. van Haaften EE, Duijvelshoff R, Ippel BD, Söntjens SHM, van Houtem MHCJ, Janssen HM, et al. The degradation and performance of electrospun supramolecular vascular scaffolds examined upon *in vitro* enzymatic exposure. *Acta Biomater.* (2019) 92:48–59. doi: 10.1016/j.actbio.2019.05.037
 39. Duijvelshoff R, Van Engeland NCA, Gabriels KMR, Söntjens SHM, Smits AIPM, Dankers PYW, et al. Host response and neo-tissue development during resorption of a fast degrading supramolecular electrospun arterial scaffold. *Bioengineering.* (2018) 5:61. doi: 10.3390/bioengineering5030061
 40. Taddei P, Di Foggia M, Causa F, Ambrosio L, Fagnano C. *In vitro* bioactivity of poly(ϵ -Caprolactone)-apatite (PCL-AP) scaffolds for bone tissue engineering: the influence of the PCL/AP ratio. *Int J Artif Organs.* (2006) 29:719–25. doi: 10.1177/039139880602900712
 41. Yagai S, Kitamoto Y, Datta S, Adhikari B. Supramolecular polymers capable of controlling their topology. *Acc Chem Res.* (2019) 52:1325–35. doi: 10.1021/acs.accounts.8b00660
 42. Bergholt MS, Lin K, Zheng W, Lau DP, Huang Z. *In vivo*, real-time, transnasal, image-guided Raman endoscopy: defining spectral properties in the nasopharynx and larynx. *J Biomed Opt.* (2012) 17:077002. doi: 10.1117/1.JBO.17.7.077002
 43. Shu C, Zheng W, Lin K, Lim C, Huang Z. Label-free follow-up surveying of post-treatment efficacy and recurrence in nasopharyngeal carcinoma patients with fiberoptic Raman endoscopy. *Anal Chem.* (2021) 93:2053–61. doi: 10.1021/acs.analchem.0c03778
 44. Bennink G, Torii S, Brugmans M, Cox M, Svanidze O, Ladich E, et al. A novel restorative pulmonary valved conduit in a chronic sheep model: Mid-term hemodynamic function and histologic assessment. *J Thorac Cardiovasc Surg.* (2018) 155:2591–601.e3. doi: 10.1016/j.jtcvs.2017.12.046
 45. Mes T, Serrero A, Bauer HS, Cox MA, Bosman AW, Dankers PY, et al. Supramolecular polymer materials bring restorative heart valve therapy to patients. *Mater Today.* (2021) 52:175–87. doi: 10.1016/j.mattod.2021.12.003
 46. Duijvelshoff R, di Luca A, van Haaften EE, Dekker S, Söntjens SHM, Janssen HM, et al. Inconsistency in graft outcome of bilayered bioresorbable supramolecular arterial scaffolds in rats. *Tissue Eng Part A.* (2021) 27:894–904. doi: 10.1089/ten.TEA.2020.0185
 47. Witherell CE, Abebayehu D, Barker TH, Spiller KL. Macrophage and fibroblast interactions in biomaterial-mediated fibrosis. *Adv Healthc Mater.* (2019) 8:1801451. doi: 10.1002/adhm.201801451
 48. Wissing TB, Bonito V, van Haaften EE, van Doeselaar M, Brugmans MMCP, Janssen HM, et al. Macrophage-driven biomaterial degradation depends on scaffold microarchitecture. *Front Bioeng Biotechnol.* (2019) 7:87. doi: 10.3389/fbioe.2019.00087
 49. Wissing TB, van Haaften EE, Koch SE, Ippel BD, Kurniawan NA, Bouten CVC, et al. Hemodynamic loads distinctively impact the secretory profile of biomaterial-activated macrophages – implications for *in situ* vascular tissue engineering. *Biomater Sci.* (2020) 8:132–47. doi: 10.1039/C9BM01005J
 50. Uiterwijk M, Smits AIPM, van Geemen D, van Klarenbosch B, Dekker S, Cramer MJ, et al. *In situ* remodeling overrules bioinspired scaffold architecture of supramolecular elastomeric tissue-engineered heart valves. *JACC Basic Transl Sci.* (2020) 5:1187–206. doi: 10.1016/j.jacbs.2020.09.011
 51. Fukunishi T, Ong CS, Yesantharao P, Best CA Yi T, Zhang H, et al. Different degradation rates of nanofiber vascular grafts in small and large animal models. *J Tissue Eng Regen Med.* (2020) 14:203–14. doi: 10.1002/term.2977
 52. Van Gulick L, Saby C, Morjani H, Beljebbar A. Age-related changes in molecular organization of type I collagen in tendon as probed by polarized SHG and Raman microspectroscopy. *Sci Rep.* (2019) 9:7280. doi: 10.1038/s41598-019-43636-2

53. Beatty R, Lu C-E, Marzi J, Levey RE, Carvajal Berrio D, Lattanzi G, et al. The foreign body response to an implantable therapeutic reservoir in a diabetic rodent model. *Tissue Eng C Methods*. (2021) 27:515–28. doi: 10.1089/ten.tec.2021.0163
54. Biermann AC, Marzi J, Brauchle E, Schneider M, Kornberger A, Abdelaziz S, et al. Impact of T-cell-mediated immune response on xenogeneic heart valve transplantation: short-term success and mid-term failure. *Eur J Cardiothorac Surg*. (2018) 53:784–92. doi: 10.1093/ejcts/ezx396
55. Raghavan M, Sahar ND, Kohn DH, Morris MD. Age-specific profiles of tissue-level composition and mechanical properties in murine cortical bone. *Bone*. (2012) 50:942–53. doi: 10.1016/j.bone.2011.12.026

Conflict of Interest: The research labs from KS-L and AIS performed independent scientific contract work for the company Xeltis and received for this work financial compensation. MC, HB, and AS are employees of Xeltis. MC is shareholder of Xeltis and AB is a financially compensated scientific advisor to Xeltis. SS is an employee of SyMO-Chem BV. AB is an employee and shareholder in SupraPolix BV.

The remaining authors declare that the research was conducted in the absence of any commercial or financial relationships that could be construed as a potential conflict of interest.

Publisher's Note: All claims expressed in this article are solely those of the authors and do not necessarily represent those of their affiliated organizations, or those of the publisher, the editors and the reviewers. Any product that may be evaluated in this article, or claim that may be made by its manufacturer, is not guaranteed or endorsed by the publisher.

Copyright © 2022 Marzi, Munnig Schmidt, Brauchle, Wissing, Bauer, Serrero, Söntjens, Bosman, Cox, Smits and Schenke-Layland. This is an open-access article distributed under the terms of the Creative Commons Attribution License (CC BY). The use, distribution or reproduction in other forums is permitted, provided the original author(s) and the copyright owner(s) are credited and that the original publication in this journal is cited, in accordance with accepted academic practice. No use, distribution or reproduction is permitted which does not comply with these terms.



Stem Cell Based Approaches to Modulate the Matrix Milieu in Vascular Disorders

Sajeesh S, Shataakshi Dahal, Suraj Bastola, Simran Dayal, Jimmy Yau and Anand Ramamurthi*

Department of Bioengineering, Lehigh University, Bethlehem, PA, United States

OPEN ACCESS

Edited by:

Anthal Smits,
Eindhoven University of
Technology, Netherlands

Reviewed by:

Najma Latif,
The Magdi Yacoub Institute,
United Kingdom
Merle Krebber,
University Medical Center
Utrecht, Netherlands
Giselle Yeo,
The University of Sydney, Australia

*Correspondence:

Anand Ramamurthi
anr320@lehigh.edu

Specialty section:

This article was submitted to
Heart Valve Disease,
a section of the journal
Frontiers in Cardiovascular Medicine

Received: 20 February 2022

Accepted: 20 May 2022

Published: 15 June 2022

Citation:

S S, Dahal S, Bastola S, Dayal S,
Yau J and Ramamurthi A (2022) Stem
Cell Based Approaches to Modulate
the Matrix Milieu in Vascular Disorders.
Front. Cardiovasc. Med. 9:879977.
doi: 10.3389/fcvm.2022.879977

The extracellular matrix (ECM) represents a complex and dynamic framework for cells, characterized by tissue-specific biophysical, mechanical, and biochemical properties. ECM components in vascular tissues provide structural support to vascular cells and modulate their function through interaction with specific cell-surface receptors. ECM-cell interactions, together with neurotransmitters, cytokines, hormones and mechanical forces imposed by blood flow, modulate the structural organization of the vascular wall. Changes in the ECM microenvironment, as in post-injury degradation or remodeling, lead to both altered tissue function and exacerbation of vascular pathologies. Regeneration and repair of the ECM are thus critical toward reinstating vascular homeostasis. The self-renewal and transdifferentiating potential of stem cells (SCs) into other cell lineages represents a potentially useful approach in regenerative medicine, and SC-based approaches hold great promise in the development of novel therapeutics toward ECM repair. Certain adult SCs, including mesenchymal stem cells (MSCs), possess a broader plasticity and differentiation potential, and thus represent a viable option for SC-based therapeutics. However, there are significant challenges to SC therapies including, but not limited to cell processing and scaleup, quality control, phenotypic integrity in a disease milieu *in vivo*, and inefficient delivery to the site of tissue injury. SC-derived or -inspired strategies as a putative surrogate for conventional cell therapy are thus gaining momentum. In this article, we review current knowledge on the patho-mechanistic roles of ECM components in common vascular disorders and the prospects of developing adult SC based/inspired therapies to modulate the vascular tissue environment and reinstate vessel homeostasis in these disorders.

Keywords: ECM, regenerative repair, cardiovascular, elastin, collagen, exosomes

INTRODUCTION

The structural and functional homeostasis of mammalian organs is maintained by support provided by their connective tissue components comprising of a three-dimensional network of cells and ECM (1, 2). The ECM provides support and anchorage for the parenchymal cells, and regulates cell fate processes including cell survival, proliferation, adhesion, and migration (3). Fibroblasts resident within most connective tissues, are the primary cell types responsible

for secreting the interstitial ECM, which further determines tissue architecture, stiffness and flexibility. Neo-assembly and remodeling of ECM structures mostly occur during fetal development and during the organ differentiation stage. In adulthood, ECM remodeling is usually associated with wound healing and matrix regeneration/repair, following an injury stimulus and subsequent inflammation cascade (4). This is also typical of cardiovascular (CV) disease conditions, which involves some degree of ECM degradation and remodeling, resulting in loss of tissue elasticity and fibrotic tissue formation (5). Both these aspects can lead to impaired tissue and organ function (6). Therapeutic strategies aimed at attenuating adverse fibrotic responses and in stimulating biomimetic ECM regeneration and repair in CV disorders are of prime significance. However, this is still at a nascent stage owing to an incomplete understanding of the activation mechanism, regulation, and modulation of ECM regenerative and reparative processes (6, 7). Challenges include the intrinsically poor matrix regenerative capacity of adult vascular tissues, which primarily contain stable (slow renewing/remodeling) cells, and the limited capability of adult vascular cells to synthesize and organize elastic fibers, and their inability to replicate the biocomplexity of developmental elastic matrix assembly (8–12). In this article, we review current knowledge on how ECM changes serve as the etiological basis for vascular disease manifestations and the prospects of developing SC-based ECM regenerative therapies to reverse vascular pathophysiology.

ECM COMPOSITION AND STRUCTURE IN THE VASCULAR WALL

The walls of healthy blood vessels exhibit a lamellar structure, with the concentric layers variably containing endothelial cells (EC), smooth muscle cells (SMC), and fibroblasts distributed in a layer-specific ECM milieu (13). Medium-sized muscular arteries and large elastic arteries exhibit 3 distinct tissue layers, namely tunica intima, tunica media, and tunica adventitia (**Figure 1**). The tunica intima lines the blood vessel lumen and comprises a monolayer of ECs that organize along blood flow and are anchored on a proteoglycan (PG) rich basement membrane that separates these cells from the underlying mesenchymal tissues. ECs regulate thrombosis, fibrinolysis, leukocyte adhesion and extravasation, and also serve to regulate vascular tone through their signaling of SMCs in the underlying medial layer. The middle layer, the tunica media, is separated from the innermost tunica intima layer by internal elastic lamina, a dense layer of concentric elastic fibers generated by intervening SMCs. The tunica media layer accounts for the bulk of the vessel wall thickness in the muscular and elastic arteries and is the chief determinant of mechanical compliance of the wall. The tunica media is composed of circumferentially arranged elastic lamellae, interspersed with SMCs, matrix collagens, microfibrillar glycoproteins, PGs, and amorphous ground substances. In this specific arrangement, the cells and the ECM play major roles in mechano-sensing and in providing force resistance with direct implications to maintenance of vascular wall homeostasis. More

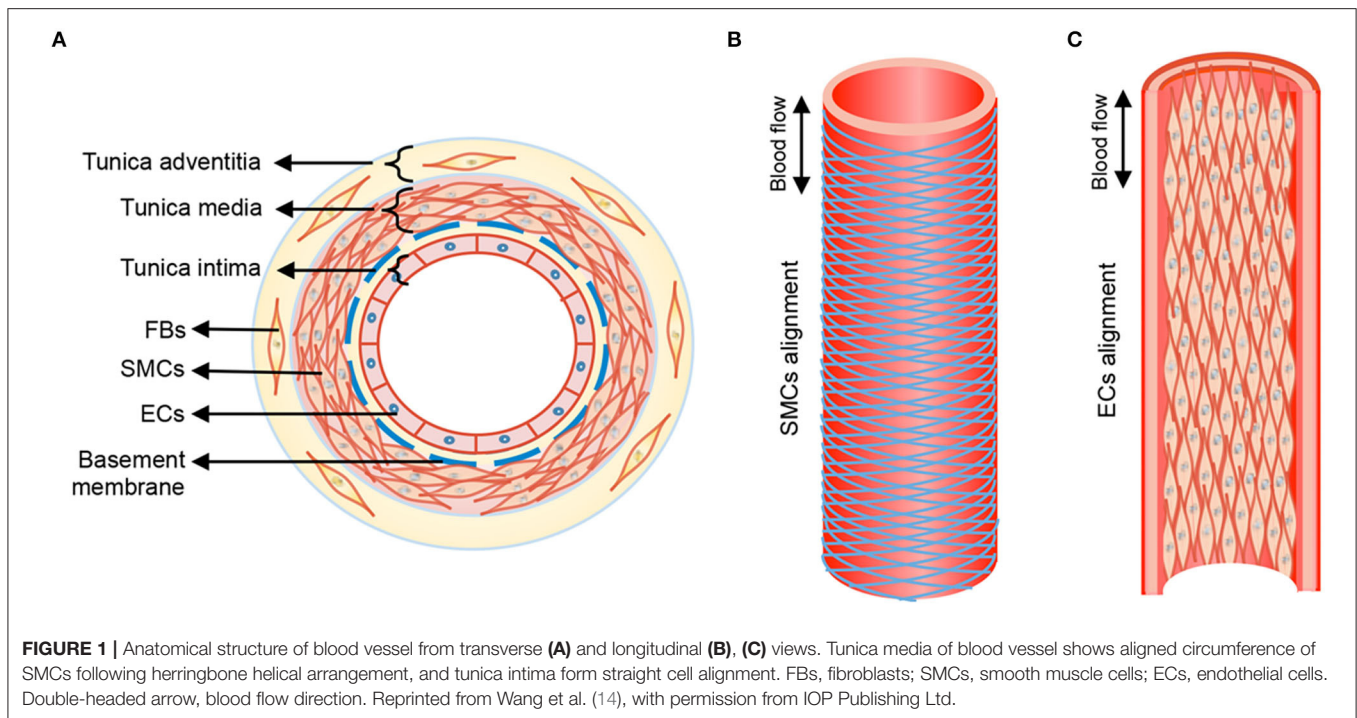
broadly, the tunica media is the primary load bearing layer of the vessel at physiologic blood pressures, but it also provides the vessel compliance to accommodate changes to blood flow toward regulating blood pressure. The outermost tunica adventitia, also called the tunica externa, is separated from tunica media by the external elastic lamina. The tunica adventitia is composed of compact (closer to tunica media) and looser (toward outer edge) collagenous ECM, fibroblasts, perivascular nerves, lymphatic vessels, vasa vasorum, and inflammatory cells. However, the exact composition of this layer depends on arterial size and their function. The tunica adventitia serves to prevent vessel over-expansion and rupture at super-physiologic blood pressures and anchor the vessels to the surrounding tissue/organs.

The ECM secreted by vascular cell types (SMCs, fibroblasts, and less so, ECs) allows the vessel wall to adapt to mechanical forces encountered. The mechanical and viscoelastic properties of the vessel wall (i.e., high resilience, low hysteresis, and non-linear elasticity) are mostly imparted by 3 main structural ECM components: elastic fibers, collagen fibers, and large aggregating PGs (3, 13) (**Figure 2**).

Elastin in the Vessel Wall

Elastin is the chief protein constituent of elastic fibers, and accounts for ~90% of its composition by mass (15, 16). Elastic fibers provide stretch and recoil properties to soft, pliable tissues of vertebrates, including in blood vessels. Elastin also play a critical role in influencing the phenotype and cell fate processes of interacting cell types, primarily, the SMCs (17). Elastin is formed through the multimerization and subsequent cross-linking of its hydrophobic monomers, called tropoelastins (18) (**Figure 3**).

In the aorta, elastin is predominantly produced by medial SMCs, though adventitial fibroblasts and ECs also exhibit limited elastogenic capacity. The process of elastic fiber neo-assembly is initiated during fetal development, and this serves as counterbalance to the mechanical forces acting on the forming vascular conduits, to enable their elastic recoil. Repeated stretch and relaxation cycles allow the tropoelastin monomers to polymerize through a process termed as coacervation (19). Tropoelastin isoforms demonstrate a specific pattern of the molecular arrangement, in which hydrophobic regions alternate with hydrophilic cross-linking domains containing lysyl residues (20). The proximity of lysine residues further allows covalent cross-linking, through oxidative deamination facilitated by lysyl oxidase (LOX), to form linkages called desmosines and isodesmosines. This process, directed by arranging hydrophobic and hydrophilic sequences in the tropoelastin molecule determines the intermolecular alignment in the protein and leads to the formation of durable and metabolically inert cross-linked tropoelastin arrays (21, 22). Mature elastic fibers are formed by deposition and aggregation of these crosslinked tropoelastin coacervates on microfibrillar pre-scaffolds which are laid down by cells in the extracellular space (23). These microfibrillar pre-scaffolds are mainly composed of heterogeneous glycoproteins (such as fibrillin-1 and fibrillin-2), microfibril-associated glycoproteins (MAGP1 and MAGP2) and latent transforming growth factor β (TGF- β)-binding proteins. The interaction of these microfibrils with chondroitin sulfate PGs



(e.g., versican, biglycan, and decorin) and other proteins present at the elastin–microfibril interface or at the cell surface–elastic fiber interface, known as elastin microfibril interface-located proteins (EMILINs), also serves to play a role in elastogenesis process (24).

Tropoelastin molecules are rich in hydrophobic amino acid residues and are amenable to robust crosslinking. Thus, fully polymerized mature elastin is practically insoluble in aqueous environments, metabolically inert, and extremely resistant to thermal and chemical onslaught (15, 17). For these reasons, elastin has an estimated half-life of about 40 years and under optimal conditions, might be expected to last over the normal human life span. However, defects in vascular elastic fibers or their assembly, either driven by genetic factors and/or disease/injury can compromise the biomechanics and biochemical regulation of vascular cells leading to the adverse remodeling characteristic of several vascular disorders (25).

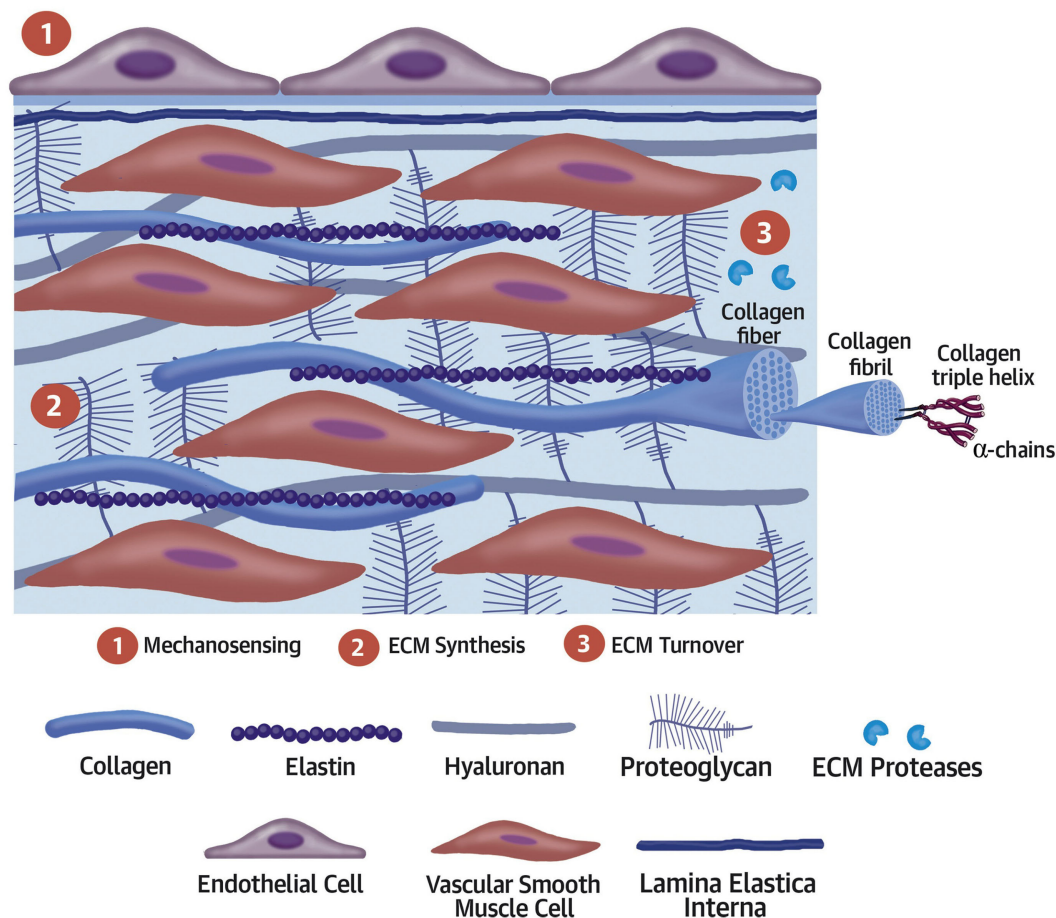
Deregulation of vascular SMCs impairs their ability to switch between a differentiated phenotype (also referred as “contractile”) and dedifferentiated phenotype (also referred as “synthetic”). Differentiated vascular SMCs exhibit high levels of contractile gene expression and demonstrate low levels of proliferation, migration and ECM synthesis, while the dedifferentiated state is often linked to increased rates of proliferation, migration and production of ECM (26). Upon injury, SMCs acquire a dedifferentiated state to promote vessel repair and cells return to a non-proliferative phenotype once the injury is resolved. Phenotype modulation of vascular SMCs is critical to maintaining vessel wall homeostasis. Several physiological and non-physiological stimuli can deregulate the vascular SMC phenotype switch, contributing to the initiation and progression of several vascular disorders.

Differently, chronic proteolytic breakdown of elastic fiber structures due to localized imbalances between elastin degrading matrix metalloproteases (e.g., MMPs 2, 9) and their inhibitors (tissue inhibitors of MMPs, TIMPs), with increased levels of the former, can also lead to the same adverse remodeling outcomes (27). In the latter situation, the pathological scenario is exacerbated by the generation of elastic fiber breakdown products, elastin derived peptides (EDPs), which contrary to intact elastic fibers, promote a differentiated SMC phenotype characterized by increased cytokine and MMP release, reduced cell contractility and increased proliferation, enhanced intracellular calcium ion uptake, and apoptosis, all of which enhance vascular ECM breakdown *via* positive feedback (28).

Collagen in the Vessel Wall

Collagen is one among the major structural components of the ECM that provide integrity and stability to the vascular wall (29). Collagens are typically transcribed and secreted by fibroblasts as a precursor, procollagen, which undergoes several post translational modifications and LOX-mediated crosslinking to form triple helical collagen superstructures (30). Collagens with their unique architectural compositions and polypeptide α -chains curled around each other resulting in the formation of triple helix structure, can form intricate ECM networks. Additionally, collagens also contain non-triple-helical domains, which usually serve as the attachment sites for other ECM proteins. Collagens vary by the length of these amino acid repeat motifs, and this permits the formation of supramolecular aggregates that can arrange into varying geometric networks to allow functional diversity. The supramolecular assembly of collagen fiber bundles is further directed through a combination

CENTRAL ILLUSTRATION: Key Elements of the Arterial Wall and Vascular Extracellular Matrix Components



Barallobre-Barreiro, J. et al. *J Am Coll Cardiol.* 2020;75(17):2189-203.

FIGURE 2 | Key elements of the arterial wall and vascular extracellular matrix components. Reprinted from Barallobre-Barreiro et al. (5), with permission from Elsevier.

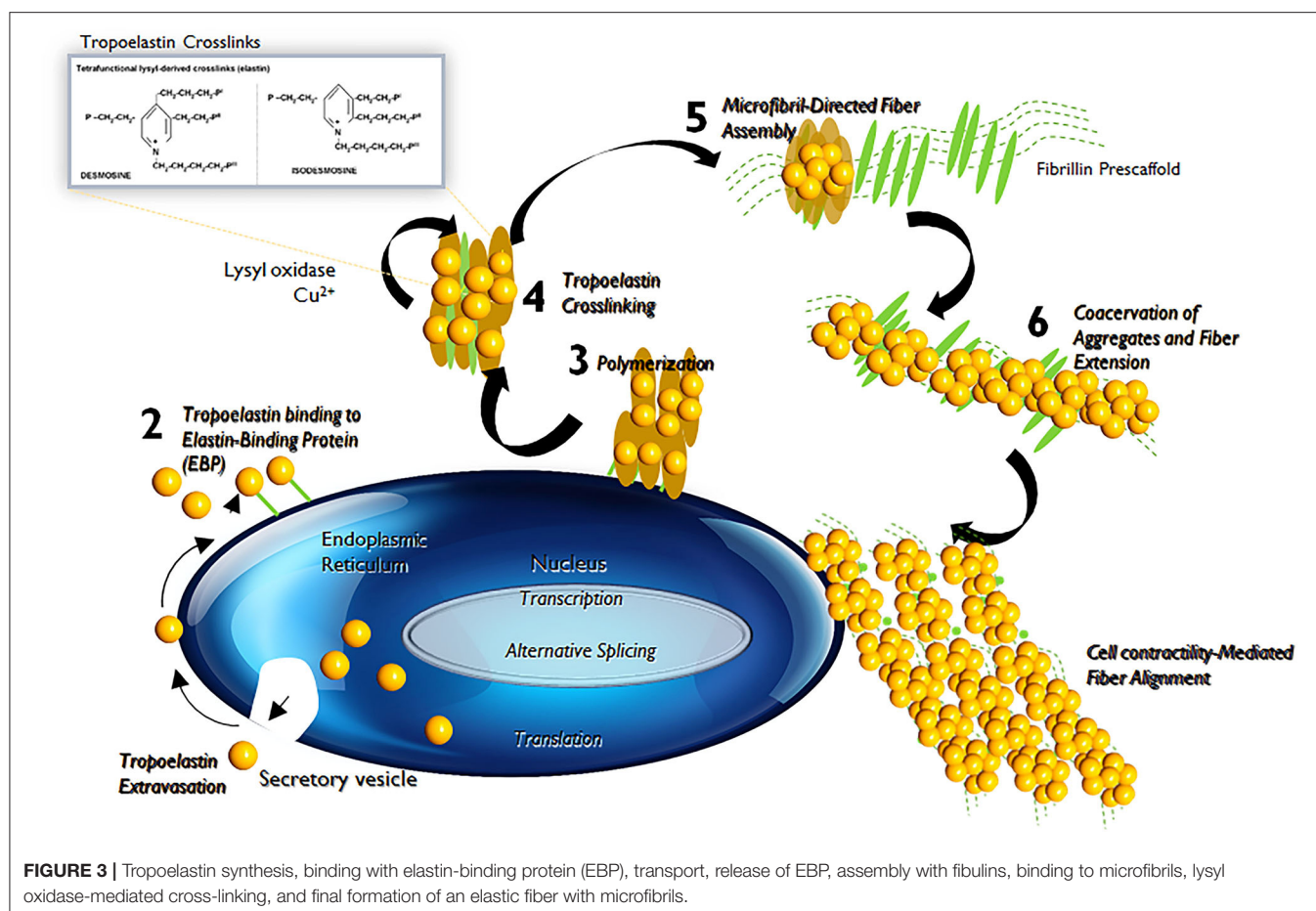
of tissue-specific matrix macromolecules, such as fibronectin and PGs, cell surface integrins, and intracellular forces.

The major collagens in large elastic arteries are the fibrillar collagens (types I, III, V) that provide structural/biomechanical functions. Non-fibrillar collagens (type IV and VI), which form part of the basement membrane, are involved in anchoring and organizing fibrillar collagens and have cytoprotective roles (31). Collagen type I (70–75%) and type III (20–25%) are the prominent subtypes found in human arterial wall, while type V accounts for 1–2% of total collagen content. Fibrillar collagens are enzymatically cross-linked during deposition stage *via* LOX and LOX-like proteins and small leucine-rich proteoglycans (SLRPs) contain collagen-binding domains. This allows the formation of a protein coat on the surface of the fibrils and further protects them from protease degradation (32). The interaction

of fibromodulin with collagen cross-linking sites further activates LOX-like proteins and enhances collagen cross-linking process. Thus, collagen plays a key role in maintaining structural integrity of the vessel wall and impaired collagen metabolism has been associated with several CV inflammatory conditions (33).

Proteoglycans in the Vessel Wall

PGs composed of protein cores that are decorated with glycosaminoglycan (GAG) side chains (34). GAGs are linear, anionic, unbranched polysaccharides made up of repeating disaccharide units and are divided into two groups: sulfated (e.g., chondroitin sulfate, heparan sulfate, and keratan sulfate) and non-sulfated (hyaluronic acid) GAGs. Often, GAG chains are attached to a single protein core and may link at one end to another GAG resulting in the formation of a huge



macromolecule. Despite of their small constituting fraction in the normal arterial wall, studies have shown that interaction of GAGs/PGs aggregates with other ECM constituents play a key role in maintaining the bio-mechanical properties of the vessel wall.

PGs are extremely diverse in size, shape and chemistry, and their structure is based on their core proteins, location, and GAG composition. PG content in ECM of normal vascular tissue is low, however this dramatically increases in almost all stages of vascular diseases. PGs accumulate largely in lesions of the vasculature that are prone to disease initiation and are frequently coincident with early phases of atherosclerotic lesion formation through the retention of cholesterol-rich lipoproteins (35). PGs are also involved in ECM related metabolic processes and crosstalk with other inflammatory cells that extravasate to the subendothelial regions (36).

ECM DEGRADATION AND REMODELING

The vascular ECM is critical to maintain vascular wall integrity, to impart tensile strength, viscoelasticity, elastic recoil and compressibility to the vessel wall. The ECM also plays a key role in regulating the phenotype and cellular fate of vascular cell types, through the distinct properties of its different constituents (4, 5,

7). ECM degradation and remodeling are hallmarks of several vascular diseases, including hypertension and arterial stiffness, atherosclerosis (AS), and aortic aneurysms (AA; **Table 1**).

Arterial Stiffness and Hypertension

Arterial stiffness, also referred as arteriosclerosis, is one of the earliest clinically detectable manifestations of impaired vascular ECM remodeling (37). Altered collagen metabolism is often considered as the major contributor to the pathogenesis of arterial stiffness (38). Remodeling of the arterial wall is mainly driven by collagenases or MMPs and stiffened vessels usually show increased deposition of collagen and higher expression of MMPs. These vessels also have fragmented and reduced elastin content, disorganized endothelium, and infiltrated macrophages and other mononuclear cells (37). Calcium deposition within the arterial wall increases with increased elastic matrix breakdown and generation of bioactive EDPs increases with growing age, contributes to wall stiffening (39). The proportion of senescent cells within the vasculature also increases with age and this further exacerbates the state of chronic inflammation. Thus, the combination of chronic inflammatory events with reduced cross-linked elastin content, accompanied by the elevated levels of activated MMPs and other proteases can seriously compromise the integrity of the elastin-collagen networks and

TABLE 1 | List of major vascular disorders caused by ECM degradation and remodeling.

| Disease | Etiology | Features | References |
|---|----------|---|------------|
| Hypertension and arterial stiffening (Arteriosclerosis) | Acquired | Altered collagen metabolism, higher MMP expression, reduced amount of elastin or compromised fiber assembly, altered ECM composition, generation of elastin derived peptide etc. causes arterial stiffening and leads to hypertension and other complications. | (37–41) |
| Atherosclerosis | Acquired | Chronic inflammation, infiltration of lipids and macrophages, accumulation of PGs, degradation ECM components in the aortic wall leads to formation of AS plaque. Leading cause for myocardial infraction and stroke. | (42–47) |
| Abdominal Aortic Aneurysm | Acquired | Infiltration of inflammatory cells, chronic over expression of MMPs (MMP 2 and 9) cause medial SMC apoptosis and ECM degradation, destruction and fragmentation of elastic fibers in the arterial wall. Compensatory collagen deposition mechanically stabilizes weakened aortic wall, but eventually leads to a fatal hemodynamic stress-induced wall rupture. | (48–58) |
| Thoracic Aortic Aneurysm | Genetic | Abnormalities in elastin-associated microfibrils caused dysfunctional FBN1 gene and increase tissue level of TGF- β , leads to breakdown of elastin. | (59–64) |

the basement membranes (39). The compensatory increase in collagen production at this stage, directed toward restoring the integrity of vessel wall, often results in the formation of poorly organized and highly cross-linked (stiffer) collagens.

Arterial stiffness increases with advancing age and is associated with a higher risk of developing hypertension (38). However, vascular stiffening and hypertension appear to be bidirectionally associated (40). High blood pressure may induce vascular damage and accelerate the artery stiffening process, while aortic stiffening increases pressure pulsatility and affects systolic blood pressure (40). The chronological relationships between vascular stiffness and blood pressure remain ambiguous, whether with the cause-effect relationship between vascular stiffness and hypertension or vice versa yet to be completely elucidated (41). Nevertheless, the clinical combination of hypertension and arterial stiffness marks a major step toward the development of serious CV complications.

Atherosclerosis

AS is a common cause of coronary artery disease and stroke and is a leading cause of morbidity and mortality worldwide (42). AS refers mainly to the lipid deposition that occurs within lesions around the tunica intima, followed by the migration and proliferation of SMCs from the tunica media layer. These events subsequently lead to the formation of atherogenic lesions or fibroid plaque lesions. Even though the exact reason for AS plaque formation is currently unknown, experimental and clinical evidence suggest that AS is a chronic inflammatory disease (42–45). Hypercholesterolaemia is considered one of the main causes of AS formation; an increase in plasma cholesterol levels alter arterial endothelial permeability and allows the accumulation of lipids, especially low-density lipoprotein cholesterol (LDL-C) particles, to the arterial wall (43). At this stage, blood leukocytes (primarily lymphocytes and monocytes) migrate and adhere to the damaged ECs, further express vascular adhesion molecule-1 (VCAM-1) and selectins (43). Once attached, these cells produce inflammatory factors, promoting monocytes differentiation into macrophages and leads to the formation of foam cells by engulfing oxidized LDL particles. Uptake of lipid particles makes macrophages less

mobile and promotes the accumulation of these lipid-laden cells in the intimal layer (43, 44). These foam cells maintain their metabolic activity and further releases a variety of cytokines and other inflammatory mediators (45). Together with damaged ECs, these foam cells initiate an inflammatory cascade to promote the proliferation of vascular SMCs toward a synthetic pro-atherogenic phenotype and supports their trans-endothelium migration. Under normal physiological conditions moderate proliferation of SMCs is associated with healthy vascular wall repair, however excessive activation is often associated with senescence, secondary necrosis, ECM formation and fibrosis. Thus, SMC proliferation and migration play a critical role in the arterial remodeling associated with AS (46).

Recent studies have indicated the role of PGs and GAGs in orchestrating AS progression (36). According to the response-to-retention hypothesis, the key initiating early event in AS is binding of cholesterol-containing lipoprotein particles to newly accumulated intimal PGs, in particular versican and biglycan, results in the gradual lipid deposition in the subintimal space (47). Accumulation of versican is seen in early stages of AS and this predisposes the vessel to lipoprotein retention (65). Peripheral literature also suggests that versican build up is detrimental to tropoelastin production and fiber assembly, and their accumulation occurs mainly in response to aging, hypertension, and other vessel injury (66). Thus, pro-atherogenic stimuli affecting versican expression or its GAG composition could contribute to plaque formation and alter ECM state to in turn trigger changes to phenotypes of contacting vascular cells (67).

In AS, ECM remodeling is considered a critical step in development and progression of the condition, the dynamic interactions between the multitude of cell types and molecular mechanisms involved in regulating the matrix remodeling process are still not fully understood (46). In AS, infiltrating leukocytes are known to release certain proteases that degrade the ECM, and lead to changes in the tissue milieu allowing SMC proliferation and plaque growth (68). AS plaques can alternate between stable and susceptible states depending on this internal environment. Lesions with large lipid core and thin fibrous cap, with higher macrophage infiltration, are usually unstable

and prone to rupturing (69–71). Once formed, SMCs maintain stability of AS plaque through secretion of interstitial collagen and MMPs secreted by the activated macrophages can effectively degrade this interstitial collagen and other ECM proteins (69). This makes the AS plaques vulnerable for rupture leading to arterial occlusion, resulting in the formation of major CV complications, including myocardial infarction (MI) and stroke (71). Collectively, these indications clearly suggest that ECM and related proteins play a critical role in the formation and progression of AS disease.

Aortic Aneurysms

Aortic aneurysms involve progressive enlargement or bulging of the aorta that has the propensity to expand and rupture (48). The most common forms of aortic aneurysms are abdominal aortic aneurysms (AAA) and thoracic aortic aneurysms (TAAs). AAAs, the more prevalent form of aortic aneurysm, are typically associated with advanced age and AS, with risk factors including hyper-cholesterolaemia, hypertension and/or diabetes (49). On the other hand, TAAs occur in all age groups and are more closely associated with hereditary factors and do not necessarily show close association with major identified risk factors for CV disease (e.g., hyper-cholesterolaemia, hypertension, diabetes etc.) (59).

Abdominal Aortic Aneurysms

AAAs are localized, focal dilatations of the abdominal aorta, the segment between the renal bifurcation and iliac bifurcation (48). An aortal expansion qualifies as an AAA if the diameter of the abdominal aortal segment increases to at least one and half times the original diameter of the healthy vessel (48). The etiology of AAAs is multifactorial (e.g., chronic hypertension, AS, smoking, or vasculitis), but in general, the pathophysiology involves breakdown and loss of aortal wall ECM structures resulting in gradual wall thinning, weakening, and ultimate rupture (50). Histology of clinical AAA tissues show infiltration of leukocytes, degradation of ECM structures, particularly the elastic matrix, and the depletion and apoptosis of medial SMCs to be the major pathological hallmarks of AAAs (51, 52). Although the mechanisms of the disease formation is unknown, studies on animal models of this disease have indicated localized injury stimulus-incited infiltration of inflammatory and immune cells (macrophages, neutrophils, mast cells, T and B lymphocytes) into the abdominal aorta wall (53). These infiltrating cells chronically overexpress cytokines and ECM proteases (mostly MMP-2 and 9) and cause medial SMC apoptosis and ECM degradation with gradual loss of aortic wall integrity. Thus, the destructive pathological remodeling of aorta in AAA involves four interrelated factors, namely (a) chronic inflammation of the outer wall of aorta along with neovascularization and upregulation of proinflammatory cytokines, (b) hyper-production and dysregulation of matrix degrading enzymes, (c) progressive destruction of elastin to generate bioactive EDPs, and of collagen and (d) apoptosis of medial SMCs incited by the EDPs (54, 55).

ECM degradation in AAAs occurs due to a chronic imbalance between elastolytic proteases (MMP2 and MMP9), generated by pro-inflammatory macrophages infiltrating the injured aorta

wall, and their natural inhibitors, the TIMPs. SMCs in the healthy adult vascular wall are of contractile phenotype and are intrinsically deficient in their capacity for elastin synthesis and have impaired ability to assemble mature elastic fibers (56). Further, diseased SMCs are even less amenable to new elastic fiber assembly and moreover, the degraded state of pre-existing fibers which are critical to the new fiber assembly process is a serious impediment to any prospects of new elastic fiber generation (57).

The decrease in total aortal elastin content in the vessel wall due to chronically upregulated proteolytic activity is compensated by the cellular deposition of collagen in response to enhanced flow-induced stresses encountered by SMCs in the thinning vessel wall. While adult cells, more so, diseased vascular cells, are intrinsically deficient in their ability to generate elastic matrix, and have impaired ability to assemble mature elastic fibers, vascular SMCs and fibroblasts readily and exuberantly regenerate collagen (58). This compensatory collagen deposition mechanically stabilizes the weakened aorta wall for short term thereby delaying AAA rupture. However, the continued degradation of elastin and generated EDPs incite SMC apoptosis, a positive stimulus for proteolytic breakdown of collagen matrix. The resulting imbalance between collagen synthesis and breakdown ultimately leads to fatal hemodynamic stress-induced wall rupture. Thus, early intervention in this pathophysiologic sequence of events to restore elastin homeostasis in the AAA wall could hold potential to slow or regress AAA growth to rupture (58, 72).

Thoracic Aortic Aneurysms and Dissections

Thoracic aneurysms are classified as aortic root or ascending aortic aneurysms (60). The common characteristic of TAADs involves cystic medial degeneration, which manifests as degenerated elastic fibers, disorganized collagen fibers, and accumulated PGs, besides a contractile to activated phenotype switch of medial SMCs, and later apoptosis of these cells (60). In healthy vessels, vascular SMCs maintain ECM homeostasis by maintaining a perfect balance between secreted proteases (MMPs) and their inhibitors (TIMPs). However, in the TAAD wall, MMPs are chronically overexpressed, causing accelerated ECM degradation. The bioavailability of cytokines and growth factors involved in signaling pathways that regulate ECM homeostasis, which are sequestered in the ECM in its latent form (e.g., TGF- β), are also enhanced (61). These pathological events progressively lead to the weakening of the aortic wall, and further reduce their ability to endure the biomechanical forces imposed by pulsatile blood flow and blood pressure.

TAADs typically demonstrate a classical Mendelian inheritance with high or complete penetrance. This possibly suggest the contribution of a single gene defect in the progression of TAADs. TAADs can be further classified into syndromic presentations that demonstrate characteristics of a systemic connective tissue disorder [e.g., Marfan syndrome (MFS), Loeys–Dietz syndrome (LDS)], and non-syndromic presentations (e.g., isolated familial TAAD syndrome). MFS is a typical heritable autosomal-dominant disorder caused by mutations in

a structural glycoprotein fibrillin 1, which is a major component of the microfibrils critical to elastic fiber assembly (62). These mutations result in a decrease in the amount of elastin in the aorta wall and lead to the disorganization of elastic fibers. Moreover, dysfunctional fibrillin-1 microfibrils impair the sequestration of TGF- β 1 in the ECM and this causes an increased bioavailability of TGF- β 1. As a consequence, the aorta exhibits progressively lower ability to stretch and recoil and increased wall stiffness and dilatation (63). Presenting similar manifestations as MFS, LDS is linked to heterozygous mutations of the TGF- β receptors I & II (TGF- β R1 and TGF- β R2), suggesting non-involvement of TGF- β 1 early signaling (64). Cystic medial degeneration in absence of overt connective-tissue disorders, now referred as familial TAA syndrome, is caused mostly through defect in ACTA2 gene which encodes smooth muscle α 2 actin. Mutation in ACTA2 leads to vascular SMCs with disorganized and aggregated actin filaments, and subsequently impairs their cellular adaptation to local mechanical stress in the aortic wall (60).

STEM CELLS FOR VASCULAR TISSUE REPAIR

SCs represent a unique population of undifferentiated cells which are capable of extensively differentiating into different tissue and cell types (73). They are characterized largely by their ability to self-renew, clonality and potency, but this can vary depending on the type of SCs (74). SCs are increasingly studied in the context of use as model systems to understand cellular mechanism involved in the disease progression, and for their utility in the treatment of a spectrum of disease conditions such as CV disorders, diabetes mellitus, chronic myeloid leukemia, cirrhosis, pulmonary fibrosis, inflammatory bowel disease and disorders of the nervous system (73, 75–77).

Types of Stem Cells

SCs are classified broadly based on origin as embryonic stem cells (ESCs), induced pluripotent stem cells (iPSCs) and adult SCs (74). ESCs are pluripotent in nature and their unlimited proliferation potential makes them excellent choice for regenerative therapy. However, their use raises several ethical issues and direct use of undifferentiated ESCs for tissue transplant pose potential tumorigenicity concerns. iPSCs are SCs generated by genetically reprogramming adult somatic cells to form an “ESC-like state” and they share similar characteristics with ESCs in terms of morphology, proliferation, and their ability to differentiate into cells of all three germ layers in culture (78). Use of iPSCs raises minimal ethical concerns and change be excellent choice for tissue regeneration and repair.

Adult SCs are the common cell type for therapy and tissue repair, specifically for CV disorders, largely due to their anti-inflammatory properties as well as tissue repair capabilities (75). Transplantation of adult SCs has shown to restore damaged organs *in vivo* and initiate revascularization of the ischemic cardiac tissue through differentiation and generation of new specialized cells (75, 77). Moreover, use of adult SCs has been associated with minimal ethical concerns. The advantage of adult

SCs in the clinics and evidence supporting their therapeutic effectiveness in regeneration and repair, makes them suitable choice for therapeutic applications. MSCs are widely used adult SC type for regenerative therapeutics (76, 77). MSCs are multipotent adult cells with the potential to differentiate into multiple cell types like osteoblasts, chondrocytes, myocytes, adipocytes, etc. (76). Mesenchyme refers to the embryonic loose connective tissue derived from the mesoderm and develops into hematopoietic and connective tissue. MSCs are mostly isolated from the bone-marrow tissues but can be obtained from other sources such as umbilical cord, endometrial polyps, menses blood and adipose tissues (75–77).

STEM CELL THERAPY FOR MAJOR VASCULAR DISORDERS

Stem Cell Treatments for Atherosclerosis

SCs, specifically MSCs, have been shown to impart strong anti-inflammatory and immunomodulatory responses against pathological events centric to vascular diseases, such as AS (79, 80). Considering AS as a chronic inflammatory disease linked to dysregulation of the immune system, an MSC-based therapy could exert protective effects on the progression of AS (81). A growing body of evidence suggests that transplanted MSC can modulate cytokine and chemokine secretion, reduce endothelial dysfunction, promote regulatory T cell function, decrease dyslipidemia, and stabilize vulnerable plaques in the AS region (82–84). **Table 2** summarizes key recent animal studies that investigated therapeutic benefits of MSCs in animal models of AS.

Undifferentiated MSCs have the capacity to modulate and reduce inflammation and can alter immune cell components within AS plaques to alleviate inflammation (83). The protective properties of MSCs on AS lesions have been largely attributed to the secretion of various anti-inflammatory mediators (80). Transplantation of BM-MSCs into AS lesions in various animal models has been found to result in increased secretion of anti-inflammatory cytokines, including Interleukin-10 (IL-10) and TGF- β 1, while the production of pro-inflammatory cytokines, such as IL-1 β , IL-6, and Tumor Necrosis Factor (TNF- α), was reduced (**Table 2**). MSC treatment enhanced IL-10 secretion, which further promoted anti-atherogenic effects primarily by inhibiting macrophage activation, MMPs, and pro-inflammatory cytokines (84). TGF- β 1 secretion by MSCs also caused the induction of CD4⁺CD25⁺Foxp3⁺ regulatory T (Treg) cells from non-regulatory cells and also suppressed the proliferation of NK cells in Apolipoprotein E (–/–) (ApoE^{–/–}) mice AS model (85). The increased ratio of Tregs over CD4⁺ T cells in turn promoted macrophage differentiation toward the M2 phenotype, and thereby reduced monocyte infiltration and inflammatory response in the plaque region (85). These results clearly indicate the beneficial anti-AS role played by MSCs, *via* (a) reducing pro-inflammatory responses, (b) promoting anti-inflammatory environment, and (c) mitigating monocyte recruitment to the lesion site.

TABLE 2 | Animal studies involving use MSCs for treatment of Atherosclerosis.

| AS model | MSC source | Major outcomes with MSC treatment | References |
|---|--------------------------|---|------------|
| Ldlr ^{-/-} mice, with high fat diet | BM-MSC (mice) | Reduction in effector T cells, circulating monocytes and serum CCL2 levels. Reduced dyslipidemia in mice. | (82) |
| ApoE ^{-/-} mice | Skin-derived MSCs (mice) | S-MSCs capable of migrating to AS plaque and selectively taking up residence near macrophages. Reduced the release of the TNF- α and increased the expression IL10 in the plaque region. | (83) |
| ApoE ^{-/-} mice | BM-MSC (ApoE-KO mice) | Reduced the size of AS plaques 3 months after treatment. Atheroprotective role by enhancing the number and function of Tregs and inhibiting the formation of macrophage foam cells. | (85) |
| New Zealand rabbits, LN2 frostbite AS model | BM-MSC (rabbit) | Downregulation of plasminogen activator inhibitor 1 (PAI-1), and MMP-9 after 4 weeks of MSC transplantation. Serum hs-CRP, TNF- α and IL-6 were significantly down-regulated, whereas IL-10 was significantly up-regulated. Formation of abundant collagen fibers at the plaque rupture areas. | (86) |
| Ldlr ^{-/-} mice, with high fat diet | CM from AD-MSC | Suppression of macrophages accumulation, downregulation of MAPKs and NF- κ B leading to M1/M2 polarization, downregulation of CAM and JNK phosphorylation with CM treatment. | (87) |
| Japanese big-ear white rabbits with high fat diet | UC-MSC | Downregulated apoptosis and proliferation of arterial cells. EC density increased in treated group. Reduced levels of TNF- α and IL6. | (88) |

Endothelial dysfunction is one of the earliest events in AS initiation (89). MSCs have been shown to successfully restore endothelial function by halting atherogenesis (90). Expression of the vasodilator molecule endothelial nitric oxide synthase (eNOS) locally in the injured vessel wall is responsible for the production of vascular nitric oxide (NO), and this often is associated with AS progression. MSC transplantation has been reported to attenuate AS by improving EC function *via* the Akt/eNOS pathway by upregulating IL8 and Macrophage Inflammatory Protein (MIP)-2 in ApoE^{-/-} mice (90). Since IL-8 is an important pro-atherogenic cytokine involved in the early stages of plaque formation, this study implies the importance of proper timing of cell therapy to be able to prevent growth of an early plaque.

Hyperlipidemia is another well-established risk factor for AS formation and studies have revealed that MSC treatment can reduce lipid levels in various hyperlipidemic animal models (91, 92). MSCs seems to have indirect effect on cholesterol metabolism through immune modulation, however the exact mechanism remains vague. MSC treatment has been effective in reducing plasma cholesterol level in low-density lipoprotein-receptor knockout mice (LDLR^{-/-} mice) due to reduction in very-low-density-lipoproteins (VLDLs) levels (92). This was attributed mainly due to the reduced activation of Kupffer cells, which express mediators promoting VLDL secretion. MSC treatment was effective in reducing SREBP-1c expression, a transcription factor involved in fatty acid biosynthesis, and an increase in PPAR- α expression, a transcription factor modulating fatty acid β -oxidation (93). Overall, this study suggests that MSC administration lowers serum lipid levels and might subsequently reduce lipid accumulation in plaques. MSC-mediated anti-inflammatory signaling appears to be the mechanism behind lipid reduction *via* altered lipid metabolism, however further studies are required to validate these observations.

MSCs have the potential to treat advanced AS plaque lesions through the regeneration of the inner endothelial lining and

collagen fiber formation in the vessel wall (94, 95). MSC transplantation stabilized vulnerable plaques in AS rabbit model through immune modulation, by reducing the expression of pro-inflammatory cytokine TNF- α and IL-6 and by increasing IL-10 expression (86). Moreover, the expression of MMPs (MMP-1, MMP-2, and MMP-9) within the lesion was reduced upon MSC transplantation, suggesting that MSCs may protect the ECM and further stabilize the lesion (86). These studies do indicate that MSC treatment can reduce plaque vulnerability by decreasing the regional collagen degradation by inhibiting local protease activity. The apoptosis of vascular ECs, SMCs, and macrophages also contribute to formation, development, and rupture of AS plaques. MSC treatment reduced apoptotic cells within the plaque region, suggesting that MSCs may increase plaque stability (87).

Current strategy of using MSCs as a therapeutic option for AS treatment involves their use as a post-injury treatment approach, exploring the immunomodulatory properties and plaque stabilization effect of MSCs (79–81). Given the broader spectrum of therapeutic responses, MSC treatment might provide an atheroprotective effect and could change the ECM microenvironment to modulate or mitigate early progression of AS (81). Future studies must address the impact of vessel site-specific and temporal differences in the ECM milieu that contribute to AS disease progression. Recent studies have revealed that PGs and pendant GAGs orchestrate AS progression by initiating the binding and retention of atherogenic lipoproteins in the artery intima, leading to foam cell formation (35). Studying the impact of SC treatment in PG remodeling by degrading enzymes at different stages of AS might be interesting and could be used as an early intervention strategy. Likewise, elastin degradation peptides, elastokinaes, effects as modulators of macrophage functions during atherogenesis (44) and anti-proteolytic effects of MSCs could be beneficial in reducing local proteolytic activity in the plaque region.

Stem Cell Therapy for Abdominal Aortic Aneurysm Treatment

AAA pathophysiology is driven mainly by the progressive degradation and loss of ECM structures in the aorta wall, a process driven by the chronic inflammatory milieu in the tissue (48, 49). Therefore, successful AAA treatment strategy must attenuate inflammation, inhibit proteolytic activity, and provide an active stimulus to tropoelastin synthesis and elastic fiber assembly and crosslinking in the aneurysm wall (10). Almost all elastin regenerative repair strategies explored so far are focused on reversing or attenuating adverse signaling pathways or mitigating MMP overexpression within the AAA wall, with limited or no direct emphasis on addressing either poor elastogenesis and ECM regeneration (Table 3). The poor elastin generation capability of terminally differentiated adult SMCs limits their use in cell therapy (106). In this context, SCs represent a viable alternative that could be useful for regenerative tissue repair. Vascular elastin is primarily synthesized and deposited during fetal and neonatal developmental stages in tissue microenvironments rich in stem/progenitor cells. Hence it is reasonable to hypothesize that SCs or their SMC-like derivatives would retain higher elastin production and matrix assembling capabilities than adult aortic cells or AAA-SMCs. An MSC-based treatment approach has demonstrated some promise in attenuating inflammatory processes and proteolytic activity and to stimulate elastogenesis.

The anti-inflammatory and pro-matrix regenerative properties of MSCs were evaluated in several investigations, using different AAA animal models. These studies are summarized in Table 4. In a seminal study by Hashizume et al. murine MSCs attenuated enzyme activities of both elastolytic MMP2 and MMP9 and reduced production of inflammatory cytokines (i.e., TNF- α) by murine macrophages (96). These cells also stimulated elastin synthesis by murine aortal SMCs in culture. Further *in vivo* studies on male angiotensin II (Ang II) infused ApoE^{-/-} mice demonstrated that MSC implantation *via* laparotomy was effective in downregulating the expression of MMPs, IL-6, Monocyte Chemoattractant Protein-1 (MCP-1), and TNF- α , and also in upregulating Insulin-like Growth Factor-1 (IGF-1) and TIMP-1. Since laparotomy for localized cell delivery to the AAA wall was invasive, BM-MSCs were delivered *via* the intravenous (I.V.) route into an AngII-induced AAA mouse model (97). In this study, multiple BM-SMC dosing events caused a significant decrease in AAA diameter at the ascending and infrarenal levels, relative to sham controls. Reduction in AAA growth was also associated with decreased macrophage infiltration and suppressed MMP-2 and MMP-9 activity in the AAA tissues, as well as enhanced preservation of elastin content in the AAA wall. BM-MSC treatment also reduced levels of the inflammatory cytokines, IL-1 β and MCP-1, and increased expression of IGF-1 and TIMP2 in the AAA wall. In a separate study, Blose et al. showed that periadventitial delivery of Adipose derived MSCs (AD-MSCs) to be effective in slowing AAA progression and in preventing fragmentation of the elastic lamelle in a mouse elastase-perfusion model of the disease (98). Effectiveness of SC therapy to re-establish the mechanical

properties of damaged abdominal aorta was attempted using a AAA model. Results from these studies suggest that BM-MSC treatment was effective in stabilizing the geometry of AAAs, improving wall stiffness, and decreasing stress variations in the arterial wall of rat AAA model (99). Wen et al. also showed I.V. administration of Umbilical Cord MSCs (UC-MSCs) was effective in attenuating aneurysmal expansion, reducing elastin degradation and fragmentation, inhibiting MMPs and TNF α expression, and to promote contractile phenotype of SMCs in the AAA wall of elastase-induced rat model (100).

A study by Davis et al. showed BM-MSCs derived from female mice to be more effective in attenuating AAA growth in elastase perfused AAA mice model, compared to MSCs derived from male mice, suggesting sex-related differences in SC characteristics and behavior (101). However, this observation has been very inadequately studied and requires further in-depth assessment. Akita et al. on the other hand compared the therapeutic effects of allogeneic and autologous MSC on Ang II- ApoE^{-/-} model of AAAs as an attempt to create an “off-the-shelf” product as required in clinical practice (112). They observed that both allogeneic and autologous MSCs had comparable effect in terms of reducing chronic inflammation and aortic dilatation.

Despite the promise of SC therapy for AAA treatment (113), a comprehensive and systematic characterization of the elastogenic capabilities of SCs and their effects on the various steps and processes involved in the complex process of elastogenesis (i.e., elastin precursor synthesis, precursor recruitment and cross-linking, and fiber assembly and organization into superstructures) by healthy and diseased SMCs is lacking. Our research focuses on developing strategies for restoring ECM homeostasis in matrix-compromised vessels, as in the AAA wall, which involves providing a stimulus for on-site regeneration of mature elastic fibers, a deterrent to proteolytic breakdown of existing fibers, and restoring a healthy SMC phenotype. Our earlier investigations using elastase infusion injury rat AAA model provided evidence that neointimal remodeling within aneurysmal tissue is associated with new elastin deposits (114). However, these structures are nascent, do not exhibit the characteristics of mature elastic fibers, and more so, are transient in their presence. The lack of maturity of these structures was suggested to be related to deficient deposition of the fibrillin microfibrils that serve as vital pre-scaffolds on which tropoelastin coacervates get crosslinked toward forming mature elastic fibers. In separate work, we investigated SMC-like cells (BM-SMC) of a defined phenotype differentiated from BM-MSCs, for their effectiveness in (a) augmenting elastic fiber assembly in cultures of aneurysmal SMCs isolated from our elastase injury rat model, and (b) restoring elastic matrix homeostasis in the AAA wall *in vitro* (115, 116). Our cell culture studies showed that BM-SMCs exhibited superior elastogenicity compared to their parent cell (BM-MSCs; Figure 4) and provided pro-elastogenic and anti-proteolytic stimuli to cytokine injured aneurysmal SMCs in culture (117–119). Further, *in vivo* studies suggested that both BM-MSCs and BM-SMCs downregulated expression of several inflammatory and pro-apoptotic cytokines that are upregulated in the AAA wall in the elastase injury

TABLE 3 | Animal studies involving use MSCs for treatment of Abdominal Aortic Aneurysm.

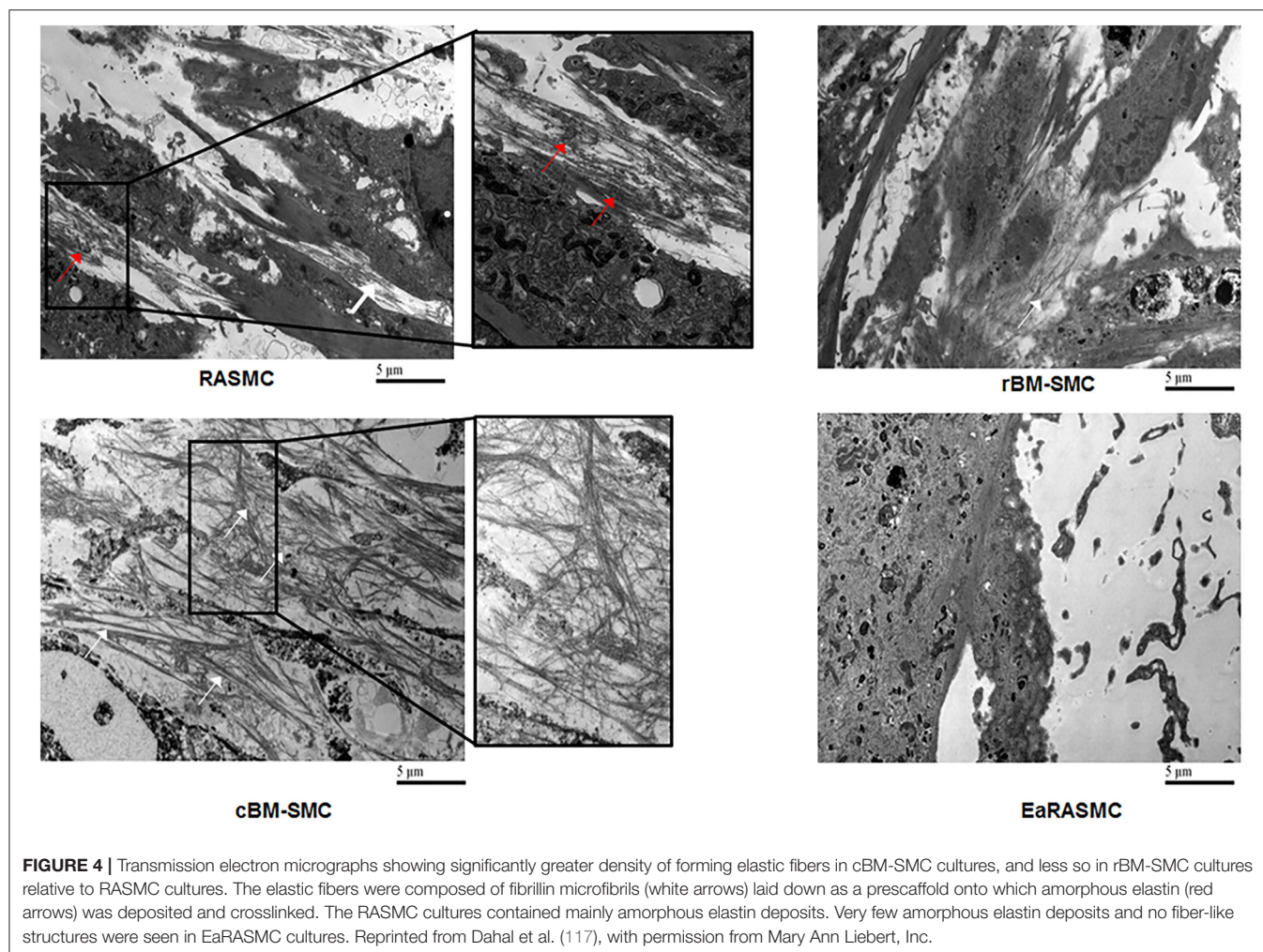
| AAA model | MSC source | Major outcomes with MSC treatment | References |
|--|--|--|------------|
| AngII infused ApoE ^{-/-} mice | BM-MSC (mice) | Reduced MMP2, TNF- α , IL-6, and MCP-1. Increased elastin expression. | (96) |
| AngII infused ApoE ^{-/-} mice | BM-MSC (mice) | Reduction in aortic diameter. Reduced MMP2, MMP9, IL-1 β , IL-6, and MCP-1 levels. Preservation of aortic elastin content, increase in IGF1 and TIMP2. | (97) |
| PPE C57BL/6 mice | AD-MSC (mice) | Reduced aortic diameter. Less fragmented elastin versus saline controls. | (98) |
| AngII infused ApoE ^{-/-} mice | BM-MSC (mice) | Reduced aortic diameter. Reduced MMP2/9 expression, inhibited infiltration of M1 macrophages and preserved elastin. | (99) |
| PPE-SD Rat | UC-MSC (human) | Reduced aneurysmal expansion, reduced elastin degradation, inhibited MMPs and TNF- α expression. | (100) |
| AngII infused ApoE ^{-/-} mice | Allogenic and Autologous BM-MSC (mice) | No major difference between allogenic and autologous MSC in reducing chronic inflammation and reduced aortic dilation. | (101) |
| PPE-SD rat | BM-MSC and BM-SMC (rat) | BM-MSC and BM-SMC downregulated expression of several inflammatory and pro-apoptotic cytokines. Deposition of thick and matured fibers were observed with BM-SMC treatment in the AAA wall; thinner and fragmented fiber | (102) |
| Cacl ₂ infused rat | AD-MSC (mice) | Reduced MMP2 and MMP9 expression Increased elastin expression | (103) |
| PPE C57BL/6 mice | AD-MSC (human) | Reduced aortic expression and pleiotropic immunomodulatory effects. No aortic engraftment following I.V, paracrine effects following lung engraftment | (104) |
| AngII infused ApoE ^{-/-} mice | BM-MSC (mice) | Regulation of the NF- κ B, Smad3, and Akt signaling pathways. | (105) |

TABLE 4 | Animal studies for treatment of vascular disorders using SC-derived exosomes.

| Disease/animal model | MSC source for exosome isolation/ exosome isolation method | Major outcomes with exosome treatment | References |
|--|--|--|------------|
| AS/ ApoE ^{-/-} mice | BM-MSC (mice)/ UC method | Selective uptake of IV injected MSC-exosomes by macrophages in plaque region, reduced plaque area and induced M2 macrophage polarization through miR-let7/HMG2/NF- κ B pathway. | (107) |
| AS/ ApoE ^{-/-} mice | BM-MSC | Exosomes containing miR-21a-5p promoted M2 polarization of macrophages, reduced plaque area and macrophage infiltration by targeting KLF6 and ERK1/2 signaling pathway. | (108) |
| AS/ ApoE ^{-/-} mice | UC-MSC (human)/UC method | miR-145-rich exosomes downregulated JAM-A, reduce AS plaque <i>in vivo</i> . | (109) |
| AAA caused by AS/ AngII infused ApoE ^{-/-} mice | BM-MSC (mice) | Attenuated AA progression decreased expression of IL-1 β , TNF- α , and MCP-1, and expression of IGF-1 and TIMP-2 increased. Also induced M2 macrophage phenotype and suppressed elastic lamella destruction. | (110) |
| AAA/ Elastase induced mice model | UC-MSC (human)/UC method | Reduction in aortic diameter, reduced expression of pro-inflammatory cytokines, increase in α SMC expression and decreased elastic fiber disruption. | (111) |

rat AAA model, which contributes to accelerated elastic matrix breakdown and suppression of elastic fiber neoassembly, repair and crosslinking (102). Our results also indicated significant improved deposition of thick and matured elastic fibers in the AAA wall upon treatment with the BM-SMCs, whereas the elastic fibers were thinner and fragmented in the BM-MSC-treated and saline-treated (control) animals with AAAs (102). This study demonstrated the promise of using an BM-MSC-derived cells of an SMC lineage for matrix regenerative cell therapy to reverse the pathophysiology of proteolytic disorders such as AAAs.

Overall, MSC therapy was effective in reducing inflammation and ECM degradation at the AAA wall site, through the secretion of several anti-inflammatory cytokines, protease inhibitors and ECM synthesis stimulators (97–100). MSC treatment was also effective in regressing the growth of already-formed AAAs (97, 98, 102, 113). However, with AAA therapy, it is critical to identify specific strategies and mechanisms that are conducive for the repair and assembly of native vascular elastic matrix with high efficiency and fidelity to the fiber assembly process. Future research should focus on understanding the exact healing



mechanism of MSCs under AAA conditions, and further assess their impact on the repair and regeneration of ECM components.

Stem Cell Therapy for Thoracic Aortic Aneurysm and Dissection Treatment

Although SC therapy could play a significant role in tissue repair associated with TAAD, with their ability to attenuate proteolytic activity and improve elastogenicity, few studies have addressed this topic. Shen et al. have demonstrated the abundant presence of SCs in the TAAD tissues obtained from patients with descending thoracic aortic aneurysms and with chronic descending thoracic aortic dissections (120). They also observed the differentiation of SCs into SMCs, fibroblasts, and inflammatory cells within the diseased aortic wall and this might suggest the reparative and destructive role of SCs in TAADs. MSC therapy was used to immunomodulate vascular inflammation and remodeling through altering microRNA (miRNAs) expression profile to attenuate TAA formation (121). Descending TAA was induced by topical elastase application in C57BL/6 mice and MSC treatment was effective in attenuating T-cell, neutrophil and macrophage infiltration and prevented elastic degradation to mitigate vascular

remodeling. This study also demonstrated miRNA modulating ability of MSCs that are linked to reduce leukocyte infiltration and vascular inflammation to mitigate the aortic diameter and TAA formation in mice. Even though the study outcome was promising, further in-depth investigations are required to evaluate the anti-proteolytic and pro-regenerative benefits of SCs under TAA conditions.

STEM CELL-INSPIRED APPROACHES FOR TREATMENT OF COMMON VASCULAR DISORDERS

It was originally assumed that SCs regenerate/repair the damaged/diseased regions by homing to the respective locations, engrafting, and subsequently differentiating into mature, functional cells (76, 77). However, this classical hypothesis was confronted by outcomes from studies indicating that SCs are neither engrafted adequately nor retained long enough to explain the tissue replacement/repair process (122). According to a more recent hypothesis, SCs largely employs alternate modes of tissue repair through secretion of paracrine signaling factors,

such as cytokines and chemokines, hormones, and extracellular vesicles (EVs) (123–125). These secreted factors, collectively referred as secretome, can be found in the SC culture medium usually mentioned as conditioned media (CM) (126). SC derived CM has been demonstrated to exert several therapeutic benefits by modulating the local immune responses to inhibit inflammation, stimulating ECM remodeling, and decrease cell apoptosis and fibrosis (126). Exosomes seems to be a critical CM component and exosomes derived from therapeutically relevant SC source represent biological functions like the parent cells, by facilitating tissue regeneration/repair through transferring active biomolecules such as peptides, proteins and RNAs to the damaged cells/tissues (122, 123).

STEM CELL DERIVED EXOSOMES FOR VASCULAR TISSUE REPAIR

Exosomes, specifically ones derived from MSC sources, have enormous benefits in a variety of diseases and injuries through the secretion of proteins and RNAs that they contain (127). Specifically, MSC-derived exosomes have been investigated for their potential for vascular regeneration and repair, and for treating diseases such as ASs, AAs, stroke, pulmonary hypertension, and septic cardiomyopathy (128–131).

Biogenesis and Secretion of Exosomes

The term extracellular vesicles (EVs) are used to broadly describe distinct sub-types of extracellular secretions comprised of small bilayer lipid membrane vesicles (132–134). EVs can be classified into three major sub-types based on their mechanism of biogenesis, and size (135). Exosomes, typically in the range of 40–150 nm diameter, are vesicles derived from an endosomal origin and released into the extracellular space following fusion of multivesicular bodies with the plasma membrane. Microvesicles, which are larger in size compared to exosomes (100–1,000 nm diameter), are vesicles that bud out directly into the extracellular space from the plasma membrane without fusion with multivesicular bodies (135). Exosomes and microvesicles are active vehicles for inter-cellular communications, as they are released and taken up by living cells. On the other hand, apoptotic bodies (>800 nm diameter) arise directly from the outward blebbing of the plasma membrane of cells undergoing apoptosis. These particles do not typically participate in cellular communication process (135). Although size is often used to generically classify these sub-types of EVs, exosomes are considered to exhibit diameters of >100 nm and microvesicles to exhibit diameters <100 nm. However, there is a lack of consensus on a strict size cut-off for classifying EVs (136). Several studies have indicated the role of exosome-mediated intercellular communications in maintaining the homeostasis of CV systems, and SC derived exosomes have emerged as an important disease diagnosis/prognosis marker for CV disease and also as a regenerative tool (128, 130).

Stem Cell Derived Exosomes for Treating Arterial Stiffness and Hypertension

In a study by Feng et al. EVs (exosomes) obtained from iPSC-MSC were used as treatment option for aging-associated arterial stiffness and hypertension (137). I.V. administration of EVs significantly attenuated aging-related arterial stiffness and hypertension, and enhanced endothelium-dependent vascular relaxation and arterial compliance in old male C57BL/6 mice. EV treatment also prevented elastin degradation and collagen I deposition (fibrosis) in older mice and promoted expression of sirtuin type 1 (SIRT1), and endothelial nitric oxide synthase (eNOS) protein expression in aortas. Substantiating this observation, Monroe et al. has reported the capability of MSC-EVs in ameliorating pathological vascular ECM changes in congenital diaphragmatic hernia (CDH)-associated pulmonary hypertension in pregnant rats (138). These studies provide a strong rationale for studying therapeutic potential of SC derived EVs for aging-related vascular diseases and potentially opens new prospect for a non-pharmacological intervention strategy.

Stem Cell Derived Exosomes for Treating Atherosclerosis

SC-derived exosomes can regulate the incidence and progression of AS and could overcome the limitations associated with conventional AS treatment strategies. MSC-derived exosomes are reported to have an anti-atherosclerotic role (139), whereas exosomes derived from non-stem cell sources, such as neutrophils, macrophages, ECs or vascular SMCs, have a multifaceted role (140, 141).

Studies with AS experimental models clearly suggest that exosomes derived from the MSC source had prominent anti-atherosclerotic effect (107–109, 142) (Table 4). These studies largely focus on the immunomodulatory effect of MSC derived exosome on AS models. MSC-exosomes treatment decreased the AS plaque area in ApoE^{-/-} mice model and greatly reduced the infiltration of macrophages into the plaques, suggesting their anti-atherosclerotic effect. Exosomes were also effective in inducing macrophage polarization toward M2 phenotype *via* up-regulation of miR-let7 (107). Exosomal miRNAs seems to play a vital role in exerting the therapeutic outcomes on AS models (142). Ma et. al. showed that MSC-derived exosomes containing miR-21a-5p promoted M2 polarization of macrophages, and reduced plaque area and macrophage infiltration by targeting KLF6 and ERK1/2 signaling pathways, in an AS model of ApoE^{-/-} mice fed on a high-fat diet (108). On the other hand, treatment with miR-145-rich MSC-exosomes downregulated expression of Junction Adhesion Molecule A (JAM-A, also known as F11R overexpressed in patients with AS) in human umbilical vein endothelial cells (HUVECs) and further reduced AS plaque area *in vivo* on AS model of ApoE^{-/-} female mice fed on high-fat diet (109). AD-MSC-derived exosomes restrained the expression of miR-324-5p in a HUVEC lesion model, and this is expected to protect ECs against AS progression (143). miR-100-5 mimic-transfected UC-MSC derived exosomes inhibited inflammatory response in eosinophils *via* a FZD5/Wnt/β-catenin

pathway and alleviated AS progression in an ApoE^{-/-} mouse model (144).

Effect of AD-MSC derived CM in ameliorating AS in Ldlr^{-/-} mice was evaluated and results from this study demonstrated that I.V. injection of MSC-CM suppressed expression of cell adhesion molecules (CAMs) and reduced AS plaque area (87). EVs isolated from these CM also demonstrated immunomodulatory effect under *in vitro* experimental conditions, suggesting the prominent role of EVs in the cell secretome (104). MSC-CM treatment has also shown to inhibit VSMC calcification through the blockade of the bone morphogenetic protein-2 (BMP2)-Smad1/5/8 signaling pathway (145). From these studies it can be assumed that MSC-derived secretomes have prominent anti-atherosclerotic role, however, further in-depth investigations are required to confirm this observation. In addition, role of MSC secreted factors in ECM regulation under AS conditions remains unknown and needs further assessment.

Stem Cell Derived Exosomes for Treating Aortic Aneurysm

MSC-derived exosomes were evaluated as a therapeutic tool for the mitigation of aortic inflammation and vascular remodeling during AAA formation, as summarized in Table 4. Macrophage derived exosomes are involved in the pathogenesis of AAAs by increasing the MMP-2 expression in VSMC *via* JNK and p38 pathways (146). However, limited studies performed on AAA animal models have demonstrated the pro-regenerative and anti-proteolytic effects of MSC derived exosomes. The therapeutic effects of MSC-exosomes on AAA formation caused by AS were evaluated in an Ang II-infused ApoE^{-/-} mouse model. The MSC exosomes significantly attenuated AAA progression, reduced expression of pro-inflammatory cytokines and induced M2 phenotype in macrophages (110). The study also confirmed the suppression of elastic lamellae destruction in the aortic wall through MSC-exosome intervention. Spinosa et al demonstrated that administration of MSC-EVs (exosomes) in an elastase-treated AAA mouse model caused significant attenuation of aortic diameter, reduced expression of proinflammatory cytokines, and decreased elastic fiber disruption, compared with untreated mice (111). The authors further elucidated the role of miR-147 in mediating inflammatory responses in murine aortic tissues treated with elastase. EVs derived from MSCs transfected with a miR-147 mimic attenuated aortic diameter, inflammation, and leukocyte infiltration in elastase-treated mice. Differently, transfection with an miR-147 inhibitor was ineffective in attenuating AAA progression (111).

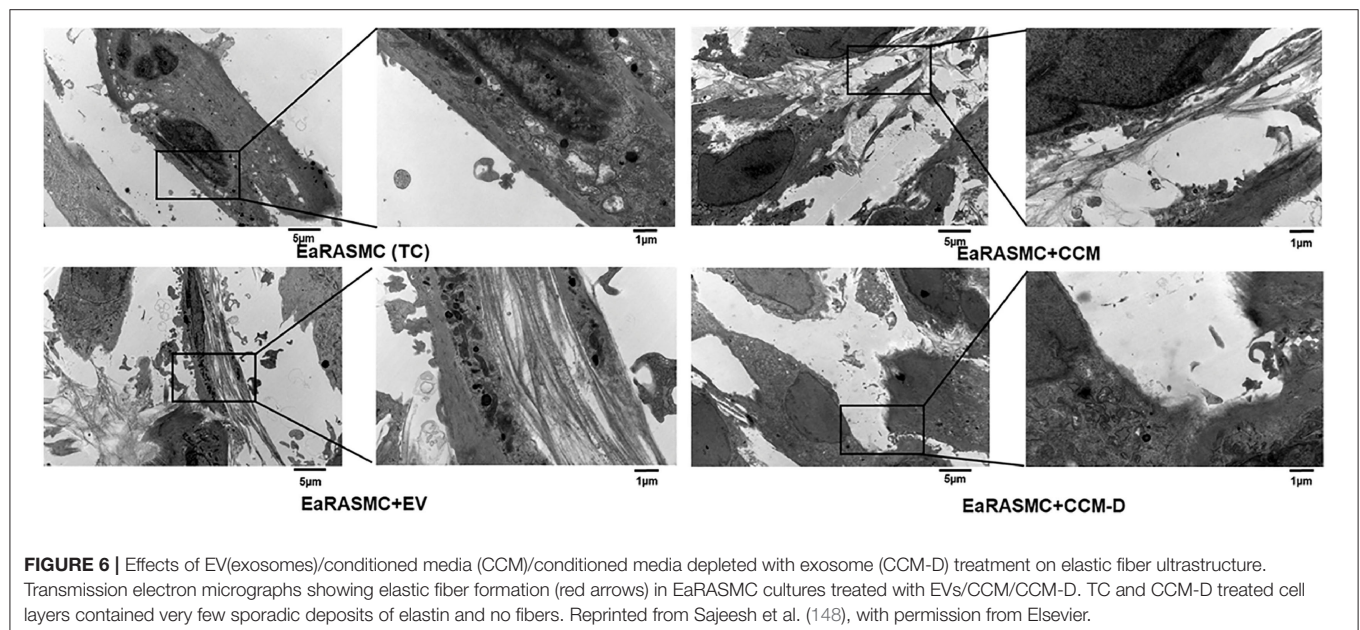
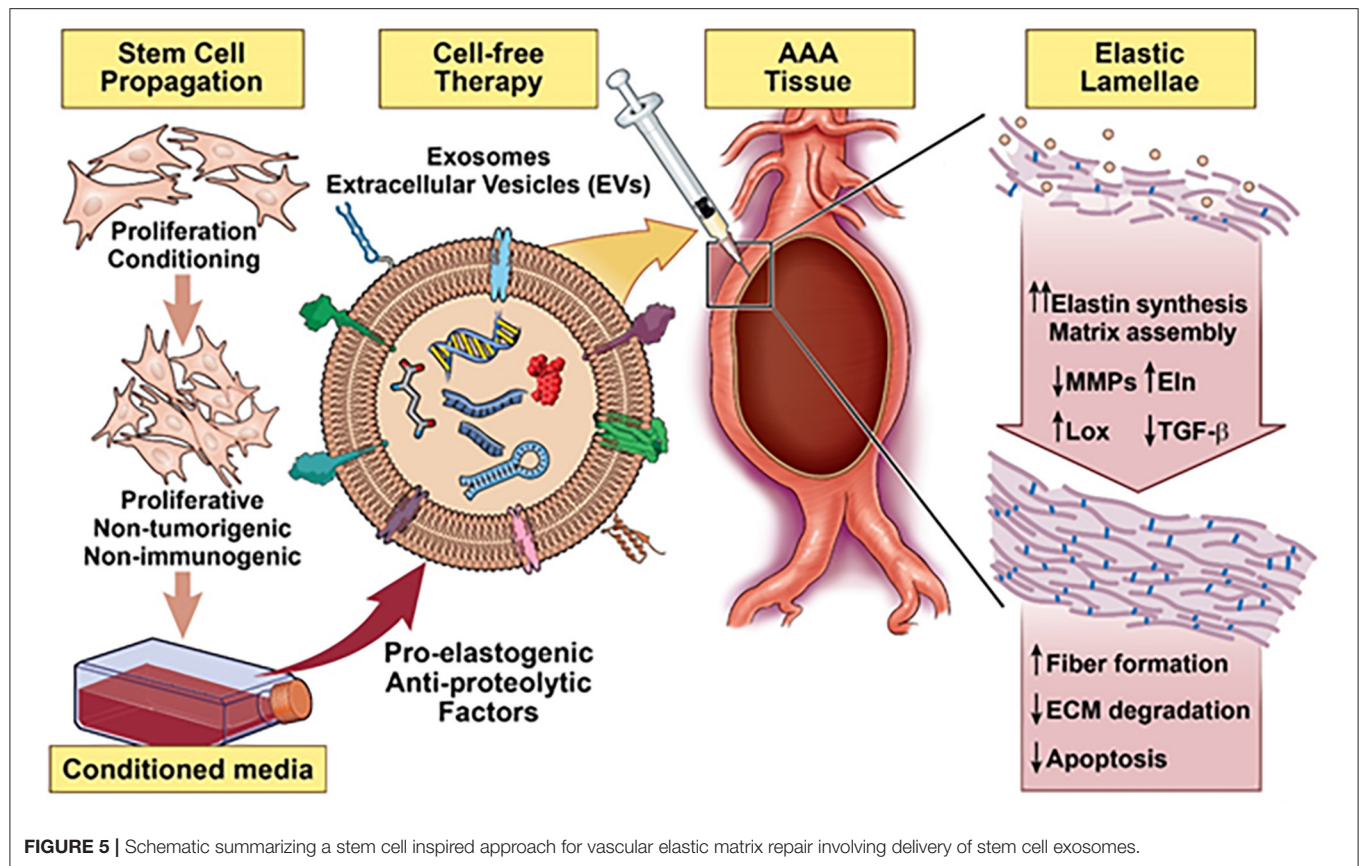
CM derived from BM-MSC cultures were utilized to treat AAA animal models (AngII-induced AAA in ApoE^{-/-} mice). The results from this study suggest that MSC-CM moderates AAA growth by potentially regulating macrophage polarization and through immunomodulation (147). Use of BM-MSC-CM obtained from male mice failed to attenuate AAA growth in elastase-perfused mice, compared to untreated group, whereas female mice derived BM-MSC-CM was effective in reducing aneurysm growth (101). However, this observation needs further validation.

Owing to evidence of the paracrine pro-elastogenic and anti-proteolytic effects of MSC, we explored the regenerative and anti-proteolytic potential of human BM-MSC derived EVs (exosomes) in cytokine-injured cultures of SMCs isolated from the elastase injury induced rat AAAs (148) (Figure 5). Apart from their strong anti-proteolytic effect, the BM-MSC-generated EVs provided effective pro-regenerative cue through the deposition of mature elastic fibers (Figure 6). Additionally, EVs demonstrated superior pro-regenerative and anti-proteolytic effect compared to MSC derived CM and CM depleted with EVs failed to demonstrate any regenerative benefits, in our study. This clearly demonstrates that EVs are necessary component in SC secretions responsible for imparting elastic matrix regenerative and anti-proteolytic properties. Thus, from these limited studies it can be assumed that exosomes recapitulate the therapeutic properties of their parent SCs and may be used as putative surrogate for conventional cell-based therapy.

LIMITATIONS OF USING STEM CELL BASED THERAPY FOR VASCULAR DISORDERS

Despite the significant advances in SC therapy, there are numerous unresolved issues that impede the clinical use of different SCs types including (a) ethical issues concerning use of ESCs, (b) potential tumorigenesis, (c) immune rejection, (d) quality control in sourcing and scale up issues, (e) their uncertain phenotypic state and fate *in vivo*, and (f) challenges to their localized delivery to the site of tissue repair (149). Even with many clinical reports and ongoing clinical trials, the long-term safety and efficacy of SC-based treatments, remain rather vague (150, 151). MSCs are often composed of a heterogeneous mix of different cell population and MSCs from different sources also show variations in their therapeutic efficacy (151, 152). These differences arise largely due to the variation in donors (autologous vs. allogeneic, age, sex, genetics, environmental factors, etc.), different administration routes, dosages, epigenetic reprogramming and senescence followed by culture expansion and cryopreservation (152). Lack of standardized products is a serious impediment for the clinical application of MSCs therapy and limit their therapeutic potential. Systemic administration of MSCs is another major challenge, following reports of MSC entrapment in the microvasculature or lung, usually referred as pulmonary first-pass effect, causing deleterious consequences (153). To overcome these limitations, implementation of good quality control systems is required, and more standardized protocols are mandatory for cell culture and their differentiation, expansion, and cryopreservation.

Efforts should be also made to capitalize the paracrine signaling pathways, as an effort to develop a cell-free approach for regenerative therapeutics. While exosomes promise unparalleled advantages over cell-based therapy (122), their future clinical translation is contingent on overcoming several critical impediments. Lack of standardized method for the collection, isolation, and analysis of exosomes is a significant barrier for the comparability and reproducibility of the results



(154). Their variable composition and presence of large number of bioactive agents might induce undesirable effects (155). Site specific delivery of exosomes remains another major challenge to tackle. I.V. administrated exosomes usually have short half-life

in the body and are quickly cleared by immune cells and specific strategies must be devised to home exosomes to the pathological sites (156). Implementation of a standardized approach is required for isolation, purification and analysis of exosomes, and

precise understanding of their interaction with damaged tissues is required for their potential application.

Another limitation in studying in chronic immunometabolic vascular diseases is the fact that most of these diseases evolve in humans over a period through the involvement of several organs and immune cell type (157). Animal models frequently used to study these diseases are generated in a short time frame and have variations in their metabolism and other inflammatory responses. Most of these vascular diseases are multifactorial in nature and many physiological processes contribute for their progression. Models generated of small laboratory animals (rats, mice etc.) might provide some valuable insights (158, 159), however these models have certain limitations in assessing the exact immunomodulatory responses imparted by SC therapy and their long-term implications. Additionally, most of these studies have not evaluated the impact of SC treatment in ameliorating pathological ECM changes associated with vascular disorders, which is critical toward the re-instatement normal vascular hemostasis. Future studies should aim to identify and establish new triggers and mechanisms involvement in vascular disease development and be more adaptive for evaluating novel treatment approach that accelerate translational cardiovascular research.

SUMMARY AND FUTURE OUTLOOK

Changes in the vascular ECM microenvironment is pervasive across a wide spectrum of vascular disorders. In many instances, these changes have been shown to drive the progressive pathophysiology of these disorders through signaling feedback. Our comprehensive understanding of the dynamic interplay between altered ECM state and dysregulation of vascular cell signaling provides new insight that might guide toward development of new treatment approaches to either prevent or to actively regress these vascular pathophysiology.

REFERENCES

- Halper J. Basic components of vascular connective tissue and extracellular matrix. *Adv Pharmacol.* (2018) 81:95–127. doi: 10.1016/bs.apha.2017.08.012
- Theocharis AD, Skandalis SS, Gialeli C, Karamanos NK. Extracellular matrix structure. *Adv Drug Deliv Rev.* (2016) 97:4–27. doi: 10.1016/j.addr.2015.11.001
- Karamanos NK, Theocharis AD, Piperigkou Z, Manou D, Passi A, Skandalis SS, et al. A guide to the composition and functions of the extracellular matrix. *FEBS J.* (2021) 288:6850–912. doi: 10.1111/febs.15776
- Bonnans C, Chou J, Werb Z. Remodelling the extracellular matrix in development and disease. *Nat Rev Mol Cell Biol.* (2014) 15:786–801. doi: 10.1038/nrm3904
- Barallobre-Barreiro J, Loeys B, Mayr M, Rienks M, Verstraeten A, Kovacic JC. Extracellular matrix in vascular disease, Part 2/4: JACC Focus Seminar. *J Am Coll Cardiol.* (2020) 75:2189–203. doi: 10.1016/j.jacc.2020.03.018
- Jacob MP, Badier-Commander C, Fontaine V, Benazzoug Y, Feldman L, Michel JB. Extracellular matrix remodeling in the vascular wall. *Pathol Biol.* (2001) 49:326–32. doi: 10.1016/S0369-8114(01)00151-1
- Frangogiannis NG. The extracellular matrix in myocardial injury, repair, and remodeling. *J Clin Invest.* (2017) 127:1600–12. doi: 10.1172/JCI87491
- Shao Y, Li G, Huang S, Li Z, Qiao B, Chen D, et al. Effects of extracellular matrix softening on vascular smooth muscle cell dysfunction.

Recent advancement in SC technologies have brought MSCs to progress closer to clinical applications for disease therapy and tissue reconstruction, even though challenges might seem daunting. The immunomodulatory effect of SCs at vascular injury sites, followed by ECM regenerative effect induced *via* secretion of growth factors have demonstrated efficacy not only in prevention of diseases but also in the regression of damaged vascular tissues. This synergistic immunoregulatory effect combined with matrix regenerative abilities of SC-based and inspired products may help in developing novel therapeutic strategies for preventing and treating vascular disorders. The clinical translation of these therapeutic strategies is however conditional on progress in addressing key challenges associated with the clinical translation of SC technology.

AUTHOR CONTRIBUTIONS

SS and AR conceptualized and wrote the manuscript. SDah, SDay, SB, and JY helped in the collection of literature and critically discussed the content. All authors reviewed the manuscript before submission and have read and agreed to the publication of the manuscript.

FUNDING

The AR lab has been funded by the following agencies in the USA for the following projects: National Institutes of Health (NHLBI), HL 139662-01. Title: Matrix Regenerative Nanotherapeutics for Abdominal Aortic Aneurysm Repair. National Science Foundation, CBET 1926939, Collaborative Research: Design and development of a multifunctional nanoplatform for augmented elastic matrix repair. American Heart Association, 19TPA34890029, Matrix regenerative siRNA nanotherapeutics for small aneurysm repair. Discretionary funds from Lehigh University usable to cover publishing costs.

Cardiovasc Toxicol. (2020) 20:548–56. doi: 10.1007/s12012-020-09580-8

- Shi J, Yang Y, Cheng A, Xu G, He F. Metabolism of vascular smooth muscle cells in vascular diseases. *Am J Physiol Heart Circ Physiol.* (2020) 319:H613–H31. doi: 10.1152/ajpheart.00220.2020
- Bashur CA, Venkataraman L, Ramamurthi A. Tissue engineering and regenerative strategies to replicate biocomplexity of vascular elastic matrix assembly. *Tissue Eng Part B Rev.* (2012) 18:203–17. doi: 10.1089/ten.teb.2011.0521
- Sivaraman B, Bashur CA, Ramamurthi A. Advances in biomimetic regeneration of elastic matrix structures. *Drug Deliv Transl Res.* (2012) 2:323–50. doi: 10.1007/s13346-012-0070-6
- Michel JB, Li Z, Lacolley P. Smooth muscle cells and vascular diseases. *Cardiovasc Res.* (2012) 95:135–7. doi: 10.1093/cvr/cvs172
- Tennant M, McGeachie JK. Blood vessel structure and function: a brief update on recent advances. *Aust N Z J Surg.* (1990) 60:747–53. doi: 10.1111/j.1445-2197.1990.tb07468.x
- Wang Z, Zhang W, Xie C, Wen F, Ma C, Lin N, et al. Geometric anisotropy on biomaterials surface for vascular scaffold design: engineering and biological advances. *J Phys Mat.* (2019) 2:032003. doi: 10.1088/2515-7639/ab1c68
- Mithieux SM, Weiss AS. Elastin. *Adv Protein Chem.* (2005) 70:437–61. doi: 10.1016/S0065-3233(05)70013-9

16. Ramirez F. Pathophysiology of the microfibril/elastic fiber system: introduction. *Matrix Biol.* (2000) 19:455–6. doi: 10.1016/S0945-053X(00)00098-6
17. Rosenbloom J. Elastin: an overview. *Methods Enzymol.* (1987) 144:172–96. doi: 10.1016/0076-6879(87)44178-5
18. Mecham RP. Elastin synthesis and fiber assembly. *Ann N Y Acad Sci.* (1991) 624:137–46. doi: 10.1111/j.1749-6632.1991.tb17013.x
19. Wise SG, Weiss AS. Tropoelastin. *Int J Biochem Cell Biol.* (2009) 41:494–7. doi: 10.1016/j.biocel.2008.03.017
20. Wise SG, Yeo GC, Hiob MA, Rnjak-Kovacina J, Kaplan DL, Ng MK, et al. Tropoelastin: a versatile, bioactive assembly module. *Acta Biomater.* (2014) 10:1532–41. doi: 10.1016/j.actbio.2013.08.003
21. Yeo GC, Keeley FW, Weiss AS. Coacervation of tropoelastin. *Adv Colloid Interface Sci.* (2011) 167:94–103. doi: 10.1016/j.cis.2010.10.003
22. Fawzi NL. Elastin phase separation - structure or disorder? *Nat Rev Mol Cell Biol.* (2020) 21:568–9. doi: 10.1038/s41580-020-00291-0
23. Muiznieks LD, Weiss AS, Keeley FW. Structural disorder and dynamics of elastin. *Biochem Cell Biol.* (2010) 88:239–50. doi: 10.1139/O09-161
24. Randell A, Daneshmand N. Elastin microfibril interface-located protein 1, transforming growth factor beta, and implications on cardiovascular complications. *J Am Soc Hypertens.* (2017) 11:437–48. doi: 10.1016/j.jash.2017.04.010
25. Cocciolone AJ, Hawes JZ, Staiculescu MC, Johnson EO, Murshed M, Wagenseil JE. Elastin, arterial mechanics, and cardiovascular disease. *Am J Physiol Heart Circ Physiol.* (2018) 315:H189–205. doi: 10.1152/ajpheart.00087.2018
26. Davis-Dusenbery BN, Wu C, Hata A. Micromanaging vascular smooth muscle cell differentiation and phenotypic modulation. *Arterioscler Thromb Vasc Biol.* (2011) 31:2370–7. doi: 10.1161/ATVBAHA.111.226670
27. Nagase H, Visse R, Murphy G. Structure and function of matrix metalloproteinases and TIMPs. *Cardiovasc Res.* (2006) 69:562–73. doi: 10.1016/j.cardiores.2005.12.002
28. Duca L, Blaise S, Romier B, Laffargue M, Gayral S, El Btaoui H, et al. Matrix ageing and vascular impacts: focus on elastin fragmentation. *Cardiovasc Res.* (2016) 110:298–308. doi: 10.1093/cvr/cvw061
29. Kolárná L, Bakesová J, Varga F, Kostáková E, Plánka L, Necas A, et al. Biochemical and biophysical aspects of collagen nanostructure in the extracellular matrix. *Physiol Res.* (2007) 56 Suppl 1:S51–s60. doi: 10.33549/physiolres.931302
30. Shoulders MD, Raines RT. Collagen structure and stability. *Annu Rev Biochem.* (2009) 78:929–58. doi: 10.1146/annurev.biochem.77.032207.120833
31. Mienaltowski MJ, Gonzales NL, Beall JM, Pechanec MY. Basic structure, physiology, and biochemistry of connective tissues and extracellular matrix collagens. *Adv Exp Med Biol.* (2021) 1348:5–43. doi: 10.1007/978-3-030-80614-9_2
32. Vallet SD, Ricard-Blum S. Lysyl oxidases: from enzyme activity to extracellular matrix cross-links. *Essays Biochem.* (2019) 63:349–64. doi: 10.1042/EBC20180050
33. Rodriguez-Feo J, Sluijter J, de Kleijn D, Pasterkamp G. Modulation of collagen turnover in cardiovascular disease. *Curr Pharm Des.* (2005) 11:2501–14. doi: 10.2174/1381612054367544
34. Kjellén L, Lindahl U. Proteoglycans: structures and interactions. *Annu Rev Biochem.* (1991) 60:443–75. doi: 10.1146/annurev.bi.60.070191.002303
35. Wight TN. A role for proteoglycans in vascular disease. *Matrix Biol.* (2018) 71:2:396–420. doi: 10.1016/j.matbio.2018.02.019
36. Viola M, Karousou E, D'Angelo ML, Moretto P, Caon I, Luca G, et al. Extracellular matrix in atherosclerosis: hyaluronan and proteoglycans insights. *Curr Med Chem.* (2016) 23:2958–71. doi: 10.2174/0929867323666160607104602
37. Ziemann SJ, Melenovsky V, Kass DA. Mechanisms, pathophysiology, and therapy of arterial stiffness. *Arterioscler Thromb Vasc Biol.* (2005) 25:932–43. doi: 10.1161/01.ATV.0000160548.78317.29
38. Ishikawa J, Kario K, Matsui Y, Shibasaki S, Morinari M, Kaneda R, et al. Collagen metabolism in extracellular matrix may be involved in arterial stiffness in older hypertensive patients with left ventricular hypertrophy. *Hypertens Res.* (2005) 28:995–1001. doi: 10.1291/hypres.28.995
39. Milan A, Tosello F, Fabbri A, Vairo A, Leone D, Chiarlo M, et al. Arterial stiffness: from physiology to clinical implications. *High Blood Press Cardiovasc Prev.* (2011) 18:1–12. doi: 10.2165/11588020-000000000-00000
40. Kaess BM, Rong J, Larson MG, Hamburg NM, Vita JA, Levy D, et al. Aortic stiffness, blood pressure progression, and incident hypertension. *J Am Med Assoc.* (2012) 308:875–81. doi: 10.1001/2012.jama.10503
41. Miyauchi S, Nagai M, Dote K, Kato M, Oda N, Kunita E, et al. Visit-to-visit blood pressure variability and arterial stiffness: which came first: the chicken or the egg? *Curr Pharm Des.* (2019) 25:685–2. doi: 10.2174/1381612825666190329122024
42. Herrington W, Lacey B, Sherliker P, Armitage J, Lewington S. Epidemiology of atherosclerosis and the potential to reduce the global burden of atherothrombotic disease. *Circ Res.* (2016) 118:535–46. doi: 10.1161/CIRCRESAHA.115.307611
43. Falk E. Pathogenesis of atherosclerosis. *J Am Coll Cardiol.* (2006) 47(8Suppl.):C7–12. doi: 10.1016/j.jacc.2005.09.068
44. Wu MY, Li CJ, Hou MF, Chu PY. New insights into the role of inflammation in the pathogenesis of atherosclerosis. *Int J Mol Sci.* (2017) 18:2034. doi: 10.3390/ijms18102034
45. Wolf D, Ley K. Immunity and inflammation in atherosclerosis. *Circ Res.* (2019) 124:315–27. doi: 10.1161/CIRCRESAHA.118.313591
46. Katsuda S, Kaji T. Atherosclerosis and extracellular matrix. *J Atheroscler Thromb.* (2003) 10:267–74. doi: 10.5551/jat.10.267
47. Williams KJ, Tabas I. The response-to-retention hypothesis of early atherogenesis. *Arterioscler Thromb Vasc Biol.* (1995) 15:551–61. doi: 10.1161/01.ATV.15.5.551
48. Lu H, Daugherty A. Aortic Aneurysms. *Arterioscler Thromb Vasc Biol.* (2017) 37:e59–65. doi: 10.1161/ATVBAHA.117.309578
49. Hellawell HN, Mostafa A, Kyriacou H, Sumal AS, Boyle JR. Abdominal aortic aneurysms part one: epidemiology, presentation and preoperative considerations. *J Perioper Pract.* (2021) 31:274–80. doi: 10.1177/1750458920954014
50. Kuivaniemi H, Ryer EJ, Elmore JR, Tromp G. Understanding the pathogenesis of abdominal aortic aneurysms. *Expert Rev Cardiovasc Ther.* (2015) 13:975–87. doi: 10.1586/14779072.2015.1074861
51. Nordon IM, Hinchliffe RJ, Loftus IM, Thompson MM. Pathophysiology and epidemiology of abdominal aortic aneurysms. *Nat Rev Cardiol.* (2011) 8:92–102. doi: 10.1038/nrcardio.2010.180
52. Quintana RA, Taylor WR. Cellular mechanisms of aortic aneurysm formation. *Circ Res.* (2019) 124:607–18. doi: 10.1161/CIRCRESAHA.118.313187
53. Patelis N, Moris D, Schizas D, Damaskos C, Perrea D, Bakoyiannis C, et al. Animal models in the research of abdominal aortic aneurysms development. *Physiol Res.* (2017) 66:899–915. doi: 10.33549/physiolres.933579
54. Cai D, Sun C, Zhang G, Que X, Fujise K, Weintraub NL, et al. A novel mechanism underlying inflammatory smooth muscle phenotype in abdominal aortic aneurysm. *Circ Res.* (2021) 129:e202–e14. doi: 10.1161/CIRCRESAHA.121.319374
55. Lu H, Du W, Ren L, Hamblin MH, Becker RC, Chen YE, et al. Vascular smooth muscle cells in aortic aneurysm: from genetics to mechanisms. *J Am Heart Assoc.* (2021) 10:e023601. doi: 10.1161/JAHA.121.023601
56. Petsophonsakul P, Furmanik M, Forsythe R, Dweck M, Schurink GW, Natour E, et al. Role of vascular smooth muscle cell phenotypic switching and calcification in aortic aneurysm formation. *Arterioscler Thromb Vasc Biol.* (2019) 39:1351–68. doi: 10.1161/ATVBAHA.119.312787
57. Rombouts KB, van Merriënboer TAR, Ket JCF, Bogunovic N, van der Velden J, Yeung KK. The role of vascular smooth muscle cells in the development of aortic aneurysms and dissections. *Eur J Clin Invest.* (2021) 2021:e13697. doi: 10.1111/eci.13697
58. Menashi S, Campa JS, Greenhalgh RM, Powell JT. Collagen in abdominal aortic aneurysm: typing, content, and degradation. *J Vasc Surg.* (1987) 6:578–82. doi: 10.1016/0741-5214(87)90274-6
59. Klein DG. Thoracic aortic aneurysms. *J Cardiovasc Nurs.* (2005) 20:245–50. doi: 10.1097/00005082-200507000-00008
60. Asano K, Cantalupo A, Sedes L, Ramirez F. Pathophysiology and therapeutics of thoracic aortic aneurysm in Marfan syndrome. *Biomolecules.* (2022) 12:128. doi: 10.3390/biom12010128

61. van Dorst DCH, de Wagenaar NP, van der Pluijm I, Roos-Hesselink JW, Essers J, Danser AHJ. Transforming growth factor- β and the renin-angiotensin system in syndromic thoracic aortic aneurysms: implications for treatment. *Cardiovasc Drugs Ther.* (2021) 35:1233–52. doi: 10.1007/s10557-020-07116-4
62. Verstraeten A, Alaerts M, Van Laer L, Loeys B. Marfan syndrome and related disorders: 25 years of gene discovery. *Hum Mutat.* (2016) 37:524–31. doi: 10.1002/humu.22977
63. Dietz HC, Loeys B, Carta L, Ramirez F. Recent progress towards a molecular understanding of Marfan syndrome. *Am J Med Genet C Semin Med Genet.* (2005) 139c:4–9. doi: 10.1002/ajmg.c.30068
64. Iqbal R, Alom S, BinSaeid J, Harky A. Loeys-Dietz syndrome pathology and aspects of cardiovascular management: a systematic review. *Vascular.* (2021) 29:3–14. doi: 10.1177/1708538120934582
65. Kenagy RD, Plaas AH, Wight TN. Versican degradation and vascular disease. *Trends Cardiovasc Med.* (2006) 16:209–15. doi: 10.1016/j.tcm.2006.03.011
66. Merrilees MJ, Kang I, Hinek A, Wight TN. *Regulating Elastogenesis Using Proteoglycans. Elastic Fiber Matrices.* Boca Raton, FL: CRC Press (2018). p. 271–300. doi: 10.1201/9781315370842-13
67. Wight TN, Merrilees MJ. Proteoglycans in atherosclerosis and restenosis: key roles for versican. *Circ Res.* (2004) 94:1158–67. doi: 10.1161/01.RES.0000126921.29919.51
68. Watanabe N, Ikeda U. Matrix metalloproteinases and atherosclerosis. *Curr Atheroscler Rep.* (2004) 6:112–20. doi: 10.1007/s11883-004-0099-1
69. Newby AC. Metalloproteinases and vulnerable atherosclerotic plaques. *Trends Cardiovasc Med.* (2007) 17:253–8. doi: 10.1016/j.tcm.2007.09.001
70. Moreno PR. Pathophysiology of plaque disruption and thrombosis in acute ischemic syndromes. *J Stroke Cerebrovasc Dis.* (2001) 10:2–9. doi: 10.1053/jscd.2001.24785
71. Shah PK, Falk E, Badimon JJ, Fernandez-Ortiz A, Mailhac A, Villareal-Levy G, et al. Human monocyte-derived macrophages induce collagen breakdown in fibrous caps of atherosclerotic plaques. Potential role of matrix-degrading metalloproteinases and implications for plaque rupture. *Circulation.* (1995) 92:1565–9.
72. Mimler T, Nebert C, Eichmair E, Winter B, Aschacher T, Stelzmueller ME, et al. Extracellular matrix in ascending aortic aneurysms and dissections - what we learn from decellularization and scanning electron microscopy. *PLoS ONE.* (2019) 14:e0213794. doi: 10.1371/journal.pone.0213794
73. Kolios G, Moodley Y. Introduction to stem cells and regenerative medicine. *Respiration.* (2013) 85:3–10. doi: 10.1159/000345615
74. Laplane L, Solary E. Towards a classification of stem cells. *Elife.* (2019) 8:e46563. doi: 10.7554/eLife.46563
75. Dulak J, Szade K, Szade A, Nowak W, Józkowicz A. Adult stem cells: hopes and hypes of regenerative medicine. *Acta Biochim Pol.* (2015) 62:329–37. doi: 10.18388/abp.2015_1023
76. Pittenger MF, Discher DE, Péault BM, Phinney DG, Hare JM, Caplan AI. Mesenchymal stem cell perspective: cell biology to clinical progress. *NPJ Regen Med.* (2019) 4:22. doi: 10.1038/s41536-019-0083-6
77. Guo Y, Yu Y, Hu S, Chen Y, Shen Z. The therapeutic potential of mesenchymal stem cells for cardiovascular diseases. *Cell Death Dis.* (2020) 11:349. doi: 10.1038/s41419-020-2542-9
78. Shi Y, Inoue H, Wu JC, Yamanaka S. Induced pluripotent stem cell technology: a decade of progress. *Nat Rev Drug Discov.* (2017) 16:115–30. doi: 10.1038/nrd.2016.245
79. Lin Y, Zhu W, Chen X. The involving progress of MSCs based therapy in atherosclerosis. *Stem Cell Res Ther.* (2020) 11:216. doi: 10.1186/s13287-020-01728-1
80. Mahdavi Gorabi A, Banach M, Reiner Z, Pirro M, Hajighasemi S, Johnston TP, et al. The role of mesenchymal stem cells in atherosclerosis: prospects for therapy via the modulation of inflammatory milieu. *J Clin Med.* (2019) 8:1413. doi: 10.3390/jcm8091413
81. Kirwin T, Gomes A, Amin R, Sufi A, Goswami S, Wang B. Mechanisms underlying the therapeutic potential of mesenchymal stem cells in atherosclerosis. *Regen Med.* (2021) 16:669–82. doi: 10.2217/rme-2021-0024
82. Frodermann V, van Duijn J, van Pel M, van Santbrink PJ, Bot I, Kuiper J, et al. Mesenchymal stem cells reduce murine atherosclerosis development. *Sci Rep.* (2015) 5:15559. doi: 10.1038/srep15559
83. Li Q, Sun W, Wang X, Zhang K, Xi W, Gao P. Skin-derived mesenchymal stem cells alleviate atherosclerosis via modulating macrophage function. *Stem Cells Transl Med.* (2015) 4:1294–301. doi: 10.5966/sctm.2015-0020
84. Li F, Guo X, Chen SY. Function and therapeutic potential of mesenchymal stem cells in atherosclerosis. *Front Cardiovasc Med.* (2017) 4:32. doi: 10.3389/fcvm.2017.00032
85. Wang ZX, Wang CQ, Li XY, Feng GK, Zhu HL, Ding Y, et al. Mesenchymal stem cells alleviate atherosclerosis by elevating number and function of CD4(+)CD25(+)FOXP3(+) regulatory T-cells and inhibiting macrophage foam cell formation. *Mol Cell Biochem.* (2015) 400:163–72. doi: 10.1007/s11010-014-2272-3
86. Wang SS, Hu SW, Zhang QH, Xia AX, Jiang ZX, Chen XM. Mesenchymal stem cells stabilize atherosclerotic vulnerable plaque by anti-inflammatory properties. *PLoS ONE.* (2015) 10:e0136026. doi: 10.1371/journal.pone.0136026
87. Takafuji Y, Hori M, Mizuno T, Harada-Shiba M. Humoral factors secreted from adipose tissue-derived mesenchymal stem cells ameliorate atherosclerosis in Ldlr^{-/-} mice. *Cardiovasc Res.* (2019) 115:1041–51. doi: 10.1093/cvr/cvy271
88. Li Y, Shi G, Han Y, Shang H, Li H, Liang W, et al. Therapeutic potential of human umbilical cord mesenchymal stem cells on aortic atherosclerotic plaque in a high-fat diet rabbit model. *Stem Cell Res Ther.* (2021) 12:407. doi: 10.1186/s13287-021-02490-8
89. Davignon J, Ganz P. Role of endothelial dysfunction in atherosclerosis. *Circulation.* (2004) 109(23Suppl.1): III27–32. doi: 10.1161/01.CIR.0000131515.03336.f8
90. Lin YL, Yet SF, Hsu YT, Wang GJ, Hung SC. Mesenchymal stem cells ameliorate atherosclerotic lesions via restoring endothelial function. *Stem Cells Transl Med.* (2015) 4:44–55. doi: 10.5966/sctm.2014-0091
91. Clémot M, Sênos Demarco R, Jones DL. Lipid mediated regulation of adult stem cell behavior. *Front Cell Dev Biol.* (2020) 8:115. doi: 10.3389/fcell.2020.00115
92. Wang J-L, Ding H-r, Pan C-y, Shi X-l, Ren H-z. Mesenchymal stem cells ameliorate lipid metabolism through reducing mitochondrial damage of hepatocytes in the treatment of post-hepatectomy liver failure. *Cell Death Dis.* (2021) 12:111. doi: 10.1038/s41419-020-03374-0
93. Knight BL, Hebbachi A, Houton D, Brown AM, Wiggins D, Patel DD, et al. A role for PPARalpha in the control of SREBP activity and lipid synthesis in the liver. *Biochem J.* (2005) 389:413–21. doi: 10.1042/BJ20041896
94. Harman JL, Jørgensen HF. The role of smooth muscle cells in plaque stability: therapeutic targeting potential. *Br J Pharmacol.* (2019) 176:3741–53. doi: 10.1111/bph.14779
95. Huang NF, Li S. Mesenchymal stem cells for vascular regeneration. *Regen Med.* (2008) 3:877–92. doi: 10.2217/17460751.3.6.877
96. Hashizume R, Yamawaki-Ogata A, Ueda Y, Wagner WR, Narita Y. Mesenchymal stem cells attenuate angiotensin II-induced aortic aneurysm growth in apolipoprotein E-deficient mice. *J Vasc Surg.* (2011) 54:1743–52. doi: 10.1016/j.jvs.2011.06.109
97. Fu XM, Yamawaki-Ogata A, Oshima H, Ueda Y, Usui A, Narita Y. Intravenous administration of mesenchymal stem cells prevents angiotensin II-induced aortic aneurysm formation in apolipoprotein E-deficient mouse. *J Transl Med.* (2013) 11:175. doi: 10.1186/1479-5876-11-175
98. Blose KJ, Ennis TL, Arif B, Weinbaum JS, Curci JA, Vorp DA. Periadventitial adipose-derived stem cell treatment halts elastase-induced abdominal aortic aneurysm progression. *Regen Med.* (2014) 9:733–41. doi: 10.2217/rme.14.61
99. Zidi M, Allaire E. Mechanical behavior of abdominal aorta aneurysm in rat model treated by cell therapy using mesenchymal stem cells. *Biomech Model Mechanobiol.* (2015) 14:185–94. doi: 10.1007/s10237-014-0586-4
100. Wen H, Wang M, Gong S, Li X, Meng J, Wen J, et al. Human umbilical cord mesenchymal stem cells attenuate abdominal aortic aneurysm progression in sprague-dawley rats: implication of vascular smooth muscle cell phenotypic modulation. *Stem Cells Dev.* (2020) 29:981–93. doi: 10.1089/scd.2020.0058
101. Davis JP, Salmon M, Pope NH, Lu G, Su G, Sharma AK, et al. Attenuation of aortic aneurysms with stem cells from different genders. *J Surg Res.* (2015) 199:249–58. doi: 10.1016/j.jss.2015.04.025
102. Dahal S, Dayal S, Androina C, Peterson J, Ramamurthi A. Adult mesenchymal stem cells and derivatives in improved elastin homeostasis

- in a rat model of Abdominal Aortic Aneurysms (AAAs). *Stem Cells Transl Med.* (2022).
103. Tian X, Fan J, Yu M, Zhao Y, Fang Y, Bai S, et al. Adipose stem cells promote smooth muscle cells to secrete elastin in rat abdominal aortic aneurysm. *PLoS ONE.* (2014) 9:e108105. doi: 10.1371/journal.pone.0108105
 104. Xie J, Jones TJ, Feng D, Cook TG, Jester AA, Yi R, et al. Human adipose-derived stem cells suppress elastase-induced murine abdominal aortic inflammation and aneurysm expansion through paracrine factors. *Cell Transplant.* (2017) 26:173–89. doi: 10.3727/096368916X692212
 105. Yamawaki-Ogata A, Oshima H, Usui A, Narita Y. Bone marrow-derived mesenchymal stromal cells regress aortic aneurysm via the NF- κ B, Smad3 and Akt signaling pathways. *Cytotherapy.* (2017) 19:1167–75. doi: 10.1016/j.jcyt.2017.07.010
 106. Gacchina CE, Deb P, Barth JL, Ramamurthi A. Elastogenic inductibility of smooth muscle cells from a rat model of late-stage abdominal aortic aneurysms. *Tissue Eng Part A.* (2011) 17:1699–711. doi: 10.1089/ten.tea.2010.0526
 107. Li J, Xue H, Li T, Chu X, Xin D, Xiong Y, et al. Exosomes derived from mesenchymal stem cells attenuate the progression of atherosclerosis in ApoE(-/-) mice via miR-let7 mediated infiltration and polarization of M2 macrophage. *Biochem Biophys Res Commun.* (2019) 510:565–72. doi: 10.1016/j.bbrc.2019.02.005
 108. Ma J, Chen L, Zhu X, Li Q, Hu L, Li H. Mesenchymal stem cell-derived exosomal miR-21a-5p promotes M2 macrophage polarization and reduces macrophage infiltration to attenuate atherosclerosis. *Acta Biochim Biophys Sin (Shanghai).* (2021) 53:1227–36. doi: 10.1093/abbs/gmab102
 109. Yang W, Yin R, Zhu X, Yang S, Wang J, Zhou Z, et al. Mesenchymal stem-cell-derived exosomal miR-145 inhibits atherosclerosis by targeting JAM-A. *Mol Ther Nucleic Acids.* (2021) 23:119–31. doi: 10.1016/j.omtn.2020.10.037
 110. Kozakai M, Narita Y, Yamawaki-Ogata A, Fujimoto KL, Mutsuga M, Tokuda Y, et al. Alternative therapeutic strategy for existing aortic aneurysms using mesenchymal stem cell-derived exosomes. *Expert Opin Biol Ther.* (2022) 22:95–104. doi: 10.1080/14712598.2022.2005575
 111. Spinosa M, Lu G, Su G, Bontha SV, Gehrau R, Salmon MD, et al. Human mesenchymal stromal cell-derived extracellular vesicles attenuate aortic aneurysm formation and macrophage activation via microRNA-147. *FASEB J.* (2018) 32:6038–50. doi: 10.1096/fj.201701138RR
 112. Akita N, Narita Y, Yamawaki-Ogata A, Usui A, Komori K. Therapeutic effect of allogeneic bone marrow-derived mesenchymal stromal cells on aortic aneurysms. *Cell Tissue Res.* (2021) 383:781–93. doi: 10.1007/s00441-020-03295-6
 113. Phie J, Thanigaimani S, Golledge J. Systematic review and meta-analysis of interventions to slow progression of abdominal aortic aneurysm in mouse models. *Arterioscler Thromb Vasc Biol.* (2021) 41:1504–17. doi: 10.1161/ATVBAHA.121.315942
 114. Gacchina CE, Ramamurthi A. Impact of pre-existing elastic matrix on TGF β 1 and HA oligomer-induced regenerative elastin repair by rat aortic smooth muscle cells. *J Tissue Eng Regen Med.* (2011) 5:85–96. doi: 10.1002/term.286
 115. Swaminathan G, Gadepalli VS, Stoilov I, Mecham RP, Rao RR, Ramamurthi A. Pro-elastogenic effects of bone marrow mesenchymal stem cell-derived smooth muscle cells on cultured aneurysmal smooth muscle cells. *J Tissue Eng Regen Med.* (2017) 11:679–93. doi: 10.1002/term.1964
 116. Swaminathan G, Stoilov I, Broekelmann T, Mecham R, Ramamurthi A. Phenotype-based selection of bone marrow mesenchymal stem cell-derived smooth muscle cells for elastic matrix regenerative repair in abdominal aortic aneurysms. *J Tissue Eng Regen Med.* (2018) 12:e60–70. doi: 10.1002/term.2349
 117. Dahal S, Broekelman T, Mecham RP, Ramamurthi A. Maintaining elastogenicity of mesenchymal stem cell-derived smooth muscle cells in two-dimensional culture. *Tissue Eng A.* (2018) 24:979–89. doi: 10.1089/ten.tea.2017.0237
 118. Dahal S, Swaminathan G, Carney S, Broekelmann T, Mecham R, Ramamurthi A. Pro-elastogenic effects of mesenchymal stem cell derived smooth muscle cells in a 3D collagenous milieu. *Acta Biomater.* (2020) 105:180–90. doi: 10.1016/j.actbio.2020.01.030
 119. Swaminathan G, Sivaraman B, Moore L, Zborowski M, Ramamurthi A. Magnetically responsive bone marrow mesenchymal stem cell-derived smooth muscle cells maintain their benefits to augmenting elastic matrix neoassembly. *Tissue Eng Part C Methods.* (2016) 22:301–11. doi: 10.1089/ten.tec.2015.0349
 120. Shen YH, Hu X, Zou S, Wu D, Coselli JS, LeMaire SA. Stem cells in thoracic aortic aneurysms and dissections: potential contributors to aortic repair. *Ann Thorac Surg.* (2012) 93:1524–33. doi: 10.1016/j.athoracsur.2012.01.063
 121. Hawkins RB, Salmon M, Su G, Lu G, Leroy V, Bontha SV, et al. Mesenchymal stem cells alter microRNA expression and attenuate thoracic aortic aneurysm formation. *J Surg Res.* (2021) 268:221–31. doi: 10.1016/j.jss.2021.06.057
 122. Phinney DG, Pittenger MF. Concise review: MSC-derived exosomes for cell-free therapy. *Stem Cells.* (2017) 35:851–58. doi: 10.1002/stem.2575
 123. Barreca MM, Cancemi P, Geraci F. Mesenchymal and induced pluripotent stem cells-derived extracellular vesicles: the new frontier for regenerative medicine? *Cells.* (2020) 9:1163. doi: 10.3390/cells9051163
 124. Hade MD, Suire CN, Suo Z. Mesenchymal stem cell-derived exosomes: applications in regenerative medicine. *Cells.* (2021) 10:1959. doi: 10.3390/cells10081959
 125. Gurunathan S, Kang MH, Kim JH. A comprehensive review on factors influences biogenesis, functions, therapeutic and clinical implications of exosomes. *Int J Nanomedicine.* (2021) 16:1281–312. doi: 10.2147/IJN.S291956
 126. Pawitan JA. Prospect of stem cell conditioned medium in regenerative medicine. *Biomed Res Int.* (2014) 2014:965849. doi: 10.1155/2014/965849
 127. Maqsood M, Kang M, Wu X, Chen J, Teng L, Qiu L. Adult mesenchymal stem cells and their exosomes: sources, characteristics, and application in regenerative medicine. *Life Sci.* (2020) 256:118002. doi: 10.1016/j.lfs.2020.118002
 128. Lai RC, Chen TS, Lim SK. Mesenchymal stem cell exosome: a novel stem cell-based therapy for cardiovascular disease. *Regen Med.* (2011) 6:481–92. doi: 10.2217/rme.11.35
 129. Elahi FM, Farwell DG, Nolte JA, Anderson JD. Preclinical translation of exosomes derived from mesenchymal stem/stromal cells. *Stem Cells.* (2020) 38:15–21. doi: 10.1002/stem.3061
 130. Ma ZJ, Yang JJ, Lu YB, Liu ZY, Wang XX. Mesenchymal stem cell-derived exosomes: toward cell-free therapeutic strategies in regenerative medicine. *World J Stem Cells.* (2020) 12:814–40. doi: 10.4252/wjsc.v12.i8.814
 131. Babaei M, Rezaie J. Application of stem cell-derived exosomes in ischemic diseases: opportunity and limitations. *J Transl Med.* (2021) 19:196. doi: 10.1186/s12967-021-02863-w
 132. Kalluri R, LeBleu VS. The biology, function, and biomedical applications of exosomes. *Science.* (2020) 367:aau6977. doi: 10.1126/science.aau6977
 133. Hessvik NP, Llorente A. Current knowledge on exosome biogenesis and release. *Cell Mol Life Sci.* (2018) 75:193–208. doi: 10.1007/s00018-017-2595-9
 134. Pegtel DM, Gould SJ. Exosomes. *Annu Rev Biochem.* (2019) 88:487–514. doi: 10.1146/annurev-biochem-013118-111902
 135. Raposo G, Stoorvogel W. Extracellular vesicles: exosomes, microvesicles, and friends. *J Cell Biol.* (2013) 200:373–83. doi: 10.1083/jcb.201211138
 136. Théry C, Witwer KW, Aikawa E, Alcaraz MJ, Anderson JD, Andriantsitohaina R, et al. Minimal information for studies of extracellular vesicles 2018 (MISEV2018): a position statement of the International Society for Extracellular Vesicles and update of the MISEV2014 guidelines. *J Extracell Vesicles.* (2018) 7:1535750. doi: 10.1080/20013078.2018.1535750
 137. Feng R, Ullah M, Chen K, Ali Q, Lin Y, Sun Z. Stem cell-derived extracellular vesicles mitigate ageing-associated arterial stiffness and hypertension. *J Extracell Vesicles.* (2020) 9:1783869. doi: 10.1080/20013078.2020.1783869
 138. Monroe MN, Zhaorigetu S, Gupta VS, Jin D, Givan KD, Curylo AL et al. Extracellular vesicles influence the pulmonary arterial extracellular matrix in congenital diaphragmatic hernia. *Pediatr Pulmonol.* (2020) 55:2402–11. doi: 10.1002/ppul.24914
 139. Ling H, Guo Z, Tan L, Cao Q, Song C. Stem cell-derived exosomes: role in the pathogenesis and treatment of atherosclerosis. *Int J Biochem Cell Biol.* (2021) 130:105884. doi: 10.1016/j.biocel.2020.105884
 140. Deng W, Tang T, Hou Y, Zeng Q, Wang Y, Fan W, et al. Extracellular vesicles in atherosclerosis. *Clin Chim Acta.* (2019) 495:109–17. doi: 10.1016/j.cca.2019.04.051

141. Bouchareychas L, Duong P, Covarrubias S, Alsop E, Phu TA, Chung A, et al. Macrophage exosomes resolve atherosclerosis by regulating hematopoiesis and inflammation *via* microRNA cargo. *Cell Rep.* (2020) 32:107881. doi: 10.1016/j.celrep.2020.107881
142. Qiu G, Zheng G, Ge M, Wang J, Huang R, Shu Q, et al. Mesenchymal stem cell-derived extracellular vesicles affect disease outcomes *via* transfer of microRNAs. *Stem Cell Res Ther.* (2018) 9:320. doi: 10.1186/s13287-018-1069-9
143. Xing X, Li Z, Yang X, Li M, Liu C, Pang Y, et al. Adipose-derived mesenchymal stem cells-derived exosome-mediated microRNA-342-5p protects endothelial cells against atherosclerosis. *Aging.* (2020) 12:3880–98. doi: 10.18632/aging.102857
144. Gao H, Yu Z, Li Y, Wang X. miR-100-5p in human umbilical cord mesenchymal stem cell-derived exosomes mediates eosinophilic inflammation to alleviate atherosclerosis *via* the FZD5/Wnt/beta-catenin pathway. *Acta Biochim Biophys Sin.* (2021) 53:1166–76. doi: 10.1093/abbs/gmab093
145. Wang S, Hu S, Wang J, Liu Y, Zhao R, Tong M, et al. Conditioned medium from bone marrow-derived mesenchymal stem cells inhibits vascular calcification through blockade of the BMP2-Smad1/5/8 signaling pathway. *Stem Cell Res Ther.* (2018) 9:160. doi: 10.1186/s13287-018-0894-1
146. Wang Y, Jia L, Xie Y, Cai Z, Liu Z, Shen J, et al. Involvement of macrophage-derived exosomes in abdominal aortic aneurysms development. *Atherosclerosis.* (2019) 289:64–72. doi: 10.1016/j.atherosclerosis.2019.08.016
147. Zhou YZ, Cheng Z, Wu Y, Wu QY, Liao XB, Zhao Y, et al. Mesenchymal stem cell-derived conditioned medium attenuate angiotensin II-induced aortic aneurysm growth by modulating macrophage polarization. *J Cell Mol Med.* (2019) 23:8233–45. doi: 10.1111/jcmm.14694
148. Sajeesh S, Broekelman T, Mecham RP, Ramamurthi A. Stem cell derived extracellular vesicles for vascular elastic matrix regenerative repair. *Acta Biomater.* (2020) 113:267–78. doi: 10.1016/j.actbio.2020.07.002
149. Stocum DL, Zupanc GK. Stretching the limits: stem cells in regeneration science. *Dev Dyn.* (2008) 237:3648–71. doi: 10.1002/dvdy.21774
150. Lee SH. The advantages and limitations of mesenchymal stem cells in clinical application for treating human diseases. *Osteoporos Sarcopenia.* (2018) 4:150. doi: 10.1016/j.afos.2018.11.083
151. Kim HJ, Park JS. Usage of human mesenchymal stem cells in cell-based therapy: advantages and disadvantages. *Dev Reprod.* (2017) 21:1–10. doi: 10.12717/DR.2017.21.1.001
152. Attia N, Mashal M, Puras G, Pedraz JL. Mesenchymal stem cells as a gene delivery tool: promise, problems, and prospects. *Pharmaceutics.* (2021) 13:843. doi: 10.3390/pharmaceutics13060843
153. Fischer UM, Harting MT, Jimenez F, Monzon-Posadas WO, Xue H, Savitz SI, et al. Pulmonary passage is a major obstacle for intravenous stem cell delivery: the pulmonary first-pass effect. *Stem Cells Dev.* (2009) 18:683–92. doi: 10.1089/scd.2008.0253
154. Ludwig N, Whiteside TL, Reichert TE. Challenges in exosome isolation and analysis in health and disease. *Int J Mol Sci.* (2019) 20:4684. doi: 10.3390/ijms20194684
155. Rezabakhsh A, Sokullu E, Rahbarghazi R. Applications, challenges and prospects of mesenchymal stem cell exosomes in regenerative medicine. *Stem Cell Res Ther.* (2021) 12:521. doi: 10.1186/s13287-021-02596-z
156. Kang M, Jordan V, Blenkinsop C, Chamley LW. Biodistribution of extracellular vesicles following administration into animals: a systematic review. *J Extracell Vesicles.* (2021) 10:e12085. doi: 10.1002/jev2.12085
157. Yvan-Charvet L, Bonacina F, Guinard RR, Norata GD. Immunometabolic function of cholesterol in cardiovascular disease and beyond. *Cardiovasc Res.* (2019) 115:1393–407. doi: 10.1093/cvr/cvz127
158. Zaragoza C, Gomez-Guerrero C, Martin-Ventura JL, Blanco-Colio L, Lavin B, Mallavia B, et al. Animal models of cardiovascular diseases. *J Biomed Biotechnol.* (2011) 2011:497841. doi: 10.1155/2011/497841
159. Emini Veseli B, Perrotta P, De Meyer GRA, Roth L, Van der Donckt C, Martinet W, et al. Animal models of atherosclerosis. *Eur J Pharmacol.* (2017) 816:3–13. doi: 10.1016/j.ejphar.2017.05.010

Conflict of Interest: The authors declare that the research was conducted in the absence of any commercial or financial relationships that could be construed as a potential conflict of interest.

Publisher's Note: All claims expressed in this article are solely those of the authors and do not necessarily represent those of their affiliated organizations, or those of the publisher, the editors and the reviewers. Any product that may be evaluated in this article, or claim that may be made by its manufacturer, is not guaranteed or endorsed by the publisher.

Copyright © 2022 S, Dahal, Bastola, Dayal, Yau and Ramamurthi. This is an open-access article distributed under the terms of the Creative Commons Attribution License (CC BY). The use, distribution or reproduction in other forums is permitted, provided the original author(s) and the copyright owner(s) are credited and that the original publication in this journal is cited, in accordance with accepted academic practice. No use, distribution or reproduction is permitted which does not comply with these terms.



3D Printed Bioreactor Enabling the Pulsatile Culture of Native and Angioplastied Large Arteries

Rolando S. Matos¹, Davide Maselli¹, John H. McVey¹, Christian Heiss^{1,2} and Paola Campagnolo^{1*}

¹ Cardiovascular Section, Department of Biochemical Sciences, Guildford, United Kingdom, ² Clinical Medicine Section, Department of Clinical and Experimental Medicine, University of Surrey, Faculty of Health and Medical Sciences, University of Surrey, Guildford, United Kingdom

OPEN ACCESS

Edited by:

Anthal Smits,
Eindhoven University of
Technology, Netherlands

Reviewed by:

Monica Soncini,
Politecnico di Milano, Italy
Maurizio Pesce,
Monzino Cardiology Center
(IRCCS), Italy

*Correspondence:

Paola Campagnolo
p.campagnolo@surrey.ac.uk

Specialty section:

This article was submitted to
Heart Valve Disease,
a section of the journal
Frontiers in Cardiovascular Medicine

Received: 28 January 2022

Accepted: 13 May 2022

Published: 21 June 2022

Citation:

Matos RS, Maselli D, McVey JH,
Heiss C and Campagnolo P (2022) 3D
Printed Bioreactor Enabling the
Pulsatile Culture of Native and
Angioplastied Large Arteries.
Front. Cardiovasc. Med. 9:864580.
doi: 10.3389/fcvm.2022.864580

Routine interventions such as balloon angioplasty, result in vascular activation and remodeling, often requiring re-intervention. 2D *in vitro* models and small animal experiments have enabled the discovery of important mechanisms involved in this process, however the clinical translation is often underwhelming. There is a critical need for an *ex vivo* model representative of the human vascular physiology and encompassing the complexity of the vascular wall and the physical forces regulating its function. Vascular bioreactors for *ex vivo* culture of large vessels are viable alternatives, but their custom-made design and insufficient characterization often hinders the reproducibility of the experiments. The objective of the study was to design and validate a novel 3D printed cost-efficient and versatile perfusion system, capable of sustaining the viability and functionality of large porcine arteries for 7 days and enabling early post-injury evaluations. MultiJet Fusion 3D printing was used to engineer the *EasyFlow* insert, converting a conventional 50 ml centrifuge tube into a mini bioreactor. Porcine carotid arteries either left untreated or injured with an angioplasty balloon, were cultured under pulsatile flow for up to 7 days. Pressure, heart rate, medium viscosity and shear conditions were adjusted to resemble arterial *in vivo* hemodynamics. Tissue viability, cell activation and matrix remodeling were analyzed by immunohistochemistry, and vascular function was monitored by duplex ultrasound. Culture conditions in the *EasyFlow* bioreactor preserved endothelial coverage and smooth muscle organization and extracellular matrix structure in the vessel wall, as compared to static culture. Injured arteries presented hallmarks of early remodeling, such as intimal denudation, smooth muscle cell disarray and media/adventitia activation in flow culture. Duplex ultrasound confirmed continuous pulsatile blood flow conditions, dose-dependent vasodilator response to nitroglycerin in untreated vessels and impaired dilator response in angioplastied vessels. The scope of this work is to validate a low-cost, robust and reproducible system to explore the culture of native and injured large arteries under pulsatile flow. While the study of vascular pathology is beyond the scope of the present paper, our system enables future investigations and provides a platform to test novel therapies and devices *ex vivo*, in a patient relevant system.

Keywords: bioreactor and 3D culture, *ex vivo* culture, organotypic culture model, vascular remodeling, balloon angioplasty, blood vessel

INTRODUCTION

Vascular disease is often caused by narrowing or occlusion of blood vessels leading to decreased blood supply to important organs like the heart or brain, or to the extremities. Revascularization procedures are common interventions aimed at re-establishing blood supply to compromised tissues. Typically, a guidewire is passed through an accessible artery to reach the narrowed area and a balloon is deployed to reopen the lumen. While the immediate effect on blood flow is readily achieved, the intervention damages the blood vessel wall which triggers a cascade of acute inflammatory and regenerative responses that result in intimal hyperplasia and vascular remodeling (1). The vascular remodeling commonly leads to re-stenosis and ultimately occlusion of the intervened vessels (2). In order to maintain patency in the long term, many times additional devices like stents or balloons coated with anti-proliferative drugs are used on the intervened vessels. Clearly, a better understanding of the processes that underly the vascular response to injury and remodeling is key to develop effective treatments to improve long-term patency of revascularization procedures (1).

Largely, experiments aimed at investigating these mechanisms are conducted in small animals (mice, rats, rabbits), upon mechanical injury of a large artery or interposition of a stent (3). Besides the obvious ethical concerns, small rodent experiments have limited predictive capacity, resulting in the development of sub-optimal therapeutic strategies, leaving this critical medical need unmet (4). *In vitro* strategies for the study of vascular remodeling focus on 2D culture of vascular cells (typically smooth muscle cells) or the static culture of rings obtained from blood vessels, the latter importantly incorporates an element of intact extracellular matrix component, which is critical in the remodeling process [for an example (5)]. Interestingly, some groups have demonstrated the successful use of flow bioreactors simulating the *in vivo* hemodynamic conditions, to culture blood vessels *ex vivo* and study vascular pathophysiology (6–9). This pioneering work has demonstrated the importance and feasibility of a functional and physiological *ex vivo* approach to vascular remodeling; however, these studies present some limitations that reduce their translational power and reproducibility, which we aim to address with the present work.

In this study, we developed an open-source 3D printed and economical bioreactor (EasyFlow) which enables the multiplex culture of blood vessels from large animals in small volumes of medium. Furthermore, we have optimized conditions of flow, shear stress, pressure, pulsatility and viscosity to closely mimic the hemodynamic forces applying to an artery *in vivo*. We comprehensively characterized the effect of pulsatile flow culture and endovascular injury on the survival, activation and function of vascular resident cells by histology, immunofluorescence and by Doppler ultrasound vasoreactivity measurements.

This work will demonstrate the reproducible application of *ex vivo* bioreactor culture for large animal blood vessels, enabling the long-term culture of healthy vessels and the study of pathological mechanisms. Importantly, the open-source nature of our design enables effortless transfer of the system to other

labs and reproducibility, promoting the reduction of the use of animals in vascular studies.

MATERIALS AND METHODS

Ethics and Sample Preparation

Carotid arteries were obtained from 4–6 weeks old piglet at The Pirbright Institute, Pirbright, UK. Animal procedures were carried out under the Home Office Animals (Scientific Procedures) Act (1986) and approved by the Animal Welfare and Ethical Review Board (AWERB) of The Pirbright Institute. The animals were housed in accordance with the Code of Practice for the Housing and Care of Animals Bred.

Pigs were euthanized by an overdose of 10 ml pentobarbital (Dolethal 200 mg/ml solution for injection, Vetoquinol UK Ltd). All procedures were conducted by Personal License holders who were trained and competent and under the Project License PPL70/8852.

Upon exsanguination the neck was opened from the chest cavity to the base of the skull to expose the common carotid artery separating into the right and left carotid artery. Arteries were excised using a no-touch technique to minimize stress to the vascular tissue. Fresh tissue was immediately placed in pre cooled transport media Dulbecco's Modified Eagle's Medium (DMEM) + 20% fetal bovine serum (FBS) + 2% penicillin and streptomycin (P/S) + 1% Amphotericin B (Amp). Tissue was washed two times in transport media and placed on ice for transportation.

Following arrival tissue was transferred into laminar hood where further preparation took place. The excess connective tissue was removed in a Petri dish using precision surgical equipment, avoiding any strain to the vessel. Once cleaned, the vessel was placed in new container and washed in transport media (2 × 20 min at 4°C), followed by short term storage in DMEM + 10% FBS + 1% P/S + 1% Amp at 4°C.

For each preparation, a sample of 2–4 mm was collected at the time of preparation, as a control.

Easy Flow Design and Production

The EasyFlow insert was produced by additive manufacturing which enables for complex design choices to be manufactured with high reproducibility. The CAD model of the system was prepared using Autodesk Fusion 360 (Autodesk® Fusion 360™ 2.0.5818). Printable file is available in **Supplementary File 1**.

In planning the design, the major criteria considered were user experience, ease of handling, adaptability and reusability. MultiJet Fusion 3D printing allowed us to create fine inner structures within a space-efficient design and therefore maintain a compact outer structure. The manufacturing was outsourced to an external provider (ProtoLabs), which produced EasyFlow by Polyamide 12 (HP 3D High Reusability PA 12) Black MultiJet Fusion built in 80 µm layers, requiring no additional finish. Considering the constantly expanding list of materials available for manufacturing, the proposed design can be manufactured with alternative materials as long as the additive method resembles a Selective Laser Sintering or Stereolithography type manufacturing.

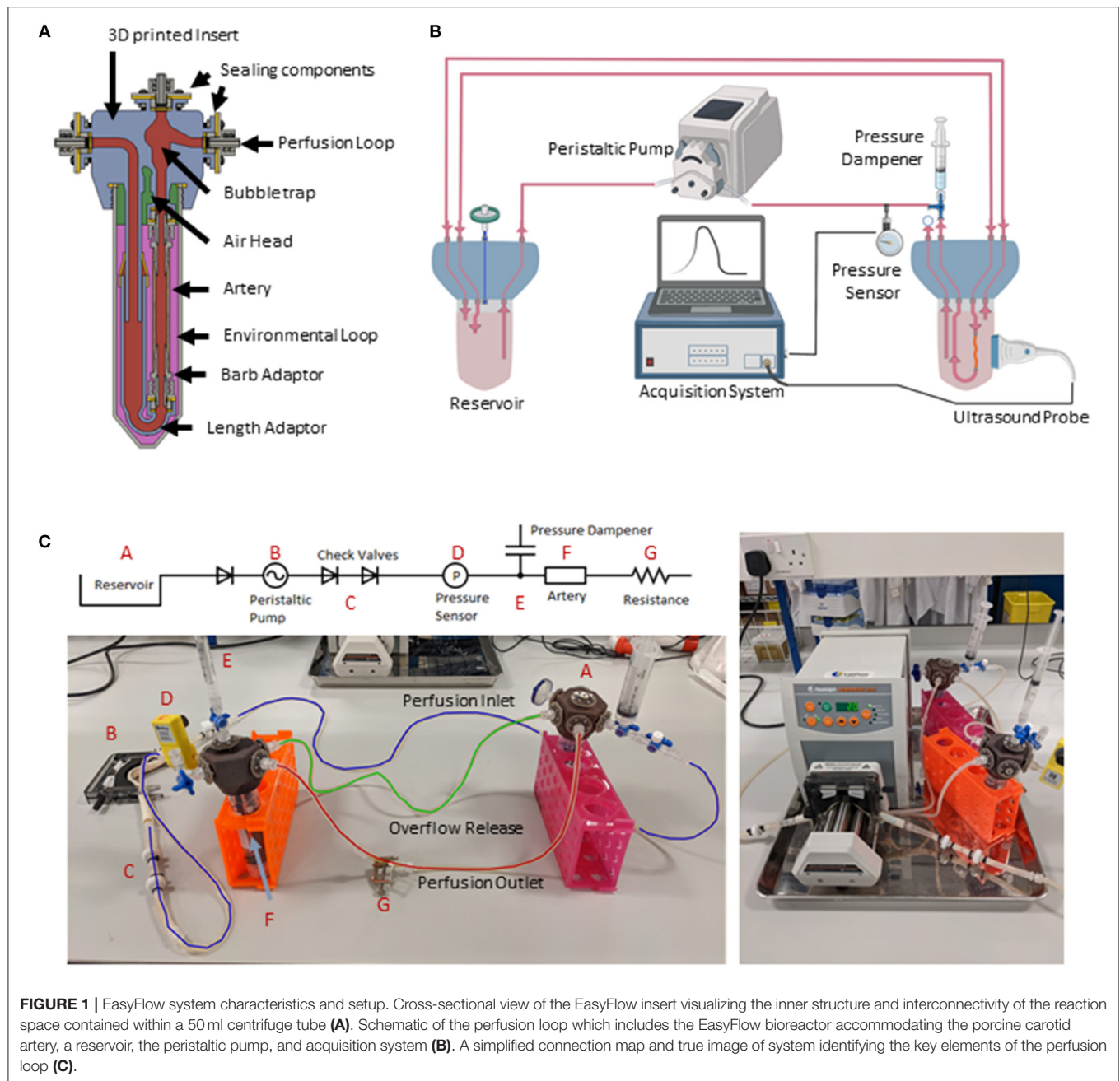


FIGURE 1 | EasyFlow system characteristics and setup. Cross-sectional view of the EasyFlow insert visualizing the inner structure and interconnectivity of the reaction space contained within a 50 ml centrifuge tube (A). Schematic of the perfusion loop which includes the EasyFlow bioreactor accommodating the porcine carotid artery, a reservoir, the peristaltic pump, and acquisition system (B). A simplified connection map and true image of system identifying the key elements of the perfusion loop (C).

EasyFlow System Set Up

Details of the EasyFlow bioreactor system are presented in **Figure 1** and in the Result section, in details.

The EasyFlow insert consists of a 3D printed part that fits as a lid of a 50 ml standard centrifuge tube. The hexagonal EasyFlow insert presents 6 inlet and outlet ports, creating two separate circulations inside and outside the blood vessel, which is lodged in its adaptor (**Figure 1A**).

The bioreactor system is composed by three main parts: a peristaltic pump (Heidolph, PD 5201, 523-52010-00-2) mounting a 4-cassette head (Heidolph, Multichannel Pump Head C8,

524-40810-00), an EasyFlow insert lodging the blood vessel sample and an equivalent EasyFlow functioning as media reservoir (**Figure 1B**). The two inserts are connected through a series of tubes. Most of the components are connected with transparent silicon tubing (RS Components, RS PRO Silicone Transparent Silicone Tubing, 3.2 mm Bore Size, 667-8444). Larger bore peristaltic pump-compatible tubing (RS Component, Verderflex Verderprene Yellow Process Tubing, 6.4 mm Bore Size, 125-4042) were used in the pump head. Unidirectional flow is ensured by check valves (Cole-Parmer, Masterflex PVDF and Viton® Barbed Check Valve, 3/16-inch, WZ-98766-50) added

downstream the peristaltic pump, and pressure is stabilized by a pressure dampener system created with a syringe loaded with liquid and air. To increase baseline pressure low bore tubing (RS Components, RS PRO Silicone Transparent Silicone Tubing, 0.8 mm Bore Size, 667-8432) was used downstream of the artery. To regulate resistance, an additional clamp (Cole-Parmer, Flow Control Clamps, 08028-00) was applied downstream of the resistance tubing. Sterile gas exchange is enabled by the presence of outlets mounted with sterility filters (Sarstedt, Syringe filter, Filtropur S, PES, pore size: 0.2 μ m, 83.1826.001) (**Figure 1C**).

The system was monitored by pressure sensors downstream of the sample-containing EasyFlow (Parker, SciLog SciPres Pressure Sensor Luer Connection, SCIPRE080699PSX), and through repeated Duplex ultrasound imaging performed with Logiq V2 (GE Healthcare).

To assure the aseptic environment necessary for the long-term incubation of tissues, all components were sterilized by autoclaving. Elements of the circulation system were assembled under a laminar flow hood and primed with *perfusion media* (DMEM + 10% FBS + 1% P/S + 1 % Amp + 3% Dextran). The circulation system was inspected for leaks, and any bubble trapped in the system was removed by flowing media across the system.

Previously harvested and cleaned tissue was then placed in the EasyFlow unit. Depending on the internal diameter of the vessel segment, an adequate barb connector was selected to facilitate the connection to the perfusion system, typically for porcine carotid arteries 2.4 or 1.6 mm ID connectors were used (Cole-Parmer, Female luer x 5/32" hose barb adapter, 45501-06). The length adaptor within EasyFlow is ultimately adjusted to create a minimal stretch on the longitudinal axis (**Figure 1A**).

Once the tissue was secured using surgical vessel bond (Vessel Loop Maxi, SKU: AR-722), the residual air was removed from the newly assembled segment before sealing the system. A sterile syringe containing 3 ml of air and 1 ml of media is connected to the port situated above the artery. This addition serves as a pressure dampener assuring that there is no extreme pressure effecting the artery. Following complete assembly, the system is sealed and transferred it to the incubator (5% CO₂ at 37°C). Circulation was connected to the peristaltic pump (**Figure 1C**) and primed overnight with low flow conditions (5 rpm). This allows system equilibrium and enables troubleshooting while minimizing unnecessary strain to the tissue. Flow was gradually increased (+1 rpm every 60 min) until the setpoint is achieved (14 rpm). The pressure of the system is constantly monitored safeguarding the vessel from any extreme condition. Once the final pump speed is reached, resistance upstream of the blood vessel is adjusted by incrementally tightening the downstream screw clamp until satisfactory pressure was reached within the system.

Balloon Injury Procedure

A standard peripheral artery angioplasty balloon catheter (Cook Medical, Advance® 35 LP Low 4 mm) was inserted into the artery. With a standard inflator pump the balloon was inflated with phosphate buffer saline (PBS) to 6 atm and the pressure was maintained for 3 min, akin to the procedure performed during

peripheral arterial angioplasties. After deflation, the balloon was extracted, the tissue rinsed and placed in the perfusion system for culture, or static culture as a control.

Artery Culture in Flow or Static Conditions

Healthy and balloon injured arteries were cultured for 7 days in static or flow conditions. In static culture, 2–4 mm long tissue segments are submerged in medium (DMEM + 10% FBS + 1% P/S + 1% Amp) in Petri dishes, and incubated at 5% CO₂, 37°C. Every 3 days 50% of the media was replaced with fresh media.

Perfusion cultures were performed using the EasyFlow bioreactor system, as described above, on segments of 2–4 cm of length. The system is filled with ~100 ml of *perfusion media* (DMEM + 10% FBS + 1% P/S + 1 % Amp + 3% Dextran). Of note, the addition of dextran exclusively to the flow culture media ensures the appropriate viscosity of the medium which in turn affects the shear stress, while avoiding reducing the diffusion of oxygen in the static cultures, that would represent a limiting factor for the culture. The peristaltic pump is set at the final speed of 14 rpm which, due to the 4 rolls mounted on the peristaltic pump, is equivalent to 56 pulse/min. This pump setting corresponds to 35 ml/min volumetric flow rate (**Supplementary Figure 1A**) and an average stroke volume of 0.6 ml (calculated as volumetric flow rate/pulse rate). To assure that the tissue is not subject to extreme pressure conditions generated by the peristaltic movement, a pressure dampener was introduced to maintain fluctuations within the physiological range (60–120 mmHg), these values were monitored across the entire experiment in one second intervals, using a pressure acquisition system (**Supplementary Figure 1B**). Lastly, conceptually similar to a heart valve and to maintain “diastolic pressure,” a one-way valve was introduced after the peristaltic pump (**Figure 1C**).

Samples in flow were monitored at day 3 and 7 by Duplex ultrasound imaging. At the end of the culture period, all samples were processed for histology and *en face* staining.

Doppler Ultrasound Imaging and Vasoreactivity Assay

Ultrasound images of the incubated arteries were obtained with a standard clinical vascular ultrasound machine with a 10 MHz linear array transducer (LOGIQ V2, GE Healthcare). Briefly, ultrasound gel was applied to the outside of the bioreactor to minimize acoustic impedance, compensate for surface incongruencies between probe and bioreactor and allow angulation of probe to obtain an insonation angle of <60°. After clear longitudinal images were obtained, the position of the ultrasound probe and B-Mode settings were adjusted until clear vessel borders with typical M and I lines were visible, and several cine video loops were acquired and saved as video files for off-line analysis. Flow velocity measurements were performed with pulsed wave Doppler. The sample volume was placed at the center of the perfused artery, insonation angle adjusted to <60° and angle correction applied. Image analysis was performed offline with an automated edge detection software (Brachial analyzer, Medical Imaging Applications). The luminal diameter was measured on video loops over several pulsation cycles. Each

diameter measurement represents the average diameter over 0.5–1.0 cm vessel area. The maximal diameter was designated systolic diameter and minimal diameter as diastolic diameter. Volumetric flow rate (Q) was calculated as follows:

$$Q = A \times \bar{V}$$

Where \bar{V} is the mean Flow Velocity and A is the Cross-sectional Area, calculated as $\pi (\text{mean diameter}/2)^2$ and mean diameter = (maximal diameter + minimal diameter)/2.

In our setup, the mean diameter of the artery was 1.2 mm and a mean velocity of ~50 cm/s (Figures 4A,B, and Supplementary Figure 1C) and this resulted in a calculated volumetric flow rate of ~35 ml/min within the artery, which confirms the calibration values obtained empirically Supplementary Figure 1A).

Wall shear stress (WSS) was estimated as:

$$\text{WSS} = 8 \times \mu \times \frac{\bar{V}}{\text{mean diameter}}$$

The viscosity of the perfusion medium (μ) was estimated at 0.035 dyn*s/cm² (10). Intimal media thickness was also measured with this software over the same vessel segment on the far side as the distance between lumen-intima (I line) and media-adventitia interface (M line).

For the functional vasoreactivity assay, syringes containing 1 ml of nitroglycerin solutions were prepared, with concentration ranging from 10⁻⁹ to 1 M. These concentrations were calculated so that added to 100 ml of medium contained in the bioreactor, they yielded final concentrations ranging from 10⁻¹¹ and 10⁻² M. Nitroglycerin boluses were injected in order of increasing concentration and the reaction of the blood vessel was recorded with a delay of 1 min, once the vessel normalized the next bolus was injected.

Histological Preparations

Portions of freshly isolated (control) and cultured arteries were fixed in 4% PFA (Paraformaldehyde, Santa Cruz Biotechnology) overnight (O/N) at 4°C. Fixed samples were either used for whole tissue *en-face* staining or were further processed for histological analysis.

To establish the maintenance of a continuous endothelial layer facing the lumen and quantify the effect of flow on the alignment of the cells, *en-face* staining was performed on samples washed with PBS and permeabilized with 1v/v% TritonX-100 in PBS for 15 min. Tissues were blocked overnight at 4°C in 20v/v% goat serum in PBS and then incubated with primary antibody solution (CD31, Abcam-ab28364, 1:50) overnight followed by goat anti-Rabbit Alexa Fluor 488[®] (Thermo Fisher Scientific) secondary antibody diluted 1:200 and Phalloidin-iFluor 594 (Abcam- ab176757) for 1 h at 37°C. Nuclei were stained with DAPI (4',6-diamidino-2-phenylindole, Merck) for 10 min at room temperature. Tissues were laid flat and mounted with Fluoromount G (Invitrogen eBioscience Fluoromount G, Thermo Fisher Scientific). Imaging was performed with Nikon Eclipse Ti A1-A confocal laser scanning microscope, obtaining stack images at 40X along the Z-axis.

For histology, tissues were washed with PBS and incubated overnight in 30w/v% sucrose (Sigma-Aldrich) solution in PBS. Following sucrose incubation, samples were embedded in OCT Compound (Agar scientific) in an Iso-Pentane bath cooled using liquid nitrogen. Frozen samples were stored at -80°C until later use. Samples were cryo-sectioned along the transverse plane, obtaining 5 μ m thick sections. Sections were collected on microscope slides in quadruplicate, where sections were separated by at least 250 μ m.

Immunofluorescent staining was performed on prepared sections to quantify luminal coverage, medial integrity and the extent of proliferation. Tissue sections underwent antigen retrieval in a water bath at 80°C for 30 min in tris-EDTA buffer (10 mM Tris Base, 1 mM EDTA Solution, pH 9.0) followed by blocking for 1 h at room temperature with 20v/v% goat serum (Sigma-Aldrich) in PBS. Primary antibodies against CD31 (Abcam-ab28364) diluted 1:200, and Proliferating cell nuclear antigen (PCNA, Sigma Aldrich-MABE288) diluted 1:100 were incubated overnight at 4°C.

Appropriate Goat anti-Mouse and Goat anti-Rabbit Alexa Fluor[®] (Thermo Fisher Scientific) secondary antibodies 488 and 567 diluted 1:200 were incubated for 1 h at 37°C. Following secondary antibodies, Human α -Smooth Muscle Actin (SMA) Alexa Fluor[®] 647-conjugated antibody (R&D Systems-IC1420R) diluted 1:200 was introduced for 1 h at 37°C. Nuclei were stained with DAPI (Merck) for 10 min at room temperature. Incubation with 0.1 w/v % Sudan Black (Sudan Black B, Santa Cruz Biotechnology) in 70% ethanol for 10 min at room temperature was performed to reduce tissue autofluorescence. Slides were then mounted in Fluoromount G (Invitrogen eBioscience Fluoromount G, Thermo Fisher Scientific) and imaged with Nikon Eclipse Ti A1-A confocal laser scanning microscope. Tile images were obtained at 20X to capture the whole tissue section where possible.

Hematoxylin and Eosin (H&E), and Masson's trichrome staining (MT) were used to estimate the overall maintenance of the tissue structure, at a cellular and extracellular matrix level. These stainings were outsourced to the Veterinary School Pathology Centre at the University of Surrey, and performed by an automated staining system (VIP[®] 6 Vacuum Infiltration Processor). Immunohistochemical assays for Caspase 3 (1:1,000, R&D systems, AF835), PDGFR- β (Santa Cruz Biotechnology, sc-374573, 1:100) and Vimentin (1:5,000 Dako, Ref M0725, Clone V9, 1:5,000) were similarly outsourced to Veterinary Diagnostic Services, School of Veterinary Medicine, University of Glasgow. Primary antibodies were followed by HRP-conjugated secondary antibody and DAB (3,3'-Diaminobenzidine) staining and counter-staining with hematoxylin. Staining was performed in the Dako Autostainer system. Slices were dehydrated and mounted with Cellpath Mounting Media (SEA-1604-00A).

Whole slice imaging was performed on the NanoZoomer 2.0-HT slide scanner by Hamamatsu.

Image Analysis

All acquired images were processed in ImageJ v1.53c (Fiji). Custom macros were composed to facilitate image analysis. Where necessary, vessel wall areas (lumen, intima, media,

adventitia) were defined manually and stored as Regions of Interest (ROIs). Resulting ROIs were used to define tissue dimensions and to measure signals specific to the predefined areas.

Quantification of Cell Activation

The quantification of PCNA was performed on the fluorescent images collected by confocal microscopy. Tile images covering the cross section of the tissue were obtained to measure distribution of PCNA across the tissue for each section (three sections/sample). PCNA+ nuclei counts were normalized against the total number of DAPI+ nuclei within each area.

To define the spatial distribution of PCNA+ cells, images were converted into distance maps where orthogonal distance of each nucleus from the lumen was calculated. Each distance was further normalized against the thickness of the tunica media, to account for differences in tissue morphology between specimens. Individual distance values were organized into a histogram representing the relative frequency of PCNA+ cells against the relative distance from the lumen.

SMA Quantification in Immunofluorescence Samples

SMA intensity in the media was quantified on the immunofluorescence samples by selecting three random, uniformly sized, representative areas within the media of each section. The average signal intensity was quantified in each of the selected areas, and normalized by the total area selected.

Signal Quantification in Histological Samples

For histological staining, whole tissue sections were loaded on ImageJ to measure specific signal expression. First an ROI was defined by high-pass gaussian filter to identify the total area of the section. Using a series of user-defined color thresholds, the specific antigen signal was selected and extracted from the image. The area of specific signal was measured and normalized toward the total tissue area.

Tissue Coherence Analysis in Using Masson's Staining

Histological samples prepared with Masson's trichomic staining were used to analyze the coherence of the tissue. Three random, uniformly sized, representative regions were selected to perform the analysis. In each region, the area occupied by the tissue vs. the empty spaces were measured and normalized toward the total area of measurement.

Endothelial Coverage Quantification

The quantification of endothelial coverage was performed on the fluorescent images obtained by confocal microscopy. To quantify the coverage, the fraction of CD31-expressing lumen over the total length of the portion of lumen perimeter captured in each picture was calculated in vessel cross-sections.

Fiber Alignment

Fiber orientation was quantified in the *en-face* confocal images compressed into a Z-Max projection. In each picture, three

random areas were selected and a vector map of the Phalloidin signal was generated using OrientationJ (ImageJ/Fiji plugin) to obtain the local orientation of the signal within the selected area. Resulting vector values were organized into a histogram to represent the relative frequency of angular orientations, where zero is the representative value of fibers perpendicular to the flow direction.

Statistics

Experiments were repeated in 3 to 5 biological replicates. In some analyses, individual samples have been excluded due to poor quality of the preparation or staining.

Difference among groups were evaluated using one-way ANOVA or Kruskal–Wallis test, based on results from normality tests, followed by Fisher's LSD *post-hoc* test (GraphPad Prism 8.1.2). A value of $p < 0.05$ was considered as statistically significant. Data are presented as mean \pm SD.

RESULTS

Design and Specifications of the EasyFlow Bioreactor Insert

The resolution of MultiJet fusion 3D printing enabled the efficient and cost-effective production of the EasyFlow insert, incorporating detailed features, and producing a non-porous surface. The resulting product is biocompatible and autoclavable multiple times. The insert is designed to fit as the lid of a 50 ml centrifuge tube, creating a versatile and self-contained bioreactor for vascular culture (Figure 1A). The EasyFlow insert is hexagonal in shape and incorporates the following functional features: de-bubbler to remove any air bubbles trapped in the system, 6 inlet/outlet ports creating the potential for 2 separate circulations (inner circulation-going through the vessel sample, and outer circulation-to exchange medium in the tube), and extra access ports for sensors, gas/pressure exchange, and endovascular probes or catheters (Figure 1A).

The EasyFlow system was created as a self-contained, off-the-shelf solution for a wide range of experimental setups, and therefore was designed to maximize the included features, while maintaining a compact design. The hexagonal shape provides ideal internal space to position the necessary features, and enables to spatially distribute the connectors externally, allowing easy handling and setup, and offering enough space flexibility to connect external components.

The blood vessel is accommodated in an adjustable adaptor, through barb connectors of interchangeable size (Figure 1A and Supplementary Video 1). Once the bioreactor containing the sample is sealed, it can be connected to an equivalent bioreactor functioning as a medium reservoir and to a peristaltic pump, though medical grade tubing (Figures 1B,C). EasyFlow is amenable to Doppler imaging, the probe can be applied directly to the exterior wall of the centrifuge tube, enabling longitudinal monitoring of the changes in hemodynamic forces and the structural/functional response of the blood vessel (Figure 1B). Additional features are added to the system to improve the performance, such as one-way valves to ensure unidirectional flow, pressure dampener to regulate the system pressure, and gas exchange filters (Figure 1C). Thanks to these

features, we ensure that the blood vessel cultured within EasyFlow would experience physiological “heart rate” (56 pulse/min) and “blood pressure” (60–120 mmHg). To maintain the simplicity of use, pulsatility was imparted by the rotation of the peristaltic pump. Pressure measurements were recorded from a pressure sensor downstream from the artery every second (**Figure 1** and **Supplementary Figure 1B**), and adjusted manually by regulating the clamp tightness according to the continuous pressure readings obtained. The media used in our culture was enriched with dextran, to obtain a media viscosity similar to that of human blood ($0.035 \text{ dyn/sec} \cdot \text{cm}^2$ or 3.5 cP).

EasyFlow Culture Preserves Extracellular Matrix Organization and Tissue Homeostasis

Next, we tested how the EasyFlow environment impacted on cellular physiology and ultrastructural components, by performing *en face* staining, immunofluorescence imaging and histology in porcine carotid artery segments cultured in EasyFlow or in static culture for 7 days, and compared them to their freshly isolated segments that were used as “untreated” controls.

Hematoxylin and eosin staining revealed that the overall structure of the tissue was preserved during culture under flow conditions. In particular, the vessel wall layers appear unaltered, and no remodeling was observed (**Figure 2A**). Some of the samples cultured in static presented a distinct displacement of the intima, and loss of structure in the media and adventitia (**Figure 2A**).

Extracellular matrix provides the mechanical support and elasticity necessary for blood vessels to perform their function, cell apoptosis and abnormal activation may affect this structure, weakening the vessel wall. We visualized the collagen content by Masson's trichrome staining and confirmed the maintenance of the extracellular matrix organization in tissues cultured in EasyFlow, while static culture produced a visible loss of tissue integrity (**Figure 2B**). These observations were reflected in the quantification of tissue coherence which indicated an increase in tissue disarrangement in static cultured samples (**Figure 2C**).

Immunofluorescence staining revealed the finer changes in cell distribution. Both endothelial coverage of the lumen and expression of smooth muscle actin in the media were slightly reduced in the static condition, as compared to the flow culture, although not to a significant level (**Figures 3A–C**). These modest changes were reflected by the histological analysis of apoptosis and proliferation. Staining for the apoptosis marker Caspase-3, indicated no significant increase in cell death following culture, although a trend is clearly visible in 3/5 static culture samples (**Figure 3D**). Quantification of the overall percentage of PCNA+ cells revealed a slight increase in proliferation over culture, but no significant differences compared to the control (**Figure 3E**). We also detected a decrease in Vimentin+ cells in the static culture, potentially reflecting a loss of adventitia (**Figure 3F**), and an overall maintenance of PDGFRβ+ expression (**Figure 3G**).

Next, *en face* staining was performed to better visualize endothelial coverage and media organization. Overall, *en face* staining revealed a good luminal coverage in both culture

conditions (**Figure 3H**), however the intensity of the expression of CD31 and the cell organization of cultured samples appeared to differ from the freshly isolated control. This could also represent an artifact of the *en face* tissue processing which is affected by the tissue stiffness and integrity. On the other hand, culture in flow produced more organized structures in the media, which were comparable to the native tissues, while static culture conditions led to fiber disarray (**Figure 3H**).

Taken together these results indicate that culture of porcine arteries in pulsatile flow conditions helps maintaining appropriate cellular organization and structural integrity.

EasyFlow Can Be Monitored Using Ultrasound, Revealing Culture Conditions Resembling *in vivo* Hemodynamics and Physico-Mechanics

We applied an ultrasound probe to the wall of the centrifuge tube, and investigated the mechanical parameters to which the cultured artery was subjected in the bioreactor. By Doppler/Duplex analysis, we established that the carotid arteries within EasyFlow were exposed to physiological arterial hemodynamic conditions. The average diameter of arteries after 7 days of culture under pulsatile flow was $1.24 \pm 0.32 \text{ mm}$ (“systolic”) and $1.19 \pm 0.30 \text{ mm}$ (“diastolic”). The ‘peak systolic velocity’ was $52 \pm 13 \text{ cm/s}$ and ‘mean velocity’ was $44 \pm 8 \text{ cm/s}$, resulting in an estimated volumetric luminal flow of $33 \pm 16 \text{ ml/min}$ (11) and wall shear stress of $10.1 \pm 2.8 \text{ dyn/cm}^2$ (12) (**Figures 4A,B**). The average IMT was $0.32 \pm 0.08 \text{ mm}$. Overall repeated measurements of vessel diameter showed that there was an average deviation (AD) of $0.00 \pm 0.03 \text{ mm}$ between two independent automated measurements of four vessel (**Figure 4C**). These measurements support that EasyFlow provides reproducible *ex vivo* hydrodynamic conditions that resemble *in vivo* hemodynamics and physico-mechanics.

EasyFlow Cultures Are Amenable to Endovascular Balloon Procedures

The study of vascular pathology *ex vivo* has the potential to reduce and replace the number of animals used as models, providing results that are more physiologically relevant and may have scope to improve the patient care.

We performed balloon injury in porcine carotid arteries before culturing them for 7 days in flow conditions. An important advantage of the EasyFlow system is the ability to monitor the structural changes and functionality of the vessel longitudinally, by Doppler ultrasound. Here, we used it to determine the luminal diameter and intima media thickness and luminal flow within the artery, providing a closer estimate of the hemodynamic environment within the vessel. We also investigated functional response of the vessel wall to increasing doses of the endothelium-independent vasodilator nitroglycerin. Ultrasound showed that at day 3 the diameter of the vessels was significantly greater after angioplasty as compared to control (systolic: $1.17 \pm 0.52 \text{ mm}$ vs. $2.79 \pm 0.12 \text{ mm}$, $p = 0.026$, diastolic: $1.09 \pm 0.52 \text{ mm}$ vs. $2.47 \pm 0.04 \text{ mm}$, $p = 0.044$). While control retained the diameter at day 7, injured

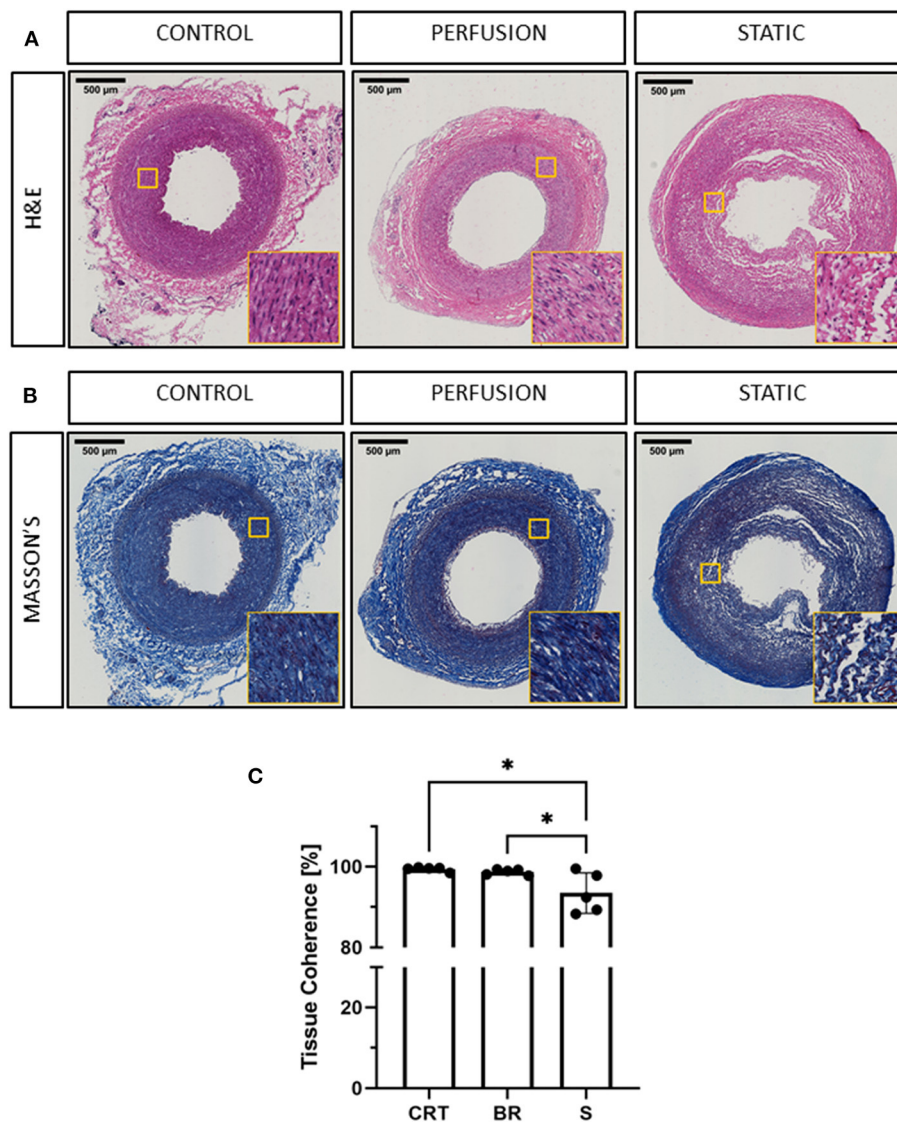


FIGURE 2 | Histological evaluation of porcine carotid arteries cultured in EasyFlow or static conditions. Hematoxylin and Eosin staining H&E (**A**) and Masson's Trichomic staining MASSON'S (**B**) of freshly isolated carotid artery tissue (CONTROL) and samples cultured for 7 days in EasyFlow (PERFUSION) or static culture (STATIC). Scale bars= 500 µm. Quantification of tissue coherence is displayed in the bar graph (**C**), $n = 5$. All data are mean \pm SD. One-Way ANOVA analysis was performed, $*p \leq 0.05$.

arteries significantly decreased diastolic diameter (control: 1.19 ± 0.30 mm, $p = 0.779$; angioplasty: 1.44 ± 0.60 mm, $p = 0.041$). There were no significant changes in luminal flow (**Figures 4D,E**, **Supplementary Videos 2, 3**). We leveraged on our ability to monitor the blood vessel in culture by ultrasound to quantify tissue remodeling using clinically relevant readouts. Intima-Media thickness (IMT) is considered a gold standard for the prediction of subclinical vascular remodeling and propensity to atherosclerosis in patients. We performed a preliminary analysis by measuring IMT in B-mode images, and showed that after injury there was an increase in IMT. While IMT remained stable between day 3 and 7 in control (0.27 ± 0.04 mm and 0.32 ± 0.08 mm, $p = 0.355$), it was decreased as compared to control

in angioplastied arteries at day 3 (0.15 ± 0.01) and increased at day 7 (0.38 ± 0.06 mm) (**Figures 4D,E**). We also compared the vascular response of the injured and control arteries cultured in flow. This identified a loss of 60–70% endothelium-independent vasodilator response upon stimulation with increasing doses of nitroglycerin (**Figure 4F**).

Next, we compared the ultrastructural effect of culturing injured arteries in static and flow conditions by histology, immunofluorescence and *en face* staining. As expected, balloon injury determined a significant loss of cells and disorganization in the extracellular matrix in the intima and the medial layers, as shown in the H&E and Masson's trichrome staining (**Figure 5A**). The effect of the injury was dramatic in tissues cultured in static,

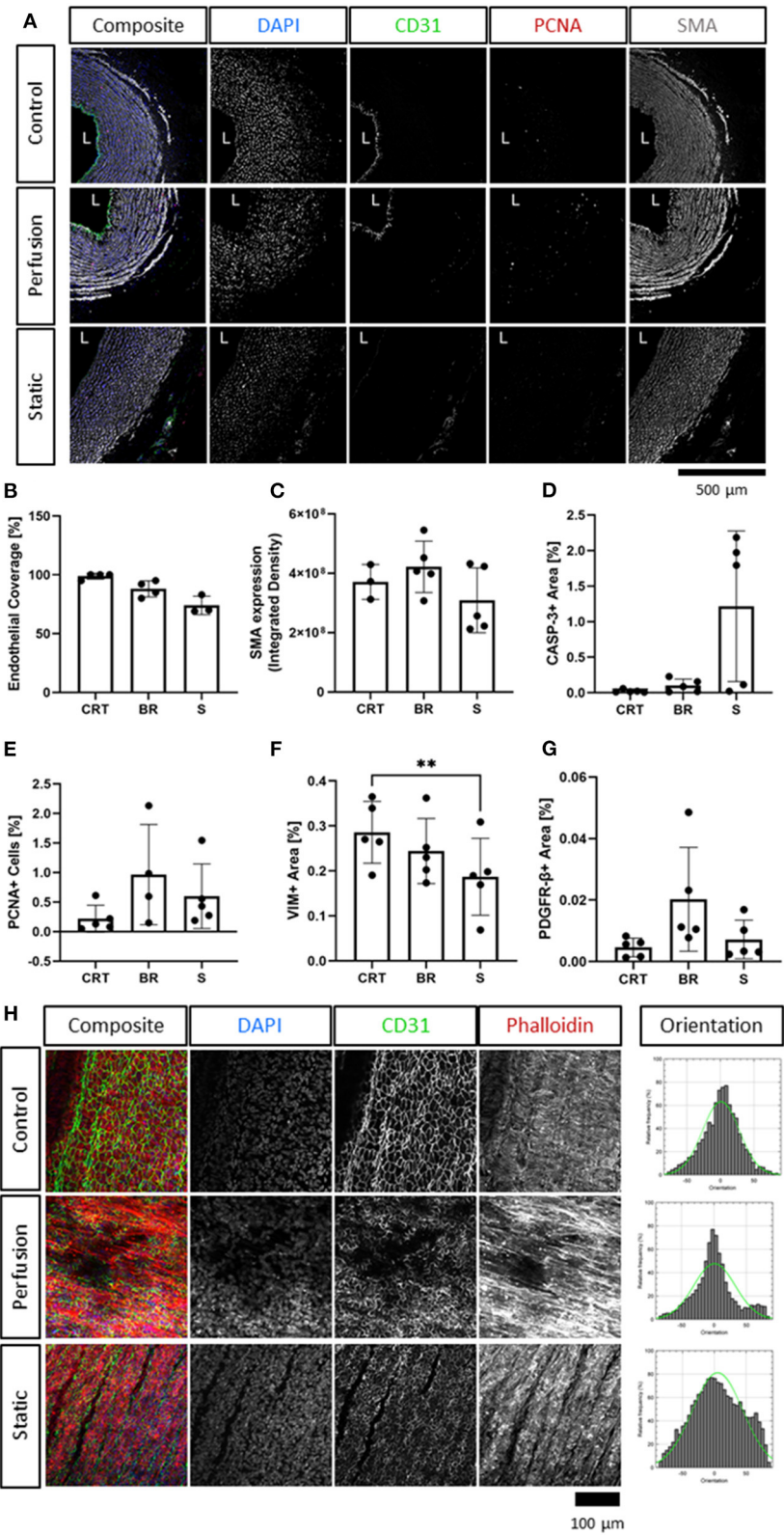


FIGURE 3 | Immunofluorescence analysis of cultured carotid arteries indicates better tissue preservation in flow. Immunofluorescence staining of freshly isolated arteries (d0, Control/CRT), EasyFlow (Perfusion/BR) and static cultured arteries (Static/S) at day 7, showing expression of endothelial marker CD31, smooth muscle (Continued)

FIGURE 3 | marker smooth muscle actin (SMA), and proliferation marker proliferating cell nuclear antigen (PCNA). Nuclei are stained with DAPI. Representative confocal images are displayed in composites and by individual marker in montage (A). Lumen is identified (L), Scalebar = 500 μ m. Quantifications of lumen coverage (B), SMA intensity (C), apoptosis caspase 3, casp-3, (D), proliferation PCNA (E), vimentin VIM (F) and platelet-derived growth factor receptor beta PDGFR β (G) are displayed in the bar graphs, $n = 3-5$. All data are mean \pm SD. One-Way ANOVA analysis was performed, $*p \leq 0.05$, $**p \leq 0.01$. *En-Face* representative images showing endothelial coverage (CD31), stress fiber (Phalloidin), and nuclei (DAPI) in samples cultured for 7 days in perfusion or static (H). Fiber alignment is quantified as vector distribution and plotted in histogram representing the relative frequency (y) against the angle (x), where zero is perpendicular to the flow direction (Orientation). An ideal normal distribution of values is represented in green over the histogram (h). Scalebar = 100 μ m.

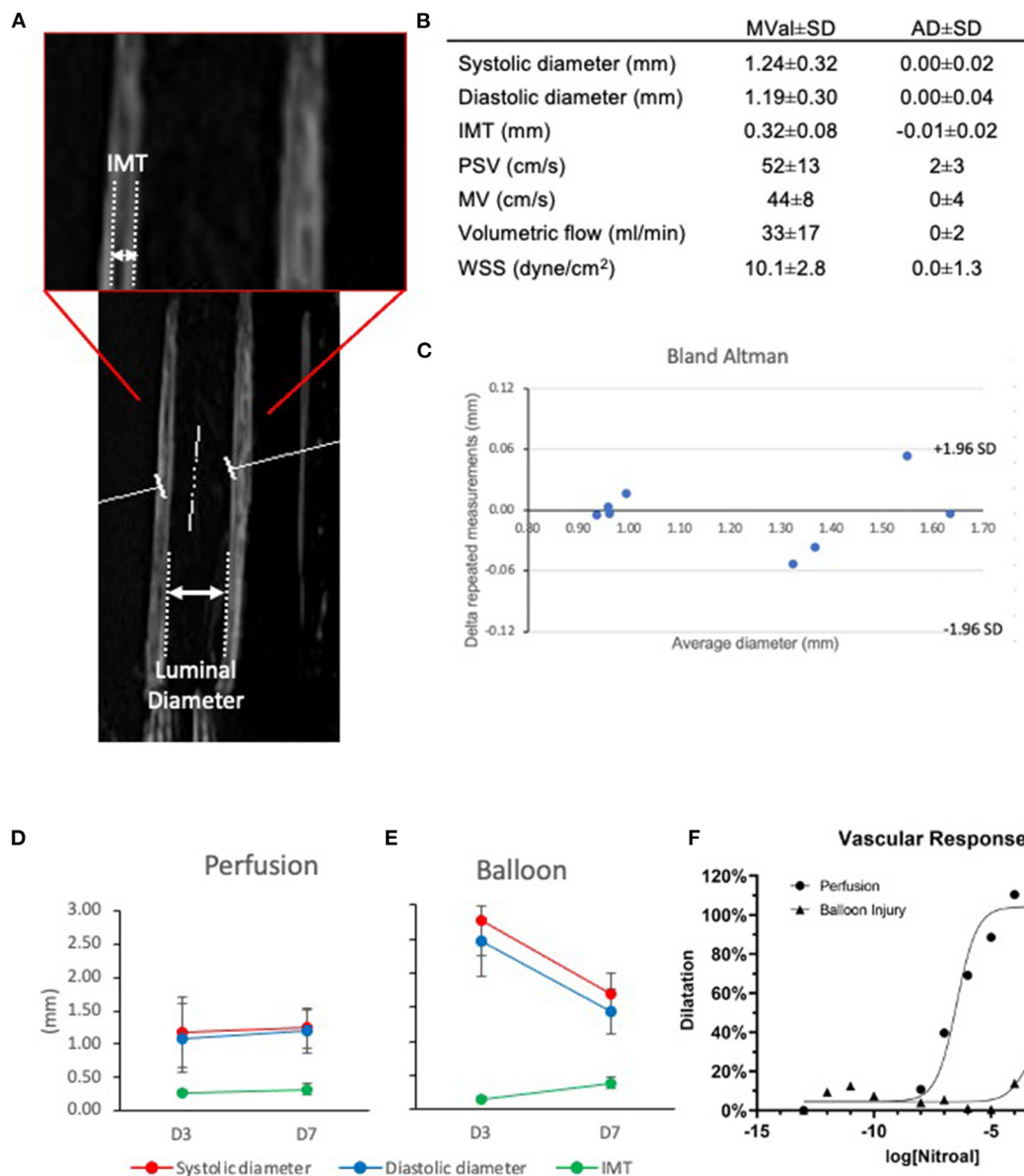


FIGURE 4 | Ultrasound evaluation of native and angioplastied carotid arteries after culture reveal *in vivo* relevant culture conditions and impairment after injury. Representative ultrasound image of an artery in culture (A), highlighting the morphological parameters captured (B). Mean value (MVal) and average deviation (AD) of vessel parameters in flow culture at day 7. IMT, intima media thickness; PSV, peak systolic velocity; MV, mean velocity; WSS, wall shear stress; Systolic, maximal pulsatile diameter; Diastolic, minimal pulsatile diameter ($n = 4$). Bland Altman plot shows the consistency of repeated measures within the samples (C). Healthy Perfusion (D) and angioplastied Balloon (E) arteries were cultured for 3 and 7 days in EasyFlow and their systolic and diastolic diameter, the intima-media thickness (IMT), and their dose-response to endothelial-independent vasodilator nitroglycerin (F) were quantified by Doppler ultrasound, $n = 2-4$.

likely due to the poor preservation in these conditions. In arteries cultured in flow conditions, the damaged media after injury corresponded to $21.7 \pm 11.6\%$ of the total vessel wall. In order to visualize the spatial effect of the injury, we quantified the distribution of nuclei within the vascular wall in culture, with or without injury. Results show that in non-injured samples, the static culture determined a baseline reduction of cell number in the media, and that the balloon injury almost completely

abolished cells in these samples (**Figure 5B**). In flow conditions, we observed a striking loss of cells close to the lumen upon injury, and an accumulation of cells in the distal part of the media, at the junction with the adventitia (**Figure 5B**). *En face* staining confirmed that balloon injury provoked extensive endothelial denudation in both culture system and that the alignment of the F-actin fibers was lost in the flow culture, as a result of extension damage (**Figures 5C,D**). Immunofluorescence analysis

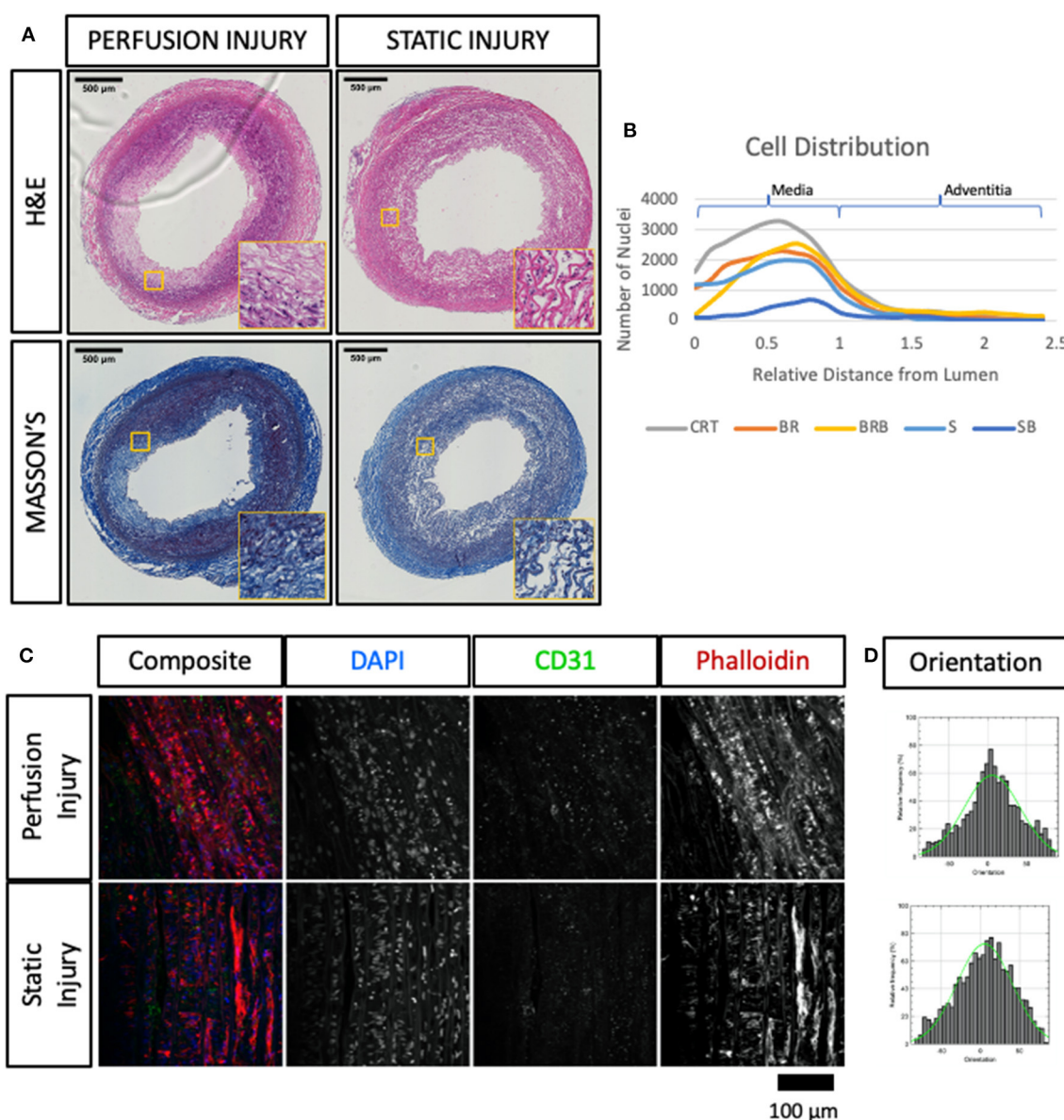


FIGURE 5 | Immuno-histological evaluation of angioplastied carotid arteries after culture reveal functional and structural damage. Injured vessels were cultured in EasyFlow (Perfusion Injury) or in static conditions (Static Injury) for 7 days and analyzed by Hematoxylin and Eosin staining (H&E) and Masson's Trichomic staining (MASSON'S) (**A**). Scale bars = 500 μm. Distribution of DAPI+ nuclei across the vessel wall is quantified in freshly isolated arteries (CRT), healthy and injured arteries cultured for 7 days in EasyFlow (BR and BRB, respectively) or static conditions (S and SB, respectively) (**B**). *En-Face* representative images showing endothelial coverage (CD31), stress fiber (Phalloidin), and nuclei (DAPI) in samples cultured for 7 days in perfusion or static after injury (**C**). Fiber alignment is quantified as vector distribution and plotted in histogram representing the relative frequency (y) against the angle (x), where zero is perpendicular to the flow direction (Orientation). An ideal normal distribution of values is represented in green over the histogram (**D**). Scalebar = 100 μm.

confirmed the significant loss of endothelial coverage, and a mild reduction in medial SMA expression in vessels cultured in flow after injury, which is likely due to large areas of damage produced in the media (**Figures 6A–C**).

Taken together these results show that EasyFlow cultured arteries subjected to endovascular damage present areas of cell loss and functional impairment, but maintain overall structural integrity.

Injured Arteries Cultured in EasyFlow Present Signs of Remodeling

In vivo, vascular injury leads to extensive apoptosis and cell replacement, which triggers the activation of the vascular wall progenitor niche and the synthetic switch of vascular smooth muscle cells. Pathological remodeling generally follows, with the formation of fibrosis, neointimal growth or atherosclerotic plaques.

We analyzed the arteries cultured for 7 days in static or EasyFlow post-injury. Overall proliferation was uniquely increased in the injured samples cultured in flow (**Figure 6D**), and the PCNA+ cells were mainly localized at the interface between the media and the intima, and in the luminal side of the media (**Figures 6A,E**). Proliferating cells mainly co-expressed SMA, and were found largely in undamaged area of the media (**Figure 7ai**), however we also detected a unique population of proliferative SMA+ cells, separated from the injured media, and located beneath the lamina elastica (**Figure 7a_{ii}**). It was also possible to identify the occasional proliferative CD31+ cell in the intima (**Figure 7ai**) and the adventitia (**Figure 7a_{iii}**). Organized microvascular structures can also be observed penetrating the media after injury (**Figure 7a**, red arrowhead), as well as infiltrating mono-nucleated cells which could potentially represent resident immune cells (**Figure 7a**, orange arrowhead).

Immunostaining also revealed that in the border zone near the medial damage, smooth muscle cells strongly expressed SMA, Vimentin and PDGFR β (**Figures 7b–d**). This indicates that smooth muscle cells in these areas were provoked into the synthetic phase by the injury.

Our results showed that culture under flow better recapitulate the early characteristics of post-injury vascular remodeling, as compared to static culture, and that early hallmarks of activation and remodeling can be identified in flow cultures by histology and ultrasound imaging.

DISCUSSION

In this study we presented a 3D printed bioreactor that is economical to produce, easily transferable to other labs and enables small volume cultures and multiplexing. EasyFlow cultures can be imaged longitudinally by Doppler ultrasound, enabling the monitoring of flow conditions and tissue integrity in a non-invasive manner. Using EasyFlow bioreactor, porcine carotid arteries can be cultured in pulsatile flow conditions closely resembling the mammalian arterial circulation. When compared to static cultures, tissue integrity and organization was superior in flow cultures. Endovascular balloon injury provoked

intimal denudation and media damage, also detected by Doppler ultrasound imaging. After injury, samples cultured in EasyFlow showed increased proliferation in the media and adventitia, and overexpression of smooth muscle markers near the injury. A small population of highly proliferative SMA+ cells was also observed at the intima/media interface. Samples cultured in static were instead significantly compromised and did not show signs of activation.

The study of vascular physiology and pathology is often pursued with the use of moderate severity animal models such as carotid ligation or wire injury, in some case presenting genetic mutations to emulate specific co-morbidities such as diabetes [db/db mice; homozygous for the diabetes-inducing spontaneous mutation (Lepr^{db})] and hypercholesterolemia (apolipoprotein E knockout mice; ApoE^{-/-}) (3). These *in vivo* experiments are routinely supported by *in vitro* work to help elucidate mechanistic insights, using static monocultures of vascular cells, which struggle to recapitulate the physiologically relevant mechanical cues and the interaction with other cell types.

Despite these limitations, these models delivered great insights in the understanding of the mechanisms of vascular homeostasis and the patterns associated with common diseases, such as atherosclerosis and restenosis (13). The striking physiological differences have however determined disappointing outcomes for some of the therapeutic approaches in clinical settings, sparking new interest in large animal models for these diseases (14). However, ethical and economic implications associated with this type of animal work demands new solutions.

Vascular bioreactors have been developed both at commercial level and in-house to provide a suitable physiological environment to maintain blood vessels in culture or enhance the maturation of tissue engineered constructs.

In this study, we present a 3D printed bioreactor that enables the culture of blood vessels within a 50 ml centrifuge tube, enabling small volume cultures and multiplexing. Previous work has demonstrated the feasibility and practicality of a bioreactor designed to fit as a lid of a 50 ml tube, however our system is distinctive as the whole insert is created entirely by 3D printing (15, 16).

EasyFlow's open-access design allows simple uptake by other labs, and the adjustable vessel compartment enables customization to different vessel sizes and tissue sources by simply exchanging the barbed connectors and adjusting the length adapters.

Dynamic bioreactors supply culture conditions that are as close as possible to the *in vivo* environment experienced by the blood vessel in its natural location. Pump revolution rate was adjusted to impose a “heart rate” of 56 beats/min to simulate resting heart rate and continue pressure monitoring confirmed a physiological range of 60–120 mmHg, which is compatible to the average healthy blood pressure in the human population. Common carotid arteries experience a mean flow velocity of 15–43 cm/s (end diastolic-peak systolic) and a wall shear stress in the range of 6–21 dyne/cm² (17, 18). EasyFlow culture conditions provide a *in vivo* relevant environment in the culture, with a mean flow velocity of 44 ± 8 cm/s, resulting in a calculated volumetric flow rate of 33 ± 16 ml/min and

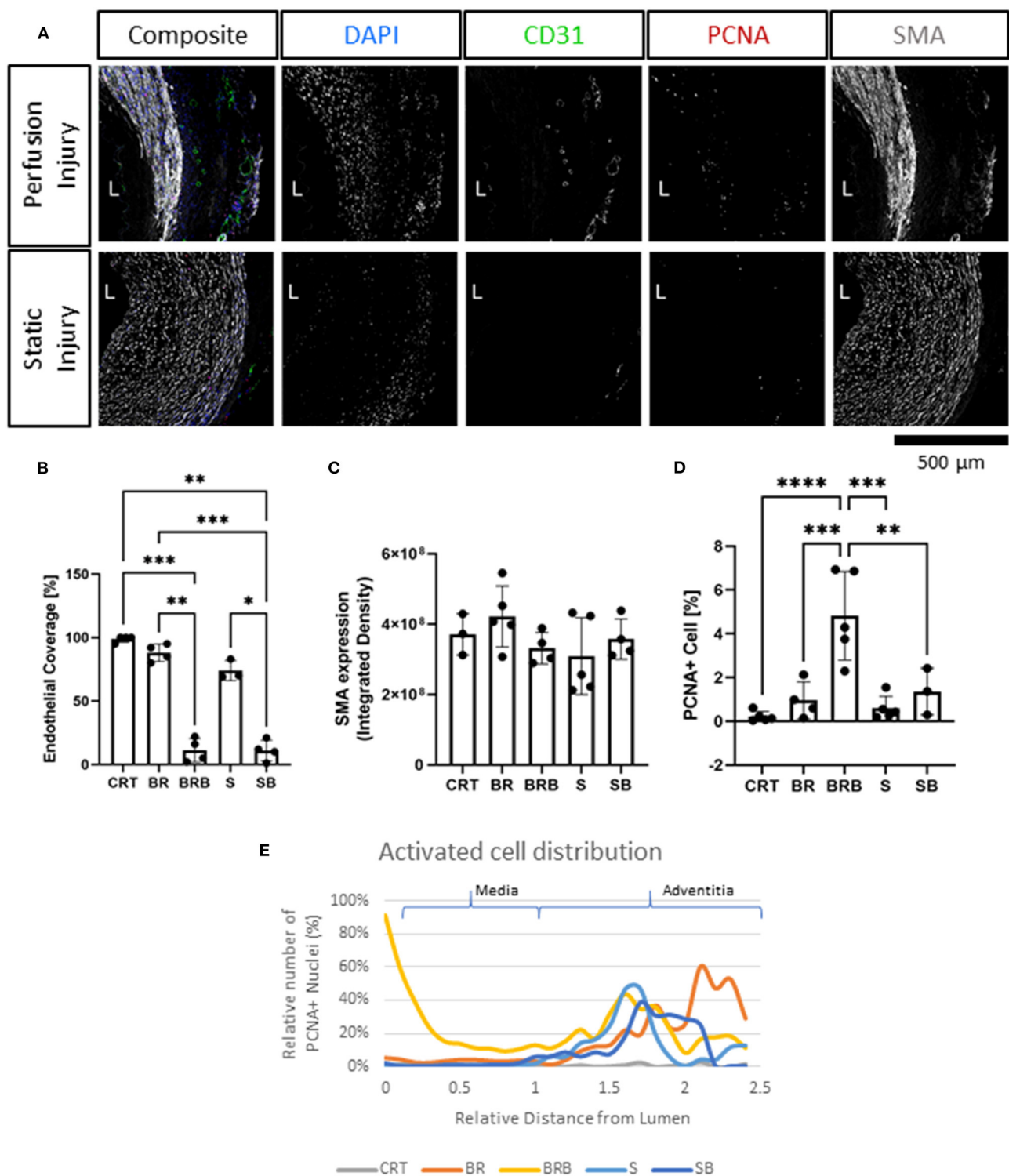
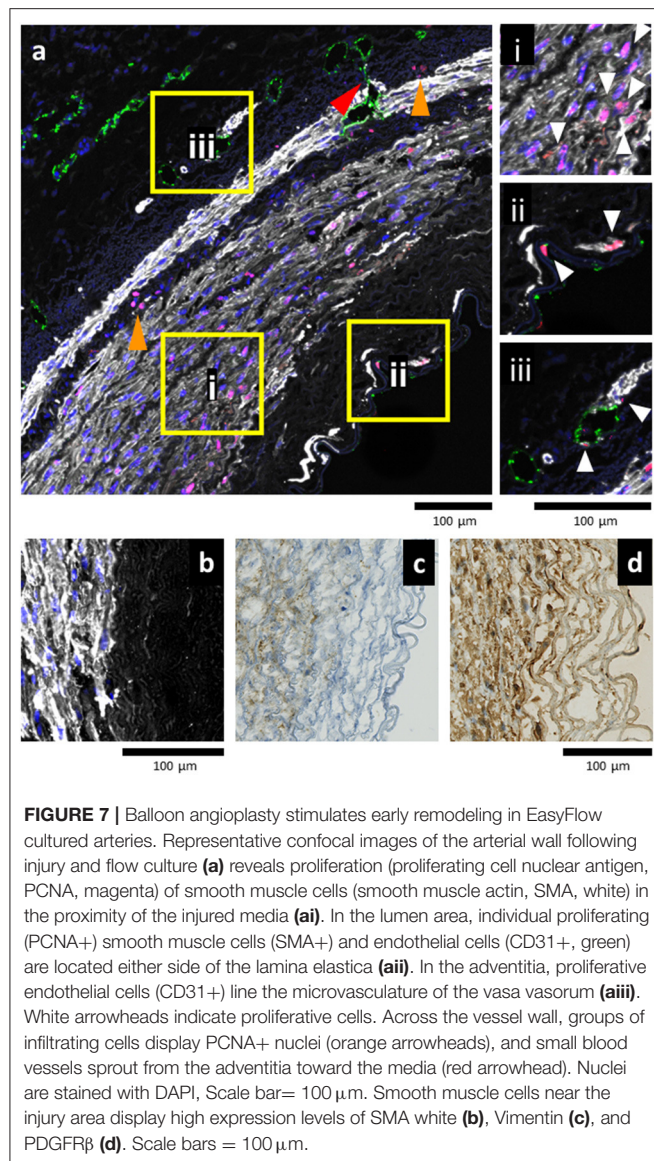


FIGURE 6 | Immunofluorescence evaluation reveals tissue injury and activation following balloon angioplasty and culture in flow. Following injury, tissues were cultured for 7 days in either perfusion (Perfusion Injury) or static conditions (Static Injury) and then stained for the endothelial marker (CD31), smooth muscle marker (smooth muscle actin, SMA), and proliferation marker (proliferating cell nuclear antigen, PCNA). Nuclei are stained with DAPI. Representative confocal images are displayed in composites and by individual marker in montage (**A**). Lumen is identified (L), Scalebar= 500 μ m. Quantifications of lumen coverage (**B**), SMA intensity (**C**), and proliferation PCNA (**D**) are displayed in the bar graphs, $n = 3-5$. All data are mean \pm SD. One-Way ANOVA analysis was performed, $*p \leq 0.05$, $**p \leq 0.01$, $***p \leq 0.001$, $****p \leq 0.0001$. Distribution of proliferating cells (PCNA+) in relation to their relative distance to the lumen is plotted for freshly isolated arteries (CRT), healthy and injured arteries cultured in EasyFlow (BR and BRB, respectively) or static conditions (S and SB, respectively) (**E**).



a mean wall shear stress of 10.1 ± 2.8 dyne/cm², which are comparable to the arterial flow forces *in vivo*. It is important to highlight that more sophisticated systems for the regulation of the pressure loop, and the shape of the pressure curve exist and have been developed for specific bioreactor applications. While EasyFlow is a more simplified version, this is a compromise that fulfills the critical characteristic of an end-user friendly system (15, 16).

In addition, we modified the medium composition to simulate the viscosity of blood (3.5–5.5 cP), this parameter closely affects the shear stress experienced by vascular cells in flow, according to the Hagen-Poiseuille equation (18).

Our in-depth consideration and characterization of the conditions and forces acting on the vessel in culture is uncommon in previously published studies (9, 19–21). Importantly, these forces were initially estimated by calculation,

but also verified within the cultured blood vessel by Doppler ultrasound imaging. While few examples exist in literature, we present a uniquely exhaustive application of the Doppler ultrasound method to a bioreactor culture. This analysis enables direct comparison with large animal and patient studies, and allows to visualize vessel structure and functionality over time (22).

When compared to static culture, EasyFlow cultured arteries demonstrated an overall better maintenance of tissue integrity and structure. In particular, the organization of the smooth muscle cells and the extracellular matrix were closer to the native tissue. Interestingly, we did not detect a critical difference in lumen coverage, apoptosis or activation of the vessel wall in the two culture systems. This is not completely unexpected as the static culture was designed to replicate the vessel ring culture, with tissue specimens of 2–5 mm in length (5, 23–25). Previous studies have demonstrated that static culture of rings can be extended up to 56 days, and can be induced to form neointima post-injury, although we did not detect such a growth in our samples (24). Samples cultured in flow were instead much longer (2–4 cm), and would not likely have survived in static culture due to limited oxygen and nutrient diffusion. We purposely elected to compare our flow culture system with the vessel ring model as this represents the most standardized and user-friendly whole vessel culture system currently available. By demonstrating that EasyFlow can not only achieve similar (or better) survival of much larger portions of the vessel, but also incorporate mechanical factors that provide crucial stimuli absent in the static culture, we effectively propose a superior and equally ingenious solution for blood vessel culture.

After verifying the feasibility of a pulsatile culture using EasyFlow, we assessed the effect of injury in the flow cultures. We delivered the injury before setting up the static or flow culture, but it is important to note that, thanks to the multiple access ports available on EasyFlow, the catheter-mediated balloon injury could potentially be implemented on the mounted sample at any point of the culture, without disturbing the system.

In vivo, mechanical damage and flow disruption, accompanied by damage to the medial layer (for example by large balloons), results in smooth muscle cells activation, proliferation and migration into the intima layer, contributing to the thickening of the vessel wall and effectively narrowing the lumen (restenosis) (26, 27). Adventitial cells, such as resident progenitor cells and pericytes, macrophages and fibroblasts also become activated after injury, releasing cytokines and growth factors and migrating toward the lumen; their contribution to neointimal lesions and the mechanisms associated with it are still highly debated (28, 29).

Following balloon application and flow culture, we observed significant damage to the intima and media layers of the tissue, which is comparable to what reported in similar animal models where intima denudation and early media apoptosis drive the regeneration process (30). In addition, the surviving smooth muscle cells in the media responded to the injury by initiating a robust proliferative response. This is akin to the results obtained after 1 week in rabbit iliac arteries, even in terms of percentage of proliferative cells (roughly 4%) (31). Other hallmarks of early remodeling included the upregulation of contractile proteins in

the smooth muscle cells adjacent the injury, and the proliferation of cells in the adventitia.

Interestingly, we did not observe the formation of neointima. This is likely due to the limited timeline of the experiment, as usually neointima forms *in vivo* after at least 2 weeks in rabbits, a typical model for vascular remodeling (31). However, we cannot exclude that large animals may react differently to angioplasty injury. For example, *in vivo* studies in pigs failed to detect significant reduction in lumen area even 2–4 weeks after balloon injury (32, 33).

On the other hand, previously published *ex vivo* work demonstrated that flow culture of porcine arteries is amenable for detection of restenosis 7 days after placement of a stent, this could be due to the smaller damage provoked by the stent as compared to the balloon, and the permanence of the ‘stimulus’ as the stent remains in place after intervention (6). Similarly, low impact stimulation such as non-physiological low flow and intima denudation reportedly led to formation of neointima in vessels cultured under flow (6, 9).

After balloon injury, the loss of contractility in the vessel wall was quantifiable in the ultrasound profile at baseline levels and following challenge with vasoconstrictors. In addition, we were able to quantify an increase in IMT, a commonly used clinical indicator of remodeling (34). In samples cultured for 7 days after vascular injury IMT was increased, a measure that is associated with increased risk of stenosis-atherosclerosis in patients.

One critical characteristic of EasyFlow is that its open-source 3D printed nature enables easy adoption by other labs, and encourages reproducibility (see **Supplementary File 1** for printing file). This is fundamentally different from previously proposed systems, which were either based on commercially available bioreactors or in house-built systems (6–9, 15, 16). Furthermore, bioreactors often leverage on the use of specialized glassware fitted with homemade connectors (6, 9) or more complex arrangements (7, 8), the details of which are regularly insufficiently described and designs undisclosed. The EasyFlow insert fits as the lid of a common laboratory 50 ml centrifuge tube, removing the need for specialized glassware. This approach was previously successfully proposed by Piola et al. (16) as the receptacle for their pulsatile pressure culture system for arterial conditioning of bypass vein material. EasyFlow entirely 3D printed design and simplified yet *in vivo* relevant culture conditions offer an improved off-the-shelf simplicity, uncommon in previously developed systems. The compactness of the EasyFlow insert enables multiplex cultures within a normal incubator where different flow/pressure conditions or interventions can be run independently by connecting each bioreactor/reservoir pair to a separate pump head. Many other designs are bulkier (6, 9) or driven by a single pump, limiting the options for parallel comparisons. In addition, EasyFlow uses small volumes of medium (~100 ml), similar to previously developed small volume bioreactors (15, 16), but much lower as compared to other published systems which required up to 500 ml (8), although in many cases the total volume of medium is not explicit and therefore cannot be compared (6, 9). Lower volume experiments (~50 ml) are also possible with EasyFlow by establishing a recirculating system without the

addition of the reservoir, enabling low-cost pharmacological studies. Lastly, commercial bioreactors exist (i.e., VABIO by LifeTec and 3DCulturePro by TA Instruments) and represent a practical solution to many users. The limitation is the cost, which is upward of £10 K, and the rigidity of the design. Even with the outsourcing of the 3D printing, the reusable EasyFlow inserts can be produced cheaply (<£100 per piece), a price that can be further reduced if in-house 3D printing is available. The multiple ports on the EasyFlow insert also permits customization by offering inlets for additional sensors and other specific applications.

This proof of principle study demonstrated with an in-depth characterization of the quality of the tissue after culture, which is uncommon in other engineering-focused papers (7, 8), the suitability of EasyFlow for pulsatile culture of large animal arteries and the study of pathological processes. Overall, our study highlighted the scientific relevance of our *ex vivo* model and the versatility for both basic and interventional studies.

DATA AVAILABILITY STATEMENT

All raw data, images, and analyses supporting the findings of this study are available through the online repository Zenodo (<https://doi.org/10.5281/zenodo.6584173>).

ETHICS STATEMENT

The animal study was reviewed and approved by Animal Welfare and Ethical Review Board (AWERB) of the Pirbright Institute. All procedures were conducted by Personal License holders who were trained and competent and under the Project License PPL70/8852.

AUTHOR CONTRIBUTIONS

RM conceived, planned the experiments, and analyzed the data with contribution by CH. DM and CH provided key experimental expertise. RM and PC wrote the manuscript and prepared the figures with support of CH. PC, CH, and JM conceived the original idea and supervised the project. All authors contributed to the article and approved the submitted version.

FUNDING

RM was supported by the Doctoral College studentship award (University of Surrey). DM and PC were supported by the National Center for the Replacement, Refinement & Reduction of Animals in Research (grant numbers: NC/R001006/1 and NC/T001216/1).

ACKNOWLEDGMENTS

The authors wish to thank the Veterinary Pathology Centre at the University of Surrey's School of Veterinary Medicine for histology services and the Histology Research Service, Veterinary Diagnostic Services, University of Glasgow. We also thank

Drs L. Dixon, A Reis and M. Henstock from the Pirbright Institute (Pirbright, UK) for their support in procuring the animal tissues, and the Department of Biochemical Sciences at the University of Surrey, especially the technical team, for their continuing support.

REFERENCES

- Beckman JA, Schneider PA, Conte MS. Advances in revascularization for peripheral artery disease: revascularization in PAD. *Circ Res.* (2021):1885–912. doi: 10.1161/CIRCRESAHA.121.318261 (accessed January 25, 2022).
- Frank U, Nikol S, Belch J, Boc V, Brodmann M, Carpentier PH, et al. ESVM guideline on peripheral arterial disease. *VASA.* (2019) 48:1–80. doi: 10.1024/0301-1526/a000834
- Xu Q. Mouse models of arteriosclerosis : from arterial injuries to vascular grafts. *Am J Pathol.* (2004) 165:1. Available online at: <https://pubmed.ncbi.nlm.nih.gov/15215157/> (accessed January 25, 2022).
- Nakazawa G, Finn A V., Joner M, Ladich E, Kutys R, Mont EK, et al. Delayed arterial healing and increased late stent thrombosis at culprit sites after drug-eluting stent placement for acute myocardial infarction patients: an autopsy study. *Circulation.* (2008) 118:1138–45. doi: 10.1161/CIRCULATIONAHA.107.762047 (accessed January 25, 2022).
- Voisard R, Zellmann S, Müller F, Fahlisch F, von Müller L, Baur R, et al. Sirolimus inhibits key events of restenosis *in vitro/ex vivo*: Evaluation of the clinical relevance of the data by SI/MPL- and SI/DES-ratio's. *BMC Cardiovasc Disord.* (2007) 7:1–10. doi: 10.1186/1471-2261-7-15 (accessed January 25, 2022).
- Wang J, Kural MH, Wu J, Leiby KL, Mishra V, Lysy T, et al. An *ex vivo* physiologic and hyperplastic vessel culture model to study intra-arterial stent therapies. *Biomaterials.* (2021) 275:120911. doi: 10.1016/j.biomaterials.2021.120911
- Maurel B, Sarraf C, Bakir F, Chai F, Maton M, Sobocinski J, et al. A new hemodynamic *ex vivo* model for medical devices assessment. *Ann Vasc Surg.* (2015) 29:1648–55. doi: 10.1016/j.avsg.2015.06.066
- Conklin BS, Surowiec SM, Lin PH, Chen C. A simple physiologic pulsatile perfusion system for the study of intact vascular tissue. *Med Eng Phys.* (2000) 22:441–9. doi: 10.1016/s1350-4533(00)00052-7
- Kural MH, Dai G, Niklason LE, Gui L. An *ex vivo* vessel injury model to study remodeling. *Cell Transplant.* (2018) 27:1375. Available online at: <https://pubmed.ncbi.nlm.nih.gov/30168986/> (accessed January 25, 2022).
- Kural MH, Dai G, Niklason LE, Gui L. An *ex vivo* vessel injury model to study remodeling. *Cell Transplant.* (2018) 27:1375–89. doi: 10.1177/0963689718792201 (accessed November 12, 2022).
- Meadow W, Rudinsky B, Raju T, John E, Fornell L, Shankararao R. Correlation of flow probe determinations of common carotid artery blood flow and internal carotid artery blood flow with microsphere determinations of cerebral blood flow in piglets. *Pediatr Res.* (1999) 45:324–30. Available online at: <https://www.nature.com/articles/pr199933> (accessed January 25, 2022).
- Irace C, Carallo C, De Franceschi MS, Scicchitano F, Milano M, Tripolino C, et al. Human common carotid wall shear stress as a function of age and gender: a 12-year follow-up study. *Age.* (2012) 34:1553. Available online at: <https://pubmed.ncbi.nlm.nih.gov/228365/> (accessed January 25, 2022).
- Qiu J, Zheng Y, Hu J, Liao D, Gregersen H, Deng X, et al. Biomechanical regulation of vascular smooth muscle cell functions: from *in vitro* to *in vivo* understanding. *J R Soc Interface.* (2014) 11:6323. Available online at: <https://pubmed.ncbi.nlm.nih.gov/25386323/> (accessed January 25, 2022).
- Shim J, Al-Mashhadi RH, Sørensen CB, Bentzon JF. Large animal models of atherosclerosis—new tools for persistent problems in cardiovascular medicine. *J Pathol.* (2016) 238:257–66. Available online at: <https://pubmed.ncbi.nlm.nih.gov/26414760/> (accessed January 25, 2022).
- Piola M, Ruitter M, Vismara R, Mastrullo V, Agrifoglio M, Zanobini M, et al. Full mimicking of coronary hemodynamics for *ex-vivo* stimulation of human saphenous veins. *Ann Biomed Eng.* (2016) 45:884–97. doi: 10.1007/s10439-016-1747-7 (accessed April 20, 2022).
- Piola M, Prandi F, Bono N, Soncini M, Penza E, Agrifoglio M, et al. A compact and automated *ex vivo* vessel culture system for the pulsatile pressure conditioning of human saphenous veins. *J Tissue Eng Regen Med.* (2016) 10:E204–15. doi: 10.1002/term.1798 (accessed April 10, 2022).
- Sui B, Gao P, Lin Y, Gao B, Liu L, An J. Assessment of wall shear stress in the common carotid artery of healthy subjects using 3.0-tesla magnetic resonance. *Acta radiol.* (2008) 49:442–9. doi: 10.1080/02841850701877349 (accessed January 25, 2022).
- Jeong SK, Rosenson RS. Shear rate specific blood viscosity and shear stress of carotid artery duplex ultrasonography in patients with lacunar infarction. *BMC Neurol.* (2013) 13:1–7. doi: 10.1186/1471-2377-13-36 (accessed January 25, 2022).
- Ma X, He Z, Li L, Liu G, Li Q, Yang D, et al. Development and *in vivo* validation of tissue-engineered, small-diameter vascular grafts from decellularized aortae of fetal pigs and canine vascular endothelial cells. *J Cardiothorac Surg.* (2017) 12:1–11. doi: 10.1186/s13019-017-0661-x (accessed January 25, 2022).
- Liao D, Lin PH, Yao Q, Chen C. Vascular smooth cell proliferation in perfusion culture of porcine carotid arteries. *Biochem Biophys Res Commun.* (2008) 372:668. Available online at: <https://pubmed.ncbi.nlm.nih.gov/182925440/> (accessed January 25, 2022).
- Halkos ME, Surowiec SM, Conklin BS, Lin PH, Lumsden AB. Effects of homocysteine on smooth muscle cell proliferation in both cell culture and artery perfusion culture models. *J Surg Res.* (2000) 88:26–33. doi: 10.1006/jsre.1999.5756
- Sansone R, Baaken M, Horn P, Schuler D, Westenfeld R, Amabile N, et al. Release of endothelial microparticles in patients with arterial hypertension, hypertensive emergencies and catheter-related injury. *Atherosclerosis.* (2018) 273:67–74. Available online at: <https://pubmed.ncbi.nlm.nih.gov/29684662/> (accessed January 25, 2022).
- Voisard R, Jensch V, Baur R, Hoher M, Hombach V. A coronary porcine organ culture system for studies of postangioplasty cell proliferation. *Coron Artery Dis.* (2022) 6:657–65. Available online at: <https://pubmed.ncbi.nlm.nih.gov/3574462/> (accessed January 25, 2022).
- Voisard R, Eicken J V., Baur R, Gschwend JE, Wenderoth U, Kleinschmidt K, et al. A human arterial organ culture model of post-angioplasty restenosis: results up to 56 days after ballooning. *Atherosclerosis.* (1999) 144:123–34. doi: 10.1016/s0021-9150(99)00046-5
- Haase D, Otto S, Romeike BFM, Figulla HR, Poerner TC. Development and characterization of an *ex vivo* arterial long-term proliferation model for restenosis research. *ALTEX - Altern to Anim Exp.* (2015) 32:307–17. Available online at: <https://www.altex.org/index.php/altex/article/view/212> (accessed January 25, 2022).
- Mayr U, Zou Y, Zhang Z, Dietrich H, Hu Y, Xu Q. Accelerated arteriosclerosis of vein grafts in inducible NO synthase(-/-) mice is related to decreased endothelial progenitor cell repair. *Circ Res.* (2006) 3:412–20. Available online at: <https://pubmed.ncbi.nlm.nih.gov/16385078/> (accessed January 25, 2022).
- Bennett MR, O'Sullivan M. Mechanisms of angioplasty and stent restenosis: implications for design of rational therapy. *Pharmacol Ther.* (2001) 91:149–66. doi: 10.1016/s0163-7258(01)00153-x
- Tang Z, Wang A, Yuan F, Yan Z, Liu B, Chu JS, et al. Differentiation of multipotent vascular stem cells contributes to vascular diseases. *Nat Commun.* (2012) 3. Available online at: <https://pubmed.ncbi.nlm.nih.gov/22673902/> (accessed January 25, 2022).
- Campagnolo P, Katare R, Madeddu P. Realities and misconceptions on the pericytes role in tissue repair. *Regen Med.* (2018) 13:119–22. doi: 10.2217/rme-2017-0091 (accessed January 25, 2022).

SUPPLEMENTARY MATERIAL

The Supplementary Material for this article can be found online at: <https://www.frontiersin.org/articles/10.3389/fcvm.2022.864580/full#supplementary-material>

30. Perlman H, Maillard L, Krasinski K, Walsh K. Evidence for the rapid onset of apoptosis in medial smooth muscle cells after balloon injury. *Circulation*. (1997) 95:981–7. doi: 10.1161/01.cir.95.4.981 (accessed January 25, 2022).
31. Strauss BH, Chisholm RJ, Keeley FW, Gotlieb AI, Logan RA, Armstrong PW. Extracellular matrix remodeling after balloon angioplasty injury in a rabbit model of restenosis. *Circ Res*. (1994) 75:650–8. doi: 10.1161/01.RES.75.4.650 (accessed January 25, 2022).
32. Houbballah R, Robaldo A, Albadawi H, Titus J, Lamuraglia GM. A novel model of accelerated intimal hyperplasia in the pig iliac artery. *Int J Exp Pathol*. (2011) 92:422–7. Available online at: <https://pubmed.ncbi.nlm.nih.gov/22050434/> (accessed April 20, 2022).
33. Kong J, Hou J, Ma L, Xing L, Jia H, Liu H, et al. Cutting balloon combined with paclitaxel-eluting balloon for treatment of in-stent restenosis. *Arch Cardiovasc Dis*. (2013) 106:79. doi: 10.1016/j.acvd.2012.10.004
34. Keymel S, Heinen Y, Balzer J, Rassaf T, Kelm M, Lauer T, et al. Characterization of macro- and microvascular function and structure in patients with type 2 diabetes mellitus. *Am J Cardiovasc Dis*. (2011) 1:68. Available online at: <https://pmc/articles/PMC3253507/> (accessed January 25, 2022).

Conflict of Interest: The authors declare that the research was conducted in the absence of any commercial or financial relationships that could be construed as a potential conflict of interest.

Publisher's Note: All claims expressed in this article are solely those of the authors and do not necessarily represent those of their affiliated organizations, or those of the publisher, the editors and the reviewers. Any product that may be evaluated in this article, or claim that may be made by its manufacturer, is not guaranteed or endorsed by the publisher.

Copyright © 2022 Matos, Maselli, McVey, Heiss and Campagnolo. This is an open-access article distributed under the terms of the Creative Commons Attribution License (CC BY). The use, distribution or reproduction in other forums is permitted, provided the original author(s) and the copyright owner(s) are credited and that the original publication in this journal is cited, in accordance with accepted academic practice. No use, distribution or reproduction is permitted which does not comply with these terms.



OPEN ACCESS

EDITED BY

Laura Iop,
University of Padua, Italy

REVIEWED BY

Bruno Reichart,
Ludwig Maximilian University
of Munich, Germany
Mitchell VeDepo,
University of Colorado, United States
Jayan Nagendran,
University of Alberta, Canada

*CORRESPONDENCE

Samir Sarikouch
sarikouch.samir@mh-hannover.de

SPECIALTY SECTION

This article was submitted to
Heart Valve Disease,
a section of the journal
Frontiers in Cardiovascular Medicine

RECEIVED 14 March 2022

ACCEPTED 13 July 2022

PUBLISHED 09 August 2022

CITATION

Oripov F, Ramm R, Falk C, Goecke T,
Ebken J, Jashari R, Böthig D, Horke A,
Avsar M, Bobylev D, Haverich A,
Hilfiker A and Sarikouch S (2022) Serial
assessment of early antibody binding
to decellularized valved allografts.
Front. Cardiovasc. Med. 9:895943.
doi: 10.3389/fcvm.2022.895943

COPYRIGHT

© 2022 Oripov, Ramm, Falk, Goecke,
Ebken, Jashari, Böthig, Horke, Avsar,
Bobylev, Haverich, Hilfiker and
Sarikouch. This is an open-access
article distributed under the terms of
the [Creative Commons Attribution
License \(CC BY\)](#). The use, distribution
or reproduction in other forums is
permitted, provided the original
author(s) and the copyright owner(s)
are credited and that the original
publication in this journal is cited, in
accordance with accepted academic
practice. No use, distribution or
reproduction is permitted which does
not comply with these terms.

Serial assessment of early antibody binding to decellularized valved allografts

Firdavs Oripov¹, Robert Ramm¹, Christine Falk²,
Tobias Goecke^{2,3}, Johannes Ebken¹, Ramadan Jashari⁴,
Dietmar Böthig³, Alexander Horke³, Murat Avsar³,
Dmitry Bobylev³, Axel Haverich^{1,3}, Andres Hilfiker^{1,3} and
Samir Sarikouch^{3*}

¹Leibniz Research Laboratories for Biotechnology and Artificial Organs (LEBAO), Hannover Medical School, Hanover, Germany, ²Institute of Transplant Immunology, Hannover Medical School, Hanover, Germany, ³Department of Cardiothoracic, Transplantation and Vascular Surgery, Hannover Medical School, Hanover, Germany, ⁴European Homograft Bank, Clinique Saint-Jean, Brussels, Belgium

Objectives: Decellularized homograft valves (DHV) appear to elicit an immune response despite efficient donor cell removal.

Materials and methods: A semiquantitative Dot-Blot analysis for preformed and new recipient antibodies was carried out in 20 patients following DHV implantation on days 0, 1, 7, and 28 using secondary antihuman antibodies. Immune reactions were tested against the implanted DHV as well as against the stored samples of 5 non-implanted decellularized aortic (DAH) and 6 pulmonary homografts (DPH).

Results: In this study, 20 patients (3 female and 17 male patients) were prospectively included, with a median age of 18 years and an IQR of 12–30 years. Six patients received DPH and 14 received DAH. The amount of antibody binding, averaged for all patients, decreased on post-operative days 1 and 7 compared to pre-operative values; and on day 28, antibody binding reached close to pre-operative levels (16.8 ± 2.5 on day 0, 3.7 ± 1.9 on day 1, 2.3 ± 2.7 on day 7, and 13.2 ± 3.7 on day 28). In comparison with the results in healthy controls, there was a higher amount of antibody binding to DAH than to DPH. The mean number of arbitrary units was 18.4 ± 3.1 in aortic and 12.9 ± 4.5 in pulmonary DHV ($p = 0.140$). Male patients exhibited higher antibody binding to aortic DHV than female patients (19.5 ± 2.1 vs. 1.6 ± 6.7). The p -value calculation was limited, as only two female patients received DAH. There was no correlation between the amount of overall antibody binding to DHV with respect to donor age (Kruskal–Wallis test $p = 0.550$). DHV recipients with a sex mismatch to the donor showed significantly less antibody binding (6.5 ± 1.8 vs. 13.7 ± 1.8 ; $p = 0.003$). Our main finding was an increase in antibody binding in younger patients receiving decellularized aortic allografts. This increase was higher in patients with early degeneration signs but was not specific to the individual DHV implanted nor previous

DHV implantation. Antibody binding toward explanted DHV was significantly increased in implicating antibody-mediated DHV degeneration.

Conclusion: Serial assessment of tissue-specific antibody binding revealed an increase in some patients within 4 weeks after surgery, who subsequently developed early signs of allograft degeneration. Further studies with larger sample sizes are needed to confirm the prognostic relevance of increased antibody activity in addition to targeted research efforts to identify the molecular agents triggering this type of antibody response.

KEYWORDS

heart valve replacement, homograft, decellularization, immune system, antibodies

Introduction

Decellularized homografts are currently the only clinically applied tissue-engineered heart valves and have shown superior performance in comparison with conventional cryopreserved allografts in a recent meta-analysis for pulmonary valve replacement. Reoperation rates in 1,418 patients who underwent outflow tract reconstructions with decellularized heart valves (DHV) were significantly lower than in the 2,725 patients who received conventional allografts (4.8 vs. 7.4%; pooled risk ratio (RR) 0.55, 95% CI: 0.36 to 0.84; $p = 0.0057$) (1).

Despite almost complete decellularization, documented by standard microscopy and very low residual DNA content, DHV seem to elicit an immune response that appears to be stronger in younger recipients, indicated by progressing valve dysfunction (2). This has been observed especially in decellularized aortic homografts (DAH) recipients and may be explained by the fact that aortic homografts are considerably thicker, thereby potentially carrying more antigenic material. Classic T-cell-mediated immune response, considered to be the leading mechanism for the usually relatively slow mode of degeneration in cryopreserved heart valves, may not be the key mechanism in DHV degeneration.

In an initial analysis of immune reactions to DHV in children and young adults, we did not find significant changes in peripheral cell counts, which were followed up to 3 years after implantation, for mature T-(CD3 +), B-(CD19 +), and natural killer-(CD16 + /CD56 +) cells and for T helper-(CD4 +) and cytotoxic T-cell-(CD8 +) subsets (3). In a systematic *in vivo* recellularization analysis of explanted DHV and biopsy material, we did not observe classic T-cell infiltration, even in the case of an adult patient following a Ross procedure with rapid degeneration of his pulmonary DHV (4). This led to the hypothesis that DHV degeneration may be predominantly antibody-mediated, based on the observed temporal increase in DHV-specific IgG levels in 14 patients following decellularized DHV (5) and the results of a newly

developed Dot-Blot technique for decellularized porcine heart valves (6). These results indicated substantial binding of preformed human antibodies to decellularized xenogeneic heart valves with considerable variance in the individual immune response toward specific porcine samples.

In our initial analysis of preformed antibody binding to DHV in healthy controls with no known contact with allogeneic tissue, we observed that DHV bind preformed recipient antibodies, which might elicit an immune response. There was considerable interindividual heterogeneity and also wide variation between specific individual decellularized human specimens. Age played an important role, as expected, with a higher immune response in younger individuals (7). Significantly higher binding of preformed antibodies was observed in male subjects. These findings correlated with a recent study from Netherlands on the outcome of standard cryopreserved pulmonary homografts, which described considerably poorer outcomes in male patients (8).

The purpose of the current analysis was to measure antibody binding to DHV in patients with repaired congenital heart disease. Our aim was to (1) compare the amount of baseline preformed antibody binding in patients who had received different patch material and different heart valve substitutes to levels of antibody binding in healthy controls, and (2) to analyze the early impact of DHV implantation in these patients using the Dot-Blot test and echocardiography.

Materials and methods

Study design and patient selection

The study was registered with and approved by the local ethics committee (EC No. 7871_BO_S_2018). Patients were not selected randomly, but 20 consecutively operated patients receiving a decellularized homograft in the period October 2019 to May 2020 were included following informed consent

provided by the patients or the parents. Since 2008, there have been a total of 199 implantations of decellularized aortic homografts and 236 implantations of decellularized pulmonary homografts at Hannover Medical School.

A serial assessment of the individual *in vivo* immune response toward decellularized homograft valves (DHV) was performed using a Dot-Blot technique at 4 time points: pre-operation, post-operation on day 1, before discharge at day 7, and at day 28. Five patients opted against attending the last session of the blood withdrawal due to the potential risk of COVID-19 infection in the pandemic situation of autumn 2020.

Individual antibody binding for each patient was measured at the above outlined time points using stored samples of 5 non-implanted decellularized aortic (A1–A5) and 6 non-implanted pulmonary homografts (P1–P6). In 18 patients, it was possible to acquire tissue samples from the implanted DHV at the time of the operation, allowing these samples to be included in the serial assessments. In four patients who underwent DHV exchange or explantation, the assessment also included samples from the explanted allograft. In one of these patients, a retained DAH sample prior to implantation was also available.

Patient characteristics are displayed in **Table 1**. Patient No. 20 underwent a bilateral lung transplantation 18 months prior to a DAH procedure and was therefore on an immunosuppressive medication regimen. None of the other included patients were receiving immunosuppressive medication, e.g., steroids, at the time of operation and 6 months prior to the surgery. In addition, none of the patients suffered from metabolic syndrome, diabetes mellitus, or acquired

heart disease, such as systemic or pulmonary hypertension or coronary heart disease.

All 20 patients underwent echocardiographic follow-up over a mean period of 16.0 ± 4.7 months following DHV implantation.

Decellularized homografts

The decellularized homografts used in this study were processed by corlife oHG,¹ a Hannover-based tissue establishment. The decellularization process comprised approximately 30 different steps using a detergent-based, non-cryopreservation approach as described previously (9). Pulmonary allografts were treated under shaking conditions with a solution of 0.5% sodium deoxycholate (Sigma) and 0.5% sodium dodecyl sulfate (Carl Roth) for 36 h at room temperature. Homografts were washed with 0.9% NaCl solution and stored at 4°C until implantation. Histologically, each homograft was assessed after processing, and the residual dsDNA content was measured before and after processing prior to final release, the upper limit for release being 25 ng/ml. Reference samples of all homografts were stored for at least 1 year according to German law.

The non-implanted homografts used in this study were procured by the European Homograft Bank (EHB), Clinic

¹ www.corlife.eu

TABLE 1 Patient cohort characteristics.

| Patient no. | Sex | Age (years) | Valve | Indication | Blood group | Follow-up |
|-------------|-----|-------------|-----------|--------------------------|-------------|------------------------------|
| 1 | M | 15 | Aortic | Stenosis, first AVR | O + | 15 months, DAH echogenicity↑ |
| 2 | M | 11 | Aortic | Stenosis, first AVR | A – | 15 months, DAH intact |
| 3 | M | 16 | Pulmonary | Regurgitation, redo DPH | A + | 13 months, DPH echogenicity↑ |
| 4 | M | 14 | Pulmonary | Regurgitation, first PVR | A + | 10 months, DPH intact |
| 5 | M | 11 | Aortic | Stenosis, first AVR | A + | 18 months, DAH intact |
| 6 | M | 9 | Aortic | Regurgitation, first AVR | O + | 14 months, DAH echogenicity↑ |
| 7 | M | 6 | Aortic | Stenosis, redo DAH | O – | 23 months, DAH intact |
| 8 | F | 17 | Pulmonary | Regurgitation, first PVR | B + | 17 months, DPH intact |
| 9 | M | 16 | Aortic | Stenosis, first AVR | O + | 18 months, DAH intact |
| 10 | M | 15 | Aortic | Stenosis, redo DAH | O + | 13 months, DAH echogenicity↑ |
| 11 | M | 20 | Pulmonary | Regurgitation, redo DPH | A + | 17 months, DPH intact |
| 12 | M | 19 | Pulmonary | Regurgitation, first PVR | A + | 20 months, DPH intact |
| 13 | F | 21 | Aortic | Stenosis, first AVR | O + | 24 months, DAH intact |
| 14 | M | 46 | Aortic | Regurgitation, first AVR | O + | 16 months, DAH intact |
| 15 | M | 30 | Pulmonary | Stenosis, fourth PVR | O + | 13 months, DPH intact |
| 16 | M | 20 | Aortic | Stenosis, first AVR | O – | 25 months, DAH intact |
| 17 | M | 30 | Aortic | Stenosis, first AVR | O + | 12 months, DAH intact |
| 18** | M | 44 | Aortic | Stenosis, first AVR | O – | 12 months, DAH intact |
| 19 | M | 41 | Aortic | Regurgitation, first AVR | O + | 20 months, DAH intact |
| 20* | F | 29 | Aortic | Regurgitation, first AVR | A + | 15 months, DAH intact |

Pat *20 underwent bilateral lung transplantation 18 months prior to DAH, Pat **18 underwent chemotherapy 6 months prior to DAH.

DAH, decellularized aortic homograft; DPH, decellularized pulmonary homograft; AVR, aortic valve replacement; PVR, pulmonary valve replacement.

St. Jean, Brussels (Material Transfer Agreement 180718); the implanted homografts were procured by the EHB and the Deutsche Gesellschaft für Gewebetransplantation (DGFG Hannover).

Dot-Blot technique

The DHV tissues (approximately 500 mg pulverized tissue) were solubilized using collagenase II digestion, dotted on nitrocellulose membranes, and exposed to human serum. Bound human serum antibodies were detected using antihuman secondary antibodies, enabling detection with an ECL reagent. The assay was conducted as previously published with minor modifications (7).

Decellularized homograft valves were dotted in triplicates (10 µg/dot in 200 µl TBS), and a dilution series of human serum (1:16,000 to 1:512,000) serving as the standard was placed in duplicates on each membrane. Loaded glutaraldehyde (Polysciences Inc., Warrington, FL, United States) fixed and blocked membranes were incubated in human serum (1:400), diluted in 10% non-fat dry milk/TBS at 4°C overnight. Bound antibodies were detected by applying goat antihuman IgG, IgA, IgM-HRP secondary antibody diluted at 1:50,000 and ECL substrate (PerkinElmer, Waltham, MA, United States). Chemiluminescence signals were imaged with the ChemiDoc imager (Bio-Rad, Hercules, CA, United States; applied software settings: “chemi Blot,” 26 photos, 56 s exposure time, accumulation signal mode) and densitometrically quantified (in arbitrary units) with Image Lab 5.0 software (Bio-Rad, Hercules, CA, United States).

Test reproducibility and statistics

Technical triplicates were generated for all Dot-Blots in this study. The experimental variance was assessed using Cronbach's Alpha as an estimate for Tau-equivalent reliability. Cronbach's Alpha is a function of the number of items in a test, the average covariance between item pairs, and the variance of the total score. A reliability score greater than 0.8 indicates good internal consistency; a Cronbach's Alpha >0.9 indicates excellent consistency.

The test robustness and reproducibility of the established Dot-Blot method have been extensively tested in decellularized xenogeneic heart valves (6). The resulting interassay variance of 9.5% and the intra-assay variance of 9.2% showed that the test is highly reproducible. As the binding of the secondary antihuman antibodies after decellularization can lead to false-positive results due to remaining donor antibodies in the DHV, we introduced a baseline by loading a membrane with DHV that was not exposed to patient serum and subtracted the result for this membrane from each specific serum-incubated specimen.

The negative values after baseline subtraction observed in some cases can be explained by steric overlays between remaining donor antibodies and serum antibodies.

We included all medians of the arbitrary antibody-binding units that resulted from matching triplicates of sera of the 20 DHV recipients at the 4 standardized time points with 11 samples of DHV non-implanted test valves and 18 samples of the implanted valves. In two patients, it was not possible to extract material from the implanted valve without causing valve function impairment.

SPSS 27 (IBM Corporation, Somers, NY, United States), MedCalc (Statistical Software version 20.015 from MedCalc Software bv, Ostend, Belgium; 2020)² and GraphPad Prism 5.0a (GraphPad Software, San Diego, CA, United States) were used for statistical analyses. Summaries of numeric data are given as means and standard errors of the mean or median and interquartile range; we used 2-sided Student's *t*-tests and the Mann-Whitney or Kruskal-Wallis tests (as appropriate) for univariate comparisons and binary logistic regression to analyze statistical significances and weights of factors, respectively. Differences were considered to be statistically significant for values of $p \leq 0.05$.

Results

In the current study, 20 patients, with a median age of 18 years and an interquartile range of 12–30 years, were prospectively included. The group was not balanced with respect to sex and included 3 female and 17 male patients. Six patients received DPH and 14 received DAH. Fifteen patients (75%) had undergone at least one previous surgical procedure, and one patient had received bilateral lung transplantation. Four patients (20%) had already obtained a decellularized allograft in the past. Five patients did not return for the blood sampling on day 28 due to the potential risk of infection during the third wave of the 2020 COVID-19 pandemic. The study cohort characteristics are described in **Table 1**.

Comparison of overall antibody binding to healthy controls

The amount of preformed antibodies which bound to DHVs preoperatively were higher in males than in the sera of female patients. The mean number of arbitrary units was 7.6 ± 4.7 (SEM, standard error of mean) in female patients and 18.5 ± 2.9 in male patients ($p = 0.060$).

The low number of female patients ($n = 3$) limited the comparison to healthy controls. The data for healthy controls

² <https://www.medcalc.org>

were taken from our previous publication (7). However, pre-operative antibody binding in male patients was almost identical to healthy male controls (18.0 ± 3.0), whereas female controls had higher antibody binding (13.6 ± 3.2).

In addition to the results in healthy controls, there was a higher amount of antibody binding to aortic DHVs compared with pulmonary DHVs in the study cohort. The mean number of arbitrary units was 18.4 ± 3.1 in aortic DHV and 12.9 ± 4.5 in pulmonary DHV. This did not reach statistical significance ($p = 0.140$), and a robust comparison was hindered by the low number of implanted pulmonary DHV ($n = 6$).

Male patients exhibited higher antibody binding to aortic DHV than female patients (19.5 ± 2.1 vs. 1.6 ± 6.7). The p -value calculation was, however, limited by the fact that only two female patients received DAH, a ratio in line with the threefold higher incidence of aortic valve disease in male patients.

Figure 1 provides an overview of generally unspecified antibody binding pre-operatively and in comparison with the results in healthy controls. Please note the different age categories in the control group, which included participants over 18 years of age.

Correlation of baseline antibody binding according to donor age and recipient blood group

There was no correlation between the amount of overall antibody binding with respect to donor age, calculated using the Kruskal–Wallis test, with a p -value = 0.550.

Figure 2A shows the high level of variance in antibody binding between the 18 implanted decellularized allografts and the respective donor age. Interestingly, DHV recipients with sex mismatch to the donor showed significantly less antibody binding (6.5 ± 1.8 vs. 13.7 ± 1.8 ; $p = 0.003$), as seen in **Figure 2B**.

Decellularized homograft valves recipients with blood group O showed significantly more antibody binding (median; IQR 11.6; -5.6 to 35.5) than A ($p < 0.001$; -7.7 ; -25.2 to 9.3) and B ($p < 0.031$; 9.1 ; -15.5 to 18.3), as seen in **Figure 2C**.

Development of antibody-binding amounts within the first month after decellularized homograft valves implantation in correlation to age, valve position, and echocardiographic follow-up

The amount of antibody binding, averaged for all patients, decreased on post-operative days 1 and 7 compared with pre-operative values and returned to levels close to pre-operative values on post-operative day 28: 16.8 ± 2.5 on day 0, 3.7 ± 1.9

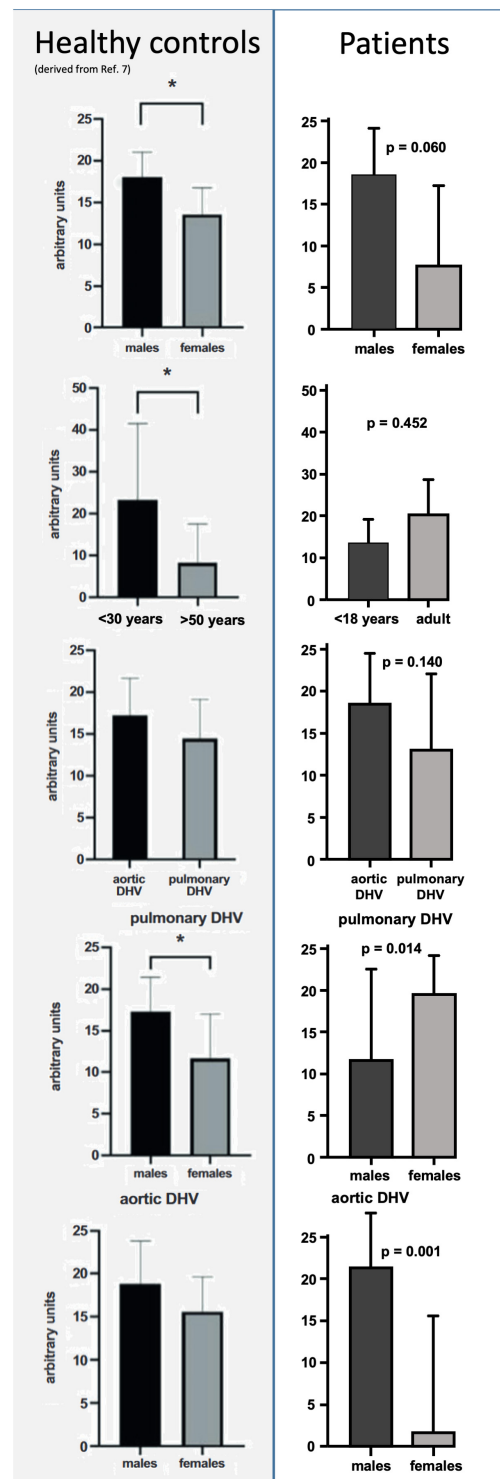
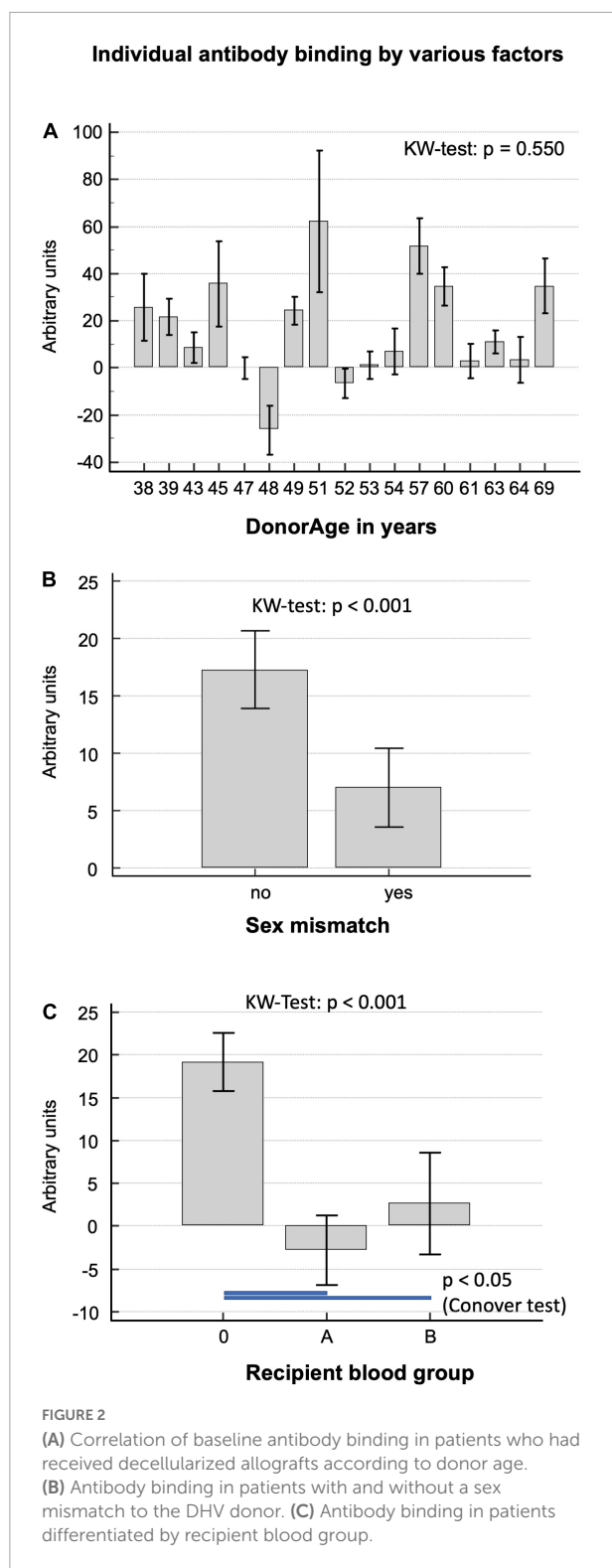


FIGURE 1

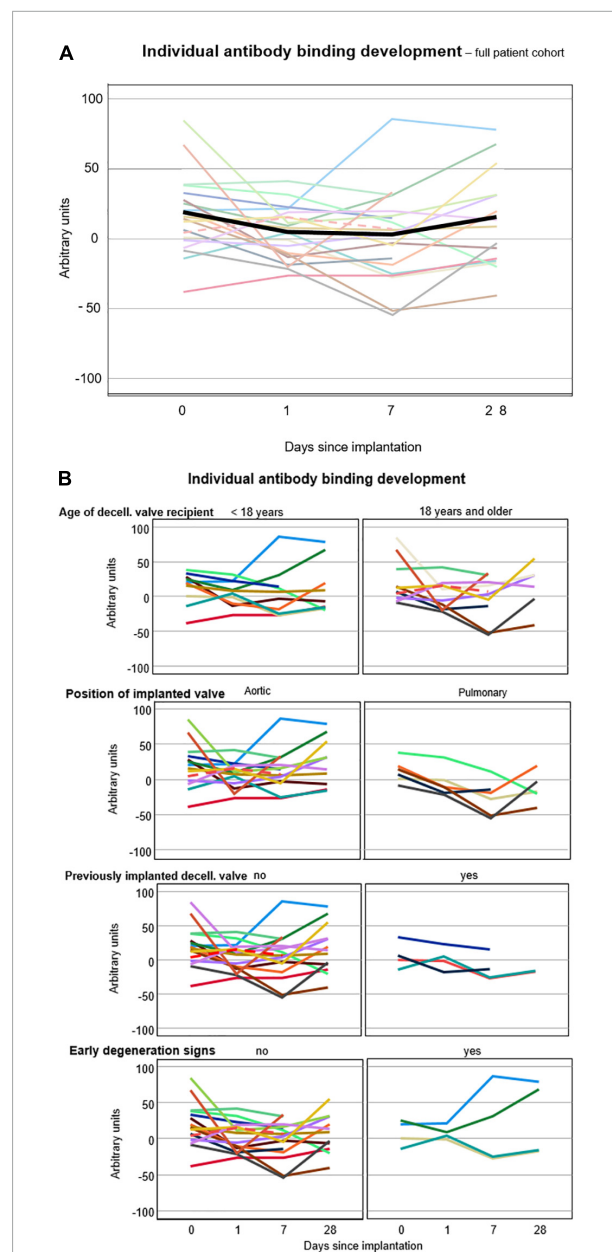
Comparison of preformed antibody binding in minced decellularized allograft samples between healthy controls and patients who had received decellularized allografts according to sex, age, and valve position. Data from healthy controls were taken from our previous publication (7). Please note the different age categories in healthy controls, which were all over 18 years of age. Asterisks indicate statistical significance.



on day 1, 2.3 ± 2.7 on day 7, and 13.2 ± 3.7 on day 28. DHV recipients with previous procedures showed less antibody binding in general (no previous operation 15.9 ± 36.5 , 1

previous operation 7.9 ± 44.2 , and 2 previous operations 9.2 ± 21.6).

Figures 3A,B exhibit the development of individual antibody binding for the overall study cohort, differentiated



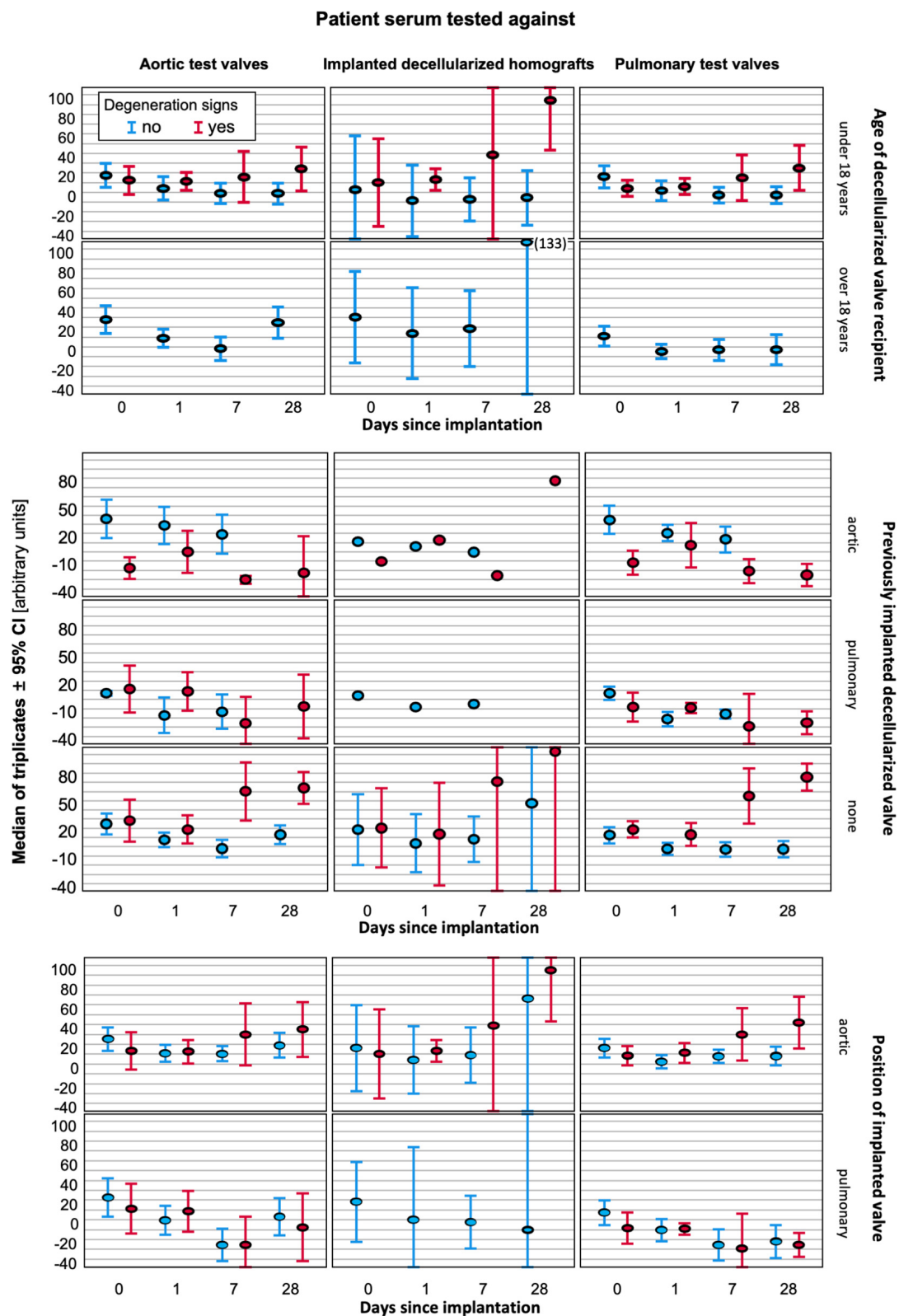


FIGURE 4

Antibody binding to implanted DHV (middle column) and test valves (left column-aortic, right column pulmonary) differentiated by age (superior block), valve position (middle block), and prior DHV implantation (inferior block). In each graph, the results for patients with signs of early degeneration are marked in red, and blue indicates no degeneration at the last follow-up.

by age, valve position, prior DHV implantation, and echocardiographic signs of early degeneration.

Four patients, 3 following DAH implantation and 1 following DPH implantation, developed echocardiographic signs of early degeneration, such as cusp thickening, enhanced echogenicity, and/or mild flow acceleration during follow-up, which was 16.0 ± 4.7 months for the whole study group. All 4 patients were under 18 years of age (13.8 ± 1.6 years.), two of whom had received a decellularized allograft in the past (1 DAH, 1 DPH).

The antibody binding (median values of all triplets, in arbitrary units) did not differ significantly between recipients under and over 18 years: the median value under 18 years was 7.9 (IQR-12.2 to 29.0) and over 18 years was 5.3 (IQR-12.8 to 22.6); $p = 0.602$, Mann-Whitney U -test.

Figure 4 provides a graphical comparison of the amount of antibody binding to the DHV implanted in the patient and graphical illustrations of the 5 non-implanted decellularized aortic and 6 non-implanted pulmonary test valves. The middle column shows the antibody binding to the implanted DHV, the left column displays the antibody binding to aortic test valves, and the right column displays the antibody binding to pulmonary test valves. Patients who exhibited early signs of degeneration are shown in red, and patients without degeneration are shown in blue. Results are also differentiated by age of the patients, prior DHV implantation, and valve position as outlined on the right side of the figure. A key finding is an increase in antibody binding in younger patients receiving decellularized aortic allografts. This increase was enhanced in patients with early degeneration signs, but this effect was not specific to the implanted DHV nor linked with previous DHV implantation.

In a stepwise logistic regression, attached as Supplementary Material, aortic position (odds ratio 3.216) and a previously implanted DHV (odds ratio 12.326) were the only significant factors relevant for the occurrence of early degeneration.

Antibody binding toward explanted degenerated decellularized homograft valves samples and decellularized homograft valves retention samples prior to implantation

In four patients, antibody binding to an explanted degenerated decellularized allograft was analyzed. In three of these patients, the amount of antibody binding to the explant was compared with the amount of binding to the newly implanted DHV. In patient no. 21, who had previously undergone a double semilunar valve replacement, a mechanical aortic valve replacement was performed due to DHV degeneration after 60 months. In this patient, who did not volunteer for the serial follow-up study, we were able to compare

the results from the explanted aortic allograft with a retained decellularized sample prior to implantation. **Figure 5** shows significantly increased antibody binding to the explanted DHV and lower binding to the non-implanted sample, indicating an antibody-mediated DHV degeneration.

Test reproducibility

All tests were performed by one experimenter (FO). Technical triplicates were generated for all Dot-Blots. Experimental variance, as assessed by Cronbach's α for Tau-equivalent reliability, was 0.979, indicating technical consistency. The interquartile range of the difference to the triplicate mean was -13.3 to 13.8 arbitrary units.

Discussion

Decellularized allogeneic heart valves have shown markedly less antigenicity than cryopreserved allogeneic heart valves, e.g., no detectable donor-specific HLA antibody response, measured by Luminex-based single beads assay, was observed after implantation of decellularized allografts (10, 11). Decellularized allografts nevertheless appear to elicit a low-grade immune response as evidenced by the diminishing freedom from explantation after 10 years among patients in the ESPOIR Registry for decellularized pulmonary homografts (12, 13).

In healthy controls, we were able to show that preformed antibodies binding to decellularized human heart valves (DHV) are present even without previous exposure to allogeneic material with high variability between individuals (7). In the current serial assessment study of antibody binding in patients undergoing heart valve replacement with DHV, we did not observe any influence in terms of donor age on the amount of patient-specific antibody binding to several different decellularized donor tissues. Regarding ABO blood type, we saw a higher amount of binding in recipients with blood group O, which, however, may be biased by the over-proportional prevalence of this blood group among the included patients.

The analysis of sex-specific factors for higher immunogenicity of DHV in male patients was limited in the current study as there were only 3 female patients among the 20 study participants. The finding of reduced antibody binding in patients with sex mismatch to the donor was unexpected and needs further analysis, in particular in the light of increasing recognition of sexual dimorphism in the immune system (12). In our study of preformed antibody binding in healthy controls, we also examined the impact of sex mismatch but did not find any clear links (unpublished data). In the serum of female control subjects, there was lower antibody binding in mismatch situations, whereas in the serum of male control subjects, higher results in mismatch situations were observed.

Individual antibody binding towards explanted DHV – serum day 0

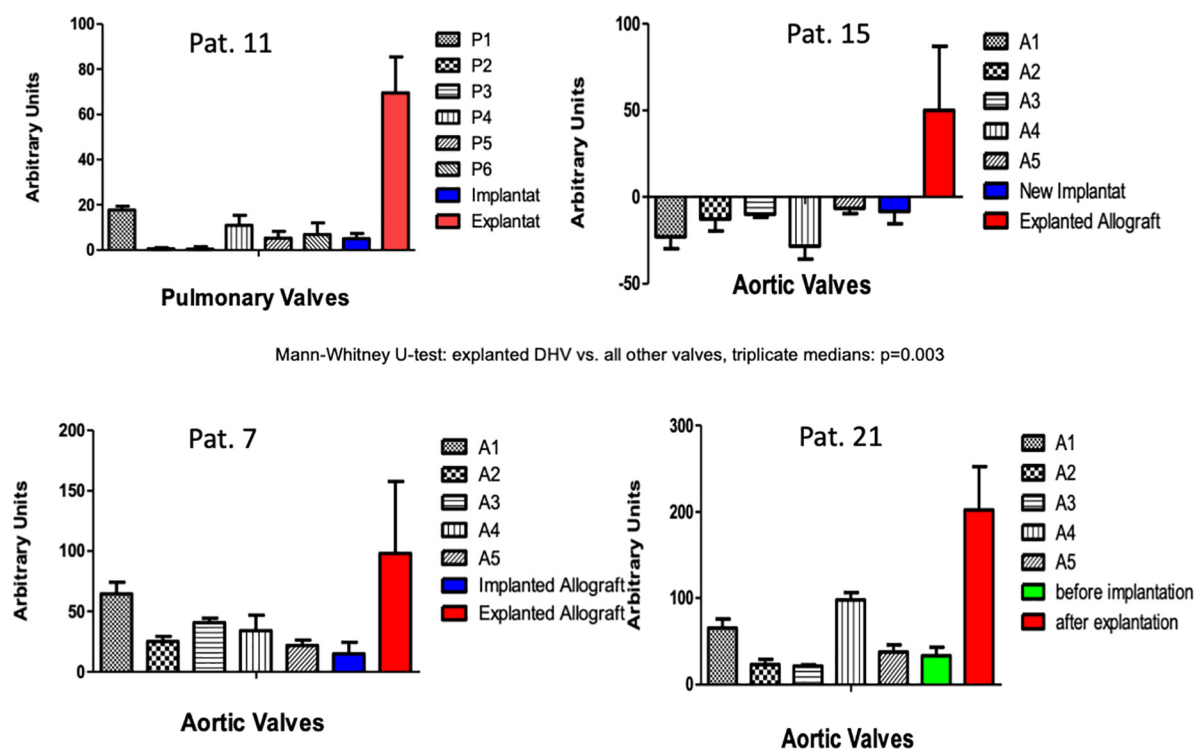


FIGURE 5

Antibody binding in patients with previous DHV and with new decellularized allografts replacing the degenerated previously implanted grafts (patients 7, 11, 15). The amount of antibody binding to one DAH retention sample 60 months after implantation and in the explanted degenerated DAH is also shown (patient 21).

There was no significantly increased antibody binding observed in the overall antibody binding pre-operatively in the four patients who had previously received a decellularized allograft. When we tested these four patients post-operatively for antibody binding to their explanted homografts, we saw markedly increased antibody binding to their explanted decellularized allografts (two aortic and two pulmonary), which we believe strongly implicates an antibody-mediated immune reaction as a co-factor in decellularized allograft degeneration.

One of these patients, a female patient who had undergone a double semilunar valve replacement with decellularized allografts and, subsequently, explantation of the degenerated aortic allograft, was also tested against a retained sample of the decellularized aortic allograft, which had been implanted 5 years earlier. Interestingly, there was only mild antibody binding toward the non-implanted test samples, but a very strong reaction toward the explanted and degenerated aortic allograft, which shows the *de novo* synthesis of antibodies directed toward the aortic allograft after implantation.

During a serial assessment of the individual antibody binding levels at the first month after implantation, we

noticed an increase in particular in patients following the implantation of decellularized aortic allografts. This finding indicates early activation of the humoral immune system of patients receiving decellularized allografts and correlates with our findings of higher rates of midterm degeneration in decellularized aortic allografts compared with pulmonary allografts (2, 13).

The amount of antibody binding was not higher in patients with prior DHV explantation. There, however, was a significantly increased amount of antibody binding after 28 days in 4 patients who, during the 19.8 months (maximum) follow-up available to date, showed mild echocardiographic signs of degeneration, such as cusp thickening and increased echogenicity of vascular parts. All 4 patients were under 18 years of age (13.8 ± 1.6 years.), which highlights the importance of age with respect to early degeneration of biological heart valves. As two of these patients previously received a DHV, the previous implantation appears to be a risk factor for early degeneration during logistic regression.

Unfortunately, this increased antibody binding was not specific to the implanted allograft, and we were unable to

demonstrate a correlation between the pre-operative antibody binding to implanted grafts and poorer early echocardiographic results in subsequent follow-up. As one of our leading goals was to enable and optimize pre-operative matching, this was a disappointing finding. The binding intensity of the currently tested antibody assays seems to indicate rather than provide a prediction of degeneration.

These results, however, are based on a small cohort of 20 patients with a limited follow-up so far. We are currently trying to establish a lateral flow test kit to replace the elaborate Dot-Blot for a clinical study of the antibody-mediated immune response following implantation of a decellularized allograft. We are also analyzing the activation of several chemokines and cytokines after the implantation of decellularized allografts to further characterize the individual immune response pathways that may ultimately lead to graft degeneration. Ideally, such analyses should also include T-cell-mediated response. Such information, however, may be impossible to obtain as serial biopsies in delicate structures such as heart valves cannot be justified ethically given the overall good performance of decellularized allografts. Despite positive findings in terms of good recipient cell repopulation (4), we postulate that, in the early post-operative period, when the graft surface has not yet been fully covered by endothelial cells, the relatively open matrix of the decellularized tissue also may be penetrable by humoral antibodies, which could bind to the matrix and subsequently induce a T-cell and B-cell response or the activation of macrophages.

We hypothesize that the so-called matrikines, specific peptides of the extracellular matrix which may become visible to the immune system after processing, are the leading target for the innate and acquired immune system (14). We do not believe that cell surface proteins or protein fragments are the specific targets of preformed and new antibodies, as we quantitatively assessed these types of proteins (e.g., ULBP-4, NT5E, Siglec-9, Nectin-2) before and after decellularization and demonstrated their absence after the process (unpublished data). Further Western-blot analysis of explanted, degenerated decellularized homografts may be an option to identify the major binding domains of preformed and newly synthesized antibodies. Once there is a better understanding of the molecular mechanisms behind the immunological activation occurring after implantation of decellularized human heart valves, the opportunity may arise to silence the respective antigens before implantation (11). As the field of xenotransplantation is rapidly evolving, new initiatives using decellularized xenogeneic heart valves will likely play a role in the future (15), possibly in combination with autologous stem cell recellularization using induced pluripotent stem cells (iPS) (16, 17). Our group already has started to use decellularized heart valves from genetically modified pigs in primate models for pulmonary valve replacement.

Limitations and conclusion

A limiting factor for the study was the low number of patients who could be included in the study due to the nature of homografts as a rare resource. This factor also limited the number of decellularized non-implanted tissue samples in comparison with the individual antibody binding.

Direct comparison of the results of antibody binding with healthy controls has technical limitations resulting from the variance in these complex experiments with the utilized biological test materials, e.g., such as different batches of secondary human antibodies. Direct comparison with the healthy controls was limited by different age and sex distribution within both groups.

Another limitation is the lack of long-term correlations of the early immunological activation, as evidenced by increasing antibody binding, with long-term DHV durability. We anticipate further insights in this regard in the future based on the ongoing follow-up of study participants.

In conclusion, serial assessment of tissue-specific antibody binding after implantation of decellularized allografts revealed increased antibody binding within 4 weeks after surgery in some patients, who subsequently developed early signs of allograft degeneration. Studies with a larger sample size are needed to confirm the prognostic relevance of antibody increase for valve performance and durability. In addition, specific research efforts to identify the molecular agents triggering this type of antibody response are required to understand the underlying processes.

Data availability statement

The raw data supporting the conclusions of this article will be made available by the authors, without undue reservation.

Ethics statement

The studies involving human participants were reviewed and approved by the Hannover Medical School Ethics Committee EC No. 7871_BO_S_2018. Written informed consent to participate in this study was provided by the participants' legal guardian/next of kin.

Author contributions

FO: investigation, formal analysis, and writing—original draft. RR, TG, and JE: validation and writing—review and editing. CF, AHo, MA, and DmB: investigation and writing—review and editing. RJ: writing—review and editing. DiB: formal analysis and writing—review and editing. AHa: funding acquisition,

resources, and writing—review and editing. AH: supervision, resources, and writing—review and editing. SS: conceptualization, supervision, and writing—review and editing. All authors contributed to the article and approved the submitted version.

Funding

This study was supported in part by a grant from the European Union's HORIZON 2020 Programme under Grant Agreement No. 643597 (www.arise-clinicaltrial.eu).

Acknowledgments

We would like to thank corlife oHG for the supply of decellularized control samples. Furthermore, the excellent technical assistance of Doreen Lenz and Stefanie Reuss was gratefully acknowledged. We also thank Nina McGuinness for her editorial assistance.

References

1. Waqanivalagi S, Bhat S, Ground MB, Milsom PF, Cornish J. Clinical performance of decellularized heart valves versus standard tissue conduits: a systematic review and meta-analysis. *J Cardiothorac Surg.* (2020) 15:260. doi: 10.1186/s13019-020-01292-y
2. Horke A, Bobylev D, Avsar M, Meyns B, Rega F, Hazekamp M, et al. Paediatric aortic valve replacement using decellularized allografts. *Eur J Cardiothorac Surg.* (2020) 58:817–24. doi: 10.1093/ejcts/ezaa119
3. Neumann A, Sarikouch S, Breyman T, Cebotari S, Boethig D, Horke A, et al. Early systemic cellular immune response in children and young adults receiving decellularized fresh allografts for pulmonary valve replacement. *Tissue Eng Part A.* (2014) 20:1003–11. doi: 10.1089/ten.TEA.2013.0316
4. Sarikouch S, Theodoridis K, Hilfiker A, Boethig D, Laufer G, Andreas M, et al. Early insight into *in vivo* recellularization of cell-free allogenic heart valves. *Ann Thorac Surg.* (2019) 108:581–9. doi: 10.1016/j.athoracsurg.2019.02.058
5. Boer U, Buettner FFR, Schridde A, Klingenberg M, Sarikouch S, Haverich A, et al. Antibody formation towards porcine tissue in patients implanted with crosslinked heart valves is directed to antigenic tissue proteins and alphaGal epitopes and is reduced in healthy vegetarian subjects. *Xenotransplantation.* (2017) 24:e12288. doi: 10.1111/xen.12288
6. Smart I, Goecke T, Ramm R, Petersen B, Lenz D, Haverich A, et al. Dot blots of solubilized extracellular matrix allow quantification of human antibodies bound to epitopes present in decellularized porcine pulmonary heart valves. *Xenotransplantation.* (2020) 28:e12646. doi: 10.1111/xen.12646
7. Ebken J, Mester N, Smart I, Ramm R, Goecke T, Jashari R, et al. Residual immune response towards decellularized homografts may be highly individual. *Eur J Cardiothorac Surg.* (2021) 59:773–82. doi: 10.1093/ejcts/ezaa393
8. Romeo JLR, Mokhles MM, van de Woestijne P, de Jong P, van den Bosch A I, van Beynum M, et al. Long-term clinical outcome and echocardiographic function of homografts in the right ventricular outflow tractdagger. *Eur J Cardiothorac Surg.* (2019) 55:518–26. doi: 10.1093/ejcts/ezy265
9. Boethig D, Horke A, Hazekamp M, Meyns B, Rega F, Van Puyvelde J, et al. A European study on decellularized homografts for pulmonary valve replacement: initial results from the prospective ESPOIR Trial and ESPOIR Registry datadagger. *Eur J Cardiothorac Surg.* (2019) 56:503–9. doi: 10.1093/ejcts/ezz054
10. Coti I, Wenda S, Andreeva A, Kocher A, Laufer G, Fischer G, et al. Donor-specific HLA antibodies after fresh decellularized vs cryopreserved native allograft implantation. *HLA.* (2020) 96:580–8. doi: 10.1111/tan.14077
11. Kneib C, von Glehn CQ, Costa FD, Costa MT, Susin MF. Evaluation of humoral immune response to donor HLA after implantation of cellularized versus decellularized human heart valve allografts. *Tissue Antigens.* (2012) 80:165–74. doi: 10.1111/j.1399-0039.2012.01885.x
12. Jaillon S, Berthenet K, Garlanda C. Sexual dimorphism in innate immunity. *Clin Rev Allergy Immunol.* (2019) 56:308–21. doi: 10.1007/s12016-017-8648-x
13. Bobylev D, Horke A, Boethig D, Hazekamp M, Meyns B, Rega F, et al. 5-year results from the prospective European multi-centre study on decellularized homografts for pulmonary valve replacement – ESPOIR Trial and ESPOIR Registry data. *Eur J Cardiothorac Surg.* (2022):ezac219. [Online ahead of print]. doi: 10.1093/ejcts/ezac219
14. Chakraborty J, Roy S, Ghosh S. Regulation of decellularized matrix mediated immune response. *Biomater Sci.* (2020) 8:1194–215. doi: 10.1039/c9bm01780a
15. Ramm R, Goecke T, Kohler P, Tudorache I, Cebotari S, Ciubotaru A, et al. Immunological and functional features of decellularized xenogenic heart valves after transplantation into GGTA1-KO pigs. *Regenerat Biomater.* (2021) 8:rbab036.
16. Carvalho-Oliveira M, Valdivia E, Blasczyk R, Figueiredo C. Immunogenetics of xenotransplantation. *Int J Immunogenet.* (2021) 48:120–34. doi: 10.1111/iji.12526
17. Neri T, Hiriart E, van Vliet PP, Faure E, Norris RA, Farhat B, et al. Human pre-valvular endocardial cells derived from pluripotent stem cells recapitulate cardiac pathophysiological valvulogenesis. *Nat Commun.* (2019) 10:1929. doi: 10.1038/s41467-019-09459-5

Conflict of interest

AHa holds shares in corlife oHG, the company providing the patented service of processing decellularized allografts used in this study. RJ was a Director of the European Homograft Bank.

The remaining authors declare that the research was conducted in the absence of any commercial or financial relationships that could be construed as a potential conflict of interest.

Publisher's note

All claims expressed in this article are solely those of the authors and do not necessarily represent those of their affiliated organizations, or those of the publisher, the editors and the reviewers. Any product that may be evaluated in this article, or claim that may be made by its manufacturer, is not guaranteed or endorsed by the publisher.



OPEN ACCESS

EDITED BY

Laura Iop,
University of Padua, Italy

REVIEWED BY

Jatin Patel,
Queensland University of Technology,
Australia
John Mayer,
Boston Childrens Hospital and Harvard
Medical School, United States

*CORRESPONDENCE

Maximilian Y. Emmert
maximilian.emmert@irem.uzh.ch;
emmert@dhzb.de
Emanuela S. Fioretta
emanuela.fioretta@irem.uzh.ch

†These authors have contributed
equally to this work and share first
authorship

‡These authors have contributed
equally to this work and share last
authorship

SPECIALTY SECTION

This article was submitted to
Heart Valve Disease,
a section of the journal
Frontiers in Cardiovascular Medicine

RECEIVED 24 May 2022

ACCEPTED 15 August 2022

PUBLISHED 13 September 2022

CITATION

Poulis N, Martin M, Hoerstrup SP,
Emmert MY and Fioretta ES (2022)
Macrophage-extracellular matrix
interactions: Perspectives for tissue
engineered heart valve remodeling.
Front. Cardiovasc. Med. 9:952178.
doi: 10.3389/fcvm.2022.952178

COPYRIGHT

© 2022 Poulis, Martin, Hoerstrup,
Emmert and Fioretta. This is an
open-access article distributed under
the terms of the [Creative Commons
Attribution License \(CC BY\)](#). The use,
distribution or reproduction in other
forums is permitted, provided the
original author(s) and the copyright
owner(s) are credited and that the
original publication in this journal is
cited, in accordance with accepted
academic practice. No use, distribution
or reproduction is permitted which
does not comply with these terms.

Macrophage-extracellular matrix interactions: Perspectives for tissue engineered heart valve remodeling

Nikolaos Poulis^{1†}, Marcy Martin^{1†}, Simon P. Hoerstrup^{1,2},
Maximilian Y. Emmert^{1,2,3,4*‡} and Emanuela S. Fioretta^{1*‡}

¹Institute for Regenerative Medicine, University of Zurich, Schlieren, Switzerland, ²Wyss Zurich, University and Swiss Federal Institute of Technology (ETH) Zurich, Zurich, Switzerland, ³Department of Cardiovascular Surgery, Charité Universitätsmedizin Berlin, Berlin, Germany, ⁴Department of Cardiothoracic and Vascular Surgery, German Heart Center Berlin, Berlin, Germany

In situ heart valve tissue engineering approaches have been proposed as promising strategies to overcome the limitations of current heart valve replacements. Tissue engineered heart valves (TEHVs) generated from *in vitro* grown tissue engineered matrices (TEMs) aim at mimicking the microenvironmental cues from the extracellular matrix (ECM) to favor integration and remodeling of the implant. A key role of the ECM is to provide mechanical support to and attract host cells into the construct. Additionally, each ECM component plays a critical role in regulating cell adhesion, growth, migration, and differentiation potential. Importantly, the immune response to the implanted TEHV is also modulated biophysically via macrophage-ECM protein interactions. Therefore, the aim of this review is to summarize what is currently known about the interactions and signaling networks occurring between ECM proteins and macrophages, and how these interactions may impact the long-term *in situ* remodeling outcomes of TEMs. First, we provide an overview of *in situ* tissue engineering approaches and their clinical relevance, followed by a discussion on the fundamentals of the remodeling cascades. We then focus on the role of circulation-derived and resident tissue macrophages, with particular emphasis on the ramifications that ECM proteins and peptides may have in regulating the host immune response. Finally, the relevance of these findings for heart valve tissue engineering applications is discussed.

KEYWORDS

collagen, fibronectin, inflammation, regenerative medicine, scaffold functionalization, immune response, extracellular matrix (ECM), macrophages

Introduction

Every tissue in the body has distinct extracellular matrix (ECM) composition, that arises from a unique combination of up to ~300 different ECM (e.g., collagen subunits, proteoglycans and glycoproteins) and ECM-related protein components (e.g., secreted factors and ECM regulators) (1). The main role of the ECM is to provide structural support to each tissue type and organ. In addition, each ECM component also plays a direct role in controlling cell adhesion, regulating cell growth, migration, proliferation, and differentiation potential (2); the native heart valve ECM being no exception.

Due to the distinct three-layer ECM composition, the heart valve leaflet structure is able to withstand constant pressure changes during the cardiac cycle (3, 4). The ventricularis or atrial is side of the leaflets, those which are exposed to pulsatile shear stress, are composed of radially oriented elastin fibers and provide the elastic recoil needed for when the valve opens and closes (5). The middle layer, or spongiosa of the valve, is comprised of proteoglycans such as chondroitin sulfate, glycosaminoglycans, and sparsely packed collagen fibers, all of which mitigate compression forces when the valve is closed (6). The circumferentially aligned, densely packed, collagen-rich (mainly collagen 1 (COL1), but also COL3) fibrosa layer is situated at the outflow tract and is the main structure that provides strength and stiffness necessary for valve sufficiency (7).

Because the ECM is the core component of heart valve functionality, diseases that abrogate ECM function, such as genetic conditions (8–11) and calcific aortic valve disease (CAVD) (12, 13), can disrupt normal valve performance and often warrants valve replacement. CAVD is the most common valve disease and is a progressive degeneration ranging from non-obstructive valve thickening to severe valve calcification, which may result in impaired leaflet movement and eventually leading to valve stenosis (12, 13). CAVD development is an active inflammatory process that culminate with the release of matrix metalloproteinases (MMPs) and cathepsins that drive pathogenic ECM remodeling and calcium deposition (14, 15). This may result in severe valve insufficiency and/or stenosis that will ultimately necessitate replacement.

In most cases, treating these severe conditions requires a valve replacement procedure (16), either using mechanical

or bioprosthetic valves, as extensively reviewed elsewhere (17, 18). Despite the remarkable heart valve prosthesis evolution (19), in particular with the advent of transcatheter techniques (20), several clinical and societal dilemmas remain (Box 1). Importantly, current clinical-grade heart valve replacement solutions lack the ability to remodel, repair and/or grow upon implantation, determining a high incidence of reoperation to replace the valve implant, in particular in the young cohort (<60 years old) (21).

In situ heart valve tissue engineering has been proposed as a promising solution to achieve “next-generation” heart valve prostheses with the potential for life-long durability (18). Remarkably, tissue engineered heart valves (TEHVs), manufactured using either decellularized allogenic/xenogeneic valves or bioresorbable polymer-based valves, have reached clinical translation (29–35). While wound healing and the foreign body response are amongst the most hypothesized mechanisms behind the integration and remodeling of TEHVs (36–38), less attention has been given to the role of ECM proteins in regulating remodeling upon implantation. Therefore, the aim of this review is to describe what is currently known about the interactions and signaling networks occurring between ECM proteins and macrophages, and how these interactions may impact the long-term *in situ* remodeling outcomes of tissue engineered ECM (TEM)-based implants. First, we provide an overview of *in situ* heart valve tissue engineering approaches with a particular focus on TEM-based TEHVs (section “*In situ* heart valve tissue engineering”). Then, we briefly summarize the fundamentals of the wound healing and remodeling cascades, specifically examining two of the first responders to injury, circulation-derived macrophages and resident tissue macrophages (RTMs) (section “The role of macrophages in tissue remodeling”). We then discuss the role of ECM proteins, such as collagens (COL), fibronectin (FN), and their corresponding peptides, in regulating the macrophage response, with particular emphasis on the implications for remodeling mechanisms (section “Immunoregulation of extracellular matrix proteins”). Finally, the relevance of these findings for heart valve tissue engineering applications is discussed by proposing examples of scaffold functionalization using ECM or ECM-related proteins to regulate the host immune response toward adaptive remodeling (section “Discussion: Relevance for *in situ* heart valve tissue engineering”).

In situ heart valve tissue engineering

In situ tissue engineering relies on the regenerative potential of the recipient's body to integrate and remodel an implanted off-the-shelf available construct. The scaffold used for this approach should withstand the native mechanical environment

Abbreviations: α SMA, α -smooth muscle actin; CAVD, calcific aortic valve disease; COL, collagen; DAMP, damage-associated molecular pattern; ECM, extracellular matrix; FGF, fibroblast growth factor; FN, fibronectin; IL, interleukin; MMP, matrix metalloproteinases; P4HB, poly-4-hydroxybutyrate; PDGF, platelet derived growth factor; PGA, polyglycolic acid; RTM, resident tissue macrophage; TEHV, tissue engineered heart valves; TEM, tissue engineered matrix; TGF β 1, transforming growth factor- β 1; VEGF, vascular endothelial growth factor.

BOX 1 Remaining clinical and societal implications for heart valve therapies.

- Heart valve replacement procedures of severely dysfunctional valves, either using mechanical or bioprosthetic valves, is expected to reach 850,000 implants annually by 2050 (22).
- Patients receiving a mechanical valve are subjected to life-long anticoagulant treatment to prevent thrombosis (23).
- For elderly patients, current guidelines recommend a bioprosthetic valve generated from glutaraldehyde-fixed xenogenic tissue (e.g., porcine valves or bovine pericardium). This prosthesis has an improved hemodynamic profile, reducing the need for anti-coagulation therapy (24).
- Bioprostheses have residual immunogenicity (i.e., xenogenic alpha-gal epitopes) that can cause chronic inflammation upon implantation (25, 26). This leads to degenerative failure, and limited durability of the prosthesis, causing the need for multiple re-interventions in the young (21, 24, 27).
- European health care costs for patients having a heart valve replacement exceed €1 billion annually (28).

immediately upon implantation, favor host cell adhesion, migration and proliferation, support ECM production, and allow for adaptive remodeling toward a native-like functional living tissue (18, 36).

To achieve this, a multitude of different tissue engineering strategies have investigated distinct scaffold materials that ensure functionality and remodeling of the implanted TEHV, as extensively reviewed elsewhere (18). Briefly, TEHVs utilizing decellularized homografts have shown favorable long-term performance and limited *in situ* cell repopulation in clinical trials (30, 39–42). However, maladaptive remodeling phenomena (i.e., fibrosis and calcification) and not favorable long-term outcomes (i.e., 51% of freedom from reoperation at 10 years compared to 80% for standard cryopreserved allografts) have been reported (43–45).

TEHVs manufactured from decellularized xenografts have been associated with controversial results, with marked discrepancy between preclinical and clinical studies. Briefly, preclinical investigations in large animal models showed promising performance of xenograft-based TEHVs, with cellular infiltration throughout the tissue thickness (46). However, clinical trials were mostly unsuccessful, with signs of maladaptive remodeling [i.e., fibrosis, leaflet thickening, calcification, lack of cellularization, and chronic inflammation (47–53)], that may have caused the observed valve insufficiency and/or stenosis.

The functionality and remodeling potential of bioresorbable polymeric valves, which are compatible with surgical and transcatheter implantation techniques, were first demonstrated in large animal models (54–59). Within these studies, the valves showed acceptable functionality for up to 12 months, rapid cellularization, ECM deposition and progressive scaffold reabsorption (56, 58). Clinical translation of this approach is currently ongoing. A first pulmonary valve conduit design was evaluated in 12 pediatric patients [Xplore-1 study (34)], but moderate-to-severe pulmonary valve regurgitation was observed in 11 out of 12 patients (60). A retrospective analysis of the implanted conduits revealed leaflet thickness heterogeneity, with the leaflets being thinner in the commissural area. Therefore, the leaflet design was modified to achieve a more homogeneous thickness distribution. The improved of pulmonary valve conduit design has been then implanted in six children [Xplore-2 study (35)]. In this trial, moderate

pulmonary valve regurgitation was reported for only 1 patient at the 12 months follow-up (60). In addition, 1 patient developed rapidly progressing stenosis and required conduit replacement (60). Given the mixed outcomes of these two clinical trials, as well as the reported intra-valve and inter-valve differences in remodeling and incomplete scaffold reabsorption after 1 year in preclinical studies (56, 58, 61–63), further data with longer follow-up time points are needed to determine the true clinical value of this approach. Alternatively, *in vitro* grown human cell-derived tissue engineered matrices (TEMs) have been recently proposed as a promising material to fulfill the need for an easily accessible and an off-the-shelf option for TEHV development (64, 65).

TEMs are obtained by *in vitro* culture of human fibroblast-like cells [e.g., human dermal fibroblasts or vascular-derived myofibroblasts (64–68)] on a biodegradable scaffold [i.e., fibrin gel or poly-4-hydroxybutyrate (P4HB) coated polyglycolic acid (PGA) (64, 67–70)] for a pre-determined amount of time to have sufficient deposition of ECM proteins. After culture, the tissue is decellularized to ensure immunocompatibility and grant off-the-shelf availability, while also preserving the ECM structure (66). The resulting TEM can then be used to manufacture off-the-shelf available TEHVs to replace (pulmonary or aortic) heart valves with promising acute performance (64, 65), and sustained functionality, up to 1 year (67), with host cell repopulation, endothelialization, integration, and remodeling potential over time being consistently observed (67, 68, 70–74).

TEMs can be described as complex materials, comprised of a multitude of ECM proteins, minimal amounts of residual DNA that may remain from the decellularization process, and possibly bioresorbable polymer remnants (64, 65, 67, 68, 70, 71, 74). Upon implantation, each of these TEM components have a potential impact on the immune response to the implant and, thus, will contribute to its remodeling process (75); the ECM proteins being no exception. Generally, the ECM components of a TEM implant are considered for their mechanical properties (64, 71). Importantly, ECM proteins also have significant biocompatible properties that can guide cell behavior (76), and can potentially regulate macrophage polarization upon implantation.

The role of macrophages in tissue remodeling

The remodeling of a tissue engineered construct is a highly complex and dynamic process characterized by the interaction of different immune cells with the implant, followed by the release of cytokines to further attract immune and specialized cells to the injury/implantation site (75). Little is known about the remodeling following an injury in native heart valve leaflets. Animal studies indicate surgically wounded valves remodel by recruiting activated macrophages, myofibroblasts, and endothelial cells that contribute to the deposition of proteoglycans and secretion of MMPs (77–79). Eventually, as a result of this healing cascade, a collagen-rich fibrous tissue is formed and, over time, the valve leaflet is re-endothelialized (79). Macrophages have been repeatedly reported as early responders that govern wound healing and remodeling processes by secreting growth factors, chemokines and cytokines [e.g., transforming growth factor beta (TGF β), fibroblast growth factor (FGF), platelet derived growth factor (PDGF) and vascular endothelial growth factor (VEGF) (80)] as extensively reviewed elsewhere (81, 82). This occurs also in the heart valves, where by secreting TGF β and FGF, macrophages play a key role in activating valvular interstitial cells (VICs), to favor proliferation and migration during valve repair and remodeling (83). However, aberrant TGF β stimulation is also the first step to pathogenic fibrosis and/or osteogenesis, potentially leading to fibrotic valve stenosis and calcific valve disease (84). Therefore, there is a fine balance between the signaling molecules secreted by macrophages that are needed to decide the fate between fibrosis and regeneration of both native and TEHV, making these cells one of the key players in the repair and remodeling cascades.

Importantly, it is very likely that the host response to an implanted engineered valve will substantially differ from the innate remodeling following an injury, in particular if an implant leads to the chronic activation of immune cells and foreign body response. After 2–4 weeks from implantation, the surface properties of the implant will modulate the foreign body reaction, by affecting protein adsorption and early responding immune cells adhesion, thereby affecting the inflammatory cascade and the subsequent cellular recruitment and activation on the implant (85). Although it is currently difficult to predict the human immune response to implanted material, we present an overview of circulation-derived and resident tissue macrophages' role in host immune response in the following sections. Traditionally, all macrophages were considered to be derived from the bone marrow through circulating monocytes (section "Circulation-derived macrophages") (Figure 1A). More recently, it has been established that resident tissue macrophages (section "Resident tissue macrophages") are derived from embryonic progenitors and can persist and proliferate throughout adulthood (86) (Figure 1B).

Circulation-derived macrophages

Circulation-derived macrophages originate from monocytes (carrying markers CD14^{Hi}, CCR2⁺ and CSFR2⁺) that circulate in a dormant steady state and are products of hematopoiesis (87, 88). Circulating monocytes are attracted to the surface of a wounded area and/or implant, where they differentiate to macrophages (87, 88) (Figure 1A). These macrophages remove cell debris as well as clear foreign materials (82). In addition, they enable collagen deposition in the injured area, or on the implanted biomaterial, in order to induce tissue restoration and support further immune cell and fibroblast recruitment *via* cytokine release (88, 89).

The cytokines secreted in the early stages of wound healing are highly dependent on the biochemical cues present in the wound or on the surface of the implanted material. Several determinants, such as the presence of cell debris, external pathogens, ECM proteins, and foreign materials (i.e., bioresorbable polymers), can impact whether the circulation-derived macrophages display a pro- or anti-inflammatory phenotype (90). Pro-inflammatory polarization, primarily comprised of M1 sub-populations, enables the formation of multinucleated foreign body giant cells (FBGCs) with the intent to engulf and clear any foreign material and remove cellular debris. Normally, when M1 macrophages have concluded the clearance of cell debris and foreign bodies, further M1 polarization is not required and the cells repolarize into an anti-inflammatory state, generally known as the M2 state. Anti-inflammatory polarization is comprised primarily of M2 (e.g., M2a, M2b, M2c, and M2d) macrophage subgroups, and promotes tissue regeneration by secreting anti-inflammatory cytokines such as interleukin 10 (IL-10), IL-4, IL-1Ra and growth factors like TGF β 1, thereby attracting fibroblasts to restore tissue integrity (91, 92). Both M1 and M2 are considered dynamic states and with inherent plasticity that depends on the stimulation they receive from their surrounding environment or the presence of paracrine factors (92), thereby enabling the spontaneous initiation and resolution of inflammation. Importantly, macrophages guide *de novo* ECM synthesis by recruiting ECM producing α -smooth muscle actin (α SMA)-positive cells, but also by directly depositing ECM proteins (89, 93). ECM production by macrophages is primarily influenced by polarization toward the M2 subgroups (92). *In vitro* studies have showcased the direct production of collagens (COLVI and COLVIII) from stimulated monocytes and macrophages (94), as well as glycosaminoglycans and α -elastin in a strain-dependent manner, identifying macrophages as direct regulator of ECM turnover and synthesis (95). *In vivo* studies focusing on the cardiac wound healing response demonstrated that macrophages can directly deposit collagen in scar formation upon cardiac injury (96), further highlighting the role of macrophage-ECM crosstalk that should to be taken into consideration for TEHV implantation. M2

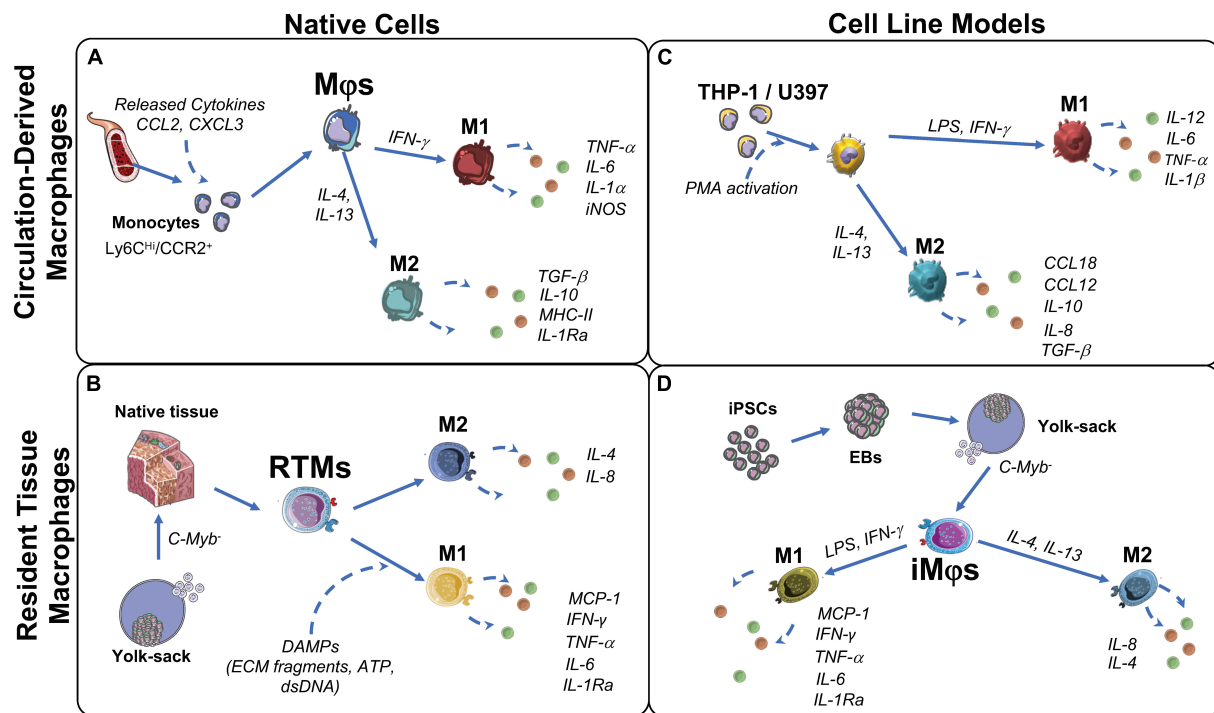


FIGURE 1

Origin and function of macrophages and their corresponding cell models. **(A)** Circulation-derived monocytes (CD14^{hi}/CCR2⁺), activated by C-C motif chemokine ligand 2 (CCL2) and C-X-C chemokine ligand 3 (CXCL3) from cells at the wound site, differentiate to macrophages (Mφs). When in contact with cell debris and ECM fragments, Mφs polarize to M1 to induce clearance of the damaged cells/proteins. M1-Mφs secrete pro-inflammatory factors to attract ECM producing stromal cells and restore tissue integrity. Over time, to resolve inflammation, Mφs polarize to M2. M2-Mφs secrete anti-inflammatory factors that favor remodeling and restore tissue integrity. **(B)** Resident tissue macrophages (RTMs) are derived from C-Myb⁻ hematopoiesis in the yolk-sac and reside in native fetal tissues, but persists into adulthood. Upon tissue damage, RTMs are activated by damage associated molecular patterns (DAMPs) and polarize to M1. M1-RTMs secrete pro-inflammatory cytokines that recruit circulating monocytes and neutrophils, but then quickly polarize to the M2 state to promote tissue restoration and homeostasis. **(C)** Immortalized leukemic cells THP-1 and U937 are used to model peripheral blood-derived monocytes and Mφs. M1 polarization is induced by lipopolysaccharides (LPS), interferon (IFN)-γ with subsequent pro-inflammatory cytokine production interleukin (IL)-12, IL-6, IL-1β, and tissue necrosis factor (TNF)-α. M2 polarization is induced by IL-4 and IL-13 with subsequent production of IL-10, IL-8, CCL18, CCL12 and transforming growth factor (TGF)β. **(D)** iMφs are a proposed model of RTMs *in vitro*. Their C-Myb independent ontogeny is similar to RTMs and have shown to polarize in a similar manner to the M1 (LPS, IFN-γ) and M2 (IL-4, IL-13) states. EB, embryoid body; iNOS, inducible nitric oxide synthase; iPSCs, induced pluripotent stem cells; LPS, lipopolysaccharides; MCP-1, monocyte chemoattractant protein 1; MHC-II, major histocompatibility complex class II; PMA, protein kinase C activator.

macrophages also enable ECM production and turnover at the wound/implantation site indirectly. For example, IL-10 and TGFβ1 secretion recruits and activates fibroblasts leading to ECM deposition in a myocardial infarction model (97). Furthermore, the paracrine effects of TGFβ1, PDGF, and MMP secretion have been shown to activate ECM producing cells, such as fibroblasts, to favor tissue repair and remodeling (96). However, the regulation of direct collagen synthesis from M2 macrophages remains unclear.

Thus, adaptive or maladaptive remodeling of a tissue engineered implant is a complex process highly dependent on the inflammatory response and, more specifically, on macrophage polarization. In the case of TEM-based cardiovascular implants, a multitude of ECM proteins such as collagens, glycoproteins and proteoglycans are in direct contact with the circulation-derived macrophages through a

network of signaling proteins such as integrins (85). These interactions may impact the long-term remodeling outcomes of *in situ* regeneration, and will be further detailed in section “Immunoregulation of extracellular matrix proteins.”

Resident tissue macrophages

While circulation-derived macrophages originate from blood monocytes, resident tissue macrophages (RTMs) can originate from: (a) embryonic development, independent of hematopoiesis, and from (b) infiltrating monocytes that arise from bone marrow hematopoiesis in adulthood (98). Compared to circulation-derived macrophages, for RTMs from embryonic origin, primitive and transient hematopoiesis is c-Myb independent (99) (Figure 1B). In adulthood, RTMs

reside in all tissues and are responsible for tissue homeostasis and immune surveillance with distinct functions specific for each tissue's microenvironment (100). However, the exact origin of adult RTMs and the mechanisms of RTMs maintenance within the adult tissue are currently not clearly defined (101).

RTMs possess self-renewal capacity and, upon tissue injury, are rapidly activated by signals released from damaged cells (i.e., calcium, ATP, H_2O_2 , and DNA) (100). As the first responders in the wound healing cascade due to their proximity to injured tissue, activation of RTMs enables immediate pro-inflammatory cytokine release (i.e., tissue necrosis factor (TNF)- α , inducible nitric oxide synthase (iNOS), and IL-1 β), which then recruits neutrophils and monocytes (102). As soon as RTMs initiate the pro-inflammatory response, they start producing ECM in order to recover tissue integrity and provide supportive matrix for cell infiltration (102). Due to their constant interaction with ECM, RTMs play an integral role in tissue remodeling for *in situ* regeneration (88). In addition to circulation-derived macrophages, RTMs may also play a role in remodeling implanted materials. When a foreign material, like the hTEM, is implanted, RTMs may be capable of infiltrating into the implant from adjacent tissues, including the heart muscle and vascular wall. Whether RTMs promote or resolve rapid inflammation and signal adaptive tissue remodeling upon contact with TEM-based implants, still remains to be further explored in the future. In terms of TEHVs, cells are known to infiltrate the implant from the arterial wall (38). However, whether RTMs may undergo such migration has not been elucidated to this date.

The role of macrophages in cardiovascular tissue development, homeostasis, and disease, has been recently examined mostly murine models, as reviewed elsewhere (103). In regards to heart tissue, cardiac-resident macrophages play a key role in homeostasis as well as in limiting damage extension following a cardiac injury, resulting in necrotic and apoptotic cell clearance, promotion of angiogenesis and reduction of inflammation (98). In the heart valve, CD45⁺ cells identified in the leaflet were originally hypothesized to differentiate toward VICs (104). However, further analyses have identified an immune population with macrophage characteristics in these CD45⁺ cells (105, 106). In addition, adult and developing heart valves have revealed the presence of multiple immune cell populations with characteristic markers of RTMs (106–108). Similar to cardiac RTMs, valvular RTMs have a role in tissue homeostasis, and have been associated to ECM remodeling, aging, and disease (106–108). Harnessing the characterization of these cell types in native heart valves, as well as in TEHVs, would greatly improve our understanding of *in situ* regeneration and remodeling.

Although RTMs have been thoroughly investigated and characterized through lineage tracing experiments in mouse

models, their detailed function has not been elucidated for every organ system in humans (109). In humans, the functional characterization of these cells has been limited primarily because RTMs are challenging to isolate, due to the minimal number available in the tissues (109). The use of macrophage cell models is therefore currently being proposed as a solution to combat these challenges (section “*In vitro* macrophage models”).

In vitro macrophage models

Macrophage behavior *in vitro* has been investigated through a variety of cell lines isolated from human donors. Peripheral blood mononuclear cells (PBMCs) are the most accessible source of macrophages and have been studied extensively to assess the early steps of the remodeling cascade, early ECM production as well as material immunocompatibility in the cardiovascular tissue engineering field (95, 110–115); their advantages and disadvantages have been extensively reviewed elsewhere (116). However, human monocytes and monocyte-derived macrophages lack *in vitro* proliferation potential, leading to the constant need for new donor material (87). This disadvantage coupled with the inter-donor variability prompted researchers to use immortalized cell lines from a similar origin, such as leukemic immortalized monocytes THP-1 and U937 cells (87, 117) (Figure 1C). Compared to PBMCs, the high proliferation rate of these cell lines make them a practical source to study monocyte and macrophage function and differentiation, manifested by their broad *in vitro* applications for immune modulation approaches and in the cardiovascular tissue engineering field (117–119). However, there have been highlighted differences between THP-1 and PBMCs. Some suggest to limit the use of THP-1 cells when studying polarization, as THP-1 cells have a bias toward phagocytosis and the M1 phenotype (116, 120). Moreover, the malignant genetic background of these immortalized cells puts their application relevance into question. Especially as *in vivo* studies would still be required to validate any *in vitro* experiments using immortalized cell lines.

Due to RTMs paucity in tissues and limited availability of human donor materials, isolation in large numbers has been an unconquered milestone. Recently, iPSC-derived macrophages (iM ϕ s) produce c-Myb independent macrophage-like cells from yolk sac-like structures (Figure 1D) and have been proposed to accurately mimic RTM biology *in vitro* (121–124). So far, due to their plasticity and adaptation potential to environmental stimuli, tissue specific resident-like iM ϕ s such as alveolar-like, brain tissue resident-like (microglia-like), skin resident Langerhans-like, and liver resident Kupffer-like iM ϕ s have been successfully produced (123, 125, 126). However, research is still ongoing into iM ϕ s that are functionally similar to cardiovascular RTMs. The use of iM ϕ s may prove to be valuable

for *in vitro* modeling of RTMs in wound healing and remodeling processes, specifically for *in situ* regeneration approaches.

Immunoregulation of extracellular matrix proteins

The multi-step process of remodeling is not only controlled biochemically by cytokines, but also biophysically by cell-ECM interactions (76, 127). Hence, implants manufactured from decellularized ECM, such as TEMs, may actively influence immune cell (i.e., macrophages) behavior *via* integrin- or non-integrin mediated signaling.

Integrin-mediated cell-ECM interactions occur when transmembrane integrin receptors, such as focal adhesions, physically bind to different ECM components and lead to signal transduction mechanisms (2, 128, 129). These connections allow cells to perceive changes in the ECM microenvironment (e.g., composition, stiffness, and orientation), as well as to migrate through the ECM (130). TEM-based TEHV have been reported to contain ECM proteins like collagens (COLI and COLIII), FN, as well as glycosaminoglycans (64, 65), therefore having a potential role in regulating macrophage response (64, 65), which should be further investigated.

Non-integrin mediated cell-ECM interactions are observed in the presence of bioactive ECM peptides or epitopes, also known as matrikines or matricryptins, generated by ECM fragmentation (2, 131). Both matrikines and matricryptins refer to ECM peptides that are usually not exposed in intact and mature ECM fibers, but that are able to regulate cellular activity when exposed after degeneration. These ECM sites become available only after structural or conformational alterations (i.e., enzymatic degradation, self-assembly, denaturation, cell-mediated mechanical forces, and adsorption to surfaces) to the ECM proteins (132). In the field of tissue repair and regeneration, it is possible to identify these ECM transformations at the site of tissue injury, suggesting that the consequent exposure of specific ECM peptides may provide new signaling cues to regulate immune cells and tissue restoration (132). It is to be expected that these protein and relative fragments are also similarly present at the site of implantation of a tissue engineered implant, as well as they may be contained in a TEM-based valve replacement. Importantly, these molecules form a class of damage-associated molecular patterns (DAMPs) that activate immune (e.g., macrophages) and differentiated (e.g., fibroblasts) cells *via* toll-like receptor (TLR2 and TLR4) signaling (133). This alerts the immune system to tissue damage and initiates tissue repair (2, 76, 134, 135). Among the ECM peptides discovered to be capable of acting as DAMPs, there are those derived by FN, fibrinogen, versican, and heparan sulfate. Overall, these peptides engage with multiple pattern recognition receptors and initiate a pro-inflammatory response (136). As

an example, biglycan and decorin have been reported to be capable of both generating a pro-inflammatory response in macrophages by interacting with TLR2 and TLR4, as well as promoting an anti-inflammatory response critical for the resolution of inflammation (137–139). In addition, bioactive ECM fragments from the basement membrane have been identified in both healthy and diseased hearts, and associated to cardiac disease (140). An example is endostatin, one of the most investigated peptides derived from enzymatic cleavage of COLXVIII. Endostatin is mostly known for its anti-angiogenic properties, but also anti-fibrotic and anti-tumor effects, *via* the reduction of anti-inflammatory cytokine (e.g., IL-4, IL-10, IL-13, and VEGF) expression and of M2 polarization (141).

In the following sections, we will discuss what is known about the effect that ECM proteins (such as collagen and FN, that have been found in TEM-based TEHV) and ECM-derived peptides have on macrophages and their relevance for repair and remodeling mechanisms (Figure 2).

Macrophage/collagen interactions

Collagens are the most abundant proteins in the human body (142) and one of the major components of *in vitro* grown TEMs. Collagens provide structural and mechanical properties to the tissue, while also playing an important role in controlling and regulating immune cells (143). In this regard, macrophages have been shown to be key players in controlling collagen homeostasis by contributing to collagen degradation and turnover (144), but also collagen synthesis *in vitro* and *in vivo* (e.g., tissue fibrosis during heart repair) (96, 144).

The immunomodulatory effect of collagen is a consequence of the different ligands that can be recognized by immune cells [e.g., integrins, discoidin domain receptors, immunoglobulin-like receptors, and mannose receptors (88, 96)]. These interactions have been reported to increase cell adhesion and integrin expression in both innate and adaptive immune cells (145), and reduce the inflammatory response of macrophages *via* the leukocyte-associated immunoglobulin-like receptor 1 (LAIR-1 or CD305) (146, 147). In addition, macrophage migration and mechanosensing in a fibrillar collagenous matrix is controlled by $\alpha 2\beta 1$ integrin binding and stretch-activated channels, resulting in macrophage migration toward the source of a dynamic force, such as the substrate deformation caused by contractile fibroblasts in the tissue (146, 148, 149). Finally, *in vitro* studies showed that macrophage infiltration into collagen-based substrates is impacted by collagen architecture (150). Taken together, these findings suggest that collagen structure and organization in tissue engineered products, such as TEM-based TEHV, may influence adhesion, infiltration and migration of macrophages, and potentially mediating the host's inflammatory response.

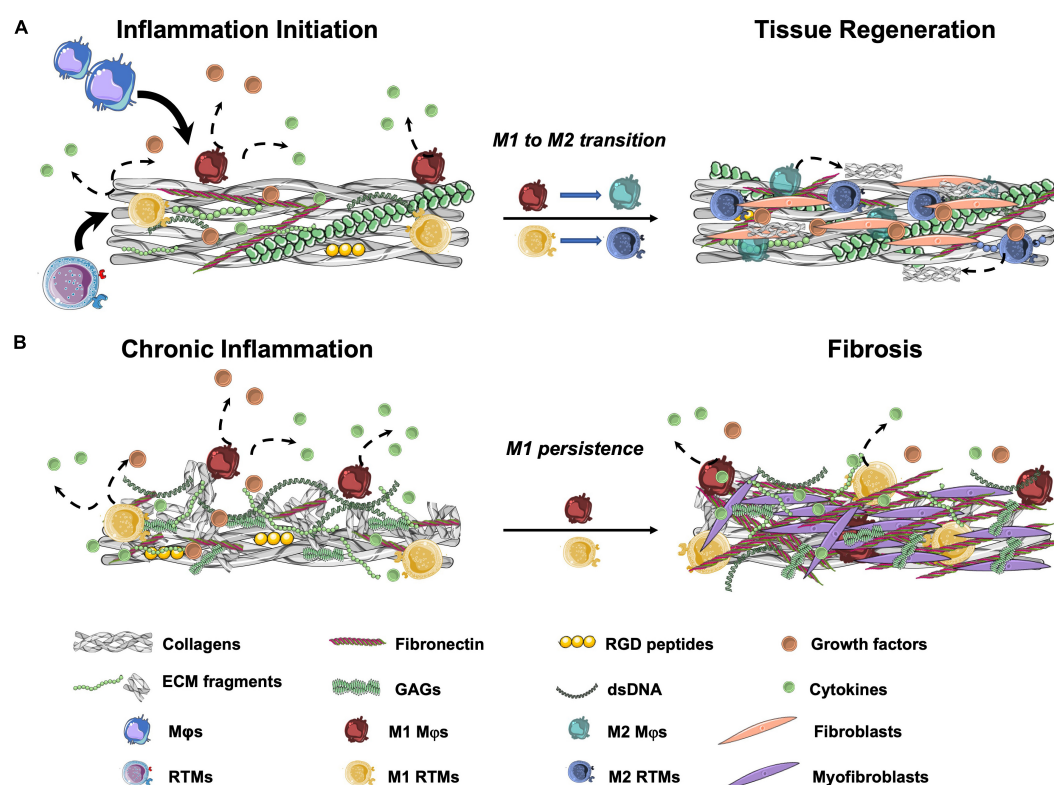


FIGURE 2

Schematic representation of wound healing outcomes after tissue injury. (A) In normal wound healing cascades, resident tissue macrophages (RTMs) and circulation-derived macrophages (Mφs) are attracted to the damaged area. When in contact with cell debris and ECM fragments, RTMs and Mφs polarize to the M1 state and produce pro-inflammatory cytokines. After the initial pro-inflammatory response, M2 polarization with progressive resolution of the inflammation occurs. Among other stromal cells, fibroblasts are recruited to site to restore tissue integrity. (B) In the presence of a high amounts of ECM fragments, peptides, cell debris and/or DNA remnants, prolonged M1 polarization with limited or absent M2 transition occurs. This results in a chronic pro-inflammatory stimulation that leads to the production of unorganized collagen-rich ECM by the activated fibroblasts (myofibroblasts) and may cause tissue fibrosis. GAGs, glycosaminoglycans; RGD, Arg-Gly-Asp.

Macrophage/fibronectin interactions

FN is a large glycoprotein that can be either present in a soluble [e.g., plasma FN (129)] or non-soluble form (e.g., cellular or tissue FN) that is produced by cells such as fibroblasts and endothelial cells (151). FN fibrils are required for the deposition of collagen and for the binding of glycosaminoglycans, thereby becoming a fundamental protein to ensure ECM remodeling during the wound healing cascade (152). FN, also one of the main ECM components of TEM-based implants, has been reported to influence the adhesion, migration, and apoptosis of monocytes and fibroblasts, among other cells (151, 153). Monocyte differentiation into macrophages was enhanced when FN-coated surfaces were used, suggesting an important role for integrin-mediated adhesion in macrophage differentiation (154, 155). FN has also demonstrated influence of macrophage polarization toward a pro-inflammatory state, characterized by increased phagocytosis activity (155, 156). In addition, the pro-inflammatory effect was further elicited in macrophages that interacted with both collagen and FN, a situation that simulates

cases of tissue damage where numerous ECM proteins are exposed or fragmented (157).

Based on these results, it is expected that TEM-based TEHV, derived by *in vitro* culture of fibroblast-like cells, have high non-soluble FN content that may therefore influence macrophage polarization toward a pro-inflammatory status. This will lead to the recruitment and activation of more immune cells and ECM-producing α SMA⁺ cells, similar to what is commonly observed in a wound healing response (81, 82). In theory, macrophages will then play a key role in attracting fibroblast-like cells to stimulate TEM-based TEHV remodeling (83).

Macrophage/extracellular matrix-derived peptide interactions

ECM-derived peptides are bioactive sites of ECM proteins such as collagens, FN, and elastin, also referred to as matrikines and matricryptins. Peptides may either be generated by

direct ECM damage (e.g., upon injury), or be exposed in immature ECM proteins (e.g., in a remodeling tissue) (2, 131). Importantly, these peptides are considered DAMP molecules that may have the potential to activate immune cells and/or stromal cells (e.g., fibroblasts) to initiate tissue repair through influencing cell migration, adhesion, and differentiation both *in vitro* and *in vivo* (2, 76, 134, 135).

RGD (Arg-Gly-Asp) is an integrin-binding peptide that results from exposed collagen, FN, vitronectin, and osteopontin proteins upon conformational changes as its active domain becomes apparent only upon substrate denaturation of collagens (158, 159), or absorption of FN and vitronectin (160). In areas of tissue injury, FN fibrils were shown to have an increased affinity for the exposed RGD sites of denatured collagens. It is hypothesized that this specific ECM composition, with abundance of exposed RGD sites as both proteins carry this sequence, is recognized by the immune system as a unique wound signal (161). Hence, it is not surprising that macrophages are affected by the presence of RGD domains, which stimulate the adhesion and M2 polarization both *in vitro* and *in vivo* (162). On the other hand, macrophage adhesion and fusion to FBGCs is supported by the presence of RGD peptides in combination with another FN-derived peptide, PHSRN (Pro-His-Ser-Arg-Asn) (163), which suggests that a combination of matricryptins—that could be found in a site of tissue injury—may be important in regulating a pro-inflammatory response. Finally, the inflammatory profile of macrophages and consequent fibrotic tissue formation could be mitigated when the RGD-binding integrins were blocked using specific antibodies (147), once again suggesting a pro-inflammatory effect of this peptide. Taken together, these results indicate a very active but controversial role of the RGD peptide in modulating macrophage response and polarization, making this peptide an interesting target for biomaterial functionalization (149).

VGVAPG (Val-Gly-Val-Ala-Pro-Gly) is an elastin-derived peptide that becomes exposed upon elastase and MMP12 digestion of elastin fibers. This peptide has repeatedly been shown to have chemotactic properties for monocytes, macrophages, and fibroblasts (164–166), and is also involved in ECM degradation *via* regulation of MMP expression (167). Specifically, the presence of elastin-derived fragments is associated with increased proliferation and decreased elastin synthesis in vascular smooth muscle cells (168). In addition, the VGVAPG peptide increased smooth muscle cell migration through the elastic lamina, thereby leading to intimal hyperplasia (168, 169). Elastin is one of the key components of vascular, valvular and heart tissue, highlighting the importance of these results for clinical translation in the cardiovascular field.

PGP (Pro-Gly-Pro) is a matricryptin derived from COL1 that plays an important role in mediating inflammation. This peptide has sequence and structural homology with one of the domains on alpha chemokines and, therefore, can mimic their chemotactic effect in inflammation models (160, 170,

171). Some bioactive ECM peptides are also involved in ECM synthesis and remodeling. Among these, the peptide GHK (Gly-His-Lys) was reported to favor wound healing and skin regeneration when combined with copper ions (Cu^{2+}), by stimulating collagen turnover, modulating MMP activity, and attracting immune cells to the wound (172).

Taken together, these studies highlight the importance of ECM and ECM-derived peptides in regulating the early steps of the inflammatory response by directly affecting macrophages (summarized in Figure 2). Because collagens and FN are among the main components of the TEM, the presence of such peptides should be carefully evaluated to better understand the intricate steps of tissue remodeling upon implantation. The possibility of using ECM proteins and fragments to favor the TEHV *in situ* remodeling potential may be an interesting strategy to influence the remodeling cascade as well as favor tissue integration and adaptive remodeling of the implant, as further discussed in section “Discussion: Relevance for *in situ* heart valve tissue engineering.”

Discussion: Relevance for *in situ* heart valve tissue engineering

The importance of ECM proteins in regulating macrophage behavior and, therefore, the consequent remodeling cascade should be considered when developing a TEHV. Macrophages are the primary mediators of host engraftment and will drive the response to the different biomaterials implanted (142), potentially deciding the fate of TEHV remodeling. Based on this, researchers are continuing to investigate ways to improve the remodeling of TEHVs with *in situ* regenerative potential.

Improving the characterization of decellularized tissue engineered matrices-based tissue engineered heart valves

Originally developed to achieve an off-the-shelf available immunocompatible product and to limit leaflet retraction observed in autologous cell-based TEHVs (173–175), decellularized TEM-based TEHVs have been developed. However, the TEM-based TEHVs have been reported to undergo adverse remodeling in chronic studies implanted in sheep, with leaflet thickening and shortening caused by fusion of the leaflet to the wall, and resulting in severe valvular insufficiency within 24 weeks after implantation (68, 73, 74). A possible explanation for this outcome was obtained by using computational modeling to simulate stress and strain distribution on the valve leaflet. Sanders et al. showed that the simplified geometry of TEM-based TEHVs led to radial leaflet

compression when subjected to physiological (pulmonary) pressure conditions (176). Based on this, further computational simulation was used to identify an improved valve geometry that could counteract the observed leaflet retraction (176). To impose this geometry, TEM-based TEHV were manufactured using a constraining bioreactor insert during tissue culture and tested in a preclinical sheep model (67). Upon implantation, the TEHV demonstrated *in vivo* performance for up to 1 year, and underwent native-like remodeling. Remarkably, no signs of adverse remodeling (i.e., leaflet thickening or leaflet-wall fusion phenomena) were observed (67). The morphological evaluation was indicative of functional native-like remodeling, with thin and shiny leaflets, complete integration within the adjacent native pulmonary artery wall, and formation of a neo-sinus. On a microscopic scale, the authors reported extensive cellular repopulation of the entire valve, improved matrix composition with elastin deposition, as well as reorganization of the collagen fibers (67). Taken together, these results indicate that valve geometry is one of the key factors in ensuring long-term TEHV function. In a subsequent study, Motta et al. investigated how the computational-inspired TEHV geometry could impact the host cell response and, therefore, tissue remodeling (177). Focused on macrophages, α SMA-positive cells, and endothelial cells as key players of the remodeling cascade, the authors found that compared to the first simple, non-physiological geometry (74), the remodeling of computational modeling-inspired TEHV having a physiological-like design had negligible amounts of macrophages and α SMA-positive cell infiltration, had the absence of thickening, and showed rapid endothelialization (177).

However, we can hypothesize that, other than TEHV geometry, also TEM composition may influence macrophage response and, therefore, the remodeling cascade, as summarized in **Figure 3**. We have previously described how ECM composition and integrity can play a role in regulating macrophage response (section “Immunoregulation of extracellular matrix proteins”). In addition, the presence of scaffold remnants may induce a foreign body response, with macrophage activation and possibly fusion to form FBGCs, as reviewed elsewhere (178). Finally, residual cellular components (i.e., DNA), may influence macrophage response and, therefore, the remodeling cascade, as detailed below.

The immunocompatibility of biomaterials made from decellularized (native or *in vitro* grown) tissues may be affected by the degree of decellularization, as the presence of cell debris may influence the immune response upon implantation. Decellularization protocols, as reviewed elsewhere (179, 180), generally aim at lysing resident cells to drastically reduce the immunogenic components of the starting tissue (i.e., DNA remnants) using a combination of chemical, physical, and enzymatic reactions, all while preserving the ECM. However, complete removal of all cellular components has not been shown so far. The presence of several antigens

and/or DAMPs released from lysed cells (e.g., calcium-binding proteins, DNA, ATP, chromatin, nuclear proteins), which has been reported to potentially cause an adverse immune response upon implantation (181). Therefore, decellularized tissues should comply with the quantitative criteria described in 2011 (182): no visible cell nuclei in H&E or DAPI staining; double stranded DNA content < 50 ng/mg of dry tissue; and DNA remnant size < 300 base pairs. It has been shown that residual cellular debris, such as DNA, mitochondria and cell membrane proteins, can promote a pro-inflammatory M1 macrophage phenotype both *in vitro* and *in vivo* (183). This is particularly striking as clinical-grade biological decellularized tissues have great variations in the amount of retained cell remnants, a parameter that may cause differences in the tissue remodeling outcome upon implantation and device efficacy (184). Indeed, the DNA amount and degree of fragmentation within decellularized tissues was reported to influence macrophage phenotype both *in vitro* and *in vivo*, with a more effective decellularization being associated with a shift from an M1 to M2-like phenotype (185, 186).

On the other hand, extensive decellularization protocols can alter the three-dimensional structure of the ECM proteins [i.e., glycoproteins, proteoglycans, fibrinogen and fibronectin domains, tenascin c, etc. (136)], thereby creating further DAMPs (187). Therefore, maintaining the integrity of ECM proteins upon decellularization is important to ensure not only sufficient mechanical properties of the tissue, but also to promote an anti-inflammatory effect (185).

Several *in vitro* studies have investigated how decellularized native tissues can modulate macrophage polarization. For example, ECM scaffolds obtained from decellularized porcine small intestine submucosa (SIS) proved to favor a M2-like macrophage phenotype, with anti-inflammatory and pro-remodeling characteristics (183, 186, 188). On the other hand, dermal tissue-derived ECM scaffolds promoted a pro-inflammatory M1-like phenotype (183). However, the cause of macrophage polarization variation on the different substrates was not clarified. Importantly, macrophage polarization is often not quantitatively apparent *in vivo* and results may differ significantly between pre-clinical and clinical data (186). In this regard, the clinical use of decellularized porcine, SIS-based or valve-based, TEHV resulted in severe adverse events for pediatric applications (47, 53). Remarkably, such an adverse effect was not observed during pre-clinical investigations in sheep models (189–192), as extensively reviewed elsewhere (18). These results suggest that decellularized xenograft-based valvular replacements may still contain α -galactose (25), a pro-inflammatory epitope that, particularly in pediatric patients, may have caused the adverse inflammatory response resulting in valve calcification and degeneration (47, 53). Therefore, independent of tissue origin, xenograft material may elicit a strong inflammatory response with detrimental consequences.

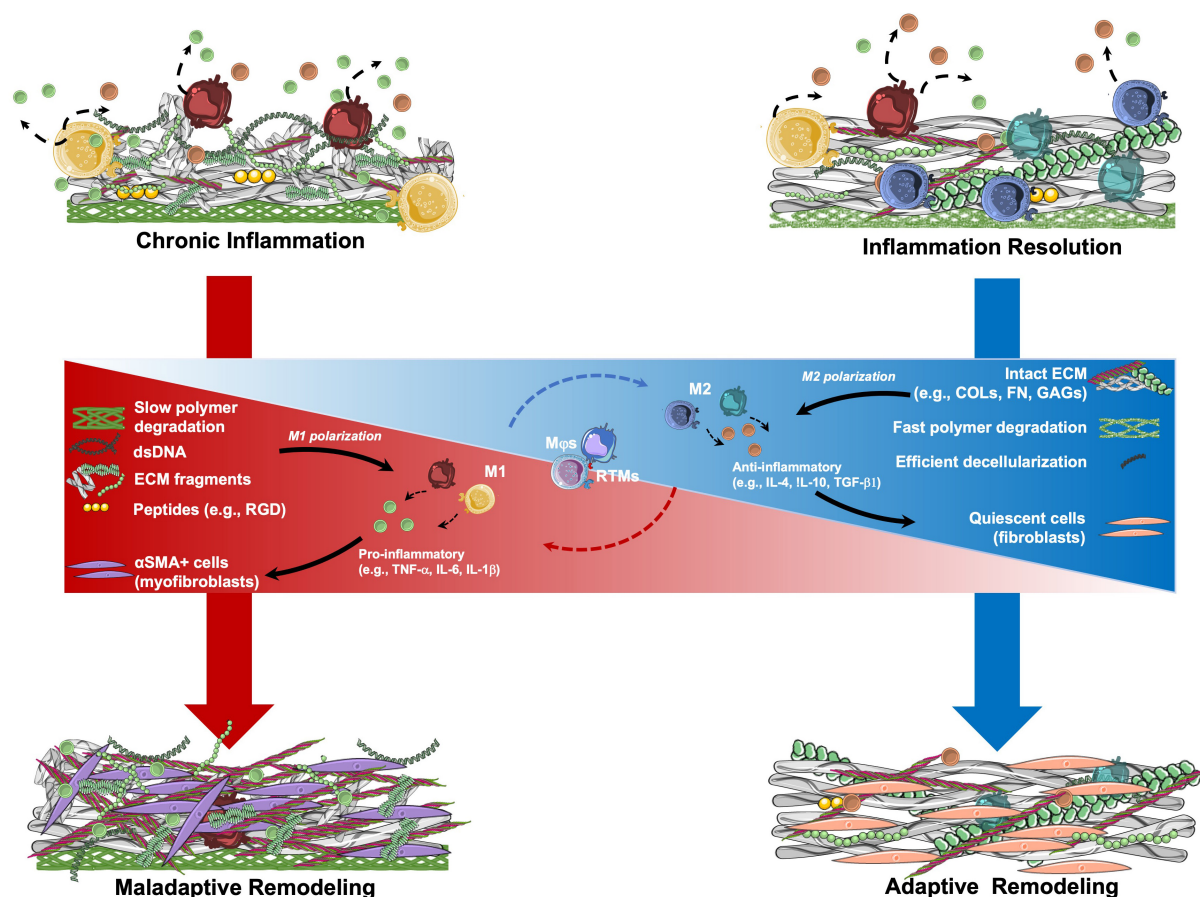


FIGURE 3

Hypothetical mechanisms involved in the remodeling of tissue engineered matrix (TEM)-based implants. TEM composition may be a crucial parameter in determining the remodeling potential of TEM-based implants. Resident tissue macrophages (RTMs) and circulation-derived macrophages (Mφs) are key mediators of the inflammatory process. Once in contact with TEMs, RTMs and Mφs may start a pro- or anti-inflammatory signaling by polarizing between M1 and M2 states, respectively. The sustained presence of polymer remnants, ECM fragments, and double stranded DNA (dsDNA) residues from incomplete decellularization, may lead to pro-inflammatory stimulation of RTMs and Mφs with consequent M1 polarization with the release of pro-inflammatory factors. This pro-inflammatory state may lead to the activation of fibroblasts into myofibroblasts, with the consequent production of a collagen-rich ECM, similarly to what is observed in tissue fibrosis (maladaptive remodeling). In contrast, TEMs having intact ECM proteins (e.g., COLs, FN, GAGs) as well as low amounts of dsDNA after optimal decellularization, may determine a short pro-inflammatory phase followed by M1 polarization resolution and transition to the M2 state. M2 RTMs and Mφs may help with provisional matrix formation. Recruited fibroblasts populate the implant and produce organized ECM until resolution of the inflammation occurs (adaptive remodeling). αSMA, alpha smooth muscle actin; COLs, collagens; FN, fibronectin; GAGs, glycosaminoglycans; IL, interleukin; RGD, Arg-Gly-Asp; TGF, transforming growth factor; TNF, tissue necrosis factor.

Taken together, these results highlight the limitations of both *in vitro* and *in vivo* preclinical models and suggest the need for an improved testing platform to assess immunocompatibility of decellularized products.

Extracellular matrix-based functionalization of bioresorbable polymeric tissue engineered heart valves

Among the different types of TEHV with *in situ* remodeling potential, polymer-based TEHV have generated considerable

interest and their clinical translation is currently ongoing with however, mixed outcomes so far, as discussed in section “*In situ* heart valve tissue engineering.” While conceptually, such materials may have multiple advantages (e.g., reasonable cost, scalability, tenability of degradation, mechanical properties and architecture), long-term safety and efficacy of this concept, especially when the initial polymer is fully resorbed, remains to be elucidated.

Nevertheless, researchers are constantly trying to improve their polymer-based scaffolds by promoting cell recruitment and endogenous tissue formation. One way to achieve this goal is to implement microstructural design features (i.e., pore size or polymer fiber orientation) to resemble native

ECM architecture of the heart valve (62, 193), as reviewed elsewhere (38). Scaffold microarchitecture can be further combined with polymer functionalization using ECM proteins and ECM-derived molecules (55, 194). It was found that non-covalent scaffold functionalization was successfully achieved by developing a hybrid polymer, which combined the durability of synthetic polymers with the biocompatibility of gelatin (55). By using a cell-free rapid jet-spinning manufacturing process, the resulting TEHV had not only mimicked the fibrous, anisotropic architecture of the native leaflet with the synthetic polymers, but also had enhanced implant biocompatibility that favored cellular attachment and infiltration with the use of gelatin. These gelatin-functionalized TEHVs have been successfully implanted in an acute sheep model, demonstrating functionality *in vitro* as well as *in vivo* (55). However, long-term comparative studies are needed to understand the benefits of gelatin functionalization may have on the remodeling potential of this hybrid TEHV.

Considering its significant role in mediating macrophage function, FN has been frequently used in biomaterial surface modification to favor implant integration and cell adhesion (142). However, the impact of FN pre-adsorption in controlling macrophage adhesion and cytokine release is often overruled by the material surface chemistry, thereby suggesting the need to better understand the macrophage response to both the material and the proteins that are immobilized on the material (195).

To date, there are no other studies where bioresorbable polymeric TEHV functionalization was evaluated in large animal models. However, in the cardiovascular field, a multitude of growth factors in combination with ECM proteins have been proposed to favor tissue integration and remodeling, as extensively reviewed elsewhere (194, 196). For example, VEGF was demonstrated to significantly inhibit the formation of calcifications in valve interstitial cells, whereas TGF β 1 stimulated calcific nodules *in vitro* (197). Remarkably, the use of FN coating proved to significantly reduce calcification formation despite TGF β 1 administration (197). These results suggest that, to limit the risk of calcifications, specific ECM proteins and growth factors, like FN and VEGF, can be combined to functionalize scaffolds for TEHV applications. Heparin and IL-4 have also been proposed to functionalize polymer. *In vitro* results showed that this functionalization effectively promoted M2 macrophage polarization and created an anti-inflammatory environment in electrospun scaffolds (112). Similarly, the use of a cytokine cocktail (i.e., IL-10 and prostaglandin-E2) was shown to promote tissue integration and to polarize macrophages into M2 pro-healing phenotype, thereby decreasing adverse immune reactions (198), suggesting a potential use of an IL-4 and IL-10 combination to improve material integration and performance.

The use of peptides to functionalize scaffolds for cardiovascular applications has been extensively reviewed elsewhere (149, 199, 200). Peptides such as RGD and REDV are mostly used to favor endothelialization of the

construct, as the sequences can be specifically recognized by the endothelial cells (199, 200). However, as discussed in section “Macrophage/extracellular matrix-derived peptide interactions,” their impact on macrophage adhesion and polarization should be further investigated. A stromal cell derived factor 1 α (SDF1 α)-derived peptide has been proposed as a potential chemokine to attract monocytes and progenitor cells and to modulate tissue remodeling. *In vitro* studies using SDF1 α -derived peptides for polymer functionalization showed reduced expression of inflammatory factors, indicating a reduction in inflammatory signaling. *In vivo* implantation of these scaffolds as rat abdominal aorta interposition grafts showed increased presence of macrophages after 7 days, thereby suggesting the potential role SDF1 α -derived peptides may have in modulating the immune response (201). However, scaffold functionalization still comes with some limitations, such as the need to ensure the functionality of the bioactive molecule included and the reduced shelf-life of the product due to diffusion of the included protein (55).

Conclusion

ECM proteins are a potent tool for the immunoregulatory function upon implantation of a tissue engineered heart valve. A multitude of studies suggest the potential role of ECM and ECM-related proteins in regulating macrophage polarization both *in vitro* and *in vivo*. However, their effect on the adaptive or maladaptive remodeling of TEM-based TEHVs should be further considered. Based on these observations, several functionalization approaches for bioresorbable polymeric TEHVs, either using ECM proteins, cytokine/growth factor cocktails, cells capable of secreting ECM-related cytokines, or ECM-derived peptides, have been evaluated both *in vitro* and *in vivo*. However, to this date, none of these approaches have reached clinical translation.

The pre-clinical use of TEM-based TEHVs for pulmonary applications has shown great potential, and their translation to aortic application is awaited. A full understanding of how ECM-based biomaterials specifically engage with the host tissue has not yet been fully elucidated. However, it is crucial to determine how the host responds to the implanted TEM-based biomaterial based on its protein composition, ECM architecture, and 3D structure, to ensure safe clinical translation. In particular, guidelines on what potential contaminants should be completely eliminated or a threshold for potential immunogenic proteins should be outlined and standardized. In addition, extensive ECM characterization of the final product, including identification of pro-inflammatory ECM components and DAMPs, should be performed. With consistent material production and comprehensive regulations on decellularized

biomaterials, TEM-based TEHV may soon become the next-generation heart valve prosthesis.

Author contributions

NP, MM, and EF drafted the manuscript. All authors reviewed the text and provided critical input to the manuscript.

Funding

This manuscript received funding through the Swiss National Science Foundation (SNSF), (Grant no. PZ00P3_180138) (MIRAvalve). EF and NP were supported by the SNSF MIRAvalve grant. ME received funding from the European Research Council (ERC) under the European Union's Horizon 2020 Research and Innovation Program (Grant no. 852814) (TAVI4Life).

References

- Werner S, Grose R. Regulation of wound healing by growth factors and cytokines. *Physiol Rev.* (2003) 83:835–70. doi: 10.1152/physrev.2003.83.3.835
- Tomlin H, Piccinini AM. A complex interplay between the extracellular matrix and the innate immune response to microbial pathogens. *Immunology.* (2018) 155:186–201. doi: 10.1111/imm.12972
- Balachandran K, Sucosky P, Yoganathan AP. Hemodynamics and mechanobiology of aortic valve inflammation and calcification. *Int J Inflamm.* (2011) 2011:1–15. doi: 10.4061/2011/263870
- Lincoln J, Lange AW, Yutzey KE. Hearts and bones: shared regulatory mechanisms in heart valve, cartilage, tendon, and bone development. *Dev Biol.* (2006) 294:292–302. doi: 10.1016/j.ydbio.2006.03.027
- Hinton RB, Yutzey KE. Heart valve structure and function in development and disease. *Annu Rev Physiol.* (2011) 73:29–46. doi: 10.1146/annurev-physiol-012110-142145
- Sacks MS, David Merryman W, Schmidt DE. On the biomechanics of heart valve function. *J Biomech.* (2009) 42:1804–24. doi: 10.1016/j.jbiomech.2009.05.015
- Hinton RB, Lincoln J, Deutsch GH, Osinska H, Manning PB, Benson DW, et al. Extracellular matrix remodeling and organization in developing and diseased aortic valves. *Circ Res.* (2006) 98:1431–8. doi: 10.1161/01.RES.0000224114.65109.4e
- Ewart AK, Morris CA, Atkinson D, Jin W, Sternes K, Spallone P, et al. Hemizygosity at the elastin locus in a developmental disorder, Williams syndrome. *Nat Genet.* (1993) 5:11–6. doi: 10.1038/ng0993-11
- Dietz HC, Cutting CR, Pyeritz RE, Maslen CL, Sakai LY, Corson GM, et al. Marfan syndrome caused by a recurrent de novo missense mutation in the fibrillin gene. *Nature.* (1991) 352:337–9. doi: 10.1038/352337a0
- Ahmad NN, Ala-Kokko L, Knowlton RG, Jimenez SA, Weaver EJ, Maguire JJ, et al. Stop codon in the procollagen II gene (COL2A1) in a family with the Stickler syndrome (arthro-ophthalmopathy). *Proc Natl Acad Sci U.S.A.* (1991) 88:6624–7. doi: 10.1073/pnas.88.15.6624
- Byers PH. Ehlers-Danlos syndrome: recent advances and current understanding of the clinical and genetic heterogeneity. *J Invest Dermatol.* (1994) 103:47S–52S. doi: 10.1111/1523-1747.ep12399038
- Lerman DA, Prasad S, Alotti N. Calcific aortic valve disease: molecular mechanisms and therapeutic approaches. *Eur Cardiol Rev.* (2015) 10:108–12. doi: 10.15420/ecr.2015.10.2.108
- Alushi B, Vathie K, Thiele H, Lauten A. Transcatheter therapies for severe tricuspid regurgitation. Quo vadis? *Herz.* (2021) 46:234–41. doi: 10.1007/s00059-020-04941-z
- Bartoli-Leonard F, Zimmer J, Aikawa E. Innate and adaptive immunity: the understudied driving force of heart valve disease. *Cardiovasc Res.* (2021) 117:2506–24. doi: 10.1093/cvr/cvab273
- Perrotta I, Russo E, Camastra C, Filice G, di Mizio G, Colosimo F, et al. New evidence for a critical role of elastin in calcification of native heart valves: immunohistochemical and ultrastructural study with literature review. *Histopathology.* (2011) 59:504–13. doi: 10.1111/j.1365-2559.2011.03977.x
- Schoen FJ. Mechanisms of function and disease of natural and replacement heart valves. *Annu Rev Pathol Mech Dis.* (2012) 7:161–83. doi: 10.1146/annurev-pathol-011110-130257
- Fanning JP, Platts DG, Walters DL, Fraser JF. Transcatheter aortic valve implantation (TAVI): valve design and evolution. *Int J Cardiol.* (2013) 168:1822–31. doi: 10.1016/j.ijcard.2013.07.117
- Fioretta ES, Motta SE, Lintas V, Loerakker S, Parker KK, Baaijens FPT, et al. Next-generation tissue-engineered heart valves with repair, remodelling and regeneration capacity. *Nat Rev Cardiol.* (2021) 18:92–116. doi: 10.1038/s41569-020-0422-8
- Russo M, Taramasso M, Guidotti A, Pozzoli A, Nietlispach F, Von Segesser L, et al. The evolution of surgical valves. *Cardiovasc Med.* (2017) 20:285–92. doi: 10.4414/cvm.2017.00532
- Cribier A, Eltchaninoff H, Bash A, Borenstein N, Tron C, Bauer F, et al. Percutaneous transcatheter implantation of an aortic valve prosthesis for calcific aortic stenosis: first human case description. *Circulation.* (2002) 106:3006–8. doi: 10.1161/01.cir.0000047200.36165.b8
- Piazza N, Bleiziffer S, Brockmann G, Hendrick R, Deutsch M-A, Opitz A, et al. Transcatheter aortic valve implantation for failing surgical aortic bioprosthetic valve. *JACC Cardiovasc Interv.* (2011) 4:721–32. doi: 10.1016/j.jcin.2011.03.016
- Yacoub MH, Takkenberg JJM. Will heart valve tissue engineering change the world? *Nat Clin Pract Cardiovasc Med.* (2005) 2:60–1. doi: 10.1038/ncpcardio0112
- Soliman Hamad MA, van Eekelen E, van Agt T, van Straten AHM. Self-management program improves anticoagulation control and quality of life: a prospective randomized study. *Eur J Cardio Thorac Surg.* (2009) 35:265–9. doi: 10.1016/j.ejcts.2008.10.020

Conflict of interest

Author SH was a shareholder at Xeltis BV and LifeMatrix AG. Author ME was a shareholder at LifeMatrix AG.

The remaining authors declare that the research was conducted in the absence of any commercial or financial relationships that could be construed as a potential conflict of interest.

Publisher's note

All claims expressed in this article are solely those of the authors and do not necessarily represent those of their affiliated organizations, or those of the publisher, the editors and the reviewers. Any product that may be evaluated in this article, or claim that may be made by its manufacturer, is not guaranteed or endorsed by the publisher.

24. Rabkin-Aikawa E, Mayer JE, Schoen FJ. Heart valve regeneration. *Adv Biochem Eng Biotechnol.* (2005) 94:141–79.
25. Choi S-Y, Jeong H-J, Lim H-G, Park S-S, Kim S-H, Kim YJ. Elimination of alpha-gal xenoreactive epitope: alpha-galactosidase treatment of porcine heart valves. *J Heart Valve Dis.* (2012) 21:387–97.
26. Leopold JA. Cellular mechanisms of aortic valve calcification. *Circ Cardiovasc Interv.* (2012) 5:605–14. doi: 10.1161/CIRCINTERVENTIONS.112.971028
27. Head SJ, Çelik M, Kappetein AP. Mechanical versus bioprosthetic aortic valve replacement. *Eur Heart J.* (2017) 38:2183–91. doi: 10.1093/eurheartj/ehx141
28. Huygens SA, Goossens LMA, Van Erkelens JA, Takkenberg JJM, Rutten-Van Mölken MPMH. How much does a heart valve implantation cost and what are the health care costs afterwards? *Open Heart.* (2018) 5:e000672. doi: 10.1136/openhrt-2017-000672
29. Cebotari S, Lichtenberg A, Tudorache I, Hilfiker A, Mertsching H, Leyh R, et al. Clinical application of tissue engineered human heart valves using autologous progenitor cells. *Circulation.* (2006) 114:132–8. doi: 10.1161/CIRCULATIONAHA.105.001065
30. Dohmen PM, Lembcke A, Holinski S, Kivelitz D, Braun JP, Pruss A, et al. Mid-term clinical results using a tissue-engineered pulmonary valve to reconstruct the right ventricular outflow tract during the ross procedure. *Ann Thorac Surg.* (2007) 84:729–36. doi: 10.1016/j.athoracsur.2007.04.072
31. Dohmen P, da Costa F. An experimental study of decellularized xenografts implanted into the aortic position with 4 months of follow up. *J Clin Exp Cardiol.* (2012) 4:2. doi: 10.4172/2155-9880.s4-004
32. Erdbrügger W, Konertz W, Dohmen PM, Posner S, Ellerbrok H, Brodde O-E, et al. Decellularized xenogenic heart valves reveal remodeling and growth potential in vivo. *Tissue Eng.* (2006) 12:2059–68. doi: 10.1089/ten.2006.12.2059
33. Bennink G, Mroczek T, Sivalingam S, Prodan Z, Herrington C, Bacha E, et al. A Novel Pulmonary Valve Homing Device – Early Feasibility Study (EFS-US) and First in Man (FIM-EU/Asia) 1&2 Year Results. *International Conference of Tissue Engineered Heart Valves.* (2020). Available online at: <https://ictev.com/abstracts/a-novel-pulmonary-valve-homing-device-early-feasibility-study-efs-us-and-first-in-man-fim-euasia-year-results> (accessed April 13, 2020).
34. US National Library of Medicine. Study to Assess Safety of the Pulmonary Valved Conduit (PV-001) in Subjects Undergoing Right Ventricular Outflow Tract Reconstruction. (2016). Available online at: <https://clinicaltrials.gov/ct2/show/NCT02700100> (accessed April 13, 2020).
35. US National Library of Medicine. Xeltis Bioabsorbable Pulmonary Valved Conduit Pivotal Study (Xplore2). (2017). Available online at: <https://clinicaltrials.gov/ct2/show/NCT03022708> (accessed April 13, 2020).
36. Wissing TB, Bonito V, Bouten CVC, Smits AIPM. Biomaterial-driven in situ cardiovascular tissue engineering—a multi-disciplinary perspective. *NPJ Regen Med.* (2017) 2:18. doi: 10.1038/s41536-017-0023-2
37. Smits AIPM, Bouten CVC. Tissue engineering meets immunoengineering: prospective on personalized in situ tissue engineering strategies. *Curr Opin Biomed Eng.* (2018) 6:17–26. doi: 10.1016/j.COBME.2018.02.006
38. de Kort BJ, Koch SE, Wissing TB, Krebber MM, Bouten CVC, Smits AIPM. Immuno-regenerative biomaterials for in situ cardiovascular tissue engineering – Do patient characteristics warrant precision engineering? *Adv Drug Deliv Rev.* (2021) 178:113960. doi: 10.1016/j.addr.2021.113960
39. Da Costa FDA, Costa ACBA, Prestes R, Domanski AC, Balbi EM, Ferreira ADA, et al. The early and midterm function of decellularized aortic valve allografts. *Ann Thorac Surg.* (2010) 90:1854–60. doi: 10.1016/j.athoracsur.2010.08.022
40. Miller DV, Edwards WD, Zehr KJ. Endothelial and smooth muscle cell populations in a decellularized cryopreserved aortic homograft (SynerGraft) 2 years after implantation. *J Thorac Cardiovasc Surg.* (2006) 132:175–6. doi: 10.1016/j.jtcvs.2006.02.038
41. Cebotari S, Tudorache I, Ciubotaru A, Boethig D, Sarikouch S, Goerler A, et al. Use of fresh decellularized allografts for pulmonary valve replacement may reduce the reoperation rate in children and young adults: early report. *Circulation.* (2011) 124:115–24. doi: 10.1161/CIRCULATIONAHA.110.012161
42. Sarikouch S, Horke A, Tudorache I, Beerbaum P, Westhoff-Bleck M, Boethig D, et al. Decellularized fresh homografts for pulmonary valve replacement: a decade of clinical experience. *Eur J Cardio Thorac Surg.* (2016) 50:281–90. doi: 10.1093/ejcts/ezw050
43. Helder MRKK, Kouchoukos NT, Zehr K, Dearani JA, Maleszewski JJ, Leduc C, et al. Late durability of decellularized allografts for aortic valve replacement: a word of caution. *J Thorac Cardiovasc Surg.* (2016) 152:1197–9. doi: 10.1016/j.jtcvs.2016.03.050
44. Konertz W, Angeli E, Tarusinov G, Christ T, Kroll J, Dohmen P, et al. Right ventricular outflow tract reconstruction with decellularized porcine xenografts in patients with congenital heart disease. *J Heart Valve Dis.* (2011) 20:341–7.
45. Sayk F, Bos I, Schubert U, Wedel T, Sievers H-H. Histopathologic findings in a novel decellularized pulmonary homograft: an autopsy study. *Ann Thorac Surg.* (2005) 79:1755–8. doi: 10.1016/j.athoracsur.2003.11.049
46. Zafar F, Hinton RB, Moore RA, Baker RS, Bryant R, Narmoneva DA, et al. Physiological growth, remodeling potential, and preserved function of a novel bioprosthetic tricuspid valve: tubular bioprosthesis made of small intestinal submucosa-derived extracellular matrix. *J Am Coll Cardiol.* (2015) 66:877–88. doi: 10.1016/j.jacc.2015.06.1091
47. Woo JS, Fishbein MC, Reemtsen B. Histologic examination of decellularized porcine intestinal submucosa extracellular matrix (CorMatrix) in pediatric congenital heart surgery. *Cardiovasc Pathol.* (2016) 25:12–7. doi: 10.1016/j.carpath.2015.08.007
48. Christ T, Paun AC, Grubitzsch H, Holinski S, Falk V, Dushe S. Long-term results after the ross procedure with the decellularized autotissue matrix P\$bioprosthesis used for pulmonary valve replacement. *Eur J Cardio Thorac Surg.* (2019) 55:885–92. doi: 10.1093/ejcts/ezy377
49. Mosala Nezhad Z, Baldin P, Poncelet A, El Khoury G. Calcific degeneration of CorMatrix 4 years after bicuspidization of unicuspid aortic valve. *Ann Thorac Surg.* (2017) 104:e431–3. doi: 10.1016/j.athoracsur.2017.07.040
50. Padalino MA, Castaldi B, Fedrigo M, Gallo M, Zucchetta F, Vida VL, et al. Porcine intestinal submucosa (CorMatrix) for semilunar valve repair in children: a word of caution after midterm results. *Semin Thorac Cardiovasc Surg.* (2016) 28:436–45. doi: 10.1053/j.semtcvs.2016.04.015
51. Hofmann M, Schmiady MO, Burkhardt BE, Dave HH, Hübner M, Kretschmar O, et al. Congenital aortic valve repair using CorMatrix\$: a histologic evaluation. *Xenotransplantation.* (2017) 24:e12341. doi: 10.1111/xen.12341
52. Zaidi AH, Nathan M, Emani S, Baird C, Del Nido PJ, Gauvreau K, et al. Preliminary experience with porcine intestinal submucosa (CorMatrix) for valve reconstruction in congenital heart disease: histologic evaluation of explanted valves. *J Thorac Cardiovasc Surg.* (2014) 148:2216–25.e1. doi: 10.1016/j.jtcvs.2014.02.081
53. Simon P, Kasimir MT, Seebacher G, Weigel G, Ullrich R, Salzer-Muhar U, et al. Early failure of the tissue engineered porcine heart valve SYNERGRAFT™ in pediatric patients. *Eur J Cardiothorac Surg.* (2003) 23:1002–6; discussion 1006. doi: 10.1016/S1010-7940(03)00094-0
54. Soliman OI, Miyazaki Y, Abdelghani M, Brugmans M, Witsenburg M, Onuma Y, et al. Midterm performance of a novel restorative pulmonary valved conduit: preclinical results. *EuroIntervention.* (2017) 13:e1418–27. doi: 10.4244/EIJ-D-17-00553
55. Capulli AK, Emmert MY, Pasqualini FS, Kehl D, Caliskan E, Lind JU, et al. JetValve: rapid manufacturing of biohybrid scaffolds for biomimetic heart valve replacement. *Biomaterials.* (2017) 133:229–41. doi: 10.1016/j.biomaterials.2017.04.033
56. Kluin J, Talacua H, Smits AIPM, Emmert MY, Brugmans MCP, Fioretta ES, et al. In situ heart valve tissue engineering using a bioresorbable elastomeric implant – From material design to 12 months follow-up in sheep. *Biomaterials.* (2017) 125:101–17. doi: 10.1016/j.biomaterials.2017.02.007
57. Miyazaki Y, Soliman O, Abdelghani M, Katsikis A, Naz C, Lopes S, et al. Acute performance of a novel restorative transcatheter aortic valve: preclinical results. *EuroIntervention.* (2017) 13:e1410–7. doi: 10.4244/EIJ-D-17-00554
58. Bennink G, Torii S, Brugmans M, Cox M, Svanidze O, Ladich E, et al. A novel restorative pulmonary valved conduit in a chronic sheep model: mid-term hemodynamic function and histologic assessment. *J Thorac Cardiovasc Surg.* (2018) 155:2591–601.e3. doi: 10.1016/j.jtcvs.2017.12.046
59. Cohan GN, D'Amore A, Matsumura Y, Pedersen DD, Luketich SK, Shanov V, et al. In vivo functional assessment of a novel degradable metal and elastomeric scaffold-based tissue engineered heart valve. *J Thorac Cardiovasc Surg.* (2019) 157:1809–16. doi: 10.1016/j.jtcvs.2018.09.128
60. Morales DL, Herrington C, Bacha EA, Morell VO, Prodan Z, Mroczek T, et al. Novel restorative pulmonary valve conduit: early outcomes of two clinical trials. *Front Cardiovasc Med.* (2021) 7:583360. doi: 10.3389/fcvm.2020.583360
61. Fioretta ES, Lintas V, Mallone A, Motta SE, von Boehmer L, Dijkman PE, et al. Differential leaflet remodeling of bone marrow cell pre-seeded versus nonseeded bioresorbable transcatheter pulmonary valve replacements. *JACC Basic Transl Sci.* (2020) 5:15–31. doi: 10.1016/j.jacbs.2019.09.008
62. Uiterwijk M, Smits AIPM, van Geemen D, van Klarenbosch B, Dekker S, Cramer MJ, et al. In situ remodeling overrules bioinspired scaffold architecture of supramolecular elastomeric tissue-engineered heart valves. *JACC Basic Transl Sci.* (2020) 5:1187–206. doi: 10.1016/j.jacbs.2020.09.011

63. De Kort BJ, Marzi J, Brauchle EM, Lichauro AM, Bauer HS, Serrero A, et al. Inflammatory and regenerative processes in bioresorbable synthetic pulmonary valves up to two years in sheep—spatiotemporal insights augmented by Raman microspectroscopy. *Acta Biomater.* (2021) 135:243–59. doi: 10.1016/j.actbio.2021.09.005
64. Lintas V, Fioretta ES, Motta SE, Dijkman PE, Pensalfini M, Mazza E, et al. Development of a novel human cell-derived tissue-engineered heart valve for transcatheter aortic valve replacement: an in vitro and in vivo feasibility study. *J Cardiovasc Transl Res.* (2018) 11:470–82. doi: 10.1007/s12265-018-9821-1
65. Motta SE, Lintas V, Fioretta ES, Dijkman PE, Putti M, Caliskan E, et al. Human cell-derived tissue-engineered heart valve with integrated valsalva sinuses: towards native-like transcatheter pulmonary valve replacements. *NPJ Regen Med.* (2019) 4:14. doi: 10.1038/s41536-019-0077-4
66. Dijkman PE, Driessen-Mol A, Frese L, Hoerstrup SP, Baaijens FPT. Decellularized homologous tissue-engineered heart valves as off-the-shelf alternatives to xeno- and homografts. *Biomaterials.* (2012) 33:4545–54. doi: 10.1016/j.biomaterials.2012.03.015
67. Emmert MY, Schmitt BA, Loerakker S, Sanders B, Spriestersbach H, Fioretta ES, et al. Computational modeling guides tissue-engineered heart valve design for long-term in vivo performance in a translational sheep model. *Sci Transl Med.* (2018) 10:eaa4587. doi: 10.1126/scitranslmed.aan4587
68. Motta SE, Fioretta ES, Dijkman PE, Lintas V, Behr L, Hoerstrup SP, et al. Development of an off-the-shelf tissue-engineered sinus valve for transcatheter pulmonary valve replacement: a proof-of-concept study. *J Cardiovasc Transl Res.* (2018) 11:182–91. doi: 10.1007/s12265-018-9800-6
69. Syedain ZH, Meier LA, Bjork JW, Lee A, Tranquillo RT. Implantable arterial grafts from human fibroblasts and fibrin using a multi-graft pulsed flow-stretch bioreactor with noninvasive strength monitoring. *Biomaterials.* (2011) 32:714–22. doi: 10.1016/j.biomaterials.2010.09.019
70. Syedain ZH, Graham ML, Dunn TB, O'Brien T, Johnson SL, Schumacher RJ, et al. A completely biological “off-the-shelf” arteriovenous graft that recellularizes in baboons. *Sci Transl Med.* (2017) 9:eaan4209. doi: 10.1126/scitranslmed.aan4209
71. Syedain Z, Reimer J, Schmidt J, Lahti M, Berry J, Bianco R, et al. 6-Month aortic valve implantation of an off-the-shelf tissue-engineered valve in sheep. *Biomaterials.* (2015) 73:175–84. doi: 10.1016/j.biomaterials.2015.09.016
72. Reimer JM, Syedain ZH, Haynie BHT, Tranquillo RT. Pediatric tubular pulmonary heart valve from decellularized engineered tissue tubes. *Biomaterials.* (2015) 62:88–94. doi: 10.1016/j.biomaterials.2015.05.009
73. Reimer J, Syedain Z, Haynie B, Lahti M, Berry J, Tranquillo R. Implantation of a tissue-engineered tubular heart valve in growing lambs. *Ann Biomed Eng.* (2017) 45:439–51. doi: 10.1007/s10439-016-1605-7
74. Driessen-Mol A, Emmert MY, Dijkman PE, Frese L, Sanders B, Weber B, et al. Transcatheter implantation of homologous “off-the-shelf” tissue-engineered heart valves with self-repair capacity: long-term functionality and rapid in vivo remodeling in sheep. *J Am Coll Cardiol.* (2014) 63:1320–9. doi: 10.1016/j.jacc.2013.09.082
75. Morris AH, Stamer DK, Kyriakides TR. The host response to naturally-derived extracellular matrix biomaterials. *Semin Immunol.* (2017) 29:72–91. doi: 10.1016/j.smim.2017.01.002
76. Barker TH. The role of ECM proteins and protein fragments in guiding cell behavior in regenerative medicine. *Biomaterials.* (2011) 32:4211–4. doi: 10.1016/j.biomaterials.2011.02.027
77. Stephens EH, Nguyen TC, Blazejewski JG, Vekilov DP, Connell JP, Itoh A, et al. Extracellular matrix remodeling in wound healing of critical size defects in the mitral valve leaflet. *Heart Vessels.* (2016) 31:1186–95. doi: 10.1007/s00380-015-0768-8
78. Han L, Gotlieb AI. Fibroblast growth factor-2 promotes in vitro heart valve interstitial cell repair through the Akt1 pathway. *Cardiovasc Pathol.* (2012) 21:382–9. doi: 10.1016/j.carpath.2011.12.001
79. Tamura K, Murakami M, Washizu M. Healing of wound sutures on the mitral valve: an experimental study. *Gen Thorac Cardiovasc Surg.* (2007) 55:98–104. doi: 10.1007/s11748-006-0085-3
80. Kao WJ. Evaluation of protein-modulated macrophage behavior on biomaterials: designing biomimetic materials for cellular engineering. *Biomaterials.* (1999) 20:2213–21. doi: 10.1016/S0142-9612(99)00152-0
81. Xia Z, Triffitt JT. A review on macrophage responses to biomaterials. *Biomed Mater.* (2006) 1:R1–9. doi: 10.1088/1748-6041/1/1/R01
82. Gurtner GC, Werner S, Barrandon Y, Longaker MT. Wound repair and regeneration. *Nature.* (2008) 453:314–21. doi: 10.1038/nature07039
83. Han L, Gotlieb AI. Fibroblast growth factor-2 promotes in vitro mitral valve interstitial cell repair through transforming growth factor- β /smad signaling. *Am J Pathol.* (2011) 178:119–27. doi: 10.1016/j.ajpath.2010.11.038
84. Liu AC, Joag VR, Gotlieb AI. The emerging role of valve interstitial cell phenotypes in regulating heart valve pathobiology. *Am J Pathol.* (2007) 171:1407–18. doi: 10.2353/ajpath.2007.070251
85. McNally AK, Anderson JM. β 1 and β 2 integrins mediate adhesion during macrophage fusion and multinucleated foreign body giant cell formation. *Am J Pathol.* (2002) 160:621–30. doi: 10.1016/S0002-9440(10)64882-1
86. Gentek R, Molawi K, Sieweke MH. Tissue macrophage identity and self-renewal. *Immunol Rev.* (2014) 262:56–73. doi: 10.1111/imr.12224
87. Lyadova I, Gerasimova T, Nenasheva T. Macrophages derived from human induced pluripotent stem cells: the diversity of protocols, future prospects, and outstanding questions. *Front Cell Dev Biol.* (2021) 9:924. doi: 10.3389/fcell.2021.640703
88. Wynn TA, Vannella KM. Macrophages in tissue repair, regeneration, and fibrosis. *Immunity.* (2016) 44:450–62. doi: 10.1016/j.immuni.2016.02.015
89. Olingy CE, San Emeterio CL, Ogle ME, Krieger JR, Bruce AC, Pfau DD, et al. Non-classical monocytes are biased progenitors of wound healing macrophages during soft tissue injury. *Sci Rep.* (2017) 7:447. doi: 10.1038/s41598-017-00477-1
90. Rayahin JE, Gemeinhart RA. Activation of macrophages in response to biomaterials. *Results Probl Cell Differ.* (2017) 62:317–51. doi: 10.1007/978-3-319-54090-0_13
91. Yao Y, Xu XH, Jin L. Macrophage polarization in physiological and pathological pregnancy. *Front Immunol.* (2019) 10:792. doi: 10.3389/fimmu.2019.00792
92. Roszer T. Understanding the mysterious M2 macrophage through activation markers and effector mechanisms. *Mediators Inflamm.* (2015) 2015:816460. doi: 10.1155/2015/816460
93. Darby IA, Zakuan N, Billet F, Desmoulière A. The myofibroblast, a key cell in normal and pathological tissue repair. *Cell Mol Life Sci.* (2016) 73:1145–57. doi: 10.1007/s00018-015-2110-0
94. Schnoor M, Cullen P, Lorkowski J, Stolle K, Robenek H, Troyer D, et al. Production of type VI collagen by human macrophages: a new dimension in macrophage functional heterogeneity. *J Immunol.* (2008) 180:5707–19. doi: 10.4049/jimmunol.180.8.5707
95. Bonito V, De Kort BJ, Bouten CVC, Smits AIPM. Cyclic strain affects macrophage cytokine secretion and extracellular matrix turnover in electrospon scaffolds. *Tissue Eng Part A.* (2019) 25:1310–25. doi: 10.1089/ten.tea.2018.0306
96. Simões FC, Cahill TJ, Kenyon A, Gavriouchkina D, Vieira JM, Sun X, et al. Macrophages directly contribute collagen to scar formation during zebrafish heart regeneration and mouse heart repair. *Nat Commun.* (2020) 11:1–17. doi: 10.1038/s41467-019-14263-2
97. O'Rourke SA, Dunne A, Monaghan MG. The role of macrophages in the infarcted myocardium: orchestrators of ECM remodeling. *Front Cardiovasc Med.* (2019) 6:101. doi: 10.3389/fcvm.2019.00101
98. Alvarez-Argote S, O'meara CC. The evolving roles of cardiac macrophages in homeostasis, regeneration, and repair. *Int J Mol Sci.* (2021) 22:7923. doi: 10.3390/ijms22157923
99. Hoeffel G, Ginhoux F. Fetal monocytes and the origins of tissue-resident macrophages. *Cell Immunol.* (2018) 330:5–15. doi: 10.1016/j.cellimm.2018.01.001
100. Minutti CM, Knipper JA, Allen JE, Zaiss DMW. Tissue-specific contribution of macrophages to wound healing. *Semin Cell Dev Biol.* (2017) 61:3–11. doi: 10.1016/j.semcdb.2016.08.006
101. Ginhoux F, Guillemin M. Tissue-resident macrophage ontogeny and homeostasis. *Immunity.* (2016) 44:439–49. doi: 10.1016/j.immuni.2016.02.024
102. Davies LC, Jenkins SJ, Allen JE, Taylor PR. Tissue-resident macrophages. *Nat Immunol.* (2013) 14:986–95. doi: 10.1038/ni.2705
103. Kim AJ, Xu N, Yutzy KE. Macrophage lineages in heart valve development and disease. *Cardiovasc Res.* (2021) 117:663–73. doi: 10.1093/CVR/CVAA062
104. Visconti RP, Ebihara Y, LaRue AC, Fleming PA, McQuinn TC, Masuya M, et al. An in vivo analysis of hematopoietic stem cell potential: hematopoietic origin of cardiac valve interstitial cells. *Circ Res.* (2006) 98:690–6. doi: 10.1161/01.RES.0000207384.81818.D4
105. Hulin A, Anstine LJ, Kim AJ, Potter SJ, DeFalco T, Lincoln J, et al. Macrophage transitions in heart valve development and myxomatous valve disease. *Arterioscler Thromb Vasc Biol.* (2018) 38:636–44. doi: 10.1161/ATVBAHA.117.310667
106. Hulin A, Hortells L, Gomez-Stallons MV, O'Donnell A, Chetal K, Adam M, et al. Maturation of heart valve cell populations during postnatal remodeling. *Development.* (2019) 146:dev173047. doi: 10.1242/DEV.173047
107. Anstine LJ, Horne TE, Horwitz EM, Lincoln J. Contribution of extra-cardiac cells in murine heart valves is age-dependent. *J Am Heart Assoc.* (2017) 6:e007097. doi: 10.1161/JAHA.117.007097

108. Shigeta A, Huang V, Zuo J, Besada R, Nakashima Y, Lu Y, et al. Endocardially derived macrophages are essential for valvular remodeling. *Dev Cell*. (2019) 48:617–30.e3. doi: 10.1016/j.devcel.2019.01.021
109. Wang X, Li Y, Feng Y, Cheng H, Li D. The role of macrophages in osseointegration of dental implants: an experimental study in vivo. *J Biomed Mater Res Part A*. (2020) 108:2206–16. doi: 10.1002/jbm.a.36978
110. Smits AIPM, Ballotta V, Driessen-Mol A, Bouten CVC, Baaijens FPT. Shear flow affects selective monocyte recruitment into MCP-1-loaded scaffolds. *J Cell Mol Med*. (2014) 18:2176–88. doi: 10.1111/jcmm.12330
111. Ballotta V, Smits AIPM, Driessen-Mol A, Bouten CVC, Baaijens FPT. Synergistic protein secretion by mesenchymal stromal cells seeded in 3D scaffolds and circulating leukocytes in physiological flow. *Biomaterials*. (2014) 35:9100–13. doi: 10.1016/j.biomaterials.2014.07.042
112. Bonito V, Smits AIPM, Goor OJGM, Ippel BD, Driessen-Mol A, Munker TJAG, et al. Modulation of macrophage phenotype and protein secretion via heparin-IL-4 functionalized supramolecular elastomers. *Acta Biomater*. (2018) 71:247–60. doi: 10.1016/j.actbio.2018.02.032
113. Battiston KG, Labow RS, Simmons CA, Santerre JP. Immunomodulatory polymeric scaffold enhances extracellular matrix production in cell co-cultures under dynamic mechanical stimulation. *Acta Biomater*. (2015) 24:74–86. doi: 10.1016/j.actbio.2015.05.038
114. Zhang X, Simmons CA, Paul Santerre J. Paracrine signalling from monocytes enables desirable extracellular matrix accumulation and temporally appropriate phenotype of vascular smooth muscle cell-like cells derived from adipose stromal cells. *Acta Biomater*. (2020) 103:129–41. doi: 10.1016/j.actbio.2019.12.006
115. Shrestha S, McFadden MJ, Gramolini AO, Santerre JP. Proteome analysis of secretions from human monocyte-derived macrophages post-exposure to biomaterials and the effect of secretions on cardiac fibroblast fibrotic character. *Acta Biomater*. (2020) 111:80–90. doi: 10.1016/j.actbio.2020.04.042
116. Bosshart H, Heinzelmann M. THP-1 cells as a model for human monocytes. *Ann Transl Med*. (2016) 4:4–7. doi: 10.21037/atm.2016.08.53
117. Chanput W, Mes JJ, Wichers HJ. THP-1 cell line: an in vitro cell model for immune modulation approach. *Int Immunopharmacol*. (2014) 23:37–45. doi: 10.1016/j.intimp.2014.08.002
118. Wissing TB, Van Haaften EE, Koch SE, Ippel BD, Kurniawan NA, Bouten CVC, et al. Hemodynamic loads distinctively impact the secretory profile of biomaterial-activated macrophages-implications for in situ vascular tissue engineering. *Biomater Sci*. (2020) 8:132–47. doi: 10.1039/c9bm01005j
119. Wissing TB, Bonito V, van Haaften EE, van Doeselaar M, Brugmans MM, Janssen HM, et al. Macrophage-driven biomaterial degradation depends on scaffold microarchitecture. *Front Bioeng Biotechnol*. (2019) 7:87. doi: 10.3389/fbioe.2019.00087
120. Shiratori H, Feinweber C, Luckhardt S, Linke B, Resch E, Geisslinger G, et al. THP-1 and human peripheral blood mononuclear cell-derived macrophages differ in their capacity to polarize in vitro. *Mol Immunol*. (2017) 88:58–68. doi: 10.1016/j.molimm.2017.05.027
121. Buchrieser J, James W, Moore MD. Human induced pluripotent stem cell-derived macrophages share ontogeny with MYB-independent tissue-resident macrophages. *Stem Cell Rep*. (2017) 8:334–45. doi: 10.1016/j.stemcr.2016.12.020
122. Takata K, Kozaki T, Lee CZW, Thion MS, Otsuka M, Lim S, et al. Induced-pluripotent-stem-cell-derived primitive macrophages provide a platform for modeling tissue-resident macrophage differentiation and function. *Immunity*. (2017) 47:183–98.e6. doi: 10.1016/j.immuni.2017.06.017
123. Lee CZW, Kozaki T, Ginhoux F. Studying tissue macrophages in vitro: are iPSC-derived cells the answer? *Nat Rev Immunol*. (2018) 18:716–25. doi: 10.1038/s41577-018-0054-y
124. Tasnim F, Xing J, Huang X, Mo S, Wei X, Tan MH, et al. Generation of mature kupffer cells from human induced pluripotent stem cells. *Biomaterials*. (2019) 192:377–91. doi: 10.1016/j.biomaterials.2018.11.016
125. Xu R, Li X, Boreland AJ, Posyton A, Kwan K, Hart RP, et al. Human iPSC-derived mature microglia retain their identity and functionally integrate in the chimeric mouse brain. *Nat Commun*. (2020) 11:1–16. doi: 10.1038/s41467-020-15411-9
126. Mucci A, Lopez-Rodriguez E, Hetzel M, Liu S, Suzuki T, Happel C, et al. iPSC-derived macrophages effectively treat pulmonary alveolar proteinosis in Csf2rb-deficient mice. *Stem Cell Rep*. (2018) 11:696–710. doi: 10.1016/j.stemcr.2018.07.006
127. Eckes B, Nischt R, Krieg T. Cell-matrix interactions in dermal repair and scarring. *Fibrogenes Tissue Repair*. (2010) 3:4. doi: 10.1186/1755-1536-3-4
128. Burridge K, Fath K, Kelly T, Nuckolls G, Turner C. Focal adhesions: transmembrane junctions between the extracellular matrix and the cytoskeleton. *Annu Rev Cell Biol*. (1988) 4:487–525. doi: 10.1146/annurev.cb.04.110188.02415
129. Yamada KM, Gailit J, Clark RAF. Integrins in wound repair. In: Clark RAF, editor. *The Molecular and Cellular Biology of Wound Repair*. Boston, MA: Springer (1988). doi: 10.1007/978-1-4899-0185-9_9
130. Chester D, Brown AC. The role of biophysical properties of provisional matrix proteins in wound repair. *Matrix Biol*. (2017) 60–1:124–40. doi: 10.1016/j.matbio.2016.08.004
131. Simon T, Bromberg JS. Regulation of the immune system by laminins. *Trends Immunol*. (2017) 38:858–71. doi: 10.1016/j.it.2017.06.002
132. Davis GE, Bayless KJ, Davis MJ, Meininger GA. Regulation of tissue injury responses by the exposure of matricryptic sites within extracellular matrix molecules. *Am J Pathol*. (2000) 156:1489–98. doi: 10.1016/S0002-9440(10)65020-1
133. McQuitty CE, Williams R, Chokshi S, Urbani L. Immunomodulatory role of the extracellular matrix within the liver disease microenvironment. *Front Immunol*. (2020) 11:574276. doi: 10.3389/fimmu.2020.574276
134. Chen GY, Nuñez G. Sterile inflammation: sensing and reacting to damage. *Nat Rev Immunol*. (2010) 10:826–37. doi: 10.1038/nri2873
135. Adair-Kirk TL, Senior RM. Fragments of extracellular matrix as mediators of inflammation. *Int J Biochem Cell Biol*. (2008) 40:1101–10. doi: 10.1016/j.biocel.2007.12.005
136. Frevert CW, Felgenhauer J, Wygrecka M, Nastase MV, Schaefer L. Danger-associated molecular patterns derived from the extracellular matrix provide temporal control of innate immunity. *J Histochem Cytochem*. (2018) 66:213–27. doi: 10.1369/0022155417740880
137. Schaefer L, Babelova A, Kiss E, Hausser HJ, Baliova M, Krzyzankova M, et al. The matrix component biglycan is proinflammatory and signals through toll-like receptors 4 and 2 in macrophages. *J Clin Invest*. (2005) 115:2223–33. doi: 10.1172/JCI23755
138. Merline R, Moreth K, Beckmann J, Nastase MV, Zeng-Brouwers J, Tralhão JG, et al. Signaling by the matrix proteoglycan decorin controls inflammation and cancer through PDCD4 and microRNA-21. *Sci Signal*. (2011) 4:ra75. doi: 10.1126/scisignal.2001868
139. Hsieh LTH, Frey H, Nastase MV, Tredup C, Hoffmann A, Poluzzi C, et al. Bimodal role of NADPH oxidases in the regulation of biglycan-triggered IL-1 β synthesis. *Matrix Biol*. (2016) 49:61–81. doi: 10.1016/j.matbio.2015.12.005
140. Okada M, Imoto K, Sugiyama A, Yasuda J, Yamawaki H. New insights into the role of basement membrane-derived matricryptins in the heart. *Biol Pharm Bull*. (2017) 40:2050–60. doi: 10.1248/bpb.b17-00308
141. Foguer K, de Braga MS, Peron JPS, Bortoluci KR, Bellini MH. Endostatin gene therapy inhibits intratumoral macrophage M2 polarization. *Biomed Pharmacother*. (2016) 79:102–11. doi: 10.1016/j.biopha.2016.01.035
142. Schmidt DR, Kao WJ. The interrelated role of fibronectin and interleukin-1 in biomaterial-modulated macrophage function. *Biomaterials*. (2007) 28:371–82. doi: 10.1016/j.biomaterials.2006.08.041
143. Gelse K, Pöschl E, Aigner T. Collagens – Structure, function, and biosynthesis. *Adv Drug Deliv Rev*. (2003) 55:1531–46. doi: 10.1016/j.addr.2003.08.002
144. Madsen DH, Leonard D, Masedunskas A, Moyer A, Jürgensen HJ, Peters DE, et al. M2-like macrophages are responsible for collagen degradation through a mannose receptor-mediated pathway. *J Cell Biol*. (2013) 202:951–66. doi: 10.1083/jcb.201301081
145. Boraschi-Diaz I, Wang J, Mort JS, Komarova SV. Collagen type I as a ligand for receptor-mediated signaling. *Front Phys*. (2017) 5:12. doi: 10.3389/fphys.2017.00012
146. Rowley AT, Meli VS, Wu-Woods NJ, Chen EY, Liu WF, Wang S-W. Effects of surface-bound collagen-mimetic peptides on macrophage uptake and immunomodulation. *Front Bioeng Biotechnol*. (2020) 8:747. doi: 10.3389/fbioe.2020.00747
147. Zaveri TD, Lewis JS, Dolgova NV, Clare-Salzler MJ, Keselowsky BG. Integrin-directed modulation of macrophage responses to biomaterials. *Biomaterials*. (2014) 35:3504–15. doi: 10.1016/j.biomaterials.2014.01.007
148. Meyard L. LAIR and collagens in immune regulation. *Immunol Lett*. (2010) 128:26–8. doi: 10.1016/j.imlet.2009.09.014
149. Rowley AT, Nagalla RR, Wang S, Liu WF. Extracellular matrix-based strategies for immunomodulatory biomaterials engineering. *Adv Healthc Mater*. (2019) 8:1801578. doi: 10.1002/adhm.201801578
150. Pakshir P, Alizadehgiashi M, Wong B, Coelho NM, Chen X, Gong Z, et al. Dynamic fibroblast contractions attract remote macrophages in fibrillar collagen matrix. *Nat Commun*. (2019) 10:1–17. doi: 10.1038/s41467-019-09709-6

151. Lenselink EA. Role of fibronectin in normal wound healing. *Int Wound J.* (2015) 12:313–6. doi: 10.1111/iwj.12109
152. Barker TH, Engler AJ. The provisional matrix: setting the stage for tissue repair outcomes. *Matrix Biol.* (2017) 60–1:1–4. doi: 10.1016/j.matbio.2017.04.003
153. Grinnell F. Fibronectin and wound healing. *J Cell Biochem.* (1984) 26:107–16. doi: 10.1002/jcb.240260206
154. Majumdar S, Kraft ML. Exploring the maturation of a monocytic cell line using self-organizing maps of single-cell Raman spectra. *Biointerphases.* (2020) 15:041010. doi: 10.1116/6.0000363
155. Fei D, Meng X, Yu W, Yang S, Song N, Cao Y, et al. Fibronectin (FN) cooperated with TLR2/TLR4 receptor to promote innate immune responses of macrophages via binding to integrin $\beta 1$. *Virulence.* (2018) 9:1588–600. doi: 10.1080/21505594.2018.1528841
156. Maclel J, Oliveira MI, Goncalves RM, Barbosa MA. The effect of adsorbed fibronectin and osteopontin on macrophage adhesion and morphology on hydrophilic and hydrophobic model surfaces. *Acta Biomater.* (2012) 8:3669–77. doi: 10.1016/j.actbio.2012.06.010
157. Digiaco G, Tusa I, Bacci M, Cipolleschi MG, Dello Sbarba P, Rovida E. Fibronectin induces macrophage migration through a SFK-FAK/CSF-1R pathway. *Cell Adhes Migr.* (2017) 11:327–37. doi: 10.1080/19336918.2016.1221566
158. Seiffert D, Smith JW. The cell adhesion domain in plasma vitronectin is cryptic. *J Biol Chem.* (1997) 272:13705–10. doi: 10.1074/jbc.272.21.13705
159. Ugarova TP, Zamarron C, Plow EF, Veklich Y, Weisel JW, Bowditch RD, et al. Conformational transitions in the cell binding domain of fibronectin. *Biochemistry.* (1995) 34:4457–66. doi: 10.1021/bi00013a039
160. Ricard-Blum S, Ballut L. Matricryptins derived from collagens and proteoglycans. *Front Biosci.* (2011) 16:674–97. doi: 10.2741/3712
161. Davis GE. Affinity of integrins for damaged extracellular matrix: $\alpha v \beta 3$ binds to denatured collagen type I through RGD sites. *Biochem Biophys Res Commun.* (1992) 182:1025–31. doi: 10.1016/0006-291X(92)91834-D
162. Kang H, Yang B, Zhang K, Pan Q, Yuan W, Li G, et al. Immunoregulation of macrophages by dynamic ligand presentation via ligand–cation coordination. *Nat Commun.* (2019) 10:1696. doi: 10.1038/s41467-019-09733-6
163. Kao WJ, Lee D. In vivo modulation of host response and macrophage behavior by polymer networks grafted with fibronectin-derived biomimetic oligopeptides: the role of RGD and PHSRN domains. *Biomaterials.* (2001) 22:2901–9. doi: 10.1016/S0142-9612(01)00037-0
164. Bisaccia F, Morelli MAC, de Biasi M, Traniello S, Spisani S, Tamburro AM. Migration of monocytes in the presence of elastolytic fragments of elastin and in synthetic derivatives structure-activity relationships. *Int J Pept Protein Res.* (1994) 44:332–41. doi: 10.1111/j.1399-3011.1994.tb01017.x
165. Senior RM, Griffin GL, Mecham RP, Wrenn DS, Prasad KU, Urry DW. Val-Gly-Val-Ala-Pro-Gly, a repeating peptide in elastin, is chemotactic for fibroblasts and monocytes. *J Cell Biol.* (1984) 99:870–4. doi: 10.1083/jcb.99.3.870
166. Hunninghake GW, Davidson JM, Rennard S, Szapiel S, Gadek JE, Crystal RG. Elastin fragments attract macrophage precursors to diseased sites in pulmonary emphysema. *Science.* (1981) 212:925–7. doi: 10.1126/SCIENCE.7233186
167. Maquart FX, Bellon G, Pasco S, Monboisse JC. Matrikines in the regulation of extracellular matrix degradation. *Biochimie.* (2005) 87:353–60. doi: 10.1016/j.biochi.2004.10.006
168. Wells SM, Sellaro T, Sacks MS. Cyclic loading response of bioprosthetic heart valves?: effects of fixation stress state on the collagen fiber architecture. *Biomaterials.* (2005) 26:2611–9. doi: 10.1016/j.biomaterials.2004.06.046
169. Hinek A, Boyle J, Rabinovitch M. Vascular smooth muscle cell detachment from elastin and migration through elastic laminae is promoted by chondroitin sulfate-induced “shedding” of the 67-kDa cell surface elastin binding protein. *Exp Cell Res.* (1992) 203:344–53. doi: 10.1016/0014-4827(92)90008-V
170. Sorokin L. The impact of the extracellular matrix on inflammation. *Nat Rev Immunol.* (2010) 10:712–23. doi: 10.1038/nri2852
171. Weathington NM, Van Houwelingen AH, Noerager BD, Jackson PL, Kraneveld AD, Galin FS, et al. A novel peptide CXCR ligand derived from extracellular matrix degradation during airway inflammation. *Nat Med.* (2006) 12:317–23. doi: 10.1038/nm1361
172. Pickart L, Vasquez-Soltero JM, Margolina A. GHK peptide as a natural modulator of multiple cellular pathways in skin regeneration. *Biomed Res Int.* (2015) 2015:648108. doi: 10.1155/2015/648108
173. Flanagan TC, Sachweh JS, Frese J, Schnöring H, Gronloh N, Koch S, et al. In vivo remodeling and structural characterization of fibrin-based tissue-engineered heart valves in the adult sheep model. *Tissue Eng Part A.* (2009) 15:2965–76. doi: 10.1089/ten.tea.2009.0018
174. Gottlieb D, Kunal T, Emami S, Aikawa E, Brown DW, Powell AJ, et al. In vivo monitoring of function of autologous engineered pulmonary valve. *J Thorac Cardiovasc Surg.* (2010) 139:723–31. doi: 10.1016/j.jtcvs.2009.11.006
175. Schmidt D, Dijkman PE, Driessen-Mol A, Stenger R, Mariani C, Puolakka A, et al. Minimally-invasive implantation of living tissue engineered heart valves. *J Am Coll Cardiol.* (2010) 56:510–20. doi: 10.1016/j.jacc.2010.04.024
176. Sanders B, Loerakker S, Fioretta ES, Bax DJp, Driessen-Mol A, Hoerstrup SP, et al. Improved geometry of decellularized tissue engineered heart valves to prevent leaflet retraction. *Ann Biomed Eng.* (2016) 44:1061–71. doi: 10.1007/s10439-015-1386-4
177. Motta SE, Fioretta ES, Lintas V, Dijkman PE, Hilbe M, Frese L, et al. Geometry influences inflammatory host cell response and remodeling in tissue-engineered heart valves in-vivo. *Sci Rep.* (2020) 10:1–14. doi: 10.1038/s41598-020-76322-9
178. Moore LB, Kyriakides TR. Molecular characterization of macrophage-biomaterial interactions. *Adv Exp Med Biol.* (2015) 865:109–22. doi: 10.1007/978-3-319-18603-0_7
179. Choudhury D, Yee M, Sheng ZLJ, Amirul A, Naing MW. Decellularization systems and devices: state-of-the-art. *Acta Biomater.* (2020) 115:51–9. doi: 10.1016/j.actbio.2020.07.060
180. Behmer Hansen RA, Wang X, Kaw G, Pierre V, Senyo SE. Accounting for material changes in decellularized tissue with underutilized methodologies. *Biomed Res Int.* (2021) 2021:6696295. doi: 10.1155/2021/6696295
181. Aamodt JM, Grainger DW. Extracellular matrix-based biomaterial scaffolds and the host response. *Biomaterials.* (2016) 86:68–82. doi: 10.1016/j.biomaterials.2016.02.003
182. Crapo PM, Gilbert TW, Badyak SF. An overview of tissue and whole organ decellularization processes. *Biomaterials.* (2011) 32:3233–43. doi: 10.1016/j.biomaterials.2011.01.057
183. Dziki JL, Wang DS, Pineda C, Sicari BM, Rausch T, Badyak SF. Solubilized extracellular matrix bioscaffolds derived from diverse source tissues differentially influence macrophage phenotype. *J Biomed Mater Res Part A.* (2017) 105:138–47. doi: 10.1002/jbm.a.35894
184. Londono R, Dziki JL, Haljasmaa E, Turner NJ, Leifer CA, Badyak SF. The effect of cell debris within biologic scaffolds upon the macrophage response. *J Biomed Mater Res Part A.* (2017) 105:2109–18. doi: 10.1002/jbm.a.36055
185. Petrosyan A, Da Sacco S, Tripuraneni N, Kreuser U, Lavarreda-Pearce M, Tamburrini R, et al. A step towards clinical application of acellular matrix: a clue from macrophage polarization. *Matrix Biol.* (2017) 57–58:334–46. doi: 10.1016/j.matbio.2016.08.009
186. Keane TJ, Londono R, Turner NJ, Badyak SF. Consequences of ineffective decellularization of biologic scaffolds on the host response. *Biomaterials.* (2012) 33:1771–81. doi: 10.1016/j.biomaterials.2011.10.054
187. Ground M, Waqanivalagi S, Walker R, Milsom P, Cornish J. Models of immunogenicity in preclinical assessment of tissue engineered heart valves. *Acta Biomater.* (2021) 133:102–13. doi: 10.1016/j.actbio.2021.05.049
188. Bm S, Ji D, Bf S, Cj M, Cl D, Sf B. The promotion of a constructive macrophage phenotype by solubilized extracellular matrix. *Biomaterials.* (2014) 35:8605–12. doi: 10.1016/J.BIOMATERIALS.2014.06.060
189. Dohmen PM, Da Costa F, Lopes SV, Yoshi S, Da Souza FP, Vilani R, et al. Results of a decellularized porcine heart valve implanted into the juvenile sheep model. *Heart Surg Forum.* (2005) 8:72–6. doi: 10.1532/HSF98.20041140
190. Iwai S, Torikai K, Coppin CM, Sawa Y. Minimally immunogenic decellularized porcine valve provides in situ recellularization as a stentless bioprosthetic valve. *J Artif Organs.* (2007) 10:29–35. doi: 10.1007/s10047-006-0360-1
191. Leyh RG, Wilhelmi M, Walles T, Kallenbach K, Rebe P, Oberbeck A, et al. A cellularized porcine heart valve scaffolds for heart valve tissue engineering and the risk of cross-species transmission of porcine endogenous retrovirus. *J Thorac Cardiovasc Surg.* (2003) 126:1000–4. doi: 10.1016/S0022-5223(03)00353-2
192. Goecke T, Theodoridis K, Tudorache I, Ciubotaru A, Cebotari S, Ramm R, et al. In vivo performance of freeze-dried decellularized pulmonary heart valve allo- and xenografts orthotopically implanted into juvenile sheep. *Acta Biomater.* (2018) 68:41–52. doi: 10.1016/j.actbio.2017.11.041
193. D'Amore A, Luketich SK, Raffa GM, Olia S, Menallo G, Mazzola A, et al. Heart valve scaffold fabrication: bioinspired control of macro-scale morphology, mechanics and micro-structure. *Biomaterials.* (2018) 150:25–37. doi: 10.1016/j.biomaterials.2017.10.011
194. Tallawi M, Rosellini E, Barbani N, Cascone MG, Rai R, Saint-Pierre G, et al. Strategies for the chemical and biological functionalization of scaffolds for cardiac tissue engineering: a review. *J R Soc Interface.* (2015) 12:20150254. doi: 10.1098/rsif.2015.0254

195. Bonfield TL, Colton E, Marchant RE, Anderson JM. Cytokine and growth factor production by monocytes/macrophages on protein preadsorbed polymers. *J Biomed Mater Res.* (1992) 26:837–50. doi: 10.1002/jbm.820260702
196. Rossi F, Van Griensven M. Polymer functionalization as a powerful tool to improve scaffold performances. *Tissue Eng Part A.* (2014) 20:2043–51. doi: 10.1089/ten.tea.2013.0367
197. Gwanmesia P, Ziegler H, Eurich R, Barth M, Kamiya H, Karck M, et al. Opposite effects of transforming growth factor- β 1 and vascular endothelial growth factor on the degeneration of aortic valvular interstitial cell are modified by the extracellular matrix protein fibronectin: implications for heart valve engineering. *Tissue Eng Part A.* (2010) 16:3737–46. doi: 10.1089/ten.tea.2010.0304
198. Barthes J, Lagarrigue P, Riabov V, Lutzweiler G, Kirsch J, Muller C, et al. Biofunctionalization of 3D-printed silicone implants with immunomodulatory hydrogels for controlling the innate immune response: an in vivo model of tracheal defect repair. *Biomaterials.* (2021) 268:120549. doi: 10.1016/j.biomaterials.2020.120549
199. Fioretta ES, Fledderus JO, Burakowska-Meise EA, Baaijens FPT, Verhaar MC, Bouten CVC. Polymer-based Scaffold designs for in situ vascular tissue engineering: controlling recruitment and differentiation behavior of endothelial colony forming cells. *Macromol Biosci.* (2012) 12:577–90. doi: 10.1002/mabi.201100315
200. Ren X, Feng Y, Guo J, Wang H, Li Q, Yang J, et al. Surface modification and endothelialization of biomaterials as potential scaffolds for vascular tissue engineering applications. *Chem Soc Rev.* (2015) 44:5680–742. doi: 10.1039/c4cs00483c
201. Muylaert DEP, van Almen GC, Talacua H, Fledderus JO, Kluin J, Hendrikse SIS, et al. Early in-situ cellularization of a supramolecular vascular graft is modified by synthetic stromal cell-derived factor-1 α derived peptides. *Biomaterials.* (2016) 76:187–95. doi: 10.1016/j.biomaterials.2015.10.052

Frontiers in Cardiovascular Medicine

Innovations and improvements in cardiovascular treatment and practice

Focuses on research that challenges the status quo of cardiovascular care, or facilitates the translation of advances into new therapies and diagnostic tools.

Discover the latest Research Topics

[See more →](#)

Frontiers

Avenue du Tribunal-Fédéral 34
1005 Lausanne, Switzerland
frontiersin.org

Contact us

+41 (0)21 510 17 00
frontiersin.org/about/contact



Frontiers in Cardiovascular Medicine

